Paving Materials and Pavement Analysis

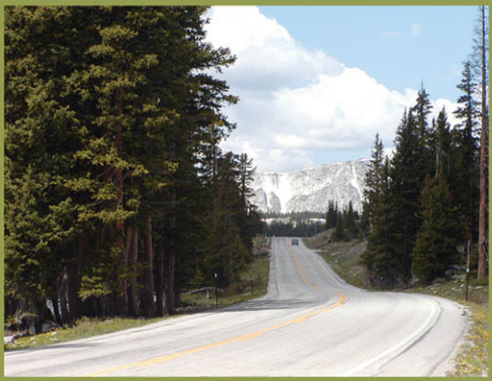

Geotechnical Special Publication No. 203

Edited by

Baoshan Huang
Erol Tutumluer
Imad L. Al-Qadi
Jorge Prozzi
Xiang Shu

ASCE

G-I
ASCE
GEO-INSTITUTE

GEOTECHNICAL SPECIAL PUBLICATION NO. 203

PAVING MATERIALS AND PAVEMENT ANALYSIS

PROCEEDINGS OF SESSIONS OF GEOSHANGHAI 2010

June 3–5, 2010
Shanghai, China

HOSTED BY
Tongji University
Shanghai Society of Civil Engineering, China
Chinese Institution of Soil Mechanics and Geotechnical Engineering, China

IN COOPERATION WITH
Alaska University Transportation Center, USA
ASCE Geo-Institute, USA
Deep Foundation Institute, USA
East China Architectural Design & Research Institute Company, China
Georgia Institute of Technology, USA
Nagoya Institute of Technology, Japan
Transportation Research Board (TRB), USA
The University of Newcastle, Australia
The University of Illinois at Urbana-Champaign, USA
The University of Kansas, USA
The University of Tennessee, USA
Vienna University of Natural Resources and Applied Life Sciences, Austria

EDITED BY
Baoshan Huang
Erol Tutumluer
Imad L. Al-Qadi
Jorge Prozzi
Xiang Shu

Published by the American Society of Civil Engineers

Library of Congress Cataloging-in-Publication Data

GeoShanghai International Conference (2010)
Paving materials and pavement analysis : proceedings of the GeoShanghai 2010 International Conference, June 3-5, 2010, Shanghai, China / edited by Baoshan Huang … [et al.].
p. cm. -- (Geotechnical special publication ; 203)
Includes bibliographical references and index.
ISBN 978-0-7844-1104-9
1. Pavements--Congresses. 2. Soil mechanics--Congresses. I. Huang, Baoshan. II. Title.

TE250.G46 2010
625.8--dc22 2010012087

American Society of Civil Engineers
1801 Alexander Bell Drive
Reston, Virginia, 20191-4400

www.pubs.asce.org

ISBN 978-0-7844-1104-9
Manufactured in the United States of America.

Preface

Pavement design and paving material selection are important for efficient, cost effective, durable, and safe transportation infrastructure. This ASCE Geotechnical Special Publication (GSP) addresses bound and unbound material characterization, modeling, and performance of highway and airfield pavements. The special issue has 73 fully refereed papers. The published papers are eligible for discussion in the *Journal of Geotechnical and Geoenvironmental Engineering* and are also eligible for ASCE awards.

The papers included in this special issue were presented during the GeoShanghai 2010 International Conference held in Shanghai, China, June 3-5, 2010. This conference was hosted by Tongji University, the Shanghai Society of Civil Engineering, and the Chinese Institution of Soil Mechanics and Geotechnical Engineering in cooperation with the ASCE Geo-Institute, the Transportation Research Board of the National Academies, the East China Architectural Design & Research Institute Company, the Deep Foundation Institute in the USA, the University of Kansas, the University of Illinois at Urbana-Champaign, the Vienna University of Natural Resources and Applied Life Sciences in Austria, the Nagoya Institute of Technology in Japan, the Georgia Institute of Technology, the University of Newcastle in Australia, the Alaska University Transportation Center, and the University of Tennessee.

The GeoShangai 2010 Conference was chaired by Professor Yongsheng Li and co-chaired by Professors Maosong Huang and Imad Al-Qadi.

Finally, we would like to acknowledge the assistance of Donna Dickert of ASCE and Carol Bowers of ASCE Geo-Institute (G-I) and the support provided by the ASCE G-I Pavements Committee. We also give special thanks to the following individuals who provided the technical review for the papers submitted to the conference:

Jose Aguiar
Armen Amirkhanian
David Arellano
Ahmet Aydilek
Ambarish Banerjee
Amanda Bordelon
David Brill
Neeraj Buch
Edwin Burdette
Francesco Canestrari
Claudia Centurion
Halil Ceylan
Dar Hao Chen
Feng Chen
Jingsong Chen
Xingwei Chen
DingXin Cheng
Trenton Clark
Andrew Collop
Lin Cong
Shongtao Dai
Jo Daniel
Eshan Dave
Andrew Dawson
Barry Dempsey
Derya Deniz
Samer Dessouky
Herve Di Benedetto
Qiao Dong
Louw du Plessis
Tuncer Edil
Mohamed El-Basyouny
Lu Gao

K. Gopalakrishnan
Sergey Grebenschikov
Runhua Guo
Jie Han
Feng Hong
Sheng Hu
Jiong Hu
Hai Huang
Shin-Che Huang
Baoshan Huang
Xiaoyang Jia
David Jones
Emad Kassem
M. Emin Kutay
Jayhyun Kwon
David Lange
Guoqiang Li
Yongqi Li
Xinjun Li
Jenny Liu
Rong Luo
Robert Lytton
Debakanta Mishra
Maziar Moaveni
Louay Mohammad
Andre Molenaar
Tongyan Pan
Manfred Partl
Onur Pekcan
Terhi Pellinen
Virgil Ping
Jorge Prozzi
Anand Puppala
Bradley Putman
Jeff Roesler
Todd Scholz
Charles Schwartz
Junan Shen
Shihui Shen
Xiang Shu
John Siekmeier
Prasad Sivaram
Andre Smit
Mark Snyder
Khaled Sobhan
Tim Stark
Marshall Thompson
David Timm
Erol Tutumluer
Bill Vavrik
Lubinda F. Walubita
Feng Wang
Kejin Wang
Linbing Wang
Haifang Wen
Hui Wu
Hao Wu
Zhong Wu
Yuanjie Xiao
Feipeng Xiao
Qinwu Xu
Jian Yin
Zhanping You
Claudia Zapata
Xiong Zhang
Fujie Zhou

Proceedings Editors
Baoshan Huang
Erol Tutumluer
Imad L. Al-Qadi
Jorge Prozzi
Xiang Shu

Contents

Asphalt Paving Materials Characterization and Modeling

Indexes

Accelerated Laboratory Polishing Device for Hot Mix Asphalt

Robert Y. Liang[1] , Mohammad Khasawneh[2] and Madhar Taamneh[3]

[1]Professor, Dept. of Civil Engineering, The University of Akron, Akron, OH 44325-3905, (corresponding author). Email: rliang@uakron.edu
[2] Assistant Professor, Dept. of Civil Engineering, Ohio Northern University, Ada, OH 45810. Email: m-khasawneh@onu.edu
[3] Ph.D, Dept. of Civil Engineering, Tafila Technical University, Tafila 66110, Jordan. Email: mmtaamneh@yahoo.com

ABSTRACT: This paper presents a newly developed accelerated polishing device used in the laboratory as a screening tool for selecting high polishing-resistant and high-friction aggregates and for optimizing the mix design to ensure satisfactory field performance in terms of preventing premature loss of friction due to vehicle tire-pavement surface polishing and wearing actions. The accelerated polishing equipment can test two types of Hot Mix Asphalt (HMA) specimen sizes: one is the 15.24 cm diameter gyratory compacted specimen, and the other one is the 45.72 cm by 45.72 cm by 5.08 cm slab specimen made by a roller compactor. The repeatability of the test results was confirmed through a series of testing and statistical analysis. Also, the polishing and friction performance of HMA specimens made by different aggregates and compaction methods (gyratory vs. roller compaction) was compared.

INTRODUCTION

The primary cause of polishing and loss of friction of asphalt concrete pavement can be attributed to loss of microtexture and macrotexture of the pavement surface through prolonged abrasive action between vehicle tires and pavement surface. Lack of adequate skid resistance of the pavement surface can create serious safety concerns to vehicles traveling at high speed, especially when the vehicle is braking suddenly on a wet pavement surface where hydroplaning can occur. It is desirable to have the ability to screen the polishing and friction characteristics of a hot mix specimen during the mix design stage. The main objective of this paper is to present a laboratory-scale accelerated HMA polishing device for the purpose of screening the polishing and friction performance of the HMA mix.

POLISHING DEVICES FOR HMA

There are four existing laboratory-scale accelerated polishing devices for polishing the HMA surface: The North Carolina State University (NCSU) Wear and Polishing Machine (ASTM E660, 2005), the National Center for Asphalt Technology (NCAT) Device, the Wehner/Schulze Polishing Device (Do, et. al, 2007), and the Penn State Reciprocating Polishing Device (Nitta et. al, 1990, ASTM E1393, 2005).

DEVELOPMENT OF NEW POLISHING DEVICE

The guiding principle of the new laboratory-scale accelerated polishing device is that the friction loss of asphalt pavement surface can be accurately measured and replicated in short test durations. The abrasive action between a rubber vehicle tire and asphalt concrete pavement surface was enacted in the accelerated polishing device by using polishing shoes (pads) made of Styrene-Butadiene-Rubber (SBR). Two specific specimen dimensions can be tested: a 45.72 cm by 45.72 cm by 5.08 cm high roller compacted slab specimen or a 15.24 cm diameter by 10.16 cm high Superpave gyratory compacted specimen. For the gyratory compacted specimen, a solid rubber disk of 15.24 cm diameter and 3.81 cm thick was used. For the slab specimen, a rubber ring of approximately 33.02 cm outside diameter and 22.86 cm inside diameter was used to fit with the required measurement area for the Dynamic Friction Tester (DFT) and Circular Texture Meter (CTM). The DFT device consists of a disk fitted with three spring-loaded rubber sliders. The disk is initially suspended above the pavement surface and is driven by a motor until the desired tangential speed of the sliders (about 90 kph) is attained. The rotating disk is then dropped onto the wet surface. The friction force and speed of the rotating disk are continuously measured and recorded as the disk slows down to stop (zero speed). The CTM uses laser techniques to measure the surface texture profile of an annulus surface area. A photograph of the completely fabricated accelerated polishing device is shown in Fig. 1. Fig. 2 shows the details on mounting the two different specimen sizes.

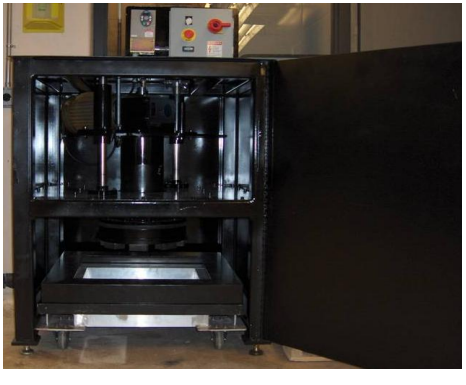

FIG. 1. Overall view of the accelerated polishing machine using rubber shoes

(a) Details on slab specimen mounting

(b) Gyratory-compacted specimen mounting

FIG. 2. Specimen mounting with the developed accelerated polishing machine

Different combinations of operation conditions were tried. The final selected operation conditions are as follows: (a) vertical force = 84 kg for 15.24 cm specimen and 127 kg for the large square specimen, and (b) the rotation speed at 30 rpm. These optimum operation conditions were selected to ensure that rubber pad would not experience rocking motion, and that more or less a flat contact surface between the rubber pad and the specimen was maintained. The water spray was used to wash off rubber debris and to prevent overheating during polishing action.

REPEATABILITY OF THE ACCELERATED POLISHING DEVICE

The repeatability of the polishing results using the developed accelerated polishing device was examined. For each set of specimens made of the same mix formula (aggregate source, aggregate gradation, optimum binder content, binder type, and compaction method and effort), three replicate specimens were tested. Both British Pendulum Test (BPT) and Mean Texture Depth (MTD) measured by the sand patch method were used. The British Pendulum tester (ASTM E303-93) consists of a rubber slider attached to the end of a pendulum arm. As the pendulum swings, it is propelled over the surface of the specimen. As the rubber slider contacts the surface of the specimen, the kinetic energy of the pendulum decreases due to friction. This energy loss is measured and reported as the British pendulum number (BPN). The Sand Patch Method (ASTM E965-96) is used to measure macrotexture of the specimen surface. This method involves taking a known volume of a spreadable material and spreading it out in a circle on the surface of the specimen. Measuring the diameter gives the area of the circle. The MTD is determined by dividing the volume by the area.

The friction values obtained from BPT and the MTD measured by the sand patch method from the three replicates were statistically analyzed using the techniques of Homogeneity of Variance (Levene statistic), one-way Analysis of Variance (ANOVA), and Multiple Comparisons to check for the repeatability of test results. The statistical analysis results are summarized in Table 1. It can be seen that the difference between the variances and the means of the results for the three replicate specimens was insignificant for all cases when considering the friction values (British Pendulum Number, BPN) and insignificant for the vast majority of the cases when considering

the macrotexture values (MTD). The repeatability of the polishing action provided by the accelerated polishing device was acceptable.

TABLE 1. Repeatability Tests for the Limestone and Gravel HMA Mixes

Aggregate Source	Factor	Homogeneity of Variances		1-Way ANOVA Table		Multiple Comparisons	
		Levene Statistic	Significance[a]	F	Significance[a]	Group	Significance[a]
Possible Medium Polish (Columbus Limestone)	BPN	0.167	0.847	0.280	0.758	1 2	0.982
						1 3	0.853
						2 1	0.982
						2 3	0.755
						3 1	0.853
						3 2	0.755
	MTD	0.384	0.685	5.705	0.009	1 2	0.964
						1 3	0.027
						2 1	0.964
						2 3	0.015
						3 1	0.027
						3 2	0.015
Possible low Polish (Stocker Sand & Gravel)	BPN	0.484	0.622	1.068	0.359	1 2	0.854
						1 3	0.334
						2 1	0.854
						2 3	0.640
						3 1	0.334
						3 2	0.640
	MTD	0.884	0.426	93.006	0.000	1 2	0.304
						1 3	0.000
						2 1	0.304
						2 3	0.000
						3 1	0.000
						3 2	0.000

a. significant at the p-value smaller than 0.05

COMPARING POLISHING BEHAVIOR BETWEEN HMA SURFACE AND AGGREGATE SURFACE

In a previous study (Liang and Chyi, 2000), different aggregates sources were tested for polishing and friction behavior using the accelerated British Polishing Wheel (ASTM E3319). The results of polishing behavior of two aggregates from Liang and Chyi (2000) and the current study of the HMA specimens made with the same two aggregate sources are statistically compared in Table 2 and Table 3 for Limestone and Sand and Gravel aggregates, respectively. It can be seen that the friction values of the aggregates, denoted by PV, are highly correlated to the friction values of the HMA made with the same aggregates, denoted by either BPN for the gyratory compacted specimens and FN_SPEED (where SPEED refers to the friction at the measuring speed) for the roller compacted slab specimens. The fact that aggregates constitute more than 90% by weight of the HMA leads us to believe that aggregate would be a dominant controlling factor on friction of HMA surface. The high correlation observed

in Tables 2 and 3 supports this. Based on the comparisons presented in this section, the developed laboratory-scale accelerated polishing device was shown to be able to polish the HMA surface and provide similar test trend as if the polishing tests were performed on the aggregates only.

TABLE 2. Simple Linear Regression between Aggregate Friction Values in (Liang and Chyi, 2000) and HMA Friction Values (This Study) for Columbus Limestone Mixes

Correlation Variables	Model Equation	R^2 (%)	ANOVA Table	
			F-value	P-value
PV vs. BPN	PV = 8.322 + 0.462 BPN	91.6	76.04	<0.0001
PV vs. FN_0	PV = 19.112 + 0.257 FN_0	92.0	80.17	<0.0001
PV vs. FN_10	PV = 19.516 + 0.347 FN_10	95.8	160.84	<0.0001
PV vs. FN_20	PV = 10.688 + 0.649 FN_20	93.9	107.34	<0.0001

TABLE 3. Simple Linear Regression between Aggregate Friction Values in (Liang and Chyi, 2000) and HMA Friction Values (This Study) for Stocker Sand and Gravel Mixes

Correlation Variables	Model Equation	R^2 (%)	ANOVA Table	
			F-value	P-value
PV vs. BPN	PV = -22.166 + 0.876 BPN	98.5	259.35	<0.0001
PV vs. FN_0	PV = -22.956 + 0.603 FN_0	72.7	10.64	0.0310
PV vs. FN_10	PV = -8.717 + 0.574 FN_10	74.2	11.49	0.0275
PV vs. FN_20	PV = -117.545 + 2.768 FN_20	92.5	49.08	0.0022

POLISHING TREND OF HMA SAMPLES PREPARED BY TWO COMPACTION METHODS

The friction values of the two types of specimen sizes, each compacted with different compaction method (i.e., roller compaction vs. gyratory compaction) were found to be correlated and the coefficients of determination were significant, as indicated in Tables 4 and 5 for Limestone and Sand and Gravel aggregates, respectively. Based on the ANOVA analysis shown, the overall significance of the models, as presented by the F-value and P-value, was found to be significant at the 0.05 significance level.

TABLE 4. Simple Linear Regression between Friction Values of Gyratory Compacted Specimens and Friction Values of Roller Compacted Slab Specimens (Limestone aggregate)

Correlation Variables	Model Equation	R^2 (%)	ANOVA Table	
			F-value	P-value
BPN vs. FN_0	BPN = 23.686 + 0.550 FN_0	98.7	522.07	0.0000
BPN vs. FN_10	BPN = 25.566 + 0.723 FN_10	97.3	248.48	0.0000
BPN vs. FN_20	BPN = 8.262 + 1.327 FN_20	91.4	74.60	0.0000

TABLE 5. Simple Linear Regression between Friction Values of Gyratory Compacted Specimens and Friction Values of Roller Compacted Slab Specimens (Sand and Gravel aggregate)

Correlation Variables	Model Equation	R^2 (%)	ANOVA Table	
			F-value	P-value
BPN vs. FN_0	BPN = -4.074 + 0.723 FN_0	81.3	17.38	0.0140
BPN vs. FN_10	BPN = 13.815 + 0.677 FN_10	80.3	16.27	0.0157
BPN vs. FN_20	BPN = -103.208 + 3.056 FN_20	87.8	28.71	0.0059

SUMMARY AND CONCLUSIONS

In this paper, an accelerated laboratory-scale polishing device that is capable of mimicking the polishing of the HMA pavement surface due to vehicle tires in an accelerated manner was developed. The accelerated polishing device was capable of testing two different sizes of HMA specimens: the 45.72 cm by 45.72 cm by 5.08 cm high slab specimens compacted using the roller compactor and the 15.24 cm diameter and 10.16 cm high cylindrical specimens compacted using the gyratory compactor. The design principles of the testing device, together with the optimized operation conditions, were presented in this paper. Results of a series of testing and comparisons can be summarized below.

- Repeatability of the accelerated polishing device was checked and affirmed using one-way ANOVA test.
- The polishing effect and trend of polishing produced by the new polishing device was ascertained through examination of the test results conducted on HMA mixes made of Limestone and Sand and Gravel aggregates, respectively.
- Good correlation of the polishing and friction behavior was found between aggregate specimens tested with standard test methods and the HMA specimens made with the same aggregates tested with the new polishing device. Therefore, it was reasonable to conclude that the new accelerated polishing device can accomplish the intended tire/pavement wearing and polishing mechanisms.
- Good correlation was found between the two specimen sizes using different compaction methods.

REFERENCES

American Society for Testing and Materials (2005). "Accelerated Polishing of Aggregates or Pavement Surfaces Using a Small-Wheel, Circular Track Polishing Machine," ASTM Standard Test Method E-660, *Book of ASTM Standards*, Volume 04.03, Philadelphia, PA.

American Society for Testing and Materials (2005). "Determining the Polishability of Bituminous Pavement Surfaces and Specimens by Means of the Penn State Reciprocating Polishing Machine," ASTM Standard Test Method E-1393, *Book of ASTM Standards*, Volume 04.03, Philadelphia, PA.

American Society for Testing and Materials (2005). "Measuring Pavement Macrotexture Depth Using a Volumetric Technique" ASTM Standard Test Method E-965-96 (2001), *Book of ASTM Standards*, Volume 04.03, Philadelphia, PA.

American Society for Testing and Materials (2005). "Measuring Surface Friction Properties Using the British Pendulum Tester" ASTM Standard Test Method E-303-93 (2003), *Book of ASTM Standards*, Volume 04.03, Philadelphia, PA.

Do, M., Tang, Z., Kane, M., and Larrad, F. (2007) "Pavement Polishing-Development of a Dedicated Laboratory Test and its Correlation with Road Results" *Wear 263*, pp. 36-42.

Kissoff, N. V. (1988) "Investigation of regional differences in Ohio pavement skid resistance through simulation modeling" PhD dissertation, University of Toledo, Toledo, Ohio.

Liang, R.Y., and Chyi, L. L. (2000). "Polishing and Friction Characteristics of aggregates Produced in Ohio" *Final Report of ODOT Project No. FHWA/OH-2000/001*, Ohio Department of Transportation.

Nitta, N., Saito, K. and Isozaki, S. (1990) "Evaluating the Polishing Properties of Aggregates and Bituminous Pavement Surfaces by Means of the Penn State Reciprocating Polishing Machine" *Surface Characteristics of Roadways, International Research and Technologie*s, ASTM SPT 1031, W. E. Meyer, and J. Reichert, Eds., American Society for Testing and Materials, Philadelphia, PA, pp. 113-126.

Voller, T.W., and Hanson, D.I. (2006). "Development of Laboratory Procedure for Measuring Friction of HMA Mixtures – Phase I," *Final Report of NCAT No. 06-06*, National Center for Asphalt Technology.

Effect of Aggregate and Asphalt on Pavement Skid Resistance Evolution

Dan ZHAO[1], Malal KANE, Minh Tan DO

Laboratoire Central des Ponts et Chaussées, LCPC, Route de Bouaye, 44341 Bouguenais Cedex, France
[1]PhD, LCPC, Tel.: +33 2 40 84 57 17; E-mail address: dan.zhao@lcpc.fr (D. ZHAO)

ABSTRACT: When designing pavement, engineers must optimize some requirements such as user safety (skid resistance), environmental impact (noise, rolling resistance…)... However, this skid resistance evolves during the entire pavement life. So it is a common practice to perform laboratory tests to forecast the evolution of skid resistance. Previous works done in the French Laboratory of Bridges and Roads (Laboratoire Central des Ponts et Chaussées, LCPC) have identified phenomena such as binder removal, aggregate polishing and seasonnal variations to be responsible of these variations. This paper focuses on the polished stone values of aggregates and the aging of asphalt on the evolution of pavement skid resistance. Skid resistance of different specimens of nude aggregates and asphalt mixes that are submitted to polishing and aging was studied. On skid resistance point of view, aging of aggregates can be neglected in comparison to those of asphalt. Rocks with high polishing resistance offer less variation of skid resistance. Aging of asphalt tends to increase skid resistance until 12 month and remains this latter constant after.

INTRODUCTION

Skid resistance is one of the fundamental requirements that provide a safe road (Diringer and Barros 1990; Roe and Hartshorne, 1998). But, unfortunately pavement skid resistance evolutes during the whole pavement life due to change on pavement surface characteristics. In the case of asphalt pavements, skid resistance is governed by, among other factors, asphalt types and aggregate properties (Michelin Company, 2000].

Research has been launched at LCPC since 2004 to investigate the polishing phenomenon of asphalt pavement. As results of this investigation, two parts was clearly observed from the evolution tendencies (see FIG.1): the friction coefficient increases firstly until reaching a maximum then decreases (Minh-Tan Do et al, 2007).

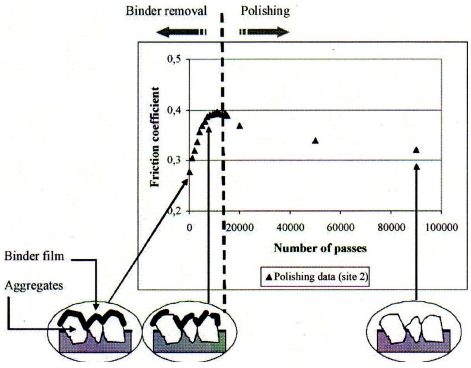

FIG. 1. Friction coefficient versus number of passes with WS machine

Comparing skid resistance evolution of asphalt mix specimen and specimen of nude aggregate (see FIG.2), the most important point is that the aggregate and asphalt curves coincide after the asphalt has reached the maximum friction. This result was explained by the fact that once the binder layer of asphalt pavement is removed, the aggregates are exposed little by little, and the surface of asphalt pavement behaves as the aggregate in this moment. For summarizing, it can be said that the skid resistance evolution is controlled by the aggregates after the binder removal [Tang, 2007; Minh-Tan Do et. al. 2008; EN 1097-8. 2000; Y. Brosseaud and V. Le Turdu., 2005].

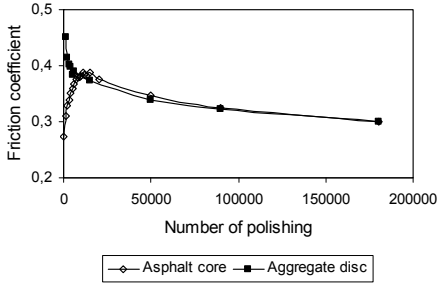

FIG. 2. Friction coefficient evolutions simulated by WS machine of asphalt and aggregate

In this paper, the effects of asphalt and aggregates characteristics on the evolution of skid resistance are analyzed. The experimental program is based on two parts. The first one focuses on the aggregate effects whereas the second consists on studying the effect of the asphalt.

EXPERIMENTAL PROGRAM

Wehner-Schulze machine

The experimental program is based on a set of tests with the Wehner-Schulze machine. This machine contains two stations for respectively performing polishing and measuring friction (see FIG.3).

FIG. 3. Wehner-Schulze machine

The polishing station contains three rubber cones mounted on a rotary disc and rolling on the specimen surface. Test parameters of this station are:

- load on all polish cone rolls is 40kg;
- revolution of polishing head is 500 r.p.m;
- flow of abrasive water mixture is 5 l/min;
- surface is polished on a ring of roughly 16 cm diameter and 6 cm width;
- temperature of abrasive water mixture is 20°C;

The friction measuring head composes of three small rubber pads (4 cm^2 area for each pad) disposed at 120° on a rotary disc. Test parameters at measurement station of friction coefficient with friction-measuring head:

- load on all measurement rubber is 26kg;
- start velocity of measurement rubbers is 100 km/h;
- flow of water is 20 l/min;
- contact surface is 82 cm^2;
- temperature of water is 12°C;

Specimens are cores of 22.5cm diameter.

Aggregate specimens

Six types of aggregates characterized by their Polished Stone Value (PSV - see Table 1) were used in this study. The used procedure for performing the polishing process can be found in the following reference (Tang, 2007).

Circular specimens are prepared in laboratory with 7.2/10 aggregate size (see FIG.7 (b)). They are fabricated by placing manually the aggregates in a single layer as closely as possible, with their flattest faces lying on the bottom of a mould, then filling the

mould with resin.

Table 1. Aggregate characteristics

Aggregate	A	B	C	D	E	F
Type	Rhyolite	Spilite	Gabbro	Diorite	Leptynite	Limestone
PSV	56	53	51	50	49	41

To study the effects of types and aging of aggregates, the following test program is elaborated (see FIG.4).

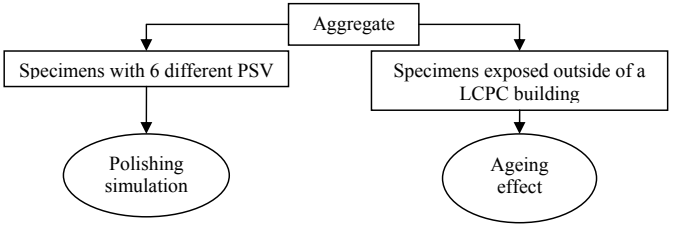

FIG. 4. Aggregate test program

Asphalt specimens

This part is planned to study the effect of asphalt on skid resistance. The studied specimen is a very thin asphalt concrete (VTAC) with STYRELF 11-40 bitumen (see Table 2) [AFNOR, NF EN 12697-33, 2004] taken on an experimental road section.

Table 2. Description of Asphalt Mixes and Aggregates

Site	Traffic(10^5 trucks/year)	Mix	Binder	Aggregates	PSV
Experimental section	1.14	VTAC	STYRELF 11-40	Gabbro	51

The program is shown by the flow charts in FIG.5.

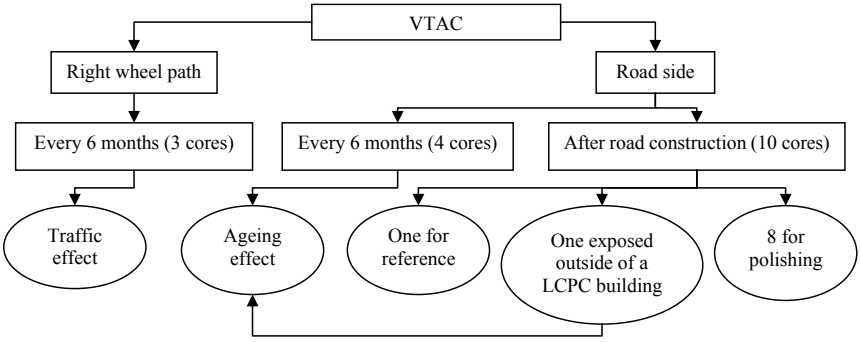

FIG. 5. Asphalt mix test program

In this road section, ten cores of 22.5cm diameter are taken from the road side just after the road construction (see FIG.6(a)) in September 2004:

- one specimen is stored in the laboratory as a reference;
- the other specimens are used for polishing tests.

Other cores are taken every 6 months of traffic in site (see FIG.6 (b)):

- three from the right wheel path;
- four from the road side (see FIG.7(c,d)).

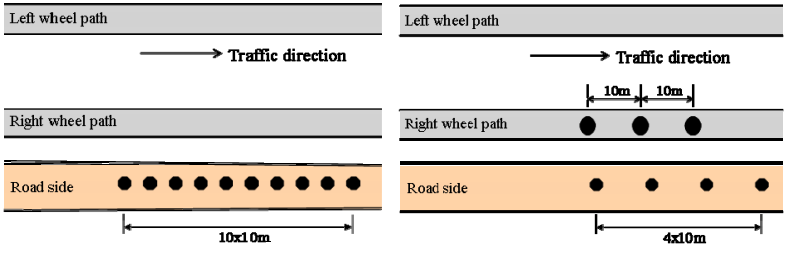

(a)just after construction (b)every 6 months

FIG. 6. Planning of in situ samples extracted Part Ⅱ

Friction measurements were made using the Wehner-Schulze machine as described in previous paragraph.

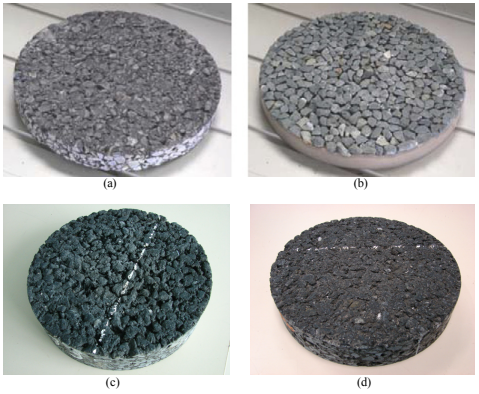

(a) specimen cored just after the road construction;
(b) specimen of nude aggregates fabricated in laboratory;
(c) specimen cored after twelve months of road side;
(d) specimen cored after forty eight months of road side.

FIG. 7. Examples of Specimens

TEST RESULTS

Influence of aggregates

Polishing of aggregates

The evolutions of skid resistance of different aggregates are shown in the FIG.8. It can be seen that the initial values are almost the same, however, after some polishing passes; each of them shows a different evolution tendency. Three groups of evolution curves can be distinguished from the PSV value. The first group consists specimen F with PSV very low (41); the second group is composed of four aggregates (specimen B to E), with an average PSV between 49 and 53; and the third group is a single specimen A with the highest PSV (56).

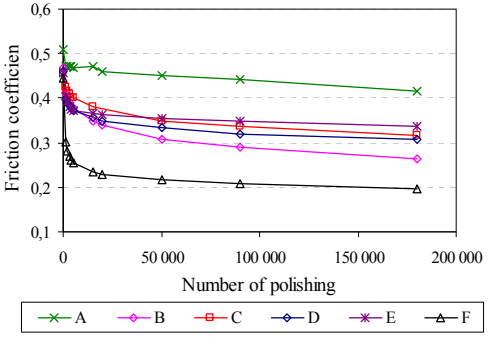

FIG. 8. Evolution of friction coefficients of different aggregates

FIG.9. shows the correlation of friction coefficient versus the PSV of aggregate after 180000 polishing. There is reasonable correlation between the aggregate PSV and their final friction coefficients. A mathematical relation can be proposed as follow:

$$\mu_{WS} = 1.18\frac{PSV}{100} - 0.29 \quad (R^2 = 0.66) \tag{1}$$

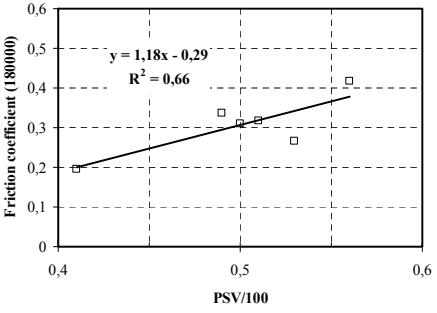

FIG. 9. Relation between friction coefficient and PSV after 180000 polishing passes

This indicates that aggregates of higher PSV may offer less decrease of skid resistance, especially at the start of the polishing process. This study confirms perfectly a linear relation of PSV versus friction coefficient of previous studies where other kinds of devices were used. For example, with the British Pendulum Number measured, Diringer proposes:

$$\mu_{\min} = C_0(1 - e^{C_1}PV) + C_2PV \tag{2}$$

with,

PV: minimum polish value; and C_0, C_1, C_2 : nonlinear regression coefficients (Diringer K.T. and Barros R.T., 1990).

And Roe proposes a relation representing the influence of traffic by SCRIM:

$$\mu_{\min} = A \cdot PSV - B \cdot \ln(CVD) + C \tag{3}$$

with,

PSV: Polished stone value of aggregate; CVD: Number of commercial vehicles per day and per lane; A, B, C: coefficients determined by fitting (P.G.Roe and S.A.Hartshorne, 1998).

Aging of aggregates

For studying the aging effect, the friction coefficient is measured at every 6 months on specimen made with aggregate C (Table 1). This latter is exposed outside, then submitted to all kinds of attacks of the nature (rain, sun, temperature…). The aggregate friction curve presents a slight decrease of only 0.05 from 0 to 24 months (see FIG.10). This low variation of friction due to the nature attacks indicates that, for this aggregate, we can ignore the aggregate aging effect.

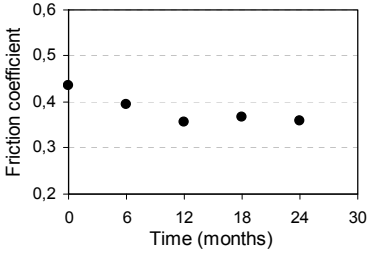

FIG. 10. Friction coefficient evolutions of aggregate

Influence of asphalt

Aging effect without traffic

FIG.11 shows the friction measured on specimen cored at each six month on the road side (untrafficked part of the road). A significant increase of the friction (+ 0.2) is observed from zero to 12 months following by stabilization.

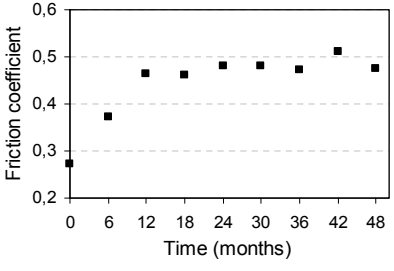

FIG. 11. Evolution of the friction coefficient of asphalt pavement due to aging alone

Pink curves with full squares of FIG.12 and FIG.13 show the friction measured on specimens extracted at 48 months after road construction. The friction coefficient starts from high value (higher than those of specimens extracted at 0 months) then decreases without ever reaching the curves of the new asphalt and the specimen of nude aggregate.

These results suggest that the mechanism of hardening of asphalt increases the friction

that tends to remain even with increasing the polishing passes.

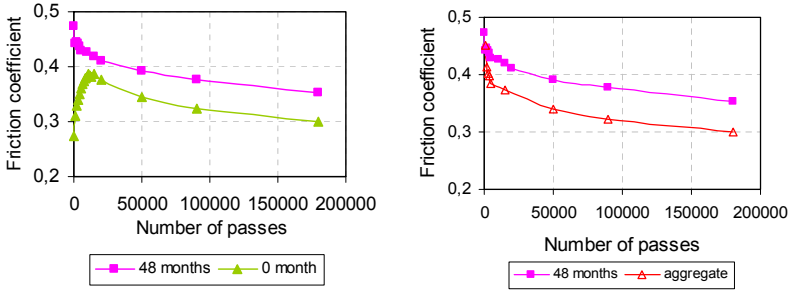

FIG. 12. Friction coefficient evolution with polishing mumber of specimens without traffic

Aging effect with traffic

We have observed that friction evolution stabilizes approximately from 12 months after road construction in site (see FIG.11).

Just after road construction, the binder of bitumen is soft and easy to be removed by polishing or traffic, so we can observe, in laboratory simulation with Wehner-Schulze machine, that the evolution curves of nude aggregate specimen (orange dotted curve) and of new asphalt specimen (green curve) coincide after a given number of polishing cycles (see FIG.12) (X Lu and Ulf Isacsson, 2002; Y.Brosseaud and J. Bellanger. 1997). And this phenomenon confirms the previous conclusion (see FIG.2). However, after some years, the chemical changes of asphalt harden the asphalt binder, and make it difficult to be removed (Fabienne Farcas, 1996).

From the part after 50 000 number of polishing passes in curves of FIG.13, the different gaps can be seen. The gap in FIG.13, between the asphalt pavement specimen with traffic (pink curve with hollow squares) and without traffic (pink curve with full squares), occurs by asphalt aging. After 48 months road traffic service, asphalt binder is removed and this makes the aggregates expose. The texture of pavement can be changed by exposed aggregates, residual asphalt, dust, etc… So the gap between the new specimen (nude aggregate and new asphalt mix) and the specimen with traffic of 48 months is less obvious but can't be neglected.

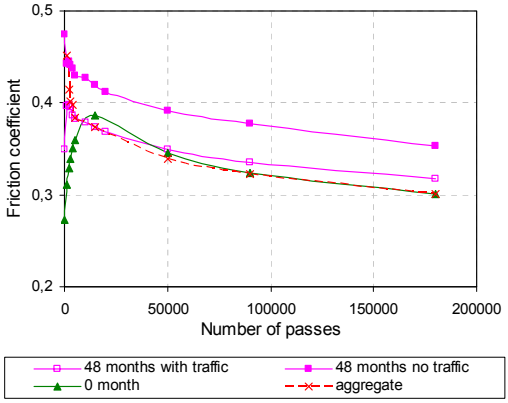

FIG. 13. Friction coefficient evolution with traffic and without traffic

Summary of findings

The aging effects of aggregates may be neglected comparing with those of asphalt on skid resistance.

Traffic tends to polish the aggregates and makes them slipper and that rocks with high polishing resistance may offer less variation of skid resistance.

Without traffic, the aging of asphalt tends to increase skid resistance until 12 month and remains this latter constant after.

On pavements submitted to traffic, the removal of asphalt exposes the aggregates on the pavement surfaces step by step to polishing.

Conclusions

In this paper, several studies have been applied to investigate the effect of aggregate and asphalt on the evolution of skid resistance. The experimental campaign was undertaken with specimens fabricated in laboratory and extracted from experimental road. All the polishing tests and skid resistance measurement are carried out with the Wehner-Schulze machine. These results obtained allow showing the importance of aggregate nature, especially the PSV (greater PSV aggregate may offer a low great variation of skid resistance). The test results also show that asphalt had a significant effect on the measured skid resistance. We have observed the importance of asphalt aging, and this effect have a tendency to increase the skid resistance.

This study allows exploiting the influence of some factors of aggregates and asphalt on the evolution of skid resistance, and indicates us the importance of considering these influences in analysis.

REFERENCES

Diringer K.T. and Barros R.T. (1990). Predicting the skid resistance of bituminous pavements through accelerated laboratory testing of aggregates, *Surface characteristics of roadways: International Research and Technologies, ASTM STP 1031, American society for testing and materials, Philadelphia,* pp. 61-67.

P.G.Roe and S.A.Hartshorne (1998). "The polished stone value of aggregates and in-service skidding resistance." *TRL Report* 332, 28.

Michelin Company. (2000). " Le pneu/l'adhérence." *Clermont-Ferrand, Michlin Technology*.

Minh-Tan Do and Zhenzhong Tang and Malal Kane and François de Larrard. (2007). " Pavement polishing: Development of a delicated laboratory test and its correlation with road results." *Wear*, 263(2007), 263:p36-42.

Tang. Z (2007). "Polishing and skid-resistance of road pavements." *PhD thesis (in French) of ENPC (Ecole Nationale des Ponts et Chaussées)*, LCPC.

Minh-Tan Do and Z. Tang and M. Kane and F. de Larrard. (2008). " Evolution of road-surface skid-resistance and texture due to polishing." *Wearing Press* , Corrected Proof.

EN 1097-8. (2000). "Tests for mechanical and physical properties of aggregates Part 8: Determination of the polished stone value."

Y. Brosseaud and V. Le Turdu. (2005). "Adhérence des revêtements de chausses routières" *Bulletin des laboratories des Ponts et Chaussées, 225: 71*.

AFNOR, NF EN 12697-33. (2004). "Test methods for hot mix asphalt Part 33: Specimen prepared by roller compactor."

Xiaohu Lu, Ulf Isacsson. (2002). "Effect of aging on bitumen chemistry and rheology." *Division of Highway Engineering Royal Institue of Technology, Sweden.*

Y.Brosseaud and J. Bellanger. (1997). "Les nouvelles formulations d'enrobés pour couches de roulement evaluation de leurs caractéristiques de surface" *Revue générale des routes et autoroutes, 752 : 51-56.*

Fabienne Farcas. (1996). "Etude d'une méthode de simulation du vieillissement sur route des bitumes." *Thèse de doctorat de l'Université Paris* VI.

Development of a New Moisture Conditioning Procedure for Bitumen Stabilized Materials

Elias M. Twagira[1] and Kim J. Jenkins[2]

[1]PhD Researcher, Stellenbosch University, Private Bag X1, Matieland, 7602, South Africa, etwagira@gmail.com
[2]Professor, SANRAL Chair of Pavement Engineering, Stellenbosch University, Private Bag X1, Matieland, 7602, South Africa, kjenkins@sun.ac.za

ABSTRACT: The presence of excess pore water in the bitumen stabilized materials (BSMs) can result in a rapid deterioration due to moisture damage. The process associated with moisture ingress and damage is complex and can occur over an extended period in-service. In the absence of a research method that realistically simulates the possible mechanisms of moisture damage, a surrogate, laboratory-based moisture conditioning method was developed. This method aims to accelerate the ingress of moisture into the mix so that the evaluation of its effect on mixture stiffness (Mr) and shear parameters (C & φ) can be made. This paper presents the results of an experiment aimed at determining whether cyclic pulses of water under pressure into BSMs induce sufficient, measurable damage to a triaxial specimen that will distinguish between BSMs with different levels of resistance to moisture damage. An additional constraint for the simulation procedure was the allowable time and cost, i.e. the conditioning has to be accomplished within a reasonable length of time with simple, cost effective laboratory equipment. The evaluation of moisture damage in this experiment was carried out using the newly developed "Moisture Induction Simulation Test" (MIST) device and triaxial testing. Mix compositions of aggregate blends with and without RAP, with different bitumen binder types (foamed bitumen or bitumen emulsion) and active filler types (cement or lime) and contents, were investigated. The findings presented in this paper show that cyclic water pressure can be used to simulate accelerated moisture damage on triaxial specimen enough to distinguish between the mixture of high resistance and high susceptibility to moisture damage. Importantly, validation of MIST device using the known laboratory Model Mobile Load Simulator (MMLS3), a one-third scale accelerated pavement tester (APT) device, shows agreeable ranking of BSMs for MMLS3 and the MIST-triaxial combination, in terms of moisture resistance.

INTRODUCTION

In order to evaluate the susceptibility of BSMs to water damage, it is ideal to have full understanding of mechanisms of moisture damage that occur under field conditions. Moisture transport mechanisms, coupled with adverse environmental conditions and dynamic loading, have found to initiate the moisture damage mechanism of the BSMs (Fu *et al.,* 2007; Birgisson *et al*. 2003; Land transport New Zealand, 2005; Bell *et al*. 1999). Fu *et al*. and Birgisson *et al*. reported that saturation of base layer slight above optimum moisture content (OMC) results in severe crocodile cracking and rutting of surface layer. Infiltration of water from pavement surface into base layer has been reported. A study on seal design by Land transport in New Zealand, confirmed that under fast dynamic loading, surface water can be forced through the chip seal without any visible signs of cracking, and into base layer. Nikajima *et al.,* (2000) and Okano *et al*. (2008) modelled the water flow under tyres as it went through a 10mm deep water film. Their results indicated that at high vehicle speeds, generation of hydrodynamic pressure increases. The water film penetrated in contact patch may be forced through the porous/voids in surface layer. The force can double from approximately 0.7KN at 60Km/h to 1.4kN at 80Km/h. An estimated pressure in terms of kilopascals, related to 1kN force, is equal to 100kPa. These magnitudes of pulsing water pressure need to be considered during conditioning of BSMs as a base layer.

RATIONALE FOR A NEW LABORATORY TEST PROCEDURE FOR CONDITIONING BSMs

BSMs mixes are characterized by partial coating of thin films of binder (bitumen) in mineral aggregates. This results in formation of high voids content between mix matrices. The presence of excess moisture in the voids, plays a major role in the damage mechanisms. The new laboratory-based representative testing procedure, and analysis protocol for the evaluation of moisture damage was developed to distinguish from current over-simplified procedures (De Beer, 1989; Jenkins, 2000; Long *et al.* 2003). Although the laboratory simulation cannot be an exact replication of mechanisms that manifest in service, it should represent the fundamental or key failure mechanism for the BSMs. In the same manner, a simplified, reliable, and cost effective procedure is required to distinguish between research and classification testing for moisture susceptibility. The testing and evaluation framework presented in this paper is based on the MIST device. Moisture conditioning followed by mechanical testing (short dynamic and static tests) was applied to numerous mixtures to determine the level of moisture damage in different representative BSMs. Different saturation levels were investigated with experimental determination of stiffness properties (Mr) and shear parameters (C and φ), before and after conditioning. These parameters are critical for the performance prediction of BSMs. Several types of aggregate blends, with and without RAP, with foamed bitumen or bitumen emulsion binders were investigated. The rating of severity of moisture related damage of the selected mixes, after conditioning using MIST test, is discussed and validation of these test results with a laboratory MMLS3 device is presented. The influence and effect of the addition of active filler (cement or lime) in the selected mixes have also been investigated.

EXPERIMENTAL PROGRAM

Materials

Two selected materials types were used in this study, that is, recycled, Hornfels-RAP (85:15, percentage composition), and crushed virgin Quartzite (G4). G4 is South African classification system of crushed or natural gravel (TRH14, 1985) The grading of the aggregates has maximum aggregate size of 19mm and percent passing 0.075mm of 10% and 6% respectively. Selected materials were stabilized in the laboratory with either foamed bitumen or bitumen emulsion binder. Two percent (2%) net bitumen content was applied to both Hornfels-RAP and Quartzite materials. The addition of 0% or 1% active filler (i.e. cement or lime) was also applied on the selected materials. The factorial design of tested mixes led into 12 mixes, as shown in Table 1, which also includes maximum dry density (MDD) and optimum moisture content (OMC).

Table 1. Constituted mix type and testing matrix

Binder type	Aggregates type	
	Hornfels-RAP + 2% net bitumen* MDD = 2177(Kg/m^3): OMC = 5.12%	Quartzite + 2% net bitumen* MDD = 2240 (Kg/m^3): OMC = 6.0%
A- Bitumen emulsion	Mix 1: 0% filler Mix 2: 1% cement Mix 3: 1% lime	Mix 7: 0% filler Mix 8: 1% cement Mix 9: 1% lime
B- Foamed bitumen	Mix 4: 0% filler Mix 5: 1% cement Mix 6: 1% lime	Mix 10: 0% filler Mix 11: 1% cement Mix 12: 1% lime

*Net bitumen is the residual binder after evaporation of water in foamed bitumen and bitumen emulsion

Sample preparation

The testing matrix was developed such that six triaxial specimens size of 250mm x 150mm are prepared for each mix. Preparation of triaxial specimens follows the new TG2 procedure (Asphalt Academy, 2009) by compacting 50mm layers in a mould of 150mm diameter, using BOSCH® vibratory hammer to the target density. Compacted specimens are cured in draft oven at 30^{o}C for 20 hours while un-sealed followed by 40^{o}C sealed in a thin plastic bag for 72 hours. After compaction and curing, the specimens are grouped into sets of two, with approximately equal void content (P_a). The voids content are calculated after determining the specimen bulk relative density (BRD) and mix maximum theoretical relative density (Rice Density).The first set comprises three specimens for wet conditioning and static (monotonic) test, and the second set comprises three specimens for dry (un-conditioned) and static (monotonic) test. From these sets, one specimen is tested for short dynamic (Mr) triaxial test prior to monotonic test. Short dynamic test is a non-destructive test. Therefore, it is possible to determine change in stiffness due to moisture damage before testing the change in shear properties.

CYCLIC PORE WATER PRESSURE CONDITIONING SYSTEM

MIST device and conditioning protocol

MIST device was developed to evaluate the effect of moisture damage in BSMs, while simulating the field water pulsing conditions. This is done under controlled laboratory condition. The designed MIST device features are presented in Figure 1a, whereas the heating unit is indicated in Figure 1b. The solenoid valves in Figure 1a, with ON-OFF timer ranging from 0 to 60 seconds are used for controlling water pulsing application. Heating unit is used to simulate different water temperature for conditioning of specimen.

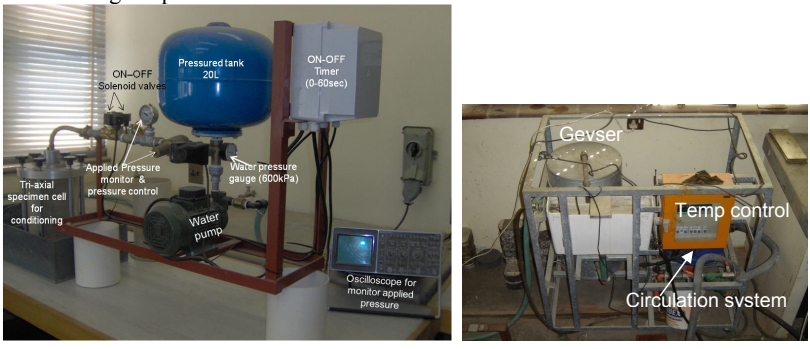

a) MIST designed features **b) Heating unit for hot water**

FIG. 1. MIST device features and conditioning set-up

The testing control variables applicable during MIST conditioning procedure include: 1) water temperature level, 2) saturation level, 3) water pressure level, 4) pulsing time or cycle number. The MIST procedure has the following major subsystems: 1) **Conditioning:** fluid saturation subsystem by pulsing moisture into triaxial specimen; 2) **Mechanical testing:** loading sub-system using material testing system (MTS) for determination of retained (shear and stiffness) properties.

The test variables of MIST device are set at 0.54 second load time, and 1.40 second rest period. Pulsing water pressure is 140 kPa. The fluid conditioning for MIST is done in triaxial cell after placing and assembling the specimen as shown in Figure 1a.

Saturation level and volumetric properties

Steady saturation is regarded as no change in water content of a material with time and additional pulsing water pressure. The steady state was determined by checking whether there is no change in bulk mass of a specimen with consecutive pulsing cycles (i.e. no more ingress of water in a specimen) or where severe (noticeable) damage occurred in specimen. At the end of conditioning i.e. reaching steady state saturation, the percentage ingress of moisture in the mix was determined. The specimen was split and moisture content of the material from the centre was determined. Calculation of steady state

saturation after MIST conditioning procedure was done by calculating the following parameters (Equations 1, 2 and 3): Volume of air voids (V_a), volume of absorbed water (V_w) in specimen [cm^3], and degree of saturation (S_r in %).

$$V_a = \frac{P_a x E}{100} \quad (1)$$

$$V_w = B - A \quad (2)$$

$$S_r = \frac{V_w}{V_a} x100 \quad (3)$$

Where B = weight of saturated-surface dry specimen [g]; A = weight of dry specimen in air after curing [g]; P_a = air void content in specimen [%]; E = volume of specimen [cm^3]. The degree of saturation was compared to OMC. The literature indicates that steady state saturation occurs when degree of saturation reaches 80% or at OMC. The degree of saturation during conditioning should therefore be at least 80% for accurate screening of BSMs. However, to achieve similar level of saturation for screening other mixes such as granular or HMA using MIST device re-evaluation of the parameters for pulsing water pressure is required.

Quantification of retained shear properties

Shear properties (C and φ) of the conditioned and unconditioned sets of specimens are determined in accordance with the procedure described in Stellenbosch triaxial test protocol. Retained cohesion (RC) is calculated as ratio of cohesion of wet mix (CoW) to cohesion of dry mix (CoD) expressed in term of percentage.

The applicability of the MIST device on conditioning of BSMs mixes could not be verified without a correlation test. In order to find more meaningful relationship on the durability of BSMs mix composition, ravelling depth (RvD) determined during module mobile load simulator (MMLS3) wet trafficking was correlated to MIST retained cohesion (RC) ratio and the tensile strength retain (TSR) after indirect tensile strength (ITS) testing. The results are presented in Section below.

ANALYSIS AND DISCUSSION OF RESULTS

The results presented in this paper are limed. However, the authors wish to refer the readers to the publication of Twagira (2009) for more test results.

Volumetric properties of specimens

The compaction levels achieved using the vibratory BOSCH® compactor shows that all mixes were compacted at more than 100% of the target density. The advantage of higher compaction levels is the simulation of field condition and minimising the influence of the void in moisture damage.

Critical steady state saturation

Figure 2 displays the accumulation (change) of moisture in a specimen with time, during MIST conditioning. It is apparent that most BSMs attain their steady state

moisture saturation after 3.2 minutes of pulsing time or 100 pulsing cycles. Although saturation graphs begin to reach a plateau after 2 minutes of pulsing time, this could be regarded as the threshold for highly moisture susceptible mixes.

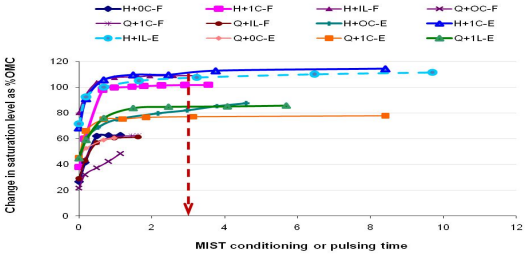

FIG. 2. Saturation levels after MIST conditioning on different BSM mixes

Moisture damage on materials properties

The results of triaxial testing on BSMs without moisture exposure and after MIST conditioning are provided in Figures 3 and 4.

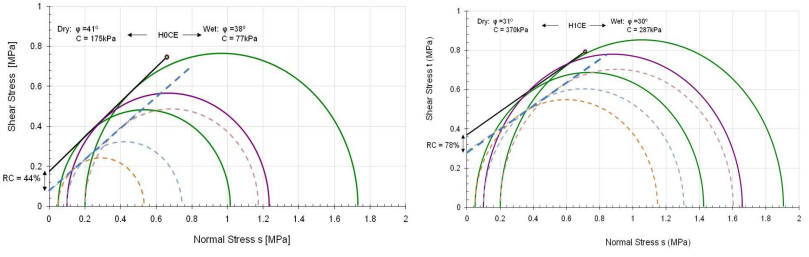

a) BSM-emulsion with no cement **b) BSM-emulsion with 1%cement**

FIG. 3. The effect of moisture damage on shear properties of BSM-emulsion

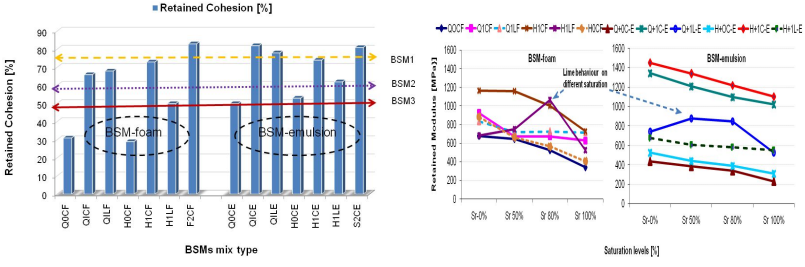

a) Retained cohesion **b) Retained stiffness**

FIG. 4. Retained cohesion and stiffness of different BSMs

The selected results in Figure 3 include shear parameters (C, & φ) for the

unconditioned and conditioned Hornfels-RAP mixes stabilised with bitumen emulsion, with or without the addition of active filler (cement). It is evident from the failure lines that reduction in cohesion occurs due to moisture ingress in the mixes. Figure 4a presents a comparison of the retained cohesion and Figure 4b presents a comparison of the retained stiffness of the BSM mixes studied. It can be seen from the retained properties (i.e. both cohesion and stiffness) that BSMs' mixes with the addition of cement or lime show significant improvement in resistance to moisture damage. At the same time, the addition of cement appears to be more effective than the addition of lime. This shows that, addition of lime into a BSM can be effective if the initial consumption of lime (ICL) is considered during mix design. Nevertheless, the general comparison between the binder types showed that BSM-emulsion mixtures are less susceptible to moisture damage than the equivalent BSM-foam mixtures.

Validation of the MIST-triaxial test results

The results presented in Figure 5 (a) and (b) show a comparison in the moisture damage behaviour predicted by using RvD (Ravelling Depth), RC (Retained Cohesion) and TSR (Tensile Strength Retained from ITS). The Hornfels-RAP stabilised with emulsion and addition of cement (H1CE) or lime (H1LE), were able to withstand wet MMLS3 trafficking of more than 40000 load applications, with RvD of 2mm and 10mm respectively . However, mix with the added lime seemed to be relatively less resistant than the mix with cement. The Hornfels-RAP and Quartzite crushed stone stabilized with foamed bitumen without addition of active filler (H0CF and Q0CF) suffered severe ravelling. It is evident from these results that, although the predicting trends of these parameters are similar, the ranking of BSMs moisture susceptibility using RC shows more sensitive correlation with RvD than ravelling behaviour with TSR.

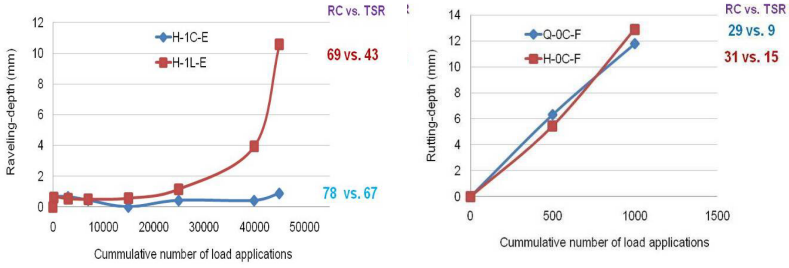

FIG. 5. Comparison of the ravelling depth (mm), retained cohesion (%) and tensile strength retain (%) on moisture damage sensitivity of BSMs

CONCLUSIONS

The findings presented in this paper show that cyclic water pressure using MIST device can be used to accelerate moisture damage on triaxial specimen enough to

distinguish between the mixture of high resistance to moisture damage and mixture susceptible to moisture damage. For this reason, the MIST device has been specified for conditioning specimens for triaxial testing as part of the new South African TG2 guidelines for bitumen stabilised materials BSMs (Asphalt Academy, 2009).

REFERENCES

Asphalt Academy (2009). " Bitumen Stabilised Materials. A Guideline for the Design and Construction of Bitumen Emulsion and Foamed Bitumen Stabilised Materials", *TG2 Technical Guideline, Second Edition*. Pretoria, South Africa

De Beer, M., (1989). "Aspects of erodibility of lightly cementitious materials". *Pretoria Division of Roads and Transport Technology*. CSIR Research Report DPVT 39, Pretoria.

Fu, P. Harvey, J.T. Jones, D.J. and Bukhari S.A. (2007). "Dry and soaked laboratory test for foamed asphalt mixes". *Accepted for publication in Transport Research record*.

Jenkins, K.J., (2000). "Mix design considerations for cold and Half-warm bituminous mixes with emphasis on foamed bitumen". *PhD Dissertation*, University of Stellenbosch, South Africa.

Land Transport New Zealand. (2005). "The waterproofiness of first coat seal." *Research report Style Guide*. New Zealand, pp 35.

Long, F. M., and Ventura, D. F. C. (2003). "Laboratory testing for the HVS Sections on the N7 (TR11/1)". *CSIR Transportek*, Contract Report CR-2003/56. Pretoria, South Africa.

Nikajima, Y., Seta, E., Kamegawa, T. and Ogawa, H. 2000. Hydroplaning analysis by FEM and FVM: Effect of the rolling and tire pattern on hydroplaning. *International journal of automotive technology*, Vol. 1 no.1 pp 26-34.

Twagira, M.E 2009. Influence of durability properties in the performance of Bitumen stabilised materials. *PhD dissertation. To be submitted at Stellenbosch University.* South Africa.

A Method to Build a Practical Dynamic Modulus Testing Protocol

Sean (Xinjun) Li

Asphalt Mixture Scientist, ESC, INC at Turner-Fairbank Highway Research Center/Federal Highway Administration, McLean, VA 22101; xinjun.li@fhwa.dot.gov

ABSTRACT: This paper presents a method for identifying a practical dynamic modulus testing procedure. The currently well adopted method of calculating the dynamic method is discussed and a more fundamental dynamic modulus calculation method is proposed in this research. A comprehensive shakedown test was performed the dynamic modulus test on one asphalt mixture. The analysis results show no permanent damage was found on tested specimens for all three test temperatures. Comparison of the master curves built by different temperature and frequency combination shakedowns the redundant test temperature and frequency. A more practical dynamic modulus test procedure is developed using this shakedown method. This research shows that three test temperatures, 4.4, 21.1 and 37.8°C, and six frequencies, 25, 10, 5, 1, 0.5 and 0.1Hz are adequate to build a smooth master curve for asphalt mixtures.

INTRODUCTION

It is generally accepted that the complex dynamic modulus of asphalt mixtures is related to major distress modes such as permanent deformation and fatigue cracking of flexible pavements (Witczak et al., 2002). A literature search on the dynamic modulus in asphalt materials results in a very large number of references and this illustrates that enormous research work has been performed on the evaluation of asphalt materials using dynamic modulus. As a consequence of the research effort, the recently released Mechanistic-Empirical Pavement Design Guide (MEPDG) proposed the dynamic modulus of asphalt mixtures as the key parameter in the flexible pavement design (ARA, 2004). Also, the dynamic modulus test is proposed as one of the Simple Performance tests to accompany the Superpave volumetric mix design process due to its ability of accurately and reliably measuring a mixture's response characteristic (Witczak et al., 2002). Consequently, increasingly pavement agencies are considering the adoption of the complex dynamic modulus test for the mixture design or to evaluate the properties of the asphalt mixtures.

Unfortunately, however, the dynamic modulus test procedure based on the AASHTO TP 62 specification, which requires testing at least two replicate specimens at five temperatures between 14°F and 130°F (-10°C and 54.4°C) and six loading rates

between 0.1 and 25 Hz, is very time consuming and costly (AASHTO, 2006). Therefore, some pavement agencies and researchers are considering other more practical dynamic modulus test protocols within the specification framework. In a recently finished study, Dougan, et al., found that the overall time required to perform the testing by AASHTO TP62-03 must be shortened if highway agencies are going to use it for routine testing (Dougan et al., 2003). In another recent study, Bonaquist and Christensen developed a procedure for developing dynamic modulus master curves for pavement structural design (Bonaquist et al., 2005). That research confirmed that the current specification leads to dynamic modulus data overlap in building master curves and alternatively this research presents a reduced testing sequence specified in AASHTO TP62 by eliminating the low test temperature of -10°C. Consequently, this alternative testing sequence will significantly reduce the testing time for most pavement agencies. While this research focused on achieving similar master curves by using the reduced testing sequence, however, a more general method that can be used by testing entities should be identified in developing their own dynamic modulus testing procedures. The objective of this study is to present a method for identifying a practical dynamic modulus testing procedure.

COMPLEX DYNAMIC MODULUS

It is well known that the asphalt mixture is a viscoelastic material at most of its' in-situ temperatures. The fundamental concepts of linear viscoelasticity are described by Ferry (Ferry, 1980). For the one-dimensional case of a sinusoidal loading, the stress can be represented by the following equation:

$$\sigma = \sigma_o \cdot \sin(\omega t) \tag{1}$$

Where σ is the stress, σ_0 is the stress amplitude and ω is the angular velocity, which is related to the frequency f by $\omega = 2\pi f$. The resulting steady state strain can be written as:

$$\varepsilon = \varepsilon_o \cdot \sin(\omega t - \phi) \tag{2}$$

Where ε is the strain, ε_0 is the strain amplitude and Φ is the phase angle related to the time the strain lags the stress, as shown in Figure 1. The ratio of the stress to strain amplitudes defines the absolute value of the dynamic modulus. The in-phase and out-of phase components are used to define the storage modulus:

$$E' = \frac{\sigma_o \cos(\phi)}{\varepsilon_o} \tag{3}$$

and the loss modulus:

$$E'' = \frac{\sigma_o \sin(\phi)}{\varepsilon_o} \tag{4}$$

The real part of the complex modulus is the storage modulus and the imaginary part is the loss modulus. The dynamic complex modulus is the absolute value of the complex modulus as represented by:

$$|E^*| = \frac{\sigma_o}{\varepsilon_o} \tag{5}$$

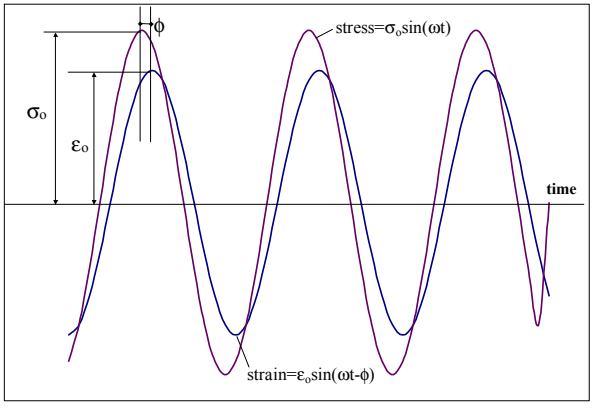

FIG. 1. Stress and strain in dynamic loading

SHAKEDOWN EXPERIMENTAL PLAN

A comprehensive shakedown test was performed the dynamic modulus test in this research to incorporate the factors of load level, test temperature and frequency. The experimental plan of the shakedown evaluation process is shown in Table 1 below.

Table 1 Experimental Plan for the Shakedown Test

Test Temperature (°C)	Test Frequency (Hz)											
	25	**15**	**10**	**7**	**5**	**2**	**1**	**0.7**	**0.5**	**0.3**	**0.1**	**5**
4.4	X	X	X	X	X	X	X	X	X	X	X	X
				X	X	X	X	X	X	X	X	X
							X	X	X	X	X	n/a
									X	X	X	n/a
21.1	X	X	X	X	X	X	X	X	X	X	X	X
				X	X	X	X	X	X	X	X	X
							X	X	X	X	X	n/a
									X	X	X	n/a
37.8	X	X	X	X	X	X	X	X	X	X	X	X
				X	X	X	X	X	X	X	X	X
							X	X	X	X	X	n/a
									X	X	X	n/a

An X in Table 1 represents the planned experimental frequency for an experimental block where five specimens were tested for each row in Table 1. Testing began with the

lowest temperature and proceeded to the next highest temperature until testing had been completed at all test temperatures. At a given temperature, the testing began with the highest frequency of loading and proceeded to the lowest. For each test temperature, a total of five replicates were tested for each strain level and frequency sequence combination to check the repeatability of the test.

TEST RESUTLS AND DATA ANALYSIS

A comprehensive analysis was done to investigate the possible damage accumulation during the test process by the frequency sequence. Here, it is assumed that significant permanent damage can be indicated by the significant change in the dynamic modulus. The main analysis tool used was the t-test, a statistical analysis method used for an evaluating means of small data populations. Analysis results show that no significant difference was found for the two 5Hz data from the same frequency sequence for all test temperatures. All specimens that were used for the first frequency were tested for the second frequency sequence. A same result in the analyses was obtained for the second sequence and the same test specimens were tested in the third frequency sequence. Another t-test was performed using the 0.1Hz data obtained from the three frequency sequences and no significant difference was found. This indicates that the load level employed in this research does not produce permanent damage to the specimen for all the three test temperatures. Therefore, the same test specimens were tested in the fourth frequency sequence. Again, the fourth t-test was executed to analyze the 0.1Hz data from the four frequency sequences. Figure 2 plots one example for the 0.1Hz data from the four frequency sequence at 4.4°C. As a summary, no obvious difference was found between the 5Hz data from the same frequency sequence or between the 0.1Hz data from different frequency sequences. Therefore, the five test specimens were used to perform the dynamic modulus test from the first frequency sequence through the fourth one.

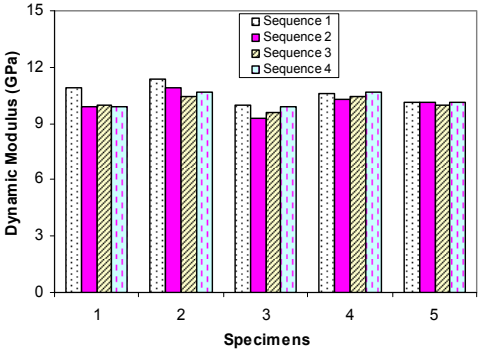

FIG. 2. Dynamic modulus data from the four test sequences at 4.4ºC and 0.1Hz

The influence of the test temperature sequence was also investigated to develop the test protocol. As described in the previous section, dynamic modulus testing was

conducted at a total of five temperatures and the data from these five temperatures of 4.4, 15.0, 21.1, 26.0 and 37.8°C and eleven frequencies (25, 15, 10, 7, 5, 2, 1, 0.7, 0.5, 0.3 and 0.1Hz) at each temperature, was compared to the data from the originally planned three test temperatures of 4.4, 21.1 and 37.8°C and six frequencies (25, 10, 5, 1, 0.5 and 0.1Hz) at each temperature. It is thought that the master curve is the best way to make this comparison. In this study, master curves were constructed fitting a sigmoidal function to the measured compressive dynamic modulus test data using non-linear least squares regression techniques (Pellinen et al., 2002). The shift can be done by solving the shift factors simultaneously with the coefficients of the sigmoidal function. The sigmoidal function is defined by equation 6.

$$\log\left|E^*\right| = \delta + \frac{\alpha}{1 + e^{\beta - \gamma(\log(f_r) + s_T)}} \tag{6}$$

Where: log|E*| = log of dynamic modulus;
δ = minimum modulus value;
f_r = reduced frequency;
α = span of modulus values;
s_T = shift factor according to temperature; and
β, γ= shape parameters.

The master curves from these two temperature groups are shown in Figures 3 and 4. It can be found that almost identical master curves were obtained from the two temperature sequences.

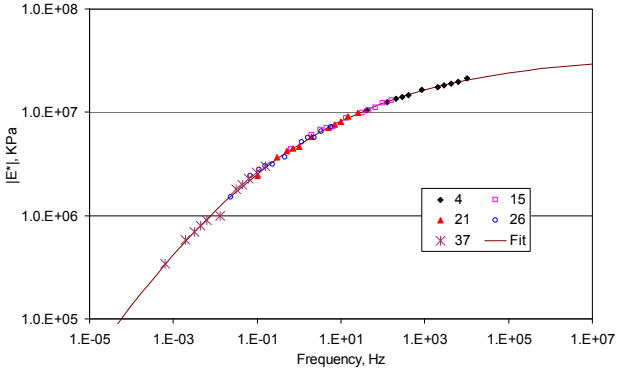

FIG. 3. Master curve from five temperature data

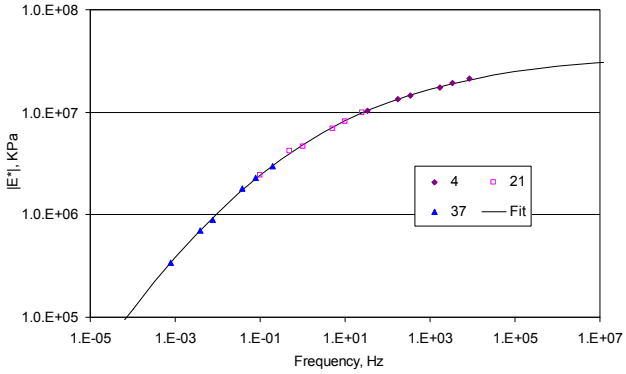

FIG. 4. Master curve from three temperature data

SUMMARY AND CONCLUSIONS

The dynamic modulus test is widely accepted by pavement agencies as the critical parameter for the newly proposed mechanistic empirical design procedure and the candidate of the simple performance test to accompany the Superpave volumetric mix design process. However, the specified dynamic modulus test procedure is time-consuming and costly. State pavement agencies are seeking more practical test protocol.

This paper presents a method for identifying a practical dynamic modulus testing procedure. A comprehensive shakedown test, which incorporates three test temperatures and eleven test frequencies, was performed the dynamic modulus test on one asphalt mixture. The analysis results show that no permanent damage was produced to specimen for all three test temperatures. Comparison of the master curves built by different temperature and frequency combination shakedowns the redundant test temperature and frequency. A more practical dynamic modulus test procedure can be developed using this shakedown method. In this research, it shows that three test temperatures, 4.4, 21.1 and 37.8°C, and nine frequencies, 25, 10, 5, 1, 0.5 and 0.1Hz is adequate to build a smooth master curve for asphalt mixtures. It is estimated that this proposed test protocol would reduce the testing time from 3 work days for the AASHTO TP62 protocol to 1.5 work days and maintain the development of quality master curves.

REFERENCES

American Association of State Highway and Transportation Officials (AASHTO, 2006): "Standard method of test for determining dynamic modulus of hot-mix asphalt concrete mixtures: TP62-03", *AASHTO Provisional Standards*.

ARA, Inc. ERES Consultants Division (2004). "Guide for mechanistic-empirical design of new and rehabilitated pavement structures", *Final Report to the National Cooperative Highway Research Program*.

Bonaquist R. and Christensen D (2005). "A practical procedure for developing dynamic modulus master curves for pavement structural design", *TRB 2005 Annual Meeting CD-ROM, National Research Council*.

Dougan C., Stephens J., Mahoney J., and Hansen G (2003). "E*-dynamic modulus test protocol – problems and solutions," *Report Number: CT-SPR-0003084-F03-3* Connecticut Department of Transportation and Federal Highway Administration.

Ferry J (1980). Viscoelastic Properties of Polymers, John Wiley, New York.

Pellinen T., and Witczak M (2002). "Stress dependent master curve construction for dynamic (complex) modulus," *Journal of the Association of Asphalt Paving Technologists*, vol. 71.

Witczak M., Kaloush K., Pellinem T., El-Basyouny M. and Quintus H. Von (2002). "Simple performance test for Superpave mix design," *National Cooperative Highway Research Program Report 465*, National Research Council.

Witczak M., Kaloush K., and Quintus H. Von (2002). "Pursuit of the simple performance test for asphalt mixture rutting," *Association of Asphalt Paving Technologists (AAPT) Symposium*, Colorado Springs, CO.

Test Method and Performance of Fire-retardant Modified Asphalt Used in Road Tunnel

Qun Yang[1] and Zhongyin Guo[2]

[1]Ph.D., Associate Professor, Department of Road and Airport Engineering,Tongji University, Cao'an Road 4800, Shanghai, China, 201804,Tel : 86-21-69585720, Email:qunyang.w@ tongji.edu.cn
[2]Ph.D., Professor, Department of Road and Airport Engineering,Tongji University, Cao'an Road 4800, Shanghai, China, 201804,Tel : 86-21-65985723,Email:zhongyin@ tongji.edu.cn

ABSTRACT: In the highway tunnel, the asphalt pavement will be used more and more common, and the corresponding fire-retardant asphalt technology research and application is still lacking. In the future, the study should be focused on the special asphalt flame retardant and the processing technology research. Using flash point and ignition point could not distinguish the combustion ability between different types of asphalt with different amount of flame retardant. The oxygen index method could evaluate the sustained combustion performance of asphalt. Based on the oxygen index method used in textiles, put forward a primary oxygen index test method for asphalt. The asphalt flame-retardant evaluation method and standard also should be further refined and adjusted in the future research and application. From the performance test results, it could be found that the addition of fire-retardant is benefit for the pavement-performance of asphalt. For the Magnesium hydroxide agent, the amount of 8% could result in compositive optimal performance of asphalt.

INSTRUCTION

Road tunnel technology has been used commonly in mountainous area such as Japan and some countries in Europe. In Japan, from 1952 to 2000 for 50 years, the number of road tunnel has an increase of nearly 5-fold from 1500 to more than 8000, and the mileage of road tunnel has 4-fold increase from less than 500 km to 2275 km (H.Mashimo 2002). In Germany, in 1998, according to Haack's statistics, the number of road tunnel only constructed by the federal government has reached 157 (Haack A. 1998).

In China, with the improvement of construction technology and cost decrease, the road tunnel has been used widely in highway construction. For example, in Zhejiang Province, there are 79 road tunnels with the mileage of 63.9 km in parts of highway constructed from the year of 2000 to 2004. The pavement in road tunnel is asphalt pavement which is a new trend in China.

Generally, tunnel fire probability is far less than the probability of occurrence in the

wild road. But because of the semi-closed characteristics of road tunnel, in the event of accident, as well as sudden disasters, will cause great casualties and property losses. The longer the road tunnel, the casualties is greater.

Since 1957, when the World Road Association (PIARC) was first established, it has set up a road tunnel group (CS) to start thinking about the safety of the tunnel traffic. At the 18th of the Word Road Conference, the discussion focused on the tunnel security, safety equipment, fire-fighting facilities and the security signs of construction. In 1992, PIARC set up a dangerous good transportation group to examine the tunnel situation in the transport of dangerous goods.

Aiming at the disaster prevention in the road tunnel such as heavy smoke, fire and so on, the international community put forward a number of design recommended value for road tunnel's design standards, such as the installation of ventilation equipment and import and export setting including the number and location (H.Mashimo 2002).

The asphalt road tunnel is increasingly common used, and the flame-retardant asphalt pavement research needs to be given more attention (Yang Qun 2005). The following text will do some preliminary study on the fire-retardant asphalt including the evaluation index, equipment and test method for fire-retardant performance of asphalt and the effect of fire-retardant agent on the asphalt road performance such as soft point, viscosity and so on.

RESEARCH ON THE FIRE-RETARDANT ASPHALT

Asphalt Combustion Evaluation Methods

Evaluation indicators of the safety of asphalt currently use flash point and ignition point. The flash point is used to evaluate asphalt storage safety, and the other is used as construction safety evaluation indicator.

In the process of operation, evaluating the asphalt combustion properties with indicators of flash point and ignition point has some limitations. The reasons are as follows:

(1) Both flash point and ignition point could not be used to evaluate the asphalt sustained combustion, because the burning time of asphalt in the test condition is very short;

(2) For different types of asphalt, including modified asphalt, the proportion of light oil is different, resulting in a weak bond broken and light oil volatilization when reaching a critical temperature. At this time, the difference of the flash point or the ignition point for different asphalts is not significant; therefore they could not be used to compare the fire-retardant properties of different asphalts effectively.

To improve the operation safety of asphalt pavement, its fire-retardant properties must be improved. At home and abroad, fire-retardant performance of asphalt is being researched (Li Zu-wei 2002, Yang Qun 2005), and has gotten some flame retardant products. But the evaluation on the flame-retardant performance of asphalt is still lack of a unified approach. Although some researchers use the oxygen index approach to evaluate asphalt's fire-retardant properties, it is still on the lack of a clear standard, resulting in the lack of comparability of results. It is urgently necessary to study on the standard method that could be used to evaluate the combustion properties of asphalt to guide the fire-retardant asphalt development and production.

Oxygen index are used to evaluate the fire-retardant materials in the textile industry and chemical industry and has formed a national standard with the standard test methods (GB/T 16581 1996, GB 10707 1989, GB/T 5454 1997). The oxygen index can be used to evaluate material's sustained combustion capacity, so it could be used to evaluate the fire-retardant properties of asphalt. But the difficulties of oxygen index test methods and standards applied to the asphalt product testing still exist. Asphalt combustion in room temperature is very difficult, and will be affected by gas flow and velocity. For this reason, we need to research the suitable evaluation procedures of oxygen index method for asphalt.

RESEARCH ON THE OXYGEN INDEX METHOD

Equipment and Test Method

Use the textile chemical industry standards for reference and adopt the equipment named LFY-606-NG oxygen index made by Shandong Province Textile Research Institute in June 2003. Its flow meter accuracy: 0.2L/min for O_2, N_2 for 0.5L/min. Combustion gas source is industrial gas with the concentration of O_2 content$\geqslant$99.5% and the concentration of nitrogen content of$\geqslant$99.5%. Pressure control requirements in accordance with the instructions within the high-pressure cylinder are not less than 15 MPa and gas pressure is between 0.1-0.5MPa. Timer is stopwatch with precision 0.2 seconds. Ignition equipment is a tube with diameter of 2 mm ± 1mm linking to LPG.

Test equipment as shown in Fig.1. The vessel with bitumen sample should be put on the brace, then adjust the gas concentration in the covering to set fire to the bitumen sample.

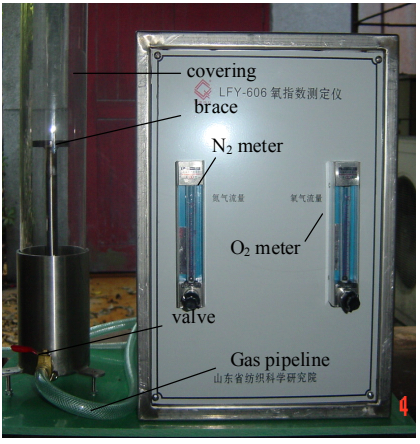

FIG.1. The oxygen-index instrument

The minimum oxygen concentration, known as Limit Oxygen Index (LOI), could provide the sample in oxygen and nitrogen mixed gas maintain a balance of combustion. The use of the formula is expressed as:

$$LOI = \frac{[O_2]}{[O_2]+[N_2]} \times 100\% \quad (1)$$

Where: $[O_2]$ = the oxygen volume flow under condition (L/min); and
$[N_2]$ = the nitrogen volume flow under condition (L/min).

Factors Analysis

Due to the nature of asphalt has great difference from that of the general textiles, the LOI method should adjust to address the inherent characteristics such as combustion performance. The key point is to find the main factors that will affect the sustained combustion test of asphalt. In this text, two main factors are considered, one is the heating temperature of the sample before combustion, and the other is the total gas flow rate to maintain combustion.

1. Heating temperature of sample before combustion

In normal temperature conditions, the asphalt sample could not be ignited, even the oxygen concentration rise nearly 60-80%. Therefore, the asphalt must be heated to a certain temperature to ignition. The specific heat of asphalt has close relation with the temperature. At 0°C, the specific heat of asphalt is 1.672-1.797× 10^{-3}J / (g •°C). when the temperature increases 1 °C, the specific heat of asphalt will increase 1.672-2.058× 10^{-3}J / (g •°C). In different temperature conditions, the asphalt combustion could produce and transfer different heat resulting in the different sustained combustion capabilities because of the different specific heat. The tested LOI will change accordingly. In the same other conditions, the greater the heating temperature of asphalt before combustion, the asphalt sustained combustion time will be longer possibly. Select original asphalt and a modified asphalt, and fix other test conditions including the sample weight, oxygen concentration and the total gas flow rate. Then heat the sample to different temperature prior to combustion. The weight of the sample is 30 g, the oxygen concentration is 19.35%, and the flow rate is 9.3L/min. The test results of sustained combustion time with the heating temperature of the sample are shown in Fig.2:

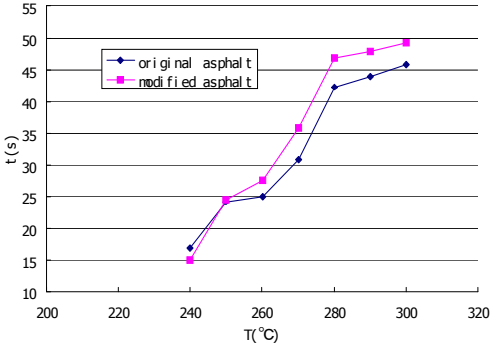

FIG.2. The relationship of heating temperature and the burning time

From the Fig.2, it could be seen that the heating temperature has good relationship with the sustained combustion time, and the combustion duration is longer with the greater heating temperature before combustion. It could also be found that the combustion duration is not change great for original asphalt or modified asphalt when the heating temperature reaches 280 °C. In other words, the heating temperature of 280 °C could provide stable sustained combustion condition for asphalt.

2. Total gas flow rate

In the process of combustion the smoke or gas flow rate has great effect on heat transfer. Great gas flow rate may lead to heat propagation countercurrent resulting in reducing the sustained burning time; meanwhile the heat transfer will speed up which will make the internal heat of the sample not sufficient to maintain the continued burning. Before burning test, fix the specimen weight 30g and heating temperature 280°C. At the same of similar oxygen concentration, test the sustained combustion time under the different total gas flow rate. The results are shown in Table 1.

Table 1. The Burning Time of Different Total Gas Flow Rate

Oxygen concentration (%)	Total gas flow rate (L/min)	Sustained combustion time (s)
19.35	12.4	26.5
19.35	9.3	114
18.8	11.7	21
18.6	8.6	65

From the experimental results, when oxygen concentration is the same as 19.35% and the difference of gas flow rate is 3.1 L / min, the combustion time difference is 87.5 seconds; when the oxygen concentration is near (18.8% and 18.6%) and the gas flow rate difference is 3.1 L / min, the burning time has 44 seconds difference. It could be seen that the gas flow rate has great effect on the burning time, accordingly affecting the determination of oxygen index. The basic rule is that the greater flow rate, the burning time is shorter. Therefore, the test should be done in the condition of controlling the total gas flow rate in a particular area. This requires test equipment to provide high precision flow control.

The Preliminary Test Standard Condition

According to the above analysis, the preliminary test standard conditions could be determined as follows: (1) The sample weight is 30g; (2) The heating temperature before combustion is 280°C; (3) The total gas flow rate is between 10-11.4L/min, and the changes shouldn't exceed 10%; (4) The oxygen index under the sustained burning time 60s is the LOI.

Selection of fire-retardant agent

In the research, choose Magnesium hydroxide as fire-retardant agent which belongs to inorganic type. The important advantage of Magnesium hydroxide is smoke-suppression and heat absorbing. The product's chemical composition is shown in Table 2:

Table 2. The Chemical Composition of Magnesium Hydroxide Product

Chemical composition	$Mg(OH)_2$	$FeO+Fe_2O_3$	SiO_2	CaO	Adsorbed Water
Weight percent (%)	95.8	0.3	2.5	1.2	0.2

Preparation of Fire-Retardant Asphalt

The production of fire-retardant asphalt by following three steps (Li Zu-wei 2002). First, the original asphalt was heated at 110ºC for 30 minutes. Second, it was cut with Styrene-Butadiene-Styrene (SBS) added for 15 min at 175ºC. Finally, it was cut with the fire retarding additive for 10 min.

Compare between Oxygen Index and Flash Point, Ignition Point

Choose a kind of original bitumen and a kind of modified asphalt, and add Magnesium hydroxide agent with 5 weight percent of asphalt respectively. Test the OI value, flash point and ignition point, and the results are shown in FIG.3. In Figure 3, A0 means original bitumen; A1 means original bitumen with Magnesium hydroxide agent; M0 means modified asphalt and M1 means modified asphalt with Magnesium hydroxide agent.

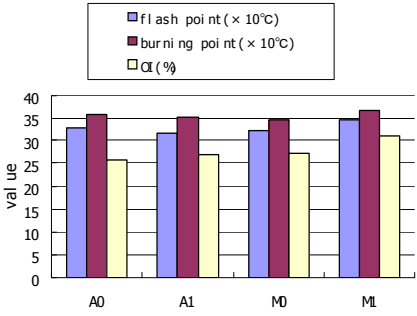

FIG.3. Test results

From the results shown in Fig.3, the difference of flash point or ignition point is not obvious between the specimens with and without Magnesium hydroxide agent for both original bitumen and modified asphalt. Even to original bitumen, the flash point and ignition point have decreased when adding Magnesium hydroxide agent. Meanwhile, the oxygen index value has increased when adding Magnesium hydroxide agent for both original bitumen and modified asphalt. This illustrates that the LOI indicator is reasonable to estimate the sustained combustion characteristic of asphalt and could used to evaluate the fire-retardant effect of different agents.

THE PERFORMANCE OF FIRE-RETARDANT MODIFIED ASPHALT

Select SHELL SBS-modified asphalt, and add Magnesium hydroxide agent with four volume, 0, 5, 8, and 10% of asphalt weight respectively. Test the oxygen index, penetration, softening point, ductility at 5° C and viscosity at 135° C. The purpose is

to analyze the effect of Magnesium hydroxide agent on the performance of asphalt. The test results are shown in from Fig.4 to Fig.7 and Table 3.

Fire-retardant's impact on penetration of asphalt

As can be seen from Fig.4, with the increase in the amount of flame retardants, the penetration will decrease which shows the linear relationship. The addition of flame retardant usually makes the consistency of asphalt become greater, so that the penetration of asphalt will become smaller.

Fire-retardant's impact on high-temperature viscosity

As can be seen from Fig.7, with the increase in the amount of flame retardant, the high-temperature viscosity will increase. This shows that the addition of flame retardant could raise the high-temperature performance of asphalt.

FIG.4. relationship of fire-retardant cont. with penetration

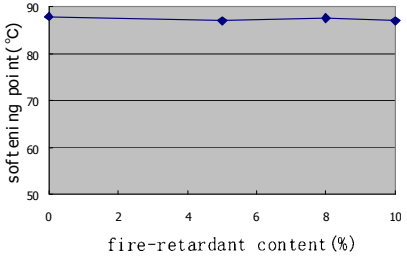

FIG.5. relationship of fire-retardant cont. with soft point

Fire-retardant's impact on softening point of asphalt

As can be seen from Fig.5, the impact on the softening point of asphalt is not obvious under the addition of flame retardant. Asphalt material is a kind of amorphous polymer materials without determined solid point and liquid point.

Fire-retardant's impact on low-temperature ductility

As can be seen from Fig.6, the addition of flame retardant could effectively increase the low-temperature ductility of asphalt. This is because when the flame-retardant

modifier usage increased, the flame-retardant modifier will take cross-linking reaction with asphalt to form the network space structure which will raise the low-temperature ductility.

FIG.6. relationship of fire-retardant cont. with ductility

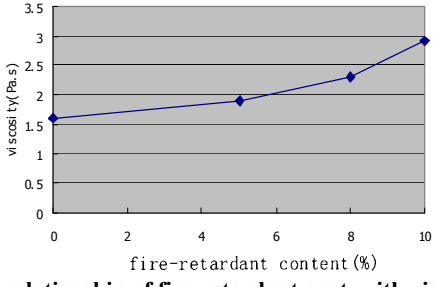

Fig.7. relationship of fire-retardant cont. with viscosity

Fire-retardant's impact on the oxygen index of asphalt

Use the oxygen index test method, and get the test result shown in Table 3. As can be seen from Table 3, with the addition of flame retardant, the asphalt oxygen index will increase rapidly, but the rate of increase will decrease when the amount of flame retardant increase. It could be seen from test results, the increase of the oxygen index is not obvious after the amount of flame retardant exceed 8%. For different bitumen, the reasonable amount of flame retardant will be different. There is a need for different bitumen to determine reasonable amount of flame retardant through the oxygen index test and other performance test, and not the higher the better.

Table 3. Test Results of LOI

Fire-retardant content	Volume of O_2 (L/min)	Volume of N_2 (L/min)	Gross volume (L/min)	LOI (%)
0%	2.5	9.0	11.5	21.74
5%	3.0	8.5	11.5	26.09
8%	3.5	8.5	12.0	29.17
10%	3.6	8.1	11.7	30.77

CONCLUSIONS

Four conclusions could be gotten from above study shown as follows:

1. In the highway tunnel, the asphalt pavement will be used more and more common, and the corresponding fire-retardant asphalt technology research and application is still lacking. In the future, the study should be focused on the special asphalt flame retardant and the processing technology research.
2. Using flash point and ignition point could not distinguish the combustion ability between different types of asphalt with different amount of flame retardant. The oxygen index method could evaluate the sustained combustion performance of asphalt.
3. The asphalt fire-retardant evaluation method and standard should be further refined and adjusted in the future research and application.
4. The addition of fire-retardant is benefit for the pavement-performance of asphalt. For the Magnesium hydroxide agent, the amount of 8% could result in compositive optimal performance of asphalt.

REFERENCES

Haack, A. (1998). "Fire Protection in Traffic Tunnels: General Aspects and Results of the EUREKA Project." *Tunnelling and Underground Space Technology*, Vol. 13, 377-381.

Mashimo, H. (2002). "State of the road tunnel safety technology in Japan." *Tunnelling and Underground Space Technology*, Vol. 17, 145-152.

Li, Z. and Chen, H. (2002). "Study on Technology to improve Flame resistant SBS Modified Bitumen and Its Mechanism." *Journal of Changsha Communications University*, Vol. 18, No. 4, 44-47.

Yang, Q. and Guo, Z. (2005). "Mixture Design of Fire-retarded OGFC in Road Tunnel." *Road Material and Pavement Design*, 221-232.

China. (1996). "Test method of burning performance of insulated liquid-Oxygen index." *GB/T 16581-1996.* The People' Communication Publishing Company, Beijing.

China. (1996). "Test method of burning performance of rubber." *GB 10707-1989.* The People' Communication Publishing Company, Beijing.

China. (1997). 'Textiles-combustion performance test-oxygen index." *GB/T 5454-1997.* The People' Communication Publishing Company, Beijing.

Resilient Modulus Characteristics of Varying Percent of Reclaimed Asphalt Pavement

Yonghui Song[1] S.M. ASCE and Phillip S.K. Ooi[2] M. ASCE, P.E.

[1] Engineer, Geolabs, Inc. 2006 Kalihi Street, Honolulu, HI 96819; yonghui@hawaii.edu
[2] Associate Professor, Department of Civil and Environmental Engineering, University of Hawaii at Manoa, Honolulu, HI 96822; ooi@eng.hawaii.edu

ABSTRACT: Utilization of reclaimed asphalt pavement (RAP) aggregate in highway projects has become common practice in the United States because it has considerable environmental and economical advantages. This study evaluates the resilient modulus (M_r) of a crushed RAP on its own, a basaltic virgin aggregate (VA) on its own as well as when the two are bended for use in pavement base and subbase courses. A series of laboratory tests were conducted to assess their fundamental properties including M_r. Test results show that under the same stress conditions, the resilient modulus of pure RAP is higher than that of VA. The factors influencing M_r are discussed and a model that captures the variation of M_r with stress level, water content and density is proposed. This model is capable of incorporating the effect of percent RAP on M_r. This M_r model will help engineers design roads using recycled materials more expediently, thereby aiding the profession's march towards greener highways.

INTRODUCTION

The concept of resilient modulus (M_r) was originally introduced by Seed et al. (1962). It is a necessary and important input parameter required in the Mechanistic-Empirical Pavement Design Guide or MEPDG (ARA Inc. 2004). The MEPDG's philosophy is that the level of engineering effort to obtain M_r should be consistent with the relative importance, size and cost of the design project. In light of this, the material stiffness characterization falls into one of the following three input levels. In Level 1, M_r is measured directly through testing representing the highest reliability. In Level 2, M_r is estimated from correlations with common soil parameters. In Level 3, M_r is estimated based on just the material classification. Clearly, increasing levels have successively lower reliabilities.

Based on *NCHRP Synthesis 382* (Puppala 2008), the overall satisfaction in the use of M_r for pavement design is low among pavement engineers. This low rating is

mainly attributable to the following 1) constant modification of test procedures; 2) complicated laboratory or field test procedures and correlations required to determine M_r, and 3) design-related issues.

PREVIOUS STUDIES

The K-θ model proposed by Seed et al. (1967) has been widely used in the past for modeling M_r of granular materials. Two limitations of this model include: (1) it is not dimensionally correct. The M_r and bulk stress should be normalized by say the atmospheric pressure prior to raising the latter to a power; (2) multiple stress conditions can give the same modulus. For example, combinations of low confining stress and high deviator stress can result in the same bulk stress and hence, the same M_r, as high confining stress and low deviator stress. The most general form of a M_r model can be expressed with the aid of the three-parameter expression as shown in Eqn. (1) (Ooi et al. 2004).

$$M_R = k_1 p_a \left[f(c)\right]^{k_2} \left[g(s)\right]^{k_3} \tag{1}$$

where

$f(c)$ is a function for confinement,
$g(s)$ is a function for shear,
k_1, k_2 and k_3 are model constants.

In this equation, the function for confinement can be expressed in terms of the minor principal stress (σ_3), bulk stress (θ), or octahedral normal stress ($\sigma_{oct} = p = \theta/3$). The function for shear can be expressed in terms of the deviator stress, σ_d or q, or octahedral shear stress ($\tau_{oct} = \sqrt{2}q/3$ in triaxial compression).

Factors that can increase an aggregate's M_r include: higher relative density; lower water content or higher suction; higher preconsolidation pressure; higher confining stress; lower applied stress; smaller number of load cycles; more well-graded as opposed to a uniform gradation; relatively lower fines content; more angular and rough particles as opposed to rounded and smooth; and larger maximum particle size.

In a repeated load triaxial test to measure M_r, only vertical and horizontal stresses are applied to the sample. They mimic the in situ principal stresses directly beneath the center of the wheel load but do not simulate rotation of principal stresses and shear stresses induced as a wheel load approaches and departs.

Past research demonstrated that RAP showed higher M_r than the dense-graded aggregate base coarse (DGABC) in New Jersey (Bennert et al., 2000); M_r decreased when RAP content increased from 0 to 25 %, then it steadily increased as the RAP content increased from 25% to 100% (Guthrie et al., 2007); M_r increased with an increase in confining pressure, while there was little change in M_r with increasing deviator stress. Specimens with water contents at ~ 65% the value at optimum were stiffer than those at optimum regardless of confining pressure. Base materials with various RAP percentages performed similar to 100% virgin aggregate in terms of stiffness and strength (Kim et al., 2007).

MATERIALS TESTED

RAP, a basaltic virgin aggregate (VA) and a 50%:50% blend of the two materials were tested as part of this work. The VA tested is the Type B crushed basalt obtained from a quarry on the island of Oahu, Hawaii, which is less superior to Type A. Generally, Type B basalt is more vesicular and is used in the layers below pavements (base, subbase and fill), while Type A basalt is used mostly in the manufacture of concrete or hot mix asphalt. Thus, RAP contains the superior Type A basalt while the VA is the inferior Type B variety.

Due to a lack of RAP fines and in an effort to test all the materials at the same gradation, the test gradation used met the State of Hawaii Department of Transportation's (HDOT) 19 mm maximum nominal base coarse requirements except for the percent fines. The gradation is 100% passing 19mm, 40% passing 4.75mm and 0% passing 0.075mm, and the materials are classified as A-1-a (AASHTO) or GW (USCS).

LA abrasion values were measured in accordance with AASHTO T96 to provide an indication of the material's potential for degradation. Specific gravity and absorption were measured in accordance with AASHTO T84 and T85 for fine and coarse aggregates, respectively. The finer aggregates consistently have lower specific gravities and higher absorptions than the coarser ones. Coarse aggregate void content test was conducted in accordance with Method A of AASHTO TP56-99. The void content depends on the particle shape and texture. Using the uncompacted void content, aggregate angularity of different materials with the same grading can be compared.

The moisture-density relationship was determined in accordance with the modified Proctor test (AASHTO T180) Method D. For RAP and its blend, the oven temperature was set at 60ºC when measuring water contents.

Table 1. Summary of Index Properties

Properties	VA		RAP	
Grading A	29		-	
Grading B	27		-	
Grading C	-		33	
Grading D	30		27	
	Fine	Coarse	Fine	Coarse
Apparent specific gravity	2.95	2.79	2.52	2.72
Absorption (%)	10.5	6.7	6.3	2.5
Void Content (%)	56.7		50.0	
Optimum water content (%)	10.8		5.6	
Maximum dry density (kgm^{-3})	1831		2003	
Asphalt content (%)	-		5.8	

TESTING SYSTEM AND SAMPLE PREPARATION

All tests were run using IPC Global Limited's Universal Testing System 25 (Ken de V 2004) consisting of a hydraulic axial stress and pneumatic confining stress

loading system. The system has two external sample LVDTs and a system LVDT. The maximum range of the sample LVDT is 10 mm. The sample LVDT measurements were used to calculate M_r.

The M_r test was run in accordance with ASHTO T 307. All samples were compacted in six equal lifts using a vibratory hammer in a split mold. The resulting compacted specimens measured 100 mm in diameter and 203 mm in height. Two rubber membranes were used in case of puncture of the first membrane. The split mold was removed after applying a vacuum to the sample. Prior to testing, all samples were subjected to 500 cycles of a deviator stress of 95 kPa under a 105 kPa confining pressure for conditioning. This is to better simulate the events occurring during compaction and before traffic loading and to reduce the effects of improper contact between the caps and the specimen.

FACTORS INFLUENCING RESILIENT MODULUS

Effect of water content As the water content increased, the stiffness decreased for VA, RAP and their blends. Water content did not significantly influence the M_r of RAP (FIG. 1), which may be attributable to the fact that it also did not show a great effect on the compaction curve of RAP.

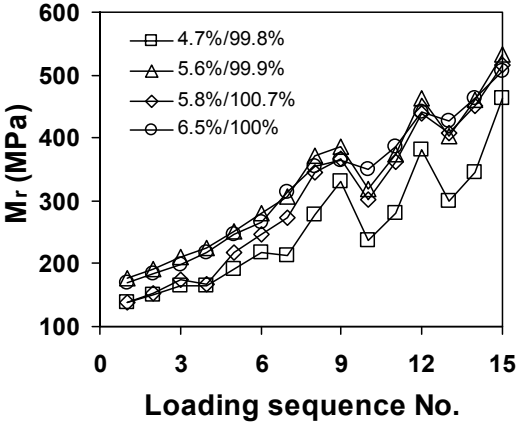

FIG. 1. Effect of water content on M_r for RAP

Effect of dry density In general, M_r increased with increasing dry density. For RAP, the dry density had relatively little influence on M_r.

Effect of stress level Increases in both the confining and deviator stresses led to higher M_r. For all materials, M_r increased approximately linearly with deviator stress at all five confining stresses. The effect of deviator stress on M_r is different for different materials (i.e. the slopes of the M_r curve with deviator stress vary with material type). In general, the RAP blend is more sensitive to confining stress and VA is more sensitive to deviator stress. FIG. 2 shows the effect of deviator stress on M_r for VA and the RAP blend at their respective optimums.

Effect of percent RAP In general, increasing the percent RAP increased the stiffness of the material.

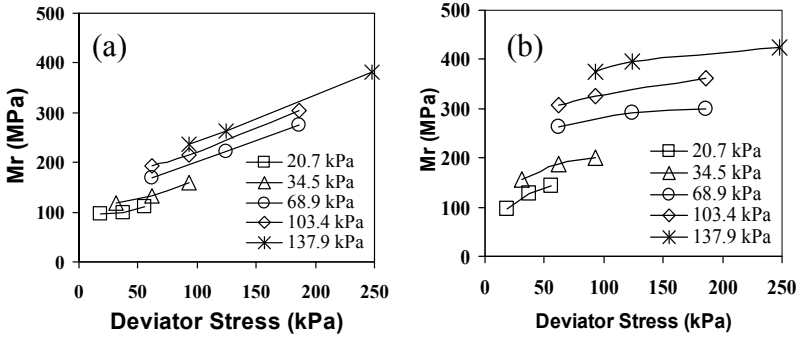

FIG. 2. Effect of Deviator Stress on M_r for VA (a) and for the RAP blend (b)

RESILIENT MODULUS MODELING

Ordinary least squares (OLS) regression analysis was performed using *SPSS Statistics GradPack* version 17.0 distributed by SPSS Inc. In total, 31 samples with 465 M_r data points were adopted in the regression. The equation proposed in the MEPDG (2004) for M_r modeling was adopted as shown below.

$$M_R = k_1 p_a \left(\frac{\theta}{p_a}\right)^{k_2} \left(1+\frac{\tau_{oct}}{p_a}\right)^{k_3} \tag{2}$$

where

θ = bulk stress, kPa,
τ_{oct} = octahedral shear stress, kPa,
p_a = 101.32 kPa, atmospheric pressure,
k_1, k_2 and k_3 are regression parameters.

By relating k_i with the amount of moisture and a measure of compaction, M_r can be correlated to the sample stress and physical states. The parameters S_{zav}-S and e-e_{zav} were adopted instead of the traditional water content and degree of compaction. The corresponding relationships are expressed in Eqn. (3). FIG. 3a illustrates the parameters S_{zav}-S and e-e_{zav} in the compaction curve for VA (left).

The parameters k_i are regressed with S_{zav}-S and e-e_{zav} as shown in Eqn. (3).

$$\begin{aligned} k_1 &= a(S_{zav}\text{-}S) + b(e\text{-}e_{zav}) + c \\ k_2 &= d(S_{zav}\text{-}S) + e(e\text{-}e_{zav}) + f \\ k_3 &= g(S_{zav}\text{-}S) + h(e\text{-}e_{zav}) + i \end{aligned} \tag{3}$$

where
S = degree of saturation,
S_{zav} = 1 = degree of saturation on the zero air void (ZAV) curve,
e = void ratio,
e_{zav} = void ratio at S = 1,
a, b, c, d, e, f, g, h and i are regression constant.

A plot of the measured and predicted M_r for VA using Eqn. (3) is shown in FIG. 3b. Regression results for RAP, VA and their blends are summarized in Table 2

To take this a step further, all the data sets for RAP, VA and their blends can be combined to account for the effect of percent RAP by rewriting Eqn.(3) as Eqn. (4). The regression results are summarized in Table 3 ($R^2 = 0.93$).

$$k_1 = a(S_{zav}-S) + b(e-e_{zav}) + c(\%R) + d$$
$$k_2 = e(S_{zav}-S) + f(e-e_{zav}) + g(\%R) + h \quad (4)$$
$$k_3 = i(S_{zav}-S) + j(e-e_{zav}) + k(\%R) + l$$

where
%R = percent RAP
a, b, c, d, e, f, g, h, i, j, k, l are regression constant.

Most parameters in Tables 2 and 3 have t-values larger than 2.0, indicating statistical significance.

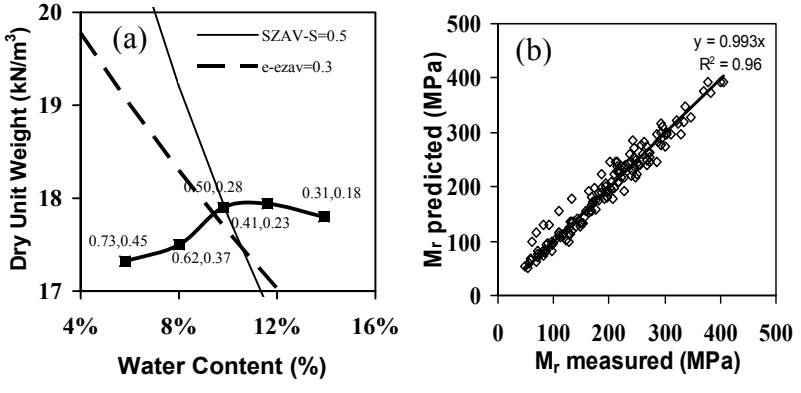

FIG. 3. S_{zav}-S and e-e_{zav} in Compaction Curve (a) and Modeling Results for VA (b)

Table 2. Summary of Regression Results for Each Material

Parameter	RAP		VA		RAP&VA	
	Estimate	t - Statistics	Estimate	t - Statistics	Estimate	t - Statistics
a	-4.08	4.17	5.53	9.03	0.80	2.24
b	6.37	3.90	-6.99	7.45	0.00	-
c	2.60	8.92	0.19	2.19	0.86	5.74
d	-1.08	1.61	-4.15	4.62	-0.35	1.66
e	2.27	2.04	5.79	4.16	0.00	-
f	0.64	3.23	0.91	7.18	0.46	4.87
g	5.75	3.54	4.37	2.16	0.00	-
h	-11.09	4.10	-6.68	2.13	0.00	-
i	-0.77	1.60	0.25	0.91	1.00	-
R^2	0.95		0.96		0.78	

Table 3. Summary of regression results for accounting the %R effect

Parameter	Estimate	Std. Error	t - Statistics	95% Confidence Interval	
				Lower Bound	Upper Bound
a	2.82	0.44	6.48	1.97	3.68
b	-3.75	0.76	4.96	-5.23	-2.26
c	0.33	0.11	2.92	0.11	0.54
d	0.49	0.06	8.34	0.37	0.60
e	-3.19	0.54	5.90	-4.25	-2.12
f	4.78	0.96	4.97	2.89	6.67
g	0.49	0.13	3.64	0.23	0.76
h	0.83	0.07	11.71	0.69	0.97
i	4.50	1.34	3.37	1.87	7.13
j	-7.41	2.40	3.08	-12.13	-2.68
k	-1.17	0.33	3.50	-1.82	-0.51
l	0.28	0.17	1.67	-0.05	0.60

CONCLUSIONS

This paper presented a model that can be used to estimate the M_r of RAP, a Hawaiian basaltic VA and their blends. All factors influencing M_r are captured by the model. They include stress level, water content and density. This model is capable of incorporating the effect of percent RAP in estimating M_r of RAP, VA and their blends. This model showed good predictive capability for the Hawaiian aggregate data set.

ACKNOWLEDGEMENTS

The financial support of the State of Hawaii Department of Transportation (HDOT) in cooperation with the Federal Highway Administration (FHWA) is greatly appreciated and acknowledged. The contents of this paper reflect the view of the authors, and do not necessarily reflect the official views or policies of HDOT and FHWA.

REFERENCES

ARA Inc. (2004). "Guide for Mechanistic-Empirical Design of New and Rehabilitated Pavement Structures - Final Report." National Cooperative Highway Research Program (NCHRP) Project 1-37A, Transportation Research Board, National Research Council.

Bennert, T., Papp, W.J. Ali, M. and Gucunski, N. (2000). "Utilization of Construction and Demolition Debris under Traffic-Type Loading in Base and Subbase Applications." *J. Transportation Research Board* (1714):33-39.

Guthrie, W.S., Cooley, D. and Dennis, L.E. (2007). "Effects of Reclaimed Asphalt Pavement on Mechanical Properties of Base Materials." *J. Transportation Research Board* (2005): 44-52.

Ken de V. (2004). "UTS 009 Unbound Materials Resilient Modulus Test Software Reference." IPC Global Limited.

Kim, W., Labuz, J.F. and Dai, S. (2007). "Resilient Modulus of Base Course Containing Recycled Asphalt Pavement." *J. Transportation Research Board* (2005):27-35.

Ooi, P.S.K., Archilla, A.R. and Sandefur, K.G. (2004). "Resilient Modulus for Compacted Cohesive Soils." *J. Transportation Research Board* (1874):115-124.

Puppala, A.J. (2008). "Correlations for Resilient Modulus Values of Subgrades and Unbound Pavement Materials." NCHRP Synthesis 382, Synthesis of Highway Practice.

Seed, H.B., Chan, C.K. and Lee, C.E. (1962). "Resilience Characteristics of Subgrade Soils and their Relation to Fatigue Failures in Asphalt Pavements." Proc., *International Conference on the Structural Design of Asphalt Pavements*, Ann Arbor:611–636.

Seed, H.B., Mitry, F.G. Monismith, C.L. and Chan, C.K. (1967). "Factors Influencing the Resilient Deformations of Untreated Aggregate Base in Two Layer Pavements Subjected to Repeated Loading." *Highway Research Record,* (190):19-55.

Evaluation of Gradation of RAP Based on Fractal Theory

Xiaoyang Jia[1] and Fen Ye[2]

[1]Ph. D. candidate, Key Laboratory of Road and Traffic Engineering of the Ministry of Education, Tongji University, Shanghai 201804, P.R. China; jxy1982@163.com
[2]Associate Professor, Key Laboratory of Road and Traffic Engineering of the Ministry of Education, Tongji University, Shanghai 201804, P.R. China; yefen@tongji.edu.cn, Corresponding Author

ABSTRACT: This paper introduced fractal theory to the description of gradation of asphalt mixture. The feasibility of description of RAP gradation by fractal theory was firstly discussed. The fractal dimension calculated by Least Square Method (LSM) was employed to evaluate gradation of RAP. Compaction tests, surface-dry condition method tests and indirect tensile strength tests were then employed to evaluate physical and mechanical performance of RAP mixtures stabilized by foamed asphalt. Relationships between fractal dimension and test results were studied. It seems that the fractal dimensions are of relevance to the performance of cold-recycling asphalt mixture. And this points out a new direction of RAP research field.

INTRODUCTION

Cold recycling becomes a technically promising and cost effective method for pavement recycling. Therefore, more attentions are being paid to recycling asphalt pavement (RAP). However, the evaluation of gradation of RAP is still a long way to go. Gradation of RAP varies largely due to the types of structures of pavements, milling speeds of machines, moisture content of pavement, etc. Therefore, it is hard to evaluate types of gradation in traditional way. And this brings difficulties for QA/QC job for cold-recycling project.

The shape of RAP is irregular and it is hard to be quantified. However, fractal theory, which can study things in meso-scope, is a useful research tools to quantify things which are irregular. The application of fractal theory into cold-recycling asphalt mixture could reduce or eliminate the inconvenience of evaluation of gradation of RAP and describe RAP in a more objective way.

LITERATURE REVIEW

Fractal concepts were introduced into the field of road engineering at 1990's: Carr et al. (1990) reported the use of fractals for the characterization of aggregate shape. Lee et al. (1990) employed fractal dimension to quantify the roughness profile of rocks.

They also described shape and angularity of rocks by fractal dimension from the measured data. Perdomo et al. (1991) applied fractal analysis into the classification of particle shape and surface texture of both crushed and uncrushed aggregates when they studied the effects of aggregates on the rutting of asphalt mixture. Ribble et al. (1992) studied macro/microtexture of aggregate particles through fractal theory, meanwhile, they concluded that the workability of concrete mixtures is directly dependent on the fractal dimension of aggregates. Their test results showed that the larger percentage of crushed particles content is, the larger fractal dimension of aggregate particles will be. Similar results were also obtained by Yeggonc et al. (1996) when they studied rutting of asphalt mixture. They thought that fractal dimension of coarse aggregates had relationship with both static and dynamic creep test of asphalt mixture. Kokkalis (1996) gave an overall presentation of fractal methods in road engineering in his paper. In China, Li et al. (1995) developed fractal gradation formula and compared it with the current gradation formula and they thought that fractal was the essence of aggregates gradation. Huang (2006) and Yang (2008) applied the fractal theory into performance evaluation of asphalt mixture synthetically.

FRACTAL THEORY AND ITS APPLICATION IN ASPHALT MIXTURE

Fractal is generally regarded as "a rough or fragmented geometric shape that can be split into parts, each of which is (at least approximately) a reduced-size copy of the whole," (Mandelbrot, B.B., 1982) Therefore, an object which has the characteristic of fractal is called self-similarity. An object is self-similar when it can be broken down into an arbitrary number of small pieces, and each of those pieces is a replica of the entire structure. In mathematics, fractal could be described by a recursive formula. According to the features of fractal, if one point set S could be written as

$$M_d = N(\delta)\delta^d \xrightarrow{\delta \to 0} \begin{cases} 0, \text{when } d > d_f \\ \infty, \text{when } d < d_f \end{cases} \tag{1}$$

Where, M_d represents size of point set S; δ represents line element; $N(\delta)$ represents times of measurement; and here "d_f" is defined as fractal dimension only if M_d is finite. Therefore, "d_f" could be calculated by equation (2). Generally, the value of fractal dimension is a fractional rather an integer.

$$d_f = -\frac{\ln N(\delta)}{\ln \delta} = \frac{\ln N(\delta)}{\ln\left(\frac{1}{\delta}\right)} \tag{2}$$

In asphalt mixture, shapes of fine aggregates are similar to those of coarse ones under the microscope. Therefore, aggregates in asphalt mixture have fractal characteristic. It seems that RAP has the characteristic of self-similarity just like virgin aggregate. Therefore, it is feasible to the application of fractal theory in both virgin aggregates and RAPs such as "black rocks". Following steps show the application of fractal theory into the evaluation of aggregates in asphalt mixture.

Given $N(r)$ represents numbers of particles, diameter of which is over r while $M(r)$ less than r. N_0 is the number of total particles. And it has (3). Distribution function of particles could be written as (4).

$$N(r) + M(r) = N_0 \tag{3}$$

$$\varphi(r) = \frac{M(r)}{N_0} \tag{4}$$

According to the fractal theory, $N(r) = Cr^{-D}$. Then N_0 and $M(r)$ will be;

$$N_0 = N(r_{\min}) - N(r_{\max}) = C\left(r_{\min}^{-D} - r_{\max}^{-D}\right) \tag{5}$$

$$M(r) = N(r_{\min}) - N(r) = C\left(r_{\min}^{-D} - r^{-D}\right) \tag{6}$$

Then, distribution function of particle size could be as follows,

$$\varphi(r) = \frac{M(r)}{N_0} = \frac{r_{\min}^{-D} - r^{-D}}{r_{\min}^{-D} - r_{\max}^{-D}} = \left(\frac{r}{r_{\max}}\right)^{-D} \tag{7}$$

When

$$r_{\max} >> r_{\min},\ \varphi(r) = \left(\frac{r}{r_{\max}}\right)^{-D} \tag{8}$$

Given that $G(r)$ represents the weight of aggregate particles whose diameter are less than r. G_0 is the weight of whole particles. The percentage of aggregates $P(r)$ could be defined as,

$$P(r) = \frac{G(r)}{G_0} \tag{9}$$

According to volume equation,

$$G(r) = M(r)K_v r^3,\ G_0 = N_0 K_v r_{\max}^3 \tag{10}$$

Where, K_v is the volume parameter for aggregate particle. Therefore, equation (9) could be rewritten as,

$$P(r) = \frac{M(r)K_v r^3}{N_0 K_v r_{\max}^3} = \left(\frac{r}{r_{\max}}\right)^{3-D} \tag{11}$$

Here, fractal dimension is D which is employed to evaluate the gradation of aggregate particles for the asphalt mixture, r represents the sieve size. D could be calculated by $r / r_{\max}$ and $P(r)$ in double logarithmic coordinates as Equation (12).

$$\log P(r) = (3 - D)\log\left(\frac{r}{r_{\max}}\right) \tag{12}$$

In double logarithm coordinate, linear fitting could be done by least square method based on $P(r)$ and r/r_{max}. Slope of linear is 3-D. Then, D and correlation coefficient (R^2) could be determined. Ordinarily, D is from 0 to 3.

FRACTAL CHARACTERISTIC OF GRADATION OF RAP

D for RAP at four different milling speeds were calculated by Least Square Method (LSM) and results were listed in Table1. It could be concluded that correlation coefficient (R^2) for RAP is from 0.9741 to 0.9935, which means there was a good linear relationship between $P(r)$ and r/r_{max} in double logarithm coordinate. In other words, the gradation of RAP has the good fractal characteristic.

Table 1 shows that the D reaches its peak at 8m/min, meanwhile, it reached the lowest at 10m/min. It is different from the common sense that milling speed determines size distribution of RAP particles. Ds for coarse and fine aggregate were calculated in Table 2, respectively. It seems that D for coarse RAP (>4.75mm) has good relationship with milling speed. D for coarse RAP decreased with the increment of milling speed which indicates that milling speed could only determine the coarse particle size distribution of RAP (>4.75mm).

D for required gradation by Asphalt Recycling and Reclaiming Association (ARRA) for cold-recycling RAP by foamed-asphalt or emulsified-asphalt agent were also calculated. D is from 2.34 to 2.69 for NMAS-25.0mm. Meanwhile, D for RAP at different speed is from 2.00 to 2.16. It means that the actually gradation of RAP is coarser than what it is required for cold-recycling. Therefore, more fine virgin aggregates should be added in order to meet the gradation requirements for RAP. Generally, range of D for RAP gradation is from 1.90 to 2.10 and the suggested range of D given by some projects or other researchers is from 2.29 to 2.69.(ARRA) So this means that more fine aggregate should be added for RAP.

Table 1. Fractal Parameters for RAP at Different Milling Speed (NMAS-25)

Parameter	Milling Speed (m/min)			
	4	6	8	10
D	2.07	2.11	2.16	2.00
R^2	0.975	0.9741	0.9838	0.9935

Table 2. D of Coarse and Fine Aggregate of RAP at Different Milling Speed

Type	Milling Speed (m/min)			
	4	6	8	10
Coarse RAP	2.56	2.50	2.40	2.14
Fine RAP	1.88	1.92	2.03	2.01

RAW MATERIALS

In this paper, foamed-asphalt mixture was involved. The raw materials employed were listed as follows.

Recycling asphalt pavement

RAP is the combination of waste asphalt pavement materials milled by milling-planing machine and virgin fine aggregates (0-4.75mm). Three test gradations of RAP were involved in this paper showed in FIG.1. All D for test gradations of RAP were calculated and listed in Table 3. And D for the RAP, coarse RAP (>4.75mm) and fine RAP (<4.75mm) were calculated respectively.

Table 3. D of RAP for Different Test Gradations

Items		No. of Test Gradation		
		1	2	3
Type of gradation	RAP	2.48	2.50	2.54
	Coarse RAP	2.57	2.61	2.67
	Fine RAP	2.46	2.47	2.48

Asphalt binder

According to the < Technical Specifications for Construction of Highway Asphalt Pavement, JTG F40-2004>, 70# asphalt (A-level) was utilized as foamed asphalt. The optimum foaming conditions in which the foamed asphalt mixture is mixed were determined by foaming experiment: foaming temperature is 150℃; foaming water content is 1.5%; expansion ratio is 11; half life is 12s.

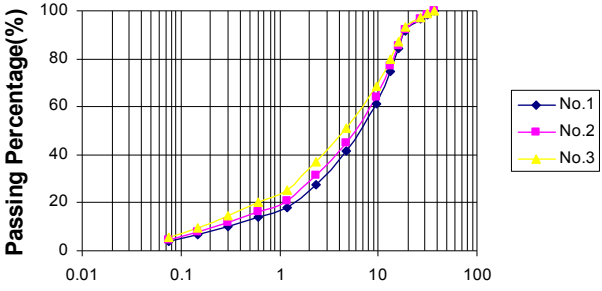

FIG. 1. Gradation curves of RAP

SPECIMENS PREPARATION AND MEASUREMENT

In this paper, compaction tests were first employed to determine optimum moisture content and maximum dry density of RAP. Then mixing water content could be determined according to optimum moisture content. Specimens were compacted according to Marshall Methods, 75 times for each side. All specimens were cured for 72 hours at 40°C. After the specimens were prepared, the bulk relative densities of specimens were measured by surface-dry method tests. Then indirect tensile stress (ITS) was measured at 25°C.

RELEVANCE OF RAP PERFORMANCE AND FRACTAL DIMENSION

Relevance of physical performance of RAP and fractal dimension

In Table 4, it seems that both the optimum water content, maximum dry density and bulk volume density increase with the increment of fractal dimension.

Reasons for this lie in the structure of mixture of foamed asphalt stabilized RAP. Larger D for RAP leads to the finer gradation. So the specific surface area for RAP will be higher. RAP then would absorb more water in the process of compaction which results in higher optimum water content of RAP.

As for the maximum dry density and bulk volume density of RAP, the increment of D makes the gradation of RAP finer. So there will be an increment in the number of particles in unit volume which results in the increase in density.

It seems that D for fine RAP mostly affect physical performance of RAP which means the distribution of fine RAP in the asphalt mixture will have more influence on the compaction characteristic of RAP material than coarse RAP. And this will give theoretical reference to the pavement construction.

Relevance of mechanical performance of RAP and fractal dimension

Indirect tensile strength test (ITST) was employed to evaluate the mechanical performance of RAP. Table 4 indicated that relationships of fractal dimension of RAP and *ITS* at different foamed asphalt content were different.

For 1.6% foamed asphalt content, *ITS* reaches its peak at the RAP fractal dimension of 2.50. Then *ITS* decreases with the increment of fractal dimension. For 2.0% foamed asphalt content, there was also a peak when D=2.50. However, D has slight influence on *ITS* after D=2.50. As for 2.5% foamed asphalt content, *ITS* increased with the increment of D.

In foamed asphalt mixture, asphalt mastic which is composed of asphalt foam mixed with fine aggregates and filler contributes the cohesion for asphalt mixture. With the increase of D, the gradation of *RAP* becomes finer. At low foamed asphalt content, there is not enough foamed asphalt mixed with fine aggregates and fillers to form asphalt mastic. Therefore, *ITS* is relatively low with the increase of D (for example, D=2.54). At higher asphalt content, there will be enough asphalt to form asphalt mastic which results in the higher *ITS* value. This showed that the increment of both D and asphalt content will lead to the increment of *ITS.* And this would determine the characteristic of compaction of RAP.

CONCLUSIONS

In this paper, fractal theory was introduced into the analysis of characteristic of gradation of RAP. D was adopted to evaluate gradation of RAP. Foamed asphalt stabilized RAP mixture was the research object in this paper. From the tests, it seems that there is a good relationship between D and performance of RAP mixtures. The main conclusions in this paper are as follows.

- Gradation of RAP has the fractal characteristic.
- Milling speed only determine distribution of coarse RAP (>4.75mm).
- Optimum water content and density increase with the increment of D.
- Increment of D and asphalt content will increase *ITS.*

Table 4. Fractal dimension of test gradations

Items		No. of Test Gradation		
		1	2	3
Optimum water content (%)		5.8	6.4	6.6
Maximum dry density (g/cm^3)		2.16	2.18	2.23
Bulk volume density @ different foamed asphalt content (%) (g/cm^3)	1.6	2.18	2.21	2.25
	2.0	2.21	2.23	2.28
	2.5	2.23	2.25	2.3
ITS @ different foamed asphalt content (%) (MPa)	1.6	0.3	0.53	0.45
	2.0	0.36	0.56	0.54
	2.5	0.33	0.55	0.65

REFERENCES

Mandelbrot, B.B. (1982). *The Fractal Geometry of Nature*. W.H. Freeman and Company. ISBN 0-7167-1186-9.

Lee, Y.H., Carr, J.R., Barr, D.J., and Haas, C.J.(1990). "Fractal dimension as a measure of the roughness of rock discontinuity profiles", *International journal of rock mechanics and mining sciences & geomechanics abstracts*, Vol 27 (6): 453-464.

Ribble, C., Szecsy, R. and Zollinger ,D.G..(1992) "Aggregate macro shape and micro texture in concrete mix design". ASCE Spring Meeting, New York.

Carr, J. R., Norris, G. M., and Newcomb, D. E., (1990) "Characterizations of aggregate shape using fractal dimension". *TRR 69th. Annual Meeting*, Washington. DC.

Perdomo, D. and Button, J. W., (1991) "Identifying and correcting rut susceptible asphalt mixtures". *TRR 1259*, TRB, Washington, DC.

Yeggonc M., Button, J. W. and Zollinger, D. G., (1996) "Fractals of aggregates correlated with creep in asphalt concrete". *ASCE Journal of Transportation Engineering*. Vol. 122 (1): 22-28

Kokkalis, A. G., (1996) "Fractal principles in highway and pavement engineering". *4th National Conference on the Complexity and Chaotic Dynamic of Non-linear Systems*, Patra, Greece.

Li, G., and Deng, X. (1995). "On Fractal Gradation of Aggregates". *Journal of Chongqing Jiaotong Institute*, Vol. 14 (2): 38-43. In Chinese.

Huang, J. (2006). "Research on asphalt mixtures performances by nonlinearity theories". PhD thesis. Tongji University. Shanghai, P.R.China. In Chinese.

Yang, R. (2008). "Study on the design theory and method for asphalt mixture based on fractal theory". PhD thesis. Tongji University. Shanghai, P.R.China. In Chinese.

Evaluation of Cracking Resistance of Recycled Asphalt Mixture Using Semi-Circular Bending Test

Xiang Shu[1], Baoshan Huang[2], and Dragon Vukosavljevic[3]

[1] Research Assistant Professor, Department of Civil and Environmental Engineering, University of Tennessee, Knoxville 37996 USA; xshu@utk.edu
[2]Associate Professor, Department of Civil and Environmental Engineering, University of Tennessee, Knoxville 37996 USA; bhuang@utk.edu
[3]Formerly research assistant, Department of Civil and Environmental Engineering, University of Tennessee, Knoxville 37996 USA

ABSTRACT: The objective of this laboratory study is to utilize the semi-circular bending (SCB) test to evaluate the effect of reclaimed asphalt pavement (RAP) on the cracking resistance of asphalt mixtures. Two type of SCB test, the tensile strength and the fracture test, were conducted on a gravel mixture containing four percentages of RAP. The results show that RAP generally increased the SCB tensile strength but significantly decreased the post-failure tenacity of asphalt mixtures. RAP also decreased the J-integral of asphalt mixture and therefore its cracking resistance. Both short-term and long-term aged asphalt mixtures exhibited similar trend in evaluating the effect of RAP.

INTRODUCTION

Recycling of reclaimed asphalt pavement started in the early 20th century (Taylor 1978) and recently has been gaining more and more popularity in the United States (McDaniel et al. 2000). Unlike with other recycled materials (such as crushed concrete), the possibility of utilizing the old asphalt binder into the newly blended mixtures, and therefore reducing the required (new) asphalt content, makes the use of RAP in hot-mix asphalt (HMA) mixtures both environmentally friendly and economically attractive (Huang et al. 2004).

Numerous research efforts has been made on the use of RAP in HMA mixtures (Huang et al. 2004, 2005a, Roberts et al. 1996, Solaimanian and Tahmoressi 1996, Kennedy et al. 1998, McDaniel et al. 2000, Kandhal and Foo 1997, Shu et al. 2008). RAP has been proven to be a reliable constituent in HMA mixtures (Paul 1996, Hossain et al. 1993, Epps et al. 1978). Recent studies indicated that RAP could be effectively used with Superpave mix design procedure as well (McDaniel et al. 2000). Using the staged extraction and recovery method, Huang et al. (2005b) found that only a small portion of aged asphalt in RAP actually participated in the remixing process. It has been

documented that when properly applied, HMA mixture with RAP can perform at least as well as conventional mixtures (Paul 1996, Hossain et al. 1993, Epps et al. 1978).

Despite the numerous studies on RAP, some concerns still exist about the possible negative impacts on the performance of asphalt mixtures. One major concern is about the resistance of HMA mixtures to fatigue cracking, which is closely related to the aged, stiffened, and embrittled asphalt in RAP (Huang et al. 2004, Shu et al. 2008). This paper presents the results from a laboratory study in which the cracking resistance of plant-produced HMA mixtures containing different percentages of RAP was evaluated using the SCB test.

OBJECTIVE AND SCOPE

The objective of this study is to utilize the SCB test to evaluate the effect of RAP on the cracking resistance of HMA mixtures. One type of coarse aggregate, gravel, and one type of asphalt binder, PG 64-22, were used in the mixtures. Both short-term and long-term aged mixtures containing four percentages of RAP, 0%, 10%, 20%, and 30%, were evaluated in this laboratory study using two types of SCB test, the tensile strength and the fracture tests.

LABORATORY EXPERIMENT

The HMA mixture used in the laboratory study was acquired from a field project in which test sections of HMA with different RAP percentages were constructed for long-term observation. The asphalt binder was a conventional PG64-22. The coarse aggregate used in the HMA mixture was gravel with a nominal maximum size of 12.5 mm. The mixtures also consisted of fine materials that included No.10 screenings, natural sand, agricultural lime, and screened RAP (materials passing No.4 sieve sizes). Fig. 1 presents the mixture gradations.

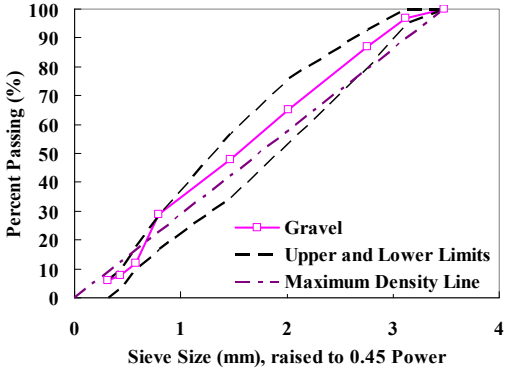

FIG. 1. Aggregate gradation

The RAP used in this study was screened through the No. 4 sieve (4.75 mm) to acquire a consistent gradation that was comparable to the fine aggregate. The optimum asphalt

cement (asphalt from RAP plus virgin asphalt) was 5.8% by the weight of the mix. HMA mixture volumetric properties are listed in Table 1. Cylindrical specimens 150 mm in diameter were compacted to the air voids of 4± percent with the Superpave Gyratory Compactor (SGC) and then cut into the semi-circular shape with a thickness of 25 mm. One half of the finished specimens were placed a drafty oven at 85℃ for 5 days to simulate the long-term aging of the asphalt mixtures.

Table 1. Volumetric Properties of HMA Mixture

AC (%)	Gmm	Gmb	Air Voids (%)	VMA (%)	Stability (kN)	Flow (mm)
5.8	2.360	2.265	4.0	17	13.0	2.77

In recent years, the SCB test has drawn more and more attention in the asphalt research community and many researchers have used it to evaluate the fracture resistance of asphalt mixtures (Mull et al. 2002, Wu et al. 2005). Two types of SCB test were conducted in this study: the SCB tensile strength and the SCB notched fracture tests (Fig. 2). In the SCB tensile strength test, the specimen was loaded at 25℃ at a constant rate of 50 mm /min. until failure occurred. The applied load and the resulting deformation at the bottom of the specimen were continuously recorded during the testing. Huang et al. (2005b) developed the following equation to calculate the SCB tensile stress under the condition the distance between the two bottom supports is two thirds of the diameter of specimen:

$$\sigma_x = 3.564\frac{P_{\text{ult}}}{Dt} \tag{1}$$

where σ_x – maximum tensile stress at the bottom of the specimen; P_{ult} – load per unit width of the specimen at failure; D – diameter of specimen; and t – thickness of specimen.

Once the SCB tensile stress and strain are known, the toughness index (TI) parameter can also be calculated in the similar way for the indirect tension test (Huang et al. 2004).

The SCB fracture test was conducted on notched specimens at 25℃ at a constant rate of 0.5mm/min to obtain the critical value of J-integral or the fracture resistance (Mull et al. 2002; Wu et al. 2005). Three notch depths were used in this study: 12.5mm, 25.4 mm, and 38 mm. The area under the load vs. vertical deflection curve up to the maximum load represents the strain energy to failure and was calculated for each notch depth. The critical value of J-integral can be determined with the following equation:

$$J_c = -\left(\frac{1}{b}\right)\frac{dU}{da} \tag{2}$$

where J_c – critical value of J-integral; b – thickness of the specimen; a – notch depth; and U – strain energy to failure.

Table 2 summarizes the test plan for the SCB tests and the parameters used for

characterization of the recycled asphalt mixtures.

(a) SCB tensile strength test

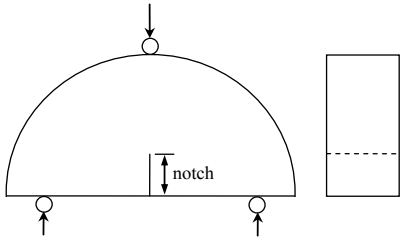

(b) SCB notched fracture test

FIG. 2. Two types of SCB test

Table 2. SCB Test Plan and Parameters

SCB Test Type	**SCB Tensile Strength Test**			**SCB Notched Fracture Test**	
Parameters	Tensile Strength	Tensile Strain at Peak Load	Toughness Index (TI)	Strain Energy	J_c

RESULTS AND DISCUSSION

The results from the SCB tensile strength test are shown in Figs. 3 – 5. It is clearly observed that HMA mixtures containing higher percentages of RAP had a higher tensile strength than those with less RAP, which indicates that RAP could increase the tensile strength of the HMA mixtures. The increased tensile strength could be attributed to the aged and stiffened asphalt binder in RAP, which has become much harder than virgin asphalt after many years of pavement service (Roberts et al. 1996). The increased strength was helpful to some extent in protecting asphalt pavements against cracking under traffic loads. Compared to the short-term aging, the long-term aging process slightly increased the SCB tensile strength of asphalt mixtures.

The strain values at peak load in the SCB tensile strength test can be used to evaluate the HMA mixture properties before failure (Huang et al. 2004). Fig. 4 shows that with the increase in RAP content, HMA mixtures experienced decreased strain at peak load. This indicates that the ability of HMA mixtures to accommodate deformation before they fail was decreased with the increase in the RAP content. This indicates that recycled asphalt mixtures were more brittle than the control mixture. The increased brittleness of HMA mixtures containing RAP was caused by the aged and embrittled asphalt binder occurring during its aging process. Fig. 4 also shows that the long-term aging process significantly reduced the strains at peak load of HMA mixtures.

The toughness index (TI) is used to characterize the post-peak load carrying capacity of asphalt mixtures (Huang et al. 2004). The TI values of recycled asphalt mixtures containing different RAP percentages are shown in Fig. 5. It can be seen that

the TI values of HMA mixtures decreased with the increase in RAP content. This means that incorporation of RAP into HMA mixture compromised its toughness and reduced its ability to further withstand traffic loads, which would significantly reduce its cracking resistance and thus the fatigue life of asphalt pavements. The higher the RAP content, the greater the decrease in the cracking resistance of asphalt mixtures. Compared to the short-term aging, the long-term aging further reduced the TI values of HMA mixtures.

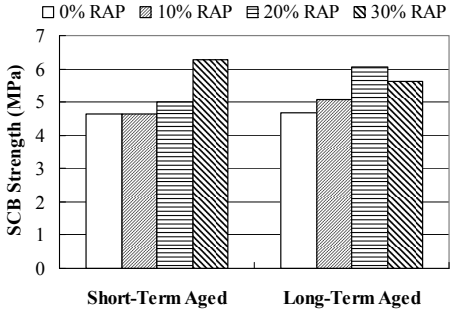

FIG. 3. SCB tensile strength results

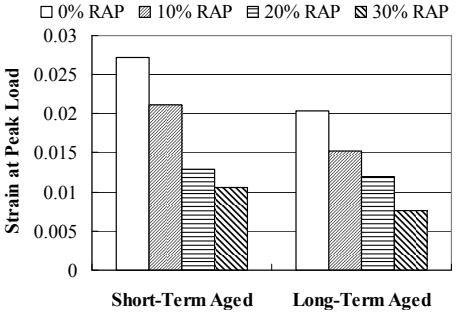

FIG. 4. Strain at peak load

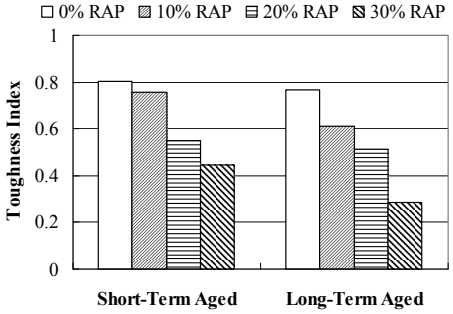

FIG. 5. TI results

The results from the SCB fracture test are presented in Figs. 6 – 7. Fig. 6 shows the change of the strain energy dissipated in one unit-thickness specimen (U/b) with the notch depth for the short-term aged specimens. The slope of the strain energy vs. notch depth represents the J-integral. The HMA mixture with a higher J-integral usually has a higher fracture resistance.

Fig. 7 shows that the J-integral values of HMA mixtures containing different percentages of RAP. It can be seen that HMA mixtures containing higher RAP contents generally exhibited lower J-integral values, which means that incorporation of RAP into asphalt mixture decreased its J-integral value and therefore its resistance to cracking. The short-term aged mixtures containing 20% and 30% of RAP experienced a significant decrease in J-integral, whereas only 30% RAP mixture showed a significant decrease in the J-integral after long-term aging. The J-integral values did not show significant differences for the long-term aged mixtures containing less than 20% RAP.

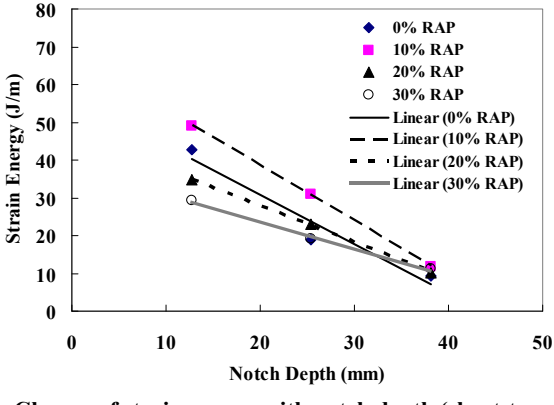

FIG. 6. Change of strain energy with notch depth (short-term aged)

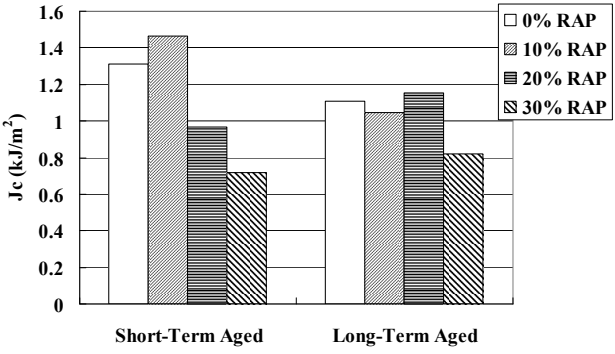

FIG. 7. Jc results

CONCLUSIONS

A laboratory study was conducted to utilize the SCB test to evaluate the effect of RAP on the cracking resistance of HMA mixtures. Based on the results from the laboratory test, the following conclusions can be summarized:

- The incorporation of RAP into HMA mixtures generally increased the tensile strength and reduced the strain at peak load and the toughness in the SCB tensile strength test.
- The addition of RAP into HMA mixtures generally reduced the J-integral values and therefore the cracking resistance, especially for the short-term aged mixtures.
- Long-term aging slightly increased the tensile strength and significantly reduced the strain at peak load and the toughness index. Long-term aging did not show a clear effect on the J-integral of HMA mixtures.
- The SCB test, including the tensile strength and the fracture tests, was a potentially effective tool in evaluating the cracking resistance of HMA mixtures.
- The conclusions are specific to the mixtures tested in this study and should not be generalized to other HMA mixtures without verification.

ACKNOWLEDGMENTS

The authors would like to acknowledge the financial support from the Tennessee Department of Transportation.

REFERENCES

Epps, J.A., Little, D.N., O'Neal, R.J., and Gallaway, B. M. (1978). "Mixture properties of recycled central plant materials.", Recycling of Bituminous Pavements (STP 662), ASTM, Philadelphia/PA: 68-103.

Hossain, M., Metcalf, D.G., and Scofield, L.A. (1993). “Performance of recycled asphalt concrete overlays in Southwestern Arizona.” *Transportation Research Record 1427*, Washington, D.C.: 30-37.

Huang, B., Kingery, W.R., Zhang, Z. (2004). “Laboratory study of fatigue characteristics of HMA mixtures containing RAP.” *Proceeding, International Symposium on Design and Construction of Long Lasting Asphalt Pavements*, Auburn/AL: 501-522.

Huang, B., Li, G., Vukosavljevic, D., Shu, X., and Egan, B.K. (2005a). "Laboratory investigation of mixing hot-mix asphalt with reclaimed asphalt pavement." *Transportation Research Record 1929*, Washington, D.C.: 37-45.

Huang, B., Shu, X., and Zuo, G. (2005b). “Laboratory evaluation of semi-circular bending tensile strength test for HMA Mixtures.” 84th Annual Meeting of the Transportation Research Board, Washington, D.C., CD-ROM.

Kandhal, P. and Foo, K.Y. (1997). “Designing recycled hot asphalt mixtures using Superpave technology.” NCAT Report No. 96-5, Auburn/AL: 7-22.

Kennedy, T.W., Tam, W.O., Solaimanian, M. (1998). “Optimizing use of relaimed asphalt pavement with the Superpave system.” *Journal of the Association of Asphalt Paving Technologists*, Vol. 67: 311-328.

McDaniel, R.S., Solymani, H., Anderson, R.M., Turner, P., and Peterson. R. (2000). *Recommended Use of Reclaimed Asphalt Pavement in the Superpave Mix Design Method*, NCHRP Project 9-12, National Cooperative Highway Research Program, Washington, D.C.

Mull, M.A., Stuart, K., and Yehia, A. (2002). "Fracture resistance characterization of chemically modified crumb rubber asphalt pavement." *J. Mater. Sci.*, Vol. 37(3): 557-566.

Paul, H.R. (1996). “Evaluation of recycled projects for performance.” *Journal of the Association of Asphalt Paving Technologists*, Vol. 65: 231-254.

Roberts, F.L., Kandhal, P.S., Brown, E.R., Lee, D.Y., Kennedy, T.W. (1996). *Hot Mix Asphalt Materials, Mixture Design, and Construction*, 2nd Edition, NAPA Education Foundation, Lanham/MD.

Shu, X., Huang, B., and Vukosavljevic, D. (2008). "Laboratory evaluation of fatigue characteristics of recycled asphalt mixture." *Constr. Build. Mater.*, Vol. 22(7):1323-1330

Solaimanian, M. and Tahmoressi, M. (1996). “Variability analysis of hot-mixed asphalt concrete containing hgh percent reclaimed asphalt pavements.” *Transportation Research Record 1543*, Washington, D.C.: 89-96.

Taylor, N.H. (1978). “Life expectancy of recycled asphalt paving.” Recycling of Bituminous Pavements (STP 662), ASTM, Philadelphia/PA: 3-15.

Wu, Z., Mohammad, L.N., Wang, L.B., and Mull, M.A. (2005). "Fracture resistance characterization of superpave mixtures using the semi-circular bending test." Journal of ASTM International, Vol. 2(3):135-149.

Deformation Characteristics of Asphaltic Concrete in Uniaxial Compression

Warat Kongkitkul[1], Patcharee Issaro[2], Pornkasem Jongpradist[3] and Sompote Youwai[3]

[1]Lecturer, Department of Civil Engineering, King Mongkut's University of Technology Thonburi, Bangkok, 10140 Thailand; warat.kon@kmutt.ac.th
[2]Graduate student, ditto
[3]Assistant Professor, ditto

ABSTRACT: A series of unconventional unconfined uniaxial compression tests were performed on cylindrical specimens of compacted hot-mix asphaltic concrete. Not only continuous monotonic loading tests at different constant strain or load rates but also sustained loading tests and minute cycles of unload/reload during otherwise monotonic loading were performed. Axial and radial strains were measured locally respectively by a pair of local deformation transducers (LDTs) and a set of three clip gauges. Therefore, it becomes possible to precisely evaluate: 1) initial Young's moduli (E_o) and Poisson's ratios (ν_o); 2) equivalent elastic Young's moduli (E_{eq}) and Poisson's ratios (ν_{eq}) for different axial stress values; and 3) tangential stiffness values (E_{tan}) and Poisson's ratios (ν_{tan}) which vary with an increase in the axial stress. Then, it becomes possible to predict the deformation of HMA from a given loading history based on the elastic theory when all parameters above can be determined.

INTRODUCTION

Hot-mixed asphalt (HMA) is popularly used as the flexible pavement of a road structure which may due likely to, for example, its good-performance and ease of construction. However, the application of HMA is currently expanded to other constructions such as impermeable sealing core of earth and embankment dams (e.g., Hoeg et al., 2007; Feizi-Khankandi et al., 2008), which requires more realistic considerations for the properties of HMA than the ones in the past for pavement design. Moreover, it was found from many researches in the past that the stress-strain curves of HMA and subsequent properties derived were determined mostly from conventional tensile and compressive tests without any local measurement to obtain the deformation values that are free from measuring errors including system compliance, bedding errors, etc. Considering all the above, the conventionally determined properties of HMA may not be sufficiently accurate and therefore it is not possible to realistically determine its stress-strain properties.

TEST MATERIALS AND PREPARATIONS

HMA specimens used in this study were prepared by hot-mixing the sieved and cleaned aggregate with asphaltic cement of AC 60/70 grade at the optimum asphaltic cement content of 5 % by weight of aggregate which was determined based on the Marshal's test results (Thaisri et al., 2007). Both asphaltic cement and aggregate were heated in an oven for about two hours at temperature of 140±5 ℃ and then brought out for mixing within one minute. Then, HMA specimens were compacted manually, by using a rubber hamper and a steel rod, into five equivalent layers in a steel mould (75 mm in diameter and 150 mm in height), with a controlled thickness of a compacted layer of about 30 mm and different controlled densities of: 1.90 g/cm^3 (HMA-1), 2.15 g/cm^3 (HMA-2) and 2.37 g/cm^3 (HMA-3). Then, after the temperature has decreased to be lower than 60 ℃, the specimen was removed from the mould and wrapped with plastic film. Subsequently, each specimen was cured at least for 16 hours before the start of test (Issaro et al., 2009).

The friction which may be mobilised at the contact between the ends of specimen and the cap and pedestal was eliminated by smearing a 50-μm thick layer of high vacuum silicone grease onto the cap and pedestal and placing respective 0.3 mm-thick latex rubber sheet onto them. In this study, it was found that irregularity associated with surface smoothening by hands after compaction at the top end of the specimen may create significantly inhomogeneous deformation of the specimen and may greatly affect the measurement of the axial strain. Therefore, in order to eliminate such errors, a thin layer of wet soft gypsum was pasted between the latex rubber sheet and the top end of specimen as well as between the latex rubber sheet and the bottom end of specimen (e.g., Abdelrahman et al., 2008).

TEST APPARATUSES AND MEASUREMENTS

In order to perform a series of unconventional unconfined uniaxial compression tests, two types of loading apparatus were used in this study. Apparatus A is of strain-controlled loading type which was used to obtain the maximum vertical stress for respective densities of HMA. And, apparatus B is of stress-controlled loading type which was used to perform tests with multiple loading histories including monotonic loading (ML) at a constant stress rate, sustained loading and cyclic loading tests during otherwise ML.

A load cell was used to measure the vertical load. On the other hand, in addition to LVDT for measuring the 'external' vertical strain from the vertical displacement of the loading piston, a pair of local deformation transducers (LDTs; Goto et al., 1999) was installed on the opposite side of a specimen to measure the 'local' vertical strain without any bedding errors associated with unexpected minute-gaps at both top and bottom ends of specimen. Moreover, the horizontal strain was measured by means of a set of clip gauges (CGs), which were positioned at the heights of 1/6, 1/2 and 5/6 of the initial height of specimen from the bottom. The locally measured vertical and horizontal strains reported in this study were those obtained by averaging the readings of a pair of LDTs and a set of three CGs, respectively.

DEFINITION OF STRESS-STRAIN PROPERTIES

In this study, a combination of tangent modulus for major principal strain increment taken place in the vertical direction, E_v, and the Poisson's ratio for major and minor principal strain increments taken place in the vertical and horizontal directions, ν_{vh}, was defined as follows:

$$E_v = \left[\frac{\Delta\sigma_v}{\Delta\varepsilon_v}\right]_{(\sigma_h=\text{constant})} \quad (1)$$

$$\nu_{vh} = -\left[\frac{\Delta\varepsilon_h}{\Delta\varepsilon_v}\right]_{(\sigma_h=\text{constant})} \quad (2)$$

Where $\Delta\sigma_v$, $\Delta\varepsilon_v$ and $\Delta\varepsilon_h$ are vertical stress increments, vertical and horizontal strain increments, respectively.

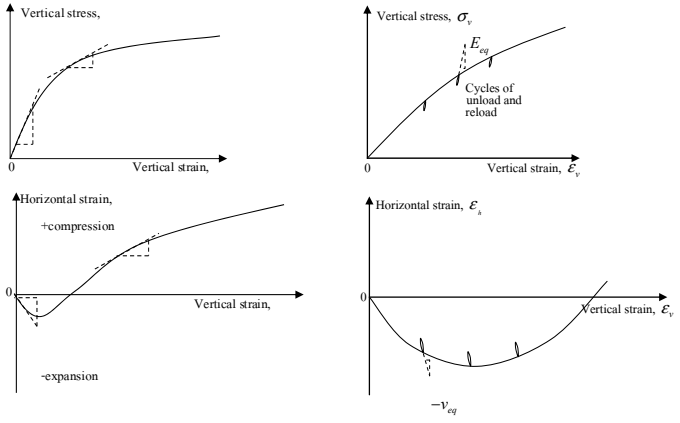

FIG. 1. a) Tangent parameters during monotonic loading; and b) equivalent parameters during cycles of unload and reload (after Abdelrahman et al., 2008)

As the stress-strain behaviour of HMA is generally non-linear, a set of Young's moduli, E_o, E_{tan} and E_{eq}, and a set of Poisson's ratios, ν_o, ν_{tan} and ν_{eq}, that are explained below are defined based on Eqns. 1 and 2 as follows:

1. From the ML tests, the initial modulus and Poisson's ratio, E_o and ν_o, were determined as shown in Fig. 1a.
2. Tangent modulus and Poisson's ratio, E_{tan} and ν_{tan}, at respective stress levels were then deduced as shown in Fig. 1a.

3. Equivalent modulus and Poisson's ratio, E_{eq} and ν_{eq}, which were defined at minute-cycles of unload and reload, were evaluated as shown in Fig. 1b. The average of readings from the last five unload branches from the total of ten cycles at each stress level was obtained.

TEST RESULTS AND DISCUSSIONS

Figure 2 compares the test results of HMA specimens at different densities of: 1.90 g/cm^3 (HMA-1), 2.15 g/cm^3 (HMA-2) and 2.37 g/cm^3 (HMA-3) obtained by continuous monotonic loading (ML) at constant vertical (axial) strain rate ($\dot{\varepsilon}_v$) of 0.0067%/min by using apparatus A. The maximum vertical stress values for respective densities were also inset in this figure. Note that the vertical strain values (ε_v) presented in this figure were the ones measured by using LVDT, as strength properties were mainly discussed in this figure. The following trends of behaviour may be seen from Fig. 2:

1. The maximum vertical stress ($\sigma_{v,\max}$) increases with an increase in the densities of HMA while the value of vertical strain at which the $\sigma_{v,\max}$ exhibited were similar.
2. The value of $\sigma_{v,\max}$ increases with an increase in density at an increasing rate. This shows the significance of compaction on HMA to obtain higher density on the strength property.

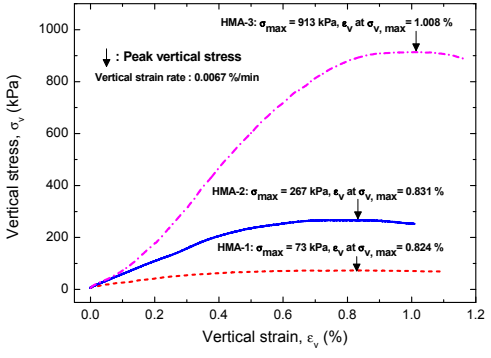

FIG. 2. Continuous monotonic loading test results of HMA with different densities

Figure 3 shows, for example, the $\sigma_v - \varepsilon_v$ relations from continuous ML tests at constant vertical stress rate ($\dot{\sigma}_v$) of 2.264 kPa/min by using apparatus B on HMA having density of 2.15 g/cm^3 (HMA-2). Tangent modulus and Poisson's ratio were defined as the tangential slopes of respective σ_v - ε_v and ε_h - ε_v relations. Figs. 4 and 5 compare $E_{\tan}$ - values and $\nu_{\tan}$ - values for different densities of HMA specimen. In addition, from the initial portions of σ_v - ε_v and ε_h - ε_v relations, the initial modulus, E_o, and Poisson's ratio, ν_o, are determined. The following trends of

behaviour may be seen from Figs. 3 – 5:

1. At the same value of σ_v, the value of ε_v measured by a LVDT is always greater than that measured by a pair of LDTs, which is due to the effect of errors consisting of system compliances and bedding errors.
2. The values of $E_{\tan}$, $\nu_{\tan}$, E_o and ν_o increased with an increase in the densities of HMA specimens.
3. For HMA-1, the $E_{\tan}$ - values decreases with an increase in vertical stress, σ_v. On the other hand, for HMA-2 and HMA-3, the $E_{\tan}$ - values increases with an increase in vertical stress, σ_v. These behaviours are consistent with the fact that the stiffness of HMA-2 and HMA-3 increased with the vertical stress while the opposite is true for HMA-1.
4. The $\nu_{\tan}$ - value increases noticeably with an increase in vertical stress, σ_v.

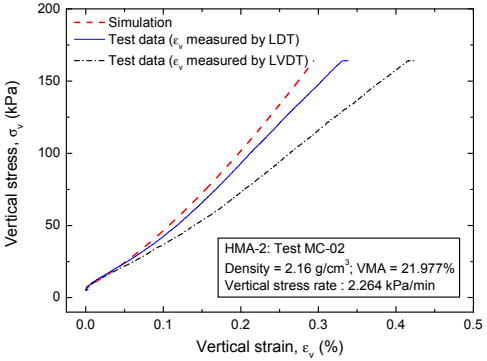

FIG. 3. Relationship between vertical stress and vertical strain obtained from continuous ML test on HMA-2, density = 2.16 g/cm^3

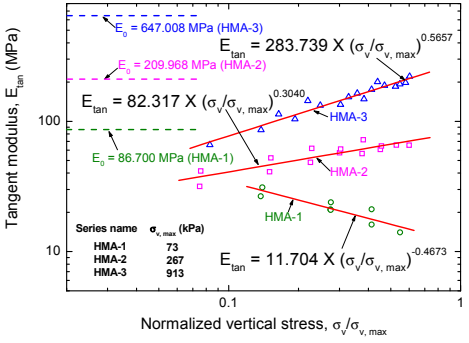

FIG. 4. Comparisons of tangent modulus values among HMA-1, HMA-2 and HMA-3

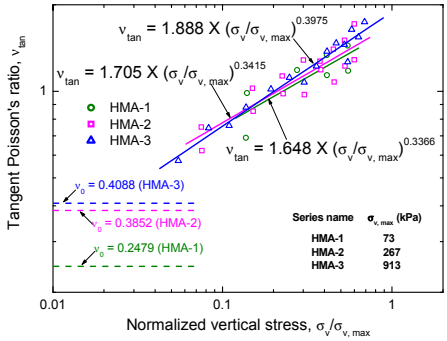

FIG. 5. Comparisons of tangent Poisson's ration values among HMA-1, HMA-2 and HMA-3

5. The $\nu_{\tan}$ - value bounds to the respective ν_o - values when σ_v approaching zero. However, there is a large difference on the values of E_o - values and $E_{\tan}$ - values when σ_v approaching zero. It is likely due to that the $E_{\tan}$ - value decreases noticeably from a value that is close to E_o - values at the initial state to a much lower value by subsequent compression. These behaviours are not true for HMA-1, but they are true for HMA-2 and HMA-3. It can be seen that, for respective density of HMA, the slope of E_o is always more than $E_{\tan}$. Moreover, the difference of the slope between E_o - slope and $E_{\tan}$ - slope on HMA-1 specimen was less significant than when compared the respective slopes in the case of HMA-2 and HMA-3 specimens.
6. Linear relations fitted to the $\nu_{\tan} - \sigma_v/\sigma_{v,\max}$ relations for different densities were nearly similar.

Figure 6 shows, for example, the σ_v - ε_v relations from continuous ML tests intervened by sustained loading (SL) after which ten minute-amplitude unload/reload cycles were performed at constant vertical stress rate $|\dot{\sigma}_v|$ of 2.264 kPa/min by using apparatus B on HMA specimen having density of 2.15 g/cm^3 (HMA-2). Equivalent modulus and Poisson's ratio are defined as the slope of the apparently linear portion from a unload cycle on σ_v - ε_v and ε_h - ε_v curves. It is known that the unload and reload cycles of axial stress give stiffness values greater than those at initial virgin loading with many materials including soils. It is also known that the vertical Young's modulus (E_{eq}) for major principal strain increments acting in the vertical direction defined in Eq. 1 for unbound granular materials (i.e., sands and gravels) increases with an increase in the vertical stress, σ_v, during triaxial compression performed at a fixed confining pressure, σ_h, unless the stress ratio, σ_v/σ_h, is close to peak value (e.g.,

Hoque and Tatsuoka, 1998; Tatsuoka et al., 1999). Therefore, it is of interest to evaluate the E_{eq} - value of the HMA having different densities against the respective values of σ_v at which these E_{eq} - value were measured. Furthermore, in order to determine the elastic lateral deformation corresponding to a vertical stress change in the elastic theory, the equivalent Poisson's ratio, ν_{eq}, is also of interest. Figs. 7 and 8 compare E_{eq} - values and ν_{eq} - values for different densities of HMA specimen. The following trends of behaviour may be seen from Figs. 6 – 8:

1. Creep strains and residual strains caused by minute-amplitude cycles performed after creep are noticeable. Therefore, the rate effect on the development of residual strain is not negligible.
2. The E_{eq} - value increases significantly with an increase in the vertical stress, σ_v. When the σ_v value approaches zero, E_{eq} bounds for E_o.
3. On the other hand, the ν_{eq} - value decreases noticeably with an increase in the vertical stress, σ_v. When the σ_v value approaches zero, ν_{eq} bounds for ν_o.
4. Observations 1) and 2) imply that, at small strain level near the origin, the $\sigma_v - \varepsilon_v$ behaviours are significantly elastic for all specimens prepared at different densities.
5. From Fig. 8, it may be seen that, the linear relations fitted to the test data for HMA-2 of ν_{eq} was nearly similar to the linear relation fitted to the entire test data for all densities for ν_{eq}.

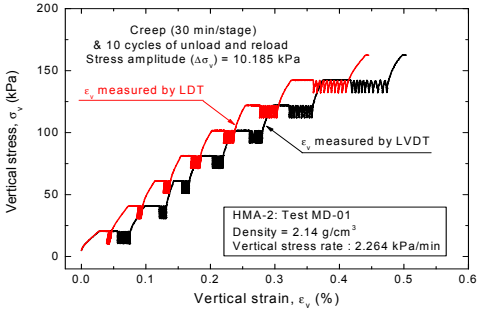

FIG. 6. Relationship between vertical stress and vertical strain obtained from minute-cycle unload/reload tests on HMA-2, density = 2.14 g/cm^3

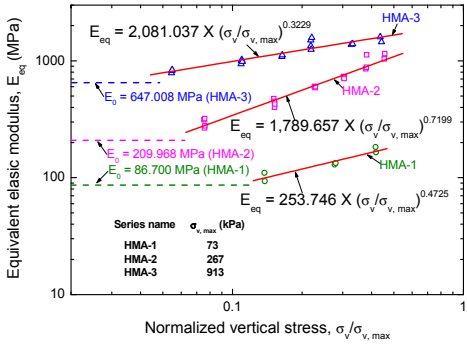

FIG. 7. Comparisons of equivalent elastic modulus values among HMA-1, HMA-2 and HMA-3

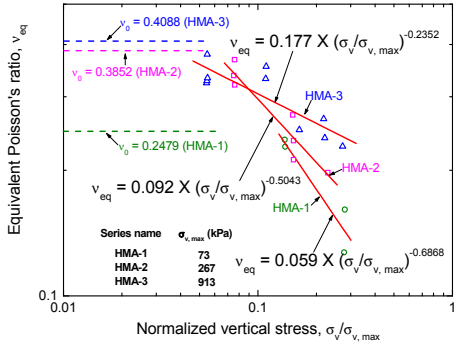

FIG. 8. Comparisons of equivalent elastic Poisson's ratio values among HMA-1, HMA-2 and HMA-3

When all E_o, E_{tan} and E_{eq} moduli and ν_o, ν_{tan} and ν_{eq} Poisson's ratios for a given HMA density prepared as shown in this study are known, it becomes possible to predict its deformation for a given loading history based on the elastic theory. Fig. 3 shows, for example, the simulated $\sigma_v - \varepsilon_v$ relation compared with the test result.

CONCLUSION

The following conclusions may be derived:

1. It is necessary to locally measure vertical and horizontal strains to realistically obtain the stress-strain properties of HMA.
2. Compressive strength and stiffness of HMA significantly increase with an increase in its density at an increasing rate. This fact implies a great importance of compaction of HMA during the construction.

3. Initial modulus, E_o and equivalent elastic modulus, E_{eq}, significantly increase with an increase in the vertical stress,σ_v, for all HMA densities investigated in this study.
4. Tangent Poisson's ratio, ν_{tan}, tends to increase while the equivalent Poisson's ratio, ν_{eq}, tends to decrease with the vertical stress.
5. Tangent and equivalent elastic moduli, E_{tan} and E_{eq}, as well as tangent and equivalent Poisson's ratios, ν_{tan} and ν_{eq}, can be expressed as a function of the vertical stress level by means of empirical equations.

REFERENCES

Abdelrahman, G.E., Kawabe, S., Tsukamoto, Y. and Tatsuoka, F. (2008): "Small-strain stress-strain properties of expanded polystyrene geofoam", *S&F*, Vol.48 (1): 61-71.

Feizi-Khankandi, S., Mirghasemi, A.A., Ghalandarzadeh, A. and Hoeg, K. (2008): "Cyclic triaxial tests on asphalt concrete as a water barrier for embankment dams", *S&F*, Vol.48 (3): 319-332.

Thaisri, K., Youwai, S. and Kongkitkul, W. (2008): "Behavior of reinforced flexible pavement under monotonic loading condition", *Proc. of the 13th National Convention on Civil Engineering*: 344-347.

Goto, S., Tatsuoka, F., Shibuya, S., Kim, Y.-S., and Sato, T. (1991): "A simple gauge for local small strain measurements in the laboratory", *S&F*, Vol.31 (1): 169-180.

Hoeg, K., Valstad, T., Kjaernsli, B. and Ruud, A.M. (2007): "Asphalt core embankment dams: recent case studies and researches", *Journal of Hydropower and Dams*, Vol.13 (5): 112-119.

Hoque, E. and Tatsuoka, F., (1998): "Anisotropy in the elastic deformation of materials", *S&F*, Vol.38 (1): 163-179.

Issaro, P., Kongkitkul, W. and Jongpradist, P. (2009): "Small-strain stress-strain properties of asphaltic concrete", *Proc. of the 14th National Convention on Civil Engineering*, Vol.1: 431-436.

Tatsuoka, F., Jardine, R.J., Lo Presti, D., Di Benedetto, H. and Kodaka, T. (1999): "Characterising the pre-failure deformation properties of geomaterials", Theme Lecture for the Plenary Session No.1, *Proc. of XIV IC on SMFE, Hamburg,* September 1997, Vol. 4: 2129-2164.

Impact of Different Extraction Recovery Method on Allowable Percentage of Reclaimed Asphalt Pavement (RAP)

Prashant Shirodkar[1], Khyati Sonpal[1], Dr. Yusuf Mehta[2], Aaron Nolan[3], Alan Norton[4], and Christopher Tomlinson[4]

[1]Graduate Students, Department of Civil and Environmental Engineering, Rowan University, Glassboro, NJ
[2]Associate Professor, Department of Civil and Environmental Engineering, Rowan University, Glassboro, NJ mehta@rowan.edu
[3]Research Associate, Department of Civil and Environmental Engineering, Rowan University, Glassboro, NJ
[4]Undergraduate Students, Department of Civil and Environmental Engineering, Rowan University, Glassboro, NJ

ABSTRACT: The objective of this paper is to capture variability from different extraction and recovery procedures. In recent years, state agencies emphasize on grading plants depending upon their RAP stockpile variability. Depending upon this grading of the plants, maximum allowable percentage of RAP for the plants will be determined. The recent NCHRP 9-33 manual "Mix design manual for Hot Mix Asphalt" gives procedure to determine RAP stockpile variability. The different extraction and recovery methods give different allowable percentage of RAP. This paper evaluates impact of different extraction recovery procedure on RAP binder property and allowable percentage of RAP which is determined by considering RAP aggregate gradation and RAP binder content. Selection of appropriate combination of extraction recovery method will not only grade the plant on uniform basis but also lead to more precise determination of allowable percentage of RAP.

INTRODUCTION

In recent years, the state agencies are increasingly emphasizing on grading of the plant depending upon RAP stockpile variability. Depending upon this grading of the plants, maximum allowable percentage of RAP for the plant will be determined. This allowable percentage of RAP depends upon standard deviation of the RAP aggregate gradation and RAP binder content. RAP aggregate gradation is determined either by ignition oven method or solvent extraction. Ignition oven method is adopted when the aggregate properties does not alter due to exposure to high temperature.

Also there are different Extraction and Recovery (ER) methods which impact the allowable percentage of RAP. The two most commonly used methods are the ER by the AASHTO T 319 (modified SHRP procedure) and the extraction by AASHTO T164 and

recovery by ASTM D5404 procedure. In addition, there are two different recovery procedures; the AASHTO T319 and the ASTM D5404. AASHTO T319 extraction procedure is in which RAP along with the solvent is allowed to agitate at the speed about 30-40 rpm to extract the RAP binder, whereas AASHTO T164 is the one which RAP and solvent rotates at a speed of 3600 rpm in a centrifuge vessel. AASHTO T319 recovery procedure is in which the solution of RAP binder and the solvent is exposed to 100^0C of oil bath for almost throughout the process, where as for ASTM D5404 the solution is exposed to 140^0 C and nitrogen gas throughout the process to recover the binder from the solution. Both the recovery procedures are based on the condensation concept. The above procedures have different configuration in terms of speed, temperatures and set up which eventually affect the time required to extract and recover the binder and the recovered binder properties.

Several researchers (Burr and Davidson, 1990), (Burr and Davidson, 1991), (Burr and Davidson, 1993) (Abson and Burton, 1960), (Bateman and Delp, 1927), (Broome, 1949), have explored various extraction and recovery methods, to optimize the time required to perform the tests and amount of solvent. However, no such study exists in recent literature that compares different combination of ER methods to determine allowable percentage of RAP. The comparison study of the different ER procedures also referred as different combinations (Table 1) would help in enhancing the understanding of the ER process and their impact on calculating percentage of RAP.

The AMRL procedure prohibits reuse of the solvent; however, the environmentally friendly n-bromopropane is very expensive. This would make the ER cost prohibitive if it is conducted regularly or on a larger scale. Therefore, there is a need to evaluate the impact of reused solvent on the recovered binder content and the binder properties.

GOAL

The goal of this paper is to study the impact different Extraction and Recovery methods on the allowable percentage of RAP.

EXPERIMENTAL PROGRAM

To achieve the above goal, the following experimental program (Table 1) was designed to evaluate the effect of different extraction and recovery procedures on binder content and the aggregate gradation. The binder content and the aggregate gradation from the following (Table 1) five combinations of extraction and recovery procedures are compared. The RAP samples collected from one of the plants from the state of New Jersey were used for this study. All samples were extracted and recovered using n-bromopropane solvent.

Table 1. Experimental Program

Combination	1	2	3	4	5
Method of Extraction	T164	T164	T164	T164	T319
Method of Recovery	T319	T319	D5404	D5404	T319
Type of Solvent	New	Reused	New	Reused	Reused
Number of Replicates	2	2	2	2	2

Sampling Method

The RAP samples were collected from the three equidistant points at the base of the stock pile. The sample used for testing was the mixture of the three samples. The RAP stockpile variability was kept to a minimum by conducting split sampling of samples.

Determination of Allowable percentage of RAP

National Cooperative Highway Research Program (NCHRP), Project 9-33 has compiled the *A Mix Design Manual for Hot-Mix Asphalt.*(Harrigan, 2009) Methods mentioned in this manual to design RAP mix are based primarily on the NCHRP report 452. As per this manual maximum amount of RAP that can be added to the mixture is governed by amount of dust (below 0.075 sieve) and the variability of the RAP. The variability of the RAP is captured by standard deviation in gradation and asphalt content. This standard deviation is used to determine allowable percentage of RAP. In this paper *HMA Tools* (Harrigan, 2009) developed during the NCHRP 9-33 is used to determined allowable percentage of the RAP. *HMA Tools* takes into account the binder content and the gradation of the different sets of extraction and recovery combinations and calculate its average and standard deviation values. There is a direct correlation of standard deviation values to allowable percentage of RAP.

RESULTS AND DISCUSSION

Gradation of RAP aggregate

Gradation of RAP aggregate for the different combination of ER procedures indicate (Figure 1) that the RAP aggregate gradation does not vary much within two replicates obtained by the same combinations of ER procedures.

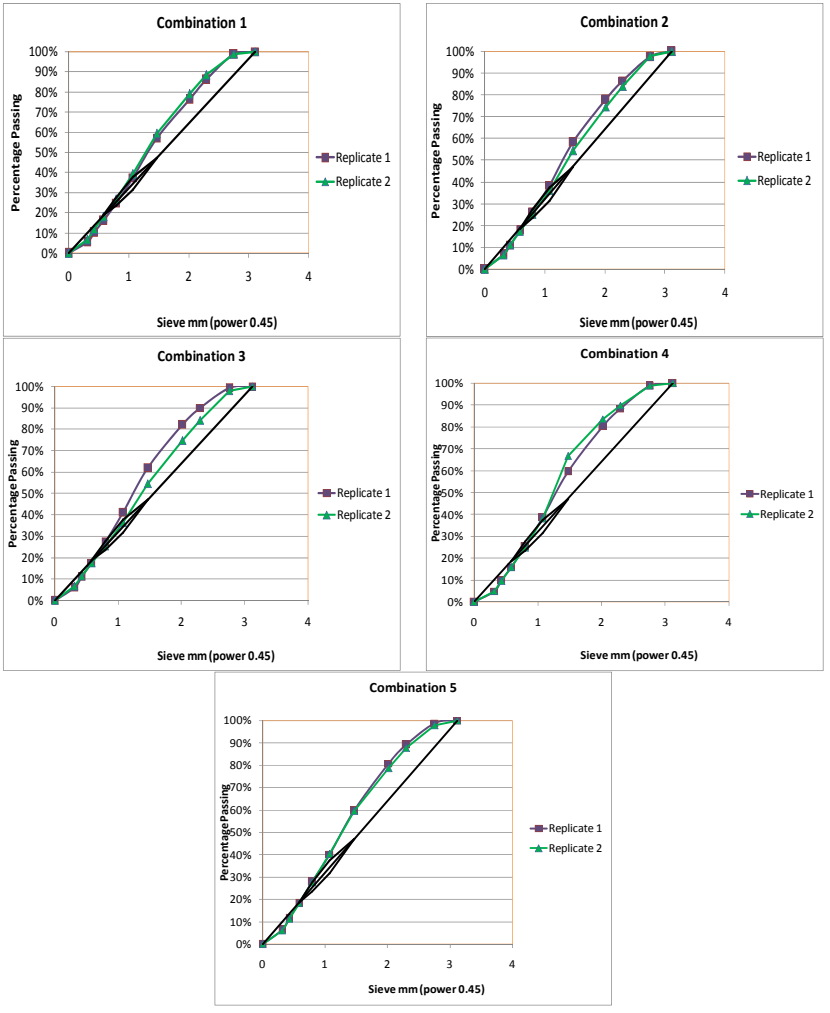

FIG. 1. Gradation of RAP aggregates for different combination of extraction and recovery procedure.

Binder Content

Binder content for the different combination of extraction and recovery procedures indicate (Figure 2) binder content determined by combination 4 and 5 is closer as compare combination 1 to 3.

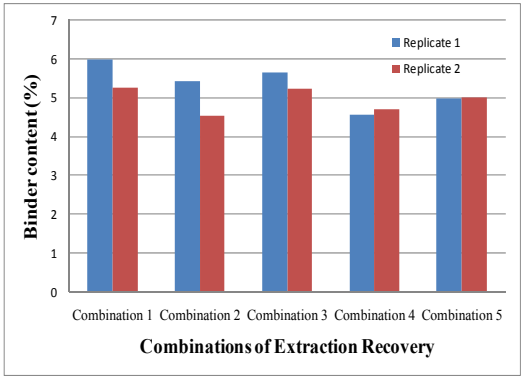

FIG. 2. Binder content of RAP for different combination of extraction and recovery procedure.

Allowable Percentage of RAP

Determination of allowable percentage of RAP strengthen the observation done while comparing RAP aggregate gradation and RAP binder content. From Table 2 it can be seen that allowable percentage of RAP determined from RAP aggregate gradation is on an average 53, 70, 64, 83, and 72% for the combinations 1 to 5, respectively. Also allowable percentage of RAP determined from RAP binder content is 39 and 100% for the combination 4 and 5 respectively and lower (0, 0 and 5%) for the combination 1 to 3 respectively.

Table 2. Allowable Percentage of RAP Determined as NCHRP9-33.

Sieve Size, mm	C 1	C2	C 3	C 4	C 5
50.000	100	100	100	100	100
37.500	100	100	100	100	100
25.000	100	100	100	100	100
12.500	100	100	100	100	100
9.500	100	100	100	100	100
6.350	25	23	63	63	100
4.750	23	15	25	15	44
2.360	24	8	17	0	15
1.180	35	20	50	100	6
0.600	23	42	100	100	19
0.300	21	100	37	100	77
0.150	22	100	26	100	100
0.075	21	100	20	100	74
AC	0	0	5	39	100
Minimum	**0**	**0**	**5**	**0**	**6**
Average Allowable %RAP	**53**	**70**	**64**	**83**	**72**

RAP binder property (Unaged G*/Sin δ)

RAP binder property (unaged G*/Sin δ) for the different combination of extraction and recovery methods show (Figure 4) binder property determined by combination 4 and 5 (0.3, 0.1) has low standard deviation as compare to combination 1 to 3 (3.7, 1.3 and 1.6).

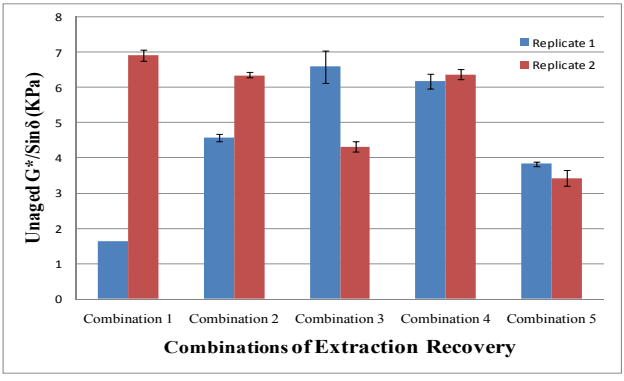

FIG. 3. Comparison of unaged G*/Sin δ for different combination of extraction and recovery procedure.

Determination of properties of RAP aggregate and binder is necessary for moderate and high percentage of RAP (above 15%). As small amount of aged binder has very less effect on HMA properties. Also some researchers have consistently shown that when RAP is mixed with virgin binder and aggregates partial blending occurs (Huang, 2005). This means that some aged binder coats the RAP aggregate even after the mixing. By considering the above two points, it can be said that combination 4 and 5 are superior over the combination 1 to 3. As combination 4 and 5 has lower standard deviation while determining RAP binder content and unaged G*/Sin δ and moderate standard deviation while determining RAP aggregate gradation (RAP variability is reduced by adopting appropriate sampling method explained above).

SUMMARY AND FINDINGS

1. RAP aggregate gradations are repeatable for all combinations of extraction and recovery.
2. Standard deviation in RAP binder content is lower in the ER combination 4 and 5 as compared to the combination 1 to 3.
3. Standard deviation in RAP binder property (unaged G*/Sin δ) is lower in the extraction recovery combination 4 and 5 as compared to the combination 1 to 3.

CONCLUSTION AND RECOMMENDATION

Extraction and Recovery combination 4 and 5 appear to have the lowest standard

deviation of RAP aggregate gradation and hence have a maximum allowable RAP. These combinations should be explored further characterization of RAP.

REFERENCE

Burr, B. L., C.J. Glover, R. R. Davidson, and J.A. Bullin. New Apparatus and Procedure for the Extraction and Recovery of Asphalt Binder from Pavement Mixtures. *In Transportation Research Record 1391, TRB*, National Research Council, Washington, D. C., 1993.

Burr, B. L., R. R. Davidson, H. B. Jemison, C.J. Glover, and J.A. Bullin. Asphalt Hardening in Extraction Solvents. In *Transportation Research Record 1323, TRB*, National Research Council, Washington, D. C., 1991, pp. 70-76.

B. L. Burr, R. R. Davidson, C. J. Glover, and J. A. Bullin. Solvent Removal from Asphalt. In *Transportation Research Record 1269, TRB*, National Research Council, Washington, D. C., 1990.

D. C. Broome. The Testing of Bituminous Mixtures, 2nd ed. Edward Arnold and Co., London, 1949.

G. Abson and C. Burton. The use of Chlorinated Solvents in the Abson Recovery Method. Proc., *Association of Asphalt Pavement Technologists*, Vol. 29, St. Paul, Minn., 1960, pp.246-252.

Harrigan E. T.A Mix Design Manual for Hot Mix Asphalt, NCHRP 9-33. Retrieved August 26, 2009, from lazerpro.com: http://lazerpro.com/projects/advanced-asphalt/manual/

Huang, B. Z, G. Li.et al. Laboratory Investigation of Mixing HMA with RAP. In *Transportation Research Board: Journal of the Transportation Research Board*, No. 1929, Transportation Research Board of the National Academies, Washington, D.C.2005, pp. 37-45.

J. H. Bateman and C. Delp. "The Recovery and Examination of the Asphalt in the Asphaltic Paving mixtures," *Proc. ASTM*, Vol.II, 1927, pp. 465-479.

Determining Compaction Temperatures based on Asphalt Mixtures Test

Guoping Qian [1], Ph.D, Hui Huang [2], M.D, Jianlong Zheng[3], Ph.D and Jinlan He[4], M.D

[1]Associate Professor, Communication and transportation Engineering school of Changsha University of Science and Technology, Changsha P.R.China, 410076; guopingqian@sina.com
[2]Instructor, Communication and transportation Engineering school of Changsha University of Science and Technology, Changsha P.R.China, 410076; huanghui19840630@163.com
[3]Professor, Communication and transportation Engineering school of Changsha University of Science and Technology, Changsha P.R.China, 410076; ZJL@csust.edu.cn
[4]Instructor, Communication and transportation Engineering school of Changsha University of Science and Technology, Changsha P.R.China, 410076; hejinlanooo000@163.com

ABSTRACT: Asphalt mixtures are granular composite materials stabilized by the presence of asphalt binder, compaction of which is one of the most important factors affecting the performance of asphalt pavement. And the quality level of compacted asphalt mixtures relies greatly on the compaction temperature determined roughly by the viscosity test of asphalt binder. So, the method for determining compaction temperature can not consider interaction between viscosity of asphalt binder and aggregate properties, such as gradation. Based on the test results of two kinds of asphalt mixtures with different combined aggregate gradations and same binder, the effects of aggregate gradation on compaction temperature are investigating in this paper.

INTRODUCTION

Asphalt mixtures are particulate composite materials consisting of interspersed aggregates, asphalt binder and air voids. And compaction of asphalt mixtures is one of the most important factors affecting the performance of asphalt pavement. The accurately controlled compaction temperature of asphalt mixtures can help to improve the degree of compaction, ensure material performance and prolong the service life of asphalt pavement.

Generally, in order to obtain the compaction temperature of asphalt mixtures, the viscosity-temperature curves of asphalt binder are established by capillary viscometers to measure kinetic viscosity or by Brookfield viscometers to measure apparent viscosity. In the curve, the compaction temperature is attained at a kinetic viscosity of 280 ± 30 centistokes or at an apparent viscosity of 0.28 ± 0.03 Pa • s(Hussain U. Bahia et al.2006).

Asphalt binders are thermoplastic materials and their rheology is highly sensitive to temperature. They exhibit semisolid behavior at ambient temperatures but can be

made fluid by heating (Hussain U. Bahia et al.2006).Viscosity is a measure of the internal friction of a fluid. If the viscosity is too high, it will be very difficult to get the desired density, and the mixtures can not be compacted properly. If the viscosity is too low, they may be difficult to get uniform distribution of asphalt binder throughout the aggregate structure (Hensey, et al.1998).It is apparent that the current method for determining compaction temperatures only considers the properties of asphalt binder and does not take the interaction between viscosity of asphalt binder and aggregate properties, such as aggregate gradation into account.

In the paper, the compaction properties of two kinds of asphalt mixtures with different combined aggregate gradations and same binder are studied by the indoor and field tests.

LABORATORY TEST AND RESULTS ANALYSIS

This paper select 30# asphalt binder and two different aggregate gradations of AC-25 and ATB-30 for investigating compaction properties of asphalt mixtures, and the viscosity test for 30# asphalt and the Superpave gyratory compactor (SGC) test for AC-25 and ATB-30 mixtures blended with 30# asphalt are studied.

Material Properties

Two combined aggregate gradations are shown in Table 1 and properties of asphalt binder (30#CNOOC in Tai Zhou) used in the paper are given in Table 2.

Table 1. Aggregate Gradation Results

Sieve Size(mm)	Combined Aggregate Gradation (Percent Passing %)			
	AC-25		ATB-30	
	Spec.	Mix Design	Spec.	Mix Design
37.5	/	/	100	100
31.5	100	100	90-100	99.3
26.5	90-100	99.2	70-90	85.2
19	75-90	84	53-72	62.4
16	65-83	73	44-66	57.7
13.2	57-76	61.6	39-60	50.4
9.5	45-65	49.4	31-51	40.8
4.75	24-52	34	20-40	33.3
2.36	16-42	24.8	15-32	23
1.18	12-33	16	10-25	17.8
0.6	8-24	10.2	8-18	10.9
0.3	5-17	7.8	5-14	7.4
0.15	4-13	6.3	3-10	5.5
0.075	3-7	5.2	2-6	4.2

Table 2. Properties of Asphalt Binder

Test Items	Value
Penetration(25ºC，5s) 0.1mm	26
Ductility (5cm/min10º C)/ (5cm/min15º C) cm	6/13
Softening Point ºC	60
Penetration Index	-0.991
60º C Dynamic Viscosity Pa • s	1626
Flash Pointº C	296
Residual Penetration Ratio % after RTFOT	85

The best oilstone ratio of AC-25 and the ATB-30 asphalt mixes were respectively 4.0% and 3.4%, by the Marshall Test of their different asphalt content.

Typical Viscosity Tests of Asphalt Binder

Kinematic viscosity and apparent viscosity of asphalt binder (30#) are measured respectively by conventional capillary viscosity test and Brookfield viscosity test. Based on test results shown in Figure 1 and 2, two different viscosity-temperature relation curves are established through mathematical analysis.

Based on the viscosity-temperature curves shown in Fig.1 and.2, two compaction temperature limits are attained at the kinetic viscosity of 280 ± 30 centistokes and the apparent viscosity of 0.28 ± 0.03 Pa • s, which are respectively 161.3 ~ 165.4 ºC and 161.7 ~ 164.5 ºC.

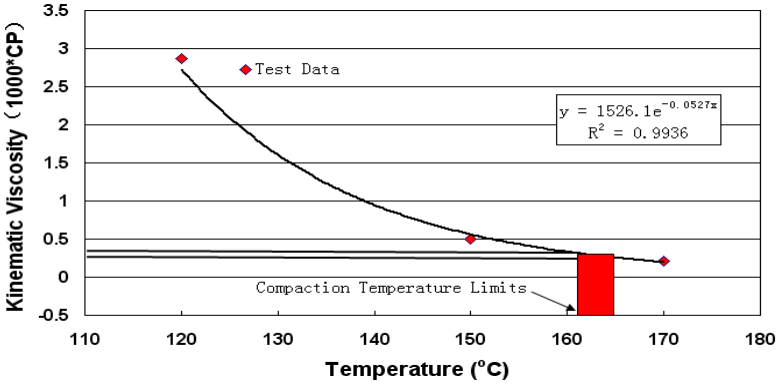

FIG.1. Kinematic viscosity –temperature relation curve.

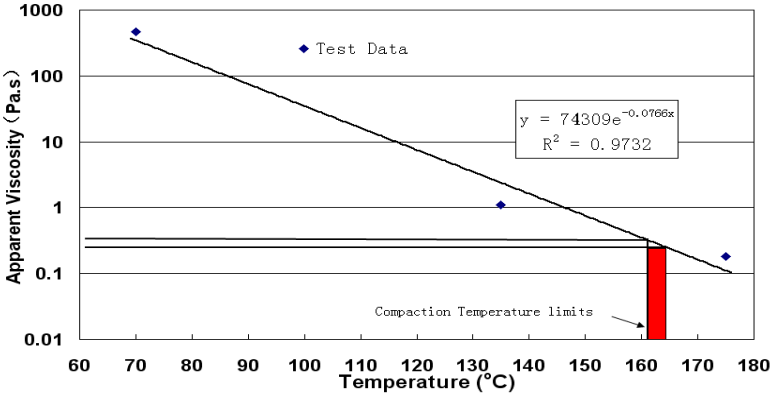

FIG.2. Apparent viscosity –temperature relation curve.

Superpave Gyratory Compactor (SGC) Test of Asphalt Mixtures

Superpave Gyratory Compactor test can well simulate field pavement compaction and provide guidance for field compaction parameters. So, the SGC tests for aggregate gradations AC-25/ATB-30 blended with 30# asphalt binder are carried out. The gyration angle for SGC is 1.25°, the rotation speed is 30r/min during the test. When the SGC specimens of asphalt mixtures reach the specified design air voids and design height shown in Fig.3 and 4, the SGC Gyratory compaction times are measured under different pressures and different temperature limits. The test conditions and results are shown Fig.3 and 4.

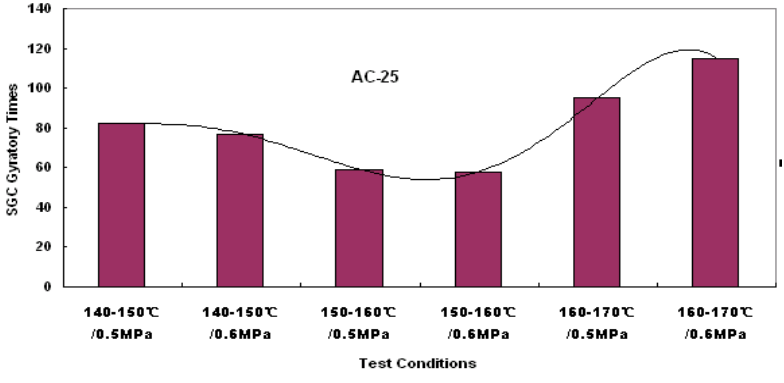

FIG.3. Gyratory compaction times of AC-25 under different temperatures (Design air voids of 4% and design height of 8cm).

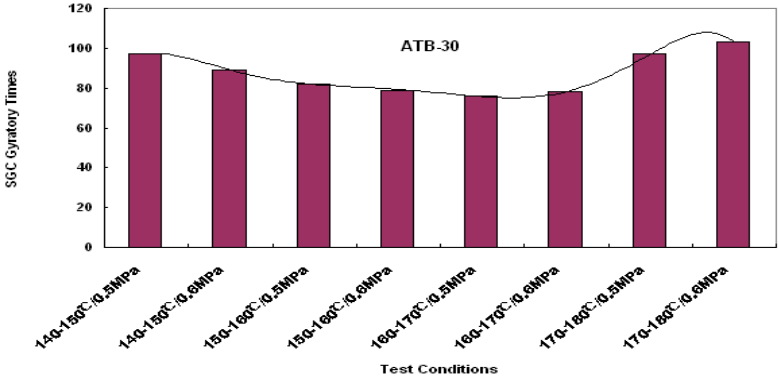

FIG.4. Gyratory compaction times of ATB-30 under different temperatures (Design air voids of 5% and design height of 9cm).

The SGC test results show that compaction properties of asphalt mixtures have significant differences at different temperatures and asphalt mixtures have an optimum compaction temperature limits. The optimum compaction temperature limit is 150～160°C for AC-25 mixtures used in this study, and 150～170°C for ATB-30 mixtures used in this study. And test results also testify that different aggregate gradations have clear influence on optimum compaction temperature limits.

FIELD TEST RESULTS ANALYSIS

The compaction temperature under compaction process for pavement layer of ATB-30 asphalt mixtures mentioned above in one expressway construction of Henan province was at 150 °C ~ 170 °C determined by SGC test. Test data for temperature of pavement layers during compaction are shown in Fig.5.

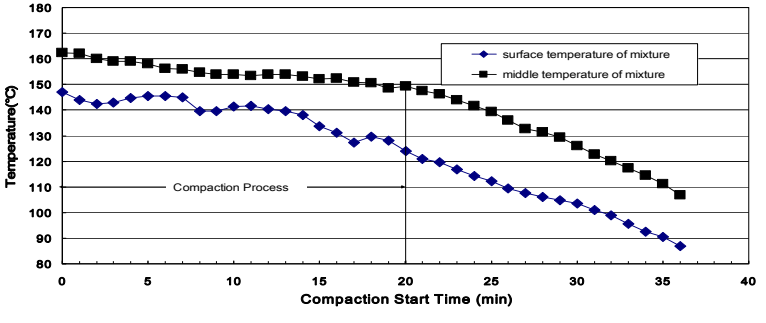

FIG.5. Temperature variation of ATB-30 during field compaction process.

Fig.5 shows that the internal temperature of ATB-30 mixtures layer is basically well controlled in required range within 20min in compaction process shown.

Cross-section was selected every one meter on the test road from K70+610 to K70+630 and totals 21 sections. Densities were measured by non-nuclear density gauge (PQI301) on every section each one meter and total 12 test points. And the degree of compaction equals the quotient of the testing density and maximum theorical density. Total 252 test results (21×12=252) are shown in Fig.6.

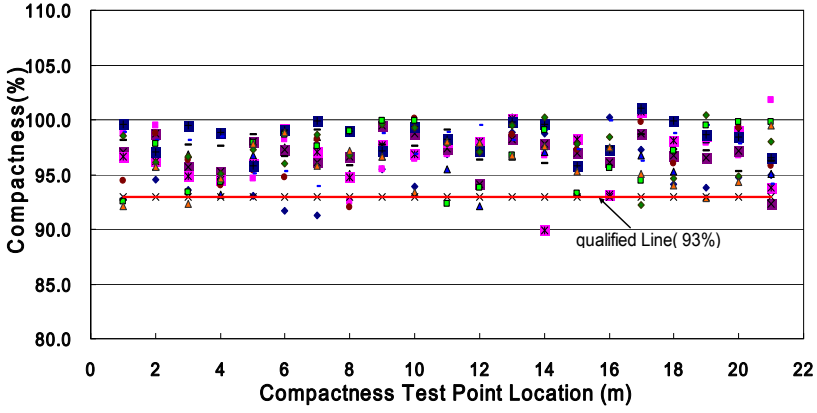

FIG.6. Variation of compaction degree in site.

Compaction is qualified when the measured filed density get to 93% of the theoretical maximum relative density. Compaction of this test road section is uniform relatively and at a higher compaction state basically shown as compaction results in Fig.6, which shows that selection and control for compaction temperature is ideal to some extent.

CONCLUSIONS AND SUGGESTION

Performance of asphalt pavement is greatly affected by the compaction of asphalt mixtures, the quality level of which relies greatly on the compaction temperature. Gradation of asphalt mixture has a clear influence on the optimum compaction temperature. The method for determining compaction temperature in view of the asphalt binder viscosity test is unable to consider above-mentioned problems and has a certain defect. It has certain rationality for the method for determining a reasonable compaction temperature limit of asphalt mixture using SGC gyratory compaction test. It is suggest that a related research should be carried on in a more in-depth level and wider scope from now on, so as to put forward a perfect determination method of optimum compaction temperature from the performance of asphalt mixtures.

ACKNOWLEDGEMENTS

The research was supported by National Natural Science Foundation of China (50778026, 50808026), Specialized Research Fund for the Doctoral Program of Higher Education (20050536001), and Scientific Research Fund of ministry of communications of P.R.China (2006319825090). The author would like to acknowledge with thanks the financial support.

REFERENCES

Hussain U. Bahia, Ahmed Fahim, and Kitae Nam.(2006) "Prediction of Compaction Temperature Using Binder Rheology" *In: Factors Affecting Compaction of Asphalt Pavements*:3-16.

Hensley, J., Palmer, A. (1998). "Establishing Hot Mix Asphalt Mixing and Compaction Temperatures at the Project Level"*Asphalt*, Asphalt Institute, Volume 12,Lexington,KY.

United States Association of Asphalt, (2005). "Superpave Basic Reference Manual".

Laboratory Evaluation of Effects of Joint Heater on Longitudinal Joint

Jingsong Chen[1,2], Baoshan Huang[2], Yongsheng Li[3], Xiang Shu[4]

[1]Ph. D candidate, Department of Geotechnical Engineering, Tongji University, Shanghai 200092, P.R.China, jchen27@utk.edu
[2]Associate Professor, Department of Civil and Environmental Engineering, University of Tennessee, Knxoville 37996 USA, bhuang@utk.edu
[3]Professor, Department of Geotechnical Engineering, Tongji University, Shanghai 200092, P.R.China, tjgiad@public3.sta.net.cn
[4]Research Assistant Professor, Department of Civil and Environmental Engineering, University of Tennessee, Knxoville 37996 USA, xshu@utk.edu

ABSTRACT: Due to the limitation of traffic condition and paving equipment, longitudinal joint is an unavoidable and common problem in hot mix asphalt (HMA) pavement construction. These longitudinal joints between lanes of HMA pavements are generally susceptible to moisture and other failures and have been one of the major problems for HMA pavements. Joint heater is one of the common techniques to improve the quality of longitudinal joint construction. This paper presents the results of a laboratory study of evaluating effects of joint heater on longitudinal joints. A test field project was conducted to evaluate the effect of joint heater on longitudinal joints and specimen cores along the longitudinal joints were taken in both conventional section and heat-treated section. Air voids, permeability tests and indirect tensile test were conducted on those field specimens. The test results showed that, with proper temperature control, the joint heater can significantly improve the behavior of pavement around longitudinal joints and is a very useful technique in improving longitudinal construction quality.

INTRODUCTION

Due to the limitation of traffic condition and paving equipment, longitudinal joint is an unavoidable and common problem in hot mix asphalt (HMA) pavement construction. These longitudinal joints between lanes of HMA pavements usually have relatively low density and high air voids, and are generally susceptible to moisture and other failures (Foster et al., 1964; Kandall and Mallick, 1996). Several factors have been identified to be the causes of HMA joint failures. First, it is difficult to achieve the desired pavement densities near the longitudinal joints with normal compaction techniques. Lower densities mean higher air voids and lower pavement strength, which will likely introduce moistures into the open voids and cause pavement failures.

Secondly, interface bond between existing cold HMA pavement lanes and newly constructed lanes can not achieve the strength of HMA inherent strength (cohesion) without joint treatments. In addition, the orientations of longitudinal joints are usually in-line with wheel loads, which result in relatively high shear stress on the weakly bonded interface.

Although echelon paving can completely eliminate longitudinal joints by using wide or multiple pavers, it inevitably affects the traffic and is costly and impracticable for multi-lane HMA pavements. Therefore, in order to achieve well-performance HMA pavements, many studies have been conducted and various construction technologies have been developed to improve the quality of longitudinal joints in the past decades (Kandhal and Rao 1994; Kandhal and Mallick 1996; Kandhal et al. 2002; Fleckenstein et al., 2002; Toepel 2003). These longitudinal joint construction techniques include Notched Wedge, Restrained Edge, Cutting Wheel, Joint Maker, Joint Adhesive, Infrared Joint Heater.

Among these longitudinal joints construction technologies, the infrared joint heater is one of common used longitudinal joint construction techniques. The main purpose of joint heater is to heat the edge of the previously placed lane when placing the adjacent lane, so both cold and hot lanes at the joint can be compacted sufficiently at suitable surface temperature. As early as 1967, Gas-fired ("Infra-Red") heater has been used to treat joints in wearing-course rolled asphalt (Buglass, 1967). However, only in recent years has it begin to be widely used for longitudinal joints construction in HMA pavement. Daniel (2005, 2006) studied the effect of infrared joint heater on the base, binder, and surface layers of a full-depth hot-mix asphalt pavement and determined the extent of heat penetration from the infrared heaters by embedding thermocouples in the pavement. However, joint heater also causes some problems and need further research. Fleckenstein (2002) found that longitudinal joints can achieve high joint density, but the surface of the asphalt was scorched in several areas and blistering was observed from overheating by using joint heater. Brown (2006) also pointed out that joint heater usually exist the problem of uneven heating of materials and it is difficult to control the joint heater so that the loose material on the cold side of the joint is consistently heated to a satisfactory temperature.

In order to evaluate the effect of infrared joint heater on asphalt mixture pavement in the joint and adjacent to the joint, a test field project was conducted and specimen cores around joint area (both cold side and hot side) were taken in conventional section and heat-treated section. Air voids, permeability tests and indirect tensile test were conducted on those field specimens. The test results showed that, with proper temperature control, the joint heater can significantly improve the behavior of pavement around longitudinal joints and is a very useful technique in improving longitudinal construction quality.

CONSTRUCTION DETAILS AND CORING PATTERN

A heater-treated (infrared heating) and a control (no special treatment) section were paved in the field. The infrared joint heater was used to preheat the cold edge of the previously compacted lane before placement of asphalt mixture in heater-treated section. The joint heating system consists of several heaters towed by a tractor and one heater attached to the paver (Figure 1). The heating equipment is propane fired joint

heater and the heater employs multiple layers of a patented ceramic and steel fabric to generate infrared heat which reheats asphalt mixes to 2.5 inches in depth. Immediately after heating, the joint temperature could reach up to 250℉. The joint temperature dropped down to approximately 230℉ before mixture placement. The joint heater should not raise the existing mat or previous overlay temperature more than 300ºF to limit the damage on asphalt mixture. In order to avoid the overheating of the asphalt mixture pavement by joint heater, the infrared camera was used for temperature control during compaction process (Figure 2).

FIG. 1. Infrared joint heater

After construction, pavement cores were taken from the longitudinal joint and its neighboring area. Three locations at joint heater section and two locations at control section were selected (Figure 4). In each location, eleven field cores (three cores in joint, two cores in each other place) were taken in the manner as shown in Figure 3.

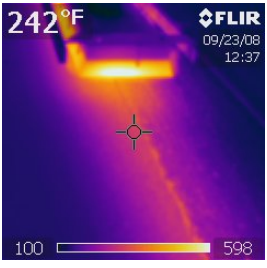

FIG. 2. Temp. monitoring

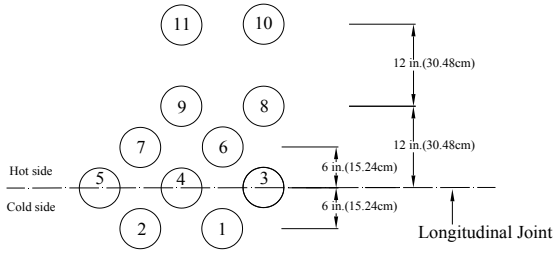

FIG. 3. Coring pattern in each location

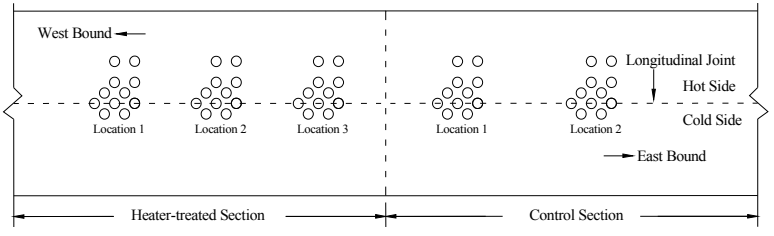

FIG. 4. Coring arrangement

LABORATORY TEST AND DISCUSSION

Air void content, permeability tests and indirect tensile test were performed on field cores to investigate the effects of infrared joint heaters on the quality of pavement in longitudinal joints and adjacent to the joints.

Air Void Content

Air voids is an important parameter of asphalt mixture, which is often closely related to the properties of HMA. Previous studies have shown that air voids in HMA can greatly affect the stability and durability (Brown, 1989; Harvey, 1996). The average air void results in each location are presented in Figure 5. It is evident that the air voids at longitudinal joint was higher than other places, which indicates that longitudinal joint was harder to be compacted than mat. As expected, the air voids in cold side around longitudinal joints is higher than that in hot side due to the unconfined edge during construction process. Comparison between the air voids in joint heater section and control section has shown that the air voids was consistently lower for joint heater section than for control section, especially along longitudinal joint. However, the difference became small as the coring locations became farther away from longitudinal joints. This finding indicates that joint heater is useful for pavement compaction and could significantly improve the quality of longitudinal joints by reducing the air voids.

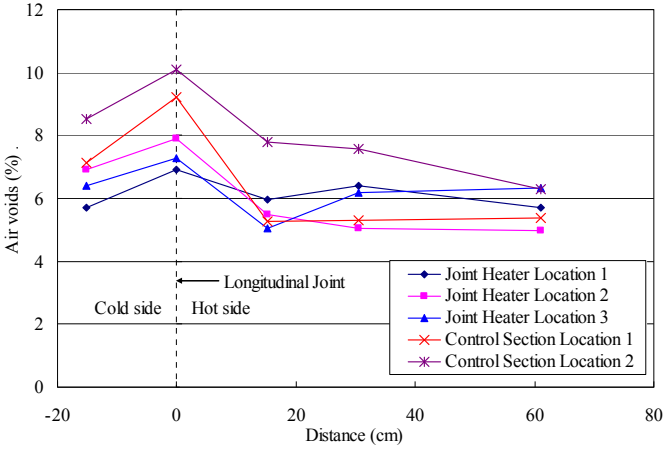

FIG. 5. Results of Air Voids Content

Permeability Test

Permeability is another important factor affecting the performance of HMA pavements and is also used to evaluate the quality of HMA pavements. Compared with density, the permeability of HMA is more directly related to durability, in terms of resistance against moisture related damage and premature oxidation and cracking (Muller 1967, Kumar and Goetz 1977). A falling head test was used to determine the permeability of field cores. The specific test procedure and calculation equation are described in Florida DOT test method (FDOT 2004)

The permeability coefficients of field cores are presented in Figure 6. It can bee seen that the distribution of permeability across the longitudinal joint is similar to that of air void content, i.e., the joint exhibited the highest permeability and the cores far from longitudinal joints have relatively low permeability coefficients. The high permeability in longitudinal joints will allow water and other materials to penetrate the pavement surface, and thus lead to premature degradation. Comparison between permeability coefficients in joint heater and control sections shows that the permeability coefficients of longitudinal joint cores in joint heater section are much lower than that in control section, which indicates joint heater can significantly improve longitudinal joints quality. The test results of field cores also showed a significant increase in permeability when the air voids is bigger than eight percent.

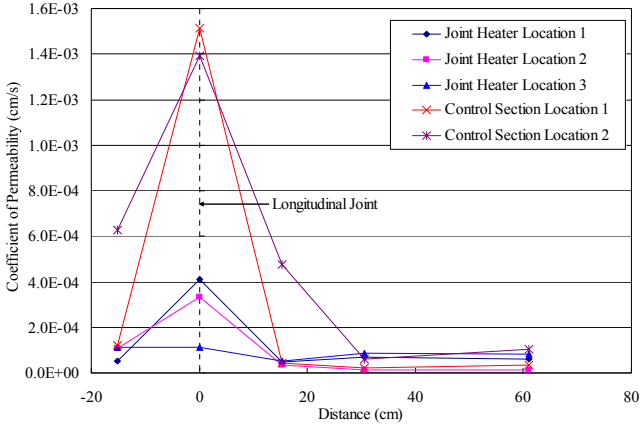

FIG. 6. Results of Permeability Coefficient

Indirect Tensile Stress

The indirect tensile test (IDT) was conducted to determine the indirect tensile strength of field cores in this paper. Indirect tensile strength can be used to establish the structural properties of asphalt mixtures and could be an indicator of adhesion between cold and hot lanes for joint cores. The field cores were properly set on the pressure pad to make sure the longitudinal joint in vertical direction (Figure 7) and the load was monotonically exerted on the samples until its failure along the vertical diametric axis at the constant rate of 76.2 mm/min. From the plot of load versus deformation, the maximum load carried by the specimen can be found, and then the indirect tensile stress at failure could be calculated.

The indirect tensile test results (Figure 8) shows that the tensile strength values of longitudinal joint field cores are previously lower than those at other places. By comparison between indirect tensile strength in jointer heater treated section and control section, it can be seen that the IDT strength of field cores around longitudinal joints considerably increased after joint heater treatment and there is no apparent changes in other places, which indicates the joint heater effectively improved the structural properties of asphalt mixture. From above test results, very good correlation

was found between air voids, permeability and IDT strength, i.e., the low air voids content usually result in low permeability coefficient and high tensile strength.

FIG. 7. Indirect tensile test

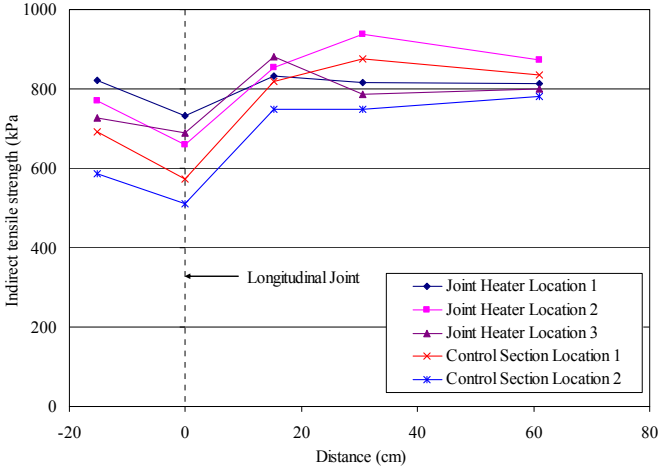

FIG. 8. Results of Indirect Tensile Test

CONCLUSIONS

In this paper, laboratory tests were conducted to evaluate the effect of joint heater on construction quality of longitudinal joints. Based on the test results in this study, the following conclusions can be summarized:

1. Longitudinal joints usually were harder to be compacted than mat and had higher air voids, permeability and low tensile strength, which would result in premature distresses such as longitudinal joint cracking.
2. Based on test results, the construction quality of cold side around longitudinal joints was worse than that of hot side due to the unconfined edge during construction process.

3. The test results indicate that, with proper temperature control, the joint heater can significantly improve the behavior of pavement around longitudinal joints. Compared with control section, the heater-treated section exhibited much lower air voids, permeability coefficients and higher tensile strength in the joint area.
4. Air voids and permeability of field cores showed general consistency in characterizing the properties of longitudinal joint, i.e., low air voids content usually result in low permeability coefficient and high tensile strength.
5. All the tests in this paper are conducted on newly paved asphalt mixture. The effect of joint heater on long term performance of asphalt mixture pavement was not studied here and need further research.

ACKNOWLEDGMENTS

This study was finally supported by the Tennessee Department of Transportation (TDOT) and the Federal Highway Administration (FHWA). The authors would also like to thank TDOT engineers and staff for their valuable help with this study.

REFERENCES

Brown, E.R. and Stephen Cross. (1989). “A study of In-Place Rutting of Asphalt Pavements.” Annual Meeting of the Association of Asphalt Paving Technologists, NCAT Report No. 89-2

Brown E. Ray. (2006). “Construction of Durable Longitudinal Joints.” Transportation Research Circular E-C105, TRB, National Research Council, Washington, DC.

Buglass, B.F. (1967). “Gas-fired ("Infra-Red") heater for use on joints in wearing-course rolled asphalt.” Great Britain. Ministry of Transport, Road Research Laboratory, RRL Report, 8p

Daniel, J. S., and W. L. Real. (2005). “New Hampshire’s Experience Using an Infrared Joint Heater to Improve Longitudinal Joint Performance.” Presented at mairepav4, Belfast, Ireland.

Daniel, J. S. (2006). “Use of an Infrared Joint Heater to Improve Longitudinal Joint Performance in HMA Pavements.” ASCE Journal of Performance of Constructed Facilities, Vol. 20, No. 2.

Fleckenstein, L.J., Allen, D.L., and Schultz, D.B. (2002). “Compaction at the Longitudinal Construction Joint in Asphalt Pavements.” Report No. KTC-02–10.

FDOT. (2004). “Florida Method of Test for Measurement of Water Permeability of Compacted Asphalt Paving Mixtures.”

Foster, C.R., S.B. Hudson, and R.S. Nelson (1964). “Constructing Longitudinal Joints in Hot Mix Asphalt Pavements.” Highway Research Record 51, TRB, National Research Council, Washington, DC.

Harvey, John T. (1996). “Effects of asphalt content and air void content on mix fatigue and stiffness.” Transportation Research Record, n 1543, p 38-45.

Kandhal, P. S., and Rao, S. S. (1994). “Evaluation of longitudinal joint construction techniques for asphalt pavements.” NCAT Rep. No. 94-1, National Center for Asphalt Technology NCAT, Auburn Univ., Auburn, Ala.

Kandhal, P. S., and Mallick, R. B. (1996). "Study of longitudinal joint construction techniques in hot-mix asphalt pavements." Transportation Research Record 1543, Transportation Research Board, Washington, D.C., 106–112.

Kandhal, P. S., Ramirez, T. L., and Ingram, P. M. (2002). "Evaluation of eight longitudinal joint construction techniques for asphalt pavements in Pennsylvania." NCAT Rep. No. 2002-03, National Center for Asphalt Technology NCAT, Auburn Univ., Auburn, Ala.

Kumar, A and Goetz, W.H. (1977). "Asphalt hardening as affected by film thickness, voids and permeability in asphaltic mixtures." Assoc. Asphalt Paving technology.

L. John Fleckenstein et al. (2002) "Compaction at the longitudinal construction joint in asphalt pavements (KYSPR-00-208)." Kentucky Transportation Center.

Muller, W.G. (1967). "Beam flexure and permeability testing of bituminous pavement samples." Assoc. Asphalt Paving Technol.

Toepel, A. (2003). "Evaluation of Techniques for Asphaltic Pavement Longitudinal Joint Construction." Report No. WI-08-03, Wisconsin Department of Transportation, Madison, WI.

Shanghai Experience with Warm Mix Asphalt

Jun Yan[1], Yadong Cao[1], Tiantong Zhu[1], Ming Cai[1], Zuguang Cao[1], Wenyuan Huang[2], and Qiao Dong[3]

[1] Shanghai Airport Road Construction Co., Ltd, Shanghai, China, 200023; yanjun216@263.net
[2] MeadWestvaco Packaging Materials Shanghai Co., Ltd
[3] Dept. of Civil and Environmental Engineering, University of Tennessee, Knoxville, TN 37996, USA; Email: qdong2@utk.edu

ABSTRACT: Warm mix asphalt (WMA) technologies have been developed to mix, transport, pave, and compact asphalt mixture at temperatures up to 40℃ lower than the conventional hot-mix asphalt (HMA). The benefits of WMA include energy savings, lower CO_2 emissions, and reduced workers' exposure to fumes, reduced binder ageing, and faster release of pavement to traffic due to shorter cooling time. Since it was introduced into Shanghai, China in 2006, WMA has been successfully used in more than 10 projects, including expressways and viaducts. The WMA in these projects performs well so far. This paper presents some of these WMA projects in Shanghai.

INTRODUCTION

Due to the good workability for paving and compaction and the benefit of saving energy and reducing emission, Warm mix asphalt (WMA) has gained more and more popularity since it was first introduced into China in 2005 (Hurley and Prowell 2005a, b, 2006; Xu et al. 2005). The two major WMA products used in China are Sasobit®, which is used as a asphalt modifier to reduce the viscosity of asphalt binder, and Evotherm®, which is a emulsion combined with a dispersed asphalt technology (DAT) delivery system (Hurley and Prowell 2005b, 2006).

Compared to the production of traditional hot-mix asphalt (HMA), the temperature for producing WMA can be lowered by 30 to 50 ºC. The lowered temperature of WMA leads to the benefits of reducing fuel consumption, decreasing emissions of fumes, and improving the working environment at mixing plants and paving sites and thus reducing the workers' exposure to potential health hazards. In addition, because of the benefits of better compaction and widened paving temperature range, WMA can be better used for ultra thin overlays, long haul distances, and paving at lower temperatures. Since the first WMA test road was paved in Shanghai, China in 2006, WMA has been used in over 10 projects including highways, urban roads, and viaducts. Evotherm® is the major WMA technology used in Shanghai.

LABORATORY PERFORMANCE OF WMA

In Shanghai, AC-13 and SMA-13 are the two major asphalt mixtures used in the surface layer of pavement and UTAC-10 and SMA-10 are the two major mixtures used for ultra thin overlays. Here, AC, SMA, and UTAC refer to asphalt concrete, stone matrix asphalt, and ultra thin asphalt concrete, respectively. The numbers, 13 and 10, are the nominal maximum aggregate size (NMAS) of asphalt mixtures.

AC-13

The AC-13 mixture was used in the first WMA test road in Shanghai. The first generation product of Evotherm® was used to produce the WMA AC-13 mixture. The Lushanwu diabase was used as coarse aggregate, the Huzhou limestone as fine aggregate, and the Taizhou #70 asphalt as binder. The Shell emulsified asphalt with a solid content of 67% was also used and the emulsifier was from the MeadWestvaco Company. The optimal asphalt content was determined to be 5.0% using the Marshall design method. The performance of WMA and HMA AC-13 mixtures were evaluated through laboratory tests as shown in Table 1.

Table 1. Laboratory Performance of WMA and HMA AC-13 Mixtures

Items	WMA	HMA	Specification Requirements
Air Voids (%)	3.1	3.8	3-5
Marshall Stability (kN)	8.4	8.9	≥8
Tensile Strength Ratio, ASTM D-4867 (%)	80	76	≥75
Dynamic Stability, rutting test (times/mm)	1500	900	≥1000

It can be seen from Table 1 that the air voids of WMA AC-13 was 0.7% lower than that of HMA AC-13, which indicates that WMA is easier to be compacted than HMA. Therefore, WMA could achieve higher density than HMA under the same compaction effort. In addition, the resistance of WMA to moisture damage was better than that of HMA.

SMA-13

The SMA-13 mixture was used in the Huqingping road reconstruction project. The second generation product of Evotherm® was used in the manufacture of the WMA SMA-13 mixture. The Lushanwu diabase was used as coarse aggregate and the Huzhou limestone as fine aggregate. The asphalt was SBS-modified Donghai asphalt from China National Petroleum Corporation. The asphalt content was 5.7% and the cellulose content was 0.3%. Table 2 compares the laboratory performance of WMA and HMA SMA-13 mixtures.

Like the AC-13 mixtures, air void content of WMA SMA-13 mixture was lower than that of HMA SMA-13. The resistance of WMA SMA-13 to moisture damage and rutting was also higher than those of HMA SMA-13.

Table 2. Laboratory Performance of WMA and HMA SMA-13 Mixtures

Items	WMA	HMA	Specification Requirements
Air Voids (%)	3.5	3.9	3-4
Marshall Stability (kN)	7.2	8.1	≥6
Tensile Strength Ratio, ASTM D-4867 (%)	93	84	≥80
Dynamic Stability, rutting test (times/mm)	7150	5445	≥3000

CASE PROJECTS

Xinshi Road Project in Hongkou District

This project is the first WMA test road in Shanghai and the second one in China. The test road was constructed on June 25, 2006. It was approximately 500 m long and 3 cm thick. Totally 260 tons of WMA AC-13 mixture were paved. The first generation product of Evotherm® was used in this project. The emulsified asphalt and aggregate were heated to 80 and 130 ºC, respectively. The mixture temperature was approximately 110 ºC immediately after production and the paving temperature was approximately 100 ºC. Figure 1 shows the paving and compacting processes at the job site.

The pavement performance was tested in the field and cores were taken immediately after construction. Two years later, the pavement performance was tested again. The test results are presented in Table 3.

(a) Paving

(b) Compaction

FIG. 1. Paving and compaction in the Xinshi road project

Table 3. Pavement Performance from Xinshi Road Project

Items	Immediately after Construction	Two Years after Construction	Specification Requirements
Texture depth (mm)	0.65	0.4	≥0.55
British Pendulum Number	66	64	≥45
Largest gap under 3m ruler (mm)	1.3	1.8	≤3
Permeability (ml/min)	85	0	≤300

Ultra Thin Overlay on the North-South Viaduct

The North-South Viaduct is a key project for the 2010 World Expo in Shanghai. Due to the low thickness of ultra thin overlay, the temperature of HMA will decrease so quickly that sufficient compaction is hard to achieve. However, WMA is easier to compact at low temperatures than HMA, which makes it more suitable for ultra thin overlay.

The WMA mixtures of both UTAC-10 and SMA-10 were used in the test section of this project in 2008. Both WMA mixtures satisfied the construction requirements and perform well. In 2009, the WMA SMA-10 mixture was selected for this project. Diabase was used for both coarse and fine aggregate. The polyester fiber was included in the mixture and the fiber content was 0.25%.

Because the project was constructed at night, the production temperature of the mixture was controlled at 145-150 ºC and the paving temperature was no less than 125 ºC. Rubber tire rollers and steel wheel rollers were combined for better compaction. Figure 2 shows the compaction at the job site.

FIG. 2. Compaction in the North-South Viaduct project

The results from field test at the job site indicate that the texture depth of the WMA SMA-10 mixture was larger than 0.8 mm. The British Pendulum Number, an indicator of the skidding resistance, was larger than 50. The surface layer was dense and impermeable to water.

Huqingping Road Project

The WMA SMA-13 mixture was used in the 4-cm thick surface layer in the Huqingping Road project. The project was 3 km long and 3000 tons of mixtures were used. The construction took place during November 22-24, 2008. The ambient temperature was 6-8 ºC during construction. The asphalt plant was 60 km away from the job site, which took more than 2h to haul paving mixture to the job site. The production temperature of the WMA mixture was controlled at 150-160 ºC and the paving temperature was no less than 140-150 ºC. Steel wheel rollers and rubber tire rollers were combined for compaction. Figure 3 shows the paving and compaction at the job site.

Field performance tests were conducted at the job site after the construction. The compaction degree, permeability, and friction number all satisfied the design requirements.


(a) Paving


(b) Compaction

FIG. 3. Paving and compaction at Huqingping Road project

Shanghai Yangtze River Tunnel Road Project

The Shanghai Yangtze River Tunnel Road project was part of the tunnel and bridge engineering project for crossing the Shanghai Yangtze River. The project was 8.74 km long. It is always a technical problem to discharge emissions from construction of asphalt surface layer in long and big tunnels. WMA technology was employed for this tunnel road project. The pavement structure consists of 4-cm thick modified WMA SMA-10 mixture as bottom layer and 4-cm thick modified WMA SMA-13 mixture as flame retarding surface layer. A 200-m long test section was constructed on June 19, 2008. The production temperature was controlled at 145-150 ºC and the paving temperature was no less than 125 ºC. Both rubber tire rollers and steel wheel rollers were used for the compaction. Figure 4 shows the paving and compaction in this project.


(a) Paving


(b) Compaction

FIG. 4. Paving and compaction in Yangtze River Tunnel Road project

The compaction degree, texture depth, and permeability tests were conducted at the job site after the construction. The average compaction degree was 97.8%. The texture depth of the surface layer was 0.9 mm. The coefficient of permeability was 72 ml/min. All test results satisfied the design requirements.

Other Projects

In addition to these projects in Shanghai, WMA technology was also applied in the Yixian viaduct, the A4 highway, the West Zhongshan Road reconstruction, new overlay on the Xing'an concrete pavement road, the Middle Jianguo Road reconstruction, and the Gumei Road reconstruction. The WMA mixtures perform satisfactorily well in all these projects. Besides, WMA technology is also being considered for use in the East-West Thoroughfare and the #-Shaped Channel in the Bund.

SUMMARY

Shanghai is of the few places in China where WMA technology was first applied. In Shanghai, a great number of laboratory experiments have been conducted on WMA and WMA mixtures have been applied in more than 10 projects. These WMA projects have performed satisfactorily well and experiences have been obtained from these projects. This paper presents several WMA projects in Shanghai as summarized in Table 4. In addition, further studies are being conducted on WMA technologies, such as WMA mixtures containing reclaimed asphalt pavement (RAP) and crumb rubber WMA mixtures. Moreover, WMA standards and specifications are being developed, which will further contribute to the spread of WMA technology.

Table 4. Summary of WMA Case Projects in Shanghai

Project Name	WMA	Thickness (cm)	Production Temp (°C)	Paving Temp (°C)
Xinshi Road	AC-13	3	110	100
North-South Viaduct	SMA-10	NA	145-150	>125
Huqingping Road	SMA-13	4	150-160	140-150
Shanghai Yangtze River Tunnel	SMA-10 (bottom) and SMA-13 (top)	4 (bottom) and 4 (top)	145-155	>125

REFERENCES

Hurley, G. C. and Prowell, B. D. (2005a). "Evaluation of Aspha-Min Zeolite for Use in Warm Mix Asphalt" *NCAT 05-04*, National Center for Asphalt Technology, Auburn, Ala.

Hurley, G. C. and Prowell, B. D. (2005b). "Evaluation of Sasobit for Use in Warm Mix Asphalt" *NCAT 05-06*, National Center for Asphalt Technology, Auburn, Ala.

Hurley, G. C. and Prowell, B. D. (2006). "Evaluation of Evotherm for Use in Warm Mix Asphalt" *NCAT 06-02*, National Center for Asphalt Technology, Auburn, Ala.

Xu, S., Yan, B., Ji, J., and Gao, Y. (2005). "The application and future of high energy-saving and low emission warm mix asphalt mixture." *Highway*, 7:195-198 (in Chinese).

Linear viscoelastic behaviour and anisotropy of bituminous mixture compacted with a French wheel compactor

Pauline Clec'h[1], Cédric Sauzéat[2] and Hervé Di Benedetto[3].

Université de Lyon, Ecole Nationale des TPE, Département Génie Civil et Bâtiment (CNRS),
Rue Maurice Audin, 69518 Vaulx-en-Velin Cedex, France
[1]Ph-D student, pauline.clech@entpe.fr
[2]Doctor, cedric.sauzeat@entpe.fr
[3]Professor, herve.dibenedetto@entpe.fr

ABSTRACT: Bituminous mixture is generally considered as isotropic. Nevertheless, its compaction on roads or in laboratory induces anisotropic properties. Anisotropic properties of bituminous mixtures compacted with a French LPC wheel compactor are highlighted in this paper, in the linear viscoelastic domain.
Tension-compression complex modulus tests have been performed on parallelepipedic specimens in two directions, i) direction of compactor wheel movement (direction I) and ii) direction of compaction (direction II). These tests consist in measuring sinusoidal axial and lateral strains as well as sinusoidal axial stress, when sinusoidal axial loading is applied on the specimen. Two parameters are investigated, loading frequency and temperature. Two complex moduli, E_I^* and E_{II}^*, and four Poisson's ratios, $\nu_{II\,I}^*$, $\nu_{III\,I}^*$, $\nu_{I\,II}^*$ and $\nu_{III\,II}^*$, can be obtained.
The vertical direction appears softer than the other one for the highest frequencies. There are few differences between the two directions I and II for parameters concerning viscous effects (phases angles $\phi(E_I)$ and $\phi(E_{II})$, and shift factors). The four Poisson's ratios reveal anisotropic properties.
In addition modeling using anisotropic version of the "2S2P1D" model developed in our laboratory at ENTPE fits well the data.

INTRODUCTION

Bituminous mixture is generally considered as isotropic. Nevertheless, its compaction on roads or in laboratory induces anisotropic properties. The objective of this paper is to highlight some anisotropic properties of bituminous mixtures compacted with a French LPC wheel compactor, in the linear viscoelastic domain. In the frequency domain, this linear viscoelastic theory uses the complex modulus (Di Benedetto and Corte 2005). Tension-compression complex modulus tests are performed on parallelepipedic shaped specimens in two directions, i) direction of compactor wheel movement (direction I) and ii) direction of compaction (direction II).

These tests consist in measuring sinusoidal axial and lateral strains as well as sinusoidal axial stress, when sinusoidal axial loading is applied on the specimen. Small axial strain amplitudes are applied (less than 10^{-4} m/m) so that the behavior remains inside the linear domain. Two complex modulus, E_I^* and E_{II}^*, can be calculated. In addition, the procedure allows to obtain four different Poisson's ratios $\nu_{II\,I}^*$, $\nu_{III\,I}^*$, $\nu_{I\,II}^*$ and $\nu_{III\,II}^*$, following the considered material direction.

Two parameters are investigated, loading frequency (from 0.01 Hz to 10 Hz) and temperature (from -26.3°C to 56.6°C).

Norms and phase angles of the two complex modulus and the four different Poisson's ratios can be compared and reveal anisotropic properties.

In addition the anisotropic version of the "2S2P1D" model (2 Springs, 2 Parabolic, 1 Dashpot) developed at ENTPE is used to model the data.

MATERIAL DESCRIPTION AND SAMPLE PREPARATION

Bituminous mixture with 6.85 % (aggregate weight) of 35/50 penetration grade bitumen and a continuous 0/6 mm La Noubleau Airvault granite aggregate grading was tested.

Parallelepipedic specimens are sawn from bigger samples tested by Nguyen (2009). These initial samples of length 550 mm, width 65 mm and height 70 mm, were sawn from slabs made with a French LPC ("Laboratoire des Ponts et Chaussées") wheel compactor according to the European standard NF EN 12697-33 (Fig. 1 and Fig. 2 a)). They were used by Nguyen (2009) for four points bending tests (Fig. 2 b)).

The specimens tested in this study have been cut far enough from the crack to be considered as non-previously loaded samples. Four specimens have been tested:

- P3EP2 and P3EP3 specimens from P3 sample which are 120 mm in height, 65 mm in width and 70 mm in depth, with a compacity of 97.2 % (Fig. 2 c)),
- P1EP2 and P1EP3 specimens from P1 sample which are 70 mm in height, 65 mm in width and 70 mm in depth, with a compacity of 97.8 % (Fig. 2 d)).

In order to measure axial and lateral strains, six strain gauges, 50 mm in length, are stuck on each specimen prior to testing:

- For P3EP2, P3EP3 and P1EP3 specimens, four strain gauges are stuck centered on each lateral face: two to measure strain along direction III (G2 and G5) and two to measure strain along direction II (G3 and G6) (Fig. 3 a) and b)). A strain gauge named G1 (respectively G4) is stuck centered at the mid height of the specimen on the same face as G2 (respectively G5) to measure strain along direction I.
- For P1EP2 specimen, four strain gauges are stuck centered on each lateral face: two to measure strain along direction I (G2 and G5) and two to measure strain along direction III (G3 and G6) (Fig. 3 c)). A strain gauge named G1 (respectively G4) is stuck centered at the mid height of the specimen on the same face as G2 (respectively G5) to measure strain along direction II.

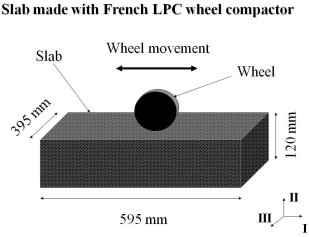

FIG. 1. Slab compaction

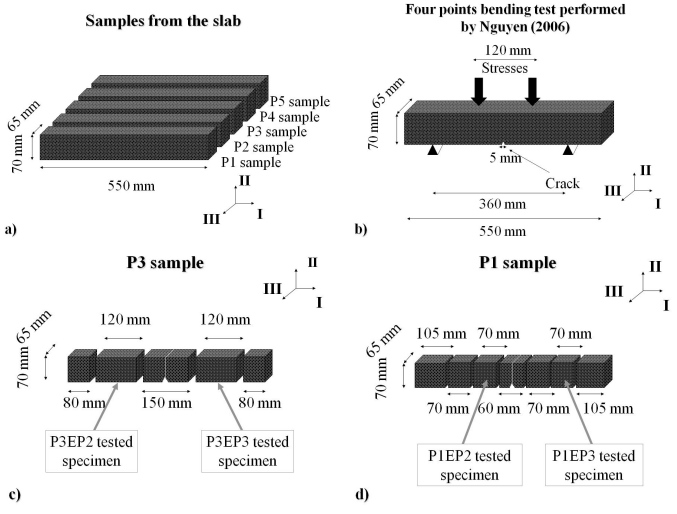

FIG. 2. a) Initial samples which are obtained from the slab, b) Test performed on the initial samples by Nguyen (2009), c) Origin and geometry of P3EP2 and P3EP3 specimens from P3 sample, d) Origin and geometry of P1EP2 and P1EP3 specimens from P1 sample.

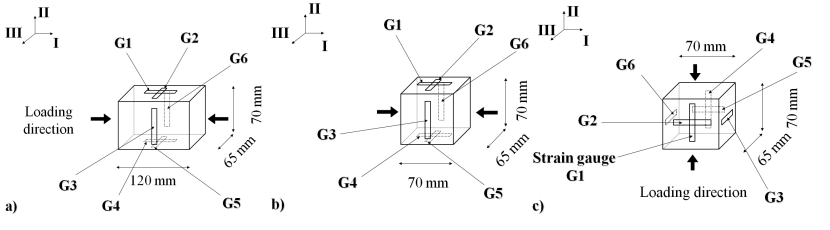

FIG. 3. Loading directions and strain gauge positions (G1 to G6) on: a) P3EP2 and P3EP3 specimens, b) P1EP3 specimen, c) P1EP2 specimen.

3 TEST DESCRIPTION

Tension-compression complex modulus tests are performed on the previously presented parallelepipedic shaped specimens with the INSTRON 1273 hydraulic press of the ENTPE/DGCB laboratory (Clec'h 2006). Sinusoidal axial and lateral strain values are measured as well as sinusoidal axial stress, when sinusoidal axial loading is applied on the specimen. Small axial strain amplitudes are applied (less than 10^{-4} m/m) so that the behavior remains inside the linear domain.

Two cases are considered:

- Axial loading is applied in the direction of compactor wheel displacement (direction I) for P3EP2, P3EP3 and P1EP3 specimens ;
- Axial loading is applied in the direction of compaction (direction II) for P1EP2 specimen.

The bituminous specimens are loaded for different temperatures (from -26.3°C to 56.6°C) at different frequencies (0.01 Hz, 0.03 Hz, 0.1 Hz, 0.3 Hz, 1 Hz, 3 Hz and 10 Hz for each temperature).

The relation between stress and strain inside the parallelepipedic specimen is defined by the following equation, expressed in axes I, II, III:

$$\underline{\varepsilon^*} = \underline{\underline{M^*}}\,\underline{\sigma^*} \quad \text{with:} \quad \underline{\underline{M^*}} = \begin{pmatrix} \frac{1}{E_I^*} & -\frac{\nu_{III}^*}{E_{II}^*} & -\frac{\nu_{IIII}^*}{E_{III}^*} \\ -\frac{\nu_{III}^*}{E_I^*} & \frac{1}{E_{II}^*} & -\frac{\nu_{IIIII}^*}{E_{III}^*} \\ -\frac{\nu_{IIII}^*}{E_I^*} & -\frac{\nu_{IIIII}^*}{E_{II}^*} & \frac{1}{E_{III}^*} \end{pmatrix} \tag{1}$$

These four homogeneous tests enable to obtain E_I^*, E_{II}^*, ν_{III}^*, ν_{IIII}^*, ν_{III}^* and ν_{IIIII}^* which gives information about the anisotropy of the bituminous mixture. The comparison between ν_{III}^*, ν_{IIII}^*, ν_{III}^* and ν_{IIIII}^* is possible.

When complex modulus test is performed in direction I, the sinusoidal evolution with time of the four measured values is defined by equations (2), (3), (4) and (5). The measured values in complex notations are also written.

$$\varepsilon_I(t) = \varepsilon_{0I}\sin(\omega t) \rightarrow \varepsilon_I^* = \varepsilon_{0I} \tag{2}$$

$$\sigma_I(t) = \sigma_{0I}\sin(\omega t + \phi_{E_I}) \rightarrow \sigma_I^* = \sigma_{0I}e^{j\phi_{E_I}} \tag{3}$$

$$\varepsilon_{II}(t) = \varepsilon_{0\,II}\sin(\omega t + \pi + \phi_{\nu_{III}}) = -\varepsilon \quad \sin(\omega t + \phi_{III}) \rightarrow \varepsilon_{II}^* = \varepsilon_{0\,II}e^{j(\pi+\phi_{\nu_{III}})} = -\varepsilon_{0\,II}e^{j\phi_{\nu_{III}}} \tag{4}$$

$$\varepsilon_{III}(t) = \varepsilon_{0\,III}\sin(\omega t + \pi + \phi_{\nu_{III}}) = -\varepsilon_{0\,III}\sin(\omega t + \phi_{\nu_{III}}) \rightarrow \varepsilon_{III}^* = \varepsilon_{0\,III}e^{j(\pi+\phi_{\nu_{III}})} = -\varepsilon_{0\,III}e^{j\phi_{\nu_{III}}} \tag{5}$$

j is considered the complex number defined by $j^2 = -1$. $\phi(E_I)$ is the phase angle between the axial strain along axis I and the axial stress along axis I, $\phi(\nu_{II\,I})$ is the phase angle between the axial strain along axis I and the opposite of strain along axis

II and $\phi(\nu_{III\,I})$ is the phase angle between the axial strain along axis I and the opposite of strain along axis III.

Complex modulus E_I^* and complex Poisson's ratios $\nu_{II\,I}^*$ and $\nu_{III\,I}^*$ can be obtained with equations (6), (7) and (8).

$$E_I^*(\omega) = \frac{\sigma_I^*}{\varepsilon_I^*} = \left|E_I^*(\omega)\right| e^{j\phi_{E_I}} = \frac{\sigma_{0I}}{\varepsilon_{0I}} e^{j\phi_{E_I}} \tag{6}$$

$$\nu_{II\,I}^*(\omega) = -\frac{\varepsilon_{II}^*}{\varepsilon_I^*} = \left|\nu_{II\,I}^*(\omega)\right| e^{j\phi_{\nu_{II\,I}}} = \frac{\varepsilon_{0II}}{\varepsilon_{0I}} e^{j\phi_{\nu_{II\,I}}} \tag{7}$$

$$\nu_{III\,I}^*(\omega) = -\frac{\varepsilon_{III}^*}{\varepsilon_I^*} = \left|\nu_{III\,I}^*(\omega)\right| e^{j\phi_{\nu_{III\,I}}} = \frac{\varepsilon_{0III}}{\varepsilon_{0I}} e^{j\phi_{\nu_{III\,I}}} \tag{8}$$

$\varepsilon_I(t)$ is measured by axial strain gauges G1 and G4.

$\varepsilon_{II\,I}(t)$ is measured by radial strain gauges G3 and G6.

$\varepsilon_{III\,I}(t)$ is measured by radial strain gauges G2 and G5.

For each of these three values, the mean of the strains given by the two gauges is considered.

Comparatively, when complex modulus test is performed in direction II, it is possible to obtain complex modulus E_{II}^* and complex Poisson's ratios $\nu_{I\,II}^*$ and $\nu_{III\,II}^*$:

$$E_{II}^*(\omega) = \frac{\sigma_{II}^*}{\varepsilon_{II}^*} = \left|E_{II}^*(\omega)\right| e^{j\phi_{E_{II}}} = \frac{\sigma_{0II}}{\varepsilon_{0II}} e^{j\phi_{E_{II}}} \tag{9}$$

$$\nu_{I\,II}^*(\omega) = -\frac{\varepsilon_I^*}{\varepsilon_{II}^*} = \left|\nu_{I\,II}^*(\omega)\right| e^{j\phi_{\nu_{I\,II}}} = \frac{\varepsilon_{0I}}{\varepsilon_{0II}} e^{j\phi_{\nu_{I\,II}}} \tag{10}$$

$$\nu_{III\,II}^*(\omega) = -\frac{\varepsilon_{III}^*}{\varepsilon_{II}^*} = \left|\nu_{III\,II}^*(\omega)\right| e^{j\phi_{\nu_{III\,II}}} = \frac{\varepsilon_{0III}}{\varepsilon_{0II}} e^{j\phi_{\nu_{III\,II}}} \tag{11}$$

$\varepsilon_{II}(t)$ is measured by axial strain gauges G1 and G4.

$\varepsilon_{I\,II}(t)$ is measured by radial strain gauges G2 and G5.

$\varepsilon_{III\,II}(t)$ is measured by radial strain gauges G3 and G6.

TEST RESULTS

Complex modulus norms $|E_I^*|$ and $|E_{II}^*|$

Figure 4 a) (respectively 4 b)) shows $|E_I^*|$ (respectively $|E_{II}^*|$) isotherm curves for the tested specimens. Complex modulus norm increases as a function of frequency and, inversely, it decreases as a function of temperature, which was expected.

The unidirectional linear viscoelastic behaviour of bituminous materials is thermorheologically simple (the Time-Temperature Superposition Principle (TTSP) is verified) (Doubbaneh 1995, Di Benedetto et al. 2001, 2004, 2005, 2007, 2008, Airey et al. 2004, Delaporte et al. 2005, 2007). This allows plotting a master curve at any chosen reference temperature (T_{ref}). The shift factor a_{TE} corresponds to the translation value, in a log scale, from any temperature T to the reference temperature (T_{ref}).

$|E_I^*|$ and $|E_{II}^*|$ master curves obtained for the tested specimens at a reference

temperature of 10°C are plotted figures 4 a) and 4 b). The shift factors a_{TEI} and a_{TEII} are given figure 5. $|E_I^*|$ and $|E_{II}^*|$ vary between 50 MPa for the lowest frequencies (or/and highest temperatures) and about 35 000 – 40 000 MPa for the highest frequencies (or/and lowest temperatures). These results fit well with the literature (De La Roche et al. 1994, Wictzack et al. 1999, Pellinen et al. 2007, Di Benedetto et al. 2008).

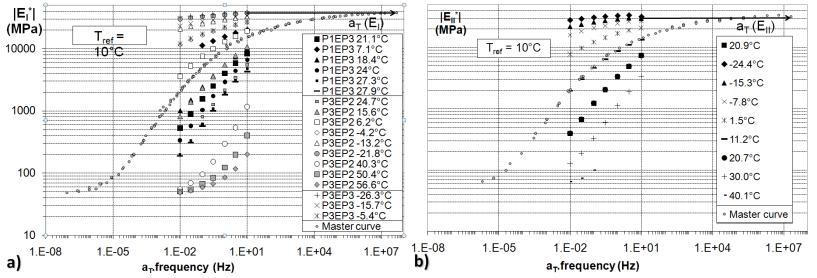

FIG. 4. a) Experimental values of $|E_I^*|$ and master curve plotted at a reference temperature of 10°C. b) Experimental values of $|E_{II}^*|$ and master curve plotted at a reference temperature of 10°C.

The classical WLF law (William, Landel and Ferry) (Ferry 1980) is used to fit the experimental shift factors a_{TEI} and a_{TEII}:

$$\log(a_T) = \frac{-C_1(T - T_S)}{C_2 + (T - T_S)} \qquad \text{with} \quad C_1 = 23.4 \text{ and } C_2 = 163.9 \tag{12}$$

Experimental and subsequently WLF a_{TEI} and a_{TEII} are really close.

$$a_{TEI} \approx a_{TEII} \approx a_T \tag{13}$$

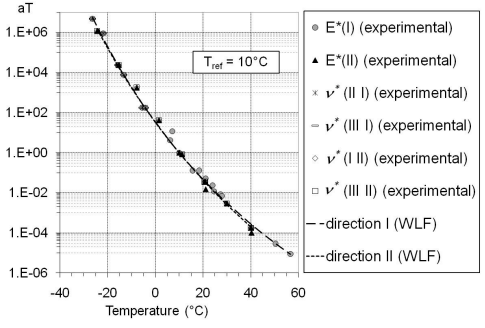

FIG. 5. Shift factors a_T of complex modulus and complex Poisson's ratios. Comparison with WLF law predictions.

Figure 6 shows $|E_I^*|$ and $|E_{II}^*|$ experimental master curves obtained at the reference temperature of 10°C and the corresponding master curves obtained with the 2S2P1D model. On this figure $|E_I^*|$ and $|E_{II}^*|$ values (23 750 MPa and 19 500 MPa) obtained from wave propagation tests performed by Di Benedetto et al. (2009) on the same bituminous mixture at a temperature of 26°C and a frequency of about 30 000 kHz are also plotted. a_{TEI} (26°C) = a_{TEII} (26°C) and equivalent frequencies have been obtained thanks to equation 12. The results which are presented in this study fit well with Di Benedetto et al.'s work (2009).

It can be seen that $|E_I^*|$ and $|E_{II}^*|$ are very close for low frequencies, while, for high frequencies, $|E_{II}^*|$ is about 10% smaller. It comes:

$$\begin{cases} |E_I^*| \approx |E_{II}^*| \text{ for low frequencies} \\ |E_I^*| \geq |E_{II}^*| \text{ for high frequencies} \end{cases} \quad (14)$$

For high frequencies, the vertical direction appears softer than the other one. The anisotropy of the specimens appears more significantly for high frequencies where the effects of geometrical organization of the granular skeleton have a visible effect.

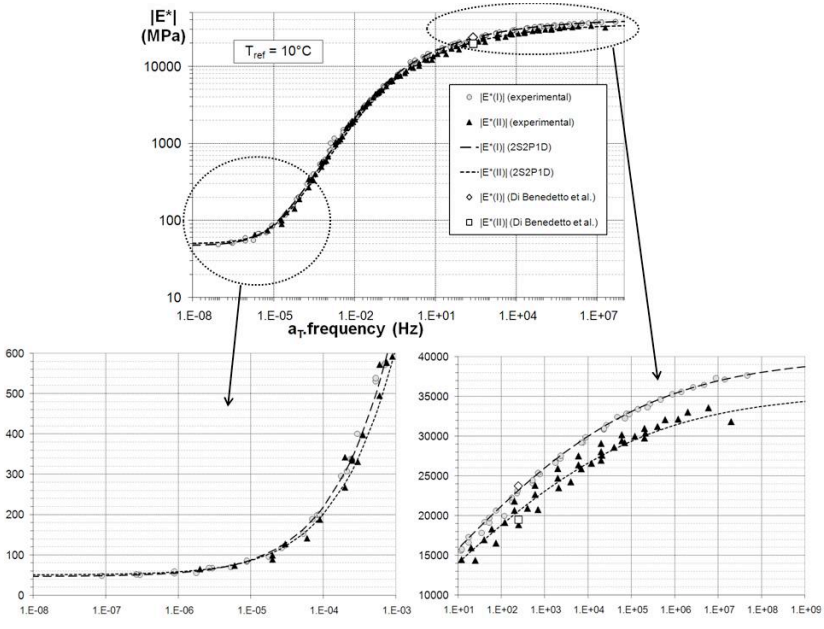

FIG. 6. Master curves of $|E_I^*|$ and $|E_{II}^*|$ plotted at a reference temperature of 10°C and 2S2P1D models.

Di Benedetto et al. (2004) presented a general model for modeling linear viscoelastic

properties of both bituminous binders and mixes. This model called 2S2P1D (2 Springs, 2 Parabolic, 1 Dashpot) consists of a generalization of the Huet-Sayegh model. It is based on a simple combination of physical elements (spring, dashpot and parabolic element). The Huet-Sayegh model (Sayegh 1965) has been adapted by adding a linear dashpot in series with the two parabolic elements (Fig. 7). One of the interest of 2S2P1D model is to be suitable for bitumens, mastics and mixtures. At a given temperature, the introduced 2S2P1D model has 7 constants and its complex modulus is given by the following expression:

$$E^*(j\omega\tau) = E_{00} + \frac{E_0 - E_{00}}{1 + \delta(j\omega\tau)^{-k} + (j\omega\tau)^{-h} + (j\omega\beta\tau)^{-1}} \quad (15)$$

With:

j: complex number defined by $j^2 = -1$,

ω: the pulsation = 2π.f, (f is the frequency)

k, h: constant exponents such as 0<k<h<1,

δ: constant

E_{00} the static modulus when $\omega \rightarrow 0$,

E_0 the glassy modulus when $\omega \rightarrow \infty$,

η: Newtonian viscosity, $\eta=(E_0 - E_{00}).\beta.\tau$; when $\omega \rightarrow 0$, then $E^*(i\omega\tau) \sim E_{00} + j\omega.(E_0 - E_{00}).\beta.\tau$; β is dimensionless.

τ: characteristic time, which value varies only with temperature. τ evolution accounts for the Time-Temperature Superposition Principle:

$$\tau(T) = a_T(T) \,.\, \tau(T_{ref}) \quad (16)$$

where $a_T(T)$: the shift factor at temperature T,

$\tau(T_{ref})$ determined at the reference temperature T_{ref}.

Only 7 constants (δ, k, h, E_0, E_{00}, β and $\tau(T_{ref})$) are needed to entirely determine the E^* linear viscoelastic behaviour of the considered material, at a given temperature. If the Time-Temperature Superposition Principle holds (TTSP), only the τ parameter depends on temperature. The two additional constants C_1 and C_2 (calculated at the reference temperature T_{ref} chosen equal to 10°C in this paper) of the WLF equation (17) are needed (Fig. 4). The total number of constants of the model then amounts to 9 (7+2).

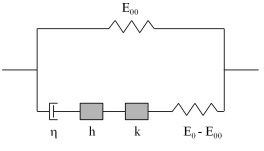

FIG. 7. 1D Representation of the considered general model "2S2P1D", h and k are two parabolic creep elements.

Table 1 shows the obtained values of the E^* (in directions I and II) 2S2P1D model parameters for the tested bituminous mixture. It can be noticed that k, h and δ parameters are independent of the direction. As shown in previous studies these constants depend only on bitumen (Di Benedetto et al. 2004, Delaporte et al. 2007).

Delaporte's k, h and δ values have been taken in this model since the same 50/70 bitumen has been used (Delaporte 2007).

Table 1. E_I^* and E_{II}^* 2S2P1D model parameters

	E_0 (MPa)	E_∞ (MPa)	k	h	δ	τ (T_{ref})	β
E_I^*	47	40 000	0.2	0.58	2.2	0.17	∞
E_{II}^*	50	35 500	0.2	0.58	2.2	0.17	∞

Complex modulus phase angle $\phi(E_I)$

Figure 8 a) presents $\phi(E_I)$ isotherms and master curve at a reference temperature of 10°C. The results fit well with the literature (Di Benedetto et al. 2008). $\phi(E_I)$ increases as a function of temperature up to a maximum (48°) and then decreases. Beyond a a time-temperature couple depending on bitumen nature (27.9°C-0.1 Hz for E_I and 30°C-0.3 Hz for E_{II}), bitumen becomes relatively fluid and rigidity is ensured by granular skeleton. Figure 8 b) shows $\phi(E_I)$ and $\phi(E_{II})$ experimental master curves obtained at a reference temperature of 10°C and the corresponding master curves obtained with the 2S2P1D model. $\phi(E_I)$ and $\phi(E_{II})$ are very close like a_{TEI} and a_{TEII}. There are very few differences between the two directions I and II for parameters concerning viscous effects.

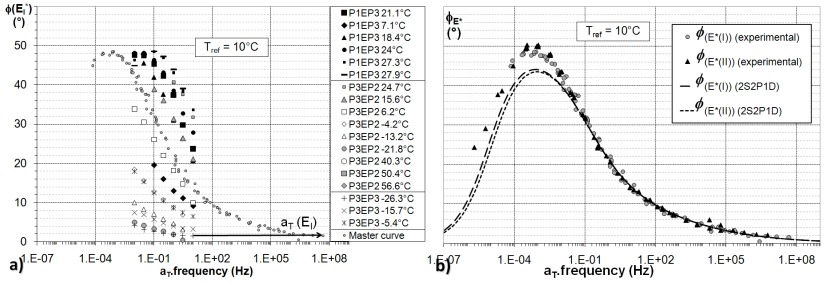

FIG. 8. a) Experimental values of ϕ_{EI} and master curve plotted at a reference temperature of 10°C. b) Master curves of ϕ_{EI} and ϕ_{EII} plotted at a reference temperature of 10°C and 2S2P1D models.

Complex Poisson's ratios norms $|\nu_{I\,II}^*|$, $|\nu_{III\,II}^*|$, $|\nu_{II\,I}^*|$ and $|\nu_{III\,I}^*|$

Poisson's ratio $|\nu^*|$ is not a constant equal to 0.35, value that is generally considered in the literature (Charif 1991, Doubbaneh 1995, Di Benedetto et al. 2008). Figure 9 a) (respectively b)) presents $|\nu_{II\,I}^*|$ (respectively $|\nu_{I\,II}^*|$) isotherm curves. The master curve at the reference temperature of 10°C is also plotted for each Poisson's ratio norm. The obtained experimental shift factor $a_{T\nu III}$ (respectively $a_{T\nu II}$) can be considered as identical to the shift factor a_{TEI} (respectively a_{TEII}) obtained for the complex modulus E_I^* (respectively E_{II}^*) (Fig. 5). $|\nu_{III\,I}^*|$ and $|\nu_{III\,II}^*|$ master curves at 10°C have also been

obtained. As Di Benedetto et al. (2008) showed, a unique shift factor can be considered for each direction:

$$\begin{cases} a_{TEI} = a_{TvIII} = a_{TvIIII} = a_{TdirectionI} \\ a_{TEII} = a_{TvIII} = a_{TvIIIII} = a_{TdirectionII} \end{cases} \quad \text{with} \quad a_{TdirectionI} \approx a_{TdirectionI'} = a_T \quad (17)$$

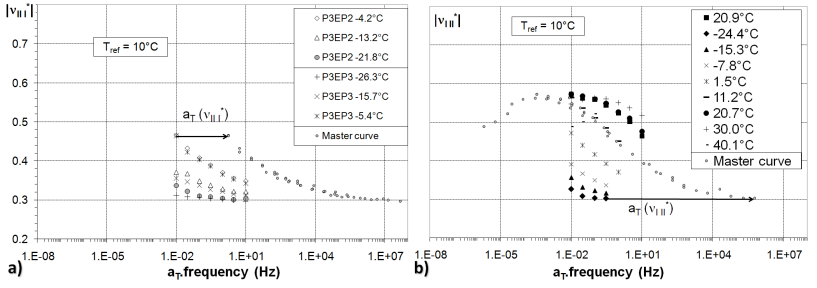

FIG. 9. a) Experimental values of $|\nu_{I\,II}^*|$ and master curve plotted at 10°C, b) Experimental values of $|\nu_{II\,I}^*|$ and master curve plotted at 10°C.

Figure 10 shows $|\nu_{I\,II}^*|$, $|\nu_{III\,II}^*|$, $|\nu_{II\,I}^*|$ and $|\nu_{III\,I}^*|$ master curves at 10°C and the corresponding master curves obtained with the 2S2P1D model. $|\nu_{II\,I}^*|$ and $|\nu_{I\,II}^*|$ are very close. $|\nu_{III\,I}^*|$ is definitely smaller. It must be noticed that two different tests give these $|\nu_{III\,I}^*|$ results. $|\nu_{III\,II}^*|$ is close to $|\nu_{II\,I}^*|$ and $|\nu_{I\,II}^*|$ for the highest frequencies (or the lowest temperatures) and is higher than the three other for the lowest frequencies (or the highest temperatures). When the material is not isotropic, it is possible to obtain Poisson's ratios higher than 0.5.

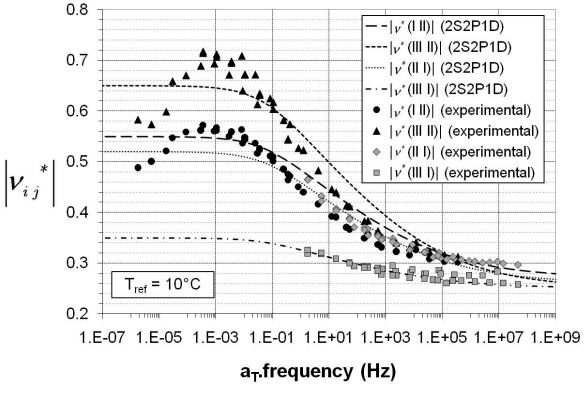

FIG. 10. Master curves of $|\nu_{I\,II}^*|$, $|\nu_{III\,II}^*|$, $|\nu_{II\,I}^*|$ and $|\nu_{III\,I}^*|$ plotted at a reference temperature of 10°C and 2S2P1D models.

$|\nu_{I\,II}^*|$, $|\nu_{III\,II}^*|$, $|\nu_{II\,I}^*|$ and $|\nu_{III\,I}^*|$ master curves can be simulated with the 2S2P1D model (Fig. 9). 2S2P1D model Poisson's ratio is given by the expression 18 (Di Benedetto et al. 2007). Table 2 shows the values of the ν^* 2S2P1D model parameters for the studied bituminous mixture.

$$\nu^*(\omega)=\nu_{00}+\frac{(\nu_0-\nu_{00})}{1+\delta(i\omega\tau)^{-k}+(i\omega\tau)^{-h}+(i\omega\beta\tau)^{-1}} \quad (18)$$

With ν_0, Poisson's ratio when $\omega \to \infty$ and ν_{00}, Poisson's ratio when $\omega \to 0$.

Other constants that are independent of the direction as shown previously, are given equation 15.

Table 2. $\nu_{I\,II}^*$, $\nu_{III\,II}^*$, $\nu_{II\,I}^*$ and $\nu_{III\,I}^*$ 2S2P1D parameters

	ν_{00}	ν_0
$\nu_{II\,I}^*$	0.52	0.26
$\nu_{III\,I}^*$	0.35	0.25
$\nu_{III\,II}^*$	0.65	0.25
$\nu_{I\,II}^*$	0.55	0.27

CONCLUSIONS

Anisotropic properties in the small strain domain, of bituminous mixtures compacted with a French LPC wheel compactor, have been measured and modeled in this paper. Tension-compression complex modulus tests are performed on parallelepipedic shaped specimens in two directions: i) direction of compactor wheel movement (direction I) and ii) direction of compaction (direction II). Two complex moduli, E_I^* and E_{II}^*, and four Poisson's ratios $\nu_{II\,I}^*$, $\nu_{III\,I}^*$, $\nu_{I\,II}^*$ and $\nu_{III\,II}^*$, were obtained.

$|E_I^*|$ and $|E_{II}^*|$ are very close for low frequencies, while, for high frequencies, $|E_{II}^*|$ is about 10% smaller. In the high frequency (and/or low temperature) domain, the vertical direction seems softer than the perpendicular one. There are very few experimental differences between the two directions I and II for parameters concerning viscous effects: $\phi(E_I)$ and $\phi(E_{II})$ can be considered as equal as well as shift factors a_{TEI} and a_{TEII} equal to a_{TE}. Concerning Poisson's ratio, $|\nu_{II\,I}^*|$ and $|\nu_{I\,II}^*|$ are very close. $|\nu_{III\,I}^*|$ is definitely smaller. $|\nu_{III\,II}^*|$ is close to $|\nu_{II\,I}^*|$ and $|\nu_{I\,II}^*|$ for the highest frequencies and is higher than the three others for the lowest frequencies. A unique shift factor can be considered for each direction and for Young's Moduli and Poisson's ratios: $a_T = a_{TE} = a_{T\nu} = a_{T\text{direction I}} = a_{T\text{direction II}}$. It can be highlighted that the rheological model called "2S2P1D model" developed by Di Benedetto et al. (2004) fits quite well the experimental values for the 6 rheological parameters (E_I^*, E_{II}^*, $\nu_{II\,I}^*$, $\nu_{III\,I}^*$, $\nu_{I\,II}^*$ and $\nu_{III\,II}^*$) on the wide range of considered temperatures and frequencies. The viscous constants that are given only by the bitumen are identical for these 6 parameters. Then, the viscous behavior introduced by the binder only appears as isotropic, which is a noticeable result.

REFERENCES

Airey, G. D. and Behzad, R. (2004). "Combined bituminous binder and mixture linear rheological properties". *Construction and Building Materials,* Vol. 18: p. 535-548.

Charif, K. (1991). "Contribution à l'étude du comportement mécanique du béton bitumineux en petites et grandes déformations", *thèse de doctorat*. *École Centrale Paris*. [in French]

Clec'h, P. (2006). "Comportement des enrobés bitumineux sous sollicitations multidirectionnelles – essais de module complexe sur éprouvettes parallélépipédique et cylindrique", *master recherche ENTPE. Lyon*. [in French]

De la Roche, C., Corté, J.-F., Gramsammer, J. C., Odéon, H., Tiret, L. and Caroff, G. (1994). "Étude de la fatigue des enrobés bitumineux à l'aide du manège de fatigue du LCPC". *Revue générale des routes et aerodromes,* n° 716: p. 62-74. [in French]

Delaporte, B., (2007). "Etude de la rhéologie des mastics bitumineux à l'aide d'un rhéomètre à cisaillement annulaire". *Thèse de doctorat. INSA de Lyon.* 250 p. [in French]

Delaporte, B., Di Benedetto, H., Sauzéat, C.and Chaverot, P. (2005). "Linear viscoelastic properties of mastics: results from a new annular shear rheometer and modelling". *Bearing Capacity of Roads, Railways and Airfileds. Trondheim.*

Delaporte, B., Di Benedetto, H., Chaverot, P. and Gauthier, G. (2007). "Linear viscoelastic properties of bituminous materials: from Binders to Mastics". *Journal of the Association of Asphalt Paving Technologists (AAPT)*, Vol. 76. p. 455-494. San Antonio.

Di Benedetto H., Partl, M.N., Francken, L. and De la Roche, C. (2001). "Stiffness testing for bituminous mixtures". *Journal Materials and Structures,* Vol. 34. p. 66-70.

Di Benedetto, H., Olard, F., Sauzéat, C. and Delaporte, B. (2004). "Linear viscoelastic behavior of bituminous materials: from binders to mixes". *International Journal of Road Materials and Pavement Design (EATA),* Vol.5, special issue: p. 163-202.

Di Benedetto, H. and Corté, J.F. (2005). *Matériaux routiers bitumineux 2: constitution et propriétés thermomécaniques des mélanges*, 288 p, Lavoisier. [in French]

Di Benedetto, H., Delaporte, B. and Sauzéat, C. (2007). "Three-dimensionnal linear behavior of bituminous materials: experiments and modelling". *International Journal of Geomechanics (ASCE),* Volume 7 (issue 2): p. 149-157.

Di Benedetto, H., Nguyen, M., Pouget, S., and Sauzeat, C. (2008). "Time-temperature superposition principle for bituminous mixtures: three dimensional approach and extension in the non-linear domain". *ICTI. Beijing.*

Di Benedetto, H., Sauzeat, C. and Sohm, J. (to be published 2009). "Stiffness of bituminous mixtures using ultrasonic waves propagation". International Journal *Road Materials and Pavement Design.*

Doubbaneh, E. (1995). "Comportement mécanique des enrobés bitumineux des " petites " aux " grandes " déformations". *Thèse de doctorat. INSA de Lyon.* 219 p. [in French]

Ferry, J.D. (1980). "Viscoelastic Properties of Polymers" John & Sons.

Nguyen, M. L. (2009). "Etude de la fissuration et de la fatigue des enrobes bitumineux". Thèse de doctorat. INSA de Lyon – ENTPE. 276 p. [in French]

Pellinen, T., Zofka, A., Marasteanu, M. and Funk, N. (2007). "Asphalt mixture stiffness predictive models" *Journal of the Association of Asphalt Paving*

Technologists (AAPT), Vol. 76. p. 575-626. San Antonio.

Sayegh, G. (1965). "Variation des modules de quelques bitumes purs et enrobés bitumineux". *Thèse de doctorat d'ingénieur. Faculté des sciences de l'université de Paris*. 74 p. [in French]

Wictzack, M. W., Andrei, D. and Mirza, W. (1999). "Developpement of Revised Predictive Model for the Dynamic (Complex) Modulus of Asphalt Mixtures". Interteam Technical Report, NCHRP Project 1-37A, University of Maryland.

Yan, X. (1992). "Comportement mécanique des enrobés au bitume et au bitume-polymère (Styrelf 13) – Utilisation de l'essai triaxial de révolution". *Thèse de doctorat. INSA de Lyon – ENTPE.* 163 p. [in French]

Deformation Prediction of Asphalt Mixtures under Repeated Load Base on Viscoelastic Mechanical Model

Li-juan Zhang [1], Xiao-ning Zhang[2], and Chi-chun Hu [3]

[1] Associate Professor, School of Civil Engineering and Transportation, South China University of Technology, Guangzhou 510641, P.R. China; tczljuan@scut.edu.cn.
[2] Professor, School of Civil Engineering and Transportation, South China University of Technology, Guangzhou 510641, P.R. China; ctxnzh@scut.edu.cn.
[3] Ph.D., School of Civil Engineering and Transportation, South China University of Technology, Guangzhou 510641, P.R. China; huchichun@gmail.com.

ABSTRACT: The deformation of asphalt mixtures can be well described by a generalized Maxwell viscoelastic model, which Prony series coefficients are obtained via static creep tests of AC-13C unmodified and modified asphalt mixtures. A half-sinusoidal load with 0.1s loading duration and 0.9s unloading duration is used to simulate the dynamic vehicle load, and the strain of AC-13C unmodified and modified asphalt mixtures under repeated load is analyzed by viscoelastic finite element method, then we obtain an excellent correlation with the measured strain. The results shows that the viscoelastic finite element method together with the parameters determined by the static creep test could well predict strain of asphalt mixtures under repeated load, and these analysis could be used in permanent deformation prediction of asphalt pavement under moving loads.

INTRODUCTION

Asphalt mixtures are a typical viscoelastic material and have elastic, viscous and viscoelastic properties. Blab et al. (2002) presented a method to derive viscoelastic material properties of asphalt concrete (AC) mixes from dynamic frequency sweep shear (FS-S) tests of lab specimens or field cores that can be used to define material behavior of the AC layers in the 3D FE pavement model. The results encourage employment of the FE pavement model for further simulation work to assess the rutting potential of AC mixes in combination with different tire types and loading situations. Mulungye et al. (2007) described the constitutive equation of asphalt mixtures as the generalized Maxwell viscoelastic model. The effect of tire pressure, wheel configuration and axle load variations of a transportation truck, on structural performance of a flexible road pavement with thin asphalt surfacing layer and soft peat soil sub-grade were evaluated using the finite element method. Kim et al. (2007) developed a computational constitutive model to predict damage and fracture failure of asphalt concrete mixtures. Complex heterogeneity and inelastic mechanical

behavior were addressed by the generalized Maxwell model by using finite-element methods and elastic–viscoelastic constitutive relations. Peng et al. (2007) deduced the finite element method of nonlinear viscoelasticity for the generalized Maxwell model, set up a nonlinear viscoelastic-elastoplastic constitutive model of permanent deformation for asphalt pavement. Then the permanent deformation of asphalt pavement was analyzed depending on its material properties, such as elasticity, nonlinear elasticity, plasticity, viscoelasticity and nonlinear viscoelasticity, etc.

The viscoelastic parameters of model can be determined by either static or dynamic material tests. In this paper, the Prony series coefficients of the generalized Maxwell model are obtained by fitting static creep test data of AC-13C unmodified and modified asphalt mixtures and the deformation response of asphalt mixtures under repeated load is predicted using viscoelastic finite element method. Then the permanent deformation rule of asphalt mixtures under repeated load is found.

VISCOELASTIC CONSTITUTIVE MODEL

For the small deformation theory, constitutive relation for an isotropic viscoelastic material can be written as(Blab,et.al., 2002; Hibbitte, Karlsson, 2005):

$$\sigma(t) = \int_0^t 2G(t-\zeta)\frac{\mathrm{d}e}{\mathrm{d}\zeta}\mathrm{d}\zeta + I\int_0^t K(t-\zeta)\frac{\mathrm{d}\Delta}{\mathrm{d}\zeta}\mathrm{d}\zeta \qquad (1)$$

where c is the Cauchy stress tensor, e the deviatoric part of the strain, Δ the volumetric part of the strain, $G(t)$ the shear modulus function, $K(t)$ the bulk modulus function, t the current time, ζ the past time, I the unit tensor.

The functions are assumed to satisfy a linear viscoelastic model of a generalized Maxwell model(Fig.1). This classical differential model(Blab,et.al.(2002),Zhang (2005))with one Kelvin model and several Maxwell models connected in parallel exhibit a solid type character with instantaneous elasticity, delayed elasticity with various retardation times, stress relaxation with various relaxation times and viscous flow.

FIG.1. The generalized Maxwell model

Shear modulus and bulk modulus function can be expressed in the form of Prony series:

$$\begin{cases} G = G_\infty + \sum_{i=1}^{n_G} G_i e^{-t/\tau_i^G} \\ K = K_\infty + \sum_{i=1}^{n_k} K_i e^{-t/\tau_i^k} \end{cases} \qquad (2)$$

where, G_∞ is the long-term shear relaxation modulus, K_∞ the long-term bulk relaxation

modulus, G_i the shear relaxation modulus corresponding with relaxation time τ_i^G, and K_i the bulk relaxation modulus corresponding with relaxation time τ_i^k.

In general, the shear relaxation modulus $G(t)$, tension and compression relaxation modulus $E(t)$ have relation shown in equation (3):

$$G(t) = \frac{E(t)}{2(1+\nu)} \tag{3}$$

where, ν is the Poisson's Ratio, and the Poisson's Ratio of asphalt mixtures in this paper is assumed to be a constant value of 0.3.

In addition, the tension and compression relaxation modulus $E(t)$ and compliance $J(t)$ of the linear viscoelastic material obey the conversion relations as follows (Park and Kim.(1999)):

$$\int_0^t E(t-\zeta)J(\zeta)\mathrm{d}\zeta = t \qquad \text{or} \qquad \int_0^t E(\zeta)J(t-\zeta)\mathrm{d}\zeta = t \tag{4}$$

LOADING MODE

A half-sinusoidal load with 0.1s loading duration and 0.9s unloading duration is selected to simulate the dynamic vehicle load(Fig.2):

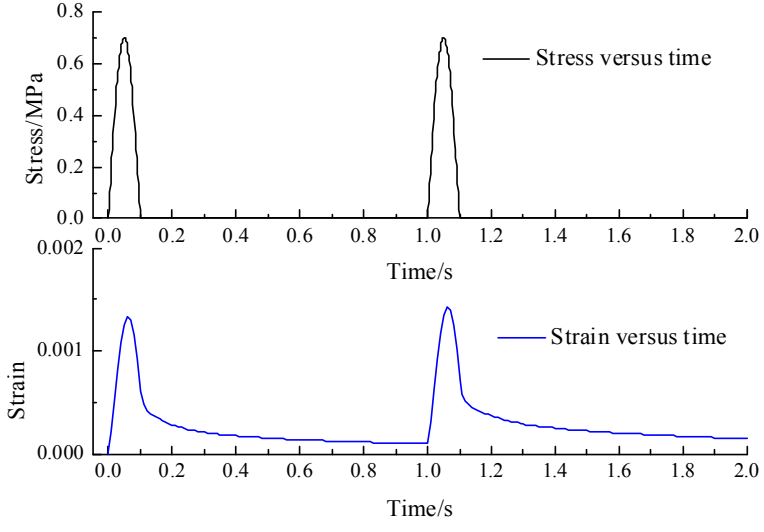

FIG.2. Loading mode of repeated creep test

MATERIALS PROPERTIES AND TEST RESULTS

The unmodified asphalt (AH-70) and SBS modified asphalt (I-D) are used in the experiments, aggregate is granite. The AC-13C aggregate gradation with 4.9% asphalt contents used is shown in Table 1.

Table 1. Aggregate Gradation of AC-13C Asphalt Mixtures

Sieve Size /mm	19	16	13.2	9.5	4.75	2.36	1.18	0.6	0.3	0.15	0.075
Total Percent Passing/%	100	100	95.7	70.3	41.4	29.3	23.9	18.4	13.7	9.3	5.4

Specimens are fabricated in the laboratory using the Superpave Gyratory Compactor (SGC), which is better simulating the field compaction of HMA mixes. Target air voids content is 4%. The test is carried out on cylindrical specimens, 100 mm in diameter and 100 mm in height. 580 and 610 MPa are obtained for elastic modulus of AC-13C unmodified and modified asphalt mixtures respectively based on the analysis results of the uniaxial compression strength test. Static creep and repeated load tests are conducted using at least three replicate test specimens for each of the mixtures to evaluate the compliance properties by MTS-810 material testing system. The loading time for static creep test is 3600s. A half-sinusoidal load with 0.1s loading duration and 0.9s unloading duration is selected in repeated load test. The experiments are performed at stress, 0.7MPa and temperature, 25□.

FITTING PRONY SERIES COEFFICIENTS OF THE GENERALIZED MAXWELL MODEL

The creep compliance-time curves of asphalt mixtures are obtained by the uniaxial static creep test, then they can be converted to the shear relaxation modulus-time curves (shown in Fig.3)via equation (3), (4).

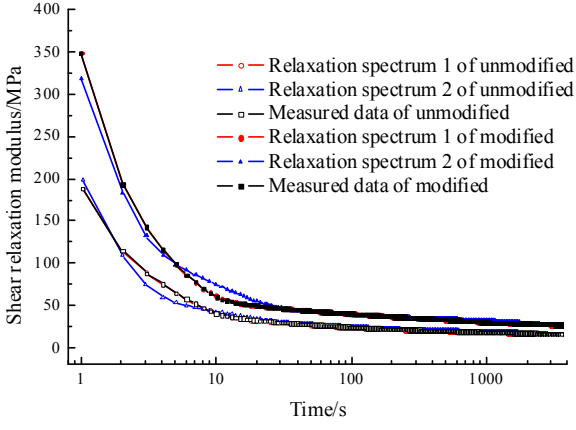

FIG.3. The fitted shear relaxation modulus curves

The Prony series coefficients of the generalized Maxwell model having 8 elements (n=8) can be obtained by fitting the shear relaxation modulus versus time curves. In fact, a lot of groups of Prony series coefficients could be fitted from the point of view of math, but not all of these groups are suitable. Two sets of fitted results about the

unmodified and modified asphalt mixtures are listed respectively in Table 2 and Fig.3. In which, relaxation spectrum 1 does not require the relaxation time values, ie. arbitrary fitting; The discrete relaxation spectrum 2 is selected as $\tau_i = 10^{(i-4)} (i = 1, \cdots, 8)$ (Park and Kim(2001)), which can cover the length of a half-sinusoidal load with 0.1s loading duration and 0.9s unloading duration.

From Table 2 and Fig.3, the Prony series expression of the generalized Maxwell model can well reflect the correlation between the shear relaxation modulus and time of the unmodified and modified asphalt mixtures, the correlation coefficient R^2 is above 0.96.

Table 2. The Prony Series Coefficients of the Generalized Maxwell Model

Coefficients	Unmodified Asphalt Mixtures		Modified Asphalt Mixtures	
	Relaxation Spectrum 1	Relaxation Spectrum 2	Relaxation Spectrum 1	Relaxation Spectrum 2
G_1/MPa	2.200	30.337	2.200	63.654
G_2/MPa	398.421	41.794	759.944	65.385
G_3/MPa	120.255	1042.967	89.708	1005.769
G_4/MPa	8.852	387.040	136.265	540.385
G_5/MPa	4.763	32.889	11.376	83.019
G_6/MPa	4.449	10.373	7.852	9.877
G_7/MPa	3.807	0.269	9.036	0.565
G_8/MPa	16.466	20.845	29.807	34.941
τ_1/s	0.015	0.001	0.015	0.001
τ_2/s	0.552	0.01	0.563	0.01
τ_3 s	3.478	0.1	3.056	0.1
τ_4/s	24.348	1	3.056	1
τ_5/s	73.999	10	20.298	10
τ_6/s	236.524	100	96.824	100
τ_7/s	1606.980	1000	568.595	1000
τ_8/s	59325.582	10000	33215.337	10000
Correlation coefficient R^2	0.99996	0.97053	0.99995	0.96399

STRAIN PREDICTION UNDER REPEATED LOAD

The strain-time curves of the unmodified and modified asphalt mixtures under repeated loading are shown in Fig.4. The permanent deformation generated by unmodified asphalt mixtures is significantly larger than modified asphalt, which shows good agreement with the test results under static load.

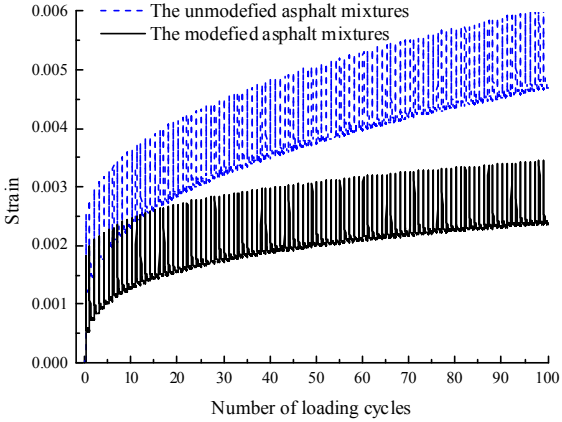

FIG.4. The strain-time curves of asphalt mixtures under repeated load

Strain response of asphalt mixtures specimen under repeated load is predicted by viscoelastic finite element method using ABAQUS. Specimen of the asphalt mixture is cylindrical, size for 100×100mm. In uniaxial repeated load tests, loads are imposed at the top and bottom of specimen, then the specimen itself and the imposed loads are axial symmetry, so the axi-symmetric model can be used. The finite element analysis model is divided into15×15 units, in which the height of model is 1/2 of specimen, i.e. 50mm and radius is 50mm(Fig.5). 8-node reduced-integration axisymmetric elements (CAX8R) are used to generate elements. Vertical displacement of cross-section at 1/2 high-specimen is zero because of the symmetry of load, so the boundary conditions of model is that the vertical displacement at the bottom is zero.

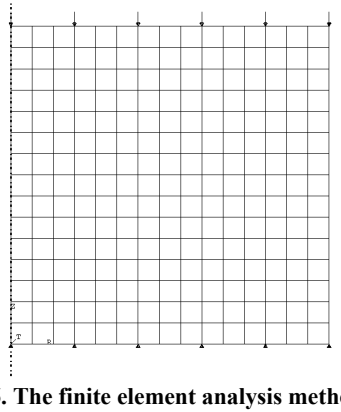

FIG.5. The finite element analysis method

The finite element calculating results of asphalt mixtures under repeated load are shown in Fig.6. The deformation of loading and unloading is predicted by finite

element analysis method based on the generalized Maxwell model. The predicted strains for different relaxation time spectrum are not the same. For example, the predicted strain by the arbitrary fitting relaxation time spectrum 1, is very different from the measured strain. But the predicted strain by the fixed relaxation time spectrum 2 shows good agreement with measured strain. And the relaxation time spectrum 2 covers loading time history of a half-sinusoidal load with 0.1s loading duration and 0.9s unloading duration. It indicates that the selected relaxation time spectrum predicted strain should cover the scope of loading time for obtaining the desired results.

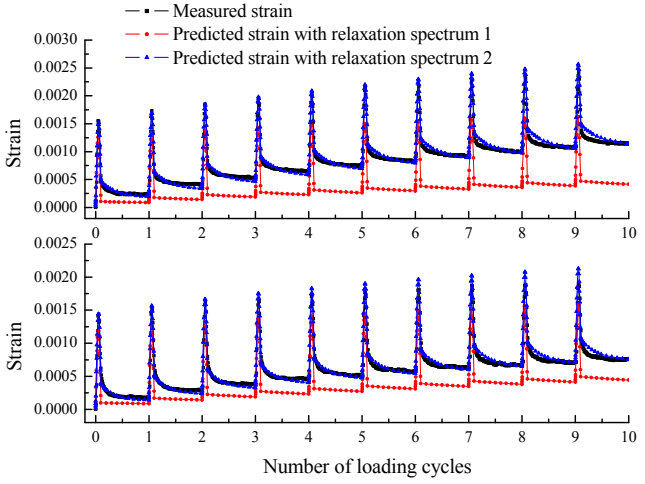

FIG.6. The measured strain compared with predicted strain for the unmodified (top) and modified (bottom) asphalt mixtures under repeated load

ANALYSIS VISCOELASTIC STRAIN UNDER REPEATED LOAD

The total strain can be divided into recoverable and irrecoverable components or time-dependent and time-independent components. Equation 5 describes the two components composing the total strain (Hibbitte, Karlsson. (2005)):

$$\varepsilon_{\text{total}} = \varepsilon_{\text{e}} + \varepsilon_{\text{cr}} \tag{5}$$

Where, $\varepsilon_{\text{total}}$ is the total strain ε_{e} the elastic strain, recoverable and time-independent; ε_{cr} the creep strain, partly recoverable and time-dependent. So the creep strain is mainly part in the total strain during the unloading condition, the irrecoverable part of creep strain is the permanent deformation of asphalt mixtures. Fig.7 illustrates viscoelastic strain composition of asphalt mixtures at 1 loading cycle. The elastic strain gets to its maximum at near 0.05s and the creep strain gets to its maximum at near 0.09s. It shows that creep strain has delayed recoverable property compared with elastic strain. Permanent deformation of the modified and unmodified asphalt mixtures is 33.1%, 40.3% of the corresponding largest creep strain,

respectively and is 9.8%, 31.1% of the corresponding largest total strain, respectively. It shows that modified asphalt mixtures possess stronger elastic recovery capacity than unmodified asphalt mixtures.

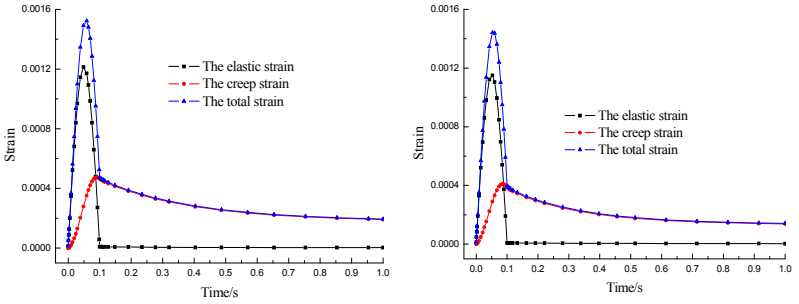

(a)The unmodified asphalt mixtures **(b)The modified asphalt mixtures**

FIG.7. The viscoelastic strain composition of asphalt mixtures

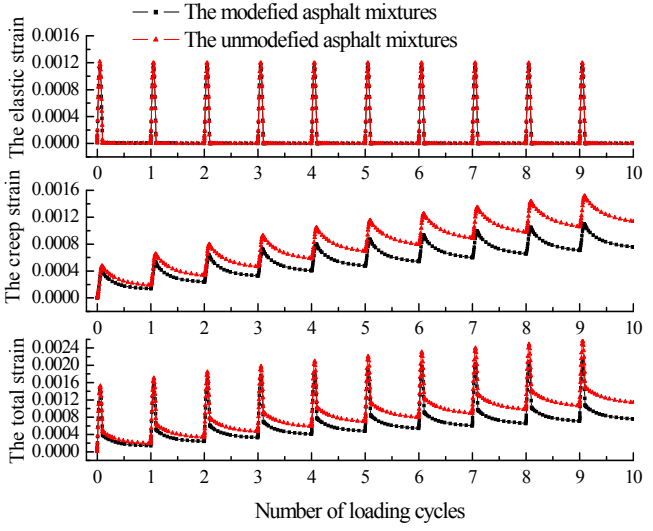

FIG.8. The contrast on viscoelastic strain of asphalt mixtures under repeated load

From the contrast on viscoelastic strain of asphalt mixtures under repeated load (Fig.8), the difference of elastic strain of two asphalt mixtures is small and the elastic strain of unmodified asphalt mixtures is a bit larger than that of modified asphalt mixtures. But the creep strain of unmodified asphalt mixtures is significantly larger

than that of modified asphalt mixtures, which elastic recovery capability is better. The greater the number of loading cycles, the greater the difference. The corresponding total strain also has similar results. The greater the number of loading cycles, the greater the difference of permanent deformation between the unmodified and the modified asphalt mixtures.

CONCLUSIONS

1. The Prony series expression of the generalized Maxwell model can well describe the relaxation modulus-time curves of unmodified and modified asphalt mixtures under static load, the correlation coefficient R^2 is above 0.96.
2. The strain response of asphalt mixtures under repeat load could be predicted by viscoelastic finite element analysis method based on the generalized Maxwell model, and thus permanent deformation could be obtained. The FE method is an effective method for researching on rutting of asphalt pavement.
3. The selected relaxation time spectrum for predicting deformation should cover the scope of loading and unloading time in order to obtain the desired results.
4. The total strain from viscoelastic FE analysis method can be divided into the elastic strain and creep strain, in which the irrecoverable part forms permanent deformation. It shows that this method could be used to efficiently separate the viscoelastic strain, and the anti-rutting performance of asphalt mixtures is estimated by analyzing recoverable capacity from deformation.
5. When the flow point of "tertiary flow" has been reached, micro cracking has begun to weaken the mixture's resistance to permanent deformation, that permanent deformation is three dimensional. In addition to that, there is the anisotropic nature of the permanent deformation which is dictated by the shape of the compacted aggregate particles. Further, 3D analysis, anisotropic nature etc. factors involved in predicting permanent deformation will be studied.

REFERENCES

Ronald Blab and John T.Harvey.(2002). "Modeling measured 3D tire contact stresses in a viscoelastic FE pavement model." *The International Journal of Geomechanics*.Vol.2(3):271-289.

R.M.Mulungye, P.M.O.Owende, K. Mellon.(2007). "Finite element modeling of flexible pavements on soft soil subgrades." *Materials and Design*, 28:739-756.

Yong-Rak Kim, D.H.Allen, and D.N.Little. (2007). "Computational constitutive model for predicting nonlinear viscoelastic damage and fracture failure of asphalt concrete mixtures." *International Journal of Geomechanics*, Vol.7(2):102-110.

Peng Miao-juan, Xu Zhi-hong. (2007). "Nonlinear viscoelastic-elastoplastic constitutive model of permanent deformation for asphalt pavement." J*ournal of Traffic and Transportation Engineering*. Vol.7(5):41-47.

Blab R, Harvey JT. (2002). "Modelling measured 3D tyre contact stresses in a viscoelastic FE pavement model." *Int J Geomech*, Vol.2(3):271–90.

Hibbitte, Karlsson. (2005).ABAQUS User Subroutines Reference Manual. HKS INC.

Zhang Xiao-ning.(2005).Theory and application of Viscoelasticity for asphalt and asphalt mixtures. Beijing:China Communications Press.

S.W. Park, Y. R. Kim.(1999). “Interconversion between relaxation modulus and creep compliance for viscoelastic solids.” *Journal of Materials in Civil Engineering*. Vol.11(1):76–82.

S.W. Park, Y. R. Kim.(2001). “Fitting Prony-Series Viscoelastic Models with Power-Law Presmoothing.” *Journal of Materials in Civil Engineering*. Vol.13(1): 26-32

Evaluation of Micromechanical Models for Predicting Dynamic Modulus of Asphalt Mixtures

Xiang Shu[1] and Baoshan Huang[2]

[1]School of Traffic and Transportation Engineering, Changsha University of Science and Technology, Changsha, Hunan, China; Research Assistant Professor, Department of Civil and Environmental Engineering, University of Tennessee, Knoxville 37996 USA; xshu@utk.edu
[2]Associate Professor, Department of Civil and Environmental Engineering, University of Tennessee, Knoxville 37996 USA; bhuang@utk.edu

ABSTRACT: Asphalt mixtures are a composite material consisting of asphalt binder, coarse and fine aggregates, mineral filler, and air voids. The overall behavior of an asphalt mixture is dependent on the properties and volumetric fractions of its individual constituents and their interactions, which is predictable with micromechanical models. This study evaluates the applicability of four different micromechanical models for predicting dynamic modulus of asphalt mixtures. The four models included a 3-D two-layered model, a differential model, the Composite Sphere model, and the Generalized Self-Consistent (GSC) model. The evaluation shows that the predicted dynamic modulus from the differential model were reasonably close to the measured value whereas the other three models under-predicted to some degree the dynamic modulus of asphalt mixture.

INTRODUCTION

Asphalt mixtures are composed of asphalt binder, coarse and fine aggregates, mineral filler, and air voids. From the viewpoint of composite mechanics, the overall behavior of an asphalt mixture can be predicted from the properties and volumetric fractions of its individual constituents and their interactions. During the past two decades, many researchers have employed micromechanical models to predict mechanical properties of asphalt mixtures (Lytton 1990; Buttlar and Roque 1996; Li et al. 1999; Huang et al. 2003, 2007; Shu and Huang 2008a,b, 2009; You and Buttlar 2004, 2006). Most of the researchers used micromechanical models to predict the modulus or stiffness of asphalt mixtures. Lytton (1990) proposed a three-phase (aggregate, asphalt binder, and air voids) model to predict the modulus of hot-mix asphalt (HMA) mixtures. Li et al. (1999) developed a 2-D two-layer built-in micromechanical model to predict the elastic modulus of HMA mixtures. With the recent incorporation of dynamic modulus of asphalt mixtures into the AASHTO mechanistic-empirical pavement design guide (MEPDG) as a basic material input, many researchers have begun to apply

micromechanical models to predict the dynamic modulus of asphalt mixtures. Shu and Huang (2008a,b, 2009) developed a 3-D two-layered model and a differential model for predicting the dynamic modulus of asphalt mixtures. The procedures they developed are capable of incorporating viscoelastic effect, aggregate gradation, and air voids in the prediction process. Research efforts have also been made to employ micromechanical models to estimate the strength of asphalt mixtures. Huang et al. (2003) successfully developed analytical equations from a micromechanical model to predict the tensile strength of HMA mixtures at low temperatures.

OBJECTIVE AND SCOPE

The objective of this study is to compare the applicability of four different micromechanical models for predicting dynamic modulus of asphalt mixtures. These four models included the 3-D two-layered model, the differential model, the Composite Sphere model, and the Generalized Self-Consistent model. The applicability was evaluated through the comparison of predicted and measured dynamic moduli of an asphalt mixture commonly used in the State of Tennessee, USA.

FORMULATIONS OF MICROMECHANICAL MODELS

Based on the 2-D two-layered micromechanical model developed by Li et al. (1999) for predicting the elastic modulus of asphalt mixtures, Shu and Huang (2008a,b) extended the model to 3-D and modified it to predict the dynamic modulus of asphalt mixtures. The 3-D two-layered model was constructed by embedding asphalt mastic-coated aggregates in the equivalent medium of asphalt mixture (Fig. 1). The elastic modulus of an asphalt mixture can be obtained using the following equation (Shu and Huang 2008a):

$$E_c = \frac{E_m(1-c)(1-2v_c)}{x_1 - \dfrac{9E_i c(1-v_m)^2}{4E_m(1-2v_i)(1-c)+4E_i x_2}} \tag{1}$$

where E_c, v_c – elastic modulus and Poisson's ratio of composite (asphalt mixture); E_i, v_i – elastic modulus and Poisson's ratio of inclusion (aggregate); E_m, v_m – elastic modulus and Poisson's ratio of matrix (asphalt mastic); $x_1 = c(1+v_m)/2+(1-2v_m)$; $x_2 = (1+v_m)/2+c(1-2v_m)$; c – volume concentration of inclusion in composite, $c = (a/b)^3$; a – radius of filler particle; and b – radius of coating film of asphalt binder.

In the differential model, the composite material is viewed as a sequence of dilute suspensions into which an increment of inclusions is added until a finite volume concentration of inclusion is reached (Shu and Huang 2009). With each incremental increase in the volume concentration of inclusion, dc, an incremental increase in the elastic modulus, dE, can be calculated (Fig. 2). Through integration, the final predictive equation for elastic modulus of an asphalt mixture is as follows (Shu and Huang 2009):

$$\left(\frac{E_c}{E_m}\right)^A \left(\frac{E_c - x_3 E_i}{E_m - x_3 E_i}\right)^B \left(\frac{E_c - x_4 E_i}{E_m - x_4 E_i}\right)^C = (1-c)^{-1} \tag{2}$$

where A, B, C, x_3, x_4 – coefficients that are dependent on v_m and v_i.

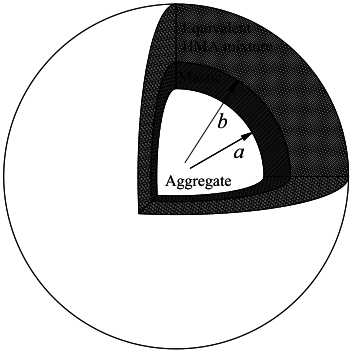

FIG. 1. 3-D two-layered model (Shu and Huang 2008b)

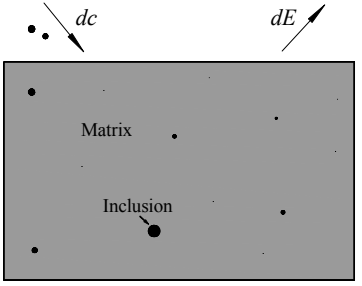

FIG. 2. Differential model (Shu and Huang 2009)

The Composite Sphere model was developed by Hashin (1962) and it consists of a series of perfectly packed spherical inclusions coated with concentric shell matrix (Fig. 3). This model assumes that all composite spheres have identical particle-to-matrix diameter ratios (a/b, Fig. 3) and are completely bounded by adjacent composite spheres. From this model, the bulk and shear moduli of the composite can be calculated using the following equations (Hashin 1962):

$$\frac{K_c}{K_m} = 1 + \frac{3(1-v_m)\left(\frac{K_i}{K_m} - 1\right)c}{2(1-2v_m) + (1+v_m)\left[\frac{K_i}{K_m} - \left(\frac{K_i}{K_m} - 1\right)c\right]} \tag{3}$$

and

$$\frac{G_c}{G_m} = 1 + \frac{15(1-v_m)\left(\frac{G_i}{G_m} - 1\right)c}{7 - 5v_m + 2(4-5v_m)\left[\frac{G_i}{G_m} - \left(\frac{G_i}{G_m} - 1\right)c\right]} \tag{4}$$

where K_c, K_m, K_i – bulk moduli of composite, matrix, and inclusion, respectively; G_c, G_m, G_i – shear moduli of composite, matrix, and inclusion, respectively.

Then, the elastic modulus of composite can be obtained using the following theoretical relationship:

$$E_c = 9K_cG_c/(3K_c + G_c) \tag{5}$$

The Generalized Self-Consistent (GSC) model developed by Christensen and Lo (1979) consists of a single composite sphere embedded in an infinite equivalent homogeneous medium of unknown properties (Fig. 4). The shear modulus of the equivalent medium can be obtained by solving the following quadratic equation (Christensen and Lo 1979):

$$D(G_c/G_m)^2 + E(G_c/G_m) + F = 0 \tag{6}$$

where G_c, G_m – shear moduli of composite and matrix, respectively; D, E, F – coefficients that are dependent on the shear modulus and Poisson's ratio of both matrix and inclusion (Christensen and Lo 1979). Then, the elastic modulus of composite can be obtained using the following relationship:

$$E_c = 2(1 + \nu_c)G_c \tag{7}$$

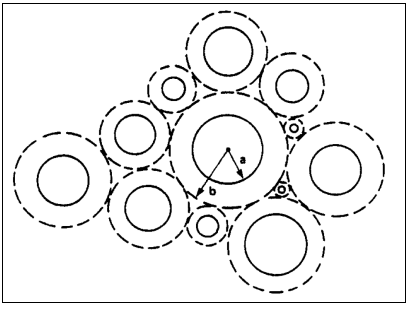

FIG. 3. Composite Spheres Model (Hashin 1962)

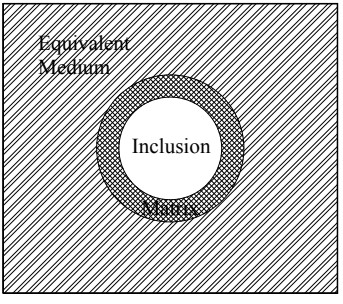

FIG. 4. Generalized Self-Consistent model (Christensen and Lo 1979)

PREDICTION OF DYNAMIC MODULUS OF ASPHALT MIXTURES

The above predictive equations are used to estimate the elastic modulus of asphalt mixtures. However, in order to predict the dynamic modulus of asphalt mixtures, the viscoelastic properties of asphalt binder should be considered. In this study, the elastic-viscoelastic correspondence principle was used to predict the complex modulus of asphalt mixtures with the predictive equations. The correspondence principle states that the complex modulus of a composite material can be obtained by replacing the elastic moduli with the corresponding complex moduli of individual constituents (Ferry 1980). Fox example, the following predictive equation for complex modulus can be obtained from Eq. (2) for the differential model:

$$\left(\frac{E_c^*}{E_m^*}\right)^A\left(\frac{E_c^*-x_1E_i}{E_m^*-x_1E_i}\right)^B\left(\frac{E_c^*-x_2E_i}{E_m^*-x_2E_i}\right)^C=(1-c)^{-1} \tag{8}$$

where E_c^*, E_m^* – complex moduli of composite and matrix.

Based on the theory of linear viscoelasticity, complex modulus E^* can be decomposed into the storage modulus E' and the loss modulus E'' as follows:

$$E^*=E'+iE'' \tag{9}$$

and the dynamic modulus $|E^*|$ and phase angle ϕ can be obtained as follows:

$$|E^*|=\sqrt{(E')^2+(E'')^2} \tag{10}$$

$$\phi=\tan^{-1}(E''/E') \tag{11}$$

It should be noted that difficulty arises regarding solving Eq. (8) for E_c^* with numerical methods. Because the complex modulus of asphalt mixture is implicitly expressed in Eq. (8) and the exponents are usually fractions, it is very hard to obtain the solution even using numerical methods. To facilitate solving Eq. (8), two special cases, $v_m=v_i=0.5$ and $v_m=v_i=0.2$, were considered in this study. In these special two cases, Eq. (8) is reduced to:

$$\left(\frac{E_c^*}{E_m^*}\right)\left(\frac{E_c^*-E_i}{E_m^*-E_i}\right)^{-2.5}=(1-c)^{-2.5} \tag{12}$$

$$\left(\frac{E_c^*}{E_m^*}\right)\left(\frac{E_c^*-E_i}{E_m^*-E_i}\right)^{-2}=(1-c)^{-2} \tag{13}$$

In addition to the viscoelastic effect of asphalt binder, the effects of aggregate gradation and air voids on the dynamic modulus were also incorporated in the predictive equations in this study. Details can be found elsewhere about the incorporation of aggregate gradation and air voids in the prediction process (Shu and Huang 2008a,b, 2009).

COMPARISON OF DIFFERENT MICROMECHANICAL MODELS

The predictive equations were applied to predict the dynamic modulus of an HMA mixture commonly used in the State of Tennessee, USA to compare the applicability of

the four micromechanical models to asphalt mixtures. The HMA mixture contains asphalt binder, PG 64-22, and crushed limestone with the nominal maximum aggregate size (NMAS) of 12.5 mm. The optimum asphalt content for the mixture was determined to be 5.0 percent. Fig. 5 shows the aggregate gradation and Table 1 presents the volumetric properties of asphalt mixture. A laboratory test was also conducted on the HMA mixture to measure its dynamic modulus values at different temperatures and loading frequencies (Shu and Huang 2008a).

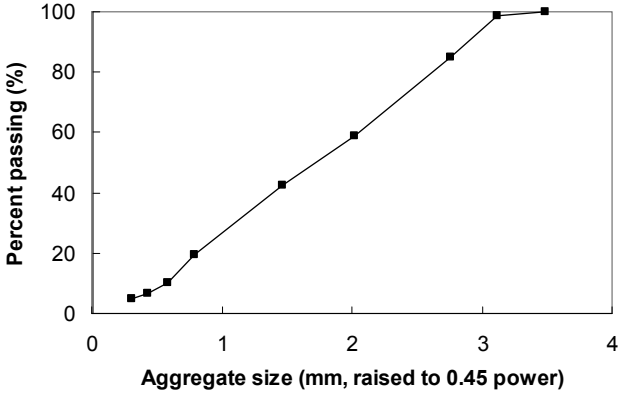

FIG. 5. Aggregate gradation

Table 1. Volumetric Properties of HMA Mixture

AC (%)	G_{mm}	G_{mb}	Air Voids (%)	VMA (%)	Stability (kN)	Flow (mm)
5.0	2.456	2.356	4.0	16	11.6	2.77

Fig. 6 presents the comparison between predicted and measured dynamic moduli of HMA mixture. It is observed that both the dynamic modulus predicted from the four micromechanical models and the measured dynamic modulus followed the general trend of dynamic modulus of asphalt mixtures, i.e., the higher the loading frequency, the higher the dynamic modulus of asphalt mixture. The relationship between the predicted dynamic modulus vs. loading frequency exhibited a sigmodal shape, which is a typical behavior for viscoelastic materials.

From Fig. 6, it can be seen that the dynamic modulus results predicted from the 3-D two-layered model were very similar to those from the Hashin model and the Christensen and Lo's GSC model. But the three micromechanical models gave much lower predicted dynamic moduli than the measured values, especially at lower loading frequencies. With the increase in loading frequency, the difference between measured and predicted dynamic moduli from the three models gradually decreased. Compared to the three models, the differential model could give much better prediction. The differential model with Poisson's ratio of 0.5 generally predicted the dynamic modulus of asphalt mixture higher than the measured value. The differential model with

Poisson's ratio of 0.2 predicted the dynamic modulus very close to the measured value at loading frequencies higher than 0.05 Hz.

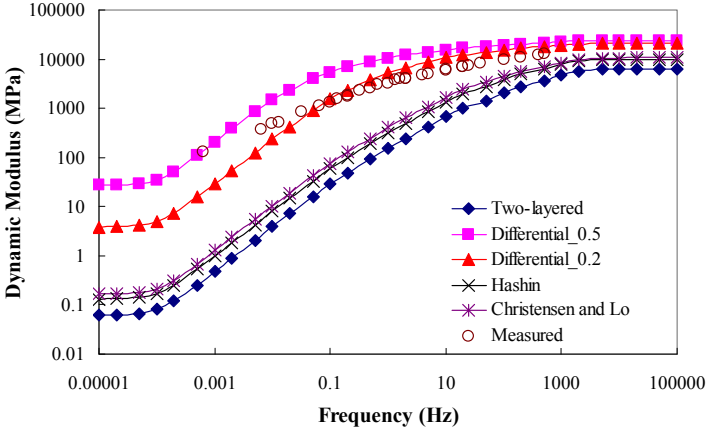

FIG. 6. Comparison of predicted and measured dynamic moduli

Fig. 7 presents the comparison between predicted and measured phase angles of asphalt mixture. It is observed that the 3-D two-layered, the Hashin, and the Christensen and Lo models gave very similar prediction results of phase angle, which were higher than the measured values. The differential model generally gave better prediction results for phase angle than the other three models. However, it appeared that the differential model predicted phase angle results higher than the measure values at lower frequencies and lower phase angle results at higher loading frequencies.

However, it is noted from Figs 6 and 7 that there is a varying discrepancy between predicted and measured dynamic modulus and phase angle. The possible reasons for the discrepancy include lack of consideration of interlocking between coarse aggregate particles (Shu and Huang 2008a), lack of consideration of the physico-chemical stiffening effects occurring at the interface between asphalt binder and aggregates (Buttlar et al. 1999), and the spherical aggregate assumption used in this study.

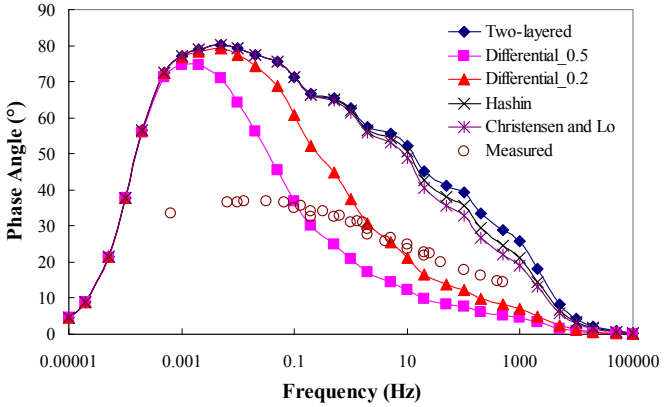

FIG. 7. Comparison of predicted and measured phase angles

SUMMARY AND CONSLUSIONS

In this study, four different micromechanical models were evaluated for predicting the dynamic modulus of asphalt mixtures. The applicability of these models to asphalt mixtures was evaluated through the comparison of predicted and measured dynamic modulus results. Based on the results from this study, the following can be summarized:

- The dynamic modulus of asphalt mixture predicted from the micromechanical models evaluated in this study could follow the general trend of dynamic modulus, i.e., the higher the frequency, the higher the dynamic modulus.
- The 3-D two-layered model predicted dynamic modulus and phase angle similar to those from the Hashin model and the Christensen and Lo model.
- The 3-D two-layered model, the Hashin model, and the Christensen and Lo model generally under-predicted dynamic modulus and over-predicted phase angle of asphalt mixtures.
- Compared to the other three models, the differential model could give better prediction results for dynamic modulus and phase angle. The differential model with Poisson's ratio of 0.2 predicted dynamic moduli reasonably close to the measured values at loading frequencies higher than 0.05 Hz.
- The differential model over-predicted phase angle at lower frequencies, but under-predicted phase angle at higher frequencies.

REFERENCES

Buttlar, W.G. and Roque, R. (1996). "Evaluation of empirical and theoretical models to determine asphalt mixtures stiffnesses at low temperatures." *Asph. Paving Technol.*, Vol. 65: 99–141.

Buttlar, W.G., Bozkurt, D., Al-Khateeb, G.G., and Waldhoff, A.S. (1999). "Understanding asphalt mastic behavior through micromechanics." *Transportation Research Record. 1681*, Transportation Research Board, Washington, D.C.,

157–169.
Christensen, R.M. and Lo, K.H. (1979). "Solutions for effective shear properties of three phase sphere and cylinder models." *J. Mech. Phys. Solids*, Vol. 27(4): 315–330.
Ferry, J.D. (1980). *Viscoelasticity properties of polymers*, 3rd Ed., Wiley, New York.
Hashin, Z. (1962). "The elastic moduli of heterogeneous materials." *J. Appl. Mech.*, Vol. 29:143–150.
Huang, B., Li, G., and Mohammad, L.N. (2003). "Analytical modeling and experimental study of tensile strength of asphalt concrete composite at low temperatures." *Composites, Part B*, Vol. 34(8): 705–714.
Huang, B., Shu, X., Li, G., and Chen, L. (2007). "Analytical modeling of three-layered HMA mixtures." *Int. J. Geomech.*, Vol. 7(2): 140–148.
Li, G., Li, Y., Metcalf, J.B., and Pang, S.S. (1999). "Elastic modulus prediction of asphalt concrete." *J. Mater. Civ. Eng.*, Vol. 11(3): 236–241.
Lytton, R. (1990). "Materials property relationships for modeling the behavior of asphalt aggregate mixtures in pavements." *Int. Memorandum*, Strategic Highway Research Program, Washington, D.C.
Shu, X. and Huang, B. (2008a). "Dynamic modulus prediction of HMA mixtures based on the viscoelastic micromechanical model." *J. Mater. Civ. Eng.*, Vol. 20(8): 530–538.
Shu, X. and Huang, B. (2008b). "Micromechanics-based dynamic modulus prediction of polymeric asphalt concrete mixtures." *Composites, Part B*, Vol. 39(4): 704–713.
Shu, X. and Huang, B. (2009). "Predicting dynamic modulus of asphalt mixtures with differential method." *Road Mater. Pavement Des.*, Vol. 10(2): 337–359.
You Z. and Buttlar W.G. (2004). "Discrete element modeling to predict the modulus of asphalt concrete mixtures." *J. Mater. Civ. Eng.*, Vol. 16(2): 140–146.
You Z. and Buttlar W.G. (2006). "Micromechanical modeling approach to predict compressive dynamic moduli of asphalt mixture using the distinct element method." *Transportation Research Record. 1970*, Transportation Research Board, Washington, D.C., 73–83.

Formulization of Asphalt Concrete Stiffness for Specific Microstructures Based on Discrete Element Method

Yu Liu[1] and Zhanping You[2]

[1,2]Department of Civil and Environmental Engineering, Michigan Technological University

ABSTRACT: This study presents an approach to formulize asphalt concrete stiffness for specific microstructures. An asphalt concrete was designed on the basis of the Superpave mix design method. Its images were obtained from X-ray Computed Tomography (X-ray CT). Through processing those X-ray CT images, two-microstructure-based models, namely the Model-I and the Model-II were rebuilt on the basis of the discrete element (DE) method. In Model-I, no air void was included, while in Model-II, the air void level was 3.1%. The DE simulation of the asphalt concrete was conducted with those two models whose primary inputs were the stiffness values of both coarse aggregate and asphalt sand mastic. The asphalt sand mastic was defined as a sub-mix of fines, fine aggregate (less than 2.36mm), and asphalt binder. Through regression analysis of the DE simulation results, the asphalt concrete stiffness values were formulized into two analytical equations for Model-I and Model-II, respectively. A potential application of those two equations is to predict effective stiffness values of the asphalt concrete at various temperatures and different loading conditions. At the end of this study, an application example is provided. It was found that compared with the measured data, the formulized equation of Model-II could more precisely predict the asphalt concrete dynamic moduli at various temperatures and different frequencies than other models.

Keywords: Asphalt Mixture, Strain Concentration Factor, Discrete Element Method, Stiffness

INTRODUCTION

Asphalt concrete consists of asphalt binder and mineral aggregate as well as air voids. Asphalt binder acts as a binder agent to glue aggregate particles into a dense mass, while mineral aggregate acts as a stone framework to impart strength and toughness to the system. The performance of asphalt concrete is affected by not only the properties of the individual components, but also their combined reaction in this system. Stiffness is one of the most important parameters of asphalt concrete. In the past one hundred years, a number of models have been developed for prediction of asphalt concrete stiffness. Most of them could be categorized into three groups, namely experiment-based regression models, two-phase micromechanical models, and microstructure-based numerical models.

The two most popularly used experiment-based regression models are the Witczak model (Dongre et al. 2005; Witczak and Fonseca 1996) and the Hirsch model (Al-Khateeb et al. 2006; Christensen et al. 2003). The shortcoming of an experiment-based regression models, however, is its laboratory dependency. First of all, a large number of laboratory tests are needed for model development or calibration. Secondly, its accuracy is dependent on the laboratory conditions and accuracy of the laboratory testing results. Also, it is only applicable at the conditions where it was developed.

Two-phase micromechanical models started about one hundred years ago. The earliest developers were Voigt (Voigt 1889) and Reuss (Reuss 1929). Subsequently, some other models were developed and used (Counto 1964; Dasgupta and Bhandarkar 1992; Hashin 1961; 1965; Hashin and Shtrikman 1963; Hirsch 1962; Paul 1960). According to the previous study (Aboudi 1991), all the existing two-phase micromechanical models could be formulized as

$$C^* = C^{(1)} + c_2 A_2 (C^{(2)} - C^{(1)}) \quad (1)$$

where $C^{(1)}$ and $C^{(2)}$ are stiffness values of the phase 1 and the phase 2, respectively; C^* and c_2 are the effective stiffness and volumetric fraction of the phase 2, respectively; A_2 is the strain concentration factor of the phase 2. Evidently, it is A_2 that has distinguished the existing two-phase micromechanical models. For example, for the Voigt model(Voigt 1889), A_2=1; for the Reuss model(Reuss 1929), $A_2 = C^{(1)}/(C^{(1)} + C^{(2)})$. In fact, the existing two-phase micromechanical models were derived from their specific microstructures on the basis of solid mechanics. For example, FIG.1(a), (b),

(c), and (d) shows the microstructures for the Voigt (Voigt 1889), the Reuss (Reuss 1929), the Hirsch (Hirsch 1962), and the Counto (Counto 1964) models, respectively. In other words, different microstructures have different formulations of A_2. Although those two-phase micromechanical models may provide useful benchmark solutions of asphalt concrete stiffness, they are limited to relatively simple microstructures and boundary conditions. Furthermore, air voids cannot be considered in those two-phase micromechanical models.

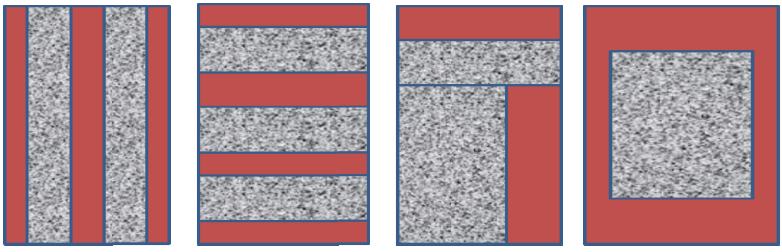

(a) Viogt Model (b) Reuss model (c) Hirsch model (d) Counto's model

FIG. 1. Examples of microstructures for two-phase micromechanical models

Microstructure-based numerical models, such as discrete element (DE) models (Liu et al. 2009; Liu and You 2009; You 2003) and finite element (FE) models (Dai and You 2007), are relatively new models. A major strong suit of a microstructure-based numerical model is that complex microstructures and micromechanics can be simulated under relatively complicated boundary conditions. It has some limitations for applying such a model for routine use to predict asphalt concrete stiffness since it is really time-consuming. For example, it took several weeks to predict the dynamic modulus of asphalt concrete with a two-dimensional viscoelastic DE model (Liu et al. 2009; Liu and You 2009). It would take much longer if a three-dimensional model was applied. Therefore, the authors believed that a microstructure-based numerical model is better suited for use as a research tool for investigating the fundamentals of asphalt mixtures rather than a routine method for prediction of stiffness. This study demonstrates the use of microstructure-based DE models as research tools.

The objective of this study is to present a method for formulizing asphalt concrete stiffness with Equation (1). Instead of deriving A_2 based on solid mechanical theories, microstructure-based DE simulation results were used to acquire the regression equations of A_2.

MICROSTRUCTURE-BASED DISCRETE ELEMENT MODELS

As is well known, asphalt concrete is a multi-phase system including coarse aggregate, fine aggregate, fines, asphalt binder, and air voids. Some researchers, however, believed that larger sizes of coarse aggregate particles act as individual components while asphalt binder, fine aggregate particles, fines, and air voids act as an integrated component to interact with the coarse aggregate (Li and Metcalf 2005). Some other researchers believed that air voids should be an isolated phase paralleled with coarse aggregate and submix of fines, fine aggregates and asphalt binder (Shashidhar and Romero 1998). In fact, air voids flow around in asphalt concrete and cannot be integrated with any component. The authors of this study believe asphalt concrete can be regarded as a three-phase system: air voids, coarse aggregates, and asphalt sand mastic. The asphalt sand mastic is a submix of fines, fine aggregates and binder. On the basis of the principle above, the major tasks for building a microstructure-based DE model of an asphalt concrete are as follows:

1) Acquire asphalt concrete X-ray Computed Tomography (X-ray CT) images
2) Process X-ray CT images with a technique developed in a previous study(Adhikari and You 2008).
3) Distinguish between coarse aggregate and asphalt sand mastic
4) Create a two-phase microstructure-based DE model
5) Create air voids by randomly deleting discrete elements from the two-phase model.

An asphalt concrete mixture was designed on the basis of the Superpave mix design method. The designed mineral aggregate gradation is shown in Table 1 and asphalt content is 5.59% by mass. The mineral aggregate was blended with the asphalt binder and compacted with Superpave Gyratory Compactor (SGC) to 3.1% of air voids by volume. The images of the finished product were acquired from X-ray CT. With those X-ray CT images, two microstructure-based models were built, namely, Model-I and Model-II. The Model-I was built by following steps one through four above, while the Model-II was built by following steps one through five. Therefore, the Model-I is a two-phase system without air voids. As shown in FIG. 2(a), a total of 148,200 discrete elements were used to build the Model-I, where dark-colored elements represent the upper and lower loading platens; white elements represent the asphalt sand mastic; and grey elements symbolize coarse aggregates. The Model-II is a three-phase system with 3.1% of air voids. The air void distribution is shown in FIG.

2(b). It should be noticed herein that both the Model-I and the Model-II were from the same asphalt concrete. Therefore, the only difference between them is the air void content.

Table 1. Aggregate Gradation

Sieve size (mm)	19	12.5	9.5	4.75	2.36	1.18	0.6	0.3	0.15	0.075
Percentage passing (%)	100	98.7	86.5	71.8	51.4	36.1	25.5	14.7	7.7	5.4

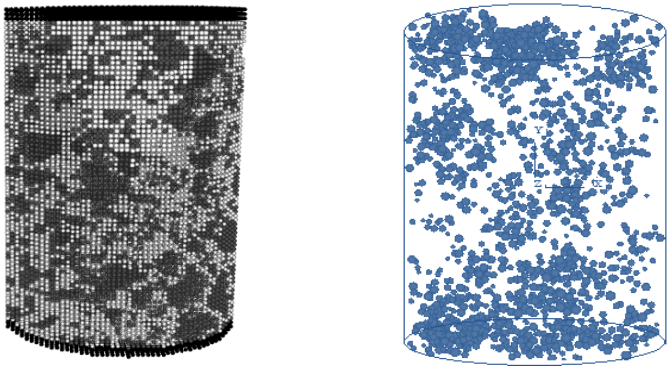

(a) Reconstructed microstructure (b) air voids distribution in the microstructure

FIG. 2. Reconstructed three-dimensional microstructure and air void distribution

To address the interactions within the Model-I and the Model-II, a micromechanical model has been developed in a previous study(You 2003). According to the previous study (Liu et al. 2009), four interactions were addressed in the micromechanical model. They were interactions between coarse aggregate and asphalt sand mastic, between two adjacent coarse aggregate particles, within a coarse aggregate particle, and within the asphalt sand mastic. Four constitutive models were assigned to those four interactions. Each of them has three parts: contact-stiffness model, contact-bond model, and slip model. The contact stiffness model relates the relative displacements

to the contact forces at a contacting point, while the other two contact models impart strength properties at the contact. Readers may refer to the previous study(You 2003) for more details.

MICROSTRUCTURE-BASED DISCRETE ELEMENT MODELING

FIG. 2(a) shows the loading setup for the microstructure-based DE modeling: the asphalt concrete specimen, either the Model-I or the Model-II, was loaded with the upper and lower loading platens. On the upper platen, a uniaxial constant load was applied while the lower platen remained fixed. The same mechanical inputs were utilized in the DE modeling with both the Model-I and the Model-II. The primary inputs include the Young's modulus for the coarse aggregate and the asphalt sand mastic. The Young's modulus of the coarse aggregate was set to 55GPa, while that of the asphalt sand mastic was varied from 0.0055GPa to 55GPa. The stiffness ratio, α, is defined as the ratio of the asphalt sand mastic stiffness to the coarse aggregate stiffness. Therefore, α, is equal to a value in the range from 0.00001 to 1. A total of 108 values were set to α, which resulted in 108 outputs from the DE modeling with either the Model-I or the Model-II. The DE modeling results are plotted in FIG.3.

From the graph in FIG. 3, it is clear that the stiffness values from the Model-I were larger than those from Model-II. Especially when α was larger than 0.1, the difference between the Model-I and the Model-II became larger. It was also noted that when α was close to 1, the difference between the two models became smaller. The observations above could be explained below:

The Equation (1) can be equivalently expressed as

$$C^{*} = C^{(2)}\left[\alpha + c_2 A_2(1-\alpha)\right] \tag{2}$$

When α is smaller (less than 0.1), A_2 plays a significant role in determining the effective stiffness. From the FIG 4 in the next section, the difference of A_2 between the two models is larger. Therefore, the stiffness difference between the two models was also larger as observed above.

When α is close to 1, A_2 has an ignorable role in determining the effective stiffness. As mentioned above, air void is considered as one of the factors which may impact A_2. Therefore, the effects of air voids became smaller and the difference between the Model-I and the Model-II was smaller when α was close to 1.

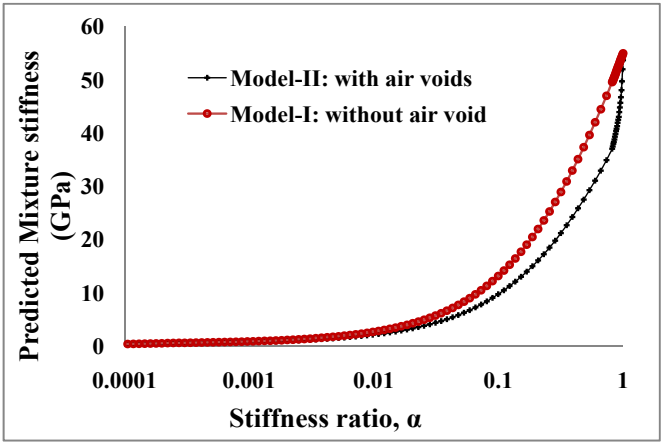

FIG. 3. DE modeling results of model-I and model-II

FORMULATION OF ASPHALT CONCRETE STIFFNESS

As discussed in the introduction, Equation (1) is a universal solution to the effective stiffness of a two-phase system. The strain concentration factor, A_2, is the key parameter which is related to the microstructure of the two-phase system. In order to formulize the effective stiffness of a two-phase composite, A_2 has to be determined. As demonstrated in the existing two-phase micromechanical models, formulations of A_2 were derived on the basis of continuum solid mechanics for relatively simple microstructures.

Unfortunately, asphalt concrete has such complex microstructures that it is impossible to derive a solution for A_2. Therefore, this study presents an indirect method through regression analysis of the DE modeling results in FIG. 3. In this indirect method, the asphalt concrete stiffness is formulized with Equation (1). To use Equation (1), the asphalt concrete was simplified into two phases. Phase 1 is the asphalt sand mastic, while phase 2 is the coarse aggregate. Therefore, the terms in Equation (1) could be interpreted as:

$C^{(1)}$ = stiffness of the asphalt sand mastic

$C^{(2)}$ = stiffness of the coarse aggregate

C^* = stiffness of the asphalt concrete;

c_2 = volumetric fraction of the coarse aggregate

A_2 = the strain concentration factor of the coarse aggregate

From Equation (1), A_2 can be determined by using the following equation:

$$A_2 = \frac{C^* - C^{(1)}}{c_2(C^{(2)} - C^{(1)})} \quad (3)$$

In Equation (3), , C^* is the predicted stiffness as shown in FIG. 3, while $C^{(2)}$ are $C^{(1)}$ are inputs for the DE modeling. c_2 may be calculated using the aggregate gradation in Table 1. In this study, $c_2 = 0.417$. Therefore, the values of A_2 could be calculated with application of Equation (3), and they are plotted in FIG. 4. From FIG. 4, the following were observed:

1) For Model-I, A_2 increases from 0 to 1 with the stiffness ratio, α increasing from 0.00001 to 1. In Model-II, however, A_2 increases and then decreases while α increases from 0.00001 to 1.

2) For Model-I, A_2 lies somewhere between the upper and lower bounds. For Model-II, however, A_2 is within the two bounds when $\alpha < 0.1$, while the curve of A_2 is below the lower bound when $\alpha > 0.1$.

3) For both Model-I and Model-II, A_2 can be fitted with a 6-order polynomial function of α. The R^2 is very close to 1.

Based on the findings above, it may be concluded that the stiffness of asphalt concrete could be formulized with Equation (1). A_2 in Equation (1) is a function of the stiffness ratio, α. For Model-I, the function is

$$A_2 = -26.539\boldsymbol{\alpha}^6 + 87.523\boldsymbol{\alpha}^5 - 110.39\boldsymbol{\alpha}^4 + 67.282\boldsymbol{\alpha}^3 - 21.519\boldsymbol{\alpha}^2 + 4.6195\boldsymbol{\alpha} + 0.0208 \quad (4)$$

For the Model-II, the function is

$$A_2 = -147.91\boldsymbol{\alpha}^6 + 357.94\boldsymbol{\alpha}^5 - 335.95\boldsymbol{\alpha}^4 + 148.23\boldsymbol{\alpha}^3 - 32.956\boldsymbol{\alpha}^2 + 3.7254\boldsymbol{\alpha} + 0.0178 \quad (5)$$

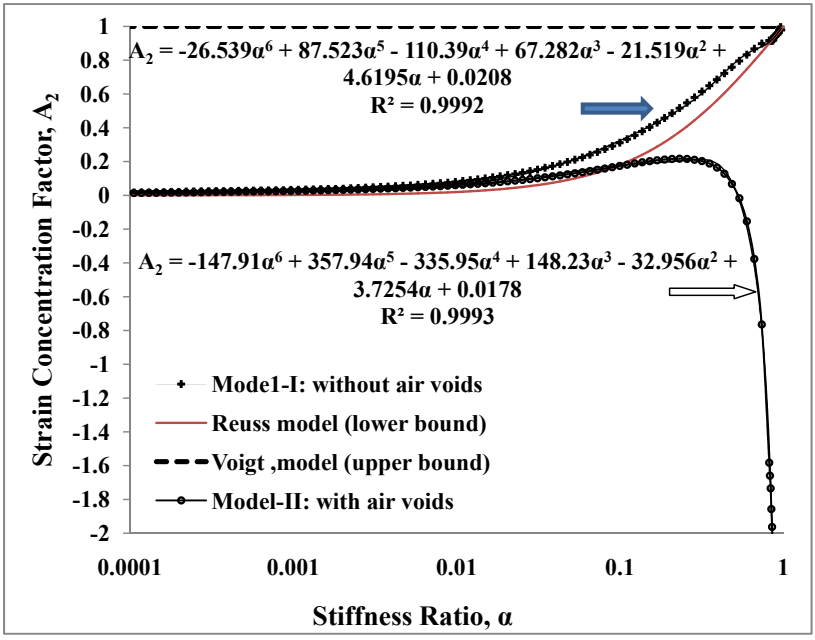

FIG. 4. Strain Concentration Factor versus Stiffness Ratio for Various Models

EXAMPLE APPLICATION

A potential application of the formulations, such as Equations (4) and (5), is to predict the asphalt concrete stiffness under various temperatures and different loading conditions. This section presents an example application to demonstrate how to use the formulations. As discussed in the previous section, Equations (1), (4) and (5) are meant to be used for prediction of asphalt concrete stiffness. Therefore, four parameters are needed: $C^{(1)}$, $C^{(2)}$, c_2 , and α. In this example application, $C^{(2)}$ =55GPa and c_2 = 0.421. Uniaxial dynamic modulus tests of the asphalt sand mastic were measured under different temperatures and frequencies as shown in Table 2. Therefore, $C^{(1)}$ could be any value in Table 2. And α is determined by dividing $C^{(1)}$ by $C^{(2)}$. An example calculation is shown below:

- At 25Hz and 4 °C, $C^{(1)}$= 13130MPa as shown in Table 2, $C^{(2)}$= 55000MPa;
- The stiffness ratio α=13130/55000=0.2387;

- $c_2 = 0.421$
- If the Model-I is used, from Equation (4), $A_2 = 0.5169$. Substitute A_2 to the Equation (1), the predicted asphalt concrete stiffness $C^* = 2224.3$ MPa
- If the Model-II is used, from Equation (5), $A_2 = 0.20468$. Substitute A_2 to the Equation (1), the predicted asphalt concrete stiffness $C^* = 16{,}738$ MPa

Table 2: Dynamic Modulus of the Asphalt Sand Mastic (MPa)

frequency / temperature	25 Hz	10 Hz	5 Hz	1 Hz	0.5 Hz	0.1 Hz
-5 °C	16,430	15,236	14,294	12,037	11,020	8,912
4 °C	13,130	11,814	10,775	8,490	7,442	5,490
13 °C	8,310	7,168	6,135	4,376	3,463	2,231
21 °C	4,685	3,752	3,240	2,035	1,533	9,49

The uniaxial dynamic modulus tests of the asphalt concrete were also conducted under the same temperatures and frequencies. The results are listed in Table 3.

Table 3 Dynamic Modulus of The Asphalt Concrete (MPa)

frequency / temperature	25 Hz	10 Hz	5 Hz	1 Hz	0.5 Hz	0.1 Hz
-5 °C	24,335	21,917	19,839	16,704	15,302	12,193
4 °C	16,848	15,272	14,073	10,977	9,724	6,990
13 °C	11,062	9,234	8,046	5,448	4,336	2,596
21 °C	7,660	6,103	4,822	2,867	2,030	1,140

At 25Hz and 4 ^{o}C, the measured dynamic modulus of the asphalt concrete is 16,848MPa. If the Equation (5) is used to calculate A_2, the predicted stiffness (16,738 MPa) is very close to the measured value. If Equation (4) is used to calculate A_2, the predicted stiffness (2224.3 MPa) is much higher than the measured value. FIG. 5 shows the comparisons of different methods for predicting asphalt concrete stiffness.

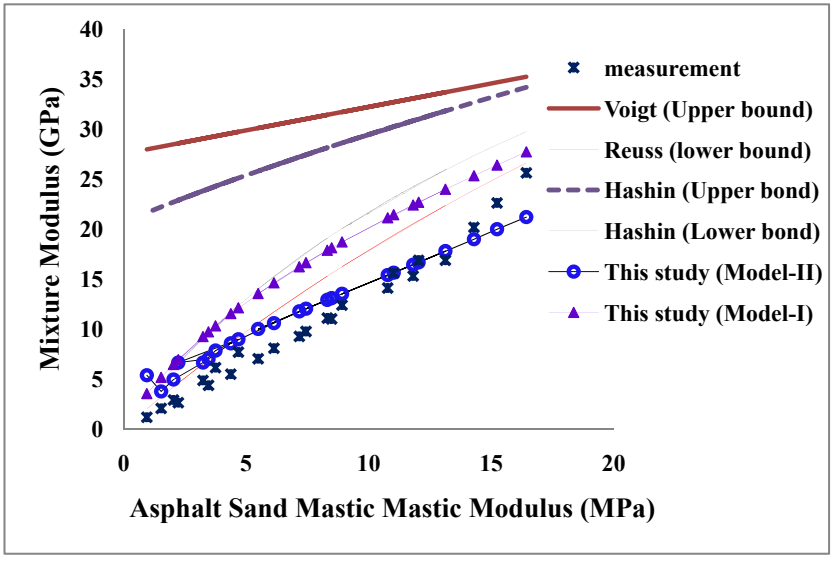

FIG. 5. Comparisons of different models as well as laboratory measurements

As shown in FIG.5, the methods include Model-I and Model-II used in this study as well as the Voigt , the Reuss , the Hashin (Hashin and Shtrikman 1963) models, and the laboratory measurements. The following findings were observed:

1) Both the measured stiffness values and predicted asphalt concrete stiffness from the Model-II are lower than those from the other models. This is due to the consideration of air voids in the Model-II and the actual samples.

2) Since no air voids were considered in Model-I of this study, the predicted stiffness is somewhere between the lower bound of the Reuss model and the lower bound of the Hashin model.

3) Compared with the results from the other micromechanical models, the predicted stiffness from Model-II is much closer to the measured value.

CONCLUSIONS

Due to the complex microstructural characteristics, it is impossible to derive an analytical solution of asphalt concrete effective stiffness. Therefore, this study has provided an indirect method to formulize asphalt concrete stiffness with specific microstructures. The universal formulation for predicting the effective stiffness of a two-phase composite was used in this study. But the key parameter, strain concentration factor of phase 2 (A_2) was determined through regression analysis of microstructure-based DE simulation results. From this study, the following conclusions were made:

1) A_2 can be a function of the stiffness ratio, α. Different microstructures of asphalt concrete have different formulations. For the specific microstructure in this study, A_2 could be expressed with a 6-order polynomial function of α as shown in FIG.4.
2) Air voids have significant effects on A_2, especially when the stiffness ratio, α is larger than 0.1.
3) Due to the effects of air voids, the measured dynamic modulus curve is lower than the lower bounds. The stiffness value of a two-phase composite is meant to fall somewhere between the upper and the lower bounds.
4) Since no air voids were considered in the Model-I of this study, the predicted stiffness is somewhere between the Reuss model and the lower bound of the Hashin model.
5) Compared with the other micromechanical models, the Model-II used in this study is much closer to the measurement in terms of dynamic modulus.

The goal of this study is to present the methodology and validate it using limited data. It should be noted herein that the DE modeling was conducted using the particular microstructure in FIG 2. Therefore, some observations and conclusions may be not applicable when the microstructure of asphalt mixture is different. However, by following the methodology presented in this paper, other asphalt mixture can be modeled.

ACKNOWLEDGEMENTS

This material is based in part upon work supported by the National Science Foundation under Grant CMMI 0701264. Any opinions, findings, and conclusions or recommendations expressed in this material are those of the authors' and do not necessarily reflect the views of the National Science Foundation.

REFERENCE

Aboudi, J. (1991). *Mechanics of Composite Materials: A Unified Micromechanical Approach*, Elsevier Science Publishing Comppany, New York.

Adhikari, S., and You, Z. (2008). "3D Microstructural Models for Asphalt Mixtures Using X-ray Computed Tomography Images." *International Journal of Pavement Research and Technology*, 3(1), 94-99.

Al-Khateeb, G., Shenoy, A., Gibson, N., and Harman, T. (2006). *A New Simplistic Model for Dynamic Modulus Predictions of Asphalt Paving Mixtures*, Association of Asphalt Paving Technologists.

Christensen, D. W., Pellinen, T., and Bonaquist, R. F. (2003). *Hirsch Model for Estimating the Modulus of Asphalt Concrete* Association of Asphalt Paving Technologists.

Counto, U. J. (1964). "Effect of elastic modulus of aggregate on elastic modulus, creep and creep recovery of concrete." *Magazine of Concrete Research*, 16(48), 129-138.

Dai, Q. L., and You, Z. (2007). "Prediction of Creep Stiffness of Asphalt Mixture with Micromechanical Finite Element and Discrete Element Models." *Journal of Engineering Mechanics, ASCE.*, 133(2), 163-173.

Dasgupta, A., and Bhandarkar, S. M. (1992). "Generalized self-consistent Mori-Tanaka scheme for fiber-composites with multiple interphases." *Mechanics of Materials*, 14(1), 67-82.

Dongre, R., Myers, L., #039, Angelo, J., Paugh, C., and Gudimettla, J. (2005). *Field Evaluation of Witczak and Hirsch Models for Predicting Dynamic Modulus of*

Hot-Mix Asphalt (With Discussion), Association of Asphalt Paving Technologists.

Hashin, Z. (Year). "Elastic moduli of heterogeneous materials." American Society of Mechanical Engineers (ASME), New York, NY, United States, 8.

Hashin, Z. (1965). "Viscoelastic behavior of heterogeneous media." *American Society of Mechanical Engineers -- Transactions -- Journal of Applied Mechanics*, 32(3), 630-636.

Hashin, Z., and Shtrikman, S. (1963). "Variational approach to theory of elastic behaviour of multiphase materials." *Journal of Mechanics and Physics of Solids*, 11(2), 127-140.

Hirsch, T. J. (1962). "Modulus of elasticity of concrete affected by elastic moduli of cement paste matrix and aggregate." *American Concrete Institute -- Journal*, 59(3), 427-451.

Li, Y., and Metcalf, J. B. (2005). *Two-Step Approach to Prediction of Asphalt Concrete Modulus from Two-Phase Micromechanical Models*, American Society of Civil Engineers.

Liu, Y., Dai, Q., and You, Z. (2009). "Viscoelastic Model for Discrete Element Simulation of Asphalt Mixtures." *Journal of Engineering Mechanics*, 135(4), 324-333.

Liu, Y., and You, Z. P. (2009). "Visualization and Simulation of Asphalt Concrete with Randomly Generated Three-Dimensional Models." *Journal of Computing in Civil Engineering*, 23(6), 340-347.

Paul, B. (1960). "Prediction of elastic constants of multiphase materials." *Metallurgical Society of American Institute of Mining, Metallurgical and Petroleum Engineers -- Transactions*, 218(1), 36-41.

Reuss, A. (1929). "Calculation of flow limits of mixed crystals on basis of plasticity of monocrystals

Berechnung der Fliessgrenze von Mischkristalle." *Zeitschrift fuer Angewandte Mathematik und Mechanik*, 9(1), 49-58.

Shashidhar, N., and Romero, P. (1998). "Factors affecting the stiffening potential of mineral fillers." *Transportation Research Record*(1638), 94-100.

Voigt, W. (1889). "Ueber die Beziehung zwischen den beiden Elasticitatsconstanten isotroper Korper." In: *Annalen Der Physik und Chemie* W. annalen, ed., Leipzig, 573-587.

Witczak, M. W., and Fonseca, O. A. (1996). *Revised Predictive Model for Dynamic (Complex) Modulus of Asphalt Mixtures*, Transportation Research Board. Volume 1540, pp. 15-23, 1996

You, Z. (2003). "Development of a Micromechanical Modeling Approach to Predict Asphalt Mixture Stiffness Using Discrete Element Method," University of Illinois at Urbana-Champaign, Illinois.

A Microstructure-Based Approach for Simulating Viscoelastic Behaviors of Asphalt Mixtures

Qingli Dai[1] and Zhanping You[2]

[1] Department of Civil and Environmental Engineering and Department of Mechanical Engineering-Engineering Mechanics, Michigan Technological University, 1400 Townsend Dr., Houghton, MI 49931-1295(corresponding author). Email: qingdai@mtu.edu.

[2] Department of Civil and Environmental Engineering Michigan Technological University, 1400 Townsend Dr., Houghton, MI 49931-1295. Email: zyou@mtu.edu.

ABSTRACT: This study developed micromechanical finite element (FE) models for simulating the viscoelastic behavior of asphalt mixtures. The two-dimensional (2D) microstructure of asphalt mixtures was captured by optically scanning the surface image of sectioned specimens. FE mesh of image samples was generated within each aggregate and asphalt mastic. Along the aggregate boundary, the FEs share the nodes to connect the deformation. The micromechanical FE model was accomplished by incorporating specimen microstructure and ingredient properties (viscoelastic asphalt mastic and elastic aggregates). The generalized Maxwell model was applied for viscoelastic asphalt mastic with calibrated parameters from nonlinear regression analysis of the mastic test data on dynamic modulus and phase angle. The displacement-based FE simulations were conducted on the digital sample under sinusoidal cyclic loadings. The predicted dynamic modulus and phase angle were compared favorably with the mixture test data over a frequency range. The simulation results of the asphalt mixture samples have good correlations with the numerical calibration of asphalt mastic specimens. These results indicate that the developed micromechanical FE model can provide a computational tool for predicting the global viscoelastic properties of asphalt mixtures with captured microstructure and ingredient properties.

INTRODUCTION

Asphalt mixtures, or Hot Mix Asphalt (HMA), are complex heterogeneous materials composed of graded aggregates, asphalt mastic (including asphalt binder and fine aggregates), additives, and void spaces. Dynamic modulus is an important factor in evaluating the field performance of asphalt mixtures. The use of micromechanical models to predict properties of asphalt mixtures and mastic has drawn increasing attention over the past ten years, and a number of approaches have been investigated. Asphalt mixtures were investigated by non-interaction particle micromechanical models without specified geometry (Buttlar and Roque 1996; 1997; Hashin and

Shtrikman 1963; Schapery and Lytton 1978; Voigt 1889), as well as, with specified geometry (Buttlar et al. 1999; Christensen and Lo 1979; Hashin 1965; Shashidhar et al. 1996).

FE modeling of asphalt concrete allows accurate prediction of mixture properties by incorporating aggregate and mastic constitutive behaviors and microstructure geometries. Research work has been conducted using FE techniques (Bahia et al. 1999; Bazant 1990; Budhu et al. 1997; Guddati et al. 2002; Kose et al. 2000; Mora 1992; Mustoe and Griffiths 1998; Papagiannakis et al. 2002; Sepehr et al. 1994; Stankowski 1990). Three-dimensional microstructures of asphalt mixtures were captured for numerical simulation (Masad 2004; Papagiannakis et al. 2002; Wang et al. 2001; Wang et al. 2004). An equivalent lattice network approach, where the local interaction between neighboring particles was modeled with a special frame-type FE, was developed and applied (Dai and Sadd 2004; Dai et al. 2005; Sadd et al. 2004a; Sadd et al. 2004b). The mixed FE approaches were developed to study asphalt mixtures by using different FEs for asphalt mastic and aggregate (Dai et al. 2006b; Dai and You 2007; Dai and You 2008). The real aggregate shape was considered in the micromechanical model (You and Dai 2007).This paper presents a micromechanical FE modeling scheme for predicting the viscoelastic properties of heterogeneous asphalt mixtures. The micromechanical model incorporates the user-defined material subroutine with viscoelastic FEs for asphalt mastic and elastic FEs for each aggregate. The inputted constitutive model parameters are determined from the lab test data of ingredients. Finally, the model predictions of the digital sample are compared with lab measurements.

SCOPE AND OBJECTIVES

The main objective of this study is to develop micromechanical finite element models that can favorably predict both complex modulus and phase angle with the captured microstructure and the measured ingredient properties. To achieve this objective, this study incorporates the generalized Maxwell viscoelastic model into a microstructure-based FE approach. The model parameters for simulating asphalt mixtures were calibrated with the measured mastic visoelastic properties over a frequency range at a low temperature. The detailed goals of this work are as follows:

- To develop microstructure-based FE models to account for the viscoelastic behavior of asphalt mixtures.
- To determine the viscoelastic model parameters with nonlinear regression analysis of laboratory test data of asphalt mastic in the frequency domain.
- To predict the dynamic modulus and phase angle of asphalt mixtures under cyclic loadings with different frequencies.

MICROSTRUCTURE AND IMAGE SAMPLE GENERATION

The 2D microstructure of asphalt concrete was captured from optically scanned images as shown in Fig.1. Asphalt mixture specimens were cut vertically and the sectioned surfaces were smoothly sawn. A high-resolution scanner was used to obtain

grayscale images from these surfaces. Fig. 1a shows a grayscale image of a vertical surface in a mixture specimen with 86mm width and 106mm height. Imaging processing techniques were used to improve the resolution and digitally sieve the coarse aggregates with a minimum size of 1.18 mm. The fine aggregates with the size less than 1.18 mm are maintained in asphalt mastic. Fig. 1b shows the digital sample A with FE mesh. In this figure, the sieved coarse aggregates are treated as polygons with Image Pro Plus software (Cybernetics 2006). This figure also illustrates the FE mesh generated within aggregate and asphalt mastic phases. Because of very irregular aggregate shapes and mastic distribution, three-node triangle elements were used to account for complex geometry. Three-node triangle elements were generated in aggregates and sand mastic domain along the irregular boundaries. The triangle elements in these two phases are perfectly bonded by sharing nodes on the boundaries as shown in Fig. 1c.

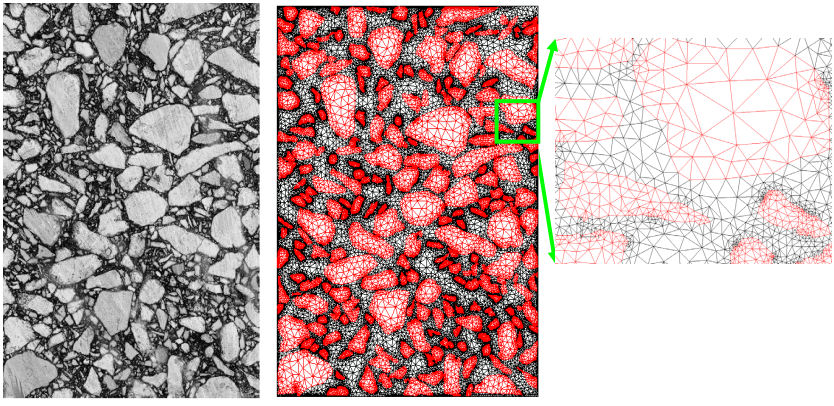

FIG. 1. The asphalt mixture image and the three-node triangle FE mesh for digital sample A, a) grayscale image of specimen surface, b) finite element mesh for the aggregates and mastic, c) enlarged meshes.

MICROMECHANICAL FINITE ELEMENT MODEL

As shown in the Fig. 1, the general modeling scheme employed viscoelastic elements to model asphalt mastic material and an elastic body for each aggregate. This model contains the real microstructure of asphalt mixture specimens. The elastic constants of aggregates are measured to input to the model. Properties of the triangle elements in asphalt mastic domain are specified through a user-defined material subroutine within the ABAQUS code (ABAQUS 2004). This subroutine allows the incorporation of the specific viscoelastic model with calibrated parameters from lab test data of the ingredients.

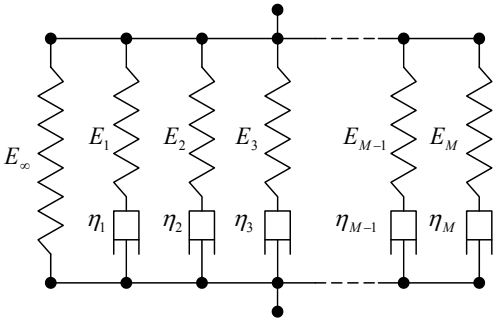

FIG. 2. The generalized Maxwell viscoelastic model for simulating sand mastic.

The generalized viscoelastic model used in this study consists of several Maxwell elements in parallel as shown in Fig. 2. This type of model has been employed to study the linear and damage-coupled viscoelastic behavior of asphalt mixtures by the author (Dai et al. 2006a; Dai and You 2007; Dai and You 2008). The constitutive behavior and FE implementation of this Maxwell-type model are briefly presented in this section. The stress-strain relations can be expressed as a hereditary integral:

$$\sigma_{ij} = E_\infty \varepsilon_{ij} + \int_0^t E_t \frac{d\varepsilon_{ij}(\tau)}{d\tau} d\tau \tag{1}$$

where E_t is expressed with a Prony series:

$$E_t = \sum_{m=1}^{M} E_m e^{-\frac{(t-\tau)}{\rho_m}}, \text{ and } \rho_m = \frac{\eta_m}{E_m} \tag{2}$$

In these equations, E_∞ is the relaxed modulus; E_t is the transient modulus as a function of the time; E_m, η_m and ρ_m are the spring constant, dashpot viscosity and relaxation time respectively for the m^{th} Maxwell element.

The reduced time (effective time) is defined by using the time-temperature superposition principle as:

$$\xi(t) = \int_0^t \frac{1}{\alpha_T} d\tau \tag{3}$$

where the term $\alpha_T = \alpha_T(T(\tau))$ is a temperature-dependent time-scale shift factor.

The 2D behaviors can be formulated with uncoupled volumetric and deviatoric stress-strain relations. A displacement-based incremental FE modeling scheme with constant strain rate over each increment is applied in the following format:

$$\Delta\sigma = K \cdot \Delta\varepsilon + \Delta\sigma^R \tag{4}$$

where $\Delta\sigma$ and $\Delta\varepsilon$ are incremental stress and strain, K is the incremental stiffness and $\Delta\sigma^R$ is the residue stress vector.

The volumetric constitutive relationship is expressed with the volumetric stress σ_{kk} and strain ε_{kk} in the general form:

$$\sigma_{kk}(t) = 3K_\infty \varepsilon_{kk}(t) + \int_0^t 3K_t(\xi-\tau)\frac{d\varepsilon_{kk}(\tau)}{d\tau}d\tau \tag{5}$$

where $K_\infty = E_\infty / 3(1-2\nu)$ is the relaxed bulk modulus; $K_t(\xi-\tau) = \sum_{m=1}^{M} K_m e^{-\frac{(\xi-\tau)}{\rho_m}}$ is the transient bulk modulus; and $K_m = E_m / 3(1-2\nu)$ is the bulk constants for the spring in the *m*th Maxwell element. The incremental formulation of the volumetric behavior is obtained with the constant volumetric strain rate $R_{kk} = \frac{\Delta\varepsilon_{kk}}{\Delta t}$,

$$\Delta\sigma_{kk} = 3\left[K_\infty + \sum_{m=1}^{N}\frac{K_m\rho_m}{\Delta\xi}\left(1-e^{-\frac{\Delta\xi}{\rho_m}}\right)\right]\Delta\varepsilon_{kk} + \Delta\sigma_{kk}^R \tag{6}$$

In this equation, incremental stiffness $K = 3\left[K_\infty + \sum_{m=1}^{N}\frac{K_m\rho_m}{\Delta\xi}\left(1-e^{-\frac{\Delta\xi}{\rho_m}}\right)\right]$ is not time-dependent if strain rate R_{kk} is constant, and the residual part $\Delta\sigma_{kk}^R$ can be expressed in a recursive relation with the history variable S_m,

$$\Delta\sigma_{kk}^R = \sum_{m=1}^{M} -\left(1-e^{-\frac{\Delta\xi}{\rho_m}}\right)S_m(\xi_n), \text{ and } S_m(\xi_n) = 3K_m R_{kk}\rho_m\left(1-e^{-\frac{\Delta\xi}{\rho_m}}\right) + S_m(\xi_{n-1})e^{-\frac{\Delta\xi}{\rho_m}} \tag{7}$$

For the initial increment, the history variable $S_m(\xi_1)$ equals to $3K_m R_{kk}\rho_m\left(1-e^{-\frac{\Delta\xi}{\rho_m}}\right)$ and is similar to the following formulations.

For the deviatoric behavior, the constitutive relationship is written using deviatoric stress $\hat{\sigma}_{ij} = \sigma_{ij} - \frac{1}{3}\sigma_{kk}\delta_{ij}$ and strain $\hat{\varepsilon}_{ij} = \varepsilon_{ij} - \frac{1}{3}\varepsilon_{kk}\delta_{ij}$,

$$\hat{\sigma}_{ij}(t) = 2G_\infty \hat{\varepsilon}_{ij}(t) + \int_0^t 2G_t(\xi-\tau)\frac{d\hat{\varepsilon}_{ij}(\tau)}{d\tau}d\tau \tag{8}$$

where $G_\infty = E_\infty / 2(1+\nu)$ is the relaxed shear modulus; $G_t(\xi-\tau) = \sum_{m=1}^{M} G_m e^{-\frac{(\xi-\tau)}{\rho_m}}$ is the transient shear modulus; and $G_m = E_m / 2(1+\nu)$ is the shear constants for the spring in the *m*th Maxwell element. The formulation of the deviatoric behavior is obtained with the constant deviatoric strain rate $\hat{R}_{ij} = \frac{\Delta\hat{\varepsilon}_{ij}}{\Delta t}$,

$$\Delta\hat{\sigma}_{ij} = 2\left[G_\infty + \sum_{m=1}^{N}\frac{G_m\rho_m}{\Delta\xi}\left(1-e^{-\frac{\Delta\xi}{\rho_m}}\right)\right]\Delta\hat{\varepsilon}_{ij} + \Delta\hat{\sigma}_{ij}^R \tag{9}$$

and the residual part $\Delta\hat{\sigma}_{ij}^{R}$ can be expressed in the recursive relation:

$$\Delta\hat{\sigma}_{ij}^{R}=\sum_{m=1}^{N}-\left(1-e^{-\frac{\Delta\xi}{\rho_m}}\right)S_m\left(\xi_n\right),\ \text{and}\ S_m\left(\xi_n\right)=2G_m\hat{R}_{ij}\rho_m\left(1-e^{-\frac{\Delta\xi}{\rho_m}}\right)+S_m\left(\xi_{n-1}\right)e^{-\frac{\Delta\xi}{\rho_m}} \quad (10)$$

For the 2D viscoelastic behavior, the incremental normal stresses can be then formulated by combining the volumetric and deviatoric behavior. For example,

$$\begin{aligned}\Delta\sigma_{yy}&=1/3\Delta\sigma_{kk}+\Delta\hat{\sigma}_{yy}\\&=\left[K_\infty+\sum_{m=1}^{N}\frac{K_m\rho_m}{\Delta\xi}\left(1-e^{-\frac{\Delta\xi}{\rho_m}}\right)\right]\Delta\varepsilon_{kk}+2\left[G_\infty+\sum_{m=1}^{N}\frac{G_m\rho_m}{\Delta\xi}\left(1-e^{-\frac{\Delta\xi}{\rho_m}}\right)\right]\Delta\hat{\varepsilon}_{yy}+1/3\Delta\sigma_{kk}^{R}+\Delta\hat{\sigma}_{yy}^{R}\end{aligned} \quad (11)$$

where $\Delta\varepsilon_{kk}=\Delta\varepsilon_{xx}+\Delta\varepsilon_{yy}$ and $\Delta\sigma_{kk}=\Delta\sigma_{xx}+\Delta\sigma_{yy}$ are the incremental volumetric strain and stress for 2D behavior; $\Delta\hat{\varepsilon}_{yy}$ and $\Delta\hat{\sigma}_{yy}$ are the incremental deviatoric strain and stress; and $\Delta\sigma_{kk}^{R}=\Delta\sigma_{xx}^{R}+\Delta\sigma_{yy}^{R}$ and $\Delta\hat{\sigma}_{yy}^{R}$ are the recursive part of the volumetric and deviatoric behavior given in Eqs. (6) and (9). Incremental stresses $\Delta\sigma_{xx}$ can be determined in the same manner.

The incremental shear stress can be formulated by using only the deviatoric behavior as:

$$\begin{aligned}\Delta\sigma_{xy}&=\Delta\hat{\sigma}_{xy}\\&=2\left[G_\infty+\sum_{m=1}^{M}\frac{G_m\rho_m}{\Delta\xi}\left(1-e^{-\frac{\Delta\xi}{\rho_m}}\right)\right]\Delta\hat{\varepsilon}_{xy}+\Delta\hat{\sigma}_{xy}^{R}\end{aligned} \quad (12)$$

where $\Delta\hat{\varepsilon}_{xy}$ and $\Delta\hat{\sigma}_{xy}$ are the incremental shear deviatoric strain and stress, and the recursive term $\Delta\hat{\sigma}_{xy}^{R}$ is also given in Eq. (9).

Once the incremental stress components are developed, the incremental stiffness terms can be calculated and then the incremental 2D linear viscoelastic behavior is formulated as:

$$\begin{bmatrix}\Delta\sigma_{xx}\\ \Delta\sigma_{yy}\\ \Delta\sigma_{xy}\end{bmatrix}=\begin{bmatrix}K_1 & K_2 & 0\\ \bullet & K_1 & K_2\\ \bullet & \bullet & K_3\end{bmatrix}\begin{bmatrix}\Delta\varepsilon_{xx}\\ \Delta\varepsilon_{yy}\\ \Delta\varepsilon_{xy}\end{bmatrix}+\begin{bmatrix}\Delta\sigma_{kk}^{R}+\Delta\hat{\sigma}_{xx}^{R}\\ \Delta\sigma_{kk}^{R}+\Delta\hat{\sigma}_{yy}^{R}\\ \Delta\hat{\sigma}_{xy}^{R}\end{bmatrix} \quad (13)$$

where

$$\begin{aligned}K_1&=\left[K_\infty+\sum_{m=1}^{N}\frac{K_m\rho_m}{\Delta\xi}\left(1-e^{-\frac{\Delta\xi}{\rho_m}}\right)\right]+\frac{4}{3}\left[G_\infty+\sum_{m=1}^{N}\frac{G_m\rho_m}{\Delta\xi}\left(1-e^{-\frac{\Delta\xi}{\rho_m}}\right)\right]\\K_2&=\left[K_\infty+\sum_{m=1}^{N}\frac{K_m\rho_m}{\Delta\xi}\left(1-e^{-\frac{\Delta\xi}{\rho_m}}\right)\right]-\frac{2}{3}\left[G_\infty+\sum_{m=1}^{N}\frac{G_m\rho_m}{\Delta\xi}\left(1-e^{-\frac{\Delta\xi}{\rho_m}}\right)\right]\\K_3&=2\left[G_\infty+\sum_{m=1}^{N}\frac{G_m\rho_m}{\Delta\xi}\left(1-e^{-\frac{\Delta\xi}{\rho_m}}\right)\right]\end{aligned} \quad (14)$$

EXPERIMENTAL CALIBRATIONS OF MODEL MATERIAL PARAMETERS

To conduct the micromechanical modeling of stone-based materials, the material parameters of elastic aggregates and viscoelastic matrix need to be determined from the lab test data. For the asphalt mixtures, the simulation results of digital sample need to be compared with the lab measurements of material specimens for the model verification. The limestone aggregates were used to prepare the mixture specimen. A modulus of 55.5GPa (You 2003) was measured and used in this study at a low temperature (-6°C) and different loading frequencies. The air void ratio of the mixture specimen was measured as 4.36%. The asphalt matrix specimens are comprised of the fine aggregates smaller than the 2.36mm combined with the volume of asphalt binder normally used in the entire asphalt mixtures (You 2003). The asphalt content of matrix specimens is about 10.4% in weight. The uniaxial compression tests were conducted to measure dynamic (complex) modulus and phase angle with asphalt matrix and mixture specimens at different loading temperatures and frequencies. The measurements of dynamic modulus and phase angle of matrix specimens at a low temperature (-6°C) and under different frequencies (0.1, 0.5, 1, 5, 10Hz) were used to determine the material parameters of the generalized Maxwell model.

The two-element Maxwell model was used to simulate the viscoelastic behavior of asphalt matrix. The detailed procedures of numerical calibration of model parameters can be found in author's publication (Dai 2009). This section briefly describes this approach. The five parameters (E_∞, E_1, E_2, ρ_1 and ρ_2) of this two-element Maxwell model were determined with the nonlinear regression analysis. The test data of dynamic modulus and phase angle of the asphalt matrix specimens were used. For the two-element Maxwell model, the imaginary and real parts (E' and E'') of complex modulus E^* are given as a function of loading radian frequency ω (Tschoegl 1989):

$$E'(\omega) = E_\infty + \frac{E_1\omega^2\rho_1^2}{1+\omega^2\rho_1^2} + \frac{E_2\omega^2\rho_2^2}{1+\omega^2\rho_2^2} \text{ and } E''(\omega) = \frac{E_1\omega\rho_1}{1+\omega^2\rho_1^2} + \frac{E_2\omega\rho_2}{1+\omega^2\rho_2^2} \tag{15}$$

where E_∞, E_1 and E_2 are the spring modulus and ρ_1 and ρ_2 are the relaxation time of each Maxwell element shown in Fig. 2. The magnitude of complex modulus $|E^*|$ (also is called as dynamic modulus in the pavement engineering) and phase angle Φ can be obtained respectively from real and imaginary parts:

$$|E^*| = \sqrt{E'(\omega)^2 + E''(\omega)^2} \text{ and } \Phi = \tan^{-1}\left(\frac{E''(\omega)}{E'(\omega)}\right) \tag{16}$$

A nonlinear regression computer program NLREG (Sherrod 1992-2008) was used to determine these five parameters. The imaginary part E'' and real part E' of complex modulus were calculated from matrix test data (dynamic modulus and phase angle) for each frequency. Nonlinear regression analysis was conducted by using the functions of imaginary part E'' and real part E' varying with the radian frequency ω. The five parameters were determined as: E_∞ = 3.489 GPa, E_1 = 5.21 GPa, E_2 = 6.309 GPa, ρ_1 = 0.579 s, and ρ_2 = 0.009 s. After determining these five parameters, the dynamic modulus and phase angle were calculated with Eq. 16. Fig. 3 shows numerical

calibration results of two-element Maxwell model parameters for asphalt matrix. The dynamic modulus and phase angle from lab test and nonlinear regression analysis were compared in Figs. 3(a-b). The average relative errors between lab test data and analysis results were calculated as 8.7% and 6.3% for dynamics modulus and phase angle respectively. These material parameters for viscoelastic asphalt matrix and elastic aggregate were input for the micromechanical FE simulation.

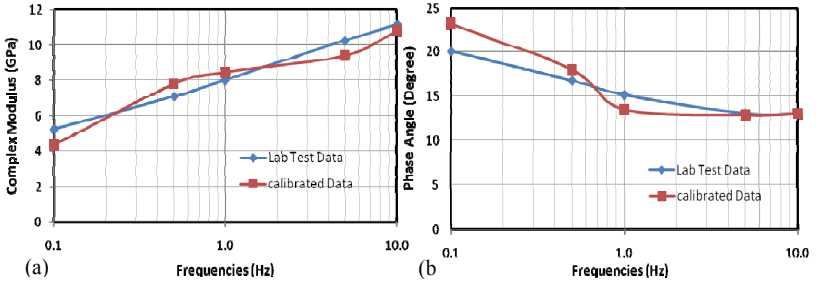

FIG. 3. Numerical calibration results of two-element Maxwell model parameters for asphalt mastic, a) dynamic modulus $|E^*|$ obtained from lab test and numerical calibration, b) phase angle Φ from lab test and numerical calibration.

COMPARISON OF SIMULATION RESULTS WITH TEST DATA

To compare with the lab test data of dynamic modulus and phase angle of mixture specimens, the FE simulations were conducted under the same sinusoidal loading with the frequencies of 0.1 Hz, 0.5 Hz, 1 Hz, 5 Hz and 10 Hz. The loading cycles were imposed as seven for the frequencies of 0.1, 0.5 and 1 Hz, and fourteen for the frequencies of 5 and 10 Hz. For each cycle, 400 time increments (computation points) were used to achieve a high resolution, 0.9 degree/computation point for phase angle. The dynamic modulus was numerically calculated with the equation within one cycle:

$$|E^*| = \frac{|\sigma_{\max} - \sigma_{\min}|}{|\varepsilon_{\max} - \varepsilon_{\min}|} \tag{17}$$

The phase angle was calculated by tracking the computation points of maximum/minimum stress and strain. The dynamic modulus and phase angle were calculated with average value of the last two cycles.

The dynamic modulus and phase angle of each loading frequency were calculated from the stress-strain curves of simulation results for digital sample A. Fig. 4 shows the comparison between these predictions and the lab test data. Fig. 4(a) shows the dynamic modulus increases with loading frequencies due to decreasing relaxation time. The result curves of mixture samples A (shown in Fig. 4(a)) have a similar trend as the numerical calibration results of dynamics modulus of asphalt mastic (shown in Fig.3(a)). It indicates that the prediction of dynamic modulus with developed FE

model is reasonable. The average relative errors between the simulation results of digital sample A and lab test data were calculated as 7.4%.

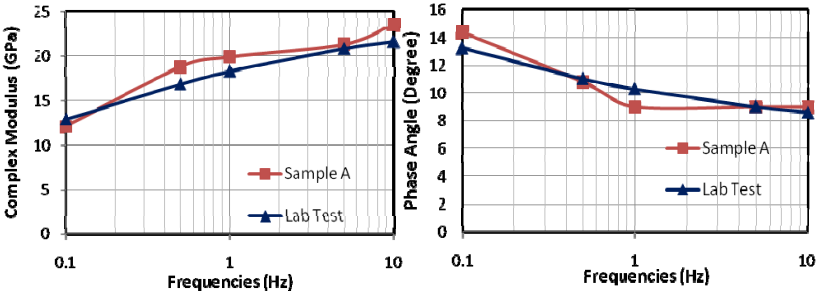

FIG. 4. Comparisons among simulation results with the digital sample A and test data under different frequencies, a) complex modulus, b) phase angle.

The comparison of phase angle is shown in the Fig. 4(b), with the prediction results of sample A and the test results of the lab specimen. It was also found that the result curve trend of the mixture samples (shown in Fig. 4(b)) is similar to the numerical calibration results of phase angle of the asphalt mastic (shown in Fig. 3(b)). This again verified the feasibility of the numerical prediction of the developed FE models. The predictions of phase angles are close to the test data at different loading frequencies. The average relative errors between the simulation results of digital sample A and lab test data were calculated as 5.6%. Overall, the predictions of dynamic modulus and phase angle with the digital sample A have a favorable comparison with the test data. It is indicated that the developed micromechanical FE model is applicable to predict the global viscoelastic properties of asphalt mixtures with generated image samples and calibrated material parameters. With the development of 3D modeling and the additional calibration of mastic and aggregates, it is expected that the prediction will be closer to the test data with more capacity to describe the micromechanical behavior of asphalt mixtures.

CONCLUSIONS

Micromechanical FE models were developed to predict the viscoelastic properties (dynamic modulus and phase angle) of asphalt mixtures. The digital sample was generated from the optically scanned surface image of a sectioned asphalt specimen. FE mesh was generated within each aggregate and asphalt mastic. Along the boundary of these two phases, the FEs share the nodes to connect the deformation. The micromechanical FE model incorporates the viscoelastic asphalt mastic and elastic aggregates. A two-element Maxwell model was used for viscoelastic asphalt mastic and its material parameters were calibrated with nonlinear regression analysis of lab test data. A viscoelastic mastic model was defined in the UMAT subroutine of the ABAQUS program. The displacement-based FE simulations were conducted on the

numerical sample A under sinusoidal cyclic loading. The predicted dynamic modulus and phase angle of sample A were compared with the lab test data under the same loading frequencies.

In general, micromechanical FE models provided reasonable predictions of the dynamic modulus and phase angle over a frequency range. For the dynamic modulus, the average relative errors between the simulation results of the digital sample A and the lab test data were calculated as 7.4% (shown in Fig.4(a)). For the phase angle, the sample A also has favorable comparison with the lab test data as shown in Fig.4(b). By comparing the simulation results of the mixture sample shown in Fig.4 and the numerical calibration of the mastic specimen shown in Fig.3, similar trends were found for the curves of dynamic modulus and phase angle as a function of loading frequencies. These comparison results indicated the developed micromechanical FE models have good capabilities to predict the global viscoelastic properties such as dynamic modulus and phase angle of asphalt mixtures.

ACKNOWLEDGEMENTS

The partial support of this research by the National Science Foundation under grants 0701264 and 0900015 is gratefully appreciated.

REFERENCES

ABAQUS. (2004). In: *Hibitt, Karlsson and Sorenson*, Version 6.5, Pawtucket, R.I.

Bahia, H., Zhai, H., Bonnetti, K., and Kose, S. (1999). "Nonlinear viscoelastic and fatigue properties of asphalt binders." *Journal of Association of Asphalt Paving Technologists*, 68, 1-34.

Bazant, Z. P., Tabbara, M.R., Kazemi, Y., Pijaudier-Cabot, G. (1990). " Random particle simulation of damage and fracture in particulate or fiber-reinforced composites. ." In: *Damage Mechanics in Engineering Materials*, Trans. ASME, AMD.

Budhu, M., Ramakrishnan, S., and Frantziskonis, G. (1997). "Modeling of Granular Materials: A Numerical Model Using Lattices , Northwestern Univ." In: *Mechanics of Deformation and Flow of Particulate Materials*, C. S. Chang, A. Misra, R. Y. Liang, and M. Babic, eds., Proc. McNu Conference, Trans. ASCE.

Buttlar, W. G., Bozkurt, D., Al-Khateeb, G. G., and Waldhoff, A. S. (1999). "Understanding asphalt mastic behavior through micromechanics (with discussion and closure)." *Journal of Transportation Research Board*, 1681, p. 157-169.

Buttlar, W. G., and Roque, R. (1996). "Evaluation of empirical and theoretical models to determine asphalt mixture stiffnesses at low temperatures (with discussion)." *Association of Asphalt Paving Technologists*, 65, p. 99-141.

Buttlar, W. G., and Roque, R. (1997). "Effect of asphalt mixture master compliance modeling technique on thermal cracking performance evaluation using superpave." In: *Eighth International Conference on Asphalt Pavements*, University of Washington, Seattle, p. 1659-1669.

Christensen, R. M., and Lo, K. H. (1979). "Solutions for Effective Shear Properties in Three Phase Sphere and Cylinder Models." *J. Mech. Phys. Solids*, 27, 315-330.

Cybernetics, M. (2006). "Image-Pro Plus."

Dai, Q. (2009). "Prediction of Dynamic Modulus and Phase Angle of Stone-Based Composites using Micromechanical Finite Element Approach " *ASCE Journal of Materials in Civil Engineering*, in press.

Dai, Q., and Sadd, M. H. (2004). "Parametric model study of microstructure effects on damage behavior of asphalt samples." *International Journal of Pavement Engineering*, 5(1), 19-30.

Dai, Q., Sadd, M. H., Parameswaran, V., and Shukla, A. (2005). "Prediction of damage behaviors in asphalt materials using a micromechanical finite-element model and image analysis." *Journal of Engineering Mechanics*, 131(7), 668-677.

Dai, Q., Sadd, M. H., and You, Z. (2006a). "A Micromechanical Finite Element Model for Linear and Damage-Coupled Viscoelastic Behavior of Asphalt Mixture." *International Journal for Numerical and Analytical Methods in Geomechanics*, 30(11), 1135-1158.

Dai, Q., Sadd, M. H., and You, Z. (2006b). "A Micromechanical Finite Element Model for Viscoelastic Creep and Viscoelastic Damage Behavior of Asphalt Mixture." *International Journal for Numerical and Analytical Methods in Geomechanics*, 30, 1135–1158.

Dai, Q., and You, Z. (2007). "Prediction of Creep Stiffness of Asphalt Mixture with Micromechanical Finite Element and Discrete Element Methods." *Journal of Engineering Mechanics, ASCE*, 133(2), 163-173.

Dai, Q., and You, Z. (2008). "Micromechanical Finite Element Framework for Predicting Viscoelastic Properties of Heterogeneous Asphalt Mixtures." *Materials and Structures, Springer Netherlands*, 41(6), 1025-1037.

Guddati, M. N., Feng, Z., and Kim, R. (2002). "Toward a micromechanics-based procedure to characterize fatigue performance of asphalt concrete." *Transportation Research Record*(1789), 121-128.

Hashin, Z. (1965). "Viscoelastic Behaviour of Heterogeneous Media." *Journal of Applied Mechanics, Trans. ASME*, 9, 630-636.

Hashin, Z., and Shtrikman, S. (1963). "A Variational Approach to the Theory of the Elastic Behaviour of Multiphase Materials." *J. Mech. Phys. Solids*, Vol. 11, 127-167.

Kose, S., Guler, M., Bahia, H. U., and Masad, E. (2000). "Distribution of Strains within Asphalt Binders in HMA Using Image and Finite Element Techniques." *J. Trans. Res. Record National Research Council, Washington, D.C.*, 1728(21-27).

Masad, E. (2004). "X-ray computed tomography of aggregates and asphalt mixes." *Materials Evaluation*, 62(7), 775-783.

Mora, P. (1992). "A Lattice Solid Model for Rock Rheology and Tectonics." In: *The Seismic Simulation Project Tech.*, Institut de Physique du Globe, Paris, 3-28.

Mustoe, G. G. W., and Griffiths, D. V. (1998). "An Equivalent Model Using Discrete Element Method(DEM), ." In: *Proc. 12th ASCE Engineering Mechanics Conf.*, La Jolla, CA.

Papagiannakis, A. T., Abbas, A., and Masad, E. (2002). "Micromechanical analysis of viscoelastic properties of asphalt concretes." *Transportation Research Record*(1789), 113-120.

Sadd, M. H., Dai, Q., Parameswaran, V., and Shukla, A. (2004a). "Microstructural simulation of asphalt materials: Modeling and experimental studies." *Journal of Materials in Civil Engineering*, 16(2), 107-115.

Sadd, M. H., Dai, Q., Parameswaran, V., and Shukla, A. (2004b). "Simulation of Asphalt Materials Using Finite Element Micromechanical Model with Damage Mechanics." *Transportation Research Record*(1832), 86-95.

Schapery, R., and Lytton, R. (1978). "Extension and Replacement of Asphalt Cement Sulfur." FHWA, US Department of Transportation.

Sepehr, K., Svec, O. J., Yue, Z. Q., and El Hussein, H. M. (Year). "Finite element modelling of asphalt concrete microstructure." Computational Mechanics Publ, Southampton, Engl, Udine, Italy, 225.

Shashidhar, N., Needham, S. P., Chollar, B. H., and Romero, P. (1996). "Prediction of the performance of mineral fillers in stone matrix asphalt." *J. Assoc. Asphalt Paving Tech.*, 222-251.

Sherrod, P. H. (1992-2008). "NLREG, Nonlinear Regression Analysis Program."

Stankowski , T. (1990). "Numerical Simulation of Failure in Particle Composite, Computers and Structures." *Computers and Structures, Great Britain*, 44(1/2), 460.

Tschoegl, N. W., ed. (1989). *The Phenomenological Theory of Linear Viscoelastic Behavior, An Introduction*, Springer-verlag.

Voigt, W. (1889). *Ueber die Beziehung zwischen den beiden Elasticitatsconstanten isotroper Korper*.

Wang, L., Frost, J. D., and Shashidhar, N. (2001). "Microstructure Study of Westrack Mixes from X-ray Tomography Images." *J. Trans. Res. Record National Research Council, Washington, D.C.*, 1767, 85-94.

Wang, L., Paul, H., Harman, T., and D'Angelo, J. (2004). "Characterization of Aggregates and Asphalt Concrete Using X-ray Computerized Tomography." *J. Assoc. Asphalt Paving Tech.*, 73(467-500).

You, Z. (2003). "Development of a Micromechanical Modeling Approach to Predict Asphalt Mixture Stiffness Using Discrete Element Method (Ph.D. Dissertation)," Ph.D. Dissertation, University of Illinois at Urbana-Champaign, Urbana, IL.

You, Z., and Dai, Q. (2007). "Complex Modulus Predictions of Asphalt Mixtures Using a Micromechanical -Based Finite Element Model." *Canadian Journal of Civil Engineering*, 34(12)(1-10).

Research and Application of Recycled Aggregate Concrete

Jian Yin[1], Yi Chi[2], Shenghui Gong[3], Wei Zou[4]

[1] Professor, postdoctor. College of Civil Engineering and Architecture, Central South University, Changsha 410075, China；csuyj@mail.csu.edu.cn
[2] Doctor. College of Civil Engineering and Architecture, Central South University, Changsha 410075, China；chiyi05@163.com
[3] Graduate student. College of Civil Engineering and Architecture, Central South University, Changsha 410075, China；agong0303@163.com
[4] Graduate student. College of Civil Engineering and Architecture, Central South University, Changsha 410075, China；csustorm@vip.qq.com

ABSTRACT: The properties of recycled aggregate concrete (RAC) incorporating mineral admixture including fly ash and slag were studied through laboratory tests and practical project. The test results indicated that by adding fly ash, the apparent density of RAC reduced significantly, and the workability of RAC improved observably. The ratio of tension strength to compression strength and the ratio of splitting tensile strength to compressive strength of RAC both increased, so the tensile capability were improved and the frangibility reduced, which were helpful to improve the crack resistance and volume stability of road RAC. The abrasion resisting property of RAC was improved. The project application of RAC showed that the compression strength of the concrete adding 80~100% recycled concrete coarse aggregate could reach C35 (35MPa~40MPa) and the flexural strength could be higher than 5.0 MPa at 28 d, both of which satisfied the requirement in the heavy and special heavy traffic road, and could open to traffic at 3 d. The overall performance of RAC pavement were excellent, and without dehiscence after working one year.

INTRODUCTION

Many scholars at home and abroad carried out extensive researches on the physical, mechanical properties and durability of recycled aggregate and RAC; but it is rare to use RAC in concrete pavement repair works. In this study, the waste concrete was used as recycled aggregate for pavement maintenance. The high-performance concrete technology was adopted, and the mechanical properties and wear resistance of RAC were studied. The RAC was applied in the pavement repair of G325 Foshan section. The overall performance of RAC pavement are excellent after working one year, which provides preliminary study basis and

technical support for the promotion and application of RAC technology.

TEST MATERIALS AND METHODS

Test materials

Cement was Yue Xiu brand ordinary Portland cement of 42.5 grade, the physical properties and chemical composition of cement met the current national specification "Common portland cement". With the mortar mixture proportion in this specification, 3, 28 d cement mortar flexural strength were 5.02, 8.10 MPa, and 3, 28 d compressive strength were 20.3, 47.6 MPa. Natural coarse aggregate was river gravel, whose gradation met the requirements of 5 ~ 31.5 mm continuous gradation. Natural fine aggregate was river sand and good graded sand, whose modulus of fineness was 2.77. The gradation of the produced recycled coarse aggregate met 5 ~ 31.5 mm continuous gradation. Table 1 presents the physical and mechanical properties of recycled aggregate. The parent rock strength of recycled aggregate was 32.5 MPa. The Bo's specific surface area of Class I fly ash was 506 m^2/Kg. The specific area of San Xia slag was 375m^2/kg. The water for concrete mixing and curing was ordinary tap water. Tanjian Superplasticizer from Xiangtan admixture production factory was used.

Table 1. Fundamental Performance of Aggregate

Material	Grain size (mm)	Apparent density ($kg \cdot m^{-3}$)	Packing density ($kg \cdot m^{-3}$)	Water absorption (%)	Crush index (%) Drying	Saturation
RA	5～31.5	2510	1230	5.7	17.2	22.3
NA	5～31.5	2650	1630	0.6	5.6	6.9
NS	<5	2670	1610	1.6	--	--

Note: RA is Recycle coarse aggregate; NA is Natural coarse aggregate; NS is Natural fine aggregate, same as other table.

Test methods

The mechanical properties of RAC were tested according to the national test specification "Testing methods for mechanical performance of ordinary concrete" (GB / T 50081-2002). 100mm×100mm×100mm cube specimen were used for compression strength tests, and 100mm × 100mm × 400mm beam specimens were used for flexural strength tests. 100mm × 100mm × 300mm beam specimens were used for prism compressive strength tests and elastic modulus tests. Test results converted into standard values according to the national test specification (GB / T 50081-2002). Before mixing RAC, the recycled aggregate were soaked in water for 15 minutes to let it absorb enough water. Table 2 presents the mix proportion and the properties of fresh concrete.

TEST RESULTS AND ANALYSIS

Performance of fresh RAC

Experimental results in Table 2 showed that: to keep the constant concrete slump value, as the content of fly ash increased, the content of superplasticizer significantly reduced, which illustrated the effect of adding fly ash to improve the workability of RAC was remarkable. The main reasons were: (1) Smooth fly ash requires less water for making the surface wet. The relatively small particles of fly ash could fill the gap of the cement particles to replace interstitial water partly. (2) Tiny particles could also play a certain role in the ball bearing among the larger cement particles and it effectively reduced the friction between the cement particles. (3) Fly ash itself had the same kind of charges. The electrostatic repulsion maintained the dispersibility of the system, which acted as ordinary mineral water reducer.

Table 2. Mix Proportion of RAC and Fresh Concrete Performance

No.	Mix proportion (kg/m^3)								Sp (%)	Slump constant (mm)	Apparent density (kg/m^3)
	C	FA	SG	W1	W2	NA	RA	NS			
NC01	450	--	--	135	0	1160	0	652	1.0	10	2437
NC02	450	--	--	135	23.2	1160	0	652	0.5	45	2439
FA-0	450	0	--	135	23.2	232	928	652	0.9	10	2382
FA-20	360	90	--	135	23.2	232	928	652	0.7	40	2353
FA-30	315	135	--	135	23.2	232	928	652	0.6	30	2358
FA-40	270	180	--	135	23.2	232	928	652	0.5	55	2362
F0+S30	315	0	135	135	23.2	232	928	652	0.8	15	2365
F10+S20	315	45	90	135	23.2	232	928	652	0.8	45	2352
F20+S10	315	90	45	135	23.2	232	928	652	0.7	40	2366
F30+S0	315	135	0	135	23.2	232	928	652	0.6	30	2358

Note: Water demand per unit by mix design of ordinary concrete (W1); Pre-soakage of waste concrete aggregate (W2). C is cement; FA is fly ash; SG is slag.

The mechanical properties of RAC

The impact of recycled aggregate on the strength

Test results of NC02 and FA-0 in Table 3 showed that, at the same water/binder ratio, the compressive strength, flexural strength at 3d of natural aggregate concrete were close to the RAC containing 80% recycled aggregate. Thus, for the 80% content of recycled aggregate, recycled aggregate had little effect on the early mechanical properties of concrete. According to JTJ 073.1-2001 "Technical Specification of Cement Concrete Pavement Maintenance for Highway", the strength of concrete materials for the slab repair should achieve more than 70% of the design strength of the original slab within 24h. In addition, 24h flexural strength of concrete should reach 3.5 MPa when the design strength of original plate was 5.0 MPa or 3.15

MPa when the design strength of original plate was 4.5 MPa. The flexural strength of the concrete with 80% recycled aggregate at 3 d reached 4.11 Mpa, which met the above requirements; meanwhile, the compressive strength at 28d was 49.2 Mpa, and the strength grade reached C40. Thus, it was feasible to use recycled aggregate instead of natural aggregate in cement concrete pavement repair project, and could be open traffic 3 days after paving.

Table 3. Experimental Results of Strength of Concrete

No.	Flexural strength (MPa)			Splitting tensile strength (MPa)			Compression strength (MPa)			Young's modulus (GPa)	
	3d	28d	56d	3d	28d	56d	3d	28d	56d	28d	56d
NC01	4.15	5.71	6.54	3.24	4.19	4.34	39.0	59.2	68.6	39.3	39.6
NC02	4.00	4.99	5.93	2.98	3.61	3.86	35.3	48.6	52.8	37.8	38.6
FA-0	4.11	5.05	6.16	2.92	3.50	3.66	38.0	49.2	53.6	35.8	37.3
FA-20	3.03	4.42	5.74	1.86	3.12	3.45	27.1	42.4	45.7	33.9	35.0
FA-30	2.87	4.17	5.20	1.46	2.83	3.38	21.2	41.4	42.5	31.1	34.7
FA-40	2.65	3.60	4.49	1.41	2.57	2.84	18.3	32.3	37.1	30.2	31.5
F0+S30	4.36	5.67	5.89	3.27	3.86	4.17	37.3	51.4	53.7	35.3	37.3
F10+S20	3.74	5.41	5.93	2.73	3.34	3.68	29.8	45.8	54.1	35.4	37.5
F20+S10	2.96	4.90	5.60	2.00	3.05	3.66	25.4	41.4	49.5	32.2	34.8
F30+S0	2.87	4.17	5.20	1.46	2.83	3.38	21.2	41.4	42.5	31.1	34.7

The impact of mixing both fly ash and slag on the mechanical properties of RAC

The test results from Table 3 and Figure 1 showed that: (1) the effect of adding both fly ash and slag was superior to only adding fly ash, especially the early strength. It can be seen from group F0 + S30 and F30 + S0 that when the total mineral additive content were the same, the RAC incorporating both fly ash and slag had higher strength and elastic modulus than those of the RAC only incorporating fly ash. The incorporation of slag could significantly improve the splitting tensile strength of RAC, which could be very beneficial to improve the crack resistance and durability of concrete. However, when the slag content was too high, its growth rate of late strength was lower. (2) When the total mineral additive content was 30%, as the fly ash content increased, strength at 3 d and 28 d of RAC decreased, which were the same with only adding fly ash. The strength increased largely from 3 d to 28 d, the growth rate was similar to the concrete of same fly ash content. (3) By Comparing F10 + S20 with F20 + S10, it could seen that, when the proportion of fly ash and slag was different, the strength and elastic modulus was significantly different. There was an optimal combination proportion of the two additives. The optimal combination proportion was determined by the optimal amount of alkaline activator formed by fly ash, slag and cement. When the ratio of fly ash and slag was 1:2, the compressive strength, flexural strength and elastic modulus at 56 d of RAC all reached the maximum. (4) When comparing F10 + S20 and F20 + S10 with F30 + S0, it could be seen that compressive strength, flexural strength and elastic modulus at 56 d of RAC containing both fly ash and slag were higher than those of

the RAC only containing fly ash. The main reason was that when mixing fly ash and slag in RAC at appropriate ratio, it could match legitimately and effectively by making full use of the different size, different shape and different activities of cement clinker, fly ash and slag. It also made morphological effects, reactive effects and micro-aggregates filling effects (lubrication, gel, refine pore effect) of slag and fly ash to complement each other, and it produced the results of superimposed effect, thereby achieving high performance RAC.

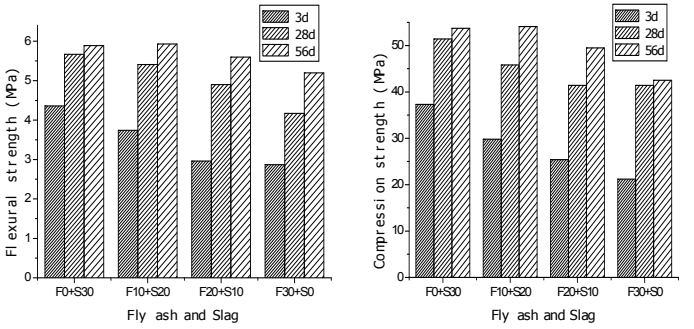

(a) Flexural strength of RAC at different age (b) Compression strength of RAC at different age

FIG. 1. Strength of RAC with different fly ash and slag content

Flexural/compression ratio and tension/compression ratio of RAC

The Flexural/compression ratio and tension/compression ratio were calculated based on the test results as shown in Table 3: the flexural/compression ratio of RAC were 0.101～0.145, and the flexural/compression ratio of natural aggregate concrete were 0.095～0.106. The tension/compression ratios of RAC were 0.068～0.092, and the tension/compression ratios of natural aggregate concrete were 0.063～0.083. Both flexural/compression ratio and tension/compression ratio of RAC were a little higher than those of the natural aggregate concrete, which means the tensile performance was improved and brittleness was reduced, thus the crack resistance and volume stability of the concrete were improved all a little.

The abrasion resistance of RAC

Concrete pavement was worn by repeated vehicle action, which would significantly reduce the anti-slide and other mechanical properties. For pavement concrete, the abrasion resistance of concrete is an important characteristic that affects safety and durability. Therefore, abrasion resistance tests were conducted according to "Testing methods of concrete for highway engineering" JTJ 053-94 for RAC incorporating 100% recycled aggregate and natural aggregate concrete. The results are shown in Table 4. Test results showed that the early compressive strength of RAC containing activating agent was higher. The abrasion value unit area of RAC

were slightly higher than the amount of the control group at 1d, but all lower than 3.6 kg/m^2, which met the requirements of abrasion resistance of concrete pavement. The abrasion value per unit area of RAC at 28 d was same with those of the control group. Thus, RAC had good abrasion resistance at both early and late age.

Table 4. Abrasion Resistance Test Results of RAC and Reference Concrete

No.	Slump constant (mm)	Flexural strength (MPa)		Compression strength (MPa)		Abrasion value unit area (kg/m^2)	
		3d	28d	3d	28d	3d	28d
1#	10	3.87	5.71	39.0	59.2	3.19	2.02
2#	10	3.74	6.33	31.0	52.4	3.44	2.05

Note: The 1# is reference concrete, and the mix proportion is C：S：G：W=450：653：1162：135 (kg·m^{-3}); The 2# is RAC with 100% RA (recycled aggregate), and the mix proportion is C：S：RA：W：FA：Activator=338：653：1162：135：112：13.5 (kg·m^{-3}).

PROJECT CASE STUDY

RAC application test was carried out on the job site of Shunde Lecong section on G325. The first test log mile of test slabs are: K23 +540 second block slab on right hand side, K23+850 second block slab on right hand side, K24+427 second block slab on right hand side. Design flexural strength at 28 d of old pavement concrete was 4.5 Mpa. Recycled aggregate content of the three groups of RAC were 100%, 80% and 60%. The mixture proportions and results are shown in Table 5. The fresh concrete slumps were 30 ~ 50 mm based on the test results at job sites. the cohesiveness and the workability of RAC were also good.

It can be seen from Table 5 that compressive strength of RAC met the design requirement of C35 (35MPa~40MPa) and the flexural strength were higher than 5.0 Mpa, which met the opening traffic requirements of heavy traffic and special heavy traffic. After opening for traffic for one year, overall performance of RAC pavement was excellent. No cracking was observed. Based on the successful application of the RAC pavement test board, RAC technology was used on 1 km deteriorated cement concrete pavement at Shunde section on G325 in Foshan. The replacement ratios of recycled aggregate were 80～100%, which brought very good technical and economic benefits.

Table 5. On-site Execution Mix Proportion and Results of RAC

No.	Macadam (kg/m^3)	Recycled Aggregate (kg/m^3)	Water (kg/m^3)	Slump constant (mm)	Group count	ompression strength of 28d (MPa)	Flexural strength of 28d (MPa)
1	--	1230	177	30	4	39.71	5.15
2	246	984	168	40	3	41.15	5.31
3	492	738	160	50	4	39.26	5.12

Note: Cement: 315 kg/m^3, Sand: 660 kg/m^3, FA:105 kg/m^3.

CONCLUSIONS

Based on the research on the performance and engineering application of RAC, several conclusions can be summarized as follows:

1. When concrete slumps remained the same, as the content of fly ash increased, the content of superplasticizer significantly reduced, indicating that improvement of workability of RAC by adding fly ash was remarkable.

2. At the same water/binder ratio, the compressive and flexural strengths at 3 d of natural aggregate concrete were close to those of RAC containing 80% recycled aggregate. The strength grade of RAC reached C40 (40MPa~50MPa). Its flexural strength reached 4.11 Mpa at 3 d, and 5.93 Mpa at 28 d. It can be opened to traffic 3 days after paving. Thus, it is feasible to use recycled aggregate instead of natural aggregate in cement concrete pavement repair project.

3. The flexural/compression ratio and tension/compression ratio of RAC were a little higher than those of the natural aggregate concrete, which means the tensile performance was improved and brittleness was reduced, thus the crack resistance and volume stability of the concrete were improved all a little.

4. RAC had good abrasion resistance at both early and late age.

5. Field test results indicated that the compressive strength of RAC containing 80~100% recycled aggregate met the design requirements of C35 (35MPa~40MPa) and the flexural strength were higher than 5.0 Mpa, which met the requirements of opening to heavy traffic and special heavy traffic. Field survey indicated no cracking was observed one year after paving.

REFERENCES

Zhang, Y., Qin, H. and Sun W., (2002). “Preliminary Study on the Proportion Design of Recycled aggregate Concrete.” *Chinal Concrete and Cement Products*, Vol. (1):7-9.

Lin, Y., Tyan, Y. and Chang, T. (2004). “An assessment of optimal mixture for concrete made with recycled concrete aggregates.” *Cement and Concrete Research*, Vol. (34):1373-1380.

Xu, Y. (2003). “Test study on high strength and high performance of recycled concrete.” *Changsha: Central South University*.

Xing, Z. and Zhou, Y. (1998). “Study on the Main Performance of Regenerated Concrete.” *Journal of North China Institute of Water Conservancy and Hydroelectric Power*, Vol. (2):30-33.

Yin, J. and Zhou, S. (2001). “A Contrastive Study of Direct Tensile Strength and Splitting Tension Strength of High Performance Concrete.” *Journal of Changsha Railway University*, Vol. 19 (2): 18-24.

Shen Y., Xie, H. and Wang, L.(2004). “Experimental Technology Study of double-doped Slag Powder and Fly Ash in Concrete.” *Shandong Building Materials*, Vol. 25(2): 34-36.

He, S. and Wang, H. (2003). “Orthogonal experimental studies on mix design of high performance concrete.” *Industrial Construction*, Vol.33(8): 8-10.

Study of the Mechanical Properties of Iowa Concrete Pavement for use in the Mechanistic-Empirical Pavement Design Guide (MEPDG)

Jiong Hu[1], Kejin Wang[2], and Zhi Ge[3]

[1] Assistant Professor, Texas State University – San Marcos, Department of Engineering Technology, 601 University Drive, San Marcos, TX, 78666, United States; jiong.hu@txstate.edu
[2]Associate Professor, Iowa State University, Civil, Construction and Environmental Engineering, 492 Town Engineering, Ames, IA 50011, United States; kejinw@iastate.edu
[3] Associate Professor, Shandong University, Department of Transportation Engineering, Jinan, 250061, China; pclabone@yahoo.com

ABSTRACT: The present research was designed to study the mechanical properties of typical portland cement concrete (PCC) used in Iowa pavements. These properties are required as input values by the AASHTO Mechanistic-Empirical Pavement Design Guide (MEPDG). In this research, over 20,000 data were collected, compiled, and statistically analyzed. The typical input values of Iowa pavement concrete, such as 28-day compressive strength (f'_c), elastic modulus (E_c), modulus of rupture (MOR), and splitting tensile strength (f'_{sp}), were obtained and compared with the MEPDG default values. The relationships among Iowa concrete material properties were established through nonlinear regression analyses. The results of the study indicated that Iowa has a good documentation on the compressive strength of pavement concrete produced during the last few decades, but there were severe shortage of complete sets of concrete test data on the properties that are required by the current MEPDG. As a result, appropriately documenting complete sets of concrete properties, including MOR, E_c, and information on concrete mix design, is essential for updating the typical material input values and providing rational prediction equations for concrete pavement design in future.

INTRODUCTION

In the new Mechanistic-Empirical Pavement Design Guide (MEPDG), material properties that characterize concrete thermal behavior, dimension stability, and strength are required for pavement distress and response computations (NAHRP 2004). The MEPDG thus also provides design engineers with a more accurate prediction for the distress development in a pavement throughout its design life. Currently, many of the material properties required by the MEPDG are not available in Iowa. Although some data may be found in literature, it is not clear whether or not those data are suitable to be incorporated in the MEPDG for the Iowa pavement design when the local materials and

mix proportions are used. To properly implement and evaluate the benefits of the new design guide for PCC pavement design in Iowa, it is essential to evaluate all Iowa concrete material properties that are required by the MEPDG.

The importance and needs for providing reliable material properties for properly implementing MEPDG have been well recognized by the researchers and engineers in Iowa. However, limited budget is available for extensive research in this area at this moment. In a consideration that Iowa Department of Transportation (DOT) has collected a large volume of the lab and field data on PCC materials, the present research is therefore focused on compiling and analyzing these existing PCC materials data.

Based on the MEPDG manual, most of the input parameters in Level 1 input need to be obtained from experiment, while Level 3 inputs generally can be estimated from typical or historical value or relate to other parameters such as compressive strength (f'_c). Level 2 inputs can be either from test results or estimation. Currently, Iowa DOT has a great amount of historical data on average compressive strength (f'_c) of PCC and a certain amount of data on elastic modulus (E_c) and modulus of rupture (MOR) of PCC, which are highly valuable for the Level 3 design. However, these existing data are not compiled as groups and are not associated with detailed mix proportion information.

The objectives of this research, therefore, are to identify typical Iowa material input values for Level 3 MEPDG design, to examine the suitability of current MEPDG default inputs for use in designing concrete pavement in state of Iowa, and to evaluate the predictive equations that describe the relationships between concrete mechanical properties used for Level 3 and Level 2 MEPDG designs.

RESEARCH APPROACH

As the purpose of this research is to serve the state of Iowa, data were primarily obtained from projects of Iowa DOT and National Concrete Pavement Technology Center (CP Tech Center) of Iowa State University. The majority of data used in this study were collected by Iowa DOT through concrete pavement construction projects in state of Iowa, and data collected from CP Tech Center and Iowa State University were mainly based upon laboratory experiments. Detail information on collected data can be found in project report associated with this study (Wang et al. 2008). A survey was performed to obtain available data (including mix design, fresh concrete properties, and strength data) from both printed materials and Iowa DOT and CP Tech Center project web site at http://www.operationsresearch.dot.state.ia.us/reports/reports.html and http://www.ctre.iastate.edu/research/reports.cfm. A total of over 20,000 sets of data obtained from Iowa DOT and CP Tech Center were used in present study. The Iowa data from Long-term Pavement Performance (LTPP) program (FHWA 2005), along with available data from three Iowa projects, were also used to estimate the long term concrete properties at approximate 20 years. The data include information on concrete compressive strength (f'_c), modulus of rupture (MOR), elastic modulus (E_c), and splitting tensile strength (f'_{sp}) at different ages (from 12 hours up to 27 years). The statistical parameters of these data, such as the mean values and standard variations, were then analyzed and compared with the MEPDG default values. Based on the study results, recommendations were made for the PCC material input values for use in state of Iowa. In addition, the existing predictive equations that describe the relationships

between concrete mechanical properties were examined. Modified equations are proposed for their potential uses in the MEPDG Level 3 and Level 2 design of Iowa pavement.

RESULTS AND DISCUSSION

In order to examine the change of compressive strength over the last few decades, approximately 19,000 sets of data obtained from Iowa DOT were collected. A statistical study was performed to obtain the mean values and standard deviations (Std Dev) of the 28-day compressive strength within each decades since the 1970s. The results as shown in Table 1 indicated that from 1970s to 1990s, the mean value of the 28-day Iowa compressive strength was approximate 32.41MPa (4700 psi) with a standard deviation approximate 4.83MPa (700 psi). After the year of 2000, the mean value of the 28-day core compressive strength decreased to 30.32MPa (4397 psi) with a standard deviation of 4.40MPa (638 psi), which is probably caused by the change of the mix design to the Quality Management Concrete (QMC) mixtures with more supplemental cementitious materials (SCMs) replacement of cement. The standard deviation, on the other hand, slightly decreased after the year of 2000, which may contributed by the better quality control of pavement concrete in state of Iowa. Based on the analysis of the data collected by Iowa DOT from 1,596 samples after the year of 2000, 28-day compressive strength of 30.32 ± 4.40 MPa (4397 ± 638 psi) was recommended for the Level 3 input values of state of Iowa.

Table 1. Statistical Analysis of Historical Iowa DOT $f'_{c,28d}$ Data

	Mean, MPa (psi)	Std Dev, MPa (psi)	Total Number of Data
1970s	32.18 (4667)	3.89 (564)	992
1980s	32.87 (4768)	5.17 (750)	8780
1990s	32.87 (4767)	5.58 (809)	7638
2000s	30.32 (4397)	4.40 (638)	1596

In the MEPDG, two of the parameters of the modulus of rupture, compressive strength, and elastic modulus are required to be known as Level 3 inputs. The 28 day strength data from state of Iowa was, therefore, analyzed under this study. Since a higher percentage of SCMs replacement were widely used in Iowa concrete pavement after the year of 2000, only data obtained from mixed made in the 2000s were included in this part of study. Based on statistical analyses of the available data, the Iowa typical concrete properties required by MEPDG as the PCC material inputs can be described in Table 2. Results showed that the 28-day MOR of Iowa concrete is 4.45MPa (646psi), similar to the MEPDG default value (4.76MPa or 690psi), but the 28-day E_c of Iowa concrete is 33.23GPa (4.82×10^6psi), very different from the MEPDG default value (27.1GPa or 3.93×10^6 psi) (NAHRP 2004). The difference may be attributed to the variation of concrete mix designs and small number of test data available. Note that the analysis of E_c and f'_{sp} in Table 2 were based on very limit data, further research is needed in order to provide statistic meaningful input values for Iowa materials.

Table 2. Typical Values to be Used in Level 3 Input

	$f'_{c,28d}$, MPa (psi)	MOR_{28d}, MPa(psi)	$E_{c,28d}$, GPa (psi)	$f'_{sp,28d}$, MPa(psi)
MEPDG Default	28.96 (4200)	4.76 (690)	27.0 (3.93×10^6)	NA
Mean	30.31 (4397)	4.45 (646)	33.3 (4.82×10^6)	2.71 (393)
Std Dev	4.40 (638)	0.35 (51)	1.93 (0.28×10^6)	0.18 (25.5)
Number of data	1596	114	2	2

In order to give a recommendation of existing pavement properties at approximately 20 years for pavement overlay design, historical data from LTPP database were obtained. Data from both general pavement studies (GPS) and specific pavement studies (SPS) from LTPP were used in present study (FHWA 2005). Pavement concrete strength data after five years were used here as long term performance study. Unfortunately, the properties of the Iowa concrete measured at different ages were from different projects, rather than given projects. No systematical data or complete sets of data are available. Therefore, the average property values of the Iowa concrete at the age of 5-30 years are simply listed in Table 3 and recommended as the long term performance pavement properties for the necessary use in MEPDG. As shown in Table 3, the typical long term mechanical values of Iowa concrete pavement are compressive strength of 52.6MPa (7,727psi), elastic modulus 30.9GPa (4.48×10^6psi), and splitting tensile strength of 4.0MPa (587psi),

Based on the available Iowa concrete test data, 20-year to 28-day compressive strength ratio was also calculated for Level 2 MEPDG input. The calculated ratio of approximate 1.60 (52.6MPa or 7,627 psi from LTPP divided by 32.97MPa or 4768psi from Iowa DOT 1980s and 1990s test data) is higher than the default value of 1.44. Considering the limited long-term property data available for Iowa concrete, the MEPDG default value for Iowa concrete pavement was recommended before further research is conducted.

Table 3. Long Term Performance Pavement Properties Analysis

		Mean	Std Dev	Number of Data
f'_c	Age of sample (year)	20.8	6.7	22
	Value, MPa (psi)	52.6 (7,627)	5.6 (811)	
E_c	Age of sample (year)	17.8	6.9	11
	Value, GPa (psi)	30.9 (4.48×10^6)	3.8 (5.55×10^6)	
f'_{sp}	Age of sample (year)	17.1	5.4	14
	Value, MPa (psi)	4.0 (587)	0.5 (71)	

Comparing with compressive strength measurement, the testing procedure of other strength related parameters, especially modulus of elasticity is much more complicated and time consuming, which often cause the lack of available data. A variety of equations with different empirical coefficients were therefore developed by researchers using different sources of data to relate these mechanical properties with compressive strength.

A number of empirical formulae are suggested to relate E_c, MOR, f'_{sp} to f'_c, most of them are of the power equation type (Mindess et al. 2003):

$$E_c = a f'^{\,m}_c \quad (1)$$

$$MOR = b f'^{\,n}_c \quad (2)$$

$$f'_{sp} = c f'^{\,ml}_c \quad (3)$$

where *a, b, c, m, n,* and *l* are coefficients related to different strength parameters. These equations can be used to relate elastic modulus, modulus of rupture, and splitting tensile strength of concrete when only compressive strength date are available.

Analysis was performed to evaluate the ability of prediction of E_c, MOR, and f'_{sp} from f'_c using Iowa testing data. Single-parameter nonlinear regressions with power equation were performed using the available data. Results of the obtained equation for Iowa pavement compared with MEPDG default equations are shown in Figure 1. Note that due to the limitation of space, only ACI equations (ACI 2008) were presented here, where the power coefficients (*m*, *n*, and *l*) were arbitrarily designated power as 0.5.

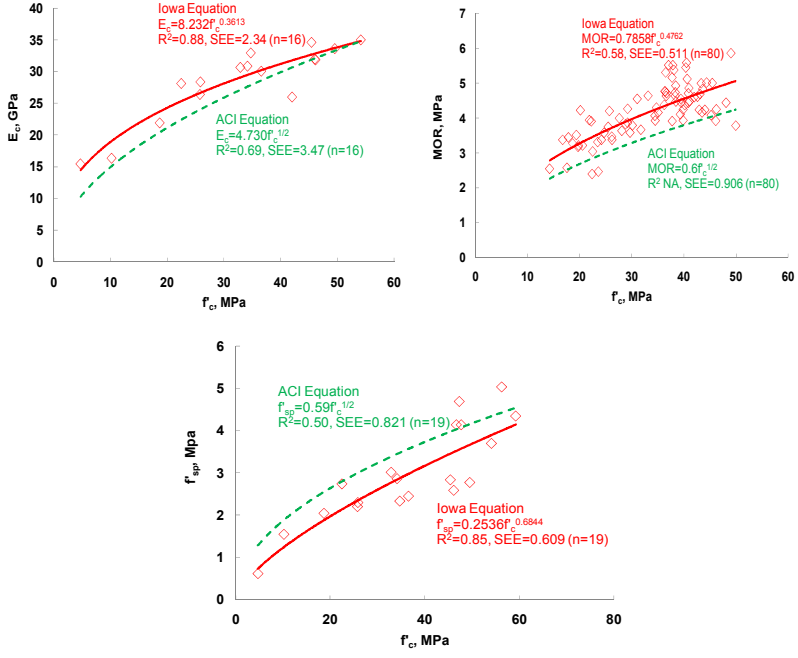

FIG. 1. Prediction of modulus of elasticity, modulus of rupture, and splitting tensile strength from compressive strength.

SUMMARY AND CONCLUSIONS

Table 4 summarizes the comparison of the default PCC input values from MEPDG and the values from the analyses of Iowa test data. Based on the discussions above, the recommendations for the Iowa PCC input values to be used in MEPDG are also included in the table.

Table 4. Comparison of Iowa PCC Properties and MEPDG Default Values

Level of Design	PCC Properties	MEPDG Default Value	Iowa Test Result	Recommended Value
3	$f'_{c,28d}$, MPa (psi)	28.96 (4200)	30.31 (4,397)	Tested data
	MOR_{28d}, MPa (psi)	4.76 (690)	4.45 (646)	As default
	$E_{c,28d}$, GPa (psi)	27.0 (3.93×10^6)	33.23 ($4.82\text{x}10^6$)*	Further research needed
2	$f'_{c,7d}$, MPa (psi) $f'_{c,14d}$, MPa (psi) $f'_{c,28d}$, MPa (psi) $f'_{c,90d}$, MPa (psi)	24.54 (3560) 26.89 (3900) 28.96 (4200) 32.41 (4700)	Not applicable	Tested data
	$f'_{c,20y}/f'_{c,28d}$	1.44	1.6*	As default
1	MOR_{7d}, MPa (psi) MOR_{14d}, MPa (psi) MOR_{28d}, MPa (psi) MOR_{90d}, MPa (psi)	4.27 (620) 4.45 (645) 4.76 (690) 5.31 (770)	Not applicable	Tested data
	$E_{c,7d}$, GPa (psi) $E_{c,14d}$, GPa (psi) $E_{c,28d}$, GPa (psi) $E_{c,90d}$, GPa (psi)	26.2 (3.8×10^6) 27.6 (4.0×10^6) 29.0 (4.2×10^6) 31.0 (4.5×10^6)	Not applicable	Tested data
	MOR_{20y}/MOR_{28d} $E_{c,20y}/E_{c,28d}$	1.2 1.2	Not applicable	As default

*Value from limited Iowa test data

The present study also suggests that appropriately documenting all commonly used concrete properties (such as compressive strength, modulus of rupture, and elastic modulus), together with the information on concrete mix design, is essential for updating the typical Iowa material input values and providing rational prediction equations for implementing MEPDG in Iowa in the future.

ACKNOWLEDGMENTS

The research was sponsored by the Iowa Department of Transportation (Iowa DOT) and the National Concrete Pavement Technology Center (CP Tech Center). The sponsorship of this research project is gratefully acknowledged. The authors would also like to express their appreciation to the project managers Mike Heitzman and Chris Williams, as well as to Halil Ceylan and Chris Brakke for their valuable inputs and suggestions on the research activities and the report. Special thanks are given to the

Iowa DOT Office of Materials, particularly to Kevin Jones and Jim Berger, for their strong supports of the concrete data collections and analyses.

REFERENCES

ACI Committee 318. (2008). "ACI 318-08, Building code requirements for structural concrete and commentary", ACI (American Concrete Institution).

IHRB Reports and Materials Laboratory Reports - Iowa Department of Transportation, http://www.operationsresearch.dot.state.ia.us/reports/reports.html.

Iowa State University, Institution of Transportation (InTrans), Center for Transportation Research and Education (CTRE) Research Projects with Online Reports, http://www.ctre.iastate.edu/research/reports.cfm.

FHWA. (2005). "Long-term pavement performance (LTPP) program - Standard data release (SDR) 20.0", VR2005.07, Federal Highway Association (FHWA).

Mindess, S., Young, J.F. and Darwin, D. (2003). "Concrete", 2nd ed., Prentice Hall, Upper Saddle River, New Jersey.

NCHRP. (2004). "Guide for mechanistic-empirical design – of new and rehabilitated pavement structures", Final Report, National Cooperative Highway Research Program, ARA, Inc., ERES Consultants Division, Champaign, Illinois.

Wang, K., Hu, J. and Ge, Z. (2008). "Task 4: Testing Iowa portland cement concrete mixtures for the AASHTO mechanistic-empirical pavement design procedure", CTRE Project 06-270, http://www.ctre.iastate.edu/reports/mepdg_testing.pdf .

Comparison of Portland Cement Concrete CTE Calculation Protocols

Shervin Jahangirnejad[1], Ph.D. and Neeraj Buch[2], Ph.D., FACI

[1] Visiting Research Associate, Michigan State University, East Lansing, MI 48824; jahangi1@msu.edu
[2] Professor, Michigan State University, East Lansing, MI 48824; buch@egr.msu.edu

ABSTRACT: A laboratory investigation was conducted to determine the coefficient of thermal expansion (CTE) of typical concrete paving mixtures made with coarse aggregate from eight different sources in the state of Michigan, USA. The primary aggregate class included limestone, dolomite, slag, gravel and trap rock. The Three replicate test specimens were fabricated for each mixture-age combination. The test specimens were moist cured for 3, 7, 14, 28, 90, 180, and 365 days prior to testing.

CTE was determined using two methods: 1) The provisional AASHTO TP60 protocol and 2) A revised test procedure based on AASHTO TP60 developed at the University of Texas at Austin. The average measured 28-day CTE values ranged from 8.11 με/°C to 10.65 με /°C based on AASHTO TP60 method and 8.12 με/°C to 10.80 με /°C based on the revised method.

In this paper, the CTE results based on the two aforementioned test procedures are compared using statistical methods and analyses. Furthermore, the paper discusses the practical impact of the statistical results by investigating the transverse cracking performance of jointed plain concrete pavements. The Mechanistic-Empirical Design Guide (M-E PDG) software developed by National Highway Cooperative Research Program (NCHRP) was employed for this investigation.

INTRODUCTION

The coefficient of thermal expansion (CTE) is defined as the unit change in length per unit change in temperature and has significant (practical) influence on the design of joints and temperature-related deformations (expansion/ contraction and curling) in jointed concrete pavements (JCPs). Furthermore, the magnitude of CTE has an impact on the amount of mid-panel cracking and spalling.

The standard protocol for CTE determination is the provisional AASHTO TP60 test method (AASHTO, 2000). A revision of this protocol is recommended by Won (this method is called the "Revised TP60" in this paper) (Won, 2005). Here, the CTE results determined by these two methods are compared using statistical methods and analyses. Furthermore, the paper discusses the practical impact of the statistical results by investigating the transverse cracking performance of jointed plain concrete pavements.

The Mechanistic-Empirical Design Guide (M-E PDG) (ARA Inc., 2004) software developed by National Highway Cooperative Research Program (NCHRP) was employed for this investigation.

EXPERIMENTAL INVESTIGATION

A local ready mixed concrete supplier supplied the concrete used in the fabrication of the test specimens. This ensured that all specimens for a given mixture were produced in a single batch, thereby reducing experiment variability. Three replicate samples were fabricated for each test. All specimens were cured at 100% relative humidity and 73 °F (23 °C) in an environment chamber until the time of testing.

Materials

Concrete made with eight different coarse aggregate sources was fabricated. Dolomite from three sources and limestone from two sources were used as coarse aggregate. Gravel, slag, and gabbro each from one source were also used as coarse aggregate. The mixture identification, physical properties, and the rock type for the various aggregate sources can be found elsewhere (Jahangirnejad, 2009). The PCC mixture design was a typical MDOT P1 paving mixture and details can be found in the aforementioned paper[4]. It should be noted that the paste content and the geological characteristics of the fine aggregate for all mixtures were similar and therefore did not influence the magnitude of the measured CTE.

Specimens

The cylinders used in CTE test were 4 in. (100 mm) in diameter and 7 in. (175 mm) in length.

CTE TEST METHODS

AASHTO TP60 and Revised TP60 were employed to determine CTE values. Specimen conditioning and heating-cooling cycle are the same in both procedures. Data collection and CTE calculation however, are different. The CTE test was performed in a way that it satisfied data collection requirements for both procedures. The relevant parts of data were then used to calculate the CTE based on each method.

AASHTO TP60

In this procedure, after the concrete specimen is conditioned, it is subjected to heating, cooling, and temperature equilibrium segments during which the temperature of the surrounding water and displacement of the specimen are monitored. A summary of the procedure is presented in the subsequent paragraphs.

The first step is to place the frame in the water bath and the specimen in the frame. LVDT is then mounted on the frame. Silicon grease is applied to the support buttons and the tip of the LVDT to prevent any sticking to the concrete specimen. The water bath is

cooled down to 50 °F (10 °C) and is kept at this temperature until thermal equilibrium of the specimen has been achieved. The thermal equilibrium is denoted by "consistent readings of the LVDT to the nearest 0.00001 in. taken every ten minutes over a one-half hour time period" (AASHTO TP60[2]). The temperature and displacement readings are recorded as initial readings. The water bath is then heated to 122 °F (50 °C) and the same process is followed to record the second readings. The system is cooled again to 50 °F (10 °C) and the final readings are recorded.

In the executed test plan, specimens were subjected to three heating-cooling cycles (Figure 1). This way, if one cycle was not suitable for CTE calculations due to problems with test conditions (specimen and LVDT misalignment, lack of proper seating of the specimen, etc.), the replicate cycles could be used for CTE calculations.

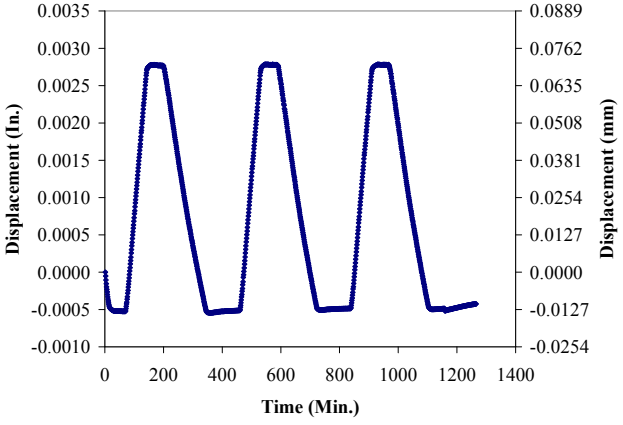

FIG. 1. Three typical heating-cooling cycles

Recorded readings mentioned above are used in computational sequences in order to calculate the CTE value. The CTE of the specimen is calculated by averaging the CTE value of the heating and cooling cycles.

Revised TP60

The Revised TP60 procedure is similar to AASHTO TP60 method with regards to specimen conditioning, heating and cooling segments. In this method however, the temperature, specimen displacement, and time are recorded every minute during heating and cooling segments.

Recorded readings are then used to plot a temperature versus displacement graph in which heating and cooling data are plotted separately (Figure 2). A typical graph such as the one explained is shown in Figure 2. A linear regression analysis is applied between temperature and displacement for the range of 59 °F (15 °C) to 113 °F (45 °C). CTE of each segment is then calculated using the regression equation and averaged to determine the CTE of the specimen.

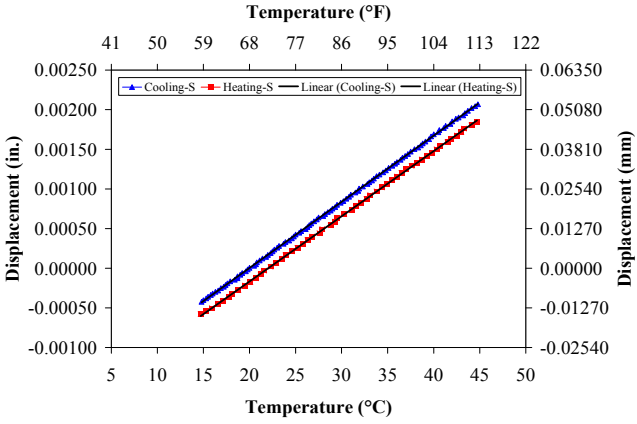

FIG. 2. A typical revised TP60 method graph

STATISTICAL APPROACH

Among the factors that affected the magnitude of concrete CTE, the method of CTE calculation was of interest in this study. Other factors that potentially affected the magnitude of the CTE in this experiment were aggregate geology and age of concrete samples at the time of testing. In order to investigate the impact of calculation method – and its interactions with other factors – on the magnitude of CTE, a "factorial treatment design" was employed. In a factorial treatment design, one factor – for example aggregate type – is tested over one or more other factors, for example sample age and method of calculation. Each factor has several categories called "levels". For example, levels of the sample age factor are 3, 7, 14, 28, 90, 180, and 365 days. The design factorial included: 1) method of calculation with two levels (AASHTO TP60 and Revised TP60); 2) aggregate geology with eight levels; and 3) sample age with seven levels. There were three replicate samples for each combination of aggregate geology and sample age. Table 1 shows the factorial design table.

Calculation method, aggregate geology, and sample age were considered as fixed effects. In fixed effects, different levels of factors are reproducible. In other words if the experiment was to be repeated, the levels could be duplicated. Individual sample ID (replications) within each aggregate geology and sample age was considered as a random effect because for each combination of aggregate type and sample age, a sample ID was assigned randomly to the three replicates from the same batch of concrete.

Because the experiment included both fixed and random effects, the statistical analysis was performed using "mixed effects" model. The following general linear model describes the relationships between factors:

$$y = \mu + Method + Agg\_Type + Age + Method \times Agg\_Type + Method \times Age + Agg\_Type \times Age + Method \times Agg\_Type \times Age + Sample\_ID(Agg\_Type\ Age) + e \quad (1)$$

Description of each term in this model is presented in Table 2.

Table 1. Factorial Design Table*

Aggregate Geology	CTE Calculation Method	Age, Days							Total
		3	7	14	28	90	180	365	
CTE 1	AASHTO TP60	X	X	X	X	X	X	X	7
	Revised TP60	X	X	X	X	X	X	X	7
CTE 2	AASHTO TP60	X	X	X	X	X	X	X	7
	Revised TP60	X	X	X	X	X	X	X	7
CTE 3	AASHTO TP60	X	X	X	X	X	X	X	7
	Revised TP60	X	X	X	X	X	X	X	7
CTE 4	AASHTO TP60	X	X	X	X	X	X	X	7
	Revised TP60	X	X	X	X	X	X	X	7
CTE 5	AASHTO TP60	X	X	X	X	X	X	X	7
	Revised TP60	X	X	X	X	X	X	X	7
CTE 6	AASHTO TP60	X	X	X	X	X	X	X	7
	Revised TP60	X	X	X	X	X	X	X	7
CTE 7	AASHTO TP60	X	X	X	X	X	X	X	7
	Revised TP60	X	X	X	X	X	X	X	7
CTE 8	AASHTO TP60	N/A	X	X	X	X	X	X	6
	Revised TP60	N/A	X	X	X	X	X	X	6
Total		14	16	16	16	16	16	16	110

* Three replicates for each combination of factors were considered totaling the CTE values to 3 × 110 = 330.

Table 2. Description of Terms in the Model for Method Comparison

Term	Description
y	Response variable which is the CTE value
μ	Overall mean
Method	Fixed effect of the calculation method
Agg_Type	Fixed effect of the aggregate geology
Age	Fixed effect of the sample age at the time of testing
Method×Agg_Type	Interaction effect of the method and aggregate geology
Method×Age	Interaction effect of the method and sample age
Agg_Type×Age	Interaction effect of the aggregate geology and sample age
Method×Agg_Type×Age	Interaction effect of the method, aggregate geology, and sample age
Sample_ID(Agg_Type Age)	Random effect of the replications
e	Random experimental error

The statistical significance of the factors and their interactions were evaluated by using the analysis of variance (ANOVA) method. The first step in the ANOVA method is checking the assumptions for the model. The assumptions require the residuals (difference between predicted and measured values) to be: 1) independent; 2) normally distributed; and 3) having a common variance for all levels of each factor. These

assumptions were checked and found to be satisfactory for the data set used in this analysis.

After checking the assumptions, the significance of the factors, and their interactions were investigated. The confidence level for this analysis was 95% ($\alpha = 0.05$). The results from the mixed effects analysis are summarized in Table 2. The impact of calculation method on CTE was found to be significant (p-value less than 0.05). This implies that the two methods produce different results with confidence level of 95%. The interactions between the method effect and other effects were not statistically significant. The significant effects are highlighted in Table 3.

An analysis of the least square means for these two methods showed that the Revised TP60 method resulted in higher CTE values in comparison with the AASHTO TP60 method. The estimated difference was 0.0234 με/°F (0.0421 με/°C).

In order to investigate the practical effect of using these two methods on jointed pavement performance, M-E PDG software (version 1.000) was used for analysis. A pavement with 15 ft (4.5 m) joint spacing and 10 in. (250 mm) slab thickness located in Lansing, MI, was modeled. The base was a 4 in. (100 mm) thick granular base on a 16 in. (400 mm) thick sand subbase. The subgrade was a fine A-7-6 soil.

Table 3. Tests of Fixed Effects for Method Comparison

Effect	F Value	p-value
Aggregate Type	421.57	<.0001
Age	50.82	<.0001
Aggregate Type×Age	7.01	<.0001
Method	11.55	0.0009
Aggregate Type×Method	1.32	0.2469
Age×Method	0.97	0.4460
Aggregate Type×Age×Method	0.62	0.9617

Two designs based on estimated CTE values (output of the least square means analysis) were considered. The two levels of CTE values were 5.51 and 5.53 με/°F (9.92 and 9.96 με/°C) for AASHTO and the Revised TP60 respectively. To study the exclusive effect of CTE on pavement performance, the mixture design and concrete strength were held constant (3500 psi [24 MPa] compressive strength).

Table 4. Percent Slabs Cracked for Two methods at Different Ages

Pavement Age (yrs.)	Percent Slabs Cracked (%)	
	AASHTO TP60	Revised TP60
5	0.6	0.6
10	2.6	2.8
15	6.2	6.6
20	11.6	12.2
25	18.5	19.5
30	26.6	27.8

It can be seen from Table 4 and Figure 3 that the using these two different calculation methods does not change the cracking performance of the JPCP significantly and subsequently, it does not affect the design.

SUMMARY AND CONCLUSIONS

A comparison between two methods of CTE determination was made. Statistical analysis showed a small difference between the two methods. However, this small difference did not prove to be practically significant.

It is suggested that if the AASHTO TP60 method is used, the data acquisition process be automated and that the Revised TP60 rate of recording be adopted.

The automation of the temperature and displacement readings with a rate of one reading per minute (as recommended by the Revised TP60 method) makes the testing process and CTE determination easier and more reliable.

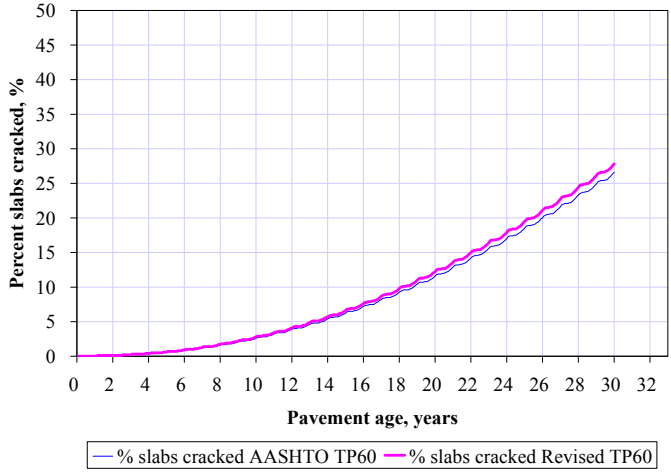

FIG. 3. M-E PDG output for the percent slabs cracked based on two methods

REFERENCES

AASHTO, (2000). Standard Test Method for the Coefficient of Thermal Expansion of Hydraulic Cement Concrete. TP60-00,

ARA Inc., (2004). ERES Consultants Division, Guide for Mechanistic-Empirical Design of New and Rehabilitated Pavement Structures. Final Report, National Cooperative Highway Research Program, 1-37A, March

Jahangirnejad, S., Buch, N., Kravchenko, A., (2009). "Evaluation of Coefficient of Thermal Expansion Test Protocol and its Impact on Jointed Concrete Pavement

Performance" American Concrete Institute Materials Journal, Vol. 106, No. 1, January-February

Won, M., (2005). Improvements of Testing Procedures for Concrete Coefficient of Thermal Expansion. Transportation Research Record: Journal of the Transportation Research Board, No. 1919, Washington D.C.

Mix design of cement-stabilized recycled aggregate base course material

Yijin Li[1], Xinpeng Sun[2], Jian Yin[3]

[1]Vice-Professor, College of Civil Engineering and Architecture, Central South University, Changsha 410075, China；csuhpc@163.com
[2]Graduate student, College of Civil Engineering and Architecture, Central South University, Changsha 410075, China；Sunxp@163.com
[3]Professor, College of Civil Engineering and Architecture, Central South University, Changsha 410075, China； csuyj@mail.csu.edu.cn

ABSTRACT: Cement-stabilized recycled aggregate base course material was prepared with lower quantities of ordinary Portland cement (only 4% and 5% by weight) and recycled aggregate replacing 30%,40%,50%,60%,75%,80%,90% and 100% of crushed stone. Compaction, un-confined compressive strength and dry shrinkage of mixture were tested. The effects of recycled aggregate replacing levels and cement dosage were analyzed based on compaction test. The results showed that the use of 100% recycled concrete aggregates increased the optimum moisture content and decreased the maximum dry density of base course materials compared to those of natural base materials. The effect of recycled aggregate replacement on un-confined compressive strength was discussed at 7, 28 and 90 days. The relational model between recycled aggregate replacement and un-confined compressive strength were established. The results of dry shrinkage tests showed that the ratio of dry shrinkage of the base materials prepared with recycled concrete aggregates increased with the increase of replacement levels of recycled concrete aggregates. The primary mix proportion parameters were determined with maximum replacement of recycled aggregates, meeting the requirements of base course road performance and lower costs.

INTRODUCTION

The base course material of highway has a lower strength requirement, but needs much natural aggregate. It is a major application of waste concrete that some or all of natural aggregate was replaced by recycled aggregate as cement stabilized recycled aggregate base course material used in the base course or sub-base of highway(JTJ034-2000).

Waste concrete was obtained from the renovation of some cement concrete pavement. Based on the optimization of aggregate gradation, the effects of recycled aggregate replacing levels and cement dosage were analyzed, The relational model between recycled aggregate replacement and un-confined compressive strength were established. The mix proportion parameters of base course material were determined

with maximum replacement of recycled aggregates, meeting the requirements of base course road performance and lower costs. It doesn't only offering theoretical guidance for the optimization of mix proportion parameters of cement-stabilized recycled aggregate base course material, but also providing technical supports for promoting practical use of waste concrete recycled aggregate technology.

RAW MATERIALS AND TEST METHODS

Raw materials

Cement: Ping tang 32.5 ordinary Portland cement, its performance indicators were showed in Table 1;

Stone: crushed limestone, its size range was 5 ~ 25 mm, the gradation was qualified, crushed limestone's crushed index is 7.4 ~ 9.0%;

Sand: Xiangjiang river sand, the gradation was qualified an meet requirements in Zone□. Fineness modulus was 2.63, clay content was 0.5%;

Fine stone: Particle size of crushed limestone was 5mm ~ 10mm;

Recycled Aggregate: discarded concrete from repairing of Changyi High-grade highway pavement, crushed by jaw crusher. The strength, packing density, apparent density, soil percentage and moisture content of broken old concrete were tested, test results shown in Table 2.

Table 1. Ordinary Portland Cement Performance Indicators

Fineness (%)	Setting time (min)		Stability	3d (MPa)		28d (MPa)	
	Initial set	Final set		Compressive strength	Flexural strength	Compressive strength	Flexural strength
4.0	150	330	eligibility	24.5	4.3	35.6	5.8

Table 2. Basic Performance of Recycled Aggregate

Loose packing void ratio (%)	Close packing void ratio (%)	Loose packing density (g/cm^3)	Close packing density (g/cm^3)	Apparent Density (g/cm^3)	Moisture content (%)	Old concrete strength (MPa)	Soil percentage (%)
41	34	1.4	1.54	2.44	0.26	46.5	4.12

Test Method

Recycled aggregate performance tests were according to "Highway Engineering Aggregates test code" (JTG E42-2005); Gradation adjustment of particle size was according to "Highway Pavement Construction Technical Specification" (JTJ034-2000); Compaction and unconfined compressive strength tests are according to the requirements of high-grade highway cement stabilized coarse-grained soil in "Testing procedures of inorganic binder stability materials in highway engineering " (JTJ057-94).

COMPACTION TEST

Test program

It is needed to determine the optimum moisture content ω (%) and maximum dry density ρ (g/cm^3) by compaction test before preparing the specimen. Test was according to the C method of compaction test in JTJ057-94. The recycled aggregate replacement were 100%, 90%, 80%, 75%, 60%, 50%, 40%, 30% and 0% ,respectively and two cement content were 4.0% and 5.0%. In order to obtain the optimum moisture content and the maximum dry density of base course material, compaction test of mixture were carried out.

Test Results Analysis

Compaction test were carried out for each mixture with different dosage of cement and different recycled aggregate replacement, then fitting the curve equation according to the compaction tests data of dry density and moisture content, deriving the maximum dry density and corresponding optimum moisture content from fitted equation, as shown in table 3, the relationship between the replacement of recycled aggregate and the optimum moisture content, the maximum dry density were shown in Figure 1.

Table 3. The Maximum Dry Density and the Optimum Moisture Content of Mixture with Different Recycled Aggregate Replacement

Aggregate proportion	Optimum moisture content (%)		Maximum dry density (g/cm^3)	
	5% cement dosage	4% cement dosage	5% cement dosage	4% cement dosage
Crushed stone：fine stone：sand=40%:30%:30%	5.34	5.06	2.29	2.28
RCA：fine stone：sand=30%:50%:20%	5.21	5.11	2.21	2.18
RCA：fine stone：sand=40%:30%:30%	7.44	6.40	2.18	2.17
RCA：fine stone：sand=50%:30%:20%	7.66	7.54	2.17	2.16
RCA：fine stone：sand=60%:20%:20%	8.01	8.01	2.13	2.13
RCA：sand=75%:25%	8.31	8.31	2.11	2.11
RCA：fine stone：sand=80%:10%:10%	8.38	8.34	2.06	2.03
RCA：sand=90%:10%	8.72	8.63	2.09	2.08
RCA=100%	9.44	9.14	2.09	2.08

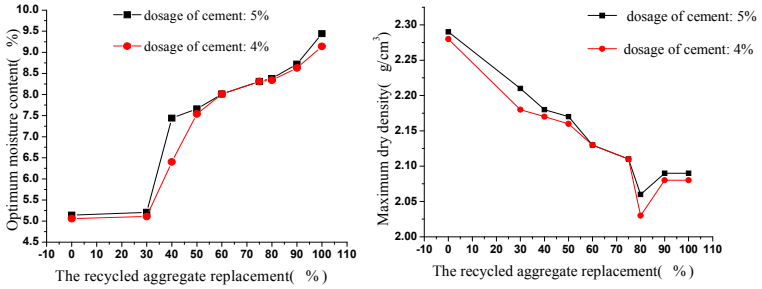

FIG.1. The effect of recycled aggregate replacement on the optimum moisture content and the maximum dry density

The effects of recycled aggregate replacement

From Table 3 and Figure 1, it could be seen whether the dosage of cement was 4% or 5%, with the increase of recycled aggregate replacement, the optimum moisture content of mixture increased, when the recycled aggregate replacement was 100%, the optimum moisture content was highest, which increased by 4.1% compared with that of mixture of 100% natural aggregate.

The main reasons were as follows. Firstly, recycled aggregate had large porosity, and its moisture content in natural condition was larger than that of natural aggregate. Secondly, recycled aggregate adhered large amounts of cement paste, its crystal water and adhered water were evaporated in the moisture content test, which was calculated to the optimum moisture content.

The maximum dry density of natural aggregate mixture was largest and that of mixture with 100% recycled aggregate was smallest, with the increase of recycled aggregate replacement, the optimum moisture content of mixture increased correspondingly, but the maximum dry density decreased. Because the apparent density of natural aggregate was larger than that of recycled aggregate, the weight of natural aggregate is bigger than that of recycled aggregate at the same volume[4].

The effects of different doses of cement

When the recycled aggregate replacement was constant, the moisture content of mixture containing 5% cement dosage increased compared to that of mixture with 4% cement dosage. With the cementitious material increased, cement hydration needed more water, it also required more water to ensure better workability of mixture, It was also the reason that the optimum moisture content of binary system containing fly ash and cement and ternary system containing lime, cement and fly ash increased.

UNCONFINED COMPRESSIVE STRENGTH

Based on mixture compaction test, the following four optimal mixture compositions were prepared to carry out unconfined compressive strength test.

A mixture: recycled aggregate replacement was 100%;

B mixture: the ratio of recycled aggregate, fine stone and sand were 80%, 10% and 10% respectively;

C mixture: the ratio of recycled aggregate, fine stone and sand were 40%, 40% and 30% respectively;

D mixture: the ratio of crushed stone, fine stone and sand were 40%, 40% and 30% respectively;

The unconfined compressive strength test results of four mixtures with various dosages of cement at different age were shown in Table 4.

Table 4 Unconfined Compressive Strength Test Results of Mixture

Mixture Composition	Dosage of cement 4%			Dosage of cement 5%		
	Unconfined compressive strength (MPa)			Unconfined compressive strength (MPa		
	7d	28d	90d	7d	28d	90d
A	4.45	5.06	5.24	4.79	5.38	5.64
B	4.21	5.13	5.51	4.97	5.52	5.89
C	3.34	4.41	4.67	3.85	4.66	5.25
D	2.71	3.95	4.33	3.65	4.47	4.93

From the test results in Table 4, It could be seen that the unconfined compressive strength of mixture at different age increased with the increase of cement dosage. With further hydrating of un-hydrated cement particles, the unconfined compressive strength of mixture at 90-d age increased compared to that of mixture at 28-d age. When the dosage of cement was same, the unconfined compressive strength of mixture at different age increased with the increase of recycled aggregate replacement, the unconfined compressive strength was the maximum when recycled aggregate replacement was 80%. On the one hand, there was always part of un-hydrated cement or partial hydrated cement in waste concrete. After waste concrete was crushed, un-hydrated cement or partial hydrated cement would continue to hydrate in case of water, which would have a favorable impact to the mixture unconfined compressive strength (Topeul.B 1997). On the other hand, aggregate particle played a skeleton role in base course material. Compared to natural aggregate, recycled aggregate had a lower strength, poorer particle size distribution, which would have a negative impact to mixture unconfined compressive strength (K Ramamurthy,et al. 1998). When the dosage of cement was same, two different kinds of effects depended on recycled aggregate replacement , so the unconfined compressive strength of mixture increased with the increase of recycled aggregate replacing levels , but it would lead to a decline in unconfined compressive strength of mixture when the recycled aggregate replacement was100%, (FIG. 2).

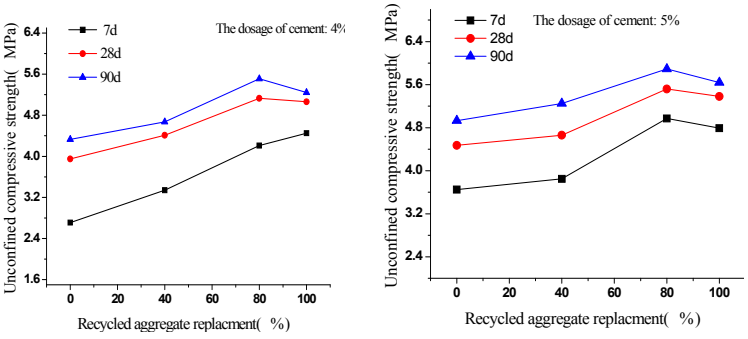

FIG.2. The effect of recycled aggregate replacement on unconfined compressive strength of mixture with 4% and 5% cement dosage

According to the correlation analysis of unconfined compressive strength of mixture at 7d, 28d and 90d, it could be drawn that there was a good linear correlation between unconfined compressive strength and recycled aggregate replacement. From Figure 3, it could be seen that all of the correlation coefficient were higher than 0.9, in which the best correlation was the fitting straight line of recycled aggregate replacement and unconfined compressive strength at 7-days age when the dosage of cement was 4%. With the increasing replacing level of recycled aggregate, the unconfined compressive strength of cement stabilized recycled aggregate mixture increased correspondingly.

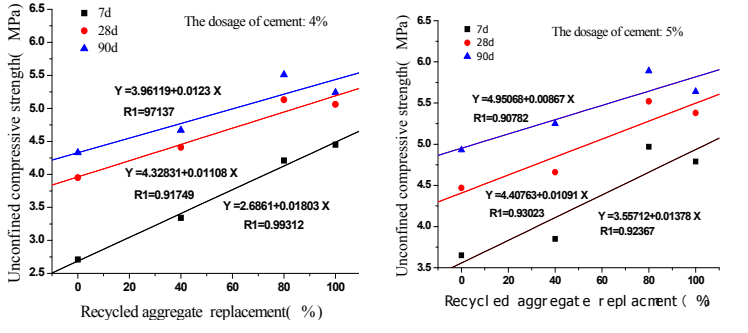

FIG. 3. The relational model between unconfined compressive strength and recycled aggregate replacement of mixture

DRY SHRINKAGE PERFORMANCE

Test Method

Mixture specimens were prepared with 5% cement dosage and 40%, 80% and 100% recycled aggregate replacement. The sample sizes are 10×10× 40 cm. There were 2

Groups specimens for mixture, a group of specimens were measured for shrinkage deformation, another group of specimens were measured for water loss ratio. The specimens for shrinkage test would be taken into a room with a constant temperature of 20±2 ℃ for 7 days, then kept flat on the glass table for natural drying, shrinkage values of specimens were measured at different age by micrometer. At the same time, the average amount of water evaporation loss another set of specimens under the same natural environment were measured, which represented the average amount of water evaporation loss of shrinkage specimens. Measuring didn't end until the micrometer readings kept unchanged and the moisture content of specimens didn't reduced (Approximately 60 days).

Test results and analysis

The dry shrinkage test results were shown in Figure 4 and Figure 5.

From Figure 4, it could be seen that the shrinkage strain of mixture gradually increased with age, the trend was growing fast at the beginning and growing slow gradually; With the increase of recycled aggregate replacement, the dry shrinkage strain of mixture increased, but the extent of growth was lesser when the replacement of recycled aggregate didn't exceed 80%. Shrinkage strain of mixture grown fastest for the first 12 days, the drying shrinkage strain at 12 days age accounted for more than 50% of the total shrinkage strain, the drying shrinkage strain at 30 days age accounted for more than 80% of the total dry shrinkage strain. Then, shrinkage strain changed slowly, which was in line with the characteristics of cement stabilize base course material.

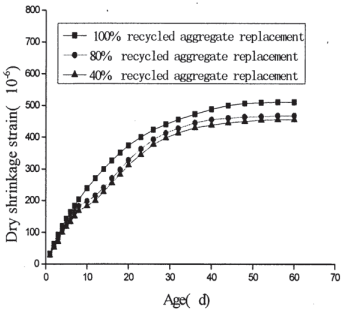

FIG. 4. Dry shrinkage strain curve of mixture at different age

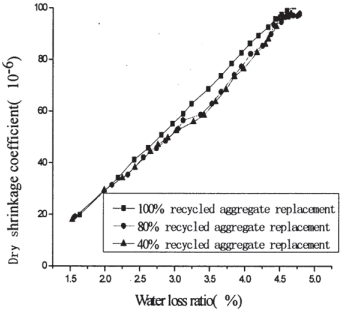

FIG.5. Correlation between shrinkage coefficient and water loss ratio

From Figure 5, it could be seen that the dry shrinkage coefficient of mixture increased with water loss ratio of mixture. When the water loss ratio of mixture was lower than 3.12%, the average dry shrinkage coefficient were almost similar for all mixture with different recycled aggregate replacement, the average dry shrinkage coefficient increased slightly with recycled aggregate replacement when the water loss ratio was larger than 3.12%, but the increasing extent would be lesser when the replacing level of recycled aggregate was not more than 80%. The final water loss ratio, dry shrinkage

coefficient and dry shrinkage strain of mixture with different replacement of recycled aggregate had a similar variation, increased slightly with the percentage of recycled aggregate, their range were 4.66%~ 4.87%, $97.58 \times 10^{-6} \sim 104.67 \times 10^{-6}$, $455 \times 10^{-6} \sim 510 \times 10^{-6}$ respectively. Xi'an Highway Institute's research about cement-stabilized gravel base indicated that the average dry shrinkage coefficient range was $41 \times 10^{-6} \sim 93 \times 10^{-6}$, that was smaller than that of cement-stabilized base course with 100% recycled aggregate replacement. It showed that the shrinkage performance of cement-stabilized gravel was better than that of cement-stabilized recycled aggregate. The main reason was that the optimum moisture content of mixture with recycled aggregate was slightly larger, it was recommend that the replacement of recycled aggregate was restrained in order to reduce the drying shrinkage strain and the average dry shrinkage coefficient of cement-stabilized recycled aggregate mixture (Mostafa Tavakoli 1996).

CONCLUSIONS

1. With the increase of recycled aggregate replacement, the optimum moisture content of mixture increased correspondingly, but the maximum dry density of mixture decreased. For high-grade highway, 5% cement dosage was recommended in cement-stabilized recycled aggregate base course material.
2. The unconfined compressive strength of mixture at different age increased with the dosage of cement. When the dosage of cement was kept constant, the unconfined compressive strength of mixture increased with the replacement of recycled aggregate, the unconfined compressive strength was at the most when 80% recycled aggregate was mixed. The unconfined compressive strength decreased when recycled aggregate was fully used. There was a good linear correlation between unconfined compressive strength and recycled aggregate replacement.
3. The dry shrinkage strain of mixture gradually increased with time, the trend was growing fast at early age and growing slow gradually. Dry shrinkage coefficient increased with the increasing water loss ratio. The final water loss ratio, dry shrinkage coefficient and dry shrinkage strain of mixture with recycled aggregate had similar variation, increasing slightly with recycled aggregate replacement.

ACKNOWLEDGMENTS

The authors appreciate the support of China Hunan Provincial Science & Technology Department.

REFERENCES

The People's Republic of China Industry Standard “Construction Technical Specification of Highway Pavement”(JTJ034-2000)”, *People's Communications Press,* 2000.

The People's Republic of China Industry Standard “Highway Engineering Aggregates test code”(JTGE42-2005) , *People's Communications Press*, 2005.

The People's Republic of China Industry Standard. (1994), “Testing procedures of inorganic binder stability materials in highway engineering”(JTJ057-94), *People's Communications Press*.

Sha, Q., (1999). High-grade highway semi-rigid base asphalt pavement, *People's Communications Press.*

Topeul. B(1997). Physical and mechanical properties of concrete produced with waste concrete. *Cement and Concrete Research*,Vol.27(12):1817-1823.

Ramamurthy, K. et al. (1998), Properties of recycled aggregate concrete. *The Indian Concrete Journal*, January, .

Tavakoli, M. et al.(1996), Drying shrinkage behavior of recycled aggregate concrete. *Concrete International*,Vol.18(2):58-61.

Study on Performance and Application of High Performance Pavement Portland Cement Concrete

Jian Yin [1], Yi Chi [2], Shenghui Gong [3], Wei Zou [4]

[1]Professor, postdoctor. College of Civil Engineering and Architecture, Central South University, Changsha 410075, China; csuyj@mail.csu.edu.cn
[2]Doctor, College of Civil Engineering and Architecture, Central South University, Changsha 410075, China; chiyi05@163.com
[3]Graduate student, College of Civil Engineering and Architecture , Central South University, Changsha 410075, China; agong0303@163.com
[4]Graduate student, College of Civil Engineering and Architecture, Central South University , Changsha 410075, China; csustorm@vip.qq.com

ABSTRACT: Because of some drawbacks including low strength, poor dimensional stability, low abrasion resistance, easy to crack and other shortcomings, Portland cement concrete has been limited in its use as a dominant pavement material in highway construction. This paper studied the feasibility of making high performance pavement concrete by adding 20~40% of high-quality composite ultra-fine fly ash (CUFA) technology to achieve high-performance of concrete roads. The test results indicated that, with cementitious material content of 360~400 kg/m^3 and CUFA content of 20% ~ 40%, adding CUFA improved the workability of concrete significantly; in the meantime, the 28d compressive strength was as high as 50 MPa, and the later strength of concrete continued growing. The designed concrete satisfied the requirements of opening to traffic 3 days after construction and heavy and extra heavy traffic in 28 days. The durability, especially the abrasion resistance, and the crack-resistance were improved significantly.

INTRODUCTION

At present, the 28d design compressive strength of cement concrete for pavement is 30~40 MPa for both Grade A and B highways in China. A series of shortcomings, which include low strength, poor dimensional stability, low abrasion resistance and early stage cracking, highly limit its application in highway construction. A large amount of domestic and foreign research results indicate that the pavement concrete expose to the atmospheric environment directly, it would have long-term effects under temperature stress, wet and dry cycles, freeze-thaw cycles and chemical erosion, it also is a subject to repeated effect of withstand bending, shock, vibration and wear, therefore its comprehensive performance put forward higher request. Using additives and mineral admixture composite technology can improve the workability, mechanical properties

and especially durability of plain concrete significantly. Furthermore, the durability of high-performance concrete will be the new requirements for the modern concrete technology. High performance concrete is also a new concrete technology to environment-friendly and sustainable development.

This paper used conventional materials, equipment and production method and utilizes new concrete super plasticizer to improve the workability. Using CUFA can reduce the cement consumption by 20% to 40% or even more. CUFA can significantly improve the efficacy of the microstructure of cement paste and concrete uniformity, compactness, durability and strength, which can make the ordinary concrete achieve high performance.

RAW MATERIALS

Cement: Grade 42.5 ordinary Portland cement; the physical and mechanical properties are shown in Table 1, which met the current national specification "Common Portland Cement".

Sand: XiangJiang rive sand, the gradation satisfied the requirement and met requirements in Zone Ⅱ according to the current national specification "Sand for building". Fineness modulus was 2.86, clay content was 0.5%.

Coarse aggregate: limstone gravel, the aggregate size range was from 5 to 31.5 mm, the gradation met the current national specification "Pebble and crushed stone for building", and the crushed indext is 7.4 ~ 9.0%.

CUFA: Grade Ⅰ fly ash could be mixed with a small amount of inorganic mineral powder and efficient surface-active substances. The fly ash content was no less than 95%, its specific surface area was 5200 cm^2/g. The chemical composition and performance indicators of fly ash, which were produced by Xiangtan Power Plant are shown in Table 2.

Table 1. Ordinary Portland Cement Properties

Fineness (%)	Setting time (min)		Stability	3d (MPa)		28d (MPa)	
	Initial set	Final set		Compressive strength	Flexural strength	Compressive strength	Flexural strength
6.9	155	350	eligibility	29.6	5.1	57.8	7.4

Table 2. The Chemical Composition of the Raw Fly Ash (%)

Ingredient	Ignition loss	Water content	SO_3	SiO_2	Fe_2O_3	Al_2O_3	CaO	MgO	K_2O	Na_2O	Specific surface area cm^2/g
1 grade FA	3.2	<1	2.5	51.8	5.0	26.4	4.1	1.0	1.3	1.0	5105

TEST METHODS

(1) FA test was according to GB 1596-91 "Fly ash used for cement and concrete". Degree of fineness was according to GB 8074－2008 "Testing method for specific

surface of cement-Blaine method";

(2) Cement mortar strength test and abrasion test, as well as the concrete's mixture performance, mechanical properties test and durability test were according to JTG E30-2005 "Test Methods of Cement and Concrete for Highway Engineering";

(3) Cube compressive strength and splitting tensile strength test were used for size specimen 100 mm * 100 mm* 100 mm , Flexural strength of specimen size was used in 100 mm * 100 mm * 400 mm. Test results converted into standard strength values. Three specimens were tested to give each value.

PREPARATION OF THE HIGH PERFORMANCE ROAD CONCRETE

For low cement concrete, higher water-cement ratio and less sand amount, the fresh concrete mixture usually had poor cohesiveness, tend to bleed segregate and thus had poor performance. Hardened concrete also often had bad surface and poor durability, and the strength of concrete was low. In order to improve the workability, strength and durability, the conception of high-performance concrete was adopted. The test results are shown in Table 3.

Table 3. Test Results of High-Performance Pavement Concrete

Group	Cement (kg/m^3)	Water (kg/m^3)	CUFA (kg/m^3)	CUFA (%)	Sand (%)	Slump (mm)	Compressive strength (MPa)			Flexural strength (MPa)	
							3d	28d	56d	3d	28d
1	400	140	0	0	38	25	52.1	61.7	64.3	4.01	6.12
2	320	138	80	20	38	50	47.3	60.1	69.9	3.65	6.99
3	280	135	120	30	38	40	40.8	58.3	75.3	3.93	7.31
4	240	130	160	40	38	55	38.8	60.3	73.5	3.51	7.24
5	160	130	240	60	34	60	21.1	54.0	60.6	3.13	6.01
6	360	130	0	0	34	15	35.7	50.7	57.4	3.66	5.78
7	288	127	72	20	34	55	36.2	58.1	63.1	3.54	6.90
8	252	125	108	30	34	65	36.2	58.1	62.8	3.47	6.90
9	216	120	144	40	34	50	31.4	53.6	59.7	3.29	5.97
10	144	120	216	60	34	50	20.9	40.1	51.2	2.91	5.06

The test results in Table 3 indicated that, when the content of cementitious material was 400 kg/m^3, as the CUFA content increased, the workability of fresh concrete was improved significantly, and so did the slump. When the CUFA content ranged from 20% to 40 %, the 3d compressive strength of high-performance pavement concrete was higher than 35 MPa and the 3d flexural strength was higher than 3.5 MPa. According to the Portland cement concrete pavement specification JTJ 073.1-2002 "Technical Specifications of Cement Concrete Pavement Maintenance for Highway" in China, the flexural strength should be no less than 70% of designed strength when the road is open to traffic. In other words, the flexural strength should be higher than 3.5 MPa when the designed flexural strength was 5.0 MPa or 3.15 MPa (the designed flexural strength was 4.5 MPa). Therefore, the concrete containing 20%~40% CUFA was applicable and met the requirement of opening to traffic three days after the construction. In comparison with the control group whose 28d flexural strength was 5.0 MPa, the flexural strength of high performance pavement concrete containing 20~40% CUFA increased by 14.0%,

19.4% and 18.3% respectively, and it met the requirement of opening to heavy traffic. When the dosage of CUFA reached to 60%, the 3 d compressive strength was low, but the 28d flexural strength was 6.01 MPa, and it was higher than that of the control group. Therefore, the content of CUFA could be higher when there is enough curing time.

When the content of cementitious materials was 360 kg/m^3 or 400 kg/m^3, the fresh concrete had good workability and consistency. In order to achieve 5.0 MPa design flexural strength and meet the requirement of 3 days traffic opening, the content of CUFA should not exceed 20%. When the content of CUFA was as high as 40%, the 3d flexural strength would be 4.5 MPa which was the design strength, and thus it would have sufficient strength to open to traffic after curing for three days.

Thus, adding 20 ~ 60% CUFA not only improved the workability of the high performance concrete, but also increased the strength significantly.

THE MICROSTRUCTURE OF CEMENT PASTE

The microstructure of cement paste of high performance pavement concrete was observed by SEM technology. Figure 1 shows the SEM photo of cement paste at 3 d, and Figure 2 shows the SEM photo of cement paste at 28 d.

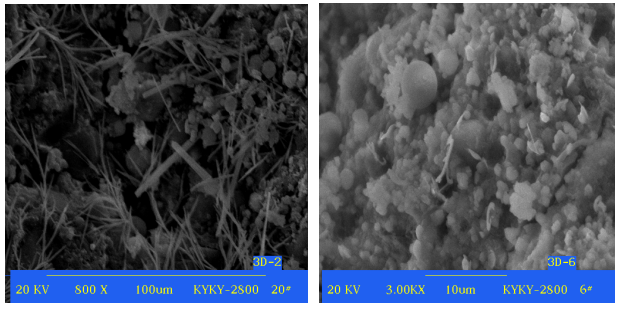

FIG. 1. The SEM photo of cement paste at 3 d

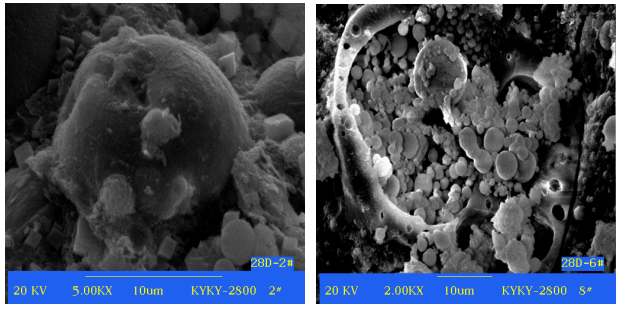

FIG. 2. The SEM photo of cement paste at 28 d

It can be seen from the Figures that, a large number of ettringite which were

needle-like crystals overlapped reciprocally with hydrated calcium silicate gel and became net structure at 3 days. Fly ash particle of all sizes filled in the hydration products. There were Hydration products precipitate on the fly ash particle surface, which indicated the fly ash had started Hydration reactions. With the extension of age, the surface of fly ash was eroded obviously, and the reaction intensified. The net and fibriform structures of hydrated calcium silicate gel became more obvious. The ettringite crystals were sturdy more, and grew better. So the strength of cement paste increased significantly.

DURABILITY AND DRYING SHRINKAGE PROPERTIES OF THE HIGH PERFORMANCE PAVEMENT CONCRETE

Permeability and freezing resistance

Table 4 and 5 present the test results of the permeability resistance under certain hydraulic pressure and resistance to rapid freez-thaw test. C40 concrete containing CUFA was used for the tests. It can be seen from Table 4 and 5 that the concrete had good resistance to hydraulic pressure (greater than S30) and freeze-thaw (greater than or equal D200).

Table 4. Permeability Test Results of the High Performance Pavement Concrete

Item		1	2	3	4	5	6
Max hydraulic pressure（MPa）		3.0					
Permeate depth （mm）	Average	15.2	16.8	18.4	12.5	12.1	13.0
	Max.	16.2	18.1	21.3	15.2	16.2	14.1
	Min.	11.0	9.2	16.1	9.3	8.9	10.9
Remark		Load the hydraulic pressure to 3.0 MPa once and steady 8 hours，all specimens no seeping.					

Note: Group No. are the same with Table 2.

Table 5. Results of Rapid Freeze-Thaw Test of High Performance Pavement Concrete

Item	100 times freeze-thaw cycle	200 times freeze-thaw cycle
Standard curing strength (MPa)	51.5	55.2
Freeze-thaw strength (MPa)	48.1	45.7
Strength losing (%)	6.6	17.2
Weight losing (%)	0.0	0.0
Max. depth of permeability (mm)	35.0	46.0

Note: When the CUFA concrete is 30%; the slump was 40 mm.

Abrasion resistant ability

Table 6 showed that the abrasion per area of the high performance pavement

concrete, which contained 15~40% CUFA, was less than ordinary concrete. Thus, the abrasion resistance ability of the high performance pavement concrete was better. On one hand, the bond property between cementitious materials and aggregates improved by adding CUFA; on the other hand, the high strength of the vitreous granule in fly ash reduced the abrasion of the high performance pavement concrete.

Table 6. Abrasion Resistance of the High Performance Road Concrete

Group	CUFA Replacement (%)	C (kg/m^3)	CUFA (kg/m^3)	28d Compressive strength (MPa)	Abrasion per area (kg/m^2)	Ratio (%)
1	0	360	0	50.0	2.048	100
2	15	306	54	52.7	1.888	92.2
3	25	270	90	56.9	1.124	54.9
4	40	216	144	56.7	1.756	85.7

Drying shrinkages

Based on the dry shrinkages test results showed in Table 7. The mixture proportion of group 1、2、3、4 and 5 concrete were shown in Table 3. The dry shrinkage value of the high performance pavement concrete increased with the increase of CUFA content. The dry shrinkage value of high performance concrete was less than the ordinary concrete as the CUFA content were less than 40%. The shrinkage values of the concrete containing 60% CUFA was much higher than those of the ordinary concrete. Thus, adding up to 40% CUFA reduced the dry shrinkage value of the high performance pavement concrete, and the crack resistance of the pavement concrete was improved.

Table 7. Dry Shrinkages Test Results of the High Performance Pavement Concrete

Group	Dry shrinkages ratio ($*10^{-6}$)							
	3d	7d	14d	28d	60d	120d	150d	360d
1	41	124	186	215	274	325		457
2	35	78	151	193	239	278	358	401
4	41	99	164	203	250	292	379	423
5	93	182	241	297	315	323	411	470

Mixture proportion of the high performance road concrete

Table 8. Mixture Design of the High Performance Pavement Concrete

Open traffic Time (day)	Cementitious materials (kg/m^3)	CUFA (%)	W/C ratio	Sand rate (%)	Remark
3	360	≯20	0.30～0.35	32～34	Crushed stone
	400	20～40		34～38	
28	360	20～40		32～34	
	400	20～40		34～38	

Based on the results above and the properties of the high performance pavement concrete, the recommended proportion is shown in Table 8.

APPLICATION OF HIGH PERFORMANCE PAVEMENT CONCRETE

Project introduction

The Ji'an section of G105 highway in Jiangxi province is 110 kilometers long. The daily traffic volume was 20 , 000~30 , 000 with 50% over loading vehicles. Because of the heavy traffic load, 40~50% of the pavement surface had deteriorated, which highly reduced the traffic speed, comfort and safety and needed rehabilitation immediately. The highway department of Ji'an city Jiangxi province decided to use high performance pavement concrete on this repair, which must satisfy the requirement of opening to traffic in 3 to 5 days after paving.

Materials and mixture ratio

(1) Materials

Cement: 32.5R ordinary Portland cement , the compressive strength and flexural strength at 3d and 28d are 20.1 MPa, 3.7 MPa and 35.3 MPa, 5.6 MPa respectively.

Sand: River sand, produced in Ganjiang with the eligible aggregate grading, M_X=2.76.

Gravel: Crushed stone, produced in Ganjing with the continuous aggregate grading from 5 to 31.5 mm. Crushed index: 9.6%; Mud content: 0.5%.

CUFA: Offered by Central South University.

(2) Mixture ratio of the high performance pavement concrete

Basing on the lab test and considering the operation feasibility and the mechanics performance of the concrete, the mixture ratio was C: W: S: G: CUFA=300:135:610:1135:100 (kg/m^3). The designed slump was 20~30mm; the compress strength at 3 d was no less than 20 MPa and the flexural strength at 3 d was no less than 4.0 MPa.

Mechanics properties of designed high performance pavement concrete

(1) Concrete performance

There were three concrete boards (5.0 m*3.75 m*0.24 m*3, all board patched) repaired on the Ji'an section of G105 highway in Jiangxi province. The average slump of the concrete was 40 mm. The test results indicated that the operation of the high performance pavement concrete which with the excellent water conservation and cohesive property was fine.

(2) Mechanics performance

Eight groups of specimens were fabricated by using insert vibrating method, 150 mm * 150 mm * 150 mm cube specimens were used for compressive strength test and 150 mm * 150 mm * 550 mm beam specimens were used for the flexural strength test. Four groups of specimens were cured in water while the other four groups were cured in the standard curing room at the job sites. As shown in Table 9, the test results indicated that

flexural strength and compressive strength at 3 d were 4.7 MPa and 30.2 MPa respectively; the 28 d strength were 7.6 MPa and 55.8 MPa respectively. The effect of the CUFA on increasing the strength of the concrete was prominent, and the high performance pavement concrete prepared with CUFA and 32.5R Portland cement met the requirement of opening traffics 3 days. No cracking or severe abrasion were found on the pavement two years after the construction.

Table 9. Mechanical Properties of the Designed Pavement Concrete on site

Group	Flexural strength (MPa)		Compressive strength (MPa)	
	3d	28d	3d	28d
Standard conserving	4.5	7.5	29.4	56.3
Conserved in the same condition	4.7	7.6	30.2	55.8

Application and economic benefit of the high performance pavement concrete

Based on the successful application of the high performance pavement concrete on the test road, the concrete had been widely used on other three sections of highway in Ji'an city of Jiangxi province. Compared with the ordinary concrete, which incorporated hardening accelerator admixture, the new technology of high performance pavement concrete saved ￥1，000，000. Besides, the society and environment benefits were obvious for opening to traffic earlier, alleviating traffic jam, reducing bypass expenditure and extending the application of fly ash.

CONCLUSIONS

Based on the test results above and the site application experience, some conclusions were summarized as follows:

1. With cementitious material amount of 360~400 kg/m^3 and CUFA content of 20% ~ 40%, the incorporation of CUFA could significantly improve the workability of concrete properties. In the meantime, it could obtain the high performance pavement concrete with a compressive strength as high as 50MPa, and the later strength of concrete continued to grow. This would meet the requirements of opening of traffic in 3 days after paving and to heavy traffic in 28 days.
2. The high performance pavement concrete containing 30% CUFA had good resistance to permeation, freeze-thaw and abrasion; dry shrinkages of the high performance pavement concrete mixed containing 20% to 40% CUFA decreased largely, which improved the crack resistance of the concrete.
3. Mixture proportion of the high performance pavement concrete used in this paper were suggested.
4. The site application showed that the 3 d flexural compressive strength of the high performance pavement concrete were 4.7 MPa and 30.2 MPa, and the 28 d flexural and compressive strength were 7.6 MPa and 55.8 MPa, which satisfied the requirement of opening to traffics in 3 days. No cracking or severe abrasion were found on the pavement two years after construction.

REFERENCES

Nehdi, M., Mindess, S., Aitcin, P.C. (1998). "Rheology of high performance concrete Effect of ultrafine particles." *Cement and Concrete Research*, Vol.28 (5):687~697.

Sharma, R. L. and Pandey, S. P. (1999). "Influence of mineral additives on the hydration characteristics of ordinary Portland cement." *Cement and Concrete Research*, Vol. 29(9): 1525~1529.

Ferraris, C.F., Obla, K.H. and Hill, R. (2001). "The influence of mineral admixtures on the theology of cement paste and concrete." *Cement and Concrete Research*, Vol. (31): 201~206.

Grzeszczyk, S. (2000). "Effect of superplasticizers on the rheological properties of fly ash suspensions containing activators of the pozzolanic reaction." *Cement and Concrete Research*, Vol. (30): 1263~1266.

Feng, N. (1996). "High Performance Concrete." Beijin: *China Construction Industry Press*.

Wu, Z. (1999). "High performance concrete and its fine mineral admixtures." *Architecture Technology*, Vol. 30 (3): 160-163.

Zhou, S., Liu, B., Xie, Y., Yin, J. and Yuan, Q. (1999). "Ultra pulverized Fuel Ash composite Powder used for HPC.", *Construction Technology*, Vol. 28(5):13-14.

Yin, J., Zhou, S. and Xie Y (2002). "Investigation on Preparation and Application of High Strength Performance Concrete.", *Journal of Changsha Railway University*, Vol. 20(2):17-22.

Yin, J. and Zhou, S. (2005). "Study and Application on High-performance Rapid Repair Concrete.", China Railway Science, Vol. 26(3):136-138.

Influence of the Micro-gradation of Fly ash and Slag on the Properties of Cement Mortar

Jianan Cao

Doctor, College of Civil Engineering and Architecture, Central South University, Changsha, P.R. China, 410075, cja6328@126.com

ABSTRACT: The particle size distributions of the mixture of fly ash, slag and cement were studied. The micro gradation of the mixture of fly ash and slag, also named as Ultra Fly ash and Slag (UFS), was analyzed and optimized. The properties of cement mortar containing fly ash, slag and UFS were studied through laboratory tests. The hydration of UFS when adding the activator was also analyzed. Test results indicated that best ratio of fly ash to slag was 4:1, which would achieve the best filling effect, much better micro gradation and the highest density for UFS, and thus improve the early strength. Both the early and late stage strength of cement mortar containing fly ash was lower than those of the cement mortar containing slag or UFS. At the environment provided by the activator, the strength performance of cement mortar would be highly improved because of the secondary hydration of the cementitious material due to the water reducing and densifying effect of the UFS.

INTRODUCTION

As the development of cement concrete pavement technology, the mineral additives have already been an important component in the concrete for rigid pavement. The mineral additives have lots of advantages including improve the micro structure of concrete, the mechanical properties and the durability. However, there are still some deficiencies of those additives. For example, the early strength of the concrete incorporating fly ash was low and the concrete strength decreases as the fly ash content increases. Yang et. al. (2005) found that although the early strength of concrete can be improved by adding slag, slag also tends to excrete water and generate more harmful air voids in the concrete, which reduced the mechanical properties and the durability. A potential promising method to utilize the advantages of the two mineral additives is to add both fly ash and slag into concrete simultaneously. Research results indicated that adding both fly ash and slag would reduce the amount of the harmful voids and the size of the voids and improve the water-retaining property, the compatibility with other additives, the density of the cement paste and the strength at both early and late stage (Liu et. al., 1995; Sun et. al., 2004; Long et. al., 2002).

This paper investigated the particle size distributions and micro gradations of the mixture of fly ash, slag and cement. The mechanical properties of cement mortar incorporating fly ash, slag, and mixed additives were evaluated through laboratory tests. The hydration of UFS at the existence of activator was also investigated.

MATERIAL PROPERTIES AND TEST METHOD

42.5 grade regular Portland cement was used in this study. The 3d and 28d compressive strength of the cement mortar are 27.7 MPa and 52.2, respectively. The 3d and 28d flexural strength of that are 5.03 MPa and 8.10 MPa, respectively. The physical and chemical properties of the cement all met the requirement of the current Chinese specification. Natural sand was used as fine aggregate. The gradation of the natural sand met the requirement of region II of the Chinese specification and the fines modulus was 2.61. An ultra fine fly ash was used, the specific surface of which was 5500 cm^2/g. The density of slag was 2.87g/cm^3, the specific surface was 3500 cm^2/g. A polycarboxylate type super plasticizer and a naphthalene type super plasticizer (SP) were used. Table 1 presents the different components of cement, fly ash and slag. 40mm*40mm*160mm beam specimens were prepared and cured in the standard curing room. The strength and fluidity of the cement mortar were tested according to the Chinese specification.

Table 1. Chemical Components of Cement, Fly Ash, and Slag (%)

Material	SiO_2	Al_2O_3	Fe_2O_3	CaO	MgO	K_2O	Na_2O	SO_3	Loss on ignition
Cement	22.05	4.34	4.42	62.68	4.58	—	—	2.21	2.84
Fly ash	50.15	30.51	2.08	12.50	0.088	1.08	0.53	0.40	3.43
Slag	28.99	14.22	1.49	49.83	0.35	0.34	0.22	3.25	1.99

DISCUSSION OF TEST RESULTS

Optimizing the Ratio of Fly Ash to Slag

The strength and durability of concrete is mainly determined by the properties of cement paste, aggregate and the bonding between cement paste and aggregate. The cement paste is composed of cement, water, mineral additives and other chemical additives. Recent research indicated that the bulk density of the dry mixture of cement, fly ash and slag could be maximized by optimizing the gradation of cement and mineral additives, which would improve the density of cement paste and thus the strength, density and durability of the cement paste and the concrete could also be improved. 5 groups of fly ash and slag mixture were prepared. The ratios of fly ash to slag for the 5 groups were 1:1, 1:2, 1:3, 1:4 and 1:5, respectively. Table 2 and Figures 1 and 2 present the air voids and particle size distribution of the 5 groups of mixture as well as the cement.

It can be seen from Figure 1 that, the volume fraction of all the 6 groups reached peak values around 0.23 μm and dropped to low values around 0.42 μm, indicating that the gradations were discrete around 0.42 μm. Actually, the ideal gradation, which would achieved the highest bulk density, should be continuous and less discrete. With the increase of the fly ash content, the gradations tended to be more continuous. By adding

more fly ash, the volume fraction around 0.23 μm was increased, the discrete gradation around 0.42 μm was improved and thus the density of the mixture was highly improved. When the ratios of fly ash to slag was 4:1 or 5:1, the fraction between within 0-30 μm were between 89.55% to 89.89%, which is consistent with the results in Table 2. Besides, the fraction smaller than 1 μm increased as the content of fly ash increased, which would also improve the density of the cement paste and thus the early strength of the concrete would be improved.

Figure 2 presents the particle size distributions of the mixed fly ash, slag and cement. The new compound mixture was made of the 5 groups of fly ash and slag mixture mixed with cement at the ratio of 3:7. Test results indicated that the fraction around 0.42 μm of the compound mixture was higher than that of cement. Some discrete gradations were improved. Thus, the micro gradation of the compound mixture was more continuous. The fine particles filled the voids and the densities of the cementitious materials mixture were improved.

In general, high densities were achieved by mixing fly ash and slag at the ratio of 4:1 or 5:1. However, considering the fact that more slag would improve the early strength of concrete, the ratio of fly ash to slag was selected as 4:1. At this ratio, both density and early strength would be satisfied. This mineral additive mixture was named as Ultra Fly ash and Slag (UFS).

Table 2. Air Voids and Volume Fraction of the Mixture of Fly ash and Slag

Items		Ratios of fly ash to slag				
		1：1	2：1	3：1	4：1	5：1
Percent of total volume (%)	0-3μm	30.61	34.27	36.10	37.19	37.92
	3-30μm	55.90	53.93	52.95	52.36	51.97
Apparent density (g/cm^3)		2.56	2.47	2.45	2.39	2.21
Bulk apparent density (g/cm^3)		0.780	0.759	0.754	0.746	0.777
Air voids (%)		70.00	69.27	69.22	68.92	64.84

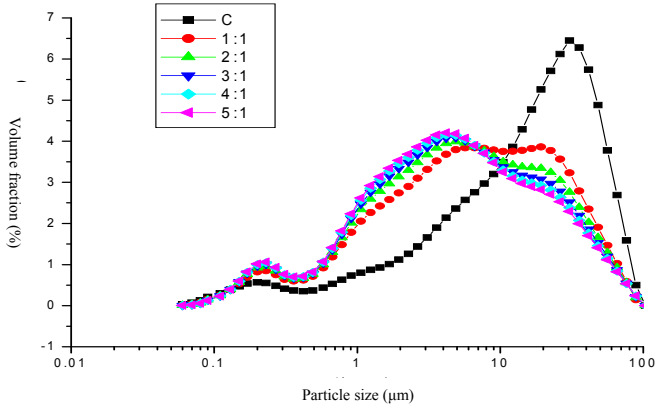

FIG. 1. Volume fractions of the fly ash and slag mixtures and cement

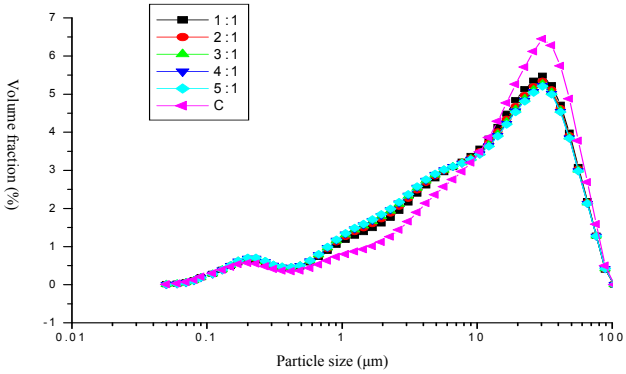

FIG. 2. Volume fraction of the mixture of fly ash, slag and cement

Influence of Fly Ash, Slag and UFS on the Properties of Cement Mortar

Laboratory tests were carried out to investigate the influence of UFS on the properties of cement mortar. The water/cement ration was 0.5. Three groups of cement mortar specimens incorporating fly ash, slag and UFS respectively were prepared and tested. The fluidity of fresh mixed cement mortar was controlled at 108±5mm. The 1d and 28d compressive and flexural strength and the water reducing rate were measured. The test results are shown in Table 3 and Figure 3.

It can be seen from Table 3 and Figure 3 that, the early (1d) compressive and flexural strength of cement mortar incorporating either flay ash or slag were lower than that of the original cement mortar. However, the early (1d) compressive and flexural strength of cement mortar incorporating UFS at the dosage of 10%-30% were higher than those of the original cement mortar. At the UFS content of 10%, 20% and 30%, comparing with the original cement mortar, the flexural strength were improved by 14.96%, 21.78% and 6.04%, respectively; and the compressive strength were improved by 32.66%, 38.57% and 7.42%, respectively. The 28d compressive and flexural strength of cement mortar incorporating slag and UFS at the dosage of 10%-50% were much higher than those of the original cement mortar. At the UFS dosage of 50%, comparing with the original cement mortar, the 28d compressive and flexural strength were improved by 25.4% and 11.1%, respectively. Besides, the water reducing rate of the cement mortar incorporating 50% UFS was 9.33%, indicating UFS also had the effect of reducing water.

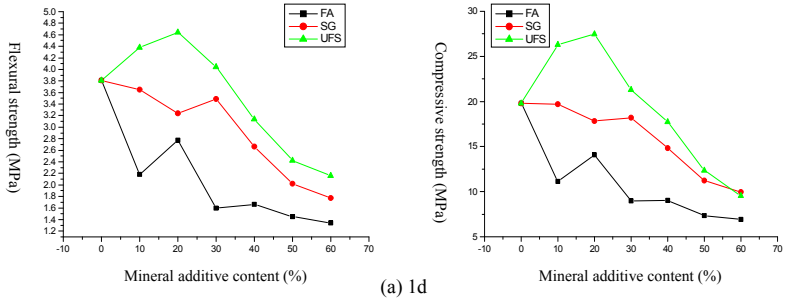

(a) 1d

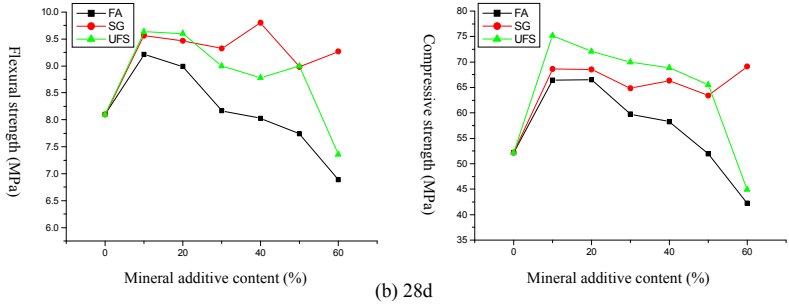

(b) 28d

FIG. 3. The influence of mineral additives on the strength of cement mortar

Table 3. Test Results of Cement Mortar Incorporating Fly Ash, Slag, and UFS

Group	Cement (kg/m^3)	Water (kg/m^3)	Sand (kg/m^3)	Fly ash (%)	Slag (%)	UFS (%)	Water reducing rate (%)	Flexural strength(MPa)		Compressive strength(MPa)	
								1d	28d	1d	28d
1	450	225	1350	0	--	--	0	3.81	8.10	19.81	52.22
2	405	218		10	--	--	3.11	2.18	9.21	11.13	66.46
3	360	213		20	--	--	5.33	2.77	8.99	14.06	66.48
4	315	206		30	--	--	8.44	1.60	8.17	9.00	59.78
5	270	199		40	--	--	11.56	1.66	8.03	9.04	58.22
6	225	192		50	--	--	14.57	1.45	7.74	7.35	51.96
7	180	184		60	--	--	18.22	1.34	6.89	6.90	42.25
8	405	220		--	10	--	2.22	3.65	9.56	19.71	68.60
9	360	218		--	20	--	3.11	3.24	9.47	17.80	68.51
10	315	216		--	30	--	4.00	3.49	9.32	18.18	64.83
11	270	214		--	40	--	4.89	2.66	9.80	14.83	66.35
12	225	212		--	50	--	5.78	2.02	8.98	11.25	63.36
13	180	210		--	60	--	6.67	1.77	9.27	9.94	69.15
14	405	219		--	--	10	2.67	4.38	9.63	26.28	75.21
15	360	216		--	--	20	4.00	4.64	9.60	27.45	72.07
16	315	211		--	--	30	6.22	4.04	9.00	21.28	70.01
17	270	208		--	--	40	7.56	3.14	8.78	17.73	68.90
18	225	204		--	--	50	9.33	2.42	9.00	12.34	65.48
19	180	197		--	--	60	12.44	2.16	7.36	9.52	56.01

Influence of UFS on the Properties of Cement Mortar Containing Activator

When only adding fly ash and slag, or the UFS content was higher than 30%, the early strength of cement mortar were lower. In order to solve this deficiency, activator was used to improve sufficient early strength of cement mortar. Sharma and Pandey (1999) compared the 28d micro structure of cement mortar incorporating fly ash and slag with that of the plain cement mortar and found that the only difference was the content of NaOH was lower for the mortar including mineral additives, indicating that the hydration of those mineral additives was very slow at the early stage.

The influence activator on the strength performance of cement mortar was investigated in this study as shown in Table 4. It can be seen from Table 4 that, the 1d and 28d strength of cement mortar were improved by adding activator A. When the activator content was 2%, the 1d compressive and flexural strength were increased by 21% and 10%, respectively. When the activator content was 3%, the 1d compressive and flexural strength were increased by 28% and 12%, respectively.

Table 4. Influence of Activator on the Strength Performance of Cement Mortar

C	Content of activator A (%)	SP (g)	Slump (mm)	Water/cement ratio	UFS content (%)	Compressive strength (MPa)		Flexural strength(MPa)	
						1d	28d	1d	28d
450	0	2.0	125	0.3	20	28.81	76.32	5.44	10.89
	2	2.0	125			34.86	80.00	5.98	11.91
	3	2.1	120			36.88	85.09	6.09	12.03

Figure 4 shows the micro structure of the cement mortar incorporating activator and UFS by Scanning Electron Microscope (SEM). It can be seen that, the fly ash particle were covered by the hydrates of calcium silicate. No clear sphere particle was found, but more crystal columns of ettringite were observed. Thus, with the help of activator, the fly ash hydrated faster, generated large amount of hydrates, accelerate the hydration speed of the cementitious materials at early stage. Thus, the density of the cement mortar was improved, the air voids inside of the cement mortar were reduced, and the early strength of the cement mortar was highly improved.

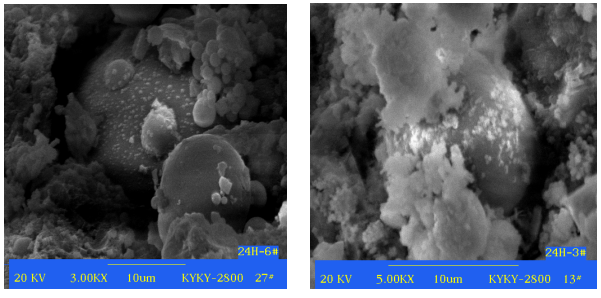

FIG. 4. SEM photo of cement mortar incorporating UFS and activator

CONCLUSIONS:

1. The optimal ratio of fly ash to slag was found to be 4:1 to maximize the density of the additive mixture, produce more continuous micro gradation and improve the early strength of the cement mortar.
2. The early (1d) strength of cement mortar incorporating either fly ash or slag were lower than that of the original cement mortar, whereas that of the cement mortar incorporating UFS at the dosage of 10%-30% were clearly higher than those of the original cement mortar. The 28d strength of cement mortar incorporating slag and UFS at the dosage of 10%-50% was much higher than that of the original cement mortar. For the 50% UPS content, the 28d compressive and flexural strength of cement mortar incorporating UFS at the dosage of 50% were 25.4% and 11.1% higher than those of the original cement mortar; besides, and the water reducing rate of UFS was 9.33%, indicating that it could be used as a water reducer.
3. Due to the activator, in the first 24 hours of hydration, fly ash hydrated faster, fly ash particles were covered with hydrates of calcium silicate and more crystal columns of ettringite were formed. Activator accelerated the hydration rate of fly ash at early stage, improved the density and of the structure of the cement paste, reduced the air voids in the cement paste and thus the early strength of cement mortar were improved.

REFERENCE

Yang, H., Dong, W., and Wang, Z. (2005). “Research on the micro properties of cement concrete incorporating slag and fly ash.” *Journal of Yangtze River Scientific Research Institute*, Vol. 22 (1): 46-49 (in Chinese).

Liu, Z., Hu, D., and Liu, Z. (1995). “Cement concrete incorporating slag and fly ash.” *Highway*, No. 2: 43-45 (in Chinese).

Sun, J., Cheng, D., Song, H., and Fang, Q. (2004). “High performance concrete incorporating compound slag mineral additive.” *Building Materials & Applications*, No. 3: 43-46 (in Chinese).

Long, G., Wang, X., and Xie, Y. (2002). “Very-high-performance with ultrafine powders.” *Cement and Concrete Research*. Vol. 32(4): 601-605.

Sharma, R.L. and Pandey, S.P. (1999). “Influence of mineral additives on the hydration characteristics of ordinary Portland cement.” *Cement and Concrete Research*, Vol. 29(9):1525-1529.

Dynamic Pavement-Vehicle Interaction of Rigid Pavement Resting on Two-Parameter Soil Medium

V. A. Sawant[1], Kousik Deb[2], and V. A. Patil[3]

[1]Assistant Professor, Department of Civil Engineering, I.I.T. Roorkee, Roorkee 247667, India; sawntfce@iitr.ernet.in

[2] Assistant Professor, Department of Civil Engineering, I.I.T. Kharagpur, Kharagpur 721302, India; kousik@civil.iitkgp.ernet.in

[3]Research Scholar, Department of Civil Engineering, I.I.T. Roorkee, Roorkee 247667, India; vikrampatil_1970@yahoo.com

ABSTRACT: An improved solution algorithm based on Finite Element Method is adopted to analyze rigid pavements under moving vehicular or aircraft loads. Analysis is based on the classical theory of thick plates resting on two-parameter elastic soil medium. The pavement is discretized by four node thick plate elements that account for the transverse shear deformation and bending. The underlying soil medium is modeled by Pasternak shear layer and linear elastic spring and dashpot systems. The dynamic interaction between the moving load and the pavement is considered by modeling the vehicle by spring-dashpot unit. The pavement-vehicle interaction force is modeled with Dirac-delta function. It has been observed that the dynamic interaction between the moving load and the pavement has significant effect on pavement response.

INTRODUCTION

Study of the dynamic response of pavements due to moving loads such as vehicles and aircraft has received significant attention in recent years because of its relevance to the design of pavements and airport runways. Most of the available analytical solutions represent the pavement by an infinitely long beam or plate, and neglect dynamic interaction between the moving load and pavement. Some of these limitations of analytical solutions have been largely overcome by the development of high-speed computers and efficient numerical technique such as Finite Element Method. By using the Finite Element technique, concrete pavements can be effectively and accurately modeled including dynamic interaction between the moving load and pavement and a realistic representation of suspension system.

The moving load problems were first encountered in the design of railroad bridges. By assuming the bridge as simply supported beams, several researchers solved this problem analytically. Thompson (1963) carried out investigations assuming the pavement as an infinitely long thin plate. Lewis and Harr (1969) analyzed the dynamic response of

concrete pavements subjected to moving loads and temperature gradient. The structural impedance method based on the principle of superposition for vehicle and structural system has been used by Ting et. al. (1974) and later modified by Genin et. al (1975) to include a mechanism by considering a vehicle with air cushion suspension. Subsequently, Taheri and Ting (1989) presented solution algorithms for bridges based on the structural impedance method. The most of the analytical solutions discussed above can not be effectively applied to pavement design, since they are obtained for an infinitely long beam or plate and neglect the dynamic vehicle-pavement interaction. A simplified spring-dashpot suspension system was used to represent the moving vehicles. Alvappillai et al. (1992) and Zaman et al (1993) presented an algorithm based on finite element analysis for dynamic response of a thick plate on viscoelastic foundation to moving loads. Sun (2001) presented a closed form solution, for the response of a beam resting on a Winkler foundation subjected to a moving line load, by means of two-dimensional Fourier transform and using Green's function. The steady-state response of a uniform beam resting on two parameter soil medium and subjected to moving load with a constant speed has been investigated by Mallik et al (2006). Sawant (2009) considered dynamic vehicle-pavement interaction in the analysis and observed significant effect of velocity of moving load on pavement response. Two clear peaks were observed in deflection – velocity response curve.

In the present study, approach suggested by Zaman et al (1993) is adopted to analyze rigid pavements under moving vehicular or aircraft loads. The concrete pavement is discretized by four node thick plate elements. The underlying soil medium is modeled by two-parameter Pasternak model and dashpot systems in which the soft subgrade soil (existing soil) is modeled by spring elements and the base course is modeled by Pasternak layer. Pasternak layer provides the continuity between the spring elements. The dynamic interaction between the moving load and the pavement is considered by modeling vehicle by spring-dashpot unit.

FINITE ELEMENT ANALYSIS

The finite element analysis adopted for pavement analysis is based on the classical theory of thick plates resting on two-parameter foundation that accounts for the transverse shear deformation of the plate. The formulation is based on the assumptions that deflections are small compared with the thickness of plate, and that a normal to the middle surface of the undeformed plate remains straight, but not necessarily normal to the middle surface of deformed plate. Four node, isoparametric rectangular elements with three degree of freedom per node (transverse displacement w, rotation about x axis θ_x and about y axis θ_y) are considered with independent bilinear shape functions are assumed for displacement and rotational degrees of freedom. The strain displacement transformation matrix [B] and constitutive relationship matrix [D] for plate element are defined as follows:

$$[B] = [B_1 \quad B_2 \quad B_3 \quad B_4] \quad and \quad [D] = \begin{bmatrix} D_b & \\ & D_s \end{bmatrix} \quad in \quad which$$

$$[B_i]=\begin{bmatrix} 0 & N_i^x & 0 \\ 0 & 0 & -N_i^y \\ 0 & N_i^y & -N_i^x \\ N_i^y & 0 & -N_i \\ N_i^x & N_i & 0 \end{bmatrix} \quad [D_b]=\frac{E t_p^3}{12(1-\nu^2)}\begin{bmatrix} 1 & \nu & 0 \\ \nu & 1 & 0 \\ 0 & 0 & \frac{1-\nu}{2} \end{bmatrix} \quad , \quad [D_s]=\frac{E t_p \kappa}{2(1+\nu)}\begin{bmatrix} 1 & 0 \\ 0 & 1 \end{bmatrix} \tag{1}$$

E is Young's modulus, ν is Poisson's ratio, κ is shear correction factor, and t_p is plate thickness. N represents shape function and superscript indicates derivative.

The force-deflection equation for plate-foundation element can be expressed as

$$[[k_1]+[k_2]+[k_3]]\{d\}=\{Q\} \tag{2}$$

where $[k_1]=\int_{-1}^{1}\int_{-1}^{1}[B]^T[D][B]\,|J|\,d\xi\,d\eta$ $\quad [k_2]=\int_{-1}^{1}\int_{-1}^{1}[B_2]^T G_p H [B_2]\,|J|\,d\xi\,d\eta$

$[k_3]=\int_{-1}^{1}\int_{-1}^{1}[N_w]^T k_s [N_w]\,|J|\,d\xi\,d\eta$ $\quad \{Q\}=\int_{-1}^{1}\int_{-1}^{1}[N_w]^T q\,|J|\,d\xi\,d\eta$

$[B_2]^T=\begin{bmatrix}[N^x]^T & [N^y]^T\end{bmatrix}$ ..(3)

The dynamic interaction between pavement and a moving vehicle/aircraft is taken into account by treating the vehicle/aircraft and the pavement as an integrated system. A simplified idealization involving a concentrated load supported by a linear spring-dashpot system is assumed to represent the aircraft. For the idealized system, the load $q(x,y)$ acting on the element due to vehicle-pavement interaction can be expressed as

$$q(x,y)=F_i\delta(x-\xi,y-\eta)+mg-m\ddot{w}-c_s\dot{w} \tag{4}$$

where F_i is the pavement-vehicle interaction force, w is transverse plate displacement, mg is the plate weight, $m\ddot{w}$ is the plate inertia force, and $c_s\dot{w}$ is the force due to foundation damping. In the above equation $\delta(x-\xi,y-\eta)$ denotes a Dirac-delta function which equals unity at $x=\xi$ and $y=\eta$, and zero elsewhere. Applying d'Alembert principle for vehicle

$$M_i\ddot{u}_i+c_i[\dot{u}_i-\dot{w}(\xi,\eta)]+k_i[u_i-w(\xi,\eta)]=M_i g \tag{5}$$

where M_i is the mass, u_i is the vertical displacement, c_i is the damping coefficient, k_i is the spring constant and (ξ,η) denotes the location of vehicle. The dynamic interaction force F_i can be expresses as

$$F_i=M_i g-M_i\ddot{u}_i \tag{6}$$

From above equations dynamic force equilibrium can be expressed as

$$[[k_b]+[k_s]+[k_f]]\{d\}=\int_{-1}^{1}\int_{-1}^{1}[N]^T\{[mg-m\ddot{w}-c_s\dot{w}][M_i g-M_i\ddot{u}]\delta(x-\xi,y-\eta)\}|J|\,d\xi\,d\eta \tag{7}$$

By expressing the derivative of plate deflection w in the right hand side in terms of nodal variable $\{d\}$, and by assembling the individual element matrices, the dynamic equilibrium equation can be expressed in the form

$$[k]\{d\}=[W]-[M]\frac{\partial^2}{\partial t^2}\{d\}-[C]\frac{\partial}{\partial t}\{d\}+\left[\tilde{N}(\xi,\eta)\right]^T M_i g-\left[\tilde{N}(\xi,\eta)\right]^T M_i\ddot{u}_i \tag{8}$$

$$\text{where} \quad [k] = \sum \{ [k_1] + [k_2] + [k_3] \} \qquad [W] = \sum \int_{-1}^{1} \int_{-1}^{1} [N]^T mg \, |J| \, d\xi \, d\eta$$
$$[M] = \sum \int_{-1}^{1} \int_{-1}^{1} [N]^T m \, [N] |J| \, d\xi \, d\eta \qquad [C] = \sum \int_{-1}^{1} \int_{-1}^{1} [N]^T c_s \, [N] |J| \, d\xi \, d\eta \tag{9}$$

$[M]$ is consistent mass matrix, $[C]$ damping matrix, $[W]$ load vector due to self weight. The tilde above $[N]$ denotes that the shape functions are evaluated for a specific element where the mass is located. Rearranging Eq (8) yields

$$[M] \frac{\partial^2}{\partial t^2} \{d\} + [C] \frac{\partial}{\partial t} \{d\} + [k] \{d\} = [W] + \left[\widetilde{N}(\xi, \eta)\right]^T M_i g - \left[\widetilde{N}(\xi, \eta)\right]^T M_i \ddot{u}_i \tag{10}$$

Similarly, the dynamic equilibrium equation of the aircraft suspension system can be transformed into following form

$$M_i \ddot{u}_i + c_i \dot{u}_i + k_i u_i = M_i g + c_i \left[\widetilde{N}(\xi, \eta)\right] \frac{\partial}{\partial t} \{d\} + c_i \left[\frac{\partial \widetilde{N}(\xi, \eta)}{\partial t} \right] \{d\} + k_i \left[\widetilde{N}(\xi, \eta)\right] \{d\} \tag{11}$$

Before solving above two equations of dynamic equilibrium, it is convenient to change the time variable t, by using position x of the vehicle as a pseudo-time variable. By applying Newmark-Beta integration method, the equations of dynamic equilibrium given by Eq (10) and (11) for pavement and vehicle, are transformed as follows:

$$\begin{aligned} &\{ [k] + C_0 [M] + C_V [C] \} \{d_i\} + C_0 \left[\widetilde{N}(\xi, \eta)\right]^T M_i u_i = [W] + \left[\widetilde{N}(\xi, \eta)\right]^T M_i g \\ &+ \left[\widetilde{N}(\xi, \eta)\right]^T M_i \left[v_m^2 (C_m) + a_m (C_n) \right] + v_m^2 [M] \{p_1\} + \left(a_m [M] + v_m [C]\right) \{p_2\} \\ &\left\{ -v_m c_i \left[\frac{\partial \widetilde{N}(\xi, \eta)}{\partial \xi} \right] - C_V c_i \left[\widetilde{N}(\xi, \eta)\right] - k_i \left[\widetilde{N}(\xi, \eta)\right] \right\} \{d_i\} + \{k_i + C_0 M_i + C_V c_i\} u_i \end{aligned} \tag{12}$$

$$= M_i g + v_m^2 M_i C_m + \left(a_m M_i + v_m c_i\right) C_n - v_m c_i \left[\widetilde{N}(\xi, \eta)\right] \{p_2\} \tag{13}$$

$$\text{where} \quad C_1 = 1/\beta h^2 \quad C_2 = 1/\beta h \quad C_3 = (0.5/\beta) - 1 \quad C_4 = \alpha/\beta h \quad C_5 = (\alpha/\beta) - 1$$
$$C_6 = 0.5h\{(\alpha/\beta) - 2\}; \quad C_0 = C_1 v_m^2 + C_4 a_m; \quad C_V = C_4 v_m; C_m = C_1 u_{i-1} + C_2 \dot{u}_{i-1} + C_3 \ddot{u}_{i-1}$$
$$C_n = C_4 u_{i-1} + C_5 \dot{u}_{i-1} + C_6 \ddot{u}_{i-1};$$
$$\{p_1\} = C_1 \{d_{i-1}\} + C_2 \{\dot{d}_{i-1}\} + C_3 \{\ddot{d}_{i-1}\} \quad \{p_2\} = C_4 \{d_{i-1}\} + C_5 \{\dot{d}_{i-1}\} + C_6 \{\ddot{d}_{i-1}\}$$

The unknown nodal displacements $\{d_i\}$ and u_i are computed by matrix inversion. Then nodal velocities and acceleration are calculated which are used in the computation of next time step. v_m and a_m represents the velocity and acceleration of moving aircraft, respectively. $|J|$ is determinant of the Jacobian matrix, h is the time step, β and α are the constants in Newmark-Beta integration method, H and G_p are thickness and shear modulus of shear layer, respectively, k is stiffness of vehicle and k_s is subgrade modulus for existing soil. $\widetilde{N}$ is the shape functions evaluated for a specific element where the mass is located.

RESULTS

A parametric analysis is conducted to study the effect of selected parameters on the dynamic response of concrete pavements. One slab section of 7.62 m x 3.81m has been considered in the analysis. It is usually assumed that the main landing gear carries 90%

of the total aircraft weight and the remaining 10% is assigned to the nose gear. Therefore, each gear in the main twin assembly carries approximately 343 kN. For simplicity, only the main landing gear represented by single suspended moving mass is considered in the analysis with the assumption of symmetry in longitudinal direction. Other properties for slab and suspension assumed in the analysis are reported below.

Pavement: Slab-7.62 × 3.81 m, E_p=2.48 × 10^7 kN/m^2, ν=0.15, density 2325 kg/m^3
t_p = 0.1524 m to 0.5334 m. Damping ratio 0.5%

Foundation: k_s= 8140 and 81400 kN/m^3, G_p=7000 kN/m^2 H = 0.0, 0.5, 1.0 m

Aircraft : k =17500 kN/m, Weight 343 kN, Damping ratio 0.5%

One of the important parameters that affect the level of the dynamic loading is the aircraft speed. Under the normal ground operations, the aircraft speed varies within the runway from about 5 to 70 m/sec during the takeoff and landing operations. A detailed study is carried to study the effect of velocity. Velocities are varied from 8 to 78 m/sec at the increment of 0.1 m/sec. Variations in maximum deflections with velocity for all pavement thickness ratios are presented in Figure 1.

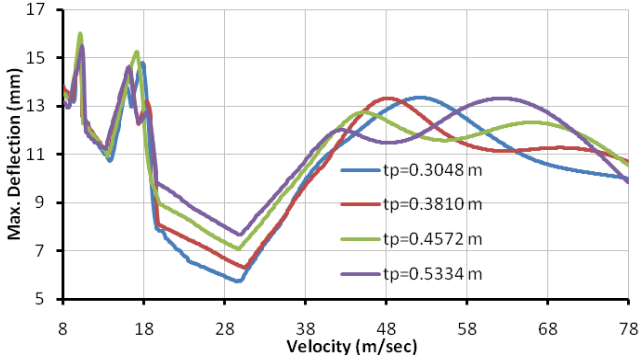

FIG. 1. Velocity- maximum deflection response curves (H = 0)

Two clear peaks were indicated in the graph similar to resonance phenomenon. Critical velocities V_1 corresponding to first peak are summarized in Table 1 along with maximum deflections. V_1 was found to be in the range of 10 to 11 m/sec. Range of V_2 was observed to be 16 to 18.4 m/sec. This is quite close to the value of 22.2 m/sec reported by Alvappillai et al. (1992) for maximum dynamic magnification. Range of V_3 was observed to be 42 to 52 m/sec. No definite trend was found out towards effect of pavement thickness when maximum deflections are considered.

CONCLUSIONS

The dynamic interaction between the moving load and the pavement has significant effect on pavement response. Study highlights the effect of dynamic loading due to aircraft speed. Two prominent speed zones are observed between 10 to 20 m/sec and 40 to 55 m/sec. Critical velocity V_1 was found to be in the range of 10 to 11 m/sec, and range of V_2 was observed to be 16.1 to 18.4 m/sec. This is in close agreement with the

value of 22.2 m/sec reported by Alvappillai et al. (1992) for maximum dynamic magnification.

Table 1. Critical Velocity and Maximum Deflection

	V_1 (m/sec)						Max. Deflection (mm)					
	k_s =8140 kN/m^3			k_s =81400 kN/m^3			k_s =8140 kN/m^3			k_s =81400 kN/m^3		
$H(m)\rightarrow$	0	0.5	1.0	0	0.5	1.0	0	0.5	1.0	0	0.5	1.0
t_p (m)												
0.1524	9.9	9.8	9.9	17.86	17.90	17.92	16.68	16.78	16.73	3.26	3.23	3.20
0.2286	10.0	10.0	10.0	18.56	18.58	18.60	15.49	15.31	15.18	2.76	2.74	2.73
0.3048	10.2	10.2	10.2	10.96	10.96	10.96	15.25	15.22	15.01	2.38	2.37	2.36
0.3810	10.0	10.1	10.1	10.60	10.60	10.60	15.39	15.40	15.38	2.18	2.18	2.17
0.4572	10.1	10.2	10.2	10.88	10.88	10.86	16.03	15.90	15.64	2.07	2.06	2.06
0.5334	10.4	10.5	10.5	18.42	18.42	18.42	15.49	15.03	14.57	1.99	1.99	1.98

REFERENCES

Alvappillai, A., Zaman, M. and Laguros, J. (1992). "Finite Element Algorithm for Jointed Concrete Pavements Subjected to Moving Aircraft." *Computers and Geotechnics*, Vol. 14: 121-147.

Genin, J., Ginsberg, J.H. and Ting, E.C. (1975). "A Complete Formulation of Inertial Effects in the Guideway-Vehicle Interaction Problem." *Journal of Sound and Vibration*, Vol. 38(1): 15-26.

Lewis, K.H. and Harr, M.E. (1969). "Analysis of Concrete Slabs on Ground Subjected to Warping and Moving Loads." *HRB*, Vol. 291: 194-211.

Mallik, A.K., Chandra, S. and Singh, A. B. (2006). "Steady-state response of an elastically supported infinite beam to a moving load." *Journal of Sound Vibration*, Vol. 291: 1148–1169.

Taheri, M.R. and Ting, T.C. (1989). "Dynamic Response of Plates to Moving Loads: Structural Impedance Methods". *Computers and Structures*, Vol. 33(6): 1379-1393.

Thompson, W.E. (1963). "Analysis of dynamic behaviour of roads subject to longitudinally moving loads". *HRB*, Vol. 39:1-24.

Ting, E.C., Genin, J. and Ginsberg, J.H. (1974). "A General Algorlthmfor Moving Mass Problems." *Journal of Sound and Vibration*, Vol. 33(1): 49-58.

Sawant, V. (2009). "Dynamic Analysis of Rigid Pavement with Vehicle-Pavement Interaction." *International Journal of Pavement Engineering*, Vol. 10(1): 63-72.

Sun, L. (2001). "Dynamic displacement response of beam on elastic foundation for moving load." *International Journal of Solids and Structures*, Vol. 38: 8869-8878.

Zaman, M., Alvappillai, A. and Taheri, M..R. (1991). "Dynamic analysis of concrete pavements resting on a two-parameter medium." *International Journal for Numerical Methods in Engineering*, Vol. 36:1465-1486.

Bearing Capacity Evaluation of Ultra Thin Reinforced Concrete Pavement Sections through Accelerated Pavement Testing and Modeling in South Africa

L du Plessis[1], P.J Strauss[2] and A Kilian[3]

[1]Research Group Leader, CSIR-Built Environment, PO Box 395 Pretoria 0001, South Africa: lplessis@csir.co.za
[2]Consultant, PO Box 395 Pretoria 0001, South Africa; pieterst@lantic.net
[3]Gauteng Department of Public Transport, Roads and Works, South Africa; Andre.Kilian@gauteng.gov.za

ABSTRACT: The CSIR Built-Environment, in conjunction with the University of Pretoria and the Cement and Concrete Institute of South Africa, developed a low cost option for the upgrading of unsurfaced (gravel) roads. The proposed solution is the placing of a thin layer of normal concrete reinforced with 5.6mm diameter steel with a mesh grid size of 200mm. This thin layer is placed on top of the existing unsurfaced road with minimal preparation to the existing road surface using labour-intensive construction methods.

Through full-scale trials this type of upgrading proved to be adequate for low-volume traffic applications (e.g. residential streets) as well as for higher-volume applications (e.g. bus routes). During the trials test sections were subjected to a total of over 700,000 ESALs over a period of 5 years without showing any deterioration.

In order to determine the structural capacity of this type of overlay full-scale Heavy Vehicle Simulator (HVS) tests were conducted. This paper summarizes the first results from the accelerated pavement testing (APT) tests and is aimed at building confidence in the use of Ultra Thin-layer Reinforced Concrete Pavement (UTRCP), with cognizance being taken of the pavement structure, support conditions, construction, climate and traffic.

INTRODUCTION

The upgrading of unsurfaced residential roads has become a priority for many metropolitan areas in South Africa. Coupled with this is the need to construct roads using labour-intensive construction techniques. One solution is the use of an ultra thin reinforced concrete pavement (UTRCP). UTRCP has been shown to offer good performance during a previous trial study (1,2) but a number of questions still remain to be answered, particularly with regard to the limits of application of this technology

(Bergh, A.O., McKay, A. Semmelink, C.J., Steyn, W.J.vdm., 2005; W.J.vdm. Steyn, P J Strauss, B D Perrie, and L du Plessis, 2005).

The primary objective of this project is to assess the performance of 50-mm thick UTRCP placed on various support conditions through accelerated pavement testing (APT), coupled with a laboratory-testing program. The aim is to determine the limits for safe application of the technology in South Africa. The outcomes of the project will also be used to update the South African design method for rigid pavements (cncPAVE) (Strauss P.J., Slavik, M. and Perrie, B.D., 2001).

This study is aimed at building confidence in the use of UTRCP, taking cognizance of the pavement structure, construction, climate and traffic, by providing practitioners with reliable design information.

EXPECTED BENEFITS

The use of UTRCP on roads offers multiple benefits by comparison with more conventional approaches. The benefits include:

- UTRCP is labour-friendly and is highly suitable for labour-based construction;
- Only simple, inexpensive construction equipment is required;
- Existing subgrade and alignment can be used;
- It can be used as an overlay on existing roads;
- It requires less lighting energy at night by comparison with bituminous surfaces because of the reflectivity of the surface; and
- Significant reduction in construction energy can be realised as the mix is hand-placed at ambient temperatures.

THE CONSTRUCTION OF THE UTRCP SECTIONS

The Ultra Thin Reinforced Concrete Pavement sections were constructed on a 130m long test section using a mix of 13mm and 9mm quartzite aggregate to achieve dense aggregate packing. High-strength cement (CEM I-42.5N) was used and the mix was reinforced with a steel mesh consisting of a 200 x 200mm grid size using 5.6mm diameter steel wire. The total thickness of concrete was 50mm and the steel was placed on the neutral axis, 25mm from the surface using plastic chairs. The mix was hand placed using shutters to control the width and thickness of the concrete. A double vibrating roller screed was used for compaction and the pavement was cured under plastic for 7 days to minimize differential shrinkage. The sections were constructed on the R80 Highway north-east of Pretoria, South Africa and Figure 1 shows some aspects of the construction process.

FIG. 1. The UTRCP Construction Process

The average 28-day cube crushing strength was 37.5 MPa (without the steel).

The UTRCP was placed on a prepared road bed consisting of various support types, which included a granular base section, a cemented base section, and sections with a 50mm of emulsion-treated base. One section was constructed using bottom dump ash (from a coal-fired power station) as a replacement for the quartzite aggregate. The aim of this was to determine the structural bearing capacity of the UTRCP under various support conditions with the aid of the HVS.

ENVIRONMENTAL INFLUENCE ON SLAB CURL AND WARPING

Prior to the start of APT loading (during the curing period), a set of measurements was taken to measure the slab curl and warping movements as a result of daily temperature fluctuations and differential shrinkage under the influence of the environment. Joint Deflection Measuring Devices (JDMDs) were installed immediately after placement of the concrete to record the vertical movements of the edges of the concrete slab. Thermocouples (TCs), which measured both top and bottom temperatures were also installed in the concrete at each JDMD location. The data captured during the first 23 days are graphically represented in Figure 2.

JDMD Placed at the Edge of the Concrete

This graph shows the maximum movements as captured by instrument JDMD 10. The instruments were installed as soon as the concrete had developed enough strength to carry the weight of the slugs of the various LVDTs.

Two distinct edge movements were identified:

a) The daily (elastic) up/down movement due to daily temperature variations. As the temperature increased during daytime, the concrete expanded elastically but, because the surface was hotter at the top (being exposed to the sun) than the bottom, the top expanded at a faster rate than the bottom, causing the longitudinal edge of the slab to curl downwards. This process was reversed at night when the top was cooler than the bottom, causing upwards slab movement along the edge of the concrete slab.

b) Slab warping. During the initial curing period in particular, a significant amount of shrinkage in concrete took place but, because the top was exposed to the environment, the degree of hydration was greater towards the top than the bottom of the slab. This differential shrinkage caused the longitudinal edge of the slab to curl upwards. This permanent non-recoverable movement is termed 'slab warping'. The degree of slab warping depends on environmental factors such as humidity, temperature and wind, as well as on the type of concrete and of the reinforcement.

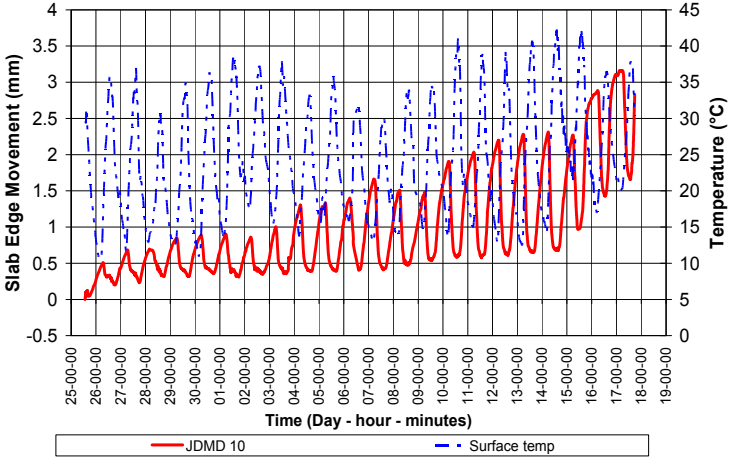

FIG. 2. Maximum slab edge movements and associated surface temperatures

Both these movements can be identified in Figure 2. Analysis of the first 23 days of curing showed that the maximum separation of the concrete from the base was 1.6mm during the day and increased to 3.1mm during the night. The data are summarized in

Table 1. Unfortunately data collection was stopped after 23 days to accommodate the HVS tests which followed directly afterwards.

Table 1. Summary of Slab Edge Movements Due to Environmental Fnfluences

Instrument	Permanent Warp (upward) (mm)	Daily Curl up (mm)	Daily Curl down (mm)	Total daily elastic curling movement (mm)
JDMD 10	2.30	0.80	0.70	1.50

Maximum surface temperature (Deg C)	42.40
Minimum surface temperature (Deg C)	10.50
Maximum positive temperature differential (top - bottom) (Deg C)	3.60
Maximum negative temperature differential (top - bottom) (Deg C)	-3.40

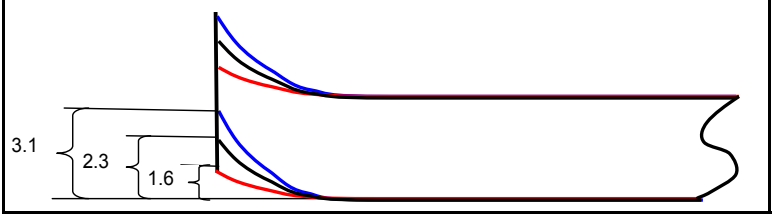

APT TESTING PLAN

In order to address the aims of this study a series of Heavy Vehicle Simulator tests (HVS) were planned as shown in Figure 3. The rectangular boxes indicate possible HVS testing areas. During the first phase of testing interior loading was applied but provisions have been made during the second phase of testing to evaluate the effects of edge loading as well.

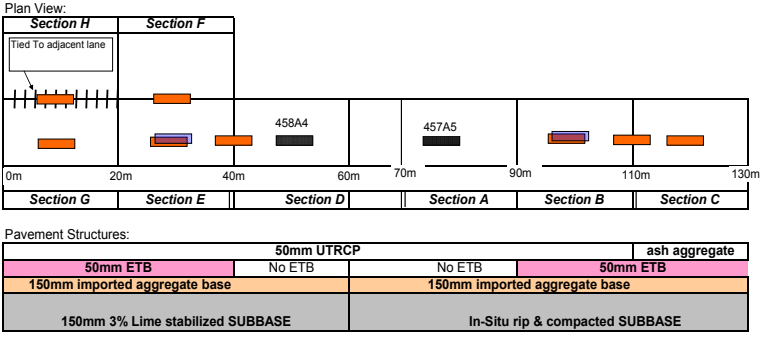

FIG. 3. Planned HVS testing areas

The main objectives of these tests can be summarized as:

- To assess the effects of various input parameters (i.e. type of aggregate, support conditions, longitudinal joints, traffic loading) on the structural integrity and performance of the UTRCP layer;
- To determine the structural strength across joints and transverse cracks as these are believed to be the weak areas in the UTRCP system; and
- To establish the success of patchwork and rehabilitation options in the event of the early UTRCP layer failure.

The rehabilitation of this type of pavement is of concern as localized failures, re-instatements due to utility cuts, and normal patchwork will be a reality. In order to address these issues, certain HVS testing will be conducted until complete failure has been observed. Those failed areas will then be patched using the standard fixing techniques for continuously reinforced pavements. The same areas will then be subjected to a second round of accelerated loading. This will be dealt with during the second phase of the UTRCP evaluation and is not discussed in this paper.

HVS RESULTS

To date eight tests have been conducted (tests 457 through to 464A4) although details of only the first two tests are presented in this paper. These tests (457A5 and 458A4) are according to the layout in Figure 3. A picture of the HVS with its dual wheel loading configuration can bee seen in Figure 4. The HVS is equipped with standard dual truck tyres and ½ axle loads (40kN) were applied to all the test sections simulating the effects of a standard 80kN axle load.

FIG. 4. HVS with its dual wheel loading configuration

The first test (457A5) was conducted on a natural gravel base section (Figure 3). The test pad was in the middle of the pavement (interior loading) and channelized traffic was applied. Although, edge loading would have resulted in a reduction of structural life of the UTRCP pavement, the first series of tests were executed to simulate real traffic without the aggressive concentrated edge loading effect. The test plan (Figure 3) makes provisions for edge loading tests to study the influence of this type of loading on the structural capacity of the UTRCP pavement system, but this paper is limited to the results stemming from interior loading only.

A total of 2 million standard ½ axle loads (40kN) were applied in the dry state to the section without any signs of structural failure. During this testing period (31 October 2008 and 15 April 2009) 900mm of rain fell at the testing site. After 2 million load applications only a few transverse cracks could be seen on the surface. Due to time and budget constraints it was decided to aggressively add water to all cracks in the hope to accelerate the deterioration of the pavement. A normal garden irrigation drip system was installed at all visible cracks. Water application at a rate of approximately 5 litres per hour and was done in a cyclic manner, i.e. two days of continuous water followed by five dry days. This was done to simulate real field conditions where naturally dry and wet periods occur. The total water added simulated an annual rainfall of approximately 2 000 mm which is more than the extreme maximum yearly rainfall in South Africa.

The section failed in its third watering cycle after a total of 2.35 million load applications. Figure 5 shows the peak elastic surface deflections with repetitions. This amount of traffic is significantly more that the total amount of traffic expected to drive over a residential street throughout its design life (20 years).

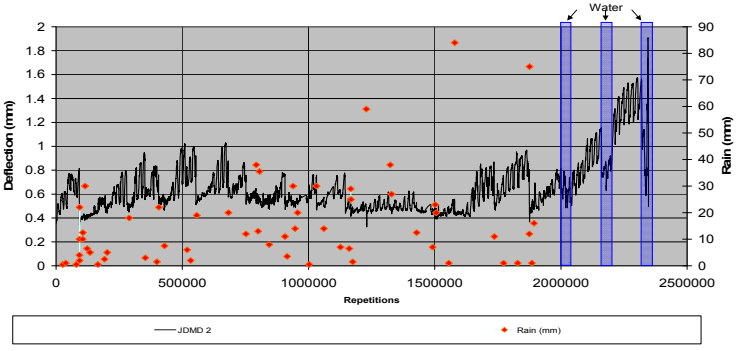

FIG. 5. 40kN deflections and rainfall data

The variations in the data are due to daily temperature and rainfall effects. From the graph it is evident that no significant degree of deterioration in terms of deflections could be detected until the start of the watering cycle (after 2 million repetitions). The rapid increase in deflections after that is due to a loss of support after significant degree of pumping was observed due to the application of surface water to the cracks.

Test 458A4: Testing on the lime stabilised subbase

Test 458A5 was conducted on a 3% lime stabilised subbase section (see Figure 3). Similar to the first test, channelized loading was applied to the middle part of the pavement.

No significant degree of deterioration was observed during the dry testing part of the test. After 1.150 million load repetitions (80kN axle load) water was added to all existing cracks to accelerate the deterioration similar than the previous test. The

section failed after a total of 1.243 million repetitions. Figure 6 shows the localized failures observed at both testing sections.

457A5: Failure after 2.235 million reps

Test 458A4: Failure after 1.243 million reps

FIG. 6. Failure patterns at test sections 547A5 and 458A4

MODELING THE BEHAVIOR OF THE PAVEMENT

The purpose of modelling was to develop a model which could be used for the design of a UTRCP and to update the design procedures in cncPAVE (3).

cncPAVE is a mechanistically based design method developed in South Africa to facilitate interaction with the mechanistic flexible pavement design methods currently in use, and to promote use of concrete to rehabilitate flexible pavements. cncPAVE, a user friendly computer program, is based on models developed from finite element and multi-layer evaluations. The design method has been calibrated against actual performance of different concrete pavement sections (roads and streets) under normal traffic loading, as well as under the HVS.

The UTRCP pavement that was modelled and tested consisted of a thin reinforced concrete pavement on top of a layered system. Properties of the model include:

- Generation of a generic finite element model of a representative piece of road provided with a reinforced concrete slab on top and various layers underneath;
- Application of wheel loads as circular patches of constant pressure moving at a given speed; and
- Non-linear dynamic FE analyses using explicit time integration.

The results from the analyses included principal stress values at the top and bottom of the concrete, as well as vertical deflections of the concrete. The results were presented as contour fringe plots as well as in tabular form.

The mesh of the model was selected per layer to be finer at the top and coarser at the bottom in order to reduce computational effort. The finest mesh was directly in the wheel path. At both ends of the wheel path, for a distance of about 1m, the mesh was coarser, allowing basically for the wheel speed to increase to a constant value in these areas.

The boundary conditions were such that all displacements at the bottom (x, y and z directions) were fixed. On the plane of symmetry at y=0, the displacement in the y direction was constrained to zero. At the ends, as well as along the sides, non-reflective boundaries were prescribed, meaning that pressure waves that propagated radially outwards from the wheel positions were not reflected back into the modelled part.

Two circular load patches, 200mm in diameter, simulated the dual-wheel loading of a typical truck. A surface pressure of 700 kPa was applied to the top concrete surface along a path that ran at a distance of 900mm from the plane of symmetry.

A transverse crack in the concrete was modelled at the center of the wheel path over the full width of the model. The crack was through the total thickness of the concrete and was modelled in such a way that compression forces, but not tension forces, could develop on the two adjacent surfaces of the crack. Vertical shear could also be carried in the crack, which meant that there was no vertical slip between the surfaces of the crack. The reinforcement was modelled as a continuous sheet of steel in both the x and y directions.

In order to create a void below the slab, the interlayer stiffness was reduced to practically zero and, for the transition areas at both ends of the void area, reduced stiffness were introduced by linear interpolation.

A non-linear dynamic analysis was required since the wheel patches are moving objects in the wheel path and sliding contact is defined between the wheels and the concrete surface. At the simulated crack in the concrete non-linear contact was also defined between the surfaces of the crack.

The results of the analyses were available after a run as time history displacements, strains and stresses. These could be presented as time history plots or as fringe or contour plots at selected time intervals. Deformed plots scaled to enlarge the actual deformation were also generated.

In view of the time and cost of using sophisticated Finite Element Analysis (FEA), a limited number of cases were evaluated. The data generated by the FEA was used to re-calibrate the equations used in cncPAVE and cncPAVE was subsequently used as a tool to illustrate the relative effect of different parameters on the performance of a UTRCP. Figure 7 shows the reliability of the predicted maximum tensile stress on the surface of the pavement using cncPAVE compared to the values generated by FEA. The correlation coefficient R^2 for the data in Figure 7 is 0.91.

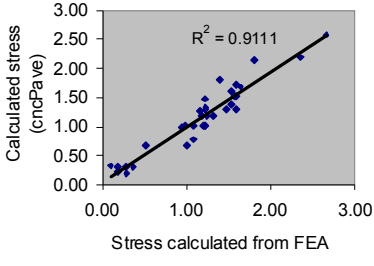

FIG. 7. Comparison between FEA and cncPAVE calculated tensile stress

MODE OF FAILURE

Combinations of FEA results and cncPAVE equations can now be used to explain the behaviour of UTRCP as observed on the test sections under HVS testing and to establish the consequences if parameters that may vary during the design, construction and loading of a UTRCP.

The modelling and the output of program cncPAVE can be used to establish the possible mode of failure and to demonstrate the sensitivity of certain characteristics of UTRCP:

1. Transverse cracks will develop as a result of shrinkage. It is also inevitable that transverse construction joints will be introduced into the pavement. Since steel bar reinforcement will be going through this joint, the joint or crack can be regarded as a hinge that allows shear but no moment to be transferred across.
2. High stresses develop when a wheel load crosses from one side of the crack or joint to the other side. According to FEA analyses the critical stresses are tensile stresses at the bottom of the pavement about 450mm from the crack, those between the wheel loads at the top of the pavement and the compression stress at the top of the crack when the wheel is crossing the crack. It was found that the tensile stress is at its greatest about 450mm away from the crack and that a second crack will rapidly develop due to the high tensile stress at that point. The crack itself may initially not be visible but the stiffness of the slab is reduced, resulting in an increase in deflection and in a greater vertical stress at the top of the supporting layer. At the same time high compression stresses develop at the top of the slab in the crack, resulting in spalling and a risk of loss of shear resistance, as well as in a risk of water entering the slab. The crack between the wheels will later extend from the surface into the pavement itself.
3. Water that enters the supporting layer through the spalled crack results in a loss of bond and, with an increase in deflection, a void will develop between the slab and the supporting layer. The effect of a loss of bond is shown in Figure 8 below where the maximum stress at the surface of the slab, calculated with cncPAVE, is plotted as a function of bond and crack width. Figure 9 indicates the effect of the void size once bond between the slab and the supporting layer is lost. The crack widths in both Figures 8 and 9 are used to indicate the loss of shear and thus load transfer at the crack.

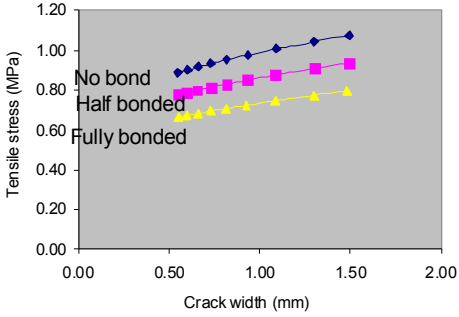

Figure 8. Maximum tensile stress at the surface as a function of crack width and bond between slab and support layer

The FEM analysis shows that the estimated pavement life for this type of structure is approximately 2 million 80kN load applications.

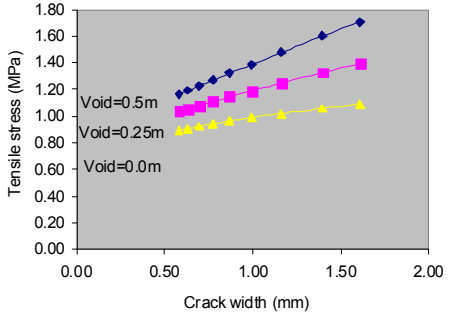

FIG. 9. Maximum tensile stress at the surface as a function of crack width and the size of the void between the slab and the supporting layer

CONCLUSION

This aim of this study was to characterize the structural performance of a 50mm thick Ultra Thin Reinforced Concrete Pavement under various types of realistic support conditions with the aid of the Heavy vehicle Simulator.

Early indications are that this type of structure is prone to curling and warping. Separation of over 3 mm between the bottom of the slab and the base along the longitudinal edge of the test section was recorded. Special attention will be required to mitigate the harmful effects of the loss of bond between the concrete and the support structure.

Through APT testing is has been shown that this type of pavement has exceptionally good performance if used on a low volume road such as a residential

street. Even in the wet state the pavement type should last its design life (20+ years of traffic). The weak point of the system is at cracks and construction joints where the ingress of water can lead to excessive pumping and early failures. It is postulated that the UTRCP overlay system will perform even better if placed on a less water sensitive base material that is less prone to pumping and subsequent loss of support.

The visual and structural evaluation of the pavement ties in with the predictions from the dynamic Finite Element Analysis.

ACKNOWLEDGEMENTS

This HVS research is supported by the Gauteng Department of Public Transport, Roads and Works (GDPTRW) and their contribution towards this study is acknowledged.

REFERENCES

Bergh, A.O., McKay, A. Semmelink, C.J. and Steyn, W.J.vdm. (2005). "Roodekrans thin concrete experiment sections 4, 5 and 6: Continuously reinforced thin concrete pavements." Paper presented at the *South African Transport Conference*, July 2005, Pretoria, South Africa.

W.J.vdm. Steyn, P J Strauss, B D Perrie, and L du Plessis. "Roodekrans trail sections: The role of structural support under very thin jointed CRCP pavements subjected to heavy traffic." *9th International Conference on Concrete Pavements*, August 2005, Colorado Springs, USA

Strauss P.J., Slavik, M. and Perrie, B.D., 2001. A mechanistically and Risk Based Design Method for Concrete Pavements in South Africa, *Proceedings of the 7th International Conference on Concrete Pavements*, September 2001, Orlando, Florida, USA.

Comparison and Analysis Method for Identifying the Voids Beneath Concrete Pavement

Zhong Yan-hui[1], Zhang Bei[2], Wang Fu-ming, Liu Yong, Qi Yue-hua

[1]Associate Professor, Ph.D, School of Water and Environment Conservancy, Zhengzhou University, Zhengzhou, Henan, 450002, P.R.China, zhong_yanhui@163.com
[2]Professor, Ph.D, School of Water and Environment Conservancy, Zhengzhou University, Zhengzhou, Henan, 450002, P.R.China, beizhang@126.com

ABSTRACT: Voids beneath slab is one of the common distresses of cement concrete pavement, which seriously influences the service ability and the tired life-span of the cement concrete pavement, and the Falling Weight Deflectometer(FWD) gets more and more applications on identifing the voids beneath the cement concrete slab because of its advantages such as speediness, nondestructiveness, etc. The formula for calculating the stresses, strains and deflections of the PCC pavement slab are deduced for different void shapes, and the displacement calculation models of the slab are established for winkler foundation, then the displacements for different void size and position are solved, and also the deflection basin curves are simulated. Through contrasting the deflection curves with voids and without voids beneath slab, the comparison analysis method for identifying the voids beneath slab is put forward based on the FWD measured deflection data. By applying this method in engineering, it is showed that it is a brief and effective method for evaluating the voids for PCC pavement. The achievements of this paper offer a new method and theoretic support for identifying the voids of concrete pavement.

INTRODUCTION

Cement concrete pavement, which is a kind of high stiffness, strong load dispersal ability and good stability surface structure, has been widely used due to its improving technical and economic advantages (Lei, 2002). However, many kinds of various distresses will be arised to this kind of pavement in the course of its application and voids beneath slab is a common one. Lots of experiments and theoretical calculations show that the local voids are abound beneath cement concrete pavement slab, especially in cement concrete pavement which is on the basic of fine-grained materials. Voids are extremely detrimental for slabs to bear stress, especially in the angle and the side of the site (Tang, 1992). Under the influence of the wheel loads, the stress state is similar to cantilever beam, which produces too much stress, strain and vertical deformation, and easily causes rupture and fragmentation damage in the cement concrete slabs. Therefore,

how to judge the location of the void as well as the degree in the slabs accurately becomes the key issue for the highway maintenance department to carry out road maintenance work.

THE CAUSES AND FORMATION MECHANISM OF VOIDS

The warping deformation is always occured to cement concrete pavement under the environment factors and repeated vehicle loads. The edge, the central part or the cube corner of the slabs may form voids because of the disengagement from the upper surface of the foundation. Meanwhile, the cube corner of the slabs may also form voids because the base materials bear pressures which lead to cumulated plastic deformation. Rainwater pass through cracks and slab edges then seep into the bottom, and water pressure which formed under the repeated vehicle loads flowed with high speed between the bottom cracks and the edges. The top surface of the base is flushed, the fine particles are taken to the road side from the cracks and the slab edges, then mud is produced. With the fine particles are taken out continuously, the voids are formed under the slabs. The voids beneath the slabs were further expanded due to mud, which led to the cement concrete slab fracture breakage under the heavy vehicles.

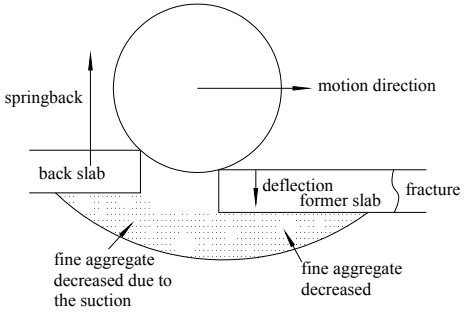

FIG.1. Principle of Void Formation

MODEL OF VOIDS UNDER CEMENT CONCRETE SLABS

The mechanics analysis of cement concrete slab with voids

(1). Deflection calculation of rigid pavement slabs under rectangular voids conditions

The mechanics analysis of cement concrete slab where the voids developed at the angle, may be regarded as elastic thin plate force problem with part of no support (void areas) and part of elastic support(no voids and the support from the base) (Zhong, 2007; Yao, 1997).

Assuming that the voids are rectangular shape under the slabs, the critical plane is fixed boundary and the other three sides are free surfaces, the problem can be simplified as the internal force and deflection for cantilever beam. C（x_0,y_0）is for the center of a circle of uniformly distributed load, a for its radius, L and LAB for the vertical length

and horizontal length of the voids slab respectively. AB cross section as shown in Figure 2 is the void critical plane. The distance from the center coordinates to any cross section is as follow: Lce = x-x_0. According to the theory of elastic thin plate, the deflection of the left beam can be calculated from equation (1).

$$v = (x_0 - x)tg[\frac{6\mu P\pi a^2 z^2}{EL_{AB}h^3} - \frac{6P\pi a^2 (L - x_0)^2}{EL_{AB}h^3}] + \frac{4P\pi a^2 (L - x_0)^3}{EL_{AB}h^3} \quad (1)$$

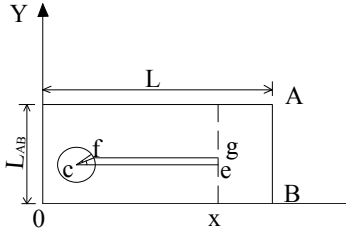

FIG.2. The rectangular voids slabs under circular uniform load

(2). Deflection calculation of rigid pavement slabs under triangle voids conditions

Assuming that the voids are triangle shape under the slabs, the critical plane is fixed boundary and the other two sides are free surface. C（x0,y0）is for the centre of a circle of uniformly distributed load, a for its radius, Lz and Lh for the vertical length and horizontal length of the voids slab respectively. The distance from the center coordinates to any cross section is as follow: Lcd = x-x0. According to the theory of elastic thin plate, the deflection of the left beam can be calculated from equation (2).

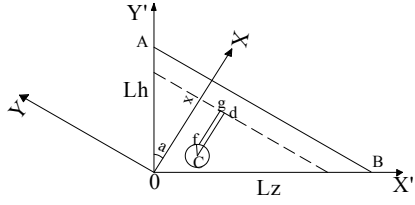

FIG. 3. The triangle voids slabs under circular uniform load

$$v = (x_0 - x)tg[\frac{6\mu P\pi a^2 z^2}{E(\frac{L_z}{L_h} + \frac{L_h}{L_z})h^3 x_0} - \frac{6P\pi a^2 (L_h \cos\alpha - x_0)^2}{E(\frac{L_z}{L_h} + \frac{L_h}{L_z})h^3 x_0} - \frac{4P\pi a^2 (L_h \cos\alpha - x_0)^3}{E(\frac{L_z}{L_h} + \frac{L_h}{L_z})h^3 x_0^2} + \frac{4P\pi a^2 (L_h \cos\alpha - x_0)^3}{E(\frac{L_z}{L_h} + \frac{L_h}{L_z})h^3 x_0}$$

(2)

The finite element model of cement concrete slab with voids

The foundation stiffness matrix embodies the elastic foundation supporting the pavement slab in finite element model. So, how to deal with the voids problem is transformed to modify to the foundation stiffness matrix (Zhou, 2007; Wang, 2003;

Zhong, 2009; Zhang, 2009; Ying, 2001). In this paper, Winkler foundation is used and the unit control equation is as follow:

$$([K]^e + [K']^e)\{\delta\}^e = \{F\}^e \quad (3)$$

From equation (3), it is seen that the ground reaction force on the slabs is reflected in the foundation stiffness matrix. The formula for element stiffness matrix in Winkler foundation is as follow.

$$[K']^e = k_0 \iint_{\Omega} [N]^T [N] \mathrm{d}x\mathrm{d}y \quad (4)$$

where, Ω is unit area, k_0 is the reaction modulus in Winkler foundation.

From the equation (4), it is seen that if the slabs are completely contact with foundation in unit region, the foundation stiffness matrix $[K']^e$ is the integral result of the entire unit area. If the unit areas exists voids, the foundation stiffness matrix should deduct the results of stiffness integral of the voids areas, because the ground reaction force only exists in the contact areas. Accordingly, the formula of element stiffness matrix under Winkler foundation voids can be established.

$$[K']^e = k_0 \iint_{\Omega} [N]^T [N] dxdy - k_0 \iint_{\Phi} [N]^T [N] dxdy \quad (5)$$

where, Φ refers to the voids areas.

THE COMPARATIVE ANALYSIS METHOD OF VOIDS IDENTIFICATION BASED ON FWD

The basic principle of comparative analysis

The method of identifying void in this paper is based on the measured deflection basin curves to evaluate the voids beneath the slab corner. The principle of the method is: the deflection of the concrete pavement slab of uniform support with load decreasing while the distance between the deflection point and the load point increasing. It shows that the void exists beneath the slab. The theory is shown in Fig 4.

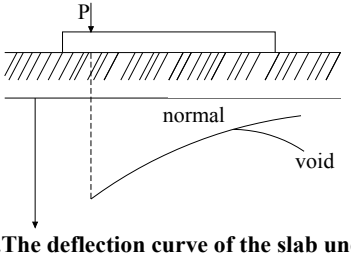

FIG. 4 .The deflection curve of the slab under load P

Procedures of comparative analysis method

FORTRAN is used to compile the program in this paper. In the program, the slab void problem is transformed through modifying the foundation stiffness matrix. Finally,

the deflection of concrete pavement under the condition of void slab is obtained , the deflection curves are drawn according to the calculation results. Then the character of the deflection curves under the condition of foundation void is obtained through comparing and analyzing the curves. Specific steps are as follows:

(1) Determine the location and size of voids, modify foundation slab total stiffness matrix.

(2) Using the program to simulate FWD load, as shown in figure 5, D1~D7 represent the position of seven sensors respectively, then the deflections of the position of seven sensors are calculated through the program.

(3)To deal with the displacement of simulated sensors and draw deflection basin curve by excel.

(4) According to contrasting the deflection basin curves of healthy foundation with void foundation, the general characteristics of foundation voids deflection basin curves are obtained.

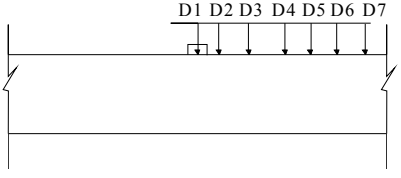

FIG.5. The loading mode and the location of the sensor array in the slab

THE ENGINEERING APPLICATION

A rigid pavement is a square plate with 5 meters long, 0.2 m thick. Its elastic modulus was 2.6e4 MPa, Poisson ratio was 0.16, the modulus of the foundation response 5.0e3 Pa, the voids at the slab edge are 0, 1.0m×1.0m, and there are 30KN, 60KN and 90KN loading on the slab center respectively, with reflection radius is 0.3m.They can be simplified as concentrated load. Using 10×10 grid to divide, the calculation results are shown in table 1 to 3, compared results are shown in figure 6 to 9.

Table 1. The Calculated Results of Plate Displacement (F = 30KN)(Units:μm)

Coordinates / voids size	(2500, 2500)	(2700, 2500)	(3000, 2500)	(3400, 2500)	(3650, 2500)	(3900, 2500)	(4200, 2500)
1.0×1.0	85.6	79.6	72.9	64.6	55.1	45.9	56.2
0	85.9	79.6	72.6	64.9	55.2	45.9	43.6

Table 2. The Calculated Results of Plate Displacement (F=60KN)(Units:μm)

Coordinates / voids size	(2500, 2500)	(2700, 2500)	(3000, 2500)	(3400, 2500)	(3650, 2500)	(3900, 2500)	(4200, 2500)
1.0×1.0	197.3	185.6	172.5	159.9	153.3	142.3	150.2
0	197.6	185.4	172.5	156.0	153.9	142.8	140.5

Table 3. The calculated results of plate displacement (F=90KN)(Units:μm)

Coordinates / voids siz	(2500, 2500)	(2700, 2500)	(3000, 2500)	(3400, 2500)	(3650, 2500)	(3900, 2500)	(4200, 2500)
1.0×1.0	301.5	282.4	263.2	240.2	220.9	200.6	215.6
0	301.8	283.9	264.8	240.5	222.6	201.3	198.6

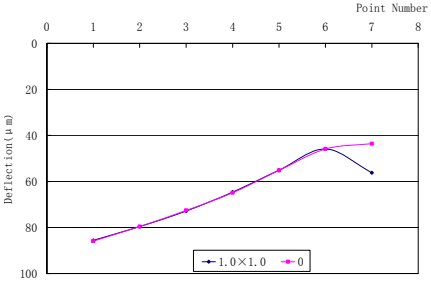

FIG. 6. The deflection basin curves when F=30KN

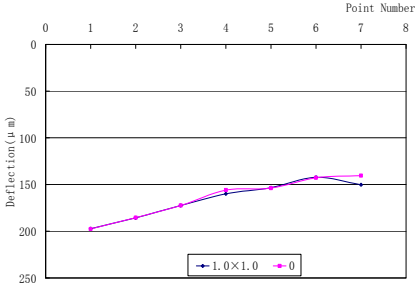

FIG.7. The deflection basin curves when F=60KN

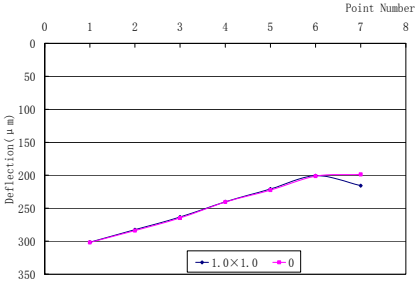

FIG.8. The deflection basin curves when F=90KN

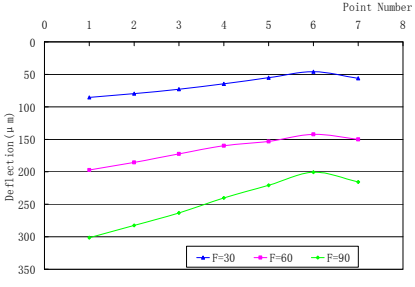

FIG.9. The deflection basin curves when the void size is certain but the loads are different

From the diagrams above, it is shown that the deflection value increases correspondingly with the load increasing when the voids sizes are certain. In this example, the whole data in deflection basin curves increase, from which the deflection increases from 85.6 to 197.3 at loading point when the load increases from 30KN to 60KN. So it can be seen that the load has a significant influence on deflection. When the voids sizes are certain, the deflection value increases correspondingly at the location of the voids with the load increasing. For example, when the load increases from 30KN to 60KN, the deflection value at the location of the voids increases from 56.2 to 150.2, which increases nearly three times, but the general trend of the deflection basin curves are basically the same. It is proved that the comparison and analysis method for identifying the voids of concrete pavement mentioned in this paper is feasible.

CONCLUSIONS

1. The formulae of the calculating the deflections under different void models are established.
2. Considering rigid pavements as thin elastic slabs, displacement calculation model is established under the condition of foundation void aiming at Winkler foundation, based on thin plate theory of elastic foundation. This method can accurately simulate the deflection basin curve, and is the premise and foundation to identify the void of rigid pavement slab.
3. According to comparing the deflection basin curves of healthy foundation to that of foundation with voids, the comparison and analysis method for identifying the voids beneath concrete pavement is put forward based on FWD measuring deflection basin curve. The engineering example shows that it is a simple and effective method to evaluate the voids beneath rigid pavement slab.
4. The research results not only provide a new thought and theoretical basis to evaluate the voids beneath rigid pavement slab, but also offer the technical support for making scientific and reasonable maintenance measures, which has theoretical significance and engineering value.

REFERENCES

Lei, L.. (2002). “Cement Concrete Pavement Void Plate and Grouting Technique Research.” Chang-an university Dissertation. China. pp 1-4.

Tang, B. (1992). “Rigid Pavement Evaluation and Analysis of the Slab Condition.” China Journal Daily. Vol. 5(1):40-44.

Wang, T.,Wang, F.,Wang, Z. (2003). “Modulus Back Analysis and Void Identification of Jointed Slab on Elastic Foundation.” Rock and Soil Mechanics. Vol. 24(4).

Yao, Z. (1997). “Cement concrete pavement design.” Anhui science and technology publishing house. China.

Ying, R., Zhang, Q. (2001). “Assessment of Separate State between Concrete Slab and Ground Base by FWD.” The old road monitoring and evaluation (cover face) and FWD Application technology Proceedings.

Zhou, Y.,Tan, Z., Liu, B. (2007). “Loading Stresses in Cement Concrete Pavement Slab with Void Underneath.” Journal of Tongji University (Science Edition), Vol. 35(3):341-345.

Zhong, Y., Zhang, B., Qi, Y. (2007). “Mechanical Analysis of PCC Pavement Slab Under Void Condition.” Subgrade Engineering. Apr. (4):26-27.

Zhong, Y., Zhang, B., Liu, Q., Wang, F. (2009). “Theoretical Research on Three Points Regression Method for Identifying the Voids of Concrete Pavement.The 5th International Conference on Natural Computation (ICNC'09) & The 6th International Conference on Fuzzy Systems and Knowledge Discovery (FSKD'09). Tianjin. Vol.1. pp341-345.

Zhang, B., Liu, Q., Zhong, Y., Wang, F. (2009). “Analysis of Dynamic Response of Rigid Pavement Deflection under FWD Load. Journal of Highway and Transportation Research and Development. Vol.26. No.7. pp33-37.

Estimation of Cement Concrete Pavement Slab Void Ratio Based on FAHP Method

Sheng Zeng[1] and Jia Xu[2]

[1]Professor, School of Traffic and Transportation Engineering, Changsha University of Science and Technology, Hunan Changsha, 410076, P. R. China; (86) 731-82309896; zszs35@sohu.com
[2]Graduate Student, School of Traffic and Transportation Engineering, Changsha University of Science and Technology, Hunan Changsha, 410076, P. R. China; (86) 731-82309896; jilinxujia@sina.com

ABSTRACT: Slab void is one of the most serious diseases. Maintenance workers need to repair them in time otherwise the whole slab will be damaged. It is very important to ensure the engineering quantity in maintenance. The pavement diseases analysis model relating to void have been established and the weight are calculated by FAHP. Heavy traffic loads have an effect on void, thus the traffic grade affection coefficient ξ to modify the calculation model has been introduced in order to meet the practice. Damage blocks are multiplied by corresponding weight and traffic grade affection coefficient, and then the void ratio is the sum blocks calculated divided by the whole blocks. The results of test section in Hunan expressway show that void ratio estimation by FAHP is contiguous to that by FWD (Falling Weight Deflectometer). In view of this, the method has good practical significance in void slab treatment plan.

INTRODUCTION

The CCP slab void is one of the most common diseases which results in the structural damage easily, such as crushed plates and faulted slabs etc. (Tang, 1992). All these damages reduce the driving comfort and the road service cycle. Slab bottom grouting is an effective way for void treatment, so the engineering quantity in maintenance plan depends on the void ratio. Nowadays, the main method of void detection is FWD, but the cost is high and the detection cycle is long, thus the equipment test is always behind the maintenance. In our practice experience, a method to solve the problem has been set up.

ESTABLISHMENT OF FAHP

After multiple comparison among the influence factors have been made by experts, the fuzzy judgment matrix $A=(a_{ij})_{n\times n}$ can be gotten. If $a_{ii}=0.5$ and $a_{ij}+a_{ji}=1$ ($i, j=1, 2, \ldots, n$) , A is fuzzy complementary judgment matrix. Scale method is shown in Table 1 (Jiang et al., 2007). If $a_{ij}\in[0.1, 0.5)$, it means that x_j is more important than x_i.

Table 1. 0.1~0.9 Scale Method

Scale	0.5	0.6	0.7	0.8	0.9	0.1,0.2 0.3,0.4
Definition	Equal Importance	Slight Importance	Obvious Importance	Special Importance	Top Importance	Opposite Comparison

Reference (Xu, 2001) has given the general formula for the weight of fuzzy complementary judgment matrix:

$$W_i = \frac{\sum_{j=1}^{n} a_{ij} + \frac{n}{2} - 1}{n(n-1)},\ i = 1, 2, \cdots, n \tag{1}$$

If A=$(a_{ij})_{n\times n}$ and $B=(b_{ij})_{n\times n}$ are both fuzzy complementary judgment matrix, compatibility index $I(A, B)$ is shown as Formula (2) (Chen et al. , 2004):

$$I(A,B) = \frac{1}{n^2}\sum_{i=1}^{n}\sum_{j=1}^{n}\left|a_{ij} - b_{ij}\right| \tag{2}$$

If $W=(W_1, W_2, \ldots, W_n)^T$ is the weight vector of fuzzy complementary judgment matrix A, and $\sum_{i=1}^{n} W_i = 1$, $W_i \geq 0$ (i=1, 2, …, n), taken $W_{ij} = \frac{W_i}{W_i + W_j}$ $(\forall i, j = 1, 2, \cdots, n)$, the characteristic matrix W^* is:

$$W^* = (W_{ij})_{n\times n} \tag{3}$$

When the compatibility index $I\ (A,\ W^*) \leq \alpha$, the judgment matrix is regarded as satisfying consistency, and generally α=0.1.

If there are k experts，the consistency test need two steps:

(1) Test consistency of m judgment matrixes, $I(A_k, W^{(k)}) \leq \alpha$, k=1, 2, …, m;

(2) Test satisfying consistency among the judgment matrixes, $I(A_k, A_l) \leq \alpha$, $k \neq l$; k, l=1, 2, …, m.

As conditions (1) and (2) are satisfied, the weight matrix can be gotten as follows (Ji et al. , 2006):

$$W = [W_1, W_2, \ldots, W_n],\ W_i = \frac{1}{n}\sum_{k=1}^{m} W_i^{(k)},\ i = 1, 2, \cdots, n \tag{4}$$

EVALUATION INDEXES SELECTION

Several pavement damages connected with slab void as the evaluation indexes have been selected, based on JTJ073.1-2001 and JTG H20-2007 two Chinese standards. Void appears while there are the damages such as faulted slabs, pumping, bow-up generally. The weight of these three damages is taken 1 and they are neglected in AHP calculation model.

The AHP evaluation model is established as Figure 1 except faulted slabs, pumping, and bow-up.

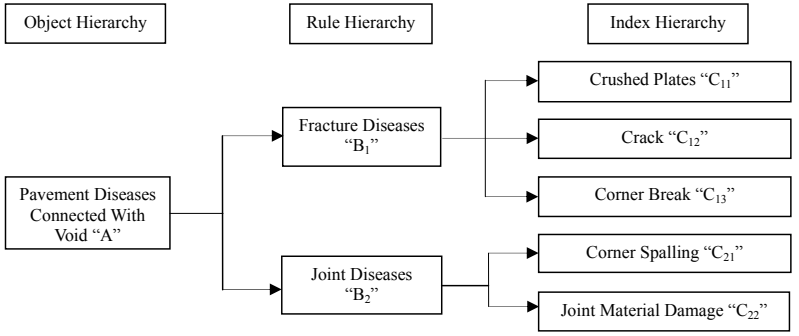

FIG. 1. AHP model of CCP slab void

RULE HIERARCHY WEIGHT CALCULATION

Fuzzy complementary judgment matrix given by the first expert:

$$A_1 = \begin{array}{c} \\ B_1 \\ B_2 \end{array} \begin{array}{c} \begin{array}{cc} \textit{criterion}\ B_1 & B_2 \end{array} \\ \begin{bmatrix} 0.5 & 0.8 \\ 0.2 & 0.5 \end{bmatrix} \end{array}$$

According to Formula (1) and (3): $W_1 = [0.650 \quad 0.350]$, $W_1^* = \begin{bmatrix} 0.5 & 0.650 \\ 0.350 & 0.5 \end{bmatrix}$.

According to Formula (2), $I\ (A_1,\ W_1^*) = 0.075 < 0.1$, therefore A_1 is satisfying consistency and W_1 is reasonable.

Similarly, the weight matrix by the second expert is obtained: $W_2 = [0.700 \quad 0.300]$; and the third expert: $W_3 = [0.700 \quad 0.300]$. The consistency test among A_1, A_2, A_3 are satisfied. According to Formula (4), W_1 is gotten as followed.

$$W_1 = [\frac{1}{3}(0.650+0.700+0.700) \quad \frac{1}{3}(0.350+0.300+0.300)] = [0.683 \quad 0.317]$$

INDEX HIERARCHY WEIGHT CALCULATION

Similarly, the weight matrixes are obtained as follows.

(1) Weight matrix of fracture diseases: $W_2 = [0.389 \quad 0.278 \quad 0.333]$;

(2) Weight matrix of joint diseases: $W_3 = [0.583 \quad 0.417]$.

WEIGHT NORMALIZATION

Weights of cement concrete pavement diseases (except faulted slabs, pumping, and bow-up) in void ratio calculation are normalized in order to ensure the sum to be 1. The results are shown as Table 2.

Table 2. Weight of CCP Disease in Void Ratio Calculation

Damage Types	Crushed Plates	Crack	Corner Break	Corner Spalling	Joint Material Damage	∑
Weights	0.266	0.190	0.227	0.185	0.132	1
Extent	Slight 0.8 Severe 1.0	Slight 0.6	Slight 0.6	Slight 0.6	Slight 0.6 Severe 1.0	—
		Moderate 0.8	Moderate 0.8	Moderate 0.8		—
		Severe 1.0	Severe 1.0	Severe 1.0		—

TRAFFIC GRADE AFFECTION COEFFICIENT ξ

There is a close relationship between traffic loads and slab void. Therefore the traffic grade affection coefficient ξ is introduced according to the experiences in Hunan Province. The axle loads are graded into 4 levels shown in Table 3.

Table 3. Traffic Grade Affection Coefficient ξ

Traffic Grades	Specific Heavy	Heavy	Medium	Light
Standard Axle Loads on The Design Lane $N_e(10^4)$	>2000	100～2000	3～100	<3
ξ	3	2	1	0.8

ENGINEERING EXAMPLE

There are four selected sections. The damage with the biggest weight of every slab have been record. The arrangement data are shown as Table 4. The length and width in test section are 10km and 3.75m.Unit of every damage type is block.

VOID RATIO (VR) CALCULATION

$$VR = [\xi(\sum_{i=1}^{n} M_i W_i) + F] / BS \tag{5}$$

Where: ξ is the traffic grade affection coefficient, the standard axle loads in the test section N_e are 3000×10^4, thus traffic grade is specific heavy, ξ=3;

M_i are the total modified slabs of i disease (except faulted slabs, pumping, and bow-up), blocks;

W_i is the weight of i disease (except faulted slabs, pumping, and bow-up), according to Table2;

F are the total slabs of faulted slabs, pumping and bow-up, blocks;

BS are total slabs in test section, blocks.

There are 2000 blocks in the test section; the void ratio is shown as follows.

$$VR = \frac{3\times(138.2\times0.266+476.2\times0.190+121.2\times0.227+18.4\times0.185+23.8\times0.132)+(10+9+2)}{2000} = 25.24\%$$

The sections have been verified by Dynatest8000 FWD, and the void has been calculated by intercept method. Results are shown in Table 5. The void ratio of the other three sections is estimated by the same method (Line 3 to 5 in Table 5).

Table 4. Investigation Data Arrangement

Damage Types	Extend	Weight	Data (Blocks)	Correction of The Extend Weigh	Total Modified Slabs
Crushed Plates	Slight	0.8	44	35.2	138.2
	Severe	1.0	103	103.0	
Crack	Slight	0.6	171	102.6	476.2
	Moderate	0.8	182	145.6	
	Severe	1.0	228	228.0	
Corner Break	Slight	0.6	8	4.8	121.2
	Moderate	0.8	48	38.4	
	Severe	1.0	78	78.0	
Faulted Slabs	—	1.0	10	10.0	10.0
Pumping	—	1.0	9	9.0	9.0
Corner Spalling	Slight	0.6	9	5.4	18.4
	Moderate	0.8	5	4.0	
	Severe	1.0	9	9.0	
Joint Material Damage	Slight	0.4	43	17.2	23.8
	Severe	0.6	11	6.6	
Bow-up	—	1.0	2	2.0	2.0
∑			960	798.8	798.8

Table 5. Comparison the Void Ratio of FWD Intercept Method and FAHP

Test Section	VR by FWD Intercept Method (%)	VR by FAHP (%)	Relative Error (%)
1	26.33	25.24	4.1
2	34.92	33.04	5.7
3	5.91	5.47	7.4
4	9.16	9.82	6.7

The results of Table 5 indicate that the biggest relative error is 7.4%, which satisfies the need of engineering. The engineering example shows that this method has a practical significance in making CCP slab void treatment.

CONCLUSIONS

The weight of pavement damages in void ratio calculation is gotten by FAHP, and the most important step is the index selection and model establishment. The damages selected include: (1) fracture diseases: crushed plates, crack, and corner break; (2) joint diseases: faulted slabs, pumping, bow-up, corner spalling, and joint material damage.

The traffic grade affection coefficient ξ has been introduced to modify the calculation model in order to meet the practice that traffic loads have an effect on void to some extend, especially heavy traffic.

The tests of Hunan expressway show that this method has a good practical

significance in void slab treatment plan.

ACKNOWLEDGMENTS

The support from Hunan National Science Foundation, my assistants Dr. Jian Zhao, Hongyi Yang, Xiaojun Zeng and my research team are much appreciated.

REFERENCES

Chen, H.Y. and Zhao, J.B. (2004). "Research on compatibility of fuzzy judgment matrices". *Operations Research and Management Science*. 13(1): 44-47.

Jiang, J. Song, B.W. Chang, M. et al. (2007). "Fuzzy weight evaluation method based on AHP". *Journal of Projectiles*, *Rockets*, *Missiles and Guidance*. 27(1): 294-296.

Ji, D.C. Song, B.F. and Yu, T.X. (2006). "FAHP and its application in the selection of design scheme". *Journal of Systems Engineering and Electronics*. 28(11): 1692-1694.

Tang, B.M. (1992). "Detection of voids beneath the rigid pavement slab". *China Journal of Highway and Transport*. 5(1): 40-44.

Xu, Z.S. (2001). "Algorithm for priority of fuzzy complementary judgment matrix". *Journal of Systems Science and Systems Engineering*. 16(4): 311-314.

EVALUATION OF A NEW GENERATION OF ASPHALT TREATED MIXTURES

Louay N. Mohammad[1], Munir D. Nazzal[2], and Aaron Austin[3]

[1] Corresponding Author, Professor, Department of Civil and Environmental Engineering and Louisiana Transportation Research Center, Louisiana State University, 4101 Gourrier Ave, Baton Rouge, LA 70808, Email:louaym@lsu.edu , Tel: 225-767-9126, Fax: 225-767-9108
[2] Assistant Professor, Department of Civil Engineering, Ohio University, Athens, OH 45701
[3] Geotechnical Engineer, Fugro Consultants, Inc., Baton Rouge, LA 70816

ABSTRACT: This paper summarizes the results of a study that was conducted to compare the performance of new generation asphalt treated base (ATB) mixtures to unbound granular materials (UGM) currently used in construction of base layers. A laboratory testing program was initially conducted on two types of ATB and UGM materials. The program included performing permanent deformation and resilient modulus repeated loading triaxial on the UGM materials. The dynamic modulus and flow number tests were used to examine the intermediate and high temperature response of the ATB mixtures under cyclic loading. In addition, the new Mechanistic Empirical Design Guide (MEPDG) software was used to compare the performance of pavement sections with ATB mixtures to existing pavement sections. The results of the laboratory testing program showed that the asphalt treated base mixtures have several folds improvement of UGM in terms of stiffness and permanent deformation resistance. In addition, the MEPDG analysis showed that pavement sections with ATB mixtures exhibited much lower rutting and fatigue cracking than the conventional pavement section.

INTRODUCTION

Asphalt treated mixtures are hot mix asphalt (HMA) mixtures consisting of crushed rock or natural gravel mixed with low percentages (2.5-4.5) of paving grade asphalt cement. Those mixtures cost less than typical HMA mixtures because they can be produced with less expensive aggregates and lower percentages of asphalt cement binder. Asphalt treated mixtures can be used in the construction of base course layers as well as shoulders of a pavement structure. Limited studies were conducted in past decades to evaluate the use of asphalt treated mixtures in pavement construction (Benkelman et al.,1962; Rostron et al. 1971). The results of those studies showed that asphalt treated mixtures had several advantages over untreated granular base material.

Currently, state agency's specifications for asphalt treated mixtures are similar to those required for HMA mixtures. As a result, those mixtures currently have a limited use in pavement construction. However, a design methodology for asphalt treated mixtures that are durable, stable, and cost effective was recently developed in a study conducted by the Louisiana Transportation Research Center (LTRC) (Mohammad et al., 2009). This paper summarizes the results of a study that was conducted to compare the performance of a new generation of asphalt treated base (ATB) mixtures to that of unbound granular materials (UGM) currently used in construction of base layers.

Unbound Granular Materials

Three types of unbound granular materials were considered in this study. These materials included: limestone (LS), sandstone (SS), and a 75% limestone and 25% coarse sand blend (LS-CS). The tested limestone and sandstone materials were taken from selected samples used in the construction of base course layers in Louisiana. The gradation curves of the considered materials are shown in Figure 1. It is noted that there were some differences between the gradation curves of the considered materials. The LS, SS, and LS-CS materials have maximum dry unit weights of 138.8, 136.5, and 143.9 lb/ft^3, respectively, and optimum moisture contents of 6.5, 7.1, and 5.9 %, respectively, as measured by the standard Proctor test.

Asphalt Treated Base Mixtures

The asphalt treated mixtures evaluated in this paper were designed based on the methodology developed in a previous study (Mohammad et al., 2009). In this design methodology, the aggregate structure consists of 75% of -1.5-inch sieve crushed run materials from the selected aggregate source and 25% of coarse sand. In addition, 3% asphalt content is used in those mixtures. The asphalt binder used in all mixtures evaluated was PG 70-22m. The design number of gyrations required to produce a sample with the same density as that expected in the field is determined to 30 gyrations based on the Superpave gyratory compactor (SGC) locking point. This is the number of gyrations after which the rate of change in height of asphalt mixture sample is equal to or less than 0.05 mm for three consecutive gyrations. For further information on the design of the asphalt treated mixtures evaluated in this study, one can refer to Mohammad et al. (2009).The job mix formula (JMF) of all mixtures considered in this study are summarized in Table 1.

Laboratory Testing Program

A laboratory testing program was conducted to characterize the asphalt treated mixtures considered in this paper. Triplicate samples were tested for each asphalt treated mixture considered. Mixtures' stiffness at was evaluated using the dynamic modulus test. In addition, a flow number test was used to assess high temperature permanent deformation resistance of the asphalt treated mixtures. Cylindrical samples for the |E*| and FN tests were fabricated by coring and sawing 3.94-in. diameter by 5.91-in. high test specimens from the middle of 5.91-in. diameter by 6.69-in. high Superpave Gyratory Compactor (SGC) compacted cylindrical specimens.

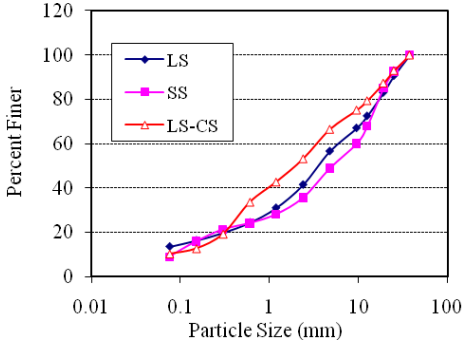

FIG. 1. Gradation curves of unbound granular materials

Table 1. Job Mix Formula for Asphalt Rreated Mixtures

Mixture Designation	Asphalt treated-LS	Asphalt treated-SS
Mix type	25 mm	25 mm
Aggregate blend	75% LS & 25% CS	75% SS & 25% CS
Binder content, %	3	3
Air void at N=30, %	7.8	11
Metric (U.S.) Sieve	Blend Gradation	
37.5 mm (1½ in.)	100	100
25 mm (1 in.)	93	94
19 mm (¾ in.)	87	89
12.5 mm (½ in.)	79	76
4.75 mm (No.4)	67	61
2.36 mm (No.8)	53	49
1.18 mm (No.16)	43	41
0.3 mm (No.50)	19	20
0.075 mm (No.200)	10	7

Two types of repeated load triaxial (RLT) tests were also used in this study to characterize the mechanical properties of unbound granular base course materials at their field construction conditions. The two types of RLT tests included: resilient modulus and single-stage tests. Resilient modulus tests were performed in accordance with AASHTO-T307 standard method for determining the resilient modulus of base course materials. The single-stage RLT tests were performed to determine the permanent and resilient deformations of the considered materials at different number of load cycles. The test consisted of applying 10,000 load cycles at a constant confining pressure of 3 psi and peak cyclic stress of 30 psi. The peak cyclic stress was selected based the one used in flow number tests. It is noted that the single-stage RLT procedure is similar to those followed in previous studies (Mohammad et al. 2006).

All triaxial tests were performed using the Material Testing System (MTS) 810 machine with a closed loop and a servo hydraulic loading system. The applied load was measured using a load cell installed inside the triaxial cell. This type of set up reduces the equipment compliance errors as well as the alignment errors. The capacity of the load cell used was ± 22.25 kN. The axial displacement measurements were made using two Linearly Variable Differential Transducers (LVDT) placed between the top platen and base of the cell to reduce the amount of extraneous axial deformation measured compared to external LVDTs. Air was used as the confining fluid to the specimens.

Performance Evaluation Using MEPDG

The new Mechanistic Empirical Pavement Design Guide (MEPDG) software was used to compare the performance of three pavement sections that incorporated LS I asphalt treated mixture layer(s) to a typical section designed for intermediate traffic volume. The cross section of the evaluated pavement sections is presented in Figure 9. Section 1, the control section, consisted of four layers: 2 inches of ½ -in. Superpave Level 2 wearing course, 2 inches of ¾ -in. Superpave Level 2 binder course, 4 inches of crushed limestone base course, and 10 inches of cement treated soil sub-base. In section 2 and 3, the LS I asphalt treated mixture replaced the ¾-in. Superpave Level 2 binder course mixture and the crushed limestone base course material. Finally, in section 4 the binder course layer was eliminated, and the asphalt treated mixture was used as base course layer.

The analysis was conducted for a 20 year design period. The initial two-way average annual daily truck traffic (AADTT) was assumed to be 2000 vehicles/day with 50% trucks in the design direction and 95% trucks in the design lane. The default values in the MEPDG software for vehicle class distribution, number of axles per truck of each class, and axle configuration were used in the analysis. The monthly adjustment factors were set at 1.0. The traffic growth rate was 5% per year. Level I input was used for the HMA and asphalt treated mixtures layers. While, Level II inputs were used for the base, subbase, and subgrade layers. The input parameters for the HMA wearing and binder course mixture were obtained from values reported in a previous study. In addition, the asphalt treated mixture and the unbound granular base material input parameters were obtained from the results of test conducted in this study. Finally, the input parameters of subbase and subgrade layers were based on a experimental studies that were previously conducted by the research team. Table 2 presents a summary of the input parameters used in the MEPDG analysis. For further information on the layers' input parameters used in this study, one can refer to Mohammad et al. (2009).

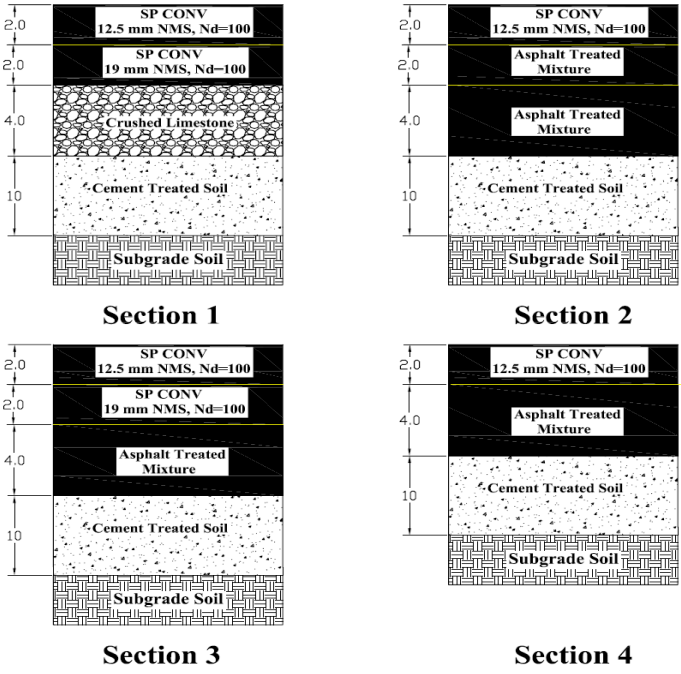

FIG. 2. Pavement sections evaluated in MEPDG

Table 2. MEPDG Input Parameters of Pavement Layers

Material	Input Level	Input Parameter
½ -in. Superpave Level 2 Mixture	Level I	E* at 6 frequencies and 5 temperatures
½-in. Superpave Level 2 Mixture	Level I	E* at 6 frequencies and 5 temperatures
LS I Asphalt treated Mixture	Level I	E* at 6 frequencies and 5 temperatures
Crushed limestone Base	Level II	Mr = 40 ksi
Subbase	Level II	Mr = 25 ksi
Subgrade	Level II	Mr = 5 ksi

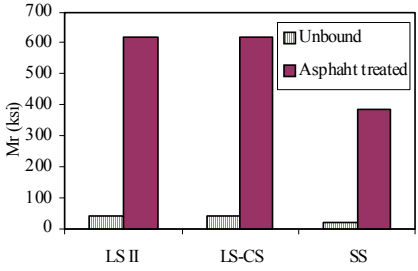

FIG. 3. Modulus of the unbound base materials and asphalt treated mixtures

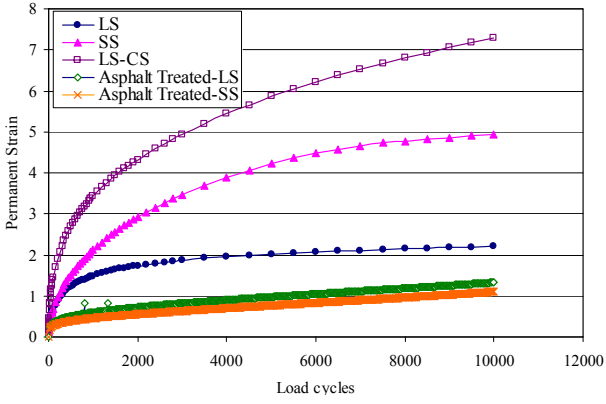

FIG. 4. Permanent strain curves for the unbound base materials and asphalt treated mixtures

Results of Laboratory Testing Program

The results of the tests conducted on the asphalt treated mixtures and unbound granular base materials were used to investigate the effect of asphalt treatment on the behavior of unbound granular base materials. Stiffness and permanent deformation resistance were used for conducting this investigation. Figure 3 compares the resilient modulus of the considered unbound materials to the dynamic modulus of the LS and SS asphalt treated mixtures measured at a temperature of 25°C and a frequency of Hz (the frequency used in the resilient modulus test). It is noted that the asphalt treated binder resulted in increasing the moduli of unbound aggregates significantly. This suggests that the asphalt treated base layer will be much stiffer than unbound granular base materials, thus it will be able to better distribute the loads to underlying layers.

Figure 4 shows permanent deformation curves obtained from the single stage RLT and flow number tests conducted on the unbound materials and the asphalt treated

mixtures evaluated in study. It is noted that although the same stress level was used in the single stage RLT and flow number tests, the asphalt treated mixtures exhibited a much lower permanent strain than the unbound materials. Furthermore, the LS-CS blend (the same aggregate blend used the LS asphalt treated mixture, not only showed a much higher permanent strain that the LS asphalt treated mixture) but also exhibited an unstable behavior as indicted by the permanent strain curve. This indicates that the asphalt binder significantly improved the permanent deformation resistance of unbound granular materials, hence their performance.

Results of MEPDG Performance Evaluation Analysis

The MEPDG software was used to predict the distress parameters for the four sections evaluated in this study. The distress parameters included: rutting and fatigue cracking. Figure 5 presents the total rutting curves predicted from the MEPDG analysis. It is noted that the use of the asphalt treated mixture in the binder and base course layers resulted in a significant reduction in the total rutting through the pavement service life. In addition, the replacing the unbound granular base layer with an asphalt treated mixture layer resulted in reducing the total rutting more than 33%. Figure 5 shows that section 4 in which the asphalt treated layer replaced the binder course and crushed limestone layers exhibited lower rutting than the control section, section 1.

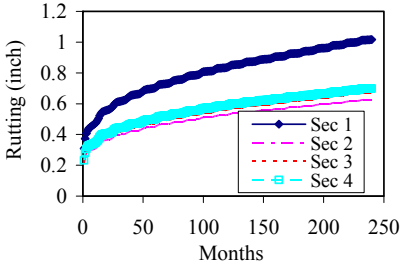

FIG. 5. Rutting curves predicted using MEPDG

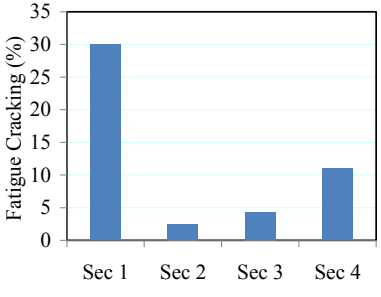

FIG. 6. Fatigure Cracking predicted using MEPDG

Figure 6 shows the fatigue cracking at the end of the design period for the four sections evaluated. It is clear that the asphalt treated mixture improved the pavement performance by reducing the fatigue cracking developed in the pavement section. Thus the results of the MEPDG suggest that the asphalt treated mixture can be used to extend the service life of a pavement structures and reduce its design thickness.

CONCLUSIONS

This paper presents the results of a study that compared the performance of a new generation of asphalt treated base (ATB) mixtures to unbound granular materials (UGM) currently used in construction of base layers. A laboratory testing program was initially conducted on two types of ATB and UGM materials. The MEPDG software was also used to compare the performance of pavement sections with ATB mixtures to the existing moderate volume pavement section. Based on the results of this paper, the following conclusions can be drawn:

- The asphalt treated base mixtures have several folds improvement of UGM in terms of stiffness and permanent deformation resistance.
- The use of the asphalt treated mixture in the binder and base course layers resulted in a significant reduction in the total rutting through the pavement service life.
- The asphalt treated mixture improved the pavement performance by reducing the fatigue cracking developed in the pavement section.
- Based the MEPDG analysis, asphalt treated mixtures can be used to extend the service life and/or reduce the design thickness of pavement structures.

ACKNOWLEDGMENTS

This research was supported by the Louisiana Transportation Research Center (LTRC) and the Louisiana Department of Transportation and Development (LADOTD) through LTRC project No. 04-4B. The authors would like to express thanks to personnel that helped in this research.

REFERENCES

Benkelman, A.C.; Kingman, R I; Schmitt, H.M. (1962). "Performance Of Treated and Untreated Aggregate Bases." *Highway Research Board Special Report*, No. 73.

Mohammad, L., A. Herath, M. Rasoulian, and Z. Zhang. "Laboratory evaluation of untreated and treated pavement base materials from a repeated load permanent deformation test." *The 85th Transportation Research Board Annual Meeting*. CD-ROM, National Research Council, Washington, D.C., 2006.

Mohammad, L.N., Nazzal, M., King, W., and Austin, A. (2009). "Development of a Design Methodology for Asphalt Treated Base," *Final report, Louisiana Transportation Research Center*, Baton Rouge.

Rostron, J.P., Busching, H.W., and Roberts, F.L. (1971). "Relative Strength of Flexible Pavement Bases." *Journal of the Association of Asphalt Paving Technologists*, Vol. 41.

Permanent Deformation Analysis on Various Base Materials under Accelerated Pavement Testing

Zhong Wu[1], M. ASCE, Xingwei Chen[1] and Zhongjie Zhang[1], M. ASCE

[1] Louisiana Transportation Research Center, 4101 Gourrier Ave, Baton Rouge, LA 70808, zhongwu@ltrc.lsu.edu

ABSTRACT: Six asphalt pavement test sections with five base materials (i.e. four chemically stabilized base materials and a crushed stone) were tested under accelerated loading. The performance of test sections was analyzed based on the instrument responses, field non-destructive tests as well as forensic investigation. Among four chemically stabilized base materials, both slag and fly ash stabilized Blended Calcium Sulfate (BCS) bases performed significantly better than a crushed stone base course. However, two foamed asphalt (FA) treated base materials exhibited an inferior field performance than the stone base studied. Field measurements indicated that the majority of test sections failed due to rutting. To predict the rutting development, a modified plastic model was introduced in this study and subsequently implemented into a finite element (FE) simulation analysis. The FE simulation results indicated that the predicted rutting development on selected test sections agreed reasonably well with the measured deformation results.

INTRODUCTION

The results from recent laboratory studies (Zhang and Tao, 2006; Mohammad et. al., 2003) have indicated that both the stabilized blended calcium sulfate (BCS) material and foamed asphalt (FA) stabilized reclaimed asphalt pavement (RAP) would provide better or similar performance as a stone base course does. To verify and validate the laboratory findings in a field environmental condition and obtain design parameters for future field implementation, a full-scale accelerated pavement testing (APT) experiment was recently conducted at the Louisiana Transportation Research Center (LTRC).

ACCELERATED PAVEMENT TESTING

Six pavement test sections were constructed at the Louisiana Pavement Research Facility (PRF) in Port Allen, Louisiana, using normal highway construction equipment and procedures. Figure 1 presents the pavement structure of ALF test sections. Each

section was about 4.0 m wide by 33.0 m long. All sections had similar 50.8 mm hot mix asphalt (HMA) top layer, but base and sub-base layers varied between sections. The combinations of base and sub-base materials are presented below. Detailed material properties may be referred to elsewhere (Wu et al., 2006).

Section I: 10 percent blast furnace slag stabilized BCS base (hereafter called BCS/Slag), and 15 percent lime treated sub-base (LTS);

Section II: 15 percent fly ash stabilized BCS base (hereafter called BCS/Flyash), and the LTS;

Section III: crushed stone base, and the LTS;

Section IV: crushed stone base, and an 8 percent cement treated sub-base (CTS);

Section V: foamed-asphalt treated blend of 50 percent RAP with 50 percent soil cement base (hereafter called FA/50RAP), and the CTS;

Section VI: foamed-asphalt treated with 100 percent RAP base (hereafter called FA/100RAP), and the CTS.

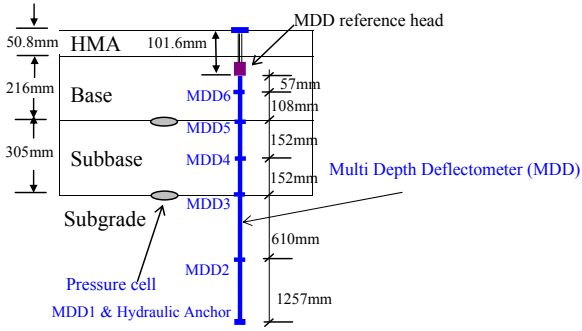

FIG. 1. Pavement structure of ALF test sections

As shown in Figure 1, one Multi Depth Deflectometer (MDD) was installed at a middle station on each test section to measure load-induced pavement vertical displacements at six specified locations below pavement surface. Two Geokon model 3500 earth pressure cells were installed in a middle station on each test section on tops of sub-base and sub-grade layers at each test section.

The APT loading device used was an Australia-designed Accelerated Load Facility (ALF), which simulated one half of a single axle with dual tires. Four different load levels were used in the APT experiments. Note that traffic wander, 380 mm at each side of the centerline, was considered in this experiment (Wu et al., 2006).

For every 25,000 ALF load repetitions, the falling weight deflectometer (FWD) test was performed on eight stations of each section. The surface rutting and cracking were also measured at this interval.

APT EXPERIMENTAL RESULTS

Measured Surface Rutting

Figure 2 provides the average rutting development for the six sections tested. As shown in Figure 2a, both stabilized BCS base test sections (sections I and II) were observed to substantially out-perform the stone base control section (section III). The slag stabilized BCS base was also proved to perform better than the fly ash stabilized BCS base, which was consistent with the laboratory results (Zhang and Tao, 2006). As shown in Figure 2b, Section IV with a stone base had a slightly higher pavement life than both foamed asphalt base sections (sections V and VI). Further, by comparing the two stone base sections, Section IV with a CTS sub-base had approximately three times longer pavement life than Section III with a LTS sub-base.

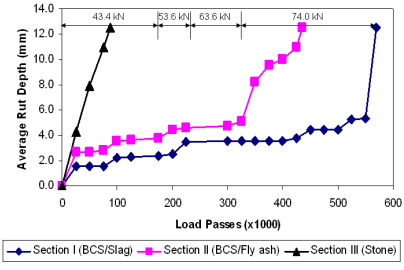

a) Sections over LTS

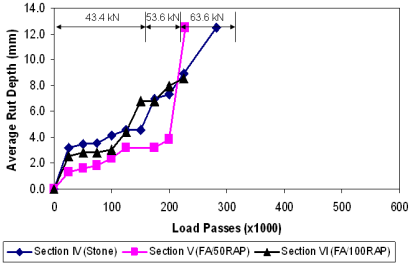

b) Sections over CTS

FIG. 2. Rut depth development on test sections

Vertical Stress at Bottom of Base Layer

Table 1 presents the mean vertical stress results measured at bottom of a base layer under a 43.4 kN ALF wheel load up to 175,000 load passes. Sections I, II and III were with LTS sub-base, a highest stress developed under section III indicated that the stone layer had less structural capacity than both BCS materials. Also, the vertical stress on top of a LTS layer (e.g. section III) was significantly higher than that on top of a CTS layer (e.g. section IV), which is consistent to the measured rutting results.

Table 1. Measured Vertical Stress at Bottom of Base Layer

Section	I	II	III	IV	V	VI
Vertical Stress (kPa)	6.2	35.8	235	130	65.5	62

FWD Results

EVERCALC back calculation program (Pierce and Mahoney, 1996) was used in the FWD modulus back calculation. The back calculation base modulus results are

presented in Table 2. The FWD modulus results generally confirmed that the in-situ BCS materials were much stiffer than the stone material.

Table 2. FWD Back calculated Base Modulus

Section	I	II	III	IV	V	VI
Modulus (MPa)	8,410	599	190	397	510	625
RMS Error (%)	2.1	3.7	3.8	2.22	3.82	1.08

Both vertical stress measurements and FWD back calculated modulus results seemed to indicate that the two foamed asphalt materials would be structurally stronger than the stone, if the load was kept at 43.4 kN after 175,000 load repetitions (Fig.2). It was, thus, further analyzed using the Shakedown Theory [Sharp and Booker, 1984], which indicated that both foamed asphalt base materials might have a lower "shakedown stress" limit than the stone base, which was thought to be the direct cause to the drastic increase in the rate of rutting when a higher ALF load level was applied on the two foamed asphalt base sections (Fig. 2).

Trench Results

By both visual observation and trench results, the major permanent deformation developed on sections I, II, IV and VI were deemed due to consolidation. An example of rutting due to consolidation is presented in Figure 3(a). However, the rutted profiles on sections III and V were found to include not only material densification but also "shear flow". The "shear flow" represents a shear failure of foamed asphalt base materials as shown in Figure 3(b).

(a) Densification on Section I

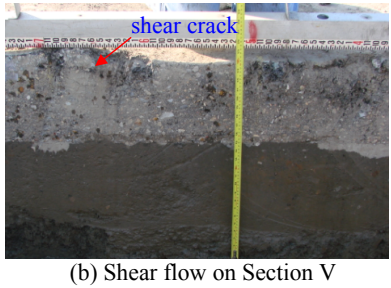

(b) Shear flow on Section V

FIG. 3. Trench results

PERMANENT DEFORMATION ANALYSIS OF BASE MATERIALS

An axisymmetric finite element (FE) model was developed in ABAQUS to predict the base layer rutting development for the APT test sections at the PRF site. As shown in Figure 4(a), the axisymmetric FE model was 3.95 m deep and 1.98 m wide. The horizontal boundary (the depth of the FE model) was chosen based on the maximum

vertical stress at the bottom of sub-grade less than 0.5 percent of the applied load pressure, whereas, the vertical boundary used one half of the APT section width. Both horizontal and vertical boundaries were restrained by roller supports. As shown in Figure 4(b), a repeated load with a triangle-shape was applied sequentially to simulate the APT repeated loading in the current FE model.

The FE model included four pavement layers similar to the APT test sections. The FE mesh, built using ABAQUS's eight-node bi-quadratic axisymmetric quadrilateral elements (CAX8R), was finer near the load and progressively coarser as the distance from the load increased. Based on the mesh sensitivity analysis results, the finally adopted mesh included a total of 3,400 CAX8R elements.

A permanent deformation model for materials under repeated loading was proposed in this study and used for all materials except the HMA layer in the developed FE model with required input model parameters derived from a triaxial permanent deformation test. The proposed model consists of a conventional elastic-plastic model for the first cycle of loading. The subsequent loading/ unloading cycles after yielding are simulated by different secant modulus values. Figure 4(c) presents the schematic representation of the permanent deformation model. More details can be referred to elsewhere (Wu et al., 2009). Temperature dependence of the asphaltic material was also considered in the FE simulation analysis. Specifically, the loading elastic moduli of asphaltic layers (the HMA and foamed asphalt base layers) were adjusted at every 25,000 load repetitions based on the average pavement temperatures.

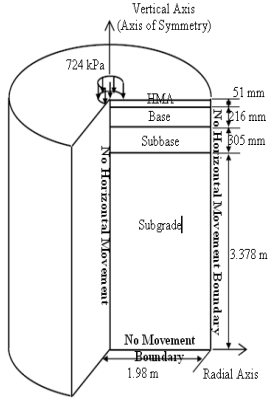

(a) FE model and boundaries

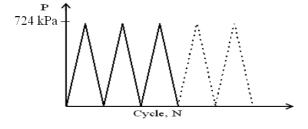

(b) Schematic of repeated loading

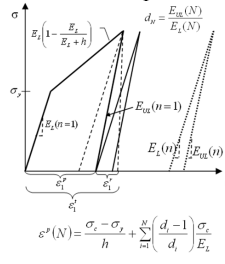

(c) Schematic of Proposed Model

FIG. 4. Axisymmetric finite element model.

In addition, three key techniques were considered in FE simulation analysis: 1) accelerated analysis procedure: only the permanent deformation developed for a reference number of cycles (N_r) was calculated by ABAQUS, then, the growth of permanent deformation was extended via a similar equation proposed by Desai and

Whitenack (*2001*); 2) load level effects: the permanent deformation curves under different load levels were first predicted separately in different FE simulation models and then connected at the cycle where the load level was changed. Limited cycles of FE analysis was conducted on both un-deformed and deformed mesh boundary conditions to investigate the effects of deformed mesh at the end of simulation cycles under one load level on the subsequent prediction results under a different load level; and 3) wander loading (380 mm at each side of the centerline): Such wander loading were considered in the FE permanent deformation prediction.

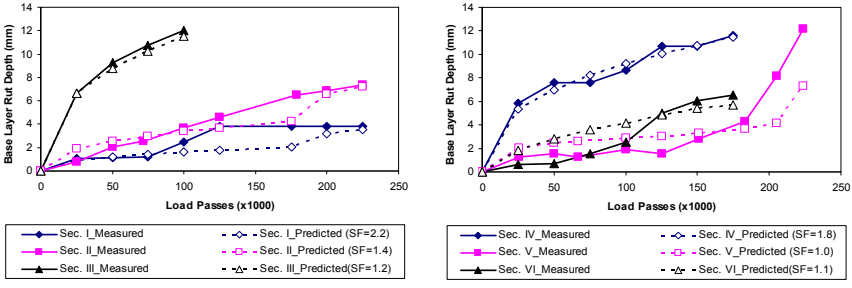

a) Sections on LTS b) Sections on CTS

FIG. 5. Comparison between measured and predicted rutting development on various base layers under APT loading

Figure 5 compares the MDD measured base rut depths at APT test sections to the FE calculated ones. The FE simulation results indicated that the predicted rutting development matched reasonably well with the measured rut depths for all test sections investigated when the lab over field shift factors (measured over predicted) ranged from 1.0 to 2.2 were applied.

CONCLUSION

Six asphalt pavement test sections with five base materials were tested under accelerated loading. Among four chemically stabilized base materials, both slag and fly ash stabilized BCS bases performed significantly better than a crushed stone base course. However, two foamed asphalt treated base materials possessed an inferior field performance than the stone base studied. A finite element model was developed to simulate the permanent deformation of APT sections under accelerated loading. A numerical permanent deformation material model, which was developed for rutting prediction of various pavement materials, was used in the FE simulation analysis. The predicted permanent deformation results for various base materials matched reasonably well with the APT measured ones.

ACKNOWLEDGEMENTS

This study was supported by the Louisiana Transportation Research Center and the

Louisiana Department of Transportation and Development. The authors would like to express thanks to all those who provided valuable help in this study.

REFERENCES

Desai, C.S. and Whitenack, R. (2001). "Review of models and the disturbed state concept for thermomechanical analysis in electronic packaging." *J. Electron. Packag.*, 123, pp. 1-15.

Mohammad, L.N., Farsakh, M., Wu, Z. and Abadie, C. (2003). "Louisiana experience with foamed recycled asphalt pavement base materials." *Journal of Transportation Research Record*, No. 1832, pp.17-24.

Pierce, L. M. and Mahoney, J.P. (1996) "Asphalt concrete overlay design case studies." *Journal of the Transportation Research Board,* No. 1543, pp. 3-9.

Sharp, R. and J. Booker. (1984). "Shakedown of pavements under moving surface loads." *Journal of Transportation Engineering*, ASCE, 110(1), 1–14

Wu, Z., Zhang, Z., King, B. Raghavendra, A. and Martinez, M. (2006). "Instrumentation and accelerated testing on Louisiana flexible pavements." *Airfield and Highway Pavements – Meeting Today's Challenges with Emerging technologies*, ASCE Special Publication, Edited by I. L. AL-Qadi.

Wu, Z., Chen, X. and Zhang, Z. (2009). "A simplified numerical model proposed for simulation of permanent deformation of pavement base and subgrade materials." *CD-ROM, Transportation Research Board of the National Academies*, Washington, D.C.

Zhang, Z. and Tao, M. (2006). "Stability of Calcium Sulfate Base Course in a Wet Environment." Final Report No. FHWA/LA-06/419, Louisiana Transportation Research Center, Baton Rouge, LA.

Laboratory Evaluation of Physical and Mechanical Properties of Recycled Asphalt Pavement

Subhash C. Thakur[1], Jie Han[2], Wai Kiong Chong[3], and Robert L. Parsons[4]

[1]Graduate Research Assistant, the University of Kansas, Department of Civil, Environmental, and Architectural Engineering, Lawrence, KS 66045, PH (785) 218-1584; email; subhash_33@hotmail.com
[2]Associate Professor, the University of Kansas, Department of Civil, Environmental, and Architectural Engineering, Lawrence, KS 66045, PH (785) 864-3714; email: jiehan@ku.edu
[3]Assistant Professor, the University of Kansas, Department of Civil, Environmental, and Architectural Engineering, Lawrence, KS 66045, PH (785) 864-2891; email: Oswald@ku.edu
[4]Associate Professor, the University of Kansas, Department of Civil, Environmental, and Architectural Engineering, Lawrence, KS 66045, PH (785) 864-2496; email: raparsons@ku.edu

ABSTRACT: In many states, the use of RAP in surface, base, and sub-base courses is limited and large quantities of RAP aggregate remain unused. To explore the possibility of more or complete use of milled RAPs, it is necessary to study physical and mechanical properties of RAPs. In this study, RAPs from two sources were selected. Binder contents and properties of coarse and fine aggregates after removing asphalt binders were determined. RAPs were also tested for their maximum densities and California Bearing Ratios (CBRs). The influence of binder contents and aggregate properties on the physical and mechanical properties of RAPs was discussed. The binder content of RAPs was found to be higher than that in the original mix designs. The coarse aggregate angularity (CAA) of the RAPs was increased compared to that of the original mixes. The combined bulk specific gravities of aggregates from RAPs decreased slightly as compared with those in the original mixes. The percentage of fine particles in the RAPs was increased from that in the original mixes. The RAP with a higher binder content and a lower fine aggregate angularity had a higher optimum moisture content, a higher maximum dry density, and lower CBR values. The aggregates from the RAPs were not of uniform hardness based on the LA abrasion tests.

INTRODUCTION

Recycled asphalt pavement (RAP) is recovered by milling or full depth of reclamation of existing pavement layers, and is to be reused partly or fully in a new pavement by mixing it with other virgin aggregate or asphalt. RAP is one of the most recycled materials in the United States. Out of 90 million metric tons of RAP produced, 73 million metric tons of RAPs are recycled each year in the United States.

Incorporating higher percentages of RAP into surface and base courses has economic, environmental, and technical benefits because it conserves energy, aggregate, and landfill space. In many states, the percentage of RAP to be used in the base course and subbase courses is limited. Therefore, it is necessary to explore the probability of using increased amounts of RAP in base and subbase courses. It is also known that RAP is a highly variable material, therefore, it is necessary to study the effect of such variability on the mechanical properties of RAP.

RAP is typically variable in its gradation, binder content, milling process, etc. Huang and Vukosavljevic (2006) conducted a laboratory study on fatigue characteristics of HMA mixtures containing RAPs and their variability. The uniformity of screened RAPs was evaluated based on the properties of binder and aggregate. The properties of aggregate were evaluated by its gradation, specific gravity, and fine aggregate angularity tests. Their sieve analysis showed no significant difference in gradation between the stockpiles at each site. However, there were slight variations in gradation between stockpiles at four job sites. They also found no significant difference in fine aggregate angularity (FAA) and specific gravity among three samples collected from different locations in the same stockpile but slight variations in specific gravity and FAA among different job sites. Locander (2009) conducted a study to evaluate the use of RAPs as a base course material. The results from this study indicated that RAPs might be used for unbound aggregate base courses because their laboratory tested properties were similar to those of the aggregate base materials included in the Colorado Department of Transportation (CDOT) specification. Bennert and Maher (2005) conducted strength tests, such as CBR and triaxial shear tests, and permeability tests on the RAPs and their blends with the regular base material. Their results showed that an increase in the percentage of RAPs used in the blend reduced both the CBR and permeability values. At 100% RAP, the measured CBR values were found to be 18% and 20% at 2.54 mm and 5.08 mm penetrations, respectively. However, when the RAP was mixed with 50% regular base course aggregate, the CBR values reached 83% and 94% at 2.54 mm and 5.08 mm penetrations, respectively.

The objective of this study is to characterize and compare the physical properties of RAPs selected from two job sites in Kansas and to investigate the effect of these properties on mechanical properties of the RAPs. The physical properties of the RAPs include binder content, particle size distribution, specific gravity, absorption, fine aggregate angularity (FAA), coarse aggregate angularity (CAA), and moisture-density relationships. The mechanical properties include Los Angeles Abrasion (LA) values and CBR values.

Materials and Test Methods

Materials

Two RAP samples were collected from K-25 Highway in Grant County, and US-083 Highway in Scott County, Kansas. The RAP sample from K-25 was composed of bituminous surface (SM-12.5A and PG64-22). Similarly, the RAP samples from US-083 contained HMA surface (SR-12.5A and PG64-22) with 14 % of previous RAP.

The moisture contents of the RAPs (three samples from each site) collected from K-25 and US-083 were measured as 0.20% and 0.21%, respectively.

Physical Property Testing

Binder Content

The ignition test (ASTM D6307) is one of the widely used methods to separate asphalt and aggregate by burning off asphalt at 540^{o}C. In this method, RAPs are heated in an oven to burn the asphalt binder within the mixture and the difference before and after burning in the ignition oven gives a measure of the asphalt binder content. The binder content of three samples from each source was determined following ASTM D6307 in this study.

Gradation

After the removal of asphalt from the RAPs in the ignition oven, three aggregate samples from each source were washed and a sieve analysis was conducted to obtain the gradation of the aggregate in accordance with the KDOT standard (KT-34).

Specific Gravity and Absorption

Specific gravity of aggregate is useful for weight-volume conversions. Bulk specific gravity, SSD bulk specific gravity, apparent specific gravity, and absorption of the aggregates were determined using three samples from each source following ASTM C127 in this study.

Fine Aggregate Angularity (FAA)

The FAA test is used to evaluate fine aggregate angularity by measuring loose uncompacted void content of a fine aggregate sample and ensure that the blend of fine aggregates has sufficient angularity to resist permanent deformation. Three aggregate samples from each source were evaluated for FAA in accordance with ASTM C1252 in this study.

Coarse Aggregate Angularity (CAA)

The CAA test is a method of determining the angularity of coarse aggregate by visually inspecting a sample of coarse aggregates and separating the sample into the aggregates with fractured faces and those without fractured faces. An increase in the angularity is considered to increase the friction resistance of the aggregate. This test was performed using two 2.5-kg aggregate samples from each source in accordance with the KDOT standard (KT-31).

Moisture-density Curve

In the laboratory, the RAP samples were compacted and tested for the optimum moisture content (OMC) and the maximum dry density (MDD) for each RAP with the modified Proctor compaction energy in accordance with ASTM D1557. These specimens were also used to determine the CBR values in accordance with ASTM D1883.

Mechanical Property Testing

Los Angeles Abrasion

One 5-kg aggregate sample from each source was prepared according to Grading D and subjected to a Los Angeles Abrasion test following ASTM C131. This test required that aggregates be placed with 6 steel spheres inside a metal drum that rotated at a speed of approximately 30 rpm for 500 revolutions. The weight loss, in percent, was computed from the initial sample weight and the final weight measured after the samples were washed on a No. 12 (1.7 mm) sieve and dried at 105^{o}C. To determine the uniformity of hardness of the samples, the samples were rotated in the drum for 100 revolutions to determine the weight loss and compare it with the weight loss after 500 revolutions.

California Bearing Ratio (CBR)

Four specimens of each RAP were compacted according to ASTM D1557 Method C to the target height of 152.4 mm and the diameter 116.5 mm. Water was added to each sample to reach a target moisture content and the sample was left for 24 hours for uniform distribution of moisture. The samples were then compacted and tested for CBR values according to ASTM D1883.

Test Results and Discussion

Physical Properties

Binder Content

The binder content for each sample was determined using the ignition oven test (ASTM D6307). Table 1 lists the measured binder content of three samples obtained from each source. The test results indicate that the RAP from K-25 had a higher binder content than that from US-83. The test results also show that both RAPs had higher binder contents than the original mixes, which may be due to the binder added during the maintenance work and the burning-off of mineral aggregates in the ignition oven.

Table 1. Binder content (%) of RAPs

Sample No.	K-25	US-83
1	6.17	5.74
2	6.22	5.58
3	6.10	5.69
Average	6.17	5.67
Original mix	4.8	4.96

Gradation

Figure 1 shows the grain size distributions of the original and RAP aggregates from K-25 and US-83 used in the mix designs. The analyses indicate that the RAP from US-83 had more fine particles than the RAP from K-25, which is consistent with the original mixes. The comparison also shows that the percentage of fine particles increased from the original mixes to the RAPs due to the milling process.

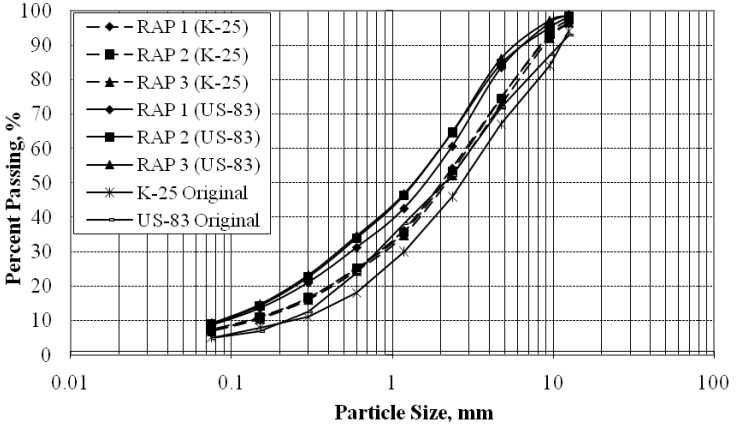

FIG. 1. Gradations of aggregates in the original and RAP mixes

Specific Gravity and Absorption

Tables 2, 3, and 4 present the measured specific gravity values of coarse, fine, and combined aggregates from both RAPs. It is shown that the RAP aggregates from K-25 had a slightly higher specific gravity than that from US-83. The aggregates from both RAPs had similar absorption. In addition, Table 4 shows that the aggregates from RAPs had lower specific gravity values than those used in the original mix designs.

Table 2. Specific gravity and absorption of coarse aggregates from RAPs

US-83				
Description	**Sample 1**	**Sample 2**	**Sample 3**	**Average**
Bulk specific gravity	2.493	2.492	2.491	2.492
Bulk specific gravity (SSD)	2.543	2.542	2.545	2.543
Apparent specific gravity	2.624	2.623	2.632	2.627
Absorption,%	2.01	2.01	2.15	2.05
K-25				
Bulk specific gravity	2.52	2.531	2.52	2.524
Bulk specific gravity (SSD)	2.571	2.583	2.55	2.568
Apparent specific gravity	2.656	2.669	2.66	2.661
Absorption,%	2.04	2.04	2.03	2.03

Table 3. Specific gravity and absorption of fine aggregates from RAPs

US-83				
Description	**Sample 1**	**Sample 2**	**Sample 3**	**Average**
Bulk specific gravity	2.554	2.562	2.543	2.553
Bulk specific gravity (SSD)	2.579	2.582	2.567	2.576
Apparent specific gravity	2.619	2.616	2.604	2.613
Absorption,%	0.98	0.81	0.92	0.9
K-25				
Bulk specific gravity	2.558	2.546	2.536	2.547
Bulk specific gravity (SSD)	2.583	2.578	2.57	2.577
Apparent specific gravity	2.624	2.631	2.626	2.627
Absorption,%	0.98	1.27	1.36	1.2

Table 4. Combined bulk specific gravity of coarse and fine aggregates

Combined bulk Sp. Gr.	**US-83**	**K-25**
Original Mix	2.598	2.575
RAP	2.533	2.540

Fine Aggregate Angularity (FAA)

The average fine aggregate angularity was determined for three samples from each source of RAPs. The measured fine aggregate angularity was 43% for the RAP from K-25 and 45% for the RAP from US-83. However, the FAA values in the original mixes were 44% for K-25 and 42% for US-83. The aggregates in the RAP from US-83 had a slightly higher measured FAA than that from K-25. As compared with the original mixes, there was a slight reduction in FAA in the RAP from K-25 but an increase in FAA in the RAP from US-83.

Coarse Aggregate Angularity (CAA)

The measured CAA values for the aggregates in the RAPs from K-25 and US-83 were both 97%. However, the CAA values in the original mix designs were 88% for K-25 and 78% for US-83. Therefore, there is an obvious increase in the CAA values in both RAPs. This increase may result from crushing of aggregates during the compaction for construction and the milling process for the recovery of RAPs.

Moisture-density Relationship

Figure 2 presents the moisture-density curves of the RAPs based on the modified Proctor test. It is shown that the optimum moisture contents and the maximum dry densities of the RAPs from US-83 and KS-25 were 3.22%, 1.78g/cm^3 and 3.78%, 1.82g/cm^3, respectively. Therefore, the RAP from KS-25 had a higher optimum moisture content and maximum dry density than that from US-83. This result may be attributed to the fact that the RAP from KS-25 had higher binder content and a lower fine aggregate angularity, which made the compaction easier.

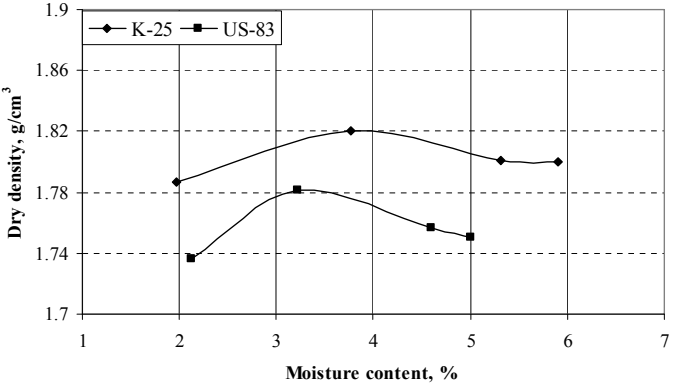

FIG. 2. Moisture-density curves

Mechanical Properties

Los Angeles Abrasion Test

The LA abrasion values for the aggregates obtained from both RAPs were 38% and the ratio of the mass loss after 100 revolutions to the mass loss after 500 revolutions was 0.3, which indicates that the aggregates from the RAPs were not of uniform hardness.

California Bearing Ratio (CBR) Test

Figure 3 presents the CBR values of both RAPs at different moisture contents. This figure shows that the RAP from K-25 had lower CBR values than that from US-83. Even though the RAP from K-25 had a higher maximum density, it had lower CBR values because of its higher binder content.

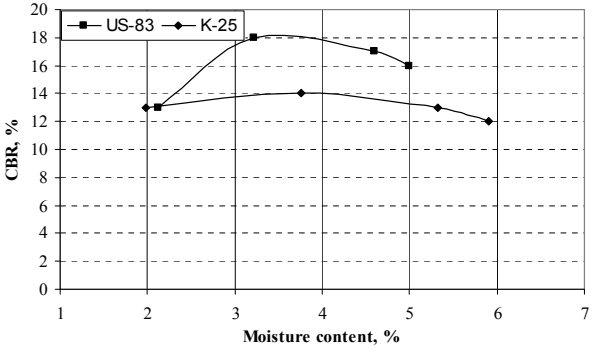

FIG. 3. CBR vs. moisture content curves

CONCLUSIONS

The following conclusions can be drawn from this study:

- The percentage of fine particles increased from the original mixes to the RAPs due to the milling process.
- The aggregates from RAPs had lower specific gravity values than those used in the mix designs.
- There was an obvious increase in the coarse aggregate angularity in the RAPs from that in the mix designs.
- The RAP with a higher binder content and a lower fine aggregate angularity had a higher optimum moisture content and maximum dry density.
- The aggregates from the RAPs were not of uniform hardness.
- The RAP with a higher binder content had lower CBR values.

ACKNOWLEDGMENTS

This research is financially sponsored by the Kansas Department of Transportation (KDOT) through the KTRAN program. KDOT engineers collected and supplied the RAP samples and the original mix designs used in this study. All the support and help are greatly appreciated.

REFERENCES

ASTM C127 – 07. Standard Test Method for Density, Relative Density (Specific Gravity), and Absorption of Coarse Aggregate.

ASTM C131 – 06. Standard Test Method for Resistance to Degradation of Small-Size Coarse Aggregate by Abrasion and Impact in the Los Angeles Machine.

ASTM C1252 – 06. Standard Test Methods for Uncompacted Void Content of Fine Aggregate (as Influenced by Particle Shape, Surface Texture, and Grading**).**

ASTM D1557 – 07. Standard Test Methods for Laboratory Compaction Characteristics of Soil Using Modified Effort (56,000 ft-lbf/ft^3 (2,700 kN-m/m^3).

ASTM D1883 - 07e1**.** Standard Test Method for CBR (California Bearing Ratio) of Laboratory-Compacted Soils.

ASTM D6307 – 05. Standard Test Method for Asphalt Content of Hot-Mix Asphalt by Ignition Method.

Bennert, T. and Maher, A. (2005). "The Development of Performance Specification for Granular Base and Sub-base Material". *Final Report, FHWA-NJ-2005-03.*

Huang, B. and Vukosavljevic, D. (2006). "Laboratory Study of Fatigue Characteristics of HMA Mixtures Containing Recycled Asphalt Pavement (RAP) ". The University of Tennessee, Knoxville.

Kansas Test Method KT-31 (2007). "Determination of Percentage of Crushed Particles in the Crushed Gravel". Kansas Department of Transportation.

Kansas Test Method KT-34 (2005). " Sieve Analysis of Extracted Aggregate". Kansas Department of Transportation.

Locander, R. (2009). "Analysis of Using Recycled Asphalt Pavement as a Base Course Material". *Final Report,* Report No. CDOT-2009-5.

Field Evaluation of Recycled Pavement Materials at MnROAD

Haifang Wen[1], M. ASCE; Wilfung Martono[2], Tuncer Edil[3], Fellow ASCE; Timothy R. Clyne[4]; and Robert Patton[5]

[1]Assistant Professor, Washington State University, Dept. of Civil & Environmental Engineering, Spokane St, Pullman, WA 99164-2910; Email: haifang_wen@wsu.edu
[2]Former Graduate Student, Department of Civil and Environmental Engineering, University of Wisconsin at Madison, 1415 Engineering Drive, Madison, WI 53706-1691
[3] Professor, Department of Civil and Environmental Engineering, University of Wisconsin at Madison, 1415 Engineering Drive, Madison, WI 53706-1691, E-mail: edil@engr.wisc.edu
[4]MnROAD Forensic Engineer, Minnesota Department of Transportation,1400 Gervais Avenue, Maplewood, Minnesota 55109-2044, E-Mail: tim.clyne@dot.state.mn.us
[5]Project Manager, National Energy Technology Laboratory, U.S. Department of Energy, Pittsburgh PA 15236; Robert.Patton@NETL.DOE.GOV

ABSTRACT: In-place recycling of asphalt pavement is an inexpensive and sustainable pavement rehabilitation method. Existing Hot Mix Asphalt (HMA) layer is pulverized and blended with some of or the entire base course to form a broadly graded material referred to as recycled pavement material (RPM). RPM can be compacted as the new base course and overlaid by a new layer of HMA. Additives may be added to improve the properties of RPM base course, such as cement or fly ash. In this study, three flexible pavement sections with different base materials were constructed at MnROAD test facility to evaluate the RPM with and without fly ash additive and to compare them with conventional crushed aggregate base course, Minnesota Department of Transportation Class 6 aggregates. The fly ash used was a high carbon and high calcium content off-specification self-cementitious fly ash. Various field tests were conducted, using dynamic cone penetrometer, lightweight deflectometer, soil stiffness gauge, and falling weight deflectometer. The backcalculated modulus of base materials from these field tests were compared with each other and with the resilient modulus from laboratory tests. It was found that there are significant differences in the moduli from different test methods. It is believed that this is due to the stress and strain dependence of these materials. However, in any case, the fly ash stabilized RPM has higher modulus than RPM, followed by Class 6.

INTRODUCTION

A majority of highways in the United States were built in 1950s and 1960's and have deteriorated significantly to date. More than 96 percent of the current highways

consist of asphalt pavement. Quarrying virgin aggregates for highway construction also results in environmental problems and energy consumption. An alternative to quarrying virgin materials is in-place recycling of asphalt pavement. This recycling process is relatively inexpensive and contributes towards sustainable pavement rehabilitation. Existing hot mix asphalt (HMA) layer is pulverized and blended with some of or the entire base course to form a broadly graded material referred to as recycled pavement material (RPM) (Li et al. 2008). There is an increasing trend towards recycling existing asphalt pavement and using as base course for the new pavement (FHWA 1995). However, there are concerns on the load-carrying capacity and deformability of a base layer made of RPM.

RPM can be directly compacted and overlaid by a new layer of HMA. Also, additives may be incorporated to improve the properties of RPM base course, such as cement or fly ash. In this study, three flexible pavement test cells with different base materials were constructed at MnROAD test facility to evaluate the effectiveness of RPM with and without fly ash addition and to compare it with traditional crushed aggregate base course which is a Minnesota DOT Class 6 granite aggregate (Clyne and Palek 2008). The MnROAD test facility is a two-lane pavement test track located 40 miles northwest of Minneapolis. The fly ash used in this study is categorized as high carbon fly ash called Cementitious High Carbon Fly Ash (CHCFA). It is one of the by-products of burning coal in power generating facilities. Fly ash is frequently described as being composed of glassy, spherical particles that are primarily the size of silt.

This study evaluated the benefit of using RPM, RPM stabilized with CHCFA, and traditional crushed aggregate base course by comparing (1) moduli measured in the laboratory; and (2) field modulus measured directly on the base layers during construction;

MATERIALS AND TEST METHODS

Materials

RPM and Class 6 Aggregate

The RPM was produced by pulverizing the in-situ asphalt pavement at MnROAD. The RPM consisted of 50% of hot mix asphalt and 50% of existing crushed aggregate base course. The Class 6 aggregate is a granite base course material used by MnDOT. The gradations of the RPM and Class 6 are shown in Table 1.

Table 1. Gradation of RPM and Class 6

Sieve Opening, mm		37.5	25	19	12.7	9.5	4.75	2	0.425	0.075
Percent Finer, %	RPM	100	99	96	86	77	60	39	13	6
	Class 6	100	100	98	73	55	32	11	4	2

Fly Ash

Fly ash obtained from Unit 8 of the Riverside Power Plant in Minneapolis, MN (operated by Xcel Energy) was used to stabilize the RPM. This fly ash has a calcium

oxide (CaO) content of 22.37% and a carbon content of 16.35%. Riverside Unit 8 fly ash is a cementitious high-carbon fly ash. A fly ash application rate of 14% by weight of dry mix was used to stabilize RPM as base course.

Test Methods

During construction, the base course materials were sampled and stored for laboratory testing. The fly ash stabilized RPM specimens were fabricated in the laboratory. The moisture-density relationship of RPM, fly ash stabilized RPM, and Class 6 were obtained in accordance with ASTM D 1557. Resilient modulus (M_r), were also characterized in accordance with the National Highway Research Program (NCHRP) 1-28A test protocol (Witzack 1997). The field evaluation included Dynamic Cone Penetrometer (DCP), Lightweight Deflectometer (LWD), FWD, and Soil Stiffness Gauge (SG) on the top of base course.

TEST RESULTS

Laboratory Tests

The laboratory summary resilient moduli (M_r) of the base materials are shown in Table 2. The Mr results were compared with moduli from other field tests. It is seen that for resilient modulus, fly ash stabilized RPM had much higher resilient modulus than RPM, followed by Class 6 crushed aggregates.

Table 2. Summary of Laboratory Test Results of Field Sampled Materials

Material	Curing Time (days)	M_r (MPa)
Class 6	-	220
RPM	-	257
Fly Ash /RPM	7	2984
	28	4334

Results of Field Tests Directly on Base Courses

During the construction, after the base courses were finished, field tests were conducted directly on the base courses. The field test results were analyzed to obtain the modulus of base materials. For the DCP measurement, 15 readings were taken in each test location. From these readings, the first two and the last two reported readings were not used in the calculation of DCP Penetration Index (DPI) (de Beer 1991*)*.

Table 3 summarizes the direct measurements of the moduli of the base layer. It can be seen that for any of M_r and field test methods, fly ash stabilized RPM had higher modulus than RPM, followed by crushed aggregate, as shown in Figure 1 in which the number after the test method indicates the days after the construction of base courses. The resilient modulus measured in the laboratory was always higher than moduli from field tests. In the field tests, DCP tests resulted in higher modulus than LWD, SSG, and FWD. The M_r of RPM was 257 MPa, while the highest modulus for RPM from field tests, 104.58MPa, was obtained from the DCP in this case. The difference

between M_r and backcalculated moduli for stabilized materials is even larger. The M_r of 28-day stabilized RPM was 4,334 MPa, while the highest modulus from field tests was 364 MPa. The M_r is more than ten times higher than moduli form field the tests. The moduli from SSG were higher than those from LWD and FWD tests, except for stabilized RPM. Between LWD and FWD tests, LWD generated higher moduli. This might be related to the stress/strain-dependence of these materials. Each of these test methods applies different load levels to the materials. The stress/strain-dependence will affect the modulus backcalculated from the response of materials. Peterson et al. (2006) attributed this variation of modulus from different field tests to sensing depth, soil heterogeneity, and vertical stress levels. However, the sensing depth and vertical stress level might be related to each other, as larger vertical stress can impact deeper soils. These heterogeneities are also affected by the volume of soil impacted by the loads and also depend on the vertical stress levels. Therefore, it is believed that load levels are most important factors for the variation of modulus from different field tests.

Table 3. Comparison between Laboratory M_r and Field measurement Moduli

Days since Placement of Fly Ash Mixtures	Test Method	Fly Ash+RPM	RPM	Class 6
		Average Moduli, MPa		
7	M_r	2984	257	220
28	M_r	4334		
8	DCP	3634	105	67
8	LWD	182	42	15
22	DCP	328	83	63
22	FWD	134	36	22
22	SSG	159	70	59
26	FWD	112		

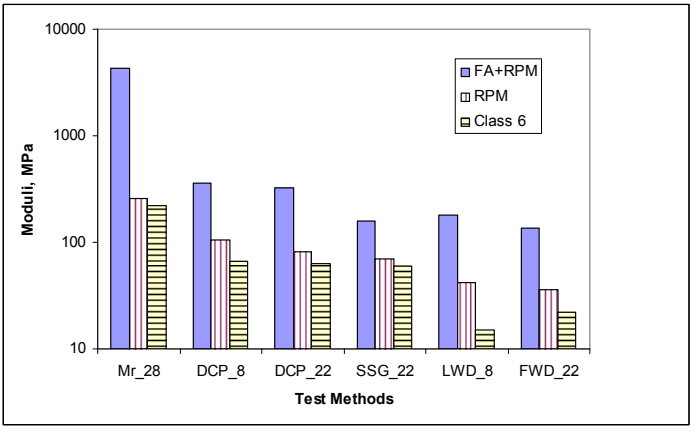

FIG. 1. Comparison of moduli from different tests methods

Another observation was that with the increase of time after the placement of the base courses, the moduli of base materials dropped slightly. For all three base materials, the 8-day DCP moduli were higher than 22-day moduli. For FWD tests, the 22-day moduli also were higher than the 28-day moduli. It is believed that moisture infiltrated into the base courses and weakened the materials. However, this finding is unexpected for the fly ash stabilized RPM, as the continuous hydration of fly ash would result in an increase of moduli with the increase of curing time. This indicated that, after the construction of base courses, surface layers should be constructed promptly, even for the stabilized layers, to prevent the weakening of base course materials, mostly due to precipitation.

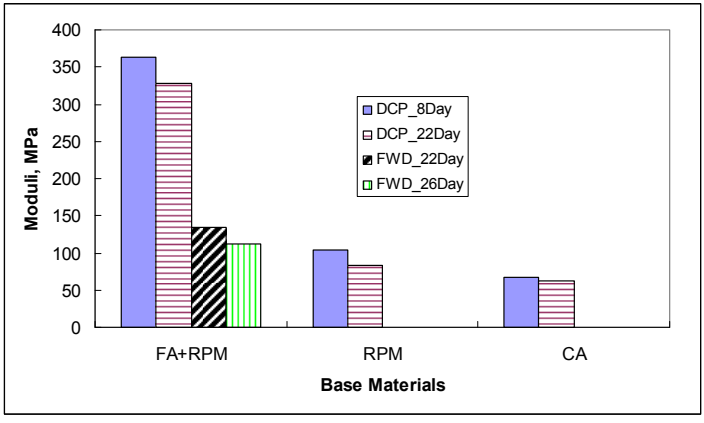

FIG. 2. Modulus from field tests as function of curing days

SUMMARY OF FINDINGS

Test sections were constructed at MnROAD test facility using three different base course materials that included a recycled pavement material (pulverized HMA layer and base layer), a recycled pavement material with a high carbon fly ash, and a crushed granite aggregate (as control). Both the field and the laboratory tests indicated that the recycled pavement material stabilized with fly ash give the best performance followed by the unstabilized recycled pavement material and the conventional crushed aggregate base course. Different field tests give different moduli for the same material, possibly due to the stress/strain-dependence of the materials. However, collectively they present a clear picture of the relative quality of the base course materials considered.

REFERENCES

Li, Lin, C.H. Benson, T.B. Edil, B. Hatipoglu, and O. Tastan. (2008). "Evaluation of Recycled Asphalt Pavement Material Stabilized with Fly Ash." *Geotechnical and*

Geological Engineering, 177-187, Netherlands

Federal Highway Administration (1995). "Pavement Recycling Executive Summary and Report." Report No. FHWA-SA-95-060, Washington, D.C.

Clyne, T.R. and L.E. Palek. (2008) "2007 Low Volume Road & Farm Loop Cells 33, 34, 35, 77, 78, 79, 83, 84 Construction Report." *Minnesota Department of Transportation*, Maplewood, MN.

Wen, H., J. Warner, and T.B. Edil. (2008) "Laboratory Comparison of Crushed Aggregate and Recycled Pavement Material with and without High-Carbon Fly Ash." *Presented at 87th Annual Meeting of Transportation Research Board*, Washington, D.C.

Witczak, M.W. (1997) "Harmonized Test Methods for Laboratory Determination of Resilient Modulus for Flexible Pavement Design." National Council Highway Research Program Report 1-28A Report, *Transportation Research Board of National Academies*, Washington, D.C.

De Beer, M. (1991). "Use of the Dynamic Cone Penetrometer (DCP) in the Design of Road Structures." *Proceedings of the tenth regional conference for Africa on Soil Mechanics & Foundation Engineering and the third International Conference on Tropical & Residual Soils*. Maseru. 23-27. Ham, M.E, 1966, Foundations ojTheoretical Soil Mechanics, McGraw-Hill, p. 81

Petersen D.L., Siekmeier J., Nelson C.R., and Peterson R.L. (2006). "Intelligent Soil Compaction Technology Results and a Roadmap Toward Widespread Use.", *Transportation Research Record: Journal of the Transportation Research Board*, No. 1975, Washington, D.C., pp. 81–88.

Laboratory Investigation of Seasonal Variations in Resilient Modulus of Alaskan Base Course Material

Lin Li[1], Juanyu Liu[2], Xiong Zhang[3], and Stephan Saboundjian[4]

[1]Graduate Research Assistant, Department of Civil and Environmental Engineering, University of Alaska, Fairbanks, AK 99775-5900; lli10@alaska.edu
[2]Assistant Professor, Department of Civil and Environmental Engineering, University of Alaska, Fairbanks, AK 99775-5900; jliu6@alaska.edu
[3]Assistant Professor, Department of Civil and Environmental Engineering, University of Alaska, Fairbanks, AK 99775-5900; xzhang11@alaska.edu
[4]Statewide Pavement Engineer, Alaska Department of Transportation & Public Facilities, Anchorage, AK 99507; steve.saboundjian@alaska.gov

ABSTRACT: In Alaska, granular base course materials, typically known as D-1 aggregate materials, undergo significant changes in resilient properties due to seasonal conditions. In the springtime, saturated base course materials are weakened due to thawing, resulting in reduced resilient properties. This paper investigates seasonal effects on the resilient modulus (M_R) of a D-1 material from southeast Alaska. Experimental work was performed on a granular material to investigate the impact of fines content, moisture and temperature on its resilient modulus. A frost heave/freezing cell was designed to condition soil specimens prior to resilient modulus testing. Depending on its thermal state, two separate prediction models were used to estimate M_R of the D-1 material.

INTRODUCTION

Since the introduction of the concept of resilient modulus (M_R) by Seed et al. (1955), a considerable amount of research has been devoted to measuring the resilient properties of granular materials (Smith and Nair 1973; May and Witczak 1981; Elliot and Thornton 1988; Elfino and Davidson 1989; Pan et. al. 2006). Resilient modulus is a required layer parameter in the recent American Association of State Highway and Transportation Officials' pavement design guide (AASHTO 2008). In Alaska, granular unbound materials, known as D-1 aggregate materials, are often used as base course layer material. Resilient properties of this material display significant variations due to seasonal conditions. Base materials saturation and weakening because of partial thawing is a typical springtime condition, which is normally reflected by reductions in the resilient properties. Due to the complexity of problem, little research has been done in this field. Simonsen et al. (2002) carried extensive resilient modulus laboratory test during full freeze-thaw cycle on various coarse and fine-grained sub-grade soils in

which a closed-system and omnidirectional freezing and thawing were used. It was found that at subfreezing temperatures, resilient moduli of the soils are dependent upon stress levels and the stress dependence varied among different soils. After completed freeze-thaw, the soils displayed a decrease of approximately 20–60% in resilient modulus depending on soil types. In never-frozen/recovered soils the universal model displayed the best overall performance. Thawed specimens generally showed highly unstable behavior and, in most cases, no significant correlations emerged from this part of the analysis. The results were extremely important for engineers in cold regions for the design of pavement structures. However, a closed-system is the most conservative test method in terms of stiffness reduction during thawing, which cannot necessarily represent the real filed conditions. In this study, an open-system was designed for sample conditioning to ensure uniaxial freezing and free water access during the freezing process. This paper investigates seasonal variations of resilient modulus for D-1 material from Juneau (southeast Alaska). Laboratory tests were conducted to investigate the impact of several factors on resilient modulus of D-1 materials under different moisture, temperatures and fines contents conditions. Prediction models were used to estimate M_R of D-1 materials under different thermal conditions.

SOIL PROPERTIES AND EXPERIEMENTAL DESIGN

Gradation curves and soil classification of four different types of D-1 materials are shown in Figure 1 and Table1, respectively. Table 2 summarizes the laboratory test factorials. Four fines contents (P200 = percent passing #200 sieve, ie. materials finer than 0.075 mm) were chosen to reflect the in-situ state of the material after placement. Occasionally in the field, the 6% specification requirement is exceeded due to material degradation (manipulation and compaction effects). Increased fines content has detrimental effects on the drainage and resilient properties of the base course layer. A moisture content of 6%, which is 0.7% above the optimum moisture content (OMC), is the greatest moisture content that the soil could hold during compaction. In this study, resilient properties of the granular materials were tested according to AASHTO T-307 by using a repeated-load triaxial testing apparatus.

Table 1. Physical Properties of D-1 Materials

D-1 material	Classification*	Maximal dry density (pcf)	OMC (%)
3.15% fines	GW	156.0	5.3
6% fines	GW-GM	156.2	5.3
8% fines	GW-GM	156.5	5.4
10% fines	GP-GM	157.1	5.5

*GW — represents well-graded gravel with sand
GW-GM — represents well-graded gravel with silt and sand
GP-GM — represents poor-graded gravel with silt and sand.

Table 2. Experimental Design Factors

Factors	No. of levels	Levels
Fines content, %	4	3.15, 6, 8, and 10
Temperature, ^{o}C	8	-10,-7,-5,-4,-3,-2,-1,and 20
Moisture content, %	3	OMC, 2 below OMC, and 0.7 above OMC

In order to simulate natural in-situ roadway freezing conditions, a frozen cell was designed for this study. Prior to placing a given specimen in the resilient test apparatus, it was conditioned (frozen) in this newly designed freezing cell. A schematic and a photo of the freezing/frost heave setup are shown in Figure 2. Figure 2a shows the cross-section of the frost heave cell. Temperatures at the top and bottom of the soil specimens were controlled at -4°C and 1°C, respectively. At the bottom of the soil sample, filter paper and porous stone were used, to allow water uptake during freezing. Soil specimens were surrounded by a thick insulation to block lateral heat transfer, ensuring that frost heave was one dimensional. Linear variable displacement transducers (LVDTs) were placed at the top of soil specimens to measure vertical displacement variation during the freezing process. Thermocouples were installed at different locations of the soil specimen to monitor the freezing process. When temperature and frost heave reached a stable value, (usually in 2-3 days period), frost heave is considered to be complete.

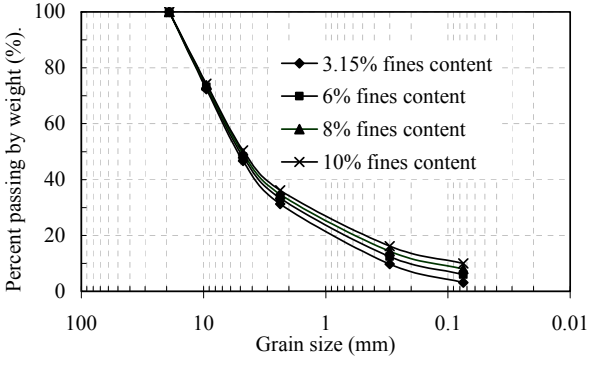

FIG. 1. Gradation curves of D-1 materials

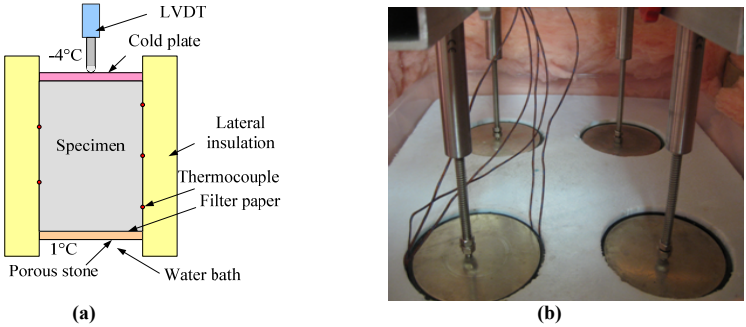

FIG. 2. Frost heave setup

TEST RESULTS AND ANALYSIS

After undergoing freezing in the frost-heave apparatus, a soil specimen was placed in the resilient modulus apparatus. In order to simulate spring thaw, resilient modulus tests were started from the lowest temperature (i.e., -10°C) to the warmest temperature (i.e., 20°C). Each specimen was generally tested at eight temperatures (i.e., -10, -7, -5, -4, -3, -2, -1 and 20°C) during one full freeze-thaw cycle. Test results indicated that when a soil sample is frozen, the variation of soil resilient moduli with varying fines and moisture contents is insignificant. In other words, effects of all influencing factors were weakened or somewhat eliminated by the frozen state. Test results also indicated that the resilient modulus of the soil is highly dependent on temperature. Figure 3a shows some typical test results. For temperatures ranging from -10°C to -5°C, there is no significant change in the resilient modulus. From -3°C to 0°C, the resilient modulus decreased significantly. There is also an unexpected increase in the resilient modulus of soil specimen temperatures ranging from -5°C to -3°C. This phenomenon might be attributed to two possible reasons: (1) due to repeated loading at each temperature, creep comes up which densifies the soil sample (see Figure3b); (2) some unfrozen water in the soil specimen refroze during conditioning at temperatures range of -5°C to -3°C. This effect however is not significant in the temperature range from -3°C to 0°C. As a result, bonding effect was strengthened by an increase of contact area after repeated load and conditioning. Soil resilient modulus was generally considered to be constant above 0°C. Therefore, for resilient modulus testing at nonfreezing temperatures, only 20°C was selected. Results for these never-frozen soils are shown in Table 3. Data in Row 2 represent moisture contents. Compared to results at subfreezing temperatures, M_R decreases significantly.

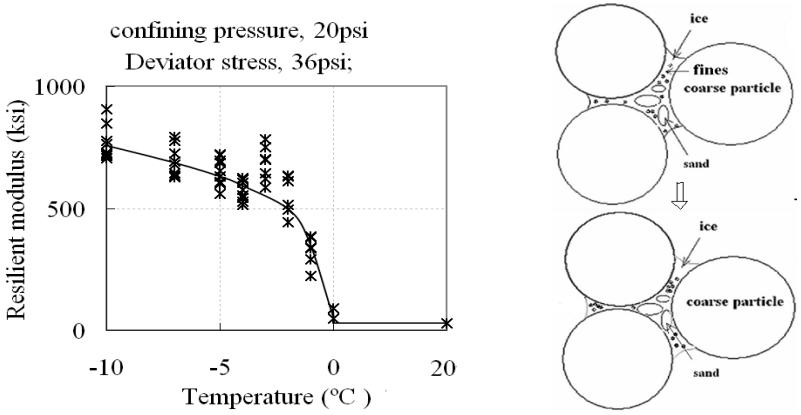

(a) Variation of M_R with Temperature **(b) Change of Soil Structure**

FIG. 3. M_R results and change of soil structure

Table 3. Results of M_R (ksi) Test at 20°C

CP*(psi)	DS*(psi)	10% fines			8% fines			6% fines			3.15% fines		
		6.0%	5.3%	3.3%	6.0%	5.3%	3.3%	6.0%	5.3%	3.3%	6.0%	5.3%	3.3%
3	2.7	6.2	11.5	46.7	5.9	12.7		4.7	7.8	22.4	5.4	12.2	20.4
	5.4	9.0	13.0	30.8	9.3	14.2	33.5	7.2	10.8	20.6	8.2	14.9	21.8
	8.1	11.8	14.5	29.5	12.3	16.2	28.8	9.7	12.0	21.2	11.0	16.7	24.5
5	4.5	8.0	11.3	45.7	7.9	19.0	39.8	5.9	8.8	25.3	7.5	12.1	32.4
	9	12.4	16.8	39.0	12.9	17.8	35.4	10.1	12.4	26.0	11.8	19.4	32.3
	13.5	15.9	18.3	39.5	16.9	19.9	36.4	13.2	14.5	28.1	15.5	20.9	31.6
10	9	13.9	19.9	60.0	15.5	22.7	53.5	11.5	20.0	38.9	15.5	27.3	45.0
	18	20.2	23.7	57.4	21.7	26.2	52.1	16.6	19.2	40.5	20.8	28.8	47.8
	27	25.0	26.5	56.6	27.1	27.0	51.8	21.0	21.0	42.7	24.8	31.0	47.6
15	9	16.8	22.8	84.0	17.8	22.4	73.8	13.9	11.5	50.1	17.9	34.9	57.6
	13.5	18.2	22.6	69.4	19.7	23.4	61.9	13.7	22.4	48.0	17.9	29.1	51.2
	27	26.3	28.3	68.3	28.4	22.1	60.8	20.6	27.9	51.4	25.6	36.2	55.8
20	13.5	20.7	23.7	85.1	21.9	30.5	78.4	15.0	18.1	58.0	21.5	35.8	64.8
	18	22.5	25.8	79.2	24.5	30.4	71.4	15.4	21.9	57.2	22.5	36.5	62.4
	36	26.3	28.0	68.4	28.2	31.3	61.9	20.3	28.6	58.7	25.9	39.3	56.8

* CP — confining pressure, DS — deviator stress

When moisture content increases, excess pore-water pressure will develop due to repeated loading. As pore-water pressure develops, effective stress decreases with a subsequent decrease of both strength and stiffness. Based on the results in Table 3, pronounced decrease of M_R can be found due to increase of moisture content.

In Table 3, impact of fines on resilient modulus is not clear. Possible reason for this may be fines are not enough to fill the voids between gravels and sands, and particle interlock was not affected by fines.

Efforts were also dedicated to determine the resilient modulus of the D-1 material

after a freeze-thaw cycle. Soil specimens were thawed without allowing water drainage. This was used to simulate Alaskan springtime thawing: during spring, thawing starts from the top of the base course layer and migrates downwards. The frozen soil beneath the thawing front is usually highly impermeable which prevents any vertical drainage. It usually causes supersaturated conditions in the upper roadbed. Excess water dramatically reduces soil strength and increases the vulnerability of the pavement structure to damage under traffic loading. However, most lab specimens cannot even sustain a preloaded process after a freeze-thaw cycle, under undrained conditions. Limited data from resilient modulus testing at room temperature after a freeze-thaw cycle indicates that M_R decreases significantly when compared to a soil specimen which did not undergo a freeze-thaw cycle.

REGRESSION

Empirical correlations for the resilient modulus have been proposed by many researchers Most of these correlations were developed from laboratory experiments (Witczak and Uzan 1988, May and Witczak 1981, Karasahin 1993, Johnson et. al. 1986). In this study, initially, an attempt was made to use all the data to develop a model valid at all temperatures. However, this proved unsuccessful due to the change of water content before and after the freezing process. Consequently, the regression analysis was divided into two parts, where resilient responses above and below 0°C were analyzed separately. For the regression analysis above 0°C, a constitutive model known as the octahedral stress model, consisting of a M_R-stress relation (Uzan 1985), is chosen to estimate the resilient modulus of D-1 material A mathematical expression for this model is shown in Equation 1.

$$M_R = k_1 P_a \left(\frac{\theta}{P_a} \right)^{k2} \left(\frac{\tau_{oct}}{P_a} + 1 \right)^{k_3} \tag{1}$$

Where, M_R = resilient modulus, psi; θ = bulk stress $= \sigma_1 + \sigma_2 + \sigma_3$, σ_1 = major principal stress; σ_2 = intermediate principal stress $= \sigma_3$ for M_R test; σ_3 = minor principal stress/ confining pressure; τ_{oct} = octahedral shear stress $= \frac{1}{3}\sqrt{(\sigma_1 - \sigma_2)^2 + (\sigma_1 - \sigma_3)^2 + (\sigma_2 - \sigma_3)^2}$; P_a = normalizing stress (atmospheric pressure, 14.7 psi); k_1, k_2, k_3 = regression constants; and deviator stress is given by:

$$\sigma_d = \sigma_1 - \sigma_3 \tag{2}$$

For a given test, since $\sigma_2 = \sigma_3$ and $\sigma_d = \sigma_1 - \sigma_3$, then $\tau_{oct} = \frac{\sqrt{2}}{3}\sigma_d$. In this model, M_R is a function of both bulk stress and octahedral shear stress. Table 4 presents the regression constants of the regression analysis.

Table 4. Results of Regression

Moisture content	Fines content	k_1	k_2	k_3	R^2
6%	10%	1.194	0.252	0.342	96.3%
	8%	1.252	0.270	0.347	95.8%
	6%	1.191	0.516	0.442	93.3%
	3.15%	1.025	0.337	0.276	94.8%
5.30%	10%	1.195	0.288	0.152	95.1%
	8%	1.023	0.386	-0.011	85.7%
	6%	1.231	0.231	0.335	86.2%
	3.15%	0.923	0.595	-0.040	95.0%
3.30%	10%	1.138	0.806	-0.427	96.2%
	8%	1.095	0.780	-0.382	97.8%
	6%	1.032	0.516	-0.183	99.6%
	3.15%	1.118	0.731	-0.232	97.2%

Multiple nonlinear regression was performed between model constant and basic soil properties, and following equations were established:

$$\log k_1 = -0.04262 + 0.8113 f_c - 0.706 m_c;\ R^2 = 33\% \quad (3)$$

$$k_2 = 1.4759 - 1.0889 f_c - 19.34 m_c;\ R^2 = 85.9\% \quad (4)$$

$$k_3 = -1.0664 - 0.4211 f_c + 23.56 m_c;\ R^2 = 84.8\% \quad (5)$$

Where, f_c = fines content, % and m_c = moisture content, %.

The model constants; namely k_1, k_2 and k_3, will be used here to study the effect of moisture content and fines content on M_R. k_1 represents the value of M_R at unit deviator stress and confining pressure. Though regression results did correlate poorly, k_1 varies in a small range and can be used for prediction of M_R. However, regression of k_2, k_3 provide R^2 s greater than 80%. The plot for M_R calculated using Equation 1 is shown in Figure 4a which displays good predicted performance.

For the regression analysis below 0°C, pavement structures are always "stronger" than that above 0°C. Hence, study of resilient properties is not considered to be of great importance. In this regression analysis part, resilient modulus at only one confining pressure and deviator stress level (i.e., confining pressure=20 psi; deviator stress= 36 psi) was conducted. The unexpected increase of resilient modulus at -3°C was not taken into consideration in this regression. According to Simonsen et al. (2002), a mathematical expression of the regression model is shown in Equation 6. Temperature is the only parameter in this model.

$$M_R = e^{k_1 + k_2/T} \quad (6)$$

Where, k_1, k_2 = regression constants and T = temperature, °C.

Performing the regression analysis, k_1 and k_2 were found to be 6.6644 and 0.9193 respectively with R^2 of 84.9%. The plot for M_R calculated using Equation 6 is shown in Figure 4b.

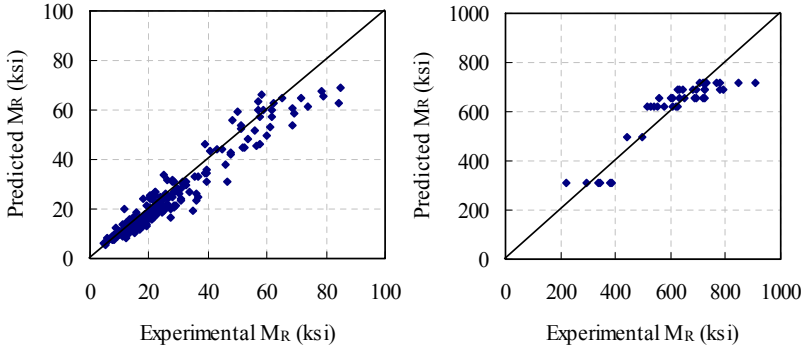

(a) nonfreezing temperature **(b) subfreezing temperature**

FIG. 4. Predicted M_R vs. Laboratory M_R for D-1 material

CONCLUSION AND FUTURE RESEARCH

In this study, the seasonal change of the resilient modulus of an Alaskan D-1 base course material was investigated. Varying the fines and moisture contents, resilient properties of the D-1 material exhibited different behaviors depending on the specimen temperature. Several conclusions can be drawn from this study:

1. With increase of moisture content, M_R significantly reduces due to increase of moisture content. Moisture content is considered to be one of the most important factors which affect resilient properties of granular material at room temperature.
2. At room temperature, when fines are not enough to fill the voids between gravels and sands, resilient properties of this material will not be significantly affected. With in the scope of this study (i.e., fines content range from 3.15% to 10%), impact of fines content on resilient modulus is not clear. While it does not mean fines content is not an important influence factor when fines content is higher.
3. When the soil is frozen, temperature is a primary factor affecting resilient properties of the granular material. Generally, resilient modulus of granular materials increases as temperature decreases.
4. During seasonal change, resilient properties of the soil are significantly affected by the freeze-thaw action. In a very dense soil the volume might increase due to freeze-thaw, making the soil structure slightly looser and leading to reduction in resilient modulus.
5. Regression models used in this study can be applied to predict M_R of Alaska D-1 material with different moisture and fines contents, under different thermal conditions.

REFERENCES

AASHTO (2008). *Mechanistic-Empirical Pavement Design guide: A Manual of Practice*. Washington, D.C.

Elfino, K. and Davidson, J.L. (1989). "Modeling Field Moisture in Resilient Moduli Testing. Resilient Moduli of Soils: Laboratory conditions." *ASCE Geotechnical Special Publication,* 24, pp. 31-51

Elliot, R.P. and Thornton, S.I.(1988). "Simplification of Subgrade Resilient Modulus Testing." *In Transportation Research Record: Journal of the Transportation Research Board*, No. 1192, Transportation Research Board of the National Academies, Washington, D.C., 1988.

Johnson, T. C., Berg, R. L. and Dimillio, A. (1986). "Frost action predictive techniques: An overview of research results". *Journal of the Transportation Research Board*, No. 1089, Washington, D.C., pp. 147–161.

Karasahin, M. (1993). "Resilient behaviour of granular materials for analysis of highway pavements", PhD thesis, Dept. of Civ. Engr., University of Nottingham, Nottingham, England.

May, R. W., and Witczak, M. W. (1981). "Effective Granular Modulus to Model Pavement Responses". *Journal of the Transportation Research Board*, No. 810, Washington, D.C., pp. 1–9.

Pan T. et. al. (2006). "Aggregate Morphology Affecting Resilient Behavior of Unbound Granular Materials*". Journal of the Transportation Research Board*, Record No. 1952, Washington, D.C., pp. 12-20.

Seed et al (1955) ''Effects of repeated loading on the strength and deformation of compacted clay''. *Proc., Highway Research Board*, 34, 541–558.

Simonsen, E., Janoo, V. C. and Isacsson, U. (2002). "Resilient Properties of unbound Road Materials during Seasonal Frost Conditions". J. *Cold Reg. Engr*. Volume 16, Issue 1, March pp. 28-50.

Smith, W. S., and Nair, K. (1973). "Development of procedures for characterization of untreated granular base course and asphalt-treated base course materials." *Rep. No. FHWA-RD-74-61*, Federal Highway Administration, Washington, D.C..

Uzan, J. (1985). "Characterization of Granular Material". *Journal of the Transportation Research Board*, No. 1022, Washington, D.C., pp. 52–59.

Witczak, M. W., and Uzan, J. (1988). "The universal airport pavement design system, *Report I of IV*: Granular material characterization". University of Maryland, College Park, Md.

Particle Shape, Type and Amount of Fines, and Moisture Affecting Resilient Modulus Behavior of Unbound Aggregates

Debakanta Mishra[1], Erol Tutumluer[2], M. ASCE, Yuanjie Xiao[3]

[1]Graduate Research Assistant, Department of Civil and Environmental Engineering, University of Illinois Urbana-Champaign, Urbana, IL, 61801, USA, dmishra2@illinois.edu
[2]Professor, Department of Civil and Environmental Engineering, University of Illinois Urbana-Champaign, Urbana, IL, 61801, USA, tutumlue@illinois.edu
[3]Graduate Research Assistant, Department of Civil and Environmental Engineering, University of Illinois Urbana-Champaign, Urbana, IL, 61801, USA, xiao8@illinois.edu

ABSTRACT: This paper presents the application of Analysis of Variance (ANOVA) approach to study effects of different aggregate properties on the resilient modulus behavior of unbound aggregates. In a recent research project at the University of Illinois, stress-dependent resilient modulus characterization models, in the form proposed for use by the Mechanistic Empirical Pavement Design Guide (MEPDG), were established for three different aggregate types (dolomite, limestone, and uncrushed gravel) using a statistically well-formulated laboratory test matrix. Such a consistent database enabled the evaluation of the model parameter dependence on different aggregate properties, such as particle shape, type and amount of fines, and moisture condition, using the Analysis of Variance (ANOVA) approach. From the statistical analyses, aggregate particle type or angularity was found to have a significant effect on the resilient moduli. At low fines content, the type of fines and moisture state in relation to optimum moisture condition were found to be somewhat insignificant as far as the regression parameter values are concerned. The effect of amount of fines became quite significant especially when the amount of fines was increased.

INRODUCTION

Recent research at the University of Illinois focused on evaluating effects of aggregate type and quality on aggregate cover thickness requirements for constructing pavement platforms on soft subgrade (Tutumluer et al., 2009; Mishra et al., 2010). The overall objective in the first laboratory phase of the study was to develop a statistically well-formulated test matrix to quantify any individual and/or combined effects of different aggregate properties on the unbound aggregate layer performance as indicated by the strength, stiffness, and deformation behavior. Three aggregate

materials, i.e., dolomite, limestone and uncrushed gravel, commonly used in Illinois for subgrade replacement and subbase were obtained to determine their particle shape and angularity quantified by an imaging based measurement system, type and amount of fines (passing No. 200 sieve size or less than 0.075 mm), and moisture state in comparison to optimum moisture content. Evaluating the effects of these properties on aggregate performance would enable researchers and practitioners to establish corresponding property ranges so as to ensure adequate performance of the pavement layers comprised of these aggregates.

For studying the effect of fines on aggregate behavior, it was decided to test the laboratory specimens at four different fines contents. These fines contents were established, to range from very low to very high, as allowed in the field by state specifications. Accordingly, the target fines contents were established to be 4%, 8%, 12% and 16% material passing No. 200 sieve size or particles smaller than 0.075 mm. All aggregate gradations were engineered to have a consistent particle size distribution across all samples and therefore eliminate unwanted variation in aggregate performance due to gradation differences. Figure 1 shows the engineered gradations used to blend samples for testing.

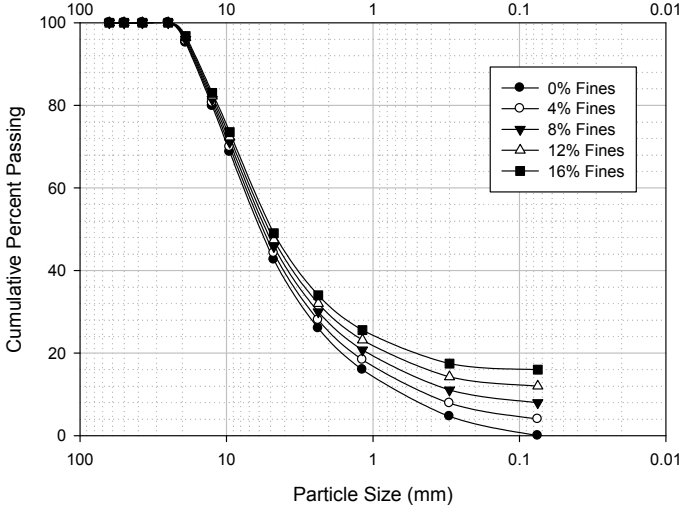

FIG.1. Engineered aggregate gradations for different fines contents

To study the effect of type of fines on aggregate behavior, two different types of fines were used. One was non-plastic in nature such as mineral filler type (with plasticity index PI = 0), and the other was plastic such as cohesive fine-grained soil type (PI in the range of 10-12). The effect of moisture state on aggregate performance was studied by testing the blended aggregate specimens at three different moisture contents: (1) optimum moisture content (OMC or w_{opt}), (2) 90% of w_{opt}, and (3) 110%

of w_{opt}, where the w_{opt} was established through the standard Proctor (AASHTO T-99) test for each aggregate gradation. Therefore, the laboratory test matrix ended up being a 4x2x3 factorial (4 different fines contents, 2 different types of fines, 3 different moisture contents) for each aggregate type. Although a comprehensive database of aggregate performance indicators was generated as a result of this research project, the current paper focuses on the resilient modulus test results only. Therefore, this paper is aimed to identify the relative significances of these aggregate properties affecting the resilient modulus behavior through the Analysis of Variance (ANOVA) approach.

RESILIENT MODULUS CHARACTERIZATION

Starting with the 1986 AASHTO Pavement Design Guide in the U.S., resilient modulus has been used to characterize the stiffness behavior of subgrade soils and granular base/subbase layers subjected to repeated traffic loading. With the routine use of resilient modulus as a primary input into mechanistic-empirical pavement design procedures, many state highway agencies are now making an effort to establish the appropriate "resilient modulus" inputs for granular materials and subgrade soils. As a measure of a material's ability to withstand loading, resilient modulus plays an integral part in the thickness design and long term performance of a pavement. Among several different characterization models proposed for expressing the stress dependent resilient modulus values of unbound aggregate materials, the following form has been adopted by the recent NCHRP 1-37A project deliverable Mechanistic Empirical Pavement Design Guide (MEPDG) software (http://www.trb.org/mepdg/):

$$M_R = K_1 p_a \left(\frac{\theta}{p_a} \right)^{K_2} \left(\frac{\tau_{oct}}{p_a} + 1 \right)^{K_3}$$

where

M_R = Resilient Modulus

p_a = Atmospheric Pressure Normalization Factor

θ = Bulk Stress (First Stress Invariant)

τ_{oct} = Octahedral Shear Stress

K_1, K_2, K_3 : Regression Parameter Estimates

The M_R test data from the research project database was fitted with the above model and values of the model parameters, K_1, K_2, and K_3, were estimated. The test results showed very good fit with the model and the R^2 (coefficient of determination) values obtained for each of the individual test samples were significantly high, above 0.96. To evaluate the dependence of the M_R model parameters with different aggregate properties, an Analysis of Variance (ANOVA) approach was adopted to conduct regression of the model parameters, K_1, K_2, and K_3, individually against each of the four classification variables, i.e., aggregate angularity, amount of fines, type of fines, and moisture condition. The statistical SAS™ software package was used for carrying out all statistical computations. When the actual nonlinear and anisotropic nature of

the resilient modulus behavior is concerned, results for the constant term K_1 were found to be primarily governing the moduli behavior at a certain stress state (Tutumluer, 2009). Accordingly, these aggregate property effects on the K_1 model parameter are presented in this paper for brevity although detailed results for the effects on K_2 and K_3 have been thoroughly investigated as part of the ongoing efforts at the University of Illinois.

The individual aggregate properties influencing K_1 values were found to be interacting with each other. In other words, the effect of amount of fines on K_1 changed depending on the moisture condition as well as the type of fines. Therefore, when studying the individual effects of these parameters on K_1, the aim was to evaluate the effect of each individual property averaged over all possible combinations of the other properties. Another research effort is currently underway to consider the combined effects of all these properties on resilient modulus model parameters and develop prediction equations for the estimates of the K values. Moreover, future work will also focus on conducting full factorial analyses of the data to evaluate the overall effects of different property combinations.

EFFECT OF PARTICLE SHAPE

Aggregate particle shape, texture and angularity have been found to affect performances of unbound and bound layers in pavement structures (Allen, 1973; Barksdale and Itani, 1989; Rao et al., 2002). Unbound aggregate layers having crushed particles have consistently performed superior compared to those with uncrushed particles. Allen (1973) and Barksdale and Itani (1989) investigated the effects of surface characteristics of unbound aggregates and found that angular materials resisted permanent deformation better than rounded particles because of improved particle interlock and higher angle of shear resistance between particles. Barksdale and Itani (1989) also concluded that blade shaped crushed particles were slightly more susceptible to rutting than other types of crushed aggregate and that cube-shaped, rounded river gravel with smooth surfaces was more susceptible than crushed aggregates. More recently, Rao et al. (2002) studied the impact of imaging based aggregate angularity index variations on the friction angle of different aggregate types and reported an improvement in aggregate performance when the percentage of crushed particles increased.

The three aggregate types studied were first tested for particle shape, texture and angularity characteristics. The use of a validated image analysis system, the University of Illinois Aggregate Image Analyzer (UIAIA), was pursued to quantify aggregate shape (flatness and elongation), angularity and surface texture characteristics. The indices computed were: Flat and Elongated (F&E) ratio (Rao et al., 2001), Angularity Index (AI) (Rao et al., 2002), and Surface Texture (ST) index (Rao et al., 2003). The average AI values obtained for the three aggregate types were: 330 for gravel, 428 for dolomite, and 481 for limestone, respectively.

The variance in K_1 with AI was analyzed, and the results are presented in Figure 2 which shows that the p-value corresponding to AI is <0.0001. Taking a significance level (or type 1 error rate α) of 0.05, it can be concluded that the mean K_1 values are not the same across all the three aggregate types. In other words, AI has some effect

on the K_1 values. Although the ANOVA results proved that the K_1 values were affected by aggregate particle angularity, they do not give direct information about whether all three aggregate types were different from each other, or only one aggregate type had different K_1 values than the other two. This question was answered by running two linear contrasts (each with an α level of 0.05) to compare the K_1 value distribution for dolomite with gravel, as well as limestone. The SAS™ output from the linear contrasts is presented in Figure 3, which clearly shows a significant difference between the K_1 values of uncrushed gravel and crushed dolomite ($p < 0.0001$). However, the K_1 values of dolomite and limestone did not have a statistically significant difference among them ($p = 0.0940$). This required grouping the commonly used aggregates into two categories "crushed" and "uncrushed" to account for the particle shape. Accordingly, crushed particles resulted in significantly higher resilient moduli.

EFFECT OF FINES TYPE

The plastic fines often found in uncrushed aggregate gradations were highlighted in a recent Illinois Department of Transportation (IDOT) field study, Experimental Feature IL 03-01, to considerably influence the performances of aggregate cover layers in subgrade applications (IDOT SSM, 2005). From the SAS ANOVA analysis output, Figure 4 indicates that the p-value corresponding to type of fines is not significant at a significance level (α) of 0.05. This is indeed interesting that the type of fines does not have any significant effect on the K_1 model parameter, and the distributions are not statistically different. Plastic fines may in fact cause stress softening behavior to be potentially dictated by the K_3 exponent of the deviator stress.

Source	DF	Sum of Squares	Mean Square	F Value	Pr > F
Model	2	1.33095985	0.66547993	18.29	<.0001
Error	62	2.25645209	0.03639439		
Corrected Total	64	3.58741194			

Source	DF	Type I SS	Mean Square	F Value	Pr > F
AI	2	1.33095985	0.66547993	18.29	<.0001

FIG.2. ANOVA output for the effect of AI on K_1

Contrast	DF	Contrast SS	Mean Square	F Value	Pr > F
Gravel vs Dolomite	1	1.26129846	1.26129846	34.66	<.0001
Dolomite vs Limestone	1	0.10528769	0.10528769	2.89	0.0940

FIG.3. Orthogonal linear contrasts for comparing the effect of AI on K_1

Source	DF	Sum of Squares	Mean Square	F Value	Pr > F
Model	1	0.06711686	0.06711686	1.20	0.2773
Error	63	3.52029508	0.05587770		
Corrected Total	64	3.58741194			

R-Square	Coeff Var	Root MSE	K1 Mean
0.018709	23.09795	0.236385	1.023401

Source	DF	Type I SS	Mean Square	F Value	Pr > F
type	1	0.06711686	0.06711686	1.20	0.2773

FIG.4. ANOVA output for the effect of fines type on K_1

EFFECT OF AMOUNT OF FINES

The samples were blended targeting fines contents (percent passing No. 200 sieve or particles smaller than 0.075 mm) of 4%, 8%, 12%, and 16%. Although the actual fines percentages achieved after blending were not exactly equal to these targeted values, still they were always close to the target values. An ANOVA analysis was conducted to study if the aggregate M_R model K_1 parameters were affected by the fines content in the sample. It should be noted that the fines contents were just treated as aggregate property variables and no correlations were developed to predict K_1 values from the fines percentages. Developing such correlations to predict M_R model parameters from different aggregate properties is currently underway and the results will be published in the future.

From the ANOVA output presented in Figure 5, it can clearly be seen, that an overall effect of the amount of fines on K_1 is not significant ($p >> \alpha = 0.05$). However, to further analyze the effect of fines content on K_1, linear contrasts were run to compare the values for 4% fines content against each of the other three. Results from the linear contrasts are presented in Figure 6. From the linear contrasts, as the amount of fines is increased from 4% to 8%, the difference in K_1 values becomes highly insignificant (shown by a p-value of 0.4055). However, as the fines content is increased gradually, the difference in K_1 values becomes more and more significant (p-value goes to 0.1512 and then to 0.0825). Although, the K_1 values for 16% fines is still not significantly different from that for 4% fines for an α level of 0.05, the difference in K_1 values becomes more and more significant as the fines contents change from 4% to 16%. Thus it may be possible to group aggregates into two broad categories, of “low fines” and “high fines” as far as resilient modulus characterization is concerned.

Dependent Variable: K1 K1

Source	DF	Sum of Squares	Mean Square	F Value	Pr > F
Model	3	0.20522458	0.06840819	1.23	0.3052
Error	61	3.38218736	0.05544569		
Corrected Total	64	3.58741194			

R-Square	Coeff Var	Root MSE	K1 Mean
0.057207	23.00849	0.235469	1.023401

Source	DF	Type I SS	Mean Square	F Value	Pr > F
pp_approx	3	0.20522458	0.06840819	1.23	0.3052

FIG.5. ANOVA output for the effect of amount of fines on K_1

Contrast	DF	Contrast SS	Mean Square	F Value	Pr > F
4 vs 8	1	0.03889878	0.03889878	0.70	0.4055
4 vs 12	1	0.11713502	0.11713502	2.11	0.1512
4 vs 16	1	0.17279231	0.17279231	3.12	0.0825

FIG.6. Linear contrasts for comparing the different amounts of fines on K_1

EFFECT OF MOISTURE CONDITION

The samples were tested at optimum, dry of optimum, and wet of optimum conditions to study the effect of moisture content on the permanent deformation and shear strength values reported elsewhere (Tutumluer et al. 2009, Mishra et al., 2010). The effects of moisture condition on the K_1 parameter were further analyzed. The ANOVA results showed that the overall effect of moisture condition (dry vs optimum, or wet) is highly insignificant (p-value of 0.7710). Further analyses through linear contrasts were also conducted to check the individual differences between dry of optimum to optimum, and also optimum to wet of optimum (see Figure 7). However, the results clearly show that moisture condition does not contribute significantly as far as the variation in the values of K_1 is concerned. Although some specimens in the sample data may differ significantly, overall, the K_1 value distributions corresponding to the three moisture conditions were not statistically different. As a result, the moisture or suction effects may need to be taken into account by the bulk stress term and the K_2 exponent in the M_R model.

Contrast	DF	Contrast SS	Mean Square	F Value	Pr > F
Dry vs Opt	1	0.02905476	0.02905476	0.51	0.4794
Opt vs Wet	1	0.00267764	0.00267764	0.05	0.8297

FIG.7. Linear contrasts for comparing the effect of moisture condition on K_1

CONCLUSIONS

This paper presented a statistical analysis approach to identify the effects of four different aggregate properties, i.e., particle shape, type and amount of fines, and moisture condition, on the resilient modulus (M_R) model parameter estimates of unbound aggregate structural layers. A statistically well-formulated laboratory test matrix was used to develop the M_R characterization model as a function of the aggregate properties. Analysis of Variance (ANOVA) analyses were conducted to study the individual effects of the four different classification variables. Aggregate angularity (crushed vs uncrushed) had a significant effect on the values of K_1, which is the constant term in the stress-dependent M_R characterization model (K_2 and K_3 are the exponents of the bulk and deviator stresses, respectively). The K_1 values for uncrushed gravel were also significantly different from those of crushed dolomite. However, there was not much difference in the K_1 values for dolomite and limestone. This was expected since both materials comprised of crushed aggregates and had similar mineralogical compositions. Type of fines (plastic vs non-plastic) or moisture condition (dry of optimum, optimum, or wet of optimum) did not have significant effect on the K_1 model parameter. Plastic fines may in fact cause stress softening behavior to be potentially dictated by the K_3 exponent of the deviator stress whereas the moisture or suction effects may need to be taken into account by the bulk stress term and the K_2 exponent in the M_R model. The overall effect of amount of fines on K_1 value was found to be insignificant. However, upon further analysis using linear contrasts, it was observed, that the difference between K_1 values of various fines percentages, i.e., 4% and 16%, becomes more and more significant, as the amount of fines increases. Further work is currently underway to develop correlations to predict the K parameters based on different aggregate properties.

REFERENCES

Allen, J. (1973). The Effect of Non-constant Lateral Pressures of the Resilient Response of Granular Materials. *Ph.D. Thesis, University of Illinois at Urbana-Champaign*, Urbana, IL.

Barksdale, R.D. and Itani, S.Y. (1989). "Influence of Aggregate Shape on Base Behavior," *Transportation Research Record 1227*, TRB, National Research Council, Washington, D.C., pp. 173-182

Rao, C., Tutumluer, E., and Stefanski, J.A. (2001). "Flat and Elongated Ratios and Gradation of Coarse Aggregates Using a New Image Analyzer," *ASTM Journal of Testing and Standard*, Vol. 29, No. 5, 2001, 79-89.

Rao, C., Pan, T., and Tutumluer, E. (2003). "Determination of Coarse Aggregate Surface Texture Using Imaging Analysis," *In Proceedings of the 16th ASCE Engineering Mechanics Conference*, University of Washington, Seattle, WA.

Rao, C., Tutumluer, E., and Kim, I.T. (2002). "Quantification of Coarse Aggregate Angularity based on Image Analysis," *Transportation Research Record 1787*, National Research Council, Washington DC, pp. 17-124.

Illinois Department of Transportation – IDOT (2005). "Subgrade Stability Manual", Bureau of Bridges and Structures, May 1, 2005, 27 pages. (http://www.dot.il.gov/bridges/pdf/subgrade stability manual.exe)

Tutumluer, E. (2009) "State of the Art: Anisotropic Characterization of Unbound Aggregate Layers in Flexible Pavements," In ASCE *Geotechnical Special Publication No. 184*, *Pavements and Materials – Modeling, Testing and Performance*, ISBN: 978-0-7844-1008-0, pp. 1-16.

Tutumluer, E., Mishra, D., and Butt, A.A. (2009). "Characterization of Illinois Aggregates for Subgrade Replacement and Subbase," *Final Report, ICT R27-1 Project*, University of Illinois Urbana Champaign, Urbana, Illinois, 61801.

Mishra, D., Tutumluer, E., and Butt, A.A. (2010). "Quantifying Effects of Particle Shape and Type and Amount of Fines on Unbound Aggregate Performance through Controlled Gradation," *Manuscript Accepted Presentation and Publication at the 89th Annual Meeting of the Transportation Research Board*, Washington, D.C., January 2010.

Assessing the Polishing Characteristics of Coarse Aggregates using Micro-Deval and Imaging System

Wenjing Xue[1], Cristian Druta[2], Linbing Wang[3], M. ASCE, and D. Stephen Lane[4]

[1]Graduate Research Student, Virginia Polytechnic Institute and State University, Blacksburg, VA 24061; wenjingx@vt.edu
[2]Senior Research Associate, Virginia Tech Transportation Institute, Blacksburg, VA 24061; cdruta1@vt.edu
[3]Associate Professor, Virginia Polytechnic Institute and State University, Blacksburg, VA 24061; wangl@vt.edu
[4]Associate Principal Research Scientist, Virginia Transportation Research Council, Charlottesville, VA 22903; stephen.lane@vdot.virginia.gov

ABSTRACT: Aggregates used in asphalt concrete should be tough and durable to withstand HMA production, transportation, construction, traffic loads and environmental effects. Aggregate morphology not only plays an important role in aggregates' mechanical properties but also influences the asphalt pavement skid resistance. The Micro-Deval apparatus, which can evaluate aggregates' hardness or wear resistance, was used for assessing the polishing resistance of aggregates. The abrasion testing in conjunction with image analysis for aggregate shape, angularity and texture, is the focus of this study.

Aggregates from ten Virginia sources were used for the Micro-Deval abrasion and digital images of twenty five particles chosen from each source were captured with a regular camera and analyzed with the MATLAB-based program to characterize the particle morphology. Due to time constraints and material availability the aggregates that were analyzed before and after abrasion were not the same aggregates. With one exception (Nolichucky quartzite), all of the aggregates exhibited very good abrasion resistance after being tested in the Micro-Deval. Also, because some of the aggregates abraded differently their morphological parameters after abrasion were larger or equal to the parameters before abrasion.

INTRODUCTION

In both, asphalt concrete and cement concrete, mineral aggregates are the main component to withstand the traffic and environment loads. The properties of aggregates are very important to the performance of the pavements, and the morphological properties, such as shape, angularity, and texture characteristics, have a significant influence on compactability, consolidation, and workability, and performance of the asphalt concrete. In civil engineering, computer imaging has been extensively researched in the last decade to characterize the properties of construction

materials. Thus, imaging and image processing and analysis provide a relatively simple means to obtain objective and quantitative measures of aggregate morphological characteristics (Masad et al. 2000; Garboczi 2002; Masad et al. 2004). In this study, a Matlab based program developed previously was used to characterize the aggregate morphology from digital images of aggregate particles (Wang et al. 2008). The program uses the unified Fourier analysis (Masad and Button 2000; Wettimuny and Penumadu 2004; Wang et al. 2005) to process and analyze images acquired with a digital camera, providing three index values for shape, angularity, and texture.

PURPOSE AND SCOPE

The primary objective of this research is to study the influence of aggregate abrasion through micro-Deval on aggregate morphology, especially on the surface texture. The study focuses on addressing two aspects:

- Accurately evaluating morphological properties (i.e., shape, angularity and texture characteristics) of aggregates using specialized software; and
- Comparing and analyzing aggregates' morphological properties before and after the polishing process

METHODS AND MATERIALS

Coarse Aggregates

In this study, groups of coarse aggregates from various quarries and plants across Virginia and of different sizes are polished and then analyzed using imaging techniques. The aggregates were selected from ten different sources to cover a wide spectrum of origin, rock type, shape and size. The sources and rock types of the aggregates tested are presented in

Table 1.

Aggregate Abrasion Methods and Equipment

Although many available abrasion test methods are discussed in the literature and state transportation agency specifications, only a few are widely used. Ninety four percent of the states use the Los Angeles abrasion test or some variation (Wu et al. 1998). Early development of LA abrasion test was studied by Woolf (1937), Shelburne (1940), and Shergold (1948). Some of these studies indicated good correlations between abrasion test results and performance of the aggregates in the field.

The Micro-Deval (MD) abrasion test, which is a wet ball mill test, was developed in France during the 1960s as an alternative of the Los Angeles abrasion test. In an MD test, the graded aggregate sample (1.5 kg), which is retained on the 9.5-mm sieve, is placed in a stainless steel jar, together with 2 l of water and a 5-kg charge of 9.5 mm diameter steel balls and rotated at a rate of 100 ± 5rpm for 2 hours. The amount of

material passing the 1.18-mm sieve was calculated as loss and expressed as a percentage of the mass of the original sample. The Micro-Deval abrasion test is used in this study to induce wear on aggregates and assess its effect on the aggregate morphology. Figure 1 shows an example of the abrasion effect from the Micro-Deval on limestone aggregates. With one exception (Nolichucky quartzite), all of the aggregates exhibited very good abrasion resistance (% loss was less than 15%) after being tested in the Micro-Deval.

Table 1. Coarse Aggregate Sources and Sizes

	Aggregate Source	Aggregate Description	Aggregate Sizes (mm)				
			37 - 25	25 - 19	19 - 12.5	12.5 - 9.5	9.5 - 4.75
Non-carbonate	Maymead	Granite	x	x	x	x	
	Salem Stone, Sylvatus	Quartzite	x	x	x	x	x
	Nolichucky	Feldspathic quartzite, weathered	x	x	x	x	
Carbonate	Staunton Lime Co.	Limestone, dolomitic	x	x	x	x	x
	S.M. Perry, Winchester	Limestone		x	x	x	
	CS Mundy, Broadway	Limestone, dolomitic	x	x	x	x	
	Rockydale, Roanoke	Limestone, dolomitic	x	x	x	x	x
	Oldcastle, Castlewood	Dolomite	x	x	x	x	x
	Carmeuse, Strasburg	Limestone	x	x	x	x	
	Frazier-North, Harrisonburg	Limestone	x	x	x	x	x

Equipment for Image Acquisition and Processing

Computer imaging can be defined as the acquisition and processing of visual information by computer. With the development of digital image processing and analysis technologies, aggregate shape characterization methods are more and more widely used in the research on asphalt concrete, cement concrete and unbound granular materials. These advances help make available automated methods for aggregate shape analysis directly from the individual aggregate. In this study, a commercially available digital camera was used to take pictures of the aggregates. The digital pictures were subsequently analyzed using MATLAB software based on Fast Fourier Transform to characterize the particle morphology from its 2D profile. A micro computer with a built-in camera and MATLAB software installed on it can be used for field analysis of aggregates.

FIG. 1. Aggregate particles after Micro-Deval (left) and before Micro-Deval (right)

Aggregate Morphological Analysis Method

In this research, the aggregate morphological analysis method by Wang et al. (2008) is used to study the effect of abrasion process on the aggregate morphology. The shape, angularity, and surface texture are three related properties in aggregate morphological analysis, which represent spatial variations (irregularities) of different dimensional scales. In this method, Fourier morphological analysis based on spatial frequency characteristics is used to analyze each of the three aggregate properties consistently. An aggregate particle profile can be represented as a Fourier series by the following function (Wang, et al. 2005):

$$R(\theta) = \alpha_0 + \sum_{m=1}^{\infty} (a_m \cos m\theta + b_m \sin m\theta) \tag{1}$$

Where α_0 is the average radius, m is the frequency, and a_m, b_m are magnitudes. The origin of the coordinate is the center of gravity. Following Fourier analysis of particle profiles, the three parameters of shape, angularity and surface texture can be described by the following functions.

$$\alpha_s(shape) = \frac{1}{2} \sum_{m=1}^{N_1} \left[\left(\frac{a_m}{a_0} \right)^2 + \left(\frac{b_m}{a_0} \right)^2 \right] \tag{2}$$

$$\alpha_r(angularity) = \frac{1}{2} \sum_{m=N_1+1}^{N_2} \left[\left(\frac{a_m}{a_0} \right)^2 + \left(\frac{b_m}{a_0} \right)^2 \right] \tag{3}$$

$$\alpha_t(texture) = \frac{1}{2} \sum_{m=N_2+1}^{\infty} \left[\left(\frac{a_m}{a_0} \right)^2 + \left(\frac{b_m}{a_0} \right)^2 \right] \tag{4}$$

Where $N_1 = 4$ and $N_2 = 25$, represent the threshold frequencies separating shape, angularity, and surface texture factors, respectively (Wang et al. 2005).

Experimental Procedure

The first step of the procedure is to take pictures of the aggregate particles with a digital camera before and after Micro-Deval testing. This is a critical step, because these pictures provide all necessary raw image data and their quality will directly affect the final analysis results (i.e., aggregate 2D profile). To obtain the clearest particle profiles (edges), the aggregates need to be placed on a contrasting background with no visible shading. In this study, 25 aggregates before M-D and 25 after M-D were chosen from each source for image processing and analysis.

In the second step, 2D images of aggregate particle profiles are analyzed, especially of aggregates from the same source before and after polishing. In this step, the analysis method described above is used to acquire the morphology of aggregates, which is the main basis of the comparison. The analysis procedure can be performed on any computer with MATLAB 6.5 software or higher version.

RESULTS AND DISCUSION

The image analysis procedure is based on measuring the grayscale variations (after conversion to binary images) of an image to quantify the shape, angularity, and surface texture of the coarse aggregate's periphery (edge). A total of 500 pictures, fifty for each aggregate source, with twenty five before and twenty five after the polishing process, were taken of individual particles to cover a broad range of shapes. All the pictures were acquired at 640 x 480 pixel resolution.

Statistical analysis was performed for quantifying the distribution of aggregate characteristics, and for comparing these properties among the different sources, before and after the Micro Deval abrasion. Table 2 and 3 present the data on the means and standard deviations.

The data in the above tables shows that:

- There is no specific development regarding aggregate morphological properties through the abrasion process, as they may increase or decrease in value, depending on their mineral composition.
- The aggregates from Salem Stone plant were the least affected by the Micro-Deval test, since the average and standard deviation of their morphological properties remained almost the same after the polishing process.
- For the aggregates from CS Mundy, Frazier-North, and Maymead sources, both the average and the standard deviation of their surface texture values became larger after abrasion, indicating a different abrasion the rate. This may be also due to the fact that the examined particles were not the same.
- For the aggregates from Nolichucky plant, both the average and the standard deviation of the surface texture became smaller after abrasion, meaning that the aggregates become smoother. Differences between shape and angularity among particles may be also due to the fact that the examined particles were not the same.

Table 2. Mean of Coarse Aggregates Morphological Properties

Aggregate Source	Aggregate Parameter					
	Shape		Angularity		Surface Texture	
	Before	After	Before	After	Before	After
Carmeuse	0.0067	0.0086	0.0007	0.0007	0.0019	0.0018
CS Mundy	0.0070	0.0083	0.0007	0.0013	0.0015	0.0020
Frazier	0.0076	0.0090	0.0007	0.0011	0.0014	0.0026
Maymead	0.0058	0.0075	0.0008	0.0008	0.0016	0.0020
Nolichucky	0.0082	0.0060	0.0011	0.0005	0.0017	0.0015
Oldcastle	0.0079	0.0069	0.0008	0.0010	0.0018	0.0021
Rockydale	0.0063	0.0089	0.0007	0.0008	0.0014	0.0021
SM Perry	0.0068	0.0065	0.0008	0.0008	0.0017	0.0026
Staunton	0.0073	0.0065	0.0006	0.0008	0.0017	0.0013
Salem Stone	0.0082	0.0084	0.0009	0.0009	0.0022	0.0024

Table 3. Standard Deviation of Coarse Aggregates Morphological Properties

Aggregate Source	Aggregate Parameter					
	Shape		Angularity		Surface Texture	
	Before	After	Before	After	Before	After
Carmeuse	0.0071	0.0059	0.0008	0.0007	0.0018	0.0014
CS Mundy	0.0066	0.0087	0.0006	0.0020	0.0012	0.0024
Frazier	0.0071	0.0085	0.0009	0.0017	0.0016	0.0034
Maymead	0.0042	0.0070	0.0007	0.0010	0.0015	0.0025
Nolichucky	0.0088	0.0056	0.0023	0.0007	0.0018	0.0016
Oldcastle	0.0099	0.0066	0.0009	0.0010	0.0023	0.0021
Rockydale	0.0071	0.0081	0.0006	0.0011	0.0008	0.0022
SM Perry	0.0082	0.0061	0.0012	0.0011	0.0016	0.0053
Staunton	0.0069	0.0057	0.0006	0.0017	0.0021	0.0012
Salem Stone	0.0067	0.0067	0.0009	0.0011	0.0025	0.0022

Asymptotic analysis was performed to determine if twenty five particle profiles would be sufficient for evaluation. Figure 2 presents the asymptotic curves of the surface texture for each type of aggregates before and after abrasion. These curves indicate that 25 particles are sufficient for obtaining a statistically stable value of the three morphological parameters.

Also, to determine if the aggregate profile characteristics were statistically different before and after the M-D tests, student T-tests were performed among all sets of aggregate parameters assuming equal variances. The parameter values for each aggregate source were based on twenty-five image profiles. For the statistical analysis, a one-tail distribution was selected at a confidence limit of 95 percent (α = 0.05). Based on the p-values given by the T-test, which were all $\geq$ 0.05 (α), the analysis indicated no significant differences among all aggregate sources in regard to their morphological properties. Table 4 presents the p-values for all aggregate sources.

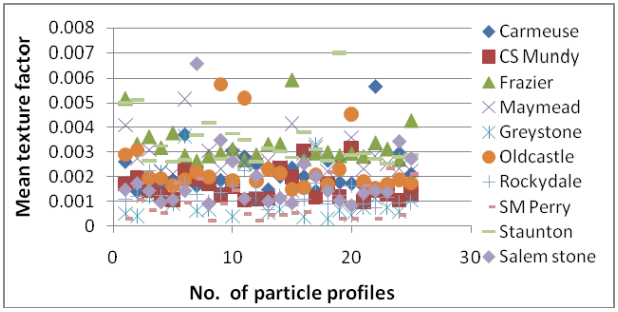

(a) After M-D polishing

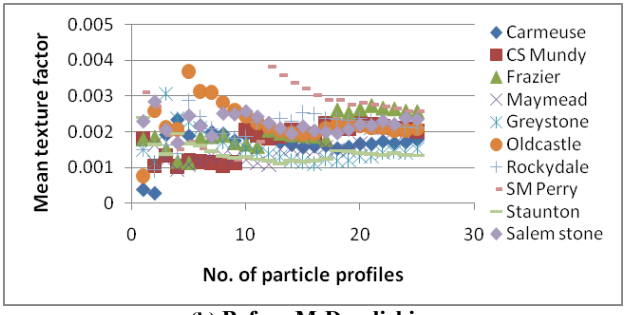

(b) Before M-D polishing

FIG. 2. Asymptotic analysis of aggregate texture

CONCLUSIONS

A method is developed to evaluate how the Micro-Deval abrasion test affects the aggregates' morphological properties. The method has the following advantages:

- Fast and easy to understand and execute;
- Assesses the aggregate morphology changes from the abrasion process;
- Evaluates the variation of morphological properties within an aggregate sample.

Although, the limited data shows that the M-D method introduces some changes to shape, angularity, and texture of aggregates, they are not significantly different. Hence, the combined shape, angularity and texture analysis obtained from the Micro-Deval procedure may contribute to a better understanding of aggregate abrasion process quantitatively.

Table 4. Coarse Aggregates T-test Statistics

Aggregate Source	T-test p-values		
	Shape	Angularity	Surface Texture
Carmeuse	0.106	0.375	0.402
CS Mundy	0.260	0.0847	0.174
Frazier	0.248	0.162	0.0837
Maymead	0.143	0.496	0.252
Nolichucky	0.166	0.128	0.346
Oldcastle	0.344	0.280	0.352
Rockydale	0.0696	0.402	0.073
SM Perry	0.411	0.485	0.236
Staunton	0.328	0.327	0.215
Salem Stone	0.452	0.368	0.428

REFERENCES

Garboczi, E. J. (2002). "Three-Dimensional Mathematical Analysis of Particle Shape using X-ray Tomography and Spherical Harmonics: Application to Aggregates Used in Concrete." *Elsevier, Cement and Concrete Res.*, Vol. 32(100), 1621-1638.

Masad, E., J.W. Button, and T. Papagiannakis (2000). "Fine-Aggregate Angularity: Automated Image Analysis Approach." In *Transportation Research Record: Journal of the Transportation Research Board, No. 1721*, TRB, National Research Council, Washington, D.C., 66-72.

Masad, E. and J.W. Button (2000). "Unified Imaging Approach for Measuring Aggregate Angularity and Texture. *J. of Comp.-Aided Civ. and Infr. Engrg*., Vol. 15, 273-280.

Masad, E., D. Little, R. Sukhwani (2004). "Sensitivity of HMA Performance to Aggregate Shape Measured Using Conventional and Image Analysis Methods." *Intl. J. of Road Mater. and Pavm. Design*, Vol. 5(4), 477-498.

Shelburne, T.E. (1940). "Surface treatment studies." Proc., Association of Asphalt Paving Technologist. Vol. 11, 44-58.

Shergold, F.A. (1948). "A review of available information on the significance of roadstone tests", *Road Research Technical Paper* 10. DSIR, H.M.S.O., London.

Wang, L., X. Wang, L. Mohammad, and C. Abadie (2005). "Unified Method to Quantify Aggregate Shape Angularity and Texture Using Fourier Analysis." *J. of Mater. in Civil Engrg*., Vol.17(5), 498-504.

Wang, L., D.S. Lane, Y. Lu, and C. Druta (2008). "Portable Image Analysis System For Characterizing Aggregate Morphology". VTRC Rep. 08-CR11.

Wettimuny, R. and D. Penumadu (2004). "Application of Fourier Analysis to Digital Imaging for Particle Shape Analysis." *J. of Comp. in Civil Engrg.*, Vol. 18(1), 2-9.

Woolf, D.O. (1937). "The relation between Los Angeles abrasion test results and the service records of coarse aggregates." HRB Proceedings.

Wu, Y., F. Parker, and P.S. Kandhal (1998). "Aggregate toughness/abrasion resistance and durability/soundness tests related to asphalt concrete performance in pavements." *Transportation Research Record*, TRB, Vol. 1638, National Research Council, Washington, D.C., 85-93.

Investigation of Aggregate Packing Using Discrete Element Modeling

Huanan Yu[1], and Shihui Shen[2], M. ASCE

[1]Research Assistant, Washington State University, Pullman, WA 99164; yu_huanan@wsu.edu
[2]Assistant Professor, Corresponding Author, Washington State University, Pullman, WA 99164; sshen2@wsu.edu

ABSTRACT: The packing of aggregate skeleton directly affects the capability of a mixture to transmit and distribute loads. It has significant impact on the performance hot mix asphalt (HMA) mixtures. This paper conducted an analysis of aggregate packing characteristics using a Discrete Element Modeling (DEM) simulation. A Washington typical HMA gradation is used as an example for the analysis. By using the *PFC*^{3D} DEM simulation to relate the gradation parameter to the volumetric properties of the structure, this paper theoretically demonstrated the different roles of aggregate particles in an HMA mixture. A new criterion to differentiate "coarse" and "fine" aggregates is developed, which is consistent with the Bailey's method definition. Aggregate contacts and contact force are also studied in this paper to evaluate the capability of the aggregate structure to transmit stresses through aggregate skeleton, and thereby, to resist permanent deformation. It is suggested that the method described in this paper based on the analysis of aggregate packing and DEM simulation provide a promising direction to theoretically understand the characteristics of a packed aggregate structure, as well as to guide the aggregate gradation design.

INTRODUCTION

Around 85 percent of the volume of dense-graded hot mix asphalt (HMA) mixture is made up of aggregates (Christensen 2009). The aggregate structure and characteristics, particularly aggregate gradation, shape (angularity), and coarse aggregate surface texture, have been considered as important factors that influence the development of aggregate skeleton, and thus rut susceptibility (Button etc. 1990; Stakston 2003; Gaudette etc. 1977; Lottman etc. 1956), strength (Vallerga etc. 1957), and fatigue resistance (Monismith 1970; Shen and Carpenter 2007) of an HMA mixture.

For dense graded mixes, traditional mix design and analysis methods including Marshall, Hveem, and Superpave method design gradations to achieve the densest packing following the maximum density line. In these methods, aggregates are categorized as coarse or fine aggregates based on a fixed size criterion. The aggregates that retained on the 4.75*mm* (No.4) sieve size were considered as coarse aggregates; while the aggregates that passed the 4.75*mm* sieve were considered as fine aggregates.

However, such definition is quite arbitrary and does not necessarily differentiate the specific roles of the aggregate particles. For the mixes with 9.5*mm* nominal maximum aggregate size (NMAS) and the ones with 25*mm* NMAS, the same 4.75*mm* was used as the breaking point for coarse and fine aggregates although in reality the 4.75*mm* aggregates can behave quite differently in these mixes.

The Bailey's Method (Vavrik etc. 2002), as an important improvement of the aggregate gradation design method, re-defined the coarse aggregates and fine aggregates based on the theory of packing and the role of certain size aggregates to the entire structure. Coarse aggregate is defined as the large aggregate particles that when placed in a unit volume, create voids; while fine aggregates are aggregate particles that can fill the voids created by the coarse aggregates. The sieve that separates the coarse and fine aggregates is called the primary control sieve (PCS), which is dependent on the nominal maximum aggregate size (NMAS) of the aggregate blend. Mathematically a diameter ratio of 0.22 between the PCS and the NMAS is selected by Vavrik (2002) based on a review of two and three dimensional analysis of the packing of different shaped particles done by various researchers. However, researchers (Shashidhar etc. 2006) have questioned the theoretical basis of the 0.22 cut-off limits because it is not clear whether the aggregates below this cut-off will actually behave as skeleton builder.

Although the packing of particles have been broadly studied in the field of composite materials (Sobolev etc. 2004), still the characteristics of aggregate packing in asphalt mixtures is less clear and requires further attention. This paper will investigate the effect of individual aggregate size to the stability of the entire aggregate structure, and evaluate the contact properties within aggregate skeleton, thereby to provide suggestions for the mix design of asphalt mixtures. Although only focused on one specific HMA gradation, the method discussed in this paper can be extended to study packing of various gradations for HMA as well as concrete mixtures.

RESEARCH APPROACH

Discrete Element Modeling (DEM) method was firstly introduced by Cundall (1971) in 1971 to solve problems in rock-mechanics. Later Cundall and Strack (1979) applied this method to soils. Because the DEM method treats particles as distinct interacting bodies, it offers an excellent opportunity to understand the micromechanical behavior of granular material and simulate the movement and interaction of stressed assemblies of rigid spherical particles. A wide application of the DEM method in asphalt materials can be found in the literature (Buttlar etc. 2001; You etc. 2002; Hossain etc. 2007; Zelelew 2007; Hashin 1965).

In this research, the packing of aggregates is studied using a DEM modeling tool, Particle Flow 3D (PFC^{3D}) commercial program from Itasca (2008). The PFC^{3D} uses balls to effectively represent the aggregates with physical properties implemented. Interactions between particles are described by contact laws that define forces and moments created by relative motions of the particles. Contact type is identified by contact properties such as normal stiffness, tangential stiffness, coefficient of friction, and adhesion between two particles. The DEM simulation in PFC^{3D} can easily examine the detailed ball contacts, and accurately measure the volumetric property changes at any time step, which is difficult to realize by using traditional laboratory and field experiments. This paper will start by simulating the packing of spherical particles, a

simplified approach popularly adopted in the particle packing analysis (Shashidhar etc. 2006). The effect of angularity and surface roughness are indirectly considered through careful model parameter assignment (such as contact friction angle), which will be calibrated based on experimental data. A complete modeling of the effect of aggregate properties such as surface roughness, angularity, and the effect of binder will be included later once the fundamental packing model has been established.

The process of simulation involves three important steps. Firstly, uniform size spherical particles (representing aggregates retained on one sieve size) are generated in the computer according to the target gradation. For the specific gradation used in this study, 68 balls with a size between 12.5*mm* and 19*mm* were randomly generated to represent the aggregates retained on 12.5*mm* sieve size. These balls are added to a square box (0.3*m**0.3*m**0.5*m*) under a unidirectional gravitational force. Secondly, balls are compacted by the assigned gravitational force to its stable position. If the unbalanced force approaches a very small value, this indicates that an equilibrium state has been reached. During the compaction, the velocities and the new positions of each ball were updated at each time step according to Newtonian motion model ($F=m*a$). Based on new particle positions, contact forces are obtained from a relative displacement of pairs of particles. Pervious study (Zelelew 2007) showed that the linear contact law is in general adequate in describing contact stiffness at aggregate-aggregate contacts and is therefore used in this study. The iteration stops when the unbalanced force reaches 0.01% of the maximum contact force. Finally, the volumetric properties and porosities are calculated.

The simulation of a complete aggregate gradation requires adding different sizes of balls to the system sequentially (from large to small) following an iteration process. Once the structure of large size particles is established and their volumetrics are determined, finer aggregates will then be added into the structure. The corresponding volumetrics and porosities will be determined and compared with the results for larger size particles to check the change in volume and contact force due to the addition of small size particles. Repeat these steps until all aggregates are added into the structure and the volumetrics are determined.

ANALYSIS OF AGGREGATE PACKING

Gradation Information & Model Parameters

A typical Washington State gradation with nominal maximum aggregate size of 12.5*mm* is used as an example for the analysis of the aggregate packing characteristics. The gradation is shown in Table 1 and plotted in Figure 1.

The initial selection of model parameters is based on the suggestions from the literature (Zelelew 2007; Abbas etc. 2005). In this study, aggregate elastic modulus of 30GPa, rigid wall stiffness of 300GPa and aggregate-to-aggregate contact friction coefficient μ=0.5 are used. These parameters will be further calibrated according to experimental results.

Table 1. Aggregate Gradation Used for Simulation

Sieve Size(*mm*)	19	12.5	9.5	4.75	2.36	1.18	0.6	0.3	0.15	0.075
% Passing	100	93.2	79.5	49.4	32.3	22.5	16.5	12.1	7.7	5.2

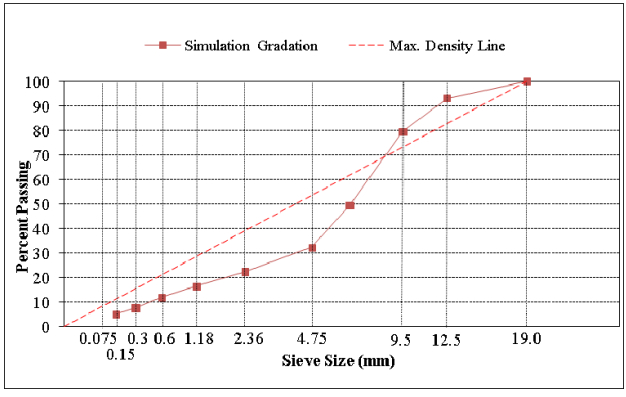

FIG. 1 Aggregate gradation for packing simulation

Roles of Particles in an Aggregate Structure

Based on the same gradation, three DEM simulation models that included different fractions of the gradation particles were established. Model 1 only includes the aggregate particles larger than 4.75*mm*; model 2 includes aggregates larger than 2.36*mm*; model 3 consists of all aggregates larger than 1.18mm. Particles smaller than 1.18*mm* are assumed to behave as fine particles which fills in the voids of the structure and are not included in the packing simulation. The number of balls and volumes for specific size group of each model were then calculated according to the proportions of the given gradation, as shown in Table 2. Also included in the Table 2 are the total volume and volume changes before and after compaction. Here the percent of volume change for model 2 and 3 are with respect to model 1 and 2, respectively.

The porosities of model 1, 2, 3 structures were also calculated in the PFC^{3D}. Porosity (p) is defined as the ratio of the volume of voids between the aggregate particles to the total volume of the structure.

$$p = \frac{V_V}{V_T} \tag{1}$$

where, V_V = the volume of voids in the aggregate structure; and

V_T = the total volume of the structure.

In order to find a representative value of the porosity, five randomly selected points were used, and their average porosity was calculated, which is 0.3374 for model 1, 0.2988 for model 2, and 0.2471 for model3.

By comparing the volume and porosity changes of model 1, 2, and 3, the role of specific particle size is determined. From model 1 to model 2 by adding in 33.5% (by volume) of 2.36-4.75*mm* particles, due to the added aggregates, the total volume of

compacted structure was increased 24.9%. In other words, most of the added particles were contributed to the increase of the total structure volume. Consequently, slight deduction in porosity (3.86%) was achieved. However, from model 2 to model 3 by adding in 14.6% (by volume) of 1.18-2.36*mm* particles, the total volume of compacted structure was increased only 5.68%. Most particles have filled in the voids created by the coarse aggregate skeleton without creating additional structure volume. And the decrease of porosity became more significant (5.17%).

Table 2. Number and Volume of Particles at Each Size for Model 1, 2, and 3

	Model 1		Model 2		Model 3	
Particle Sieve Size	**Balls No.**	**V_s (mm^3)**	**Balls No.**	**V_s (mm^3)**	**Balls No.**	**V_s (mm^3)**
12.5-19	68	1160242	68	1160242	68	1160242
9.5-12.5	412	2337546	412	2337546	412	2337546
4.75-9.5	3061	5152839	3061	5152839	3061	5152839
2.36-4.75			13848	2900605	13848	2900605
1.18-2.36					65450	1689176
total volume before compaction		8650628		11551233		13240409
Percent of volume change before compaction				33.5%		14.6%
total volume after compaction		13707000		17118000		18090000
Percent of volume change after compaction				24.9%		5.68%

To further describe the change of volume due to the addition of finer aggregates, and quantify the role of finer aggregates on the specific aggregate structure, a new gradation parameter f_s is developed. f_s is defined as the percent of volume increase due to the addition of unit finer aggregates, which can be calculated using equation 2. f_s value greater than 1 will indicate the aggregates more behave like creating the voids.

$$f_s = \frac{V_2 - V_1}{V_{a2}} \tag{2}$$

where, V_1 is the total volume of basic model, V_2 is the total volume after finer aggregate were added, and V_{a2} is the volume of finer aggregate added into the basic model. For example, to calculate f_s for 4.75*mm* sieve size, we have V_1=17118000 (mm^3), V_2=13707000 (mm^3), and V_{a2}=2900605 (mm^3), using equation (2) we can get f_s=1.176 as shown in Table 3.

Table 3 shows the f_s values of each particle size for the given gradation. As shown, f_s values are larger than 1 for aggregates passing 4.75*mm* but retained on 2.36*mm* sieve size, indicating the change of the total volume of aggregate structure is larger than the volume of the added aggregate volume, and some additional voids have been created. When particles smaller than 2.36*mm* are included into the structure, f_s becomes smaller than 1. The 2.36*mm* sieve appears to be a reasonable breaking size between coarse and fine aggregates for aggregates with NMPS equaling to 12.5*mm*. This finding is

consistent with the primary control sieve definition used in the Bailey's method.

Table 3. f_s value verse aggregate passing sieve size

Aggregate Passing Sieve Size (*mm*)	**12.5**	**9.5**	**4.75**	**2.36**
f_s	1.524	1.434	1.176	0.575

Aggregate Contact and Interlocking

The advantages of DEM computational simulation such as easily adding and deleting balls, and detecting contacts and contact force, make it an excellent tool to study the aggregate contact. In this study, a "ball hiding" technique was used to identify the particle contacts and quantify the contact force. First, all balls larger than 1.18*mm* as designated in the design gradation were generated in the PFC^{3D}, and their contact forces are calculated and plotted as shown in Figure 3a. Then the aggregates between 1.18*mm* and 2.36*mm* are made invisible in the structure (Figure 3b). By only plotting the contacts among those visible balls, we are able to identify the particle contacts due to aggregates coarser than 2.36*mm*. Following the same procedure, the contacts among coarse aggregates are able to be identified. Figure 3c-e shows the particle contacts for aggregates retained on 4.75*mm*, 9.5*mm*, and 12.5*mm*, respectively.

Also indicated in Figure 3 are the magnitudes of contact force (black lines), usually called "force chain". The more the force chain appears, the more contacts are detected. In addition, a wider force chain will indicate a stronger contact force (heavily stressed chains), and thus more stress is transmitted through the aggregate skeleton; the remaining groups of particles are only lightly loaded (Howell etc. 1999). Examining all figures in Figure 3, it is clear that very few aggregate contacts exist between particles larger than 12.5*mm* as well as 9.5*mm*; and there exists very few stress transmission through the mainly lightly stressed force chains (weak force chains). The force chains start forming a network when 4.75*mm* and 2.36*mm* particles are included into the skeleton structure, and more strong force chains are observed.

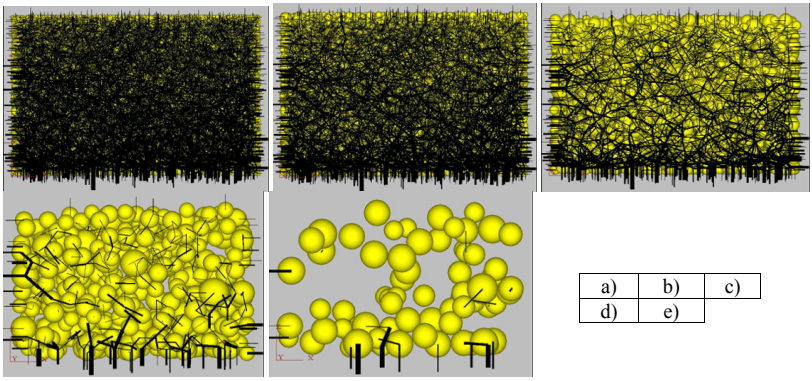

FIG. 3 "Ball hiding" technique for detecting aggregate contact and interlock in DEM simulation

SUMMARY FINDINGS

This paper conducted an analysis of aggregate packing based on DEM simulation to characterize the roles of aggregates with different sizes in the structure, and evaluate the aggregate contact with respect to different aggregate packing skeleton. One specific HMA design gradation with NMPS of 12.5*mm* is used as an example of the DEM simulation for the study of aggregate packing.

Using DEM simulation, a gradation parameter f_s is developed to theoretically link the aggregate packing to the volumetric properties of the mixture. f_s is defined as the percent of volume increase of the structure created by unit additional aggregate, which is specific to a sieve size. An f_s value greater than 1 will indicate that the corresponding size of aggregates are mainly behaving as coarse aggregates, creating the aggregate skeleton and increasing significantly the total volume of the structure. Consequently, the porosity decreases slightly with the addition of the coarse aggregates. An f_s value less than 1 will indicate the aggregates mainly behaves as fine aggregates which fill in the voids created by the coarse aggregates and only slightly increase the total volume of the structure when added in. At the same time, the decrease of porosity is much greater compared to the effect of coarse aggregates. The breaking sieve of the coarse and fine aggregates, based on the packing study using DEM simulation, agree with the primary control sieve suggested by the Bailey's Method.

A "Ball hiding" technique was developed in the DEM simulation to clearly demonstrate the degree of aggregate contact and interlocking, which is a function of aggregate size. For the gradation studied in this paper, significant amount of aggregate contacts are achieved when aggregates greater than 2.36*mm* are included in the system. In other words, all aggregates greater than 2.36*mm* have contributed to the formation of the aggregate structure, as well as the transmission of stresses through strong force chains (thick lines). Although adding smaller aggregates such as 1.18*mm* particles will increase the amount of contacts, most of such contacts are weak force chains (thin lines) which will not serve as major load bearing contacts.

By presenting a methodology of simulating aggregate packing and studying packing characteristics, this paper will help to develop meaningful gradation parameters that can be fundamentally related to the performance of overall aggregate structures, thereby to provide guidance on the improvement of aggregate gradation design for the HMA as well as concrete mixtures.

REFERENCE

Abbas, A., Papagiannakis, A.T., Masad, E., and Shenoy A. (2005). "Modelling Asphalt Mastic Stiffness using Discrete Element Analysis and Micromechanics based Models" *The International Journal of Pavement Engineering*, Vol.6(2): 137-146.

Button, J. W., Perdomo, D., and Lytton, R. L..(1990). "Influence of Aggregate on Rutting of Asphalt Concrete Pavements." *Transportation Research Record 1259*. Transportation Research Board, Washington D.C. pp 141-152.

Christensen,D., et al. (2009). "A Mix Design Manual for Hot-Mix Asphalt,." *NCHRP* 9-33 Report.

Cundall, P.A. and Strack, O.D. (1979). "Discrete Numerical Model for GranularAssemblies." *Geotechnique*, Vol.29(1): 47-65.

Cundall P.A. (1971). "A Computer Model for Simulating Progressive Large Scale Movements in Blocky Rock Systems." *In Proceedings of the Symposium of International Society of Rock Mechanics*, Nancy, France; 1 (II-8).

Gaudette, B. E., Welke, R. A., (1977). "Investigation of Crushed Aggregates for Bituminous Mixtures." *Michigan Department of State and Highway Transportation. Report* No. TB-58, 1977.

Hashin, Z. (1965). ''Viscoelastic behaviour of heterogeneous media.'' *J. Appl. Mech.*, 32(9): 630–636.

Hossain, Z., Indraratna, B., Darve, F., and Thakur, P. K., (2007). "DEM analysis of angular ballast breakage under cyclic loading." Geomechanics and Geoengineering: *An International Journal* Vol. 2(3):175-181

Howell, D., Behringer, R.P., Veje, C.T. (1999). "Fluctuations in granular flows." *Chaos*, Vol.9 (3): 559–572.

Lottman, R. R. and Goetz, W. H., (1956). "Effect of Crushed Gravel Fine Aggregate on the Strength of Asphaltic Surfacing Mixtures." *National Sand and Gravel Association Circular.* No. 63.

Monismith, C. L. (1970) "Influence of Shape, Size, and Surface Texture on the Stiffness and Fatigue Response of Asphalt Mixtures," *Highway Research Board Special Report No. 109*, pp. 4-11.

PFC^{3D} Manuals. (2008). "General Formation 1-2, verison 4.0". *Itasca Consulting Group Inc. Minneapolis, MI.*

Shashidhar, N., Gopalakrishnan, K., (2006). "Evaluating the aggregate structure in hot-mix asphalt using three-dimensional computer modeling and particle packing simulations", *Canada Journal of Civil Engineering*. 33: 945-954

Shen, S. and Carpenter, S.H.. (2007). "Development of an Asphalt Fatigue Model Based on Energy Principles", *Journal of the Association of Asphalt Paving Technologists (AAPT)*, in press, Vol.76.

Sobolev, K., Amirjanov, A., (2004). “The development of a simulation model of the dense packing of large particulate assemblies.” *Powder Technology* Vol.141 :155-160.

Stakston, A.D., Bahia, H. U., (2003). “The Effect of Fine Aggregate Angularity, Asphalt Content and Performance Graded Asphalts on Hot Mix Asphalt Performance.” *WisDOT Highway Research Study* 0092-45-98

Vallerga, B. A., Seed, H. B., Monismith, C. L., and Cooper, R.S., (1957) “Effect of Shape, Size, and Roughness of Aggregate Particles on the Strength of Granular Materials,” *Special Technical Publication*, No.212, ASTM.

Vavrik, W. R., Huber, G., Pine, W. J., Carpenter, S. H., and Bailey, R. (2002). "Bailey Method for Gradation Selection in Hot-Mix Asphalt Mixture Design." *Transportation Research E-Circular, Report No: E-C044.*

You, Z., and Buttlar, W. G. (2002). ‘‘Stiffness prediction of hot mixture asphalt (HMA) based upon microfabric discrete element modeling (MDEM).’’ Proc., *4th Int. Conf. on road and airfield pavement technology*, Vol. 1, People’s Communications, China, 409–417.

Zelelew, H, M., (2007). Doctoral Theses. “Simulation of the Permanent Deformation of Asphalt Concrete Mixtures using Discrete Element Method (DEM).”,*Washington State University.* pp130-140.

Laboratory Validation of Coal Dust Fouled Ballast Discrete Element Model

Hai Huang[1], Erol Tutumluer[2], Youssef M.A. Hashash[3] and Jamshid Ghaboussi[4]

[1] Research Assistant Professor, Department of Civil & Environmental Engineering, Washington State University, Pullman, WA 99163; hai.huang@wsu.edu
[2] Professor, Department of Civil & Environmental Engineering, University of Illinois at Urbana Champaign, IL 61801; tutumlue@illinois.edu
[3] Associate Professor, Department of Civil & Environmental Engineering, University of Illinois at Urbana Champaign, IL 61801; hashash@illinois.edu
[4] Professor Emeritus, Department of Civil & Environmental Engineering, University of Illinois at Urbana Champaign, IL 61801; jghabous@illinois.edu

ABSTRACT: Fouling refers to the condition of railroad ballast when voids in this unbound aggregate layer are filled with relatively finer materials or fouling agents commonly from the ballast aggregate breakdown, outside contamination, or from subgrade soil intrusion. When ballast gets fouled, this unbound layer may not adequately serve its primary functions to provide drainage and structural support under the repeated loading applied by trains. Coal dust fouling has been identified as one of the most critical fouling scenarios as it significantly decreases the strength and stability of railroad ballast. A Discrete Element Modeling (DEM) approach was adopted in this study to investigate the coal dust fouled ballast performances. A DEM program BLOKS3D was used to employ realistic three-dimensional polyhedrons as discrete elements generated through digital imaging of aggregate particles. An appropriate DEM model parameter calibration process was carried out to predict both the clean ballast condition and the partially to fully coal dust fouled ballast behavior as obtained from laboratory shear box tests, which properly validated the BLOKS3D DEM simulations.

INTRODUCTION

Railroad ballast is uniformly-graded coarse aggregate placed between and immediately underneath the crossties. The purpose of ballast is to provide drainage and structural support for the heavy loading applied by trains. As ballast ages, it is progressively fouled with fine-grained materials filling the void spaces. Fouling refers to the condition of railroad ballast when voids in this unbound aggregate layer are filled with relatively finer materials. Fouling agents are commonly from the ballast aggregate breakdown, outside contamination such as coal dust from coal trains, or from subgrade soil intrusion. Fouling materials in ballast have been traditionally

considered not favorable for railroad ballast performance. Recent research by Huang et al. (2009) showed that coal dust was by far the worst fouling agent for its impact on track substructure and roadbed. Approximately 15% coal dust fouling by weight of ballast was statistically significant to cause considerable strength reductions (Huang et al., 2009).

Discrete Element Modeling (DEM) uses numerical procedures to simulate problems that exhibit "gross discontinuous behavior" (Cundall, 1971; Barbosa, 1990). Cundall first proposed the discrete element method for use in rock mechanics in 1971. Essentially, the method attempts to solve problems using real world particulate interactions as opposed to finite element or elastic layer calculations that treat particulate matter as a continuum. In this research, the DEM program BLOKS3D, developed at the University of Illinois, is used to model railroad ballast (Ghaboussi and Barbosa, 1990; Nezami et al., 2004; Nezami et al., 2006; Zhao et al., 2006). The particles are simulated as non-deformable blocks represented by 3-D polyhedrons or "blocks" as the basic elements to simulate discrete element interactions such as particle interlock, contact between aggregate particles, and force transfer between particles with modeling details presented elsewhere (Ghaboussi and Barbosa, 1990; Zhao et al., 2006). Tutumluer et al. (2006, 2007) have recently applied BLOKS3D program to modeling deformation behavior of railroad ballast for the effects of multi-scale aggregate morphological properties on ballast performance by employing digital image aided element shape generation method. Figure 1 shows the comparisons between an actual aggregate particle and the corresponding DEM representative element.

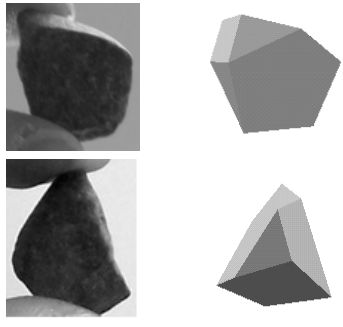

FIG.1. Comparisons of an Actual Aggregate Particle with the Discrete Element Representation Generated for the BLOKS3D DEM Program

Figure 2 shows two discrete elements representing aggregates in contact. The input variables and model parameters for the BLOKS3D DEM program include shape and size distributions, normal and shear contact stiffness properties as spring constants (Kn and Ks), and the surface friction angle (θ). In this paper, these model parameters for coal dust fouled ballast aggregates will be calibrated using laboratory direct shear (shear box) strength test data.

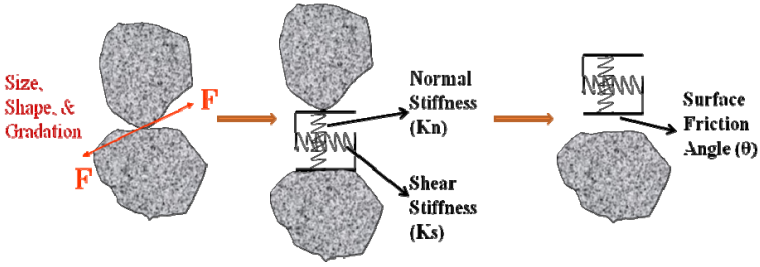

FIG.2. Input Variables and Model Parameters for the BLOKS3D DEM Program

DEM MODEL VALIDATION

Direct shear strength tests were performed on the reconstituted clean and coal dust fouled granite aggregate samples. The left image in Figure 3 shows the large shear box used for testing ballast aggregates at the University of Illinois. The test device is a square box with side dimensions of 305 mm and a specimen height of 203 mm. It has a total 102 mm travel of the bottom 152 mm high component which is large enough for ballast testing purposes to record peak shear stresses. The vertical (normal direction) and horizontal load cells are capable of applying and recording up to 50-kN load magnitudes. The device controls and the data collection are managed through an automated data acquisition system controlled by the operator through a built-in display and the test data are saved on to a personal computer. The ballast aggregate sample preparation process is as follows:

Place aggregates in the lower box by lifts (usually two 76 mm lifts).

For each lift, use vibratory compactor on top of a flat Plexiglas compaction platform and compact until no noticeable movement of particles is observed.

Record the weight of aggregate used.

For coal dust fouled ballast shear box sample, spread targeted amount of coal dust on the clean sample and compact.

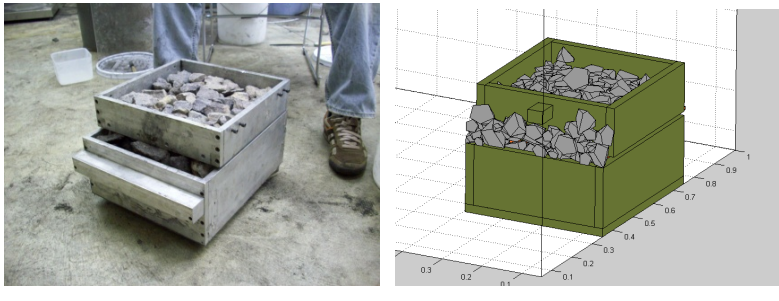

FIG.3. Direct Shear (Shear Box) Laboratory Setup and the BLOKS3D DEM Model

Figure 4 shows typical contact forces generated among aggregate particles during the direct shear test 3-D DEM simulations. The number of elements used represent actual aggregate particles was 671. Note that the major contact forces form a band connecting the upper left corner to the lower right to govern the shear strength of the ballast sample. Although aggregate friction is important on the horizontal shearing plane, the shear strength is contributed by aggregates in all locations in the shear box and changes in composition, i.e., fouling, in any region in the box would alter significantly the overall shear strength of the aggregate assembly. In accordance with the laboratory study by Huang et al. (2009), coal dust fouled ballast samples were prepared by adding coal dust into the clean ballast samples. Different fouling severities were represented by adding different percentages of coal dust by the weight of clean aggregate. In other words, in the direct shear box tests, the depth of coal dust filling the shear box determines the fouling severity. For instance, 15% coal dust fouled shear box sample will have approximately half of the lower box filled with coal dust while aggregates above are clean. This implies the fouled ballast DEM model validation should include three following steps:

Determine the DEM model parameters for clean ballast aggregate by testing clean ballast sample in direst shear strength test;

Determine the DEM model parameters for fouled ballast aggregate by testing fully coal dust fouled ballast sample in direct shear strength test;

Conduct laboratory 15% coal dust fouled ballast strength test and 15% coal dust fouled ballast strength DEM simulation by assigning coal dust fouled ballast DEM model parameters to the lower half of the shear box and the clean ballast DEM model parameters to the rest part. Compare the laboratory and DEM results to validate the coal dust fouled DEM model parameters.

DEM Simulation of Fouled Track

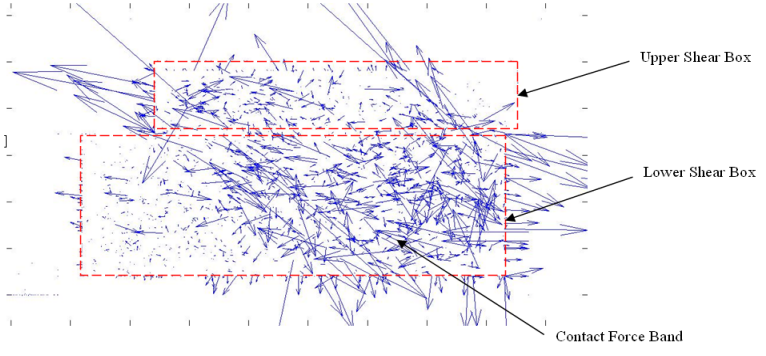

FIG.4. Contact Force Band among Aggregate Particles in Shear Box Test Simulation

Clean Ballast DEM Model Parameters

Calibration of the DEM model involves the process of matching the simulation results to the laboratory results by adjusting the model parameters. Since the element shape and size distributions have already been determined (Huang et al., 2009), the adjustable model parameters are: normal contact stiffness, shear contact stiffness, and surface friction angle. The ballast material tested was a typical AREMA No.24 graded granite aggregate with a specific gravity of 2.62 obtained from Gillette, WY and commonly used in the Powder River Basin joint line (Huang et al., 2009). Aggregates were processed through the University of Illinois Aggregate Image Analyzer (UIAIA) for quantifying their shape and angularity index properties so that representative elements could be generated with similar aggregate shape properties in BLOKS3D DEM simulations (Tutumluer et al., 2006). Three normal stresses, 172, 241, and 310 kPa, were applied at a constant shearing rate of 0.2 mm/sec in the laboratory tests.

Figure 5 shows for clean ballast samples the average shear reaction stresses plotted against the shear displacements under different normal stresses. The DEM simulation results are shown as dashed lines in Figure 5. These DEM model predictions achieved with a normal contact stiffness Kn of 20 MN/m; shear contact stiffness of 10 MN/m; and surface friction angle θ of 31 degrees as the model parameters were deemed satisfactory to represent clean granite ballast behavior.

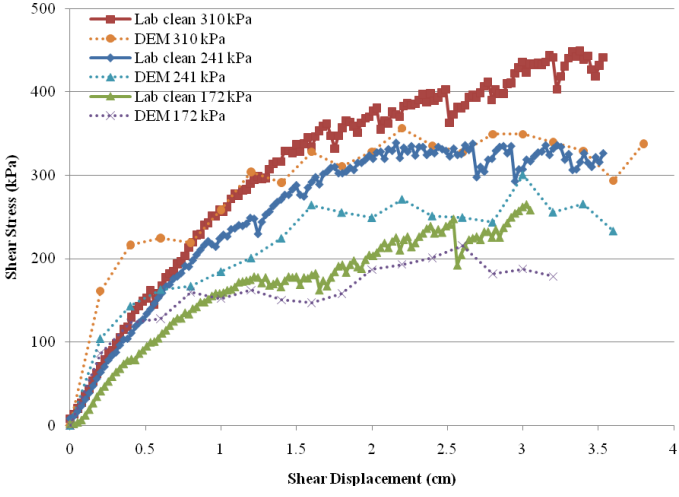

FIG.5. Average Shear Reaction Stresses from DEM Direct Shear Simulations and Laboratory Test Results for Clean Granite Ballast Aggregates (θ= 31^o)

Coal Dust Fouled Ballast DEM Model Parameters

Fully coal dust fouled ballast samples (i.e. the coal dust fills all the way up to the top of the shear box) were prepared and tested for DEM model calibration purposes. A direct way to simulate fouled ballast in DEM is to add small sized elements (representing fouling materials such as coal dust) into larger sized elements (representing clean ballast aggregates). It is however not feasible in terms of computation time since one particle of the fouling material can get as small as 0.075 mm (No. 200 sieve size). After studying the ballast fouling mechanism, an alternative way to simulate ballast fouling is proposed which is decreasing surface friction angle θ of the discrete element contact in the DEM model while keeping the contact stiffness values the same. It is based on the assumption that the coal dust would not greatly affect the contact stiffness which is reasonable in terms of the definition presented for Phase II fouling (Huang et al., 2009). How much to decrease the surface friction angle for fouled contacts needed to be obtained from a calibration process similar to the case of clean ballast sample.

Figure 6 shows for the fully coal dust fouled granite ballast samples the average shear reaction stresses plotted against the shear displacements under different normal stresses. The surface friction angle was decreased to 27 degrees. From Figure 6, it may be concluded that the DEM predictions, based on this set of parameters, match satisfactorily with the laboratory test results to represent coal dust fouled granite ballast behavior.

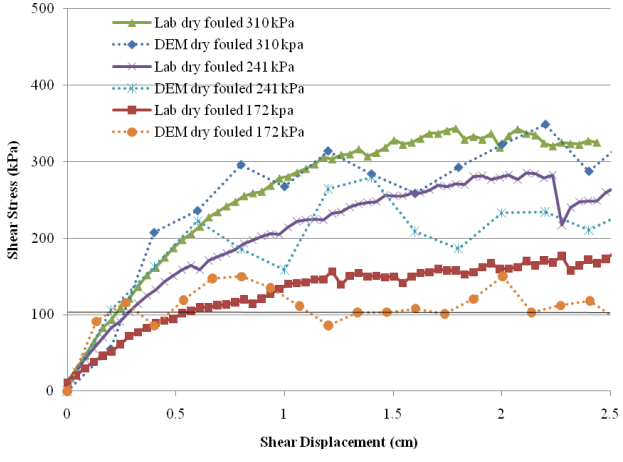

FIG.6. Average Shear Reaction Stresses from DEM Direct Shear Simulations and Laboratory Fully Coal Dust Fouled Samples ($\theta = 27^o$)

Validation of the Coal Dust Fouling Ballast DEM Model

As discussed previously, to test the validity of this statement and the applicability of the adopted DEM model parameters, laboratory direct shear tests were conducted on the partially fouled ballast samples. Solid lines shown in Figure 7 are the measured average shear stresses plotted against the shear displacements under three normal stresses for 15% coal dust fouled ballast samples tested in the laboratory. In this case, 15% fouling volumetrically equals to the condition that the coal dust fills up the voids within the lower half (76-mm) of the lower shear box. During the DEM simulations, ballast aggregate particles within this region were assigned with a surface friction angle of 27^{o}; whereas, the clean particles in other parts of the shear box were assigned with a surface friction angle of 31^{o}. The DEM simulation predictions are shown in dashed lines in Figure 7 for the three normal stresses. Although more fluctuation of the DEM results can be observed which may be due to the sharp corners of unbreakable elements assumed, it can be seen that the DEM fouling model can predict the laboratory test results reasonably well.

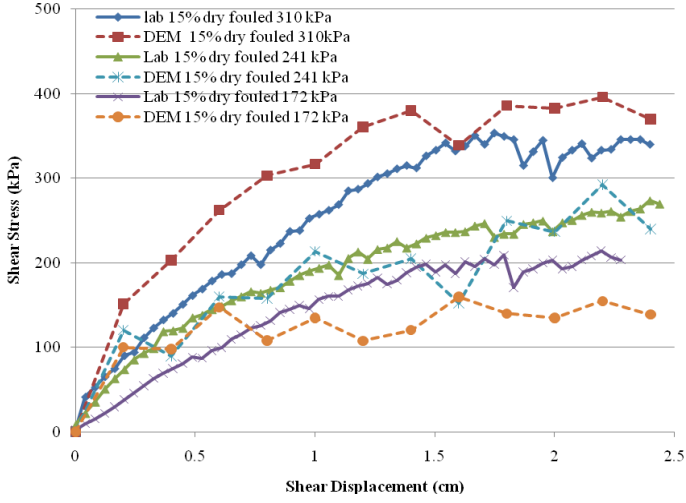

FIG.7. DEM Model Validation for the Partial Coal Dust Fouled Shear Box Test Simulation (15% by weight of coal dust filled half of the lower shear box)

SUMMARY AND CONCLUSIONS

This paper focused on using a special Discrete Element Modeling (DEM) approach, which uses realistic three-dimensional polyhedron shaped discrete elements generated through imaging based shape evaluations of aggregate particles, to simulate coal dust fouled ballast behavior. Laboratory direct shear (shear box) tests were conducted on

both clean and fouled AREMA No. 24 granite aggregates. As one of the worst fouling agents, coal dust was used to fill the voids in the ballast aggregate compacted and prepared in the shear box equipment. Both partial and full fouling conditions were studied in the laboratory for their effects on the shear strength test results.
Based on the laboratory findings, calibration of the developed DEM approach for fouled ballast was accomplished to determine DEM model parameters. By adjusting fictional contact between aggregate particles in contact through DEM model parameters and matching both clean and fouled ballast DEM simulation shear strength results to those of the experimental ones, it was possible to simulate different levels of coal dust fouling including partially fouled conditions, which was deemed essential for validating the DEM simulations.

ACKNOWLEDGEMENTS

The authors would like to thank Association of American Railroads (AAR) Affiliated Research Laboratory established at the University of Illinois at Urbana-Champaign and the Burlington Northern Santa Fe (BNSF) Railroad Company for providing the financial support needed to carry out this research study. The authors would also like to personally thank David Davis with AAR, Hank Lees with BNSF for providing ballast materials, and former graduate student William (Zach) Dombrow for conducting ballast shear box tests. The contents of this paper reflect the views of the authors who are responsible for the facts and the accuracy of the data presented herein. This paper does not constitute a standard, specification, or regulation.

REFERENCES

Barbosa, R. (1990). "Discrete Element Models for Granular Materials and Rock Mass". *Ph.D. Dissertation, University of Illinois at Urbana-Champaign*, Urbana, IL.

Cundall, P.A. (1971). "A Computer Model for Simulating Progressive, Large Scale Movements in Blocky Rock Systems". *International Symposium on Rock Fracture*, I.S.R.M., Nancy, France.

Ghaboussi, J and R. Barbosa. "Three-dimensional Discrete Element Method for Granular Materials". *International Journal for Numerical and Analytical Methods in Geomechanics*, Vol. 14, 1990: 451-72.

Huang, H., W. Dombrow, and E. Tutumluer. (2009). "Laboratory Characterization of Fouled Railroad Ballast Behavior". Manuscript 09-2065, *CD-ROM Proceedings of the 88th Transportation Research Board Meeting*, Accepted for Publication in Transportation Research Record.

Nezami, E.G., Zhao, D., Hashash, Y.M.A., and J. Ghaboussi. " A Fast Contact Detection Algorithm for 3-D Discrete Element Method". *Computers and Geotechnics*, Vol. 31, 2004: 575-587.

Nezami, E.G., Hashash, Y.M.A., Zhao, D., and J. Ghaboussi. "Shortest Link Method for Contact Detection in Discrete Element Method". *International Journal for Numerical and Analytical Methods in Geomechanics,* Vol. 30, (8), 2006: 783 - 801.

Tutumluer, E., Huang, H., Hashash, Y.M.A., and J. Ghaboussi. " Aggregate Shape Effects on Ballast Tamping and Railroad Track Lateral Stability". *Proceedings of the AREMA Annual Conference*, Louisville, Kentucky, September 17-20, 2006.

Tutumluer, E., H. Huang, Y. M. A. Hashash, and J. Ghaboussi. "Discrete Element Modeling of Railroad Ballast Settlement". *Proceedings of the AREMA Annual Conference*, Chicago, Illinois, September 9-12, 2007.

Zhao, D., Nezami, E.G., Hashash, Y.M.A., and J. Ghaboussi. "Three-dimensional Discrete Element Simulation for Granular Materials". *Journal of Engineering Computations*, Emerald Group Publishing Ltd., Vol. 23, (7), 2006: 749-770.

Evaluation of the Reinforcement Effect of Geogrids in Pavement Base Using Loaded Wheel Tester (LWT)

Hao Wu [1, 2, 3], Baoshan Huang [3], Zixin Zhang[1, 2]

[1]Ph.D. candidate, Key Laboratory of Geotechnical and Underground Engineering of Ministry of Education of Tongji University, Shanghai, 200092, P.R. China; hwu7@utk.edu
[2] Professor, Ph. D., Department of Geotechnical Engineering, School of Civil Engineering, Tongji University, Shanghai, 200092, P.R. China; zxzhang@mail.tongji.edu.cn
[3]Associate Professor, Ph.D., Department of Civil and Environmental Engineering, University of Tennessee at Knoxville, TN, 37919, US; bhuang@utk.edu

ABSTRACT: Geogrids have been widely used as an effective reinforcement in constructions, such as slopes and pavement bases. The mechanism of reinforcement action of geogrids is mainly achieved through the interlocking actions between aggregates and the grids. Different geogrids products and aggregates combinations would significantly affect the effects of interlocking. Accordingly, it is necessary to evaluate the effects of different geogrids on aggregates commonly used in potential engineering projects. In this study, laboratory experimental and analytical investigations were conducted to evaluate the performance of pavement base materials with or without geogrids reinforcement by using cyclic loading system, Loaded Wheel Tester (LWT). Meanwhile, rut depth (vertical deformation) of pavement base was considered to evaluate the effect of improvement.

INTRODUCTION

Geosynthetic materials have gained considerable popularity because of their wide applications in reinforcing various earthwork constructions. Its applications are primarily focused on pavement system, such as slope and pavement base (Haas et al. 1988, Barksdale et al. 1989). Base or subbase reinforcement is defined within as the use of geogrid reinforcement in pavements to support vehicular traffic over the life of a pavement structure. In terms of this point, in recent years, a number of applications with geogrid reinforcement in construction over low strength sub-grades or base have been developed.

Numerous studies and experiments have been carried out to investigate the mechanisms and evaluate the effects of geogrid reinforcement. The mechanisms of geogrid reinforcement in granular base were investigated under repeated load through the stress, strain and deflection measurements (Haas et al. 1988). The results showed that for low-deformation systems the interlock and confining actions of grids were

required to provide reinforcement and it also presented that highly performances could be obtained by geogrids in reinforcing the granular base material and thereby extend the life of a pavement structure. Deformation observed from the bearing capacity tests indicated that the bearing capacity of clay sub-grades was increased due to the reinforcement of geogrids (Mandal et al. 1992). A falling weight deflectometer was used to measure the dynamic response of pavement base system, and the traffic benefit ratio defined as the ratio of expected life of one section and the expected life of another section was introduced to appraise the effect of the improvement of geogrids (Kinney, 1998). Additionally, significant improvement in reducing rutting was observed in terms of the permanent strain in the pavement and soil layers in all reinforced sections by using heavy vehicle simulator (Perkins et al. 2005).

A cyclic loading test method proposed by Zhang (2007) and Han et al. (2008) was employed in this study to differentiate the effects of geogrid-aggregate reinforcement by different geogrid products using loaded wheel tester (LWT).

RESEARCH OBJECTIVE AND SCOPE

This study primarily focused on assessing the approach of using cyclic loading system to test pavement base materials with or without geogrids reinforced. Rut depth was regarded as the major factor in evaluating the effect of geogrids in reducing the vertical deflection of pavement.

In this study, LWT was introduced to simulate the actual vehicle loads on the pavement, and the rut depth of the base materials was measured through some transducers installed along the loading direction. Laboratory experiments and analysis were conducted in multi-layered geogrids with three different numbers of layers, and a well-graded angular gravel was considered as pavement base material.

TEST PROTOCOL

The LWT used in this study is shown in Figure 1. It features controllable wheel load and contact pressure provided by rubber hose with internal air pressure, which is an appropriate simulation of actual pavement loading conditions. Wheel load could be calibrated utilizing a load cell (as shown in Figure 2), and the effects for each geogrid were evaluated by comparison with the base without it.

FIG. 1. Loaded wheel tester (LWT)

FIG. 2. Load calibrating cell

LABORATORY EXPERIMENT

The grain-size distribution of the gravel used as pavement base is shown in Figure 3. The geogrids evaluated in this test are shown in Figure 4.

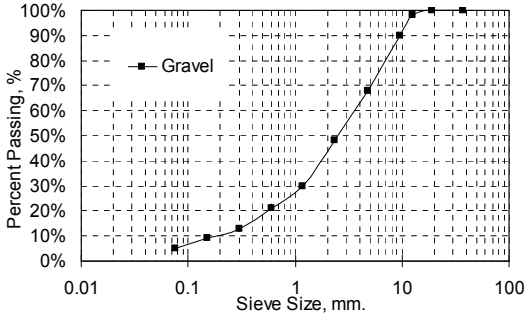

FIG. 3. Grain size distribution of the gravel

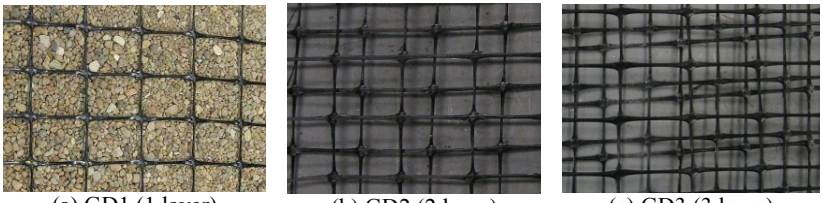

(a) GD1 (1 layer) (b) GD2 (2 layer) (c) GD3 (3 layer)

FIG. 4. Geogrids for test

In the test, the wheel load used for testing was 353 N (80 lb) and the corresponding hose pressure was 552 kPa (80 psi). An aluminum box for holding base materials was fabricated with 480mm in length, 380mm in width and 100mm in depth, and the geogrids were settled 25mm (1 in.) below the surface of the base. Each test was designed to run for 8000 cycles and the rut depths were measured automatically in different intervals in the loading direction by transducers. Before the rutting test, the base material was compacted to a certain density (70%). Considering the efficiency and quality of compacting, it was placed and compacted in three layers. To control the density of the sample, the mass of aggregate for each layer was measured. After each layer of base material was filled into the box, compaction was applied by tamping till the soil thickness reached to the satisfied thickness marked on the testing box. During tamping, the geogrids were set up into the box, making them even and level off on the required place. The testing specimen was shown in Figure 5.

The testing samples were directly put underneath the rubber hoses to be subjected to the wheel tracking action in the test. The LWT machine was connected to a computer, and software installed in the computer can automatically perform data acquisition from transducers to measure the rut depth with respect to the number of cycles. The

measurements were taken at five different locations along the pressured rubber hose, the three of which close to the center were used to obtain rutting depth.

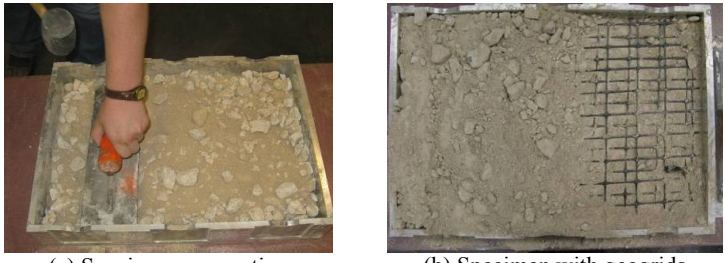

(a) Specimen preparation (b) Specimen with geogrids

FIG. 5. Specimen for the tests

TEST RESULTS

Figure 6 illustrated that the rut depth for the gravel base with geogrids were smaller than that without geogrid more or less. Geogrids GD2 and GD3 had remarkable contribution for rutting resistance, which reduced about 30% of the rut depth for the base without geogrid reinforced. However, GD1 with one layer of geogrids had no significant improvement in the reinforcement. As the number of the layer of geogrids increased, the effects were more noticeable, and GD2 and GD3 were more effective in reducing rut depth for the base than GD1. It can also be seen in Figure 6 that the gravel base with geogrid reinforced could achieve 80% of the total vertical deflection in the 8000 cycles around the 600th cycle, while the gravel base without geogrid required 3000 cycles to reach this plateau. Moreover, to this point, the geogrids GD2 and GD3 also exhibited much better effects than that of GD1. Whereas, comparing GD3 to GD2, there was no apparent difference between them in reinforcing even GD3 has one more layer of geogrids. That means two layers of this geogrids were sufficient in reinforcing the gravel with such grain-size distribution. The rut depths at the 8000th cycle for those geogrids were compared in Table 1.

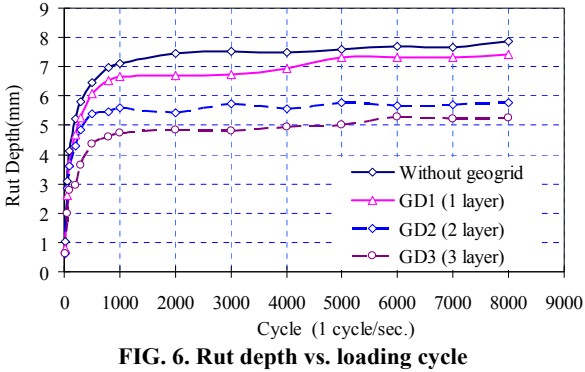

FIG. 6. Rut depth vs. loading cycle

Table 1 Rut Depth at the 8000th Cycle

Base Material	Gravel			
Geogrids	Without Geogrids	GD1 (1-layer)	GD12 (2-layer)	GD3 (3-layer)
Rut Depth (mm)	7.85	7.43	5.77	5.26
Improvement (%)	1.00	5.32	26.50	32.93

Furthermore, according to the rate of deflection in Figure 7, the effect of confinement and interlocking actions provided by geogrids in the base material were obviously reflected in this test. In addition, the vertical deflections of the gravel base with geogrid reinforced were much easier to be stabilized than the gravel base without geogrid reinforced. In the first 1000 cycles, the rate of deflection of the base without geogrid reinforced was much higher than that of the base with geogrid reinforced, but after 1000 cycles they all trended to be smooth and no distinct difference could be observed between them.

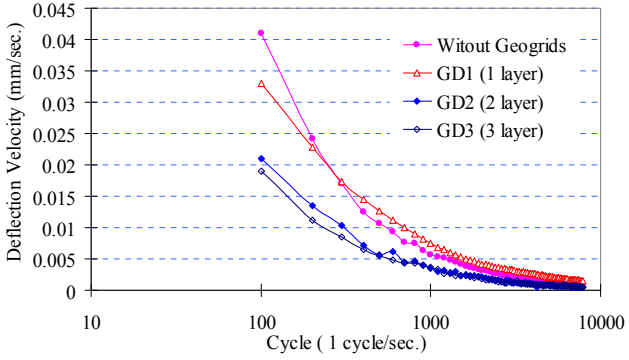

FIG. 7. Rate of deflection of rutting

SUMMARY AND CONCLUSION

Cyclic loading system, LWT, was utilized to evaluate the improvement of geogrid reinforcement on pavement base. Three multi-layer geogrid products were evaluated in the tests. Based on the laboratory experiments, the following can be summarized and concluded:

- The LWT is acceptable to evaluate the reinforcement effects of geogrids in base materials. The results were repeatable and in general agreement with an independent experiment from Han et al. with similar pavement base material.
- All three geogrids tested exhibited improvement to some extent for the performance of the base material.

- Compared to GD2 and GD3, GD1 was not significantly effective in reinforcing gravel base. GD2 and GD3 exhibited desired performance in confinement and interlock but the difference in the effects between them was not apparent, which indicates the relationship between grain-size of gravel and the apertures of geogrids has significant influence in determining the effect of geogrids, and the interaction between geogrids and pavement base could be emphasized to be more efficient based on this.

REFERENCES

Haas, R., Walls, J. and Carroll, R.G. (1988). "Geogrid reinforcement of granular bases in flexible pavements." *Transportation Research Board*, Washington, D.C. IN: 1188, pp. 19-27.

Barksdale, R.D., Brown, S.F., and Chan, F. (1989). "Potential benefits of geosynthetics in flexible pavement systems." *Transportation Research Board*, Washington, D.C. IN: 315.

Mandal, J.N. and Sah, H.S. (1992). "Bearing capacity tests on geogrid-reinforced clay." *Geotextiles and Geomembranes*, Vol. 11 (3): 327-333.

Kinney, T.C., Stone, D., and Schuler, J. (1998b). "Using geogrids for base reinforcement as measured by a falling weight deflectometer in a full scale laboratory study." *Transportation Research Board*, Washington, D.C. Vol. 1611: 70-77.

Perkins, S.W. and Cortez, E.R. (2005). "Evaluation of base-reinforced pavements using a heavy vehicle simulator." *Geosynthetics International*, Vol. 12 (2): 86-98

Zhang, Yuze (2007). "Investigation of geosynthetic-soil confinement using asphalt pavement analyzer." Dissertation for the Degree of Master's of Science, Lawrence, KS: The University of Kansas.

Han, J., Zhang, Y., and Parsons, R.L. (2008). "Development of a performance-based laboratory test method for evaluating geosynthetic-soil confinement." *Transportation Research Board*, Washington, D.C.

Utilization of Plastic Wastes for Improving the Sub-grades in Flexible Pavements

A.K.Choudhary[1], J.N.Jha[2], and K.S.Gill[3]

[1]Deptt. of Civil Engineering, NIT, Jamshedpur, India
[2,3]Deptt. of Civil Engineering, GNDEC, Ludhiana, India

ABSTRACT: The objective of this study is to demonstrate that a waste material can be used as reinforcement and for this purpose a series of experimental study was carried out to investigate the CBR behavior of waste plastic strip reinforced soil. The effect of waste plastic strip content (0.25% to 4.0%) and strip length on the CBR and secant modulus of strip reinforced soil was investigated. The study reveals that addition of waste plastic strips of appropriate size and proportions in soil results in an appreciable increase in both the CBR and secant modulus. The waste plastic strip reinforced soil can be used in low cost embankment/road construction leading to significant cost advantage as well as safe disposal of these waste materials in an environment friendly manner.

INTRODUCTION

Soil reinforcement is an effective and reliable technique to improve the strength of soil subgrade. An improved subgrade shall require relatively thinner section of a flexible pavement as compared to that required in case of an untreated and weaker subgrade resulting in significant cost advantage. Over the years the use of geotextiles and other polymeric reinforcements such as geogrids has increased drastically in geotechnical engineering practice. However; in certain cases; especially for low cost embankment/road construction, their cost becomes a prohibitive factor for their wide spread use. In comparison with systematically reinforced soil, randomly distributed fiber reinforced soil has been found effective in improving the soil CBR as reported in the literature (Gosavi et al. 2004, Yetimoglu et al. 2005). Nowadays plastic containers usually made of high density polyethylene (HDPE) are being discarded immediately after use. Though, at many places HDPE is being collected for recycling or reuse but unfortunately; the secondary markets for reclaimed HDPE have not developed as recycling programmes. According to the data published in US, plastic is occupying 20% of available landfill spaces by volume. The estimated municipal solid waste production in India upto the year 2000 was of the order of 39 million tons per year and this figure is most likely to touch 56 million tons per year

by the end of 2010 (Dutta 1997). The typical percentage of plastics in the municipal solid waste produced in India is around 1% (Rao and Dutta 2004). The best way to handle such wastes is to utilize them for engineering applications. Soil reinforcement can be a significant secondary market for waste HDPE. Soil reinforcement with reclaimed HDPE strips, if found effective can provide an easy and economical means to improve the engineering performance of the soil subgrades by replacing costly reinforcing material like geogrid. Again it can help in solving the problem of disposal of this non biodegradable waste causing environmental hazards. The feasibility of reinforcing soil with strips of reclaimed HDPE has been investigated only to a limited extent by few researchers (Benson and Khire 1994) and therefore the prediction of pavement performance will become difficult if unconventional materials are part of pavement structure (Lee and Fishman 1993). Keeping this in view an attempt has been made in the present investigation to demonstrate the potential for using reclaimed HDPE strips as soil reinforcement for improving the performance of the subgrades and thus possibility of finding applications in many real life problems especially for design and construction of low cost roads and stabilization of earth slopes. The paper describes the results of a series of laboratory CBR tests carried out with specimens of unreinforced sand as well as sand mixed uniformly with varying percentage of HDPE strip content and lengths. The results obtained from the tests are presented and discussed in this paper.

EXPERIMENTAL WORK

A brief description of the material and method (as per IS-2720-Part-I(1987)) used in this investigation is given in the following paragraph.

Sand: The investigation was carried out on locally available sand collected from Kharkai river basin at Jamshedpur, India, having specific gravity 2.62, mean particle diameter (D_{50}) 0.55 mm, coefficient of uniformity (C_u) 2.40 and coefficient of curvature (C_c) 1.67. The sand was classified as 'SP' as per the Unified Classification System. The maximum and minimum dry densities of sand as determined from the relative density test were 16.5 kN/m^3 and 14.6 kN/m^3 respectively.

HDPE: The waste plastic strip used in the present study were purchased from a rag picker who collects recycling material from the waste dump site in and around Jamshedpur, Jharkhand (India) at a price of INR 100 per kg (approximately $2per kg). They are made of HDPE having a width (b_s) of 12mm and a thickness of 0.40mm. These were cut into lengths (l_s) of 12mm [Aspect Ratio(AR)= (l_s)/ (b_s) = 1], 24mm (AR=2) and 36mm (AR=3) thus always ensuring that mould diameter remains at least 4 times the maximum strip length which will ensure that there is sufficient room for the strips to deform freely and independent of mould confinement. The waste plastic strips to be added to the soil were considered a part of the solid fraction in the void solid matrix of the soil. The content of the strip is defined herein as the ratio of weight of strips to the weight of dry sand. The tests were conducted at a strip content of 0.0%, 0.25%, 0.50%, 1.0%, 2.0% and 4.0% respectively. In the absence of standards for testing strips, the standard used for wide width tensile strength test (ASTM D 4885) for geosynthetics were used. The tensile strength of 100mm long waste plastic strip was determined at a deformation rate of 10mm/min in a computer

controlled Housefield machine. The average ultimate tensile strength of this strip was 0.36 kN and percent elongation at failure was 23%.

Method: The experimental study involved performing a series of laboratory CBR tests on unreinforced and randomly oriented HDPE strip reinforced sand specimen. Specimens were prepared by compacting sand in dry state in three equal layers to a dry density of 16.2 kN/m^3 (corresponding to a relative density of D_r= 85%) in a steel CBR mould having diameter 150mm and height 175mm. HDPE strip reinforced sand layers were prepared at the same dry density as that of unreinforced sand. Required amount of strips as well as sand for each layer were first weighed and then the strips were randomly mixed with dry sand and due care was taken to have a homogeneous mix. The mix was then transferred to the mould and a surcharge base plate 148 mm in diameter and weighing 25 N was placed over it in order to avoid segregation of the strips during vibration. The sand was compacted in the mould by vibrating it on a vibration table for 2 minutes. Similar procedure was adopted for compacting other two layers in the mould. The tests were performed as per procedures described in IS-2720-Part 16(1987). A surcharge plate of 2.44 kPa was placed on the specimen prior to testing. The loads were carefully recorded as a function of penetration up to a total penetration of 12.5 mm. Finally; load-penetration curves were drawn for each case and corrections were applied using the standard procedure. From the load-penetration curves so obtained california bearing ratio (CBR) values as well as secant modulus (defined as the ratio of load in kPa at a penetration of 5mm to the penetration of 5mm) were determined. Since for all the cases considered in the present investigation, CBR value at 5.0 mm penetration was observed higher than that of 2.5 mm penetration even on repetition, therefore the CBR value reported in the present investigation are those of 5.0 mm penetration. All the tests were performed in triplicate to obtain average results and to check reproducibility. If the test results had significant variation (more than 3% in this study) additional tests were performed before averaging.

RESULT AND DISCUSSION

The load-penetration curves obtained from the CBR tests for un-reinforced and randomly reinforced system with varying strip contents (0.25% to 4.0%) and aspect ratios (AR=1, 2 and 3) are shown through Figure 1 to Figure 3.It is evident from these figures that in general, addition of randomly oriented HDPE strips inclusion in the soil increased the piston load at a given deformation significantly as compared to that of unreinforced sand, eg. the load of the unreinforced sand corresponding to 2.5mm and 5.0mm penetration were found to be 1920N and 3880N respectively but when the soil was reinforced with 0.25% waste plastic strips having strip length equal to 12mm, the piston load increased to 3320N and 6000N respectively (Figure 1). The variation in CBR value for reinforced sand with different strip content at various aspect ratios is shown in Figure 4.Unreinforced case has been shown in Figure 4 as AR=0. From Figure 4 it can be seen that for a given strip length, the CBR values increases with increase in strip content (0.25% to 4%) and again for a given strip content any increase in strip length or aspect ratio also results in an increase in CBR value. The extent of improvement in the CBR values due to the addition of HDPE

strip inclusions has been expressed by a dimensionless term namely; California bearing ratio index, defined as the ratio of CBR value of reinforced soil (CBR_r) to the CBR value of unreinforced soil (CBR_u) [$CBRI=CBR_r/CBR_u$]. The variation of CBRI with strip content for various strip length/aspect ratio has been shown in Figure 5 whereas Figure 6 shows the variation in secant modulus of strip reinforced sand with strip content. The increase in CBRI and secant modulus is noticeably attributed to strip inclusion in the soil and the extent of improvement is observed to be governed by the parameters namely; strip content and aspect ratio. At 0.25% strip content, the range of improvement in CBRI is from 50-70% depending on aspect ratio when compared with plain soil. When the strip content is increased from 0.25% to 2%, then the range of improvement in CBRI is from 80-90% only if compared with plain soil again depending on aspect ratio. But once the strip content reaches to 4%, the improvement in CBRI is substantial and is approximately 2.2 to 3 times to that of unreinforced soil for different aspect ratio. This may be due to the fact that the number of strips required for developing friction between reinforcing material and soil may not be sufficient at less value of strip content in the range of 0.25-2 %, thus resulting less improvement in CBRI. But once the strip content becomes 4% in the mix, sufficient friction is generated between HDPE strip and sand causing substantial improvement in CBRI (Figure 5).

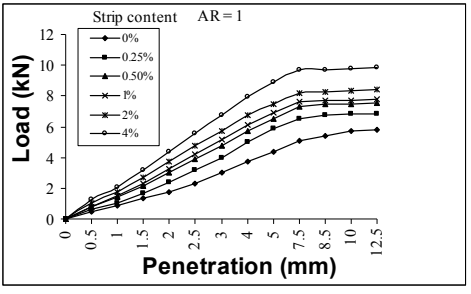

FIG. 1. Load penetration curve for different strip content at AR=1

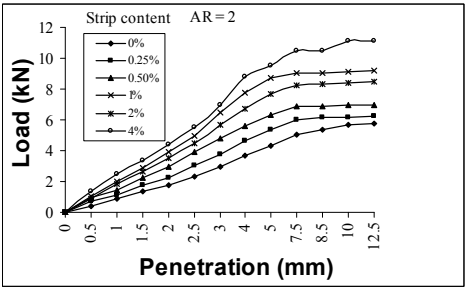

FIG. 2. Load penetration curve for different strip content at AR=2

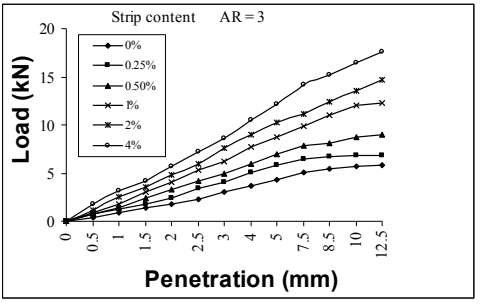

FIG. 3. Load penetration curve for different strip content at AR=3

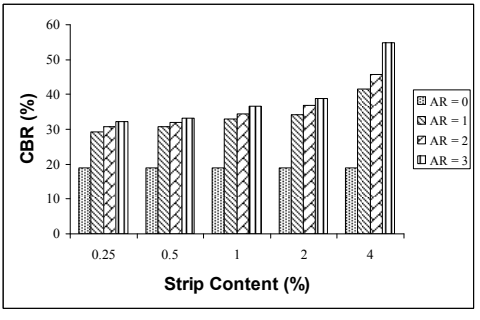

FIG. 4. Variation of CBR with Strip Content at different AR

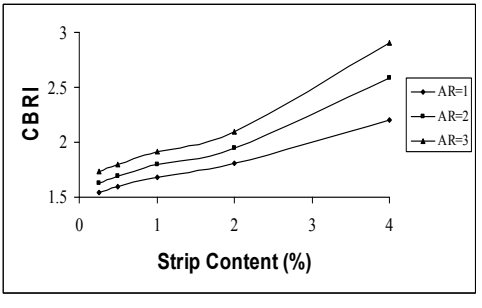

FIG. 5. Variation of CBRI with Strip Content at different AR

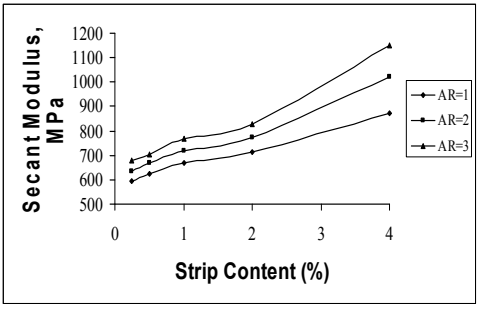

FIG. 6. Variation of Secant Modulus with Strip Content at different AR

It can again be observed from Figure 5 that at constant strip content, if aspect ratio increases CBRI value also increases. This may be due to the fact that longer strips may develop greater tension as a result of larger embedment length. Similar trend is also observed for the secant modulus when strip content varied from 0.25 to 4 %. The maximum value of secant modulus of the reinforced system is approximately 2.9 times to that of an unreinforced system (Figure 6) which occurs for the case when 4% HDPE strip having aspect ratio equal to 3 is mixed with the soil. After the completion of each test, specimens were dissected and the strips were examined. Many of the strips showed elongation, thinning and clear impression of sand particles. Apparently, as the soil sheared during penetration, strip embedded in the sand are subjected to friction and gets elongated as the soil is deformed. Though the CBR value at 2.5mm is invariably higher but in the present case, the CBR value of HDPE strip reinforced sand at 5mm penetration is found to be higher thus clearly indicating that at higher deformation the HDPE reinforcement is more effective in improving the strength of soil and the resistance to deformation is the likely cause of the increase in CBR.

CONCLUSIONS

Based on the results of the present investigation following conclusions can be drawn:

1) The addition of reclaimed HDPE strips a waste material to local sand results in an appreciable increase in the CBR and the secant modulus.
2) The reinforcement benefit increases with an increase in strip content and the aspect ratio and maximum value of CBR and secant modulus of a reinforced system is around three times of that of an unreinforced system.
3) Though the maximum improvement in CBR and secant modulus is obtained when the strip content is 4% and the aspect ratio 3 but the improvement in CBR is also appreciable even at 2% strip content.

ACKNOWLEDGEMENT

The facilities extended during the study by NIT, Jamshedpur is acknowledged.

REFERENCES

Benson, C.H. and Khire, M.V. (1994) "Reinforcing sand strips of Reclaimed High density polyethylene" *Journal of Geotechnical Engineering*, 120 (5), pp.838-855.

Dutta , M. (ed.) (1997) "Waste disposal in engineered landfills" NPH, N.Delhi,pp.3-4

Gosavi, M. Patil, K.A., Mittal, S. and Saran, S. (2004) "Improvement of Properties of black cotton soil subgrade through synthetic reinforcement" *Journal, Institution of Engineers* (India), Vol. 84, pp.257-262.

Lee,S.W. and Fishman, K.L.(1993) "Waste products as Highway Materials in flexible pavement System" *Journal of Transportation Engineering*, 119 (3) pp.433-449

Rao, G. V. and Dutta, R.K. (2004) "Ground improvement with plastic waste" *Proceeding, 5th International Conference on Ground Improvement Technique*, Kaulalumpur, Malaysia, pp.321-328.

Yetimoglu, T., Inanir, M., Inanir, O. (2005) "A study on bearing capacity of randomly distributed fibre reinforced sand fill overlying soft clay" *Geotextile and Geomembranes*, 23(2), pp.174-183.

IS:2720-Part XVI(1987). Laboratory determination of CBR. *Bureau of Indian Standards*, New Delhi, India.

Performance Prediction and Moisture Susceptibility of Anisotropic Pavement Foundations

Reza Salehi Ashtiani [1]; M. ASCE, Rong Luo [2]; and Robert L. Lytton [3], F. ASCE

[1]Post Doctoral Research Scientist, Zachary Department of Civil Engineering, Texas A&M University, College Station, Texas 77843-3135; reza@tamu.edu
[2] Assistant Lecturer, Zachary Department of Civil Engineering, Texas A&M University, College Station, Texas 77843-3135; rongluo@tamu.edu
[3]F. J. Benson Chair Professor of Civil Engineering, Texas A&M University, College Station, Texas 77843-3136; r-lytton@tamu.edu

ABSTRACT: Significant work has been done by the International Center for Aggregate Research (ICAR) to identify the effects of the anisotropic nature of compacted base courses on the stress, strain, and permanent deformation characteristics of pavement foundations. As continuation to this effort, current paper presents a mechanistic approach for determination of the variation of pore water pressure under a moving wheel load. This paper also presents a methodology as to evaluate the effect of pore water pressure on the anisotropic response of aggregate layers.

Sixty-two aggregate systems were tested with varying fine contents and water contents. The aggregate blends were molded according to AASHTO T-180 and tested using state of the art equipment called the Rapid Triaxial Tester (RaTT) at three saturation levels to capture the moisture susceptibility of the aggregate systems. Variable Dynamic Confining Pressure (VDCP) stress paths were in turn used to determine the anisotropic material properties for each aggregate system.

This approach shows that the external pressure applied on the surface of the pavement results in a reduction of the initial negative pore water pressure. The change in pore water pressure induced by traffic load for high fines content specimens at elevated saturation levels results in positive pore water pressure which is synonymous with more critical conditions for plastic deformation. Further analysis on the results shows the agreement between the proposed approach and the principle of change in pore water pressure presented by Henkel.

Mohr-Coulomb yield function was employed as a performance indicator in this study. The stress sensitive and anisotropic material model showed that the hardening component of the stiffness in vertical direction at the centerline of the load and at the top of the aggregate base layer is approximately 20% smaller when the influence of

pore water pressure is considered in the formulations.

BACKGROUND

The mechanistic response of hydraulically bonded aggregate layers subjected to traffic loads is significantly affected by the pore water pressure in the aggregate system. Significant work has been done by the International Center for Aggregate Research (ICAR) to identify the effects of the anisotropic nature of compacted base courses on the stress, strain, and permanent deformation characteristics of aggregate layers. There is another effect that has just been discovered by re-analyzing the original data that will prove to be just as significant in determining the long-term permanent deformation of those base courses. The previous analysis had determined by non-linear regression analysis the coefficients and exponents of the stress-dependent vertical, horizontal and shear modulus (Uzan 1985); (Witczak and Uzan 1988). The Uzan model for the vertical modulus is shown in equation 1 that includes coefficients k1, k2, and k3. The k1 value was the scale multiplier of the vertical modulus and the k2 value was the exponent of the mean principal stress term. The k3 value was the exponent of the octahedral shear stress term. Similar arrangements were found for the horizontal modulus and the shear modulus as shown in equations 2 and 3. It was further found that all of the nine k-values depended upon the gradation, and the statistical distributions of the form, angularity, and texture measurements as well as the dry unit weight and water content (Ashtiani et al. 2008), (Ashtiani et al. 2007).

$$E_y = k_1 P_a \left(\frac{I_1}{P_a} \right)^{k_2} \left(\frac{\tau_{oct}}{P_a} \right)^{k_3} \quad (1)$$

$$E_x = k_4 P_a \left(\frac{I_1}{P_a} \right)^{k_5} \left(\frac{\tau_{oct}}{P_a} \right)^{k_6} \quad (2)$$

$$G_{xy} = k_7 P_a \left(\frac{I_1}{P_a} \right)^{k_8} \left(\frac{\tau_{oct}}{P_a} \right)^{k_9} \quad (3)$$

where: E_x and E_y= resilient modulus in x and y directions, respectively;
G_{xy}= shear modulus in xy plane;
I_1=First invariant of the stress tensor;
τ_{oct}=shear stress on octahedral plane;
Pa=atmospheric pressure;
k-parameters= fitting parameters determined from stress path tests.

The re-analysis inserted three more k-values, called k_4, k_8 and k_{12} into the hardening component to represent the pore water pressure that was developed under the anisotropic stress path tests. The equations 4 through 6 were used to characterize the aggregate systems. According to the theory that was presented by Lytton at the First International Conference on Unsaturated Soils in Paris (Lytton 1995), these terms represent the effect of the moisture state in the base course. Under normal compaction

conditions this stress is negative, meaning that the pore water in the base course is in tension, using the common soil mechanics sign convention. The pore water pressures change as the stress states applied on the pavement varies. Highly compressive external pressures will cause the pore water pressure to become less tensile and may even become positive. A compressive state in the pore water is known to reduce both the strength and stiffness of any soil or base course and to reduce its resistance to permanent deformation and to affect, negatively, the plasticity yield function and plastic potential function.

$$E_y = k_1 P_a \left(\frac{I_1 - k_4}{P_a} \right)^{k_2} \left(\frac{\tau_{oct}}{P_a} \right)^{k_3} \tag{4}$$

$$E_x = k_5 P_a \left(\frac{I_1 - k_8}{P_a} \right)^{k_6} \left(\frac{\tau_{oct}}{P_a} \right)^{k_7} \tag{5}$$

$$G_{xy} = k_9 P_a \left(\frac{I_1 - k_{12}}{P_a} \right)^{k_{10}} \left(\frac{\tau_{oct}}{P_a} \right)^{k_{11}} \tag{6}$$

It was found that the values of the extra coefficients (k_4, k_8 and k_{12}) were highly dependent upon the stress state in the base course. Following the theory developed by Lytton in 1995, the extra k-coefficients were further determined to investigate the magnitude of the change in pore water pressure that was developed in the different aggregate systems. The analysis results revealed that the change of pore water pressure followed the principles of pore water pressure change that were set forth by (Henkel 1960). Henkel's theory states that the change in pore water pressure has two coefficients which depend upon the stress state: one of these refers to the changes of mean principal stress and the other refers to the changes in octahedral shear stress. Henkel's principal of variation of pore water pressure is presented in equation 7.

$$\Delta u = \beta \Delta \sigma_{oct} + \alpha \Delta \tau_{oct} \tag{7}$$

where: Δu = the change in pore water pressure;

$\Delta \sigma_{oct}$ = the change of mean principal stress, $\frac{\Delta \sigma_1 + \Delta \sigma_2 + \Delta \sigma_3}{3}$;

$\Delta \tau_{oct}$ = the change of octahedral stress, $\frac{1}{3}\sqrt{(\Delta \sigma_1 - \Delta \sigma_2)^2 + (\Delta \sigma_2 - \Delta \sigma_3)^2 + (\Delta \sigma_3 - \Delta \sigma_1)^2}$;

α and β = Henkel pore-water pressure coefficients.

ANALYSIS AND RESULTS

Figure 1 and figure 2 present the variation of the Henkel's pore water pressure parameters as a function of stress states for granite materials sourced from Oklahoma. The following test protocol was used to determine the Henkel's pore water pressure parameters plotted in the aforementioned figures.

The aggregate blends were molded and subjected to variable dynamic confining pressure stress path tests at three saturation levels namely the dry state (below the optimum moisture content), optimum moisture content, and the wet state (two percent above the optimum moisture content). These three water contents are symbolized by D (Dry), O (Optimum), and W (Wet). Three different gradations were considered with increasing amount of fines to capture the synergistic impact of particle size and moisture content on the performance of aggregate systems. These three gradations are symbolized by C (Coarse), W (Well), and F (Fine). Hydraulically bonded aggregate specimens were subjected to variable dynamic confining pressure stress paths in three stress regimes and ten different stress states therefore each aggregate system was tested at 30 stress points. The prescribed stresses in the lab and the resultant anisotropic material properties were in turn fitted to equations (4) through (6) to determine the k-parameters. Equations 8 and 9 were later used to calculate the net change in the pore water pressure due to change in stress states for each variant.

$$\theta = \frac{\gamma_d}{\gamma_w}\omega \tag{8}$$

$$\Delta u = \frac{k_4}{-3\theta} \tag{9}$$

where: ω=gravimetric water content

θ= volumetric water content

γ_d= dry density of the aggregate system (kg/m^3)

γ_w = dry density of water (kg/m^3)

k_4 = fitting parameter in the hardening term in equation (4)

The impact of a moving wheel load characterized by the orthogonal dynamic loading protocol on the Henkel's pore water pressure parameters for E_x (resilient modulus in x-direction) as well as G_{xy} (shear modulus in xy plane) can also be investigated using the same protocol. It was observed that the same trend exists for E_x and G_{xy} when the fitting parameters k_8 and k_{12} were used in equation 9 for E_x and G_{xy} respectively.

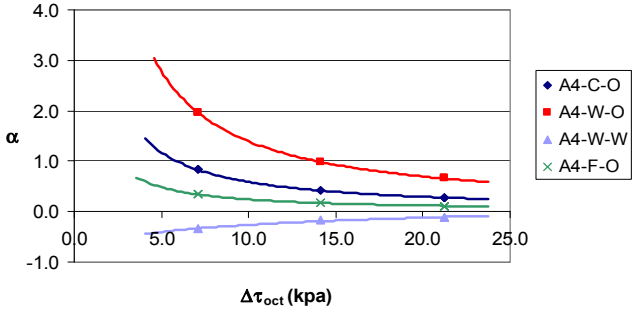

FIG. 1. Variation of Henkel's pore pressure parameter (α) with change in the octahedral shear stress.

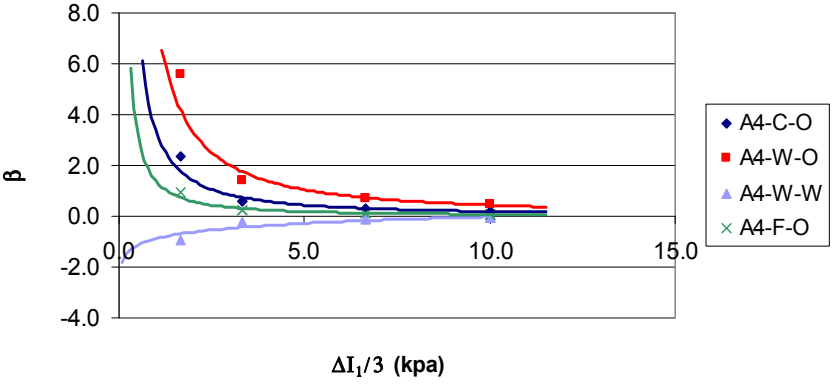

FIG. 2. Variation of Henkel's pore pressure parameter (β) with change in the first stress invariant.

The following example is provided to emphasize the significance and usefulness of this methodology for the highway design industry. Two analysis methods with two assumptions: one considering the impact of pore water pressure and the other one without taking into account the influence of the pore water pressure parameters in the base layers were employed for comparison. Cross-anisotropic solutions were used in both cases for the calculation of the pavement responses due to traffic load.

The Mohr-Coulomb yield criterion was adopted to analyze the stability of the aggregate bases. Equation 10 presents the yield function according to Mohr-Coulomb theory.

$$f = \frac{1}{3}\sin\varphi + \sqrt{J_2}\,\sin(\theta + \frac{\pi}{3}) + \frac{\sqrt{J_2}}{3}\cos(\theta + \frac{\pi}{3})\sin\varphi - c\cos\varphi \quad (10)$$

$$J_2 = \frac{1}{6}\left[(\sigma_1 - \sigma_2)^2 + (\sigma_2 - \sigma_3)^2 + (\sigma_1 - \sigma_3)^2\right] \quad (11)$$

$$J_3 = \left[(\sigma_1 - \frac{I_1}{3})\ (\sigma_2 - \frac{I_1}{3})\,(\sigma_3 - \frac{I_1}{3})\right] \quad (12)$$

$$\theta = \frac{1}{3}Cos^{-1}\left[\frac{3\sqrt{3}}{2}\frac{J_3}{J_2^{3/2}}\right] \quad (13)$$

where: f = yield function according to Mohr-Coulomb theory;
c and ϕ=cohesion and angle of internal friction, respectively;
$\sigma_1.\sigma_2$ and σ_3 = principal stresses in z, y and x directions, respectively;
J_2 and J_3 = second and third invariants of the deviatoric stress tensor, respectively; and
θ= the angle of similarity.

Figure 3 presents the influence of pore water pressure on the vertical stiffness of the aggregate layer. Figure 3 clearly indicates the shift and reduction in the hardening component of the vertical resilient modulus $[(I_1-k_4)/pa]^{k2}$ as the pore water pressure parameters were considered in the formulations. Lower hardening parameters correspond to less stiff aggregate systems, therefore taking into account the influence of the pore water pressure enables the pavement designer to have a better judgment of the stiffness of the aggregate layer and to prevent overestimation of the modulus of the base layer particularly in wet cycles. The results in this figure indicate that the hardening component is approximately 20% smaller when the influence of traffic stress-induced pore water pressure is considered in the formulations.

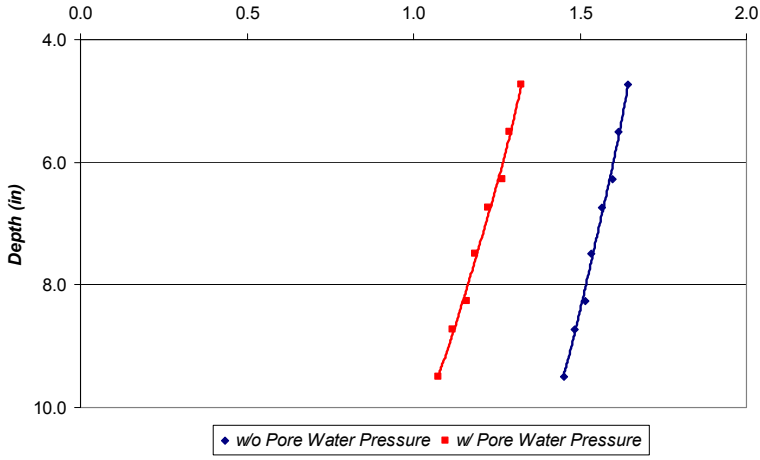

FIG. 3. Impact of pore water pressure on the hardening parameter of vertical resilient modulus (E_y).

Figure 4 presents the values of the yield function presented in equation 10. In general, negative values of the yield function correspond to stress states under which the deformation in the aggregate system is mostly recoverable and the system can sustain the external load without developing significant plastic deformations. On the other hand positive values of the yield function correspond to critical conditions at which the aggregate system is prone to develop plastic deformations. The material parameters were selected so that the yield function falls into the plastic region in this example. Higher values of the yield function correspond to more critical conditions which typically happens at the centerline of the external force.

Figure 4 shows the influence of pore water pressure on the Mohr-Coulomb yield function. Yield function values corresponding to solutions with the pore water pressure parameters resulted in more critical values than solutions without considering the pore water pressure parameters. This will help the highway design industry have better understanding of the stability and performance of the aggregate bases during different traffic and environmental cycles.

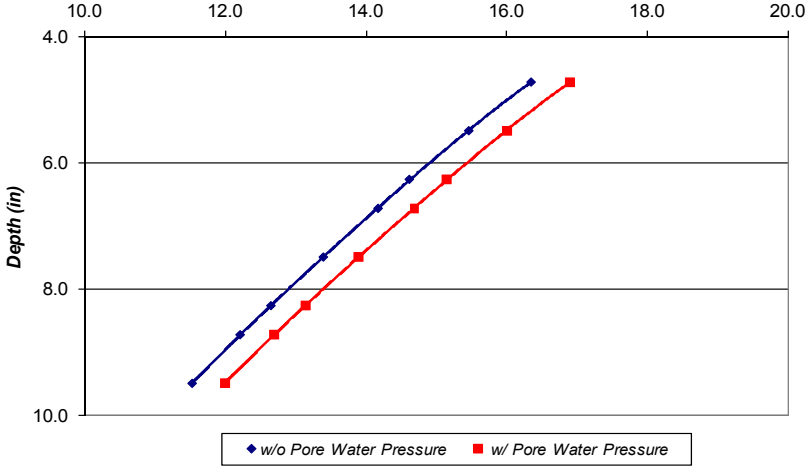

FIG. 4. Impact of pore water pressure on the Mohr-Coulomb yield function.

CONCLUSION

Extensive stress path tests were performed on several aggregate systems with different lithologies, gradations and moisture states to investigate the effect of pore water pressure on the mechanical response of aggregate samples. The mechanistic responses of the aggregate systems were considered to be nonlinear, stress sensitive and anisotropic in nature. The orthogonal load distribution capability of the systems was also considered to be influenced by the pore water pressure in the system. A methodology for determination of the variation of pore water pressure with moving wheel load is developed and presented in this study. The results were in conformity with principal of pore pressure change presented by Henkel.

Plasticity theory along with cross-anisotropic solutions was further employed to investigate the impact of pore water pressure on the performance of aggregate layers at high saturation levels. The results indicate that the hardening component of the vertical stiffness at the top of the aggregate base layer is approximately 20% smaller when the influence of traffic stress-induced pore water pressure is considered in the formulations. Yield function values corresponding to solutions considering the pore

water pressure parameters resulted in more critical conditions than solutions without considering the pore water pressure parameters.

The results presented in this study showed that repeated traffic load applications will have a direct and predictable effect on pore water pressure in the base course which, in turn, will make the estimation of the performance of these aggregate base courses more accurate and precise. The original negative pore water pressure in the base course can be measured and, in fact can be predicted using the capabilities of the Enhanced Integrated Climatic Model (EICM) that is part of the new Mechanistic-Empirical Pavement Design Guide (MEPDG).

The proposed approach in this paper will provide a valuable means for highway design industry to have a better understanding of the stability and performance of the aggregate layers subjected to different traffic loads and environmental cycles.

REFERENCES

Ashtiani, R., Little, D., and Masad, E. (2007). "Evaluation of the Impact of Fines on the Performance of Lightly Cement-Stabilized Aggregate Systems." Transportation Research Record: Journal of the Transportation Research Board, 2026(-1), 81-88.

Ashtiani, R., Little, D., and Masad, E. (2008). "Material Factors That Influence Anisotropic Behavior of Aggregate Bases." Transportation Research Record: Journal of the Transportation Research Board, 2059(-1), 20-30.

Henkel, D. J. (1960). "The Shear Strength of Saturated Remoulded Clays." Proceedings of the American Society of Civil Engineers (ASCE) Research Conference on Shear Strength of Cohesive Soils, 9, 533 - 554.

Lytton, R.L. (1995). "Foundations and Pavements on Unsaturated Soils", Keynote Address, Proceedings, First International Conference on Unsaturated Soils, International Society of Soil Mechanics and Foundation Engineering, Paris, Sept. 8-10, pp 1201-1220.

Uzan, J. (1985). "Characterization of Granular Material." Transportation Research Record: Journal of the Transportation Research Board, No. 1022, 52 - 59.

Witczak, M., and Uzan, J. (1988). "The Universal Airport Pavement Design System, Report I of IV: Granular Material Characterization." University of Maryland, Dept. Of CE.

Experimental Study on Dredged Material Improvement for Highway Subgrade soil

Yinghao Huang[1], Wei Zhu[2], Chunlei Zhang[3], Shuncai Wang[4], Nan Zhang[5]

[1]PhD student, Geotechnical Research Institute, Hohai University, Nanjing, P.R. China, 210098; ythuangyinghao@163.com
[2]Professor, College of Environmental Science and Engineering, Hohai University, Nanjing, P.R. China, 210098; weizhu863@126.com
[3]Doctor, College of Environmental Science and Engineering, Hohai University, Nanjing, P.R. China, 210098; chunleizhang@hhu.edu.cn
[4]Doctor, College of Environmental Science and Engineering, Hohai University, Nanjing, P.R. China, 210098; wshcai@hhu.edu.cn.
[5]Master student, Geotechnical Research Institute, Hohai University, Nanjing, P.R. China, 210098; zhangnanvictor@126.com

ABSTRACT: Large amount of sediments are dredged from rivers and lakes as a result of environmental dredging in China. These dredged materials (DM) have poor geotechnical properties and are normally treated as wastes. On the other hand, there is a huge demand of sub-grade materials due to the increasing number of highway construction projects in the eastern China. Thus the reuse of the DM as sub-grade material may be considered as an environmental-friendly and economical option. In this study a dredged material taken from Tai-hu lake was modified by adding fine sand, quicklime and Portland cement. Water content, Atterberg limits, and California bearing ratio (CBR) of the modified soil were determined. Test results show that fine sand significantly decreases the plasticity of the modified soil and increases its workability. However, a great amount of sand is required to meet the standard for a highway sub-grade material, which increases substantially the volume of the modified soil and the cost. Quicklime evidently decreases the water content and plasticity of the modified soil, and improved significantly its mechanical behavior. When the amount of quicklime and cement are equal, cement modified soil has larger CBR strength than that of quicklime modified soil. Test results also indicate that less amount of cement is required to meet the highway standard than that of using quicklime.

INTRODUCTION

Large amounts of waste materials are dredged from harbor construction and hydraulic projects in China. In general these dredged materials (DM) are very soft soils which have very low shear strength ($c_u < 50$ kPa) and the natural water contents are higher than their liquid limits, thus they are usually treated as waste. Ocean and land methods are

commonly used to dispose of these wastes (Zhu et al., 2007). It is reported that in recent years over 100 million m^3 of DM were disposed annually into the ocean in China (Zhang et al., 2004), it is especially serious in eastern China, for example, more than 20 million m^3 of DM were dredged from Tai-hu lake in the past few years. On the other hand, there is a huge demand for fill material for embankment and highway construction projects. The utilization of DM for beneficial uses such as fill may be considered as an environmental friendly and economical option (Zhu et al., 2008; Huang et al., 2009).

To achieve this goal, admixtures are added to the DM to modify their mechanical and physical properties. Past studies have been attempted to modify DM as the fill materials, for example, Satoh et al. (2005) used the blast furnace slag cement and quicklime as additives to modify the DM as the embankment fill; Kamali et al. (2008), Rachid et al. (2008) and Dubois et al. (2009) combined several treatment technologies to modify a DM from Dunkirk harbor to a highway sub-grade soil, which included flocculation of the sediment, initial dehydration by mechanical compression, further dehydration by adding quicklime and a thermal treatment at 40℃, aggregation by adding sand and cement and compaction of the modified soil to the target density. However, the construction cost is expensive.

Chinese specifications for design of highway sub-grade soils (JTG D30-2004, 2004), a fine grained soil shall not be used as an embankment soil if its liquid limit and plasticity index are above 50% and 26, respectively. Moreover, the minimum CBR strength of sub-grade soil for expressway and first class highway should not less than 3%, and for low-grade highway (second class, third class and fourth class highway) the CBR value should not less than 2%. In order to decrease plasticity index and enhance CBR Strength of DM, dry fine sand, quicklime and Ordinary Portland cement are added into DM separately, properties of each modified soil are studied to check for the requirements for highway sub-grade soil.

EXPERIMENTAL STUDIES

In this study, the DM was a lake sediment taken in Gong-hu bay of Tai-hu lake, Jiangsu province of China. The basic physical properties of the DM were evaluated in accordance with the procedures given in GB/T 50123-1999 (Ministry of Construction P.R. China, 1999) and are summarized in Table 1. According to the Unified Soil Classification System (USCS), the DM is classified as clay of high plasticity (CH). Three additives were used in the study: (i) type I is a fine sand, with grain sizes vary between 0.05 mm and 1 mm; (ii) type II is a quicklime, which has CaO content above 98%; and (iii) type III is Ordinary Portland cement (OPC). For a unit volume of DM, six different fine sand contents (500, 1000, 2000, 3000, 4000 and 5000kg/m^3) were used, four different contents (100, 150, 200 and 250kg/m^3) were used for quicklime, and four different contents were used for cement (50, 75, 100 and 150kg/m^3).

The specimens were prepared by mixing slurries of the DM with each type of additives by a drum mixer machine for about 10 minutes. For DM modified by fine sand, the Atterberg limits were measured immediately after mixing, then compacted and tested for CBR strengths. For DM modified by quicklime and cement, the specimens were covered by plastic sheets and put inside an environmental chamber for curing where the ambient temperature and relative humidity were maintained at 20±2℃ and higher than 90%, respectively. After curing the specimens for the target days,

Atterberg limits, compaction and CBR tests were conducted. For DM modified by quicklime, the curing periods are 1, 3, 7, 14 and 28 days; and for DM modified by cement, the curing periods are 7, 14 28 and 56 days. All tests were conducted according to GB/T 50123-1999.

Table. 1 Basic Physical Properties of Dredged Material (DM)

Water content (%)	Liquid limit (%)	Plastic limit (%)	Plasticity index	Specific gravity	Bulk unit weight (kN/m^3)	clay content (%)
65.8	53.8	22.7	31.1	2.65	16.4	23%

RESULTS AND DISSCUSSION

DM treated by fine sand

Figs. 1 and 2 show the variation of Atterberg limits and CBR strength with sand content, respectively. Where, w is the water content, w_L is the liquid limit, w_P is the plastic limit, and I_P is the plasticity index. It can be seen those w, w_L, w_P and I_P all decrease with increasing sand content but the CBR value increases with increasing sand content. For a sand content of 5000 kg/m^3, the plasticity index reduces to 9.6 and the CBR value reaches 2.63%. Both values meet the standard for low-grade highway. Although sand greatly increases the workability of the modified DM, a substantial volume increase is inevitable.

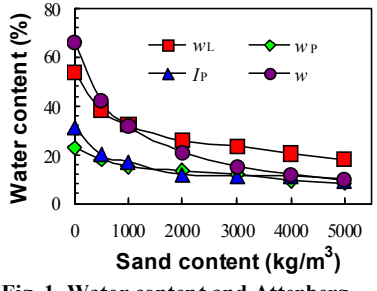

Fig. 1. Water content and Atterberg limits of sand modified DM

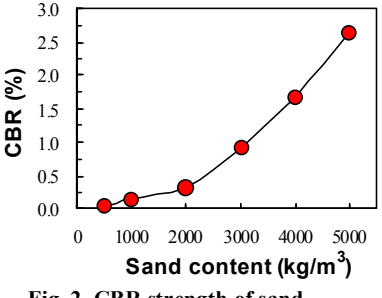

Fig. 2. CBR strength of sand modified DM

DM treated by quicklime

Test results show water content and Atterberg limits major change within the initial 7 days, and basically no more change after 28days for quicklime modified DM. Fig.3 shows the Atterberg limits change with quicklime content with the curing periods of 28days. It can be seen quicklime have great decrease effect on plasticity index and increase workability accordingly. Figure 4 shows the effect of different quicklime content on CBR strength, when the content is 250 kg/m3 and curing time is 28 days, the plasticity index decrease to 18.4, and the CBR strength increase to 2.01%, which exactly meet the specifications for low-grade highway sub-grade.

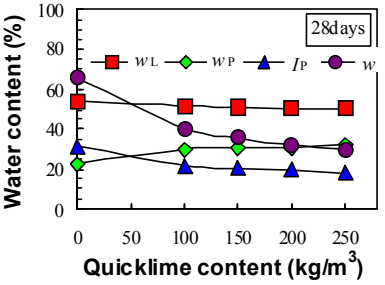

Fig. 3. Water content and Atterberg limits of quicklime modified DM

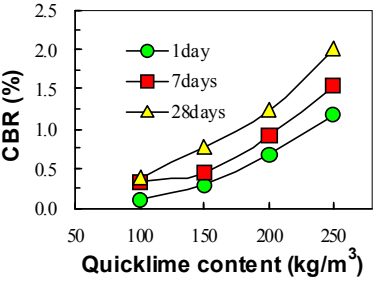

Fig. 4. CBR strength of quicklime modified DM

DM treated by cement

Fig.5 shows the Atterberg limits change with cement content for curing periods of 28days. Water content is seen to decrease with increasing cement content, but the effect is not as significant as that of the quicklime. However, the plasticity index decreases significantly with increasing cement content and the effect is better than that of quicklime. Fig. 6 shows that the CBR strength increases with increasing cement content. For a cement content of 150 kg/m^3 and curing time of 28 days, the plasticity index and CBR strength of the cement modified DM are 14 and 2.34%, respectively, which meet the requirements for the highway sub-grade material.

Figs. 4 and 6 show that for an additive content of 100 kg/m^3 and a curing time of 28days, the CBR strength of quicklime and cement modified DM are 0.4% and 1.03%, respectively. Moreover, the CBR value of quicklime and cement modified DM increase to 0.77% and 2.34%, respectively, when the additive content increases to 150 kg/m^3. For the same additive content, cement modified DM has much greater CBR strength than that of quicklime modified DM. In order to meet the CBR strength standard of 2% for low-grade sub-grade material, the required cement content is 150 kg/m^3 but the required quicklime content should be at least 250 kg/m^3. Such differences may be due to the different modification mechanisms between quicklime and cement. The former mainly depends on reduction of water content, cation exchange and carbonation reaction (Bell, 1996), while the latter depends more on bonding mechanism of the resultant hydration products such as calcium silicate hydrates (C-S-H), which form a firm framework that can resist external forces (Zhu et al., 2007).

In order to meet the minimum CBR strength specifications of 2% for highway sub-grade material, the required sand content, quicklime content and cement content are at least 5000 kg/m^3, 250 kg/m^3 and 150 kg/m^3,respectively. At present, the prices for sand, quicklime and cement are 40¥, 200¥ and 280¥ per ton, respectively, so the modified additives cost will be 200¥ for sand, 50¥ for quicklime and 42¥ for cement, thus the cement modified DM has a smaller cost relatively in the research.

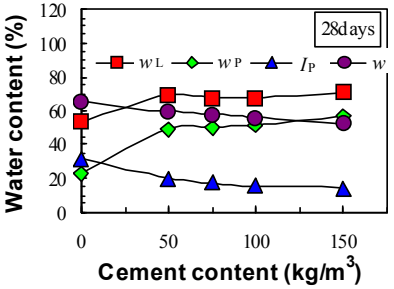

Fig. 5. Water content and Atterberg limits of cement modified DM

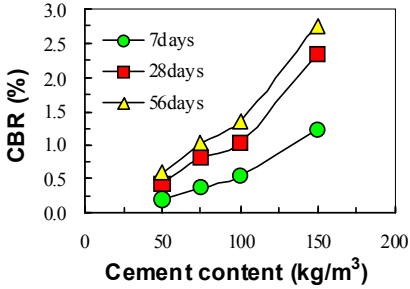

Fig. 6. CBR strength of cement modified DM

CONCLUSIONS

Three additives (fine sand, quicklime and cement) were used to modify the physical and mechanical properties of a dredged material (DM) so that it may be used as a highway sub-grade material. Test results show that fine sand decreases greatly the plasticity of DM, and increases the workability. However, a great amount of sand is required, which increases substantially the volume of the modified soil and it is considered unfavorable. Both quicklime and cement can evidently decrease the water content and plasticity of the modified soil, and improved significantly its mechanical behavior. For the same additive content and curing days, the cement modified soil has larger CBR strength and smaller plasticity index than those of the quicklime modified soil. Test results also show that less amount of cement is required to meet the highway standard for sub-grade material than that of quicklime.

ACKNOWLEDGMENTS

This study is jointly sponsored by the Hi-Tech Research and Development Program of China (863 program) through Grant No.2007AA11Z135, the State Oceanic Administration of China through Grant No.200701045 and the Fund of Technology Innovation of Graduate Student, Jiang'su Province through Grant No. CX08B-102Z. The paper was completed under help of Doctor Abraham C.F. Chiu in the Geotechnical Research Institute, Hohai University. Their support is gratefully acknowledged.

REFERENCES

Bell, F.G. (1996). "Lime stabilization of clay minerals and soils". *Engineering Geology*, Vol.42:223-237.

Dubois, V., Abriak, N.E., Zentar, R. (2009). "The use of marine sediments as a pavement base material". *Waste Management* , Vol. 29(2):774-782.

Huang, Y.H., Zhu W., Zhang, C.L., Wang, S.C. (2009). "Mechanical characteristics and strength source of remolded solidified dredged materials". *Rock and Soil Mechanics*, Vol. 30(5): 1352-1356 (in Chinese).

Kamali, S., Bernard, F., Abriak, N. E. (2008). "Marine dredged sediments as new materials resource for road construction". *waste management*, Vol. 28(5):919-928.

Ministry of Construction P.R. China. (1999). "Standard for soil test method." *GB/T 50123-1999*, Beijing (in Chinese).

Ministry of Transport P.R. China. (2004). "specifications for design of highway subgrades". *JTG D30-2004*, Beijing (in Chinese).

Rachid, Z., Vincent, D., Nor, E. A. (2008). "Mechanical behavior and environmental impacts of a test road built with marine dredged sediments". *Resources, Conservation and Recycling*, Vol.52(6):947-954.

Satoh, A., Nishimoto, S., Suzuki, T. (2005). "Strength characteristics of crushed solidified soil". *The 2nd Japan-China Joint Symposium on Geotechnical Engineering.*

Zhang, H.Q., Xie, J., Zhu, W., Huang, Y.Z. and Shi, P. (2004). "Present situation of dredged materials dumping and the study of transforming dredged mud into regenerative resources – difficulties of refuses dumping in China seas and countermeasures to deal with these problems." *Marine Science Bulletin*, Vol. 23(6): 54-60 (in Chinese).

Zhu W., Huang, Y.H., Zhang, C.L., Liu, Q. S. (2008). "Effect of curing time on mechanical behavior of crushed solidified dredged material". *Characterization, Monitoring, and Modeling of Geosystems* (GSP179), ASCE, 179: 597-604.

Zhu, W., Zhang, C. L., Chiu, C.F. (2007). "Soil-water transfer mechanism for solidified dredged materials". *Journal of Geotechnical and Geoenvironmental Engineering*, Vol. 133(5):588-598.

Air-Soil Relationships for Lime and Cement Stabilized Sub-grades

John L. Daniels[1] M.ASCE, Shaogang Lei[2], Zhengfu Bian[3], Benjamin F. Bowers[4]

[1]Associate Professor, Department of Civil and Environmental Engineering, University of North Carolina at Charlotte, Charlotte, NC 28223, USA, jodaniel@uncc.edu
[2]Associate Professor, China University of Mining and Technology, Xuzhou, China
[3]Professor and Director of Graduate Programs, China University of Mining and Technology, Xuzhou, China
[4]Graduate Student, Department of Civil and Environmental Engineering, University of North Carolina at Charlotte, Charlotte, NC 28223, USA, bfbowers@uncc.edu

ABSTRACT: Temporal and spatial relationships between air and soil temperature are relevant to many applications in geotechnical and geo-environmental engineering. However, such data are not often available for a given site-specific project, so it remains attractive to develop practical models that do not require extensive and esoteric parameters. The impetus for the work presented herein is the common use of lime and cement to stabilize soils in road construction. While these additives have been used successfully to increase shear strength and reduce moisture susceptibility, their performance is temperature dependent. This manuscript presents soil temperature data for lime and cement-stabilized sub-grades from four sites. In general, each site was instrumented for air temperature, sub-grade temperature and moisture content. For the soils tested, estimated thermal diffusivity values range between 5.7×10^{-7} and 7.8×10^{-7} m^2/s. These results are incorporated into a sinusoidal approximation of diurnal temperature fluctuations for purposes of preliminary modeling. Limitations in this approach are discussed, along with recommendations for model refinement. This work is part of a larger effort to predict subsurface temperatures and the corresponding strength of lime or cement stabilized sub-grades with little more than a standard weather forecast.

INTRODUCTION

Thermal properties of soils are relevant in agricultural, geotechnical and geo-environmental engineering, as well as in solar and geothermal energy applications (Farouki Mihalakakou 2002, Parton 1982, Ghuman et al. 1981, Tessy et al. 2002, Zheng et al. 1993). However, such data are not often available for a given site-specific project, so the notion of developing tractable models which relate soil temperature to another parameter more easily measured, e.g. air temperature, remains attractive. Motivation for

the work presented herein derives from the frequent use of lime and cement to stabilize soils in road construction. While these additives have been used successfully to increase shear strength and reduce moisture susceptibility, they are limited by their temperature sensitivity. Consequently, road construction which requires these additives is impeded or stopped altogether during cold weather conditions, often on the basis of air temperature alone (Daniels and Janardhanam 2007, Daniels et al. 2009). In this scenario, the interest lies in predicting the temperature in the stabilized soil on an hourly basis for approximately one week. As part of a larger project evaluating the influence of temperature on lime and cement stabilized soil, sub-grade temperature data were collected from various sites across North Carolina. The objective of this paper is to present some of this data in conjunction with a modeling approach that predicts soil temperature on the basis of air temperature and other accessible parameters.

MATERIALS AND METHODS

Four sites were instrumented primarily for air and sub-grade temperature, as identified in Table 1. Air temperatures were generally recorded with two sensors. The first was an EchoTemp sensor from Decagon Devices, Inc. This sensor has a range of -40^{o}C to +60^{o}C and is accurate to ± 0.25^{o}C at temperatures above 0^{o}C, and ± 1^{o}C below 0^{o}C. The temperature sensor was outfitted with a radiation shield to mitigate the effects of localized radiated and reflected heat. The EchoTemp sensor was connected to an EM5 datalogger, also from Decagon Devices and data were recorded every 30 minutes. A second temperature sensor for measuring air temperatures was an intelliRock temperature sensor from Engius, LLC. This sensor has a range from -50^{o}C to +85^{o}C and is accurate to ± 1^{o}C. Data were recorded every 60 minutes by the datalogger which is part of the sensor itself. The intelliRock sensors were also used to measure sub-grade temperatures, and three sensors were placed at different depths (ranging from ~50-200 mm below the surface) for each site. The intelliRock sensors appear as cylindrical rubber stoppers with wires emanating from the top. They have a diameter of about 1 inch and a length of 1.75 inches. For sub-grade placement, a hole was drilled to the desired depth, and the sensors were tapped into place with a hammer and then soil was backfilled and compacted over top of the sensor. The lead wires were then extended, labeled and placed out from roadway to a median or shoulder. Measurements were recorded for approximately two weeks during in the fall of 2006. The overall process is shown in Figure 1.

RESULTS AND ANALYSIS

A summary of the average, maximum and minimum temperatures, as well as the daily average variation (i.e., amplitude) in temperature is provided by Table 2. Although each of the four sites experienced different thermal regimes, the above data can be used to determine material specific values, including thermal diffusivity and thermal conductivity. This information is in turn useful when developing a predictive relationship. In particular, the following equations may be used to determine thermal diffusivity (Andersland and Ladanyi 2004):

Table 1. Field Instrumentation Locations and Details

Parameter	Location			
	U.S. 70, near Clayton, NC	**U.S. 421, near Siler City, NC**	**I-40, near Greensboro, NC**	**I-485, near Charlotte, NC**
AASHTO Soil Type	A-7-5	A-7-5	A-7-6	A-4
Type of Stabilization	Lime Slurry	Lime Slurry	Cement	Cement
Rate of Application	13 kg/m^2 (hydrated lime) 6.5 kg/m^2 (quicklime)	14 kg/m^2 (hydrated lime)	8%, by dry weight	8%, by dry weight
Depth of Stabilization (mm)	200	200	305	180
Optimum Moisture Content (%)	26	28	18	16
Maximum Dry Density (kN/m^3)	15	15	18	18
Sub-grade Temperature Measurement Depths (mm)	45, 95, 185	45, 70, 110	45, 210	45, 95, 160

FIG. 1. Individual temperature sensor installation (left) and overall array (right)

Table 2. Summary Temperature Data

Site Description and Location	Depth (mm)	Temperature (^{o}C)			
		Average	Max	Min	Average Amplitude
U.S. 70, near Clayton, NC	0	16.14	32.58	-0.14	7.50
	45	19.64	32.00	8.00	4.94
	95	19.73	29.00	11.00	3.33
	185	20.26	26.00	14.00	2.06
U.S. 421, near Siler City, NC	0	14.77	27.62	-0.22	6.50
	45	16.41	30.00	6.00	4.83
	70	16.64	28.00	7.00	3.89
	110	16.87	25.00	9.00	2.72
I-40, near Greensboro, NC	0	10.54	24.10	-1.36	6.67
	45	13.83	28.00	3.00	7.17
	210	10.91	16.00	6.00	1.89
I-485, near Charlotte, NC	0	5.34	24.32	-8.50	7.44
	45	10.06	23.00	-1.00	5.50
	95	10.97	21.00	2.00	3.06
	160	11.56	20.00	4.00	2.11

$$\alpha = \frac{p}{4\pi}\left(\frac{z_2 - z_1}{t_2 - t_1}\right)^2 \quad (1)$$

Or:

$$\alpha = \frac{p}{\pi}\left(\frac{z_2 - z_1}{\ln\left(\frac{A_{z1}}{A_{z2}}\right)}\right)^2 \quad (2)$$

In Eq. (1) and (2), α= thermal diffusivity, which is defined as $k / c\rho$, where k = thermal conductivity, c = volumetric heat capacity, ρ = material density, p = period (e.g., 24 hours), z_1, z_2 = depth at location 1, 2, t_1, t_2 = time lag at location 1, 2 and A_{z1}, A_{z2} = temperature amplitude at location 1, 2. Note that thermal conductivity values find greater use when considering steady-state heat transfer. In this case, where there is diurnal heating and cooling, thermal diffusivity is of more practical utility. Collection of temperature data with time and depth allows for thermal diffusivity to be calculated by either equation. For example, Fig. 2 illustrates how the amplitude may be obtained for various depths to solve Eq. 2.

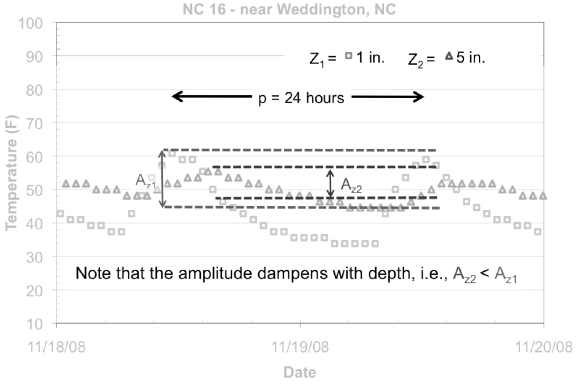

FIG. 2. Use of temperature data for calculating thermal diffusivity.

Thermal diffusivity values were obtained for each of the four sites by the method shown in Fig. 2 (use of Eq. 2), because temperature amplitudes (A_{z1}, A_{z2}) are more readily and accurately available from the collected data. The amplitude at a given depth (z_1, z_2) is calculated by averaging hourly data over a 24 hour period to compute mean, maximum and minimum values. The positive amplitude is taken as the maximum temperature minus the mean, while the negative amplitude is taken as the mean minus the minimum temperature. Note that in Fig. 2, only the bottom amplitude is highlighted for clarity. Overall daily amplitude is then computed as the average of these two values. This calculation is repeated for as much of the data as available for a given site, and then all of these daily amplitude values are averaged to compute an overall value for the site. Note that determination of thermal diffusivity via Eq. 2 requires two amplitude values, while the collected data, in general, provide several amplitude values, i.e., temperature measurements were made at the surface and then at three different levels of depth. Therefore, the thermal diffusivity can be calculated on the basis of the following six combinations: Air – Depth 1, Air – Depth 2, Air – Depth 3, Depth 1 – Depth 2, Depth 1 – Depth 3 and Depth 2 – Depth 3. The results for these values along with comparative values for Air, Water, Granite, and Iron are given as Table 3.

Table 3. Comparison of Calculated Thermal Diffusivity Values for Each Site, along with Standard Materials for Reference

Thermal Diffusivity, m^2/s							
U.S. 70	U.S. 421	I 40	I 485	Air*	Water*	Granite*	Iron*
7.34E-07	5.68E-07	7.81E-07	6.07E-07	2.10E-08	1.40E-07	1.50E-06	1.73E-05

*For comparison, as summarized in Andersland and Ladanyi (2004)

Having obtained site-specific values of thermal diffusivity, the following equation can be used to predict the temperature as a function of time or depth:

$$T_{z,t} = T_m + A_s \exp\left(-z\sqrt{\frac{\pi}{\alpha p}}\right)\sin\left(\frac{2\pi t}{p} - z\sqrt{\frac{\pi}{\alpha p}}\right) \quad (3)$$

In Eq. (3), $T_{z,t}$ = temperature as a function of specified time (t) and depth (z), T_m = average air temperature, and A_s = surface temperature amplitude. The above equation presumes a sinusoidal change in air/surface temperature whereby the minimum occurs at time t=0, or for our period of 24 hours, at 12:00 AM. However, the lowest air temperatures typically occur just before dawn. Refinements that address this issue and others with Eq. 3 are described in more detail in Lei et al. (2009).

CONCLUSIONS

Thermal diffusivity values may be derived from soil temperature data collected at various depths. For the lime and cement-stabilized sub-grade soils investigated herein, values of thermal diffusivity ranged between 5.7×10^{-7} and 7.8×10^{-7} m^2/s. These results can be incorporated into a sinusoidal approximation of diurnal temperature fluctuations for purposes of relating air and subsurface temperatures. Knowledge of thermal diffusivity enables one to estimate subsurface temperatures as demonstrated by Lei et al. (2009). Such estimates can be used to evaluate whether in situ curing conditions will assure sufficient strength gain for lime or cement-stabilized sub-grade (Daniels and Janardhanam 2009).

REFERENCES

Andersland, O.B. and Ladanyi, B. (2004). *Frozen Ground Engineering*, The American Society of Civil Engineers and John Wiley and Sons, New York, 363 p.

Daniels, J.L. and Janardhanam, R. (2007). "Cold-weather sub-grade stabilization" *Soil Improvement* (GSP 172), ASCE, Reston/VA: 1-10.

Daniels, J.L., Janardhanam, R., Starnes, J., DeBlasis, N. and Miles, K (2009). "Cold-weather concreting technology for ground modification" *Contemporary topics in ground modification, problem soils, and geo-support* (GSP 187), ASCE, Reston/VA 273-280.

Farouki, O. T. (1986) *Thermal Properties of Soils*, Series on Rock and Soil Mechanics, Vol. 11, Trans Tech Publications, Switzerland.

Ghuman B.S.and LAL R. (1981). Predicting Diurnal Temperature Regime of a Tropical Soil. *Soil Science* Vol. 132, 247-252

Lei, S., Daniels, J.L., Bian, Z and Janardhanam, R. (2009) "Practical Soil Temperature Modeling" *Environmental Earth Sciences* (in review)

Mihalakakou G. (2002), On estimating soil surface temperature profiles. *Energy and Buildings* Vol. 34, 251-259.

Parton, W. J. (1984). Predicting soil temperatures in a short grass steppe. *Soil Science* Vol. 138, 93-101.

Tessy Chacko P and G Renuka(2002). Temperature mapping, thermal diffusivity and subsoil heat flux at Kariavattom of Kerala.Proc. *Indian Acad. Sci.* Vol. 111, 79-85.

Zheng Daolan, E. Raymond Hunt Jr, Steven W. Running (1993). A daily soil temperature model based on air temperature and precipitation for continental applications. *Climate Research* Vol. 2, 183-191.

Stiffness and Strength Based In-Place Evaluation of Compacted Unbound Materials

Suppakorn Wachiraporn [1], Auckpath Sawangsuriya [2], Ph.D.,
Jutha Sunitsakul [3], Ph.D., and Wilailak Sramoon [4], D.Eng.

[1]Graduate student, Department of Civil Engineering, Mahanakorn University of Technology; Thailand, wachiraporn08@gmail.com
[2,3]Researcher, Bureau of Road Research and Development, Department of Highways, Thailand; sawangsuriya@gmail.com, sjutha@gmail.com
[4]Asistant Professor, Department of Civil Engineering, Mahanakorn University of Technology, Thailand; swilaila@mut.ac.th

ABSTRACT: Several non-nuclear and portable tools for structural properties assessment of pavement materials have been currently introduced to the market. They are capable of directly measure in-place stiffness and strength of compacted pavement materials, which are the fundamental properties for mechanistic design and performance evaluation of the pavement system. This paper presents stiffness and strength based methods for rapid in-place monitoring compaction quality control during highway construction in Thailand. Results indicated that these methods exhibited good potential for construction quality control as well as the development of performance-based specifications in Thailand.

INTRODUCTION

Long-term structural performance of the highway pavement depends on the structural properties of the pavement materials and sub-grade stability. Quality control monitoring and structural evaluation during highway construction play an important role to assure that the quality of compaction and the material used. Typical earthwork compaction acceptance criteria are currently based on the specified target dry density of the placed earthen materials achieved through appropriate moisture content (i.e., 95% of maximum dry density and near the optimum moisture content according to the Department of Highways (DOH), Thailand construction specification).

The DOH has adopted the sand-cone method for a statistical evaluation of compaction quality for several decades. However, such method is generally time consuming, labor intensive, less cost-effective, and considered destructive. A simple, rapid, and direct structural property testing in conjunction with moisture-density testing which can be conducted independently and safely by the inspector without interference with the construction process is anticipated to increase test coverage, to improve statistical basis of evaluation, and to reduce variability.

A number of innovative tools for in-place assessment of structural properties and quantitative evaluations of construction practices and materials are currently available in the geotechnical and pavement engineering communities. They include Light Weight Deflectometer (LWD), Portable Falling Weight Deflectometer (PFWD), Soil Stiffness Gauge (SSG), Briaud Compaction Device (BCD), Dynamic Cone Penetrometer (DCP), Soil Density Gauge (SDG) and others can provide in-place stiffness, strength, density, and moisture assessment of pavement materials and are therefore considered as alternative means for Thailand highway construction quality control in the near future (Sawangsuriya et al., 2009, Taesiri et al., 2009).

The study presents stiffness and strength based methods for rapid in-place monitoring compaction quality control during highway construction in Thailand. The Soil Stiffness Gauge (SSG) and the Dynamic Cone Penetrometer (DCP) were selected in this study for direct assessment of stiffness and strength of compacted unbound materials, respectively. These tools are portable, simple to use, absolutely safe for operator, and provide rapid measurement without interference with construction process.

SOIL STIFFNESS GAUGE AND DYNAMIC CONE PENETROMETER

Soil Stiffness Gauge (SSG), which is currently marketed as the Humboldt GeoGauge™ (Fig. 1a), is a portable, non-nuclear testing device that provides simple and non-destructive means of directly and rapidly measuring in-place soil stiffness. The SSG weighs about 11.4 kg, is 28 cm in diameter, 25.4 cm in height, and rests on the soil surface via a ring-shaped foot. The SSG measures near-surface stiffness by imparting small dynamic force to the soil though a ring-shaped foot at 25 steady state frequencies between 100 and 196 Hz. Based upon the force and displacement-time history, stiffness is calculated internally as the average force per unit displacement over the measured frequencies and reported. A measurement takes only about 1.5 minutes. The measured soil stiffness from the SSG can be used to calculate the elastic modulus of the materials at near surface (Sawangsuriya and Edil, 2005).

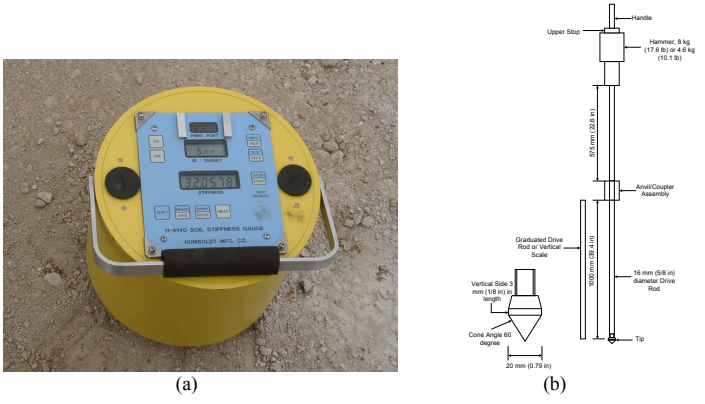

(a) (b)

FIG. 1. Soil Stiffness Gauge (a) and Dynamic Cone Penetrometer (b)

Dynamic Cone Penetrometer (DCP) (Fig. 1b) is simple, rugged, economical, and able to provide a rapid in-place index of strength of pavement structure. The DCP is used for measuring the material resistance to penetration while the cone of the device is being driven into the pavement structure. The number of blows during operation is recorded with depth of penetration. The slope of the relationship between number of blows and depth of penetration (in millimeters per blow) at a given linear depth segment is recorded as DCP penetration index (DPI), which can be correlated with California Bearing Ratio or CBR (Sawangsuriya and Edil, 2005).

MATERIAL AND FIELD TESTING PROGRAM

The field test was conducted at a highway construction site, HWY No. 3011: Ban Rai – Ban Tai section, which is located in Uthaithani, Thailand. This highway was constructed using the conventional pavement structure, which consisted of 10-cm hot mixed asphalt, 20-cm crushed rock base, and 20-cm soil-aggregate sub-base over the compacted sub-grade. Tests were performed on three types of unbound materials including: (1) sub-grade, (2) soil-aggregate sub-base, and (3) crushed rock base. The properties of these materials are summarized in Table 1.

Table 1. Properties of Unbound Materials

Properties	Sub-grade	Soil-Aggregate Sub-base	Crushed Rock Base
AASHTO Classification	A-7-5	A-2-6	A-2-4
% Passing			
50.0 (2")	100	93.07	100
25.0 (1")	95.77	71.95	100
19.0 (3/4")	-	65.78	86.20
9.5 (3/8")	88.25	-	65.46
#4	85.16	27.45	52.41
#10	78.63	20.37	34.50
#40	54.48	-	14.25
#200	41.27	8.99	9.84
D_{10} (mm)	$4.5x10^{-4}$	0.1	0.1
D_{30} (mm)	$1.5x10^{-3}$	5.1	1.6
D_{60} (mm)	0.63	10.6	7.0
LL (%)	41	27	19
PI (%)	14	19	9
O.M.C. (%)	13.2	8.5	6.8
$\gamma_{dry,\ max}$ (t/m^3)	1.9	2.1	2.4
Specific Gravity	2.65	2.68	2.77
Soaked CBR (%)	18	42	68
Unsoaked CBR (%)	56	56	74
Swell (%)	6.6	0	0.3

During the compaction, material from the stockpile was first spread out by a motor

grader. Loose layer thickness of 170-180 mm was compacted to the compacted layer thickness of 150 mm. Fig. 2 illustrates a typical layout of field test section. The test section had a total length of about 30-40 m with less than 2.5 m width. Two compaction plants of different capacities were used for the study. These included a vibratory roller and a pneumatic tire roller. The vibratory roller consisted of a single drum vibratory roller of 11,050 kg (operating weight) and 11,400 kg – 23,000 kg (centrifugal forces) capacity. The pneumatic tire roller has the capacity of 14,000 kg. The compaction plants were driven slowly forward to the end of the section and then reversed along the same track. This forward and backward movement along the same path constituting two passes was counted for one pass in this study. A water tanker was used to moisten the material when necessary.

After the compaction procedure, the SSG, DCP, and nuclear gauge (NG) were conducted instantaneously at five test locations for each material type as shown in Fig. 2. At most five SSG measurements were made first, followed by two NG measurements and a single DCP measurement, respectively per one test location. Every measurement was made at the adjacent location. In addition to these tests, three field CBR tests were performed on each material type.

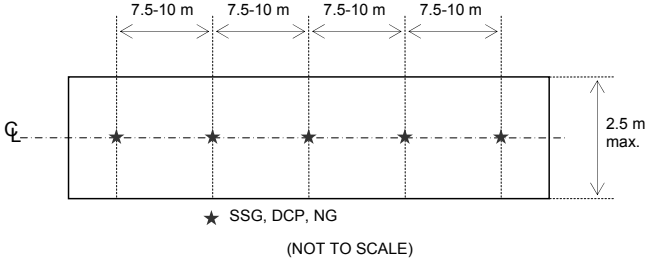

FIG. 2. Layout of field test section.

RESULTS AND DISCUSSION

Results from field testing on three unbound materials are shown in Figs. 3 to 5. The SSG stiffness (K_{SSG}) of all unbound materials tended to increase with the number of passes (i.e., compaction effort).The sub-grade exhibited the highest $K_{SSG,}$ while both soil-aggregate sub-base and crushed rock base had comparable $K_{SSG.}$ K_{SSG} seemed to be very sensitive to the contact surface of the SSG footing and thus the test materials. On the other hand, the DCP penetration index (DPI) value of all three unbound materials decreased with an increase in the number of passes (i.e., soil becomes stronger). The spatial variation in DPI value also reduced drastically as the number of passes increased. Note that the penetrations achieved after 2 and 5 blows were selected to obtain the DPI values in this study. Higher DPI indicated lower shear strength. Unlike K_{SSG}, the DCP test indicated that the sub-grade had lowest strength (i.e., highest DPI). The DPIs of soil-aggregate sub-base are comparable to those of crushed rock base. Note also that less DPI variation was observed for the crushed rock base for a given number of pass.

The dry unit weight and the associated relative compaction of the sub-grade remained

almost constant as the number of passes increased. This might be due to the applied compaction process and the initial moisture condition. The dry unit weight and the associated relative compaction of the soil-aggregate sub-base and the crushed rock base gradually increased with the number of passes as shown in Figs. 3c, 4c and 5c, respectively.

By plotting the cumulative number of blows against penetration depth (Fig. 6), the DCP can effectively capture the soil structural integrity and the uniformity of layer thickness during the compaction process. The discontinuity within a layer thickness can be identified when the slope of the plot (a ratio between the cumulative number of blows and penetration depth) deviates. For instance, the discontinuity within the layer thickness of sub-grade was observed at depths ranging between 60 and 90 mm. As the number of passes increased, the discontinuity within the layer thickness tended to disappear (i.e., soil became stronger) as clearly depicted in Fig. 6.

The average CBR for each material type was determined from the average DPI across the compacted layer thickness (~150 mm) after the final pass was achieved as indicated in Fig. 6 (CBR_{DCP} = 23.5%, 32.1% and 30.3% for sub-grade, soil-aggregate sub-base, and crushed rock base, respectively). The companion field CBR indicated higher average CBR values of 28.9% for sub-grade, 53.3% for soil-aggregate sub-base, and 57% for crushed rock base, respectively, which were however smaller than the laboratory CBR values.

CONCLUSIONS AND RECOMMENDATIONS

This study presents the implementation of the SSG and the DCP for stiffness and strength assessment for quality control during highway construction in Thailand. Both the SSG and the DCP provided simple means for the pavement material and sub-grade property evaluation during the construction phase. The in-place stiffness and strength properties of three unbound materials can be rapidly and directly monitored in companion with the conventional moisture-density control test during highway construction. Due to their rapid and instantaneous measurements, the inspector can increase test coverage, improve statistical evaluation, and reduce compaction variability, thus ensure structural uniformity during the compaction. The DCP is however highly recommended for routine quality control evaluation in Thailand. In addition to the structural integrity, the DCP can assess the uniformity of layer thickness during compaction process.

The quality control criteria for construction specification can be developed by the DCP and conventional moisture-density measurements. Since the DOH, Thailand, typically adopt the CBR for the pavement design and the compaction acceptance criteria based on the 95% of maximum dry density and near the optimum moisture content. Future comprehensive study is underway to establish such quality control criteria and specification. Moreover, further study is necessary to evaluate the CBR values obtained from different test methods and testing conditions.

ACKNOWLEDGEMENTS

The authors would like to express their sincere gratitude to the director of Tak road

construction and training center, project manager, inspectors, and engineers of highway construction site, HWY No. 3011: Ban Rai – Ban Tai section for their cooperation in arranging access to the sites and assistances during the field test.

REFERENCES

Sawangsuriya, A. and Edil, T. B. (2005). "Evaluating stiffness and strength of pavement materials." *Proceedings of the Institution of Civil Engineers-Geotechnical Engineering*, Vol. 158(4): 217-230.

Sawangsuriya, A., Sramoon, W., and Wachiraporn, S. (2009), "Innovative tools for highway construction quality control." *Research and Development Journal of the Engineering Institute of Thailand*, Vol. 20 (3): 36 – 42.

Taesiri, Y., Sawangsuriya, A., Wachiraporn, S., and Sramoon, W. (2009), "Assessment of in-situ tests for stiffness and strength characteristic of pavement materials." *13th REAAA Conference Korea*, Incheon, South Korea (in CD-ROM).

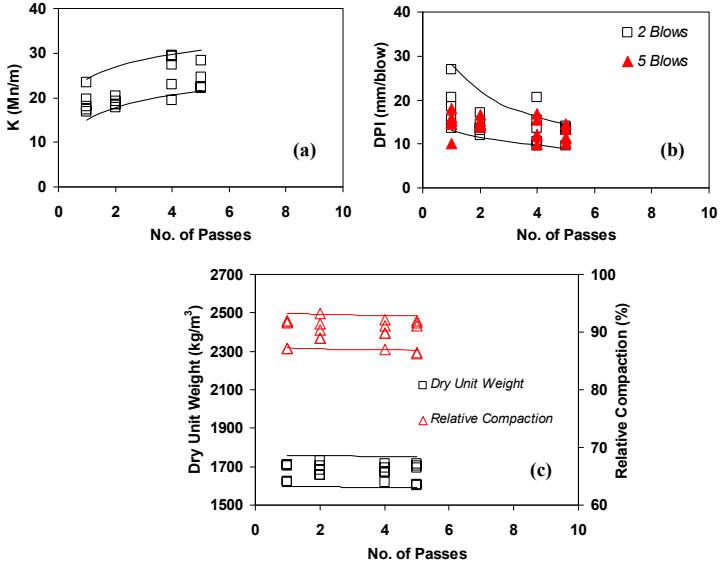

FIG. 3. Stiffness, DPI value, dry unit weight and relative compaction vs. number of passes for sub-grade.

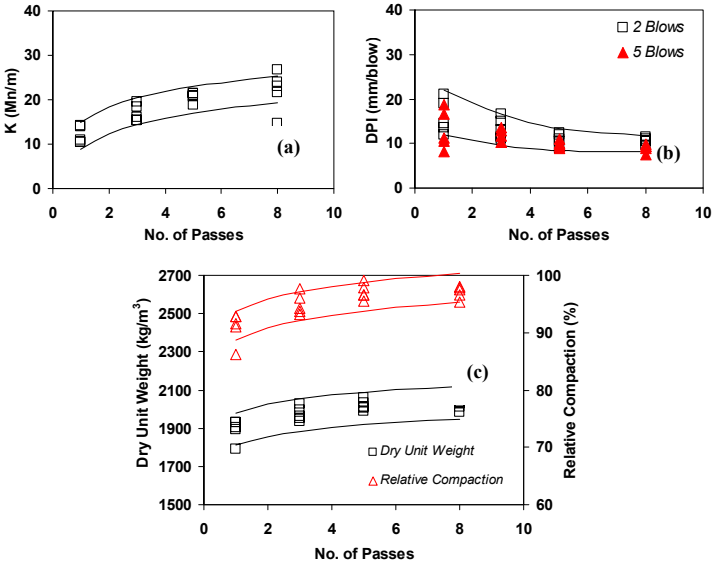

FIG. 4. Stiffness, DPI value, dry unit weight and relative compaction vs. number of passes for soil-aggregate sub-base

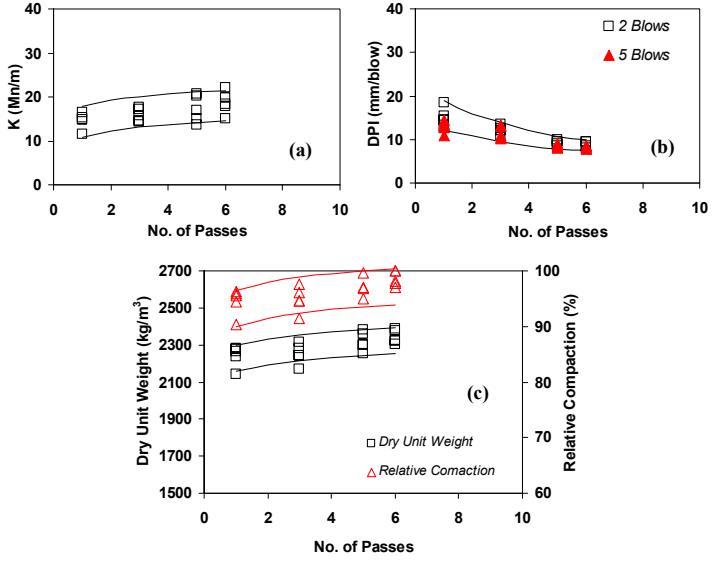

FIG. 5. Stiffness, DPI value, Dry unit weight and relative compaction vs. number of passes for crushed rock base

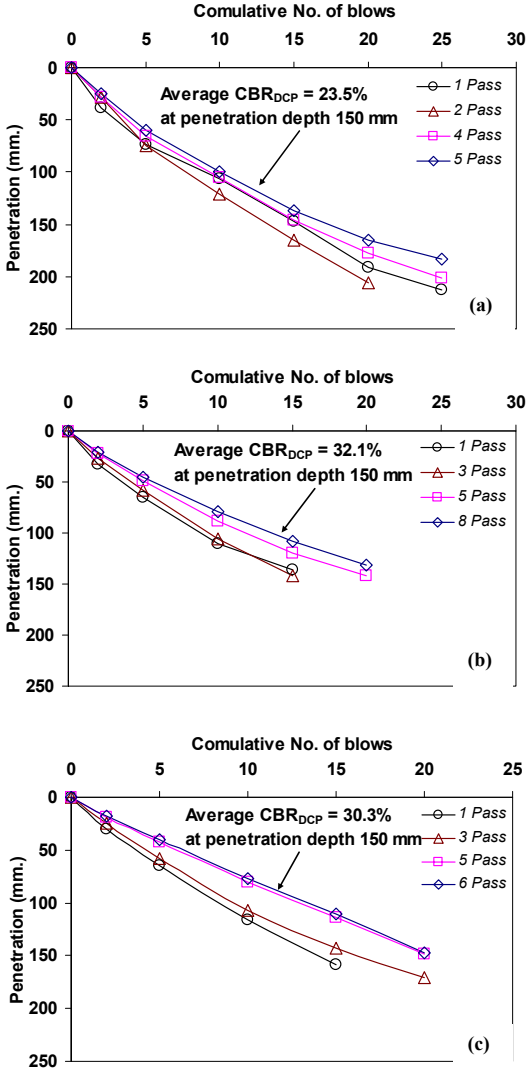

FIG. 6. Cumulative number of blows vs. penetration depth for (a) sub-grade, (b) soil-aggregate sub-base, and (c) crushed rock base under different number of passes

Characterization of Unbound Granular Materials Using Repeated Load CBR and Triaxial Testing

Alemgena Araya[1], Andre Molenaar[2], Lambert Houben[3].

[1]PhD Student, Faculty of Civil Engineering, Delft University of Technology, P.O.Box 5048, 2600 GA, Delft, Netherlands; a.a.araya@tudelft.nl
[2]Professor of Highway Engineering, Faculty of Civil Engineering, Delft University of Technology, P.O.Box 5048, 2600 GA, Delft, Netherlands; a.a.a.molenaar@tudelft.nl
[3]Associate Professor of Highway Engineering, Faculty of Civil Engineering, Delft University of Technology, P.O.Box 5048, 2600 GA, Delft, Netherlands; l.j.m.houben@tudelft.nl

ABSTRACT: Because repeated load triaxial testing is cumbersome and not readily available, especially in developing countries, characterization of unbound granular road base and subbase materials is still done using empirical methods such as California Bearing Ratio (CBR) testing. Although widely applicable and useful, the CBR does not provide information on the mechanical behavior such as the resilient and permanent deformation characteristics of the material. A relatively simple testing technique, a repeated load CBR test, is developed to characterize the mechanical behavior of unbound base and subbase materials, which can be used as an input in mechanistic design analyses. The repeated load CBR test is quite useful to estimate the mechanical behavior of unbound granular materials, especially the resilient modulus. Furthermore, big scale cyclic triaxial tests are carried out to measure the resilient modulus which is then compared with the repeated load CBR results.

INTRODUCTION

A prerequisite for the introduction of mechanistic pavement design procedures is the availability of realistic methods for characterizing the mechanical behavior of unbound materials. Considerable attention has been devoted to this matter since the introduction of the concept of resilient modulus in the mid 1950's (Seed, H. B., Chan, C. K., and Monosmith, C. L., 1955). Most road pavements in developing countries and rural roads in the developed world are commonly paved with thin asphalt layers. In such pavements the base and subbase layers are the main load bearing structures. A realistic characterization method of their mechanical properties can introduce a mechanistic design method in developing countries to develop economic and sustainable road pavements. Cyclic triaxial testing is an ideal method to characterize such mechanical behaviors, however, it is cumbersome and not readily available especially in developing countries. An ongoing PhD project at the Delft University of Technology is

investigating the behavior of six different unbound granular base and subbase materials from different countries, namely a very high quality grade 1 (G1) crushed stone and ferricrete gravel (FC) both from South Africa, weathered basalt (WB) from Ethiopia, two granite gravels from Austria and a recycled mix granulate from the Netherlands. For these materials basic tests such as gradation, Proctor density, apparent relative density, and standard CBR test have been carried out in addition to the repeated load CBR and triaxial testing. The test results for the South African high quality (G1) crushed stone will be presented in this paper. First a brief description of this material will be given followed by a description of the test methods adopted to characterize its mechanical behavior. Then the results of the repeated load CBR and triaxial testing will be summarized and finally short concluding remarks will be presented.

MATERIAL

The South African high quality (G1) base material is a crushed aggregate from Greywacke Hornfels rock. The gradation used lies, as shown in Fig. 1, within the South African standard specification for grade 1 crushed stone base (CEAC - Civil Engineering Advisory Council, 1998). Moreover the standard specifies compaction requirements of minimum 88% of apparent relative density, that is about 106 – 108% modified Proctor density.

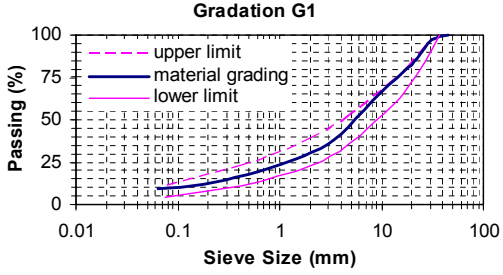

FIG. 1. Gradation of the material and South African specification for grade 1 base materials.

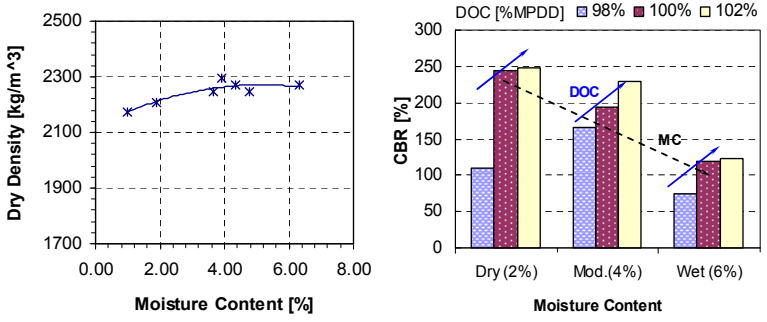

FIG. 2. Moisture-density curve and effect of moisture content and DOC on CBR

TEST METHODS

The moisture - density relation as determined by means of the modified Proctor test and the effect of the moisture content and degree of compaction (DOC) expressed as percentage of the modified Proctor dry density (MPDD), on the CBR value for this material are shown in Fig. 2.

Repeated Load CBR Test

Under loading granular materials experience deformation that is in part elastic (recoverable) and in part plastic (permanent). Upon multiple repetitions of the same magnitude of loading the material comes to a state in which almost all strain under a load application is recoverable. The principle of the repeated load CBR test is similar to the standard CBR test but repeated loads are applied (Fig. 3). First of all the CBR test is performed until a penetration of mostly 2.54 mm (0.1 inch) or a target penetration/load level is reached at a loading rate similar to the standard CBR test (1.27 mm/min = 0.05 inch/min). The force at this deformation is recorded and then unloaded at the same rate to nearly zero, with minimum contact force of about 0.1 MPa. The specimen is re-loaded repetitively to the CBR force until the elastic deformation reaches nearly a constant value. Normally that occurs after 60 - 100 load cycles.

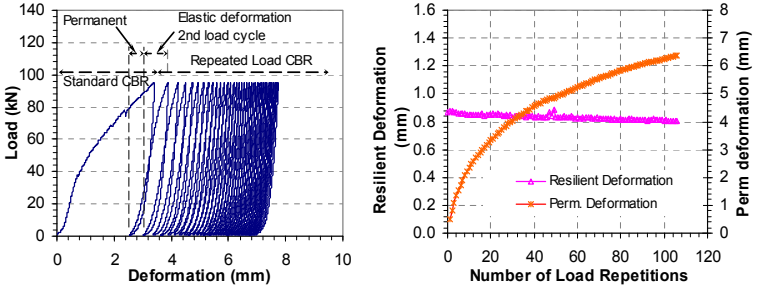

FIG. 3. Load-deformation pattern and deformations in repeated load CBR test

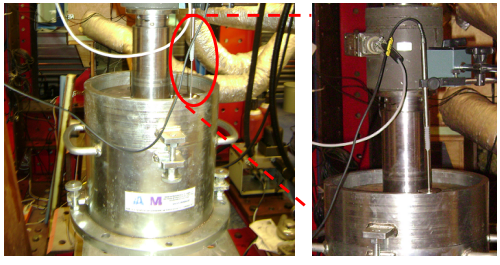

FIG. 4. RL CBR specimen during testing (left), detailed LVDT setup (right)

The elastic deformation during RL CBR testing is measured as the vertical displacement

of the plunger during loading and unloading by an external LVDT (Linear Variable Displacement Transducer) attached to the plunger with a magnetic stand. The displacement is recorded with respect to the top edge of the mould (top surface of the collar) as shown in Fig. 4. The elastic deformation for each cycle is then measured as the difference of the LVDT reading during the maximum loading and the minimum after unloading. For estimation of the modulus the average elastic deformation of the last five loading cycles of the 100 cycles is considered.

The equivalent modulus E_{equ} is computed from the stabilized elastic deformation after 100 cycles. Two methods of computing E_{equ} have been developed by Opiyo (Opiyo, T.O., 1995: Molenaar, A.A.A., 2008: Molenaar, A.A.A., 2007). The first one is an approximate solution with an assumption about how the load is spread over the height of the CBR sample i.e. an estimate has to be made about the angle of load spreading.

The second approach is based on Finite Element analysis results assuming linear elastic behavior of the material in the CBR mould. Both full-friction and no-friction between the material and the mould is assumed. The equations derived from the FE analyses are given below.

Full-friction
$$E_{equ} = \frac{1.375 \cdot (1-\nu^{1.286}) \cdot \sigma_p \cdot a}{w^{1.086}} \quad (1)$$

No-friction
$$E_{equ} = \frac{1.797 \cdot (1-\nu^{0.889}) \cdot \sigma_p \cdot a}{w^{1.098}} \quad (2)$$

Where E_{equ} = Equivalent modulus of the material,
σ_p = stress under the plunger,
a = radius of the circular load (radius of the plunger),
w = elastic deformation measured,
ν = Poisson's ratio of the material,

Granular base and subbase materials with a nominal maximum grain size above 31.5 mm cannot be tested in the standard CBR mould with a diameter of 152.4 mm. As per the standard specifications (ASTM, BS etc), if these materials are to be tested using this mould, all particles with grain size larger than 19 mm should be removed and replaced by material in the 4.75 – 19 mm range. This of course completely changes the characteristics of the material. Therefore, in order to avoid the scaling down of the gradation, a larger standard compaction mould with diameter of 250 mm is used in this project for testing the materials with maximum grain size 45 mm. Accordingly a larger plunger size of 81.5 mm proportional to the diameter of the mould is used instead of the standard plunger 49.5 mm for the repeated load CBR testing of these granular materials.

Resilient Modulus Cyclic Triaxial Test

Unbound granular materials exhibit a highly stress dependent mechanical behavior. To determine this stress dependent behavior a specimen has to be subjected to a large number of different vertical and confining stresses in cyclic triaxial testing and the resulting deformations should be measured (Van Niekerk, A.A., 2002). A triaxial setup with a diameter of 300 mm and a height of 600 mm was used in the study for testing the full 0/45 mm coarse material. The triaxial apparatus is equipped with a hydraulic

loading system actuator and MTS controller capable of cycling the axial stress and with a constant confining pressure (CCP) by partial vacuum. The test is carried out according to the European Standard, EN13286-7 test protocol (EN13286-7, 2004). The loading signals used are a haversine, Fig. 5, at a loading frequency of 10 Hz for the first 20,000 load cycles of conditioning phase and 1 Hz for the series of short loadings, 100 cycles each. The stress range used is a ratio of axial stress to their respective failure axial stress, $_1/\ _{1,f}$ = 0.05 to 0.6, where the monotonic shear failure triaxial tests are carried out prior to the repeated load triaxial tests. The objective of the cyclic conditioning is to stabilize the permanent strains of the material and attain a practically elastic behavior. Generally the conditioning is performed with a stress level corresponding to the maximum stresses applied in the test. The triaxial cell is equipped with three axial and six radial transducers (LVDT's) measuring the axial and radial strains on the middle third of the specimen, see Fig. 5.

For a cylindrical triaxial specimen the axial and radial stresses and strains are the principal stresses ($_1$ and $_3$) and strains ($_1$ and $_3$) and the resilient modulus, M_r, and Poisson's ratio, , can be expressed as:

$$M_r = \frac{\Delta\sigma_1}{\Delta\varepsilon_1} \tag{3}$$

$$\nu = -\frac{\Delta\varepsilon_3}{\Delta\varepsilon_1} \tag{4}$$

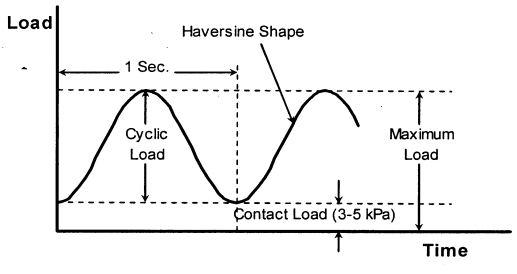

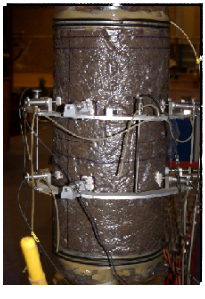

FIG. 5. Haversine triaxial repeated loading curve (left) and instrumented triaxial specimen ready for testing (right)

RESULTS

Repeated Load CBR Test Results

Repeated load CBR tests were performed at different moisture contents and at different degree of compaction (DOC) levels. Fig.6-left shows the resilient deformations due to repeated 95 kN loads for moderate (4%) moisture content at different DOC and Fig.6-right shows the resilient deformations due to repeated 85 kN loads for 100% DOC at different moisture contents. It can be observed that a low compaction level and excess moisture content increases the resilient deformation and thus, according to equation 3, reduces the stiffness of the material. On the other hand,

higher compaction improves the performance. In road construction in South Africa this high quality G1 material is compacted in the field to 108% DOC; unfortunately this high compaction level couldn't be achieved with the existing compaction facility in the laboratory.

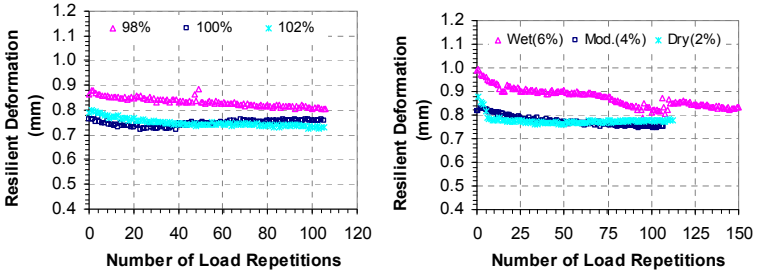

FIG. 6. Effect of DOC and moisture content on resilient deformation of G1 material

It is well known that granular materials are stress dependent. Especially the role of the confinement level is significant. Though the confinement in the CBR test is not known and its distribution in the specimen is very complex, it is proportional to the plunger load. In order to obtain the stress dependency behavior from the repeated load CBR, as shown in Fig. 7, different tests have been carried out at different plunger load levels. The equivalent modulus is estimated for the condition Poisson's ratio of 0.45 and full-friction between the mould and material (equation 1).

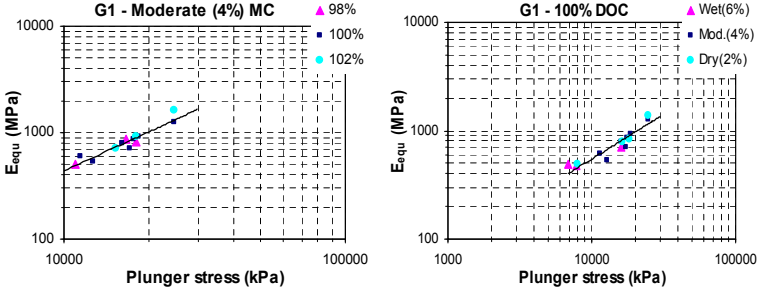

FIG. 7. Stress dependent equivalent modulus for G1 material

Resilient Modulus Triaxial Test Results

As mentioned before, also repeated load triaxial tests were performed. From these tests the stress dependency of the resilient modulus was described using the well known $M_r - \theta$model (equation 5). Results for three different compaction levels are shown in Fig. 8.

$$M_r = k_1\theta^{k2} \quad (5)$$

Where: M_r = resilient modulus (MPa)
θ = sum of principal stresses ($_1$+ $_2$+ $_3$) (kPa)
k_1 & k_2 = model parameters

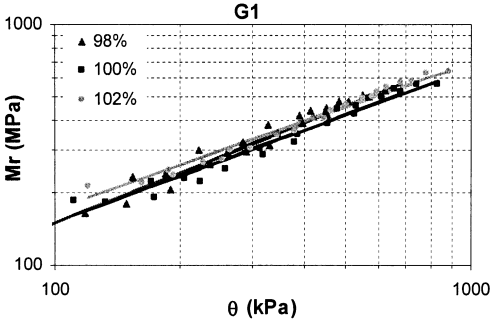

FIG. 8. Triaxial resilient modulus for G1 material for three compaction levels

Comparison of RL-CBR Equivalent Modulus & Triaxial Resilient Modulus

A direct comparison between the resilient modulus of the triaxial test and equivalent modulus of the repeated load CBR test is not possible as the test setups are completely different and they are expressed as a function of different parameters. Fig. 9 shows the trend how the modulus varies with their respective stress levels and a correlation has been developed between the triaxial resilient modulus and RL-CBR equivalent modulus.

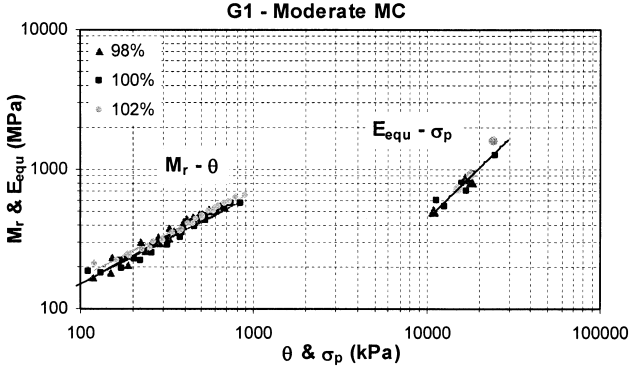

FIG. 9. Comparison of resilient modulus vs. equivalent modulus for G1 material at moderate moisture content and different DOC

In order to estimate a realistic equivalent modulus, E_{equ}, comparable to the resilient modulus, M_r, one approach is to find a corrected or reduced plunger stress.

For $E_{equ} \cong M_r$

From equations (1) and (5):

$$\frac{1.375(1-\nu^{1.286})\cdot\sigma_p\cdot a}{w^{1.086}} = k_1\theta^{k_2}$$

$$\sigma_p = \frac{w^{1.086}\cdot k_1\theta^{k_2}}{1.375(1-0.45^{1.286})\cdot(^{81.5}\!/_{2})} = \frac{w^{1.086}\cdot k_1\theta^{k_2}}{35.965} \tag{6}$$

The elastic deformation, *w*, is known from the repeated load CBR test Fig. 6-left. The parameters k_1 and k_2 are known from the triaxial test, Fig. 8. The corrected plunger stresses were computed for different stress levels, θ. Equation 7 was developed for estimation of the corrected plunger stress for the G1 material, by using non linear multidimensional least square regression, from the compaction level (DOC) of the base layer in the road and the total stress, θ, at that layer in consideration.

$$Log(\sigma_p) = 4.501 - 2.636Log(DOC) + 0.636Log(\theta) \tag{7}$$

Where σ_p = Plunger stress (MPa)
DOC = Degree of Compaction (% MPDD)
θ = Total principal stress ($\sigma_1+\sigma_2+\sigma_3$) (kPa)

Fig. 10 shows the good correlation between the plunger stress σ_p resulting from the regression equation 7 and the plunger stress σ_p calculated by means of equation 6.

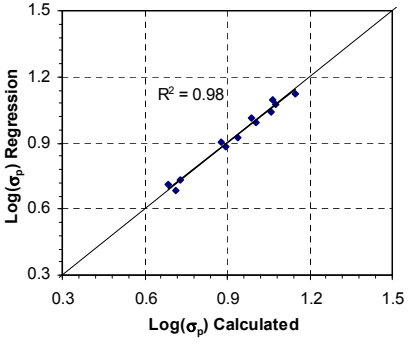

FIG. 10. Comparison of the regression fit of equation 7 with the calculated value from equation 6 for G1 material.

In practice, one has to have the feeling about the compactness of the layer based on existing specifications, experience and nature of material. Moreover from multilayer analysis one needs to have an idea of the magnitude of the stresses from traffic and surcharge loads on a particular base or subbase layer. In fact one can conduct a repeated load CBR test at different load levels and carrying out a pavement analysis for an

assumed modulus to estimate the stress level in the different layers. A new modulus can then be estimated from the repeated load CBR test using the stress level. Thus the equivalent modulus, equal to the triaxial resilient modulus, can be estimated in an iterative way from repeated load CBR test.

CONCLUSIONS

From the extensive repeated load CBR tests carried out the following remarks can be placed:

- The repeated load CBR test is relatively simple and affordable for developing countries and yields, at least for the South African G1 high quality base material, a good estimate of the resilient modulus
- A larger mould and plunger should be used for testing coarser granular materials in order to avoid scaling down of their gradation
- As shown in the above sections the repeated load CBR test is a useful method to evaluate the effect of moisture content, degree of compaction, stress level etc. on the modulus and resistance to permanent deformation of granular materials
- It is recommended to further improve the models used to estimate the equivalent modulus with less assumption on friction condition and if possible Poisson's ratio and to validate it for different types of granular materials.

REFERENCES

Seed, H. B., Chan, C. K., and Monosmith, C. L. (1955). ''Effects of repeated loading on the strength and deformation of compacted clay.'' *Proc., Highway Research Board*, Vol. 34, pp. 541–558.

CEAC - Civil Engineering Advisory Council (1998). "Standard Specification for Road and Bridge Works for State Road Authorities". The South African Institution of Civil Engineering (SAICE), South Africa.

Opiyo, T.O. (1995). "A Mechanistic Approach to Laterite-based Pavements". *MSc. thesis IP 047*, International Institute for Infrastructure, Hydraulic and Environment Engineering (IHE), Delft, Netherlands.

Molenaar, A.A.A. (2008). "Repeated Load CBR Testing, A Simple but Effective Tool for the Characterization of Fine Soils and Unbound Materials". *Transportation Research Board TRB 2008*, Annual Meeting CD-ROM. No. 08-0516. Washington DC.

Molenaar, A.A.A. (2007). "Characterization of Some Tropical Soils for Road Pavements". In *Low Volume Roads 2007. Journal of the Transportation Research Board*, No. 1989, Vol.2, pp. 186-193. Washington DC.

Van Niekerk, A.A. (2002). "Mechanical behavior and performance of granular bases and subbases in pavements*". PhD Dissertation*; Delft University of Technology; Delft.

EN13286-7, (2004). "Unbound and Hydraulically Bound Mixtures – Part 7: Cyclic Load Triaxial Test for Unbound Mixtures". *European Standard EN 13286-7*. CEN European Committee for Standardization, Brussels, January 2004.

Effects of Freeze-Thaw Action and Composition on Compression Strength of WFS-FA-EPS Fills

An Deng[1], Zhongyi He[2] and Haibo Wang[3]

[1] Associate Professor, Key Laboratory of MOE for Geomechanics and Embankment Engineering, Hohai University, Nanjing 210098, China;
[2] Geotechnical Research Institute, Hohai University, Nanjing 210098, China; a_deng@hhu.edu.cn
[3] Department of Civil Engineering, Nanjing Forestry University, Nanjing 210037, China

ABSTRACT: A frost-resistant earth fill was proposed by mixing waste foundry sand (WFS), fly ash (FA), expandable polystyrene (EPS) beads, Portland cement and water in proportions, which was known as WFS-FA-EPS fill. This study examined the unconfined compressive strength (UCS) weakening susceptibility of a range of WFS-FA-EPS specimens prepared at designated compositions which were exposed to freeze-thaw (F-T) cycling from 20 ºC to −15 ºC and up to 5 times. It was found that the inclusion of EPS reduced the unit weight of the fill materials by 20-40%. The majority of UCS loss was found suffered in the first F-T impact. Cement component clearly enhanced the anti-frost capability of materials. Components of EPS and FA also improved the F-T resistance of materials. Water was the main factor leading to F-T impairment, and should be prudentially added into the mixture. Inclusion of EPS beads was able to mitigate the frost impact by the means of reducing UCS loss. The optimal contents were 1.08% for EPS bead and 30% for FA.

INTRODUCTION

In the past two decades, waste foundry sand (WFS) has been widely reused as beneficial construction materials in civil engineering domain, e.g., cement concrete (Naik et al. 2003), asphalt concrete (Bakis et al. 2006), highway embankment (Abichou et al. 2004), earth fills (Deng and Tikalsky 2008), and hydraulic barrier (Abichou et al. 2004). This study was another attempt exploring a WFS-based earth fill incorporating expanded polystyrene (EPS) beads, which were used to reduce the weight and enhance the frost resistance of the earth fill.

The proposed earth fill was a mixture of WFS, fly ash (FA), EPS beads, cement and water in proportions, known as WFS-FA-EPS fill, which hardened into a material with an unconfined compressive strength (UCS) comparable to that of general compacted backfills. Relative to its low unit weight, the fill can be choice of construction material for backfilling situations where reduction in overburdens or lateral pressures was required (Tsuchida et al., 2001; Yoonze et al., 2004). The next merit was the frost

sustainability of the material. The EPS bead inclusion may behave as buffering media in the matrix to attenuate frost impact (Jumikis 1977). The last attractive merit of the fill material was probably the beneficial reuse of solid waste materials, i.e., WFS and FA, which were the base materials and saved the cost retrieving feed materials.

This study was conducted to investigate the gain and loss of UCS of WFS-FA-EPS fills in conjunction with frost action and mixture compositions, which, perhaps, was one of the most critical properties of a fill placed in seasonable frozen regions.

MATERIALS AND METHODS

Materials

WFS samples were retrieved from a casting facility which used clay-based system sand to cast ferrous vehicle engines. Fig. 1 plots the gradation curve of WFS samples. Table 1 shows the physical properties of WFS samples. WFS sample was classified under the Unified Soil Classification System as SP (poor-graded sand).

FA was sampled from an electricity power plant, which discarded FA in wet. The physical properties are presented in Table 1. The gradation curve of the FA sample is presented in Fig. 1, which led to a classification of SW (well-graded).

EPS bead is a super light polymer foam, pre-puffed from polystyrene resin. The beads are white, uniform and spherical, sizing between 2-4 mm. The bulk unit weight of the beads (including the voids between beads) is 0.14 kN/m^3, which is only about 1% of the unit weight of a typical soil. Portland cement was used as a binding material for the mixture. Tap water was used to activate cement hydration.

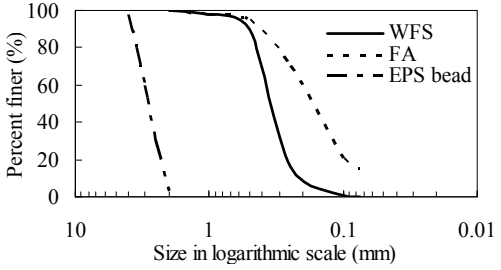

FIG. 1. Gradation curves of WFS, FA and EPS bead samples.

Table 1. Physical Properties of WFS, FA and EPS Beads Samples.

	Water Content (%)	Bulk Unit Weight (kN/m^3)	Specific Gravity	Dry Unit Weight (kN/m^3)		Void Ratio	
				Min.	Max.	Min.	Max.
WFS	1-5	12.5	2.50	12.6	15.8	0.59	0.99
FA	22.3	6.0	2.20	0.61	0.87	1.54	2.64
EPS	0	0.14	-	-	-	-	-

Testing Program

Thirteen series of WFS-FA-EPS mixtures (T1 to T13) were prepared in the laboratory. The mixing ratios are presented in Table 2. All composition were prescribed based on the dry weight of WFS component, and designated by varying the content of a single component, all other variable maintained constant. Water content was added based on the weight of the solid material in the matrix.

Table 2. Mixing Ratios of WFA-FA-WPS Mixtures.

Series	FA (%)	Cement (%)	EPS (%)	Water (%)	Unit Weight (kN/m^3)
T1-T3 and T6	30	6.15, 7.69, 11.54, 15.38	1.08	30	11.3-11.7
T4-T8	30	15.38	0, 0.62, 1.08, 1.54, 1.85	30	9.7-17.0
T6, T9 and T10	30	15.38	1.08	25, 30, 35	11.4-11.8
T6 and T11-T13	0, 13.04, 30, 52.94	15.38	1.08	30	11.2-12.3

A cylindrical specimen (50 mm in diameter and 100 mm in height) was prepared by using a steel tri-split mold, and cured in a chamber maintained at temperature of 20±2 ºC and relative humidity of 100%. UCS were tested on specimens cured through day 28, upon which the specimens were exposed to null, 1, 3 or 5 freeze-thaw (F-T) cycles.

F-T cycling was carried out by referring to the assembly and procedure specified in ASTM D5918-06. In this study, the freezing operation was configured as being unidirectional (upward), at fixed temperature (−15 ℃ at the bottom), at slow freezing rate (1.3 ℃/h), being non-surcharged, and under (hydraulic) closed or open system.

A conventional strain rate controlled uniaxial compression apparatus was used to conduct UCS tests. The compression rate was 1.38 mm/min or 1.38% strain/min. The peak UCS value was observed. At least two specimens were prepared in each test.

RESULTS AND DISCUSSION

Unit Weight

The results of unit weight are summarized in Table 2. As expected, inclusion of EPS content decreased the unit weight of the mixture. For specimens prepared in series of T4-T8, every 1% inclusion of EPS content (up to 1.85%) led to 25-40% reduction in unit weight of the mixture, all other variable maintained constant. The minimum unit weight was 9.7 kN/m^3 for specimens prepared at EPS content of 1.85%. This was a significant improvement in terms of unit weight as the unit weight of a sandy soil was between 17-19 kN/m^3. Inclusion of FA content led to minor reduction in the unit weight of the mixture. A statistical regression data indicated that every 10% inclusion of FA content (up to 52.94%) led to 10-30% reduction in the unit weight of the mixture. Cement and water contents played marginal roles in affecting the unit weight.

Stress-Strain Relation

Fig. 2 presents the stress-strain relations of specimens prepared in series T10, cured through day 7 and 28, respectively, and exposed to null, one or three F-T cycles. The peak strength decreased if the specimens were exposed to F-T action. When the F-T action was conducted over 1 cycle, the strength decreased marginally (Fig. 2b), which indicated that the majority of strength loss due to repeated frost actions was suffered in the first F-T action. Following the first F-T action, the mixture would basically maintain post-action strength in the same order, or rarely lose clearly thereafter. Furthermore, the specimen exposed to 1 F-T cycle demonstrated similar stress-strain relation as the specimen exposed to 3 F-T cycles. It was thus presumed that the binding materials (e.g., cement hydrates) was impaired mainly in the first F-T action, and a minor impairment was suffered in the subsequent frost actions, if exposed. This indication would be further verified by additional test results in the next section.

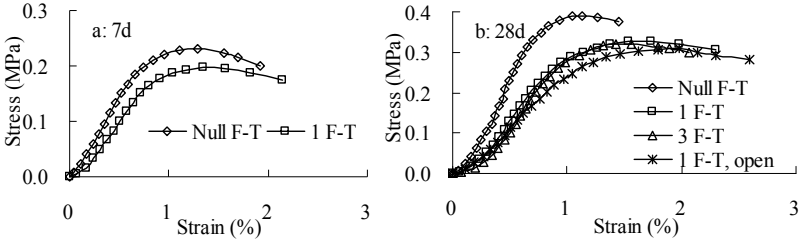

FIG. 2. Stress-strain relations before and after freeze-thaw (F-T) cycles.

The strain at the peak strength increased if the specimen was exposed to F-T action, and the increase was clearer for the specimen cured through day 28 than that cured through day 7. The increase in strain could be due to the fissures resulted in F-T cycles. Freezing action converted water into ice, during which the mixture expanded, say by 10%. The additional volume took the form of numerous fissures in the mixture when thawing action reversed the conversion. Once loaded, these fissures led to the increase in strain. Fissures also led to initial tangent modulus decrease.

The stress-strain relation was further deteriorated for the specimen exposed to frost actions conducted under an open system (Fig. 2b). The strength parameters were moderately weakened. It was reasonable to interpret that the water migration led to such deterioration. Along with the freezing interface moving upward at a slow rate in the mixture during the freezing action, the water supply on the top had the tendency to migrate downward due to suction incurred by the thermal gradient (Jumikis 1977), which eventually increased the water content in the mixture. In this context, the F-T action impaired the matrix more than did under the closed system.

Effect of Cement Content

Fig. 3 shows the effect of cement content on the UCS of specimens prepared in series T1-T3 and T6, all other variable maintained constant. As expected, the increase of

cement content led to a drastic increase in UCS. When the cement content ranges from 6.15% to 15.38%, the UCS gained from 0.12 MPa to 0.46 MPa, which fell within the UCS ranges of general compacted fills. Following the first F-T cycle, the UCS loss was 21.0%, 15.9%, 10.5% and 6.5 % for specimens prepared at cement content 6.15%, 7.69%, 11.54% and 15.38%, respectively. After 3 F-T cycles, the UCS loss increased marginally to 26.2%, 21.1%, 18.4% and 10.1%, respectively. The major UCS loss was suffered in the first F-T action out of 3 F-T cycles. That is, the binding materials (e.g., cement hydrates) were mainly impaired in the first F-T action, and the subsequent frost actions led to minor impairment of the fill materials.

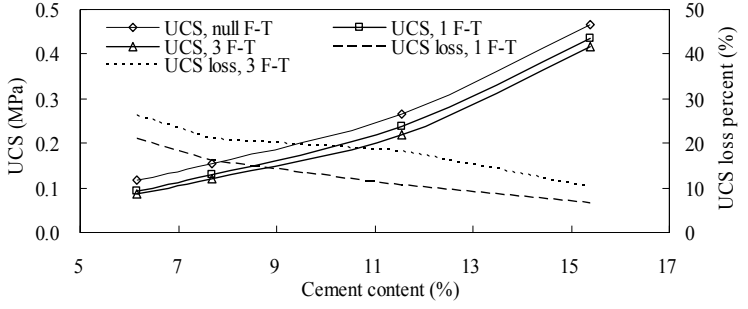

FIG. 3. UCS versus cement content.

The cement content also affected the UCS loss percentage, which estimated UCS loss due to F-T actions relative to the UCS of specimens without F-T exposures. The higher the cement content, the less the UCS loss percentage, and *vice versa*.

Effect of Expandable Polystyrene (EPS) Bead Content

Fig. 4 shows the effect of EPS content on the UCS of specimens prepared in series T4-T8, all other variable maintained constant. As seen, inclusion of EPS beads did temper the potential strength gain of the mixture. The UCS loss was positively associated with the EPS content. The more the EPS content, the more the UCS loss and the less the UCS values. The UCS ranges, however, reasonably fell within 0.4 to 0.6 MPa when the EPS contents ranged between 0.62% and 1.08%, which were still sufficiently high to be comparable to those of general compacted soils.

One of the merits including EPS into the WFS-FA-EPS matrix was to mitigate the F-T impairment. Along with the use and increase of the EPS content, the UCS loss percentage resulted in the first F-T impact decreased from 20.8% (null EPS) to the minimum 6.5% (at EPS content 1.08%) and to 9.3% (at EPS content 1.85%); the UCS loss percentage resulted in the first 3 F-T cycles decreased from 25.1% (null EPS) to the minimum 10.1% (at EPS content 1.08%) and to 18.1% (at EPS content 1.85%). The EPS content was consistently 1.08% at the bottom of the UCS loss percentage trends, which indicated that specimens prepared at EPS content 1.08% demonstrated favorable frost sustainability.

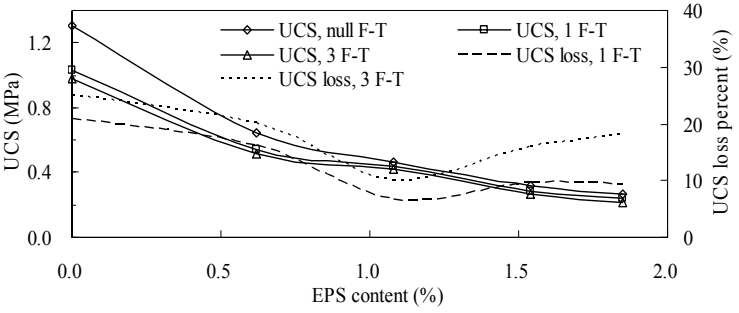

FIG. 4. UCS versus EPS bead content.

The majority of UCS loss percentage was suffered in the first F-T action, and the subsequent F-T actions (up to 3 cycles) led to minor relative loss of strength. The UCS loss percentages were 20.8%, 16.2%, 6.5%, 9.7% and 9.3% for the specimens prepared in series T4-T8, respectively, which were suffered in the first F-T action, and were 25.1%, 20.1%, 10.1%, 15.9% and 18.1% as the same, respectively, which were suffered in the first 3 F-T cycles. On average, around 70% UCS loss was suffered in the first F-T action, at least out of the first 3 F-T cycles.

There was an EPS content at which the WFS-FA-EFS mixture presented the reasonably optimal combination of critical properties, i.e., unit weight, UCS and F-T sustainability. In this context, EPS content of 1.08% (i.e., 45% in volume) seemed to be a reasonable choice, at which the specimen was 1.17 g/cm^3 in density, and 0.47 MPa for null F-T, 0.43 MPa for 1 F-T and 0.42 MPa for 3 F-T in UCS values, respectively.

Effect of Water Content

Fig. 5 shows the effect of water content on the UCS of specimens prepared in series T6 and T9-T10, all other variable maintained constant. Given water content of 30%, which was the optimal water content of the mixture, the specimen had the maximum UCS value out of the 3 series. The UCS loss percentage increased along with the increase of the water content. Given water content of 25%, the UCS loss percentages were 3.3% following the first F-T action, 6.3% following the first 3 F-T actions and 8.4% following the first 5 F-T actions, respectively. Given water content of 35%, the UCS loss percentages increased to 8.4% following the first F-T action, 15.1% following the first 3 F-T actions and 25.6% following the first 5 F-T actions, respectively.

The UCS loss in association with water content was interpreted by the freezing mechanism of water-granular matrix. Water is one of the necessities to trigger frost action and an internal factor impairing the structure of the matrix. More water volume means additional volume expansion upon freezing. The force during expansion may degrade the binding force of cement hydrates, which, apparently, led to UCS loss. Accordingly, it is suggested to control the water volume added to the mixture, given the water content required for cement hydration and mixture compaction.

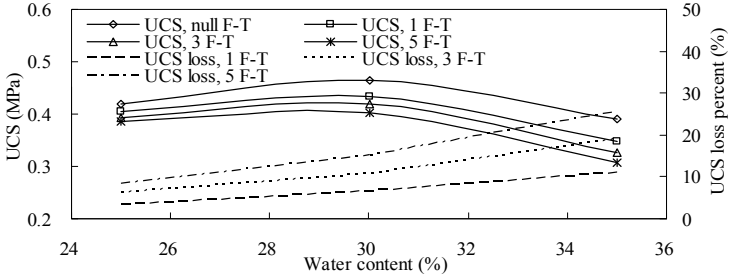

FIG. 5. UCS versus water content.

Effect of Fly Ash (FA) Content

Fig. 6 shows the effect of FA content on the UCS of specimens prepared in series T6 and T11-T13, all other variable maintained constant. Inclusion of FA mitigated the frost impairment. The specimens in series T11, which were prepared without FA content, suffered UCS loss percentage of 28.7% following the first F-T action and 42.8% following the first 3 F-T actions. In contrast, the specimens prepared with FA inclusion suffered UCS loss percentage of 6.5-16.1% following the first F-T action and 10.1-21.8% following the first 3 F-T action, respectively, which were well less than the respective percentages for specimens prepared without FA inclusion.

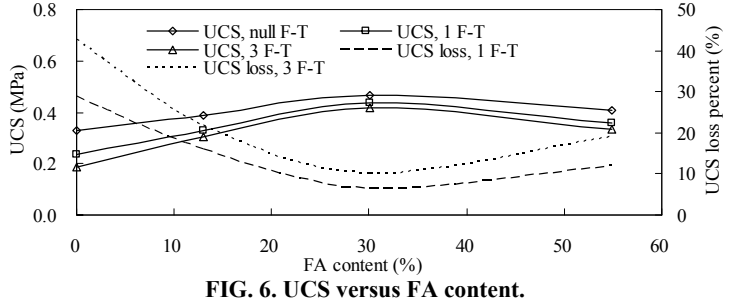

FIG. 6. UCS versus FA content.

The specimens prepared at 30% FA content consistently presented the maximum UCS and the least UCS loss percentage when exposed to null, 1 or 3 F-T cycles in this investigation, which suggests that the specimen prepared at 30% FA content and other variables prescribed as herein was a relatively weathering sustainable mixture in terms of UCS and frost resistance.

The enhancement in UCS and frost sustainability due to FA inclusion was probably associable with several mechanisms. Firstly, the cementitious materials contained in FA helped cement hydration processes and led to additional binding forces. Next, FA was less in unit weight than WFS, which means that less water volume in unit weight was required to prepare a specimen. The resulted water volume reduction mitigated the freezing expansion and thus the frost impairment to the specimen structure if exposed to

F-T actions. The last, FA inclusion was able to improve the gradation of the mixture, leading to a well graded distribution in size and thus increasing the UCS gain.

CONCLUSIONS

For specimens prepared in all series, the unit weight was 20-40% less than that of general fill materials. The 28-day UCS values ranged from 0.11 to 1.30 MPa, which can be controlled to meet almost all the requirements for backfill materials. F-T cycling impaired the binding force of WFS-FA-EPA mixtures and led to the UCS loss of the cured specimen. The majority of the UPS loss was suffered in the first F-T action, at least out of the first 5 F-T cycles in this study. EPS inclusion was one of means effectively mitigating UCS loss. Water content was the essential leading to F-T impairment and should be controlled in making the mixture. In this study, the optimal contents were 30% for FA and 1.08% for EPS. Contents for cement and water should be determined in accordance with UCS requirements.

ACKNOWLEDGEMENTS

The study presented in this paper was supported by a grant from the China National Science Foundation (50708031) and supervised under Hohai Talent Program (2009). Laboratory facilities and technical supports furnished in Nanjing Forestry University were used to complete the majority of the tests, and were appreciated.

REFERENCES

Abichou, T., Edil, T.B., Benson, C.H. and Bahia, H. (2004). "Beneficial use of foundry by-products in highway construction." *Geotechnical Engineering for Transportation Projects* (GSP 126), ASCE, Reston/VA: 715-722.

Abichou, T., Edil, T.B., Benson, C.H. and Tawfiq, K. (2004). "Hydraulic conductivity of foundry sands and their use as hydraulic barriers." *Recycled Materials in Geotechnics* (GSP 127), ASCE, Reston/VA: 186-200.

Bakis, R., Koyuncu, H. and Demirbas, A. (2006). "An investigation of waste foundry sand in asphalt concrete mixtures." *Waste Manag. Res.*, Vol. 24(3): 269-274.

Deng, A. and Tikalsky, P.J. (2008). "Geotechnical and leaching properties of flowable fill incorporating waste foundry sand." *Waste Manag.*, Vol. 28(11): 2161-2170.

Jumikis, A.R. (1977). *Thermal Geotechnics*, Rutgers, New Jersey, 251-253.

Naik, T., Viral, M., Dhaval, M. and Mathew, P. (1994). "Utilization of used foundry sand in concrete." *J. Matl. Civil Eng.*, Vol. 6(2): 254-263.

Tsuchida, T., Porbaha, A. and Yamane, N. (2001). "Development of a geomaterial from dredged bay mud." *J. Matl. Civil Eng.*, Vol. 13(2): 152-160.

Yoonz, G., Jeon, S. and Kim, B. (2004). "Mechanical characteristics of light-weighted soils using dredged materials." *Mar. Georesour. Geotechnol.*, Vol. 22(4): 215-229.

Study on Cement-treated Yangtze Hydraulic Sand Mixed with Expanded Polystyrenes (EPS) Beads as Backfill Material in Highway Embankments

Linchang Miao, Ph. D.[1], Fei Wang [2], Weihua Lu[3] and Jin Li[4]

1 Professor, Institute of Geotechnical Engineering, Southeast University, Nanjing, Jiangsu, China, 210096; lc.miao@seu.edu.cn
2 Ph. D. Candidate, Institute of Geotechnical Engineering, Southeast University, Nanjing, Jiangsu, China, 210096; feiwangseu@gmail.com
3 Doctoral student, Institute of Geotechnical Engineering, Southeast University, Nanjing, Jiangsu, China, 210096; lvweihua@yahoo.com.cn
4 Master student, Institute of Geotechnical Engineering, Southeast University, Nanjing, Jiangsu, China, 210096; lijing695_2@hotmail.com

ABSTRACT: The mechanical characteristics of the lightweight fill using hydraulic sand mixing with expanded polystyrene (EPS) beads were investigated in this paper. Unconfined compression tests, CBR tests and tri-axial shear tests were performed for the presented lightweight fill. The numerical study using a simple model in PLAXIS manual was conducted to verify the performance of embankments filling with the proposed material. Compared with the general lime stabilized soil embankments, the proposed material can significantly reduce the settlement which is beneficial for the highway serviceability. The research results show that the mixing lightweight soil is adequate to be used as the filling material of highway embankments to decrease the damage potential of the bridge-head jumping and to control the post-construction settlement. It is a new kind of filling conception for highway embankment projects.

INTRODUCTION

With the development of the economy in China, many infrastructure projects, for example highways, big bridges, and railways have been constructed, especially in the east area of China where the soft soil distributes extensively. How could the total settlement of embankment and the bridge jumping be controlled in soft soil area? Solving of those problems is very important for the severability of projects.

Numerous authors have developed different kinds of lightweight soil as filling material, including geo-foam, air-foam and waste tires, in an attempt to reduce costs, enhance project performance and have environmental benefits effects (Oh et al., 2002; Tsuchida and Kang, 2002; Gan and Tan, 2003; Tsuchida and Egashira, 2004). To solve the environmental problems caused by waste tires, Engstrom and Lamb (1994) proposed using the shredded tires as a lightweight fill material in road construction; this method was firstly used in 1985 in Minnesota. They concluded that this kind of fill

material was not only beneficial for the environment but also for construction. Stark et al. (2004) submitted a research report to the Transportation Research Board discussing the use of geo-foam blocks (i.e. EPS blocks) as fill material in highway embankments and comparing the costs of this kind of fill with that of general embankments. They concluded that geo-foam provided a safe and economical method of dealing with the embankments on soft soil. However, the geo-foam blocks are too expensive to apply widely. In Japan, Tsuchida (1995) and Tsuchida et al (1996) discussed the use of dredged soil mixed with air-foam and cement as lightweight material when constructing on soft soil and concluded the costs were offset by the reduced need for ground improvement and the benefits of utility waste material. Typically, the unit weight of lightweight soil is just 6-15kN/m3 (Kim et al., 2008), implying the total weight of an embankment could be reduced by some 50%, which is beneficial for the control of settlement, especially at the connection between bridges and embankments. In addition, it can reduce the stress transmission to a deeper soft clay layer, minimizing their compaction, and thus controlling total settlement of the local position of embankment. In this paper, the authors investigated the possibility of mixing hydraulic sand, EPS beads and cement to create an embankment filling material. The mechanical behavior of this potential new material is assessed by a series of tests, including CBR and triaxial tests on specimens with different proportions of the various components. Numerical analysis using commercial software PlaxisV8 is also conducted to analyze the feasibility of the newly material applied as embankment filling.

EXPERIMENTAL STUDIES

Proposed Lightweight Soil Preparation

The sand used in the tests is taken from the Yangtze River and air dried. The particle sizes are smaller 3 mm. EPS beads are white, rounded grains with diameters varying from 3 to 5mm depending on the manufacturing procedure. The presence of gas in EPS beads means their bulk density is only $0.0127 g/cm^3$. Cement was included in the proposed material to bind the cohesionless sand and EPS beads such that they would be easier to compact as well as stable and sufficiently strong to carry the required load after an appropriate curing time. The proportion of sand and EPS beads is measured by volume, while the proportions of sand, water and cement are determined by weight. The sand, cement, and EPS beads are first mixed to ensure that the water added was evenly distributed.

To obtain the optimum water content and the maximum dry density, compaction tests were undertaken. The cement weight percents were determined as 4%, 5%, 6%, and 7% relative to the weight of sand. The ratio of the sand/cement mix and volume of EPS beads was determined as 1:1. Figure 1 presents the compaction curves and the maximum dry densities are summarized in Table 1. Optimum water content ranges from 16% to 18%, which is not significantly affected by the cement content. It is possible that increasing the volume of EPS beads in the mixing material would significantly decrease the density of the material, however, which would increases the cost.

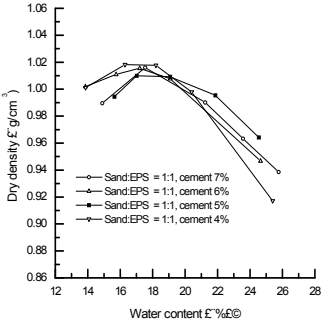

FIG. 1. Compaction Curves for Different Volume Ratios of Sand and EPS

Table 1 Summary of the Maximum Dry Density

Cement Content (%)	Maximum Dry Density (g/cm^3)	Optimum water content (%)
4	1.018	16.3
5	1.010	17.0
6	1015	17.2
7	1.016	17.5

Unconfined Compression Tests

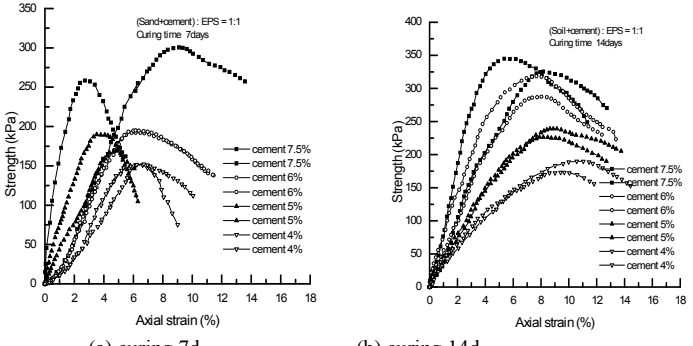

(a) curing 7d (b) curing 14d

FIG. 2. Stress-strain curves of unconfined tests curing 7 and 14 days for 4 different cement contents

The 70.7 mm x 70.7 mm x 70.7 mm unconfined compression test specimens were prepared using the maximum dry density and optimum water content determined previously. The unconfined compression test device is automatic and

computer-controlled; the deformation rate was assigned as 1mm/min. Specimens were cured at approximately 20°C for 7 and 14 days to investigate the shear strength increasing with time. Figure 2 shows the stress-strain curves for different cement contents and curing times. It can be seen that the peak stress of the specimens increases with increasing cement. The axial strain corresponding to the maximum axial stress ranges from approximately 4%-8%; no sudden failure occurs.

CBR Tests

The California bearing ratio (CBR) is a kind of penetration test for the mechanical strength evaluation of the road sub-grades and base courses. The test is performed by measuring the pressure required to penetrate a soil sample with a plunger of standard area. The CBR rating was developed for measuring the load-bearing capacity of cement-treated Yangtze hydraulic sand mixed with EPS beads as backfill material. The harder the surface should have the higher the CBR rating.

$$CBR = \frac{p}{p_s} \cdot 100 \tag{1}$$

where p = measured pressure for site soils [N/mm²], p_s = pressure to achieve equal penetration on standard soil [N/mm²]. The cement weight percents were determined as 7%, 8%, 9%, and 10% relative to the weight of sand. The ratio of the sand/cement mix and volume of EPS beads was determined as 1:1. Table 2 shows results of CBR tests of mixing light soil for different cement weight percents. The results show that cement-treated Yangtze hydraulic sand mixed with EPS beads can be used as filling material of the highway embankment.

Table 2. CBR of Mixing Light Soil for Different Cement Weight Percents

Cement weight (%)	7.0	8.0	9.0	10.0
CBR (%)	5.12	6.03	6.73	8.21

Unconsolidated Undrained (UU) Tests

Unconsolidated undrained triaxial shear tests were carried out with confining pressures of 100, 200 and 300kPa. The specimens were prepared the mixing light soil of 1:1 volume ratio of EPS beads and sand and adding cement content of 7% for sand weight. Figure 3 shows stress-strain curves and strength envelope curves of UU tests of the mixing light soil after 7 and 14 days curing. It can be seen that even with an axial strain of greater than 15%, there was no peak deviator stress. The strength envelope curves slope of UU tests of the mixing light soil is not zero, i.e. $_{uu} \neq 0$, the features show the unsaturated behavior of the mixing light soil because the existence of the EPS beads.

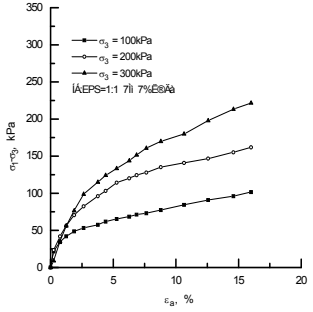

(a) Stress-strain curves for curing 7d

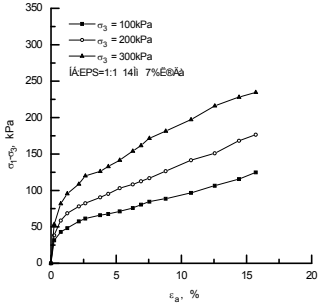

(b) Stress-strain curves for curing 14d

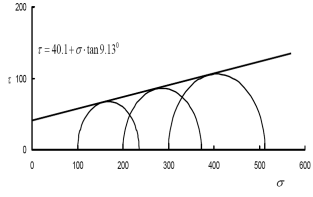

(c) Strength envelope curve for curing 7d

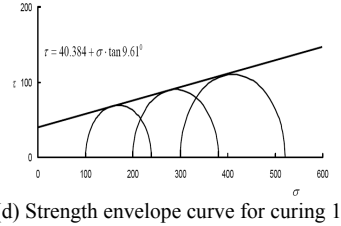

(d) Strength envelope curve for curing 14d

FIG. 3. Stress-strain curves of UU tests of mixing light soil curing 7 and 14 days

NUMERICAL STUDY

To investigate the performance of an embankment constructed using the mixing light soil, a numerical analysis was undertaken using PLAXIS and compared with the results obtained for a common fill material (i.e., lime stabilized soil). The embankment is 16.0m wide and 4.0m high with slopes of 1:1.5. Figure 4 presents the settlement profile after embankment construction for both the mixing lightweight soil and lime stabilized soil. It is clearly shown that the maximum settlement for the mixing lightweight soil embankment is approximately 100 mm compared with 220 mm for the lime-stabilized soil. The numerical analysis indicates the settlement associated with the mixing lightweight soil embankment is significantly less than that with a general lime stabilized soil embankment constructed in a soft soil area. As foundation compression is mainly related to gravity, the mixing lightweight soil embankment is particularly advantages: (1) the embankment load is smaller; (2) the total settlement of foundation can be controlled; (3) the ground improvement investment will be decreased in soft soil area.

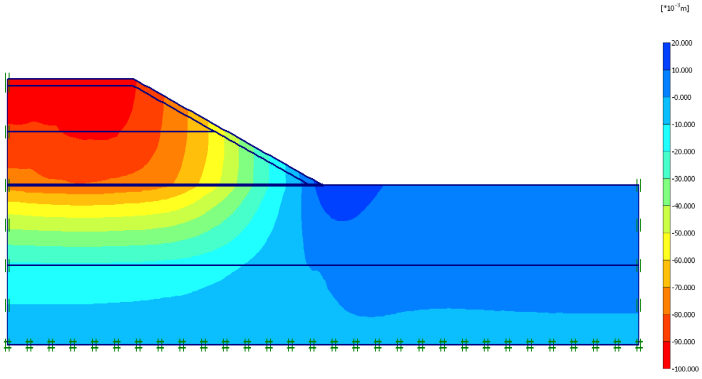

(a) Settlement of the mixing lightweight soil embankment

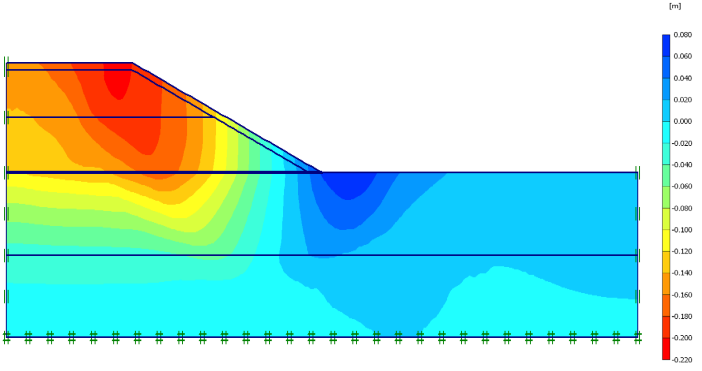

(b) Settlement of the lime-stabilized soil embankment

FIG. 4. Calculation settlement comparison for two types of embankments

CONCLUSIONS

The bridge-head jumping and controlling post-construction settlement of soft ground, which are caused by the embankment gravity loading, have become technical difficulties during the highway and bridge engineering construction and might cause damage during the project running. The optimum method decreasing the damage potential of the bridge-head jumping and controlling post-construction settlement is using lightweight embankments as the fill material to decrease the backfill loading. This paper proposed a mixing lightweight material composed of EPS beads mixed with Yangtze River sand, and cement as embankments fill material over soft soil in the Yangtze River delta. Both experimental and numerical studies are undertaken to investigate the effectiveness and the performance of the material in embankment projects. Research results show that the mixing light soil of EPS can be used as filling

material of highway embankment and it has the advantages: decreased embankment loading, decrease the damage potential of the bridge-head jumping, and controlling total settlement and post-construction settlement of soft soil foundation in highway projects.

ACKNOWLEDGMENTS

The Project No. 50878051 is supported by National Natural Science Fund of China. The work presented was carried out as a part of the project No. 50878051.

REFERENCES

Engstrom, G. M., and Lamb, R. 1994. " Using shredded waste tires as a lightweight fill material for road sub-grades." *Report MN/RD-94/10* to Minnesota Department of Transportation.

Gan, C. H., and Tan, S. M. 2003. Some construction experience on soft soil using light weight materials. Proceedings of *2nd International conference on advance in soft soil engineering and technology*, July, 2-4, 2003, Putrajaya, Malaysia.

Kim, Y. T., Kim, H.J. and Lee, G. H. 2008. Mechanical behavior of lightweight soil reinforced with waste fishing net. *Geotextiles and Geomembranes* 26, 512–518.

Oh, W. S., Lee, J. K., Kwon, Y. C. and Lee, B. J. 2002. Bearing capacity of light weight soil using recycled Styrofoam beads. Proceedings of *the Twelfth (2002) International offshore and polar engineering conference*, Kitakyushu, Japan, May 26-31, 2002.

Stark, T. D., Horvath, J. S., and Leshchinsky, D. 2004. Geofoam application in the design and construction of highway embankments. *TRB project* No. 24-14

Tsuchida, T., 1995. Super geo-material project in coastal zone. In: Proceedings of *the International Symposium on Ocean Space Utilization COSU'95*, Yokohama, pp.22–31.

Tsuchida, T., Takeuchi, D., Okumura, T., Kishida, T., 1996. Development of light-weight fill from dredgings. In: *Environmental Geotechnics*. Balkema, pp. 415–420.

Tsuchida, T., Kang, M.S., 2002. Use of lightweight treated soil method in seaport and airport construction projects. In: *Proceedings of the Nakase Memorial Symposium, Soft Ground Engineering in Coastal Areas*

In-situ Testing and Evaluation of Moisture Content in Existing Sub-grade

Jinsong Qian[1], Xin Qiu[2] and Jianming Ling[3]

[1]PH.D., Dept. of Road and Airport Engineering, Tongji Univ., 4800 Cao An Road, Shanghai 201804, China; PH(86-21)69583006; qjs1001@126.com.
[2]PH.D., Dept. of Road and Airport Engineering, Tongji Univ., 4800 Cao An Road, Shanghai 201804, China; PH(86-21)69584655; tonyxiuqiu@163.com.
[3]Professor, PH.D., Dept. of Road and Airport Engineering, Tongji Univ., 4800 Cao An Road, Shanghai 201804, China; PH(86-21)69583005; jmling01@yahoo.com.cn.

ABSTRACT: The bearing capacity of subgrade soils, which is a critical parameter for assessing pavement conditions and guiding the type and extent of maintenance and rehabilitation (M&R), is greatly influenced by soil water content. In this study, a case of long-term spatial distribution of moisture content in existing cohesive subgrade in Shanghai was investigated. The in-situ testing data revealed significant variations in the water content of the sub-asphalt soils layers in both the horizontal and vertical directions. The equilibrium moisture contents (EMC) beneath pavement were calculated based on unsaturated soil theory and Fredlund & Xing equation was chosen as the soil-water characteristic curve (SWCC). Comparison of water content estimates from investigation and from prediction shows that, the relative elevation of groundwater table (GWT) is an influential factor controlling moisture distribution in subgrade, but areas with high water content immediately beneath pavement mainly reflect the inefficacy of pavement drainage systems.

INTRODUCTION

According to the field survey and analysis, the performance of the pavement is strongly affected by the characteristics of the subgrade (Ling, 2002). Further, an important factor affecting the stiffness and strength of subgrade soils is the prevalent moisture conditions of the soil below the pavement (Chu, 1977). The soils are weaker due to the higher degree of saturation, which can be used for the lower resilient modulus (M_r) values and undergo more accumulated plastic strain. For example, Khoury (2004) found M_r of clayey soils compacted at OMC-4% was reduced by approximately 45% due to wetting them to OMC+4%, and Puppala (1999) noted the majority of rutting emanated from cohesive sub-grades, in accelerated loading facility (ALF) investigations at Louisiana, was possibly due to heavy and continuous rains, which resulted in development of the pore pressures and the loss of strength in sub-soils during loading.

Construction specifications generally require that subgrade soils be compacted in the field at or near optimum moisture content (OMC). However, subgrade is directly exposed to the natural environment and then the long-term water content is affected by precipitation, temperature and seasonal variation, groundwater table, pavement conditions, drainability, etc.(Han, 2005). A large number of field investigations have shown that the moisture content of soils beneath pavements, except for a zone close to pavement edge, reaches an equilibrium condition after several years from the construction (Chu, 1977). Moreover, the results of LTPP have shown the in-situ equilibrium moisture contents (EMC) in cohesive subgrades at 59 sites are all at the wet side of OMC (Quintus, 1998).

The paper presents the in-situ investigation at A11 expressway to get the field spatial distribution of moisture content in silty clay subgrade for analyses of M_r and permanent deformation in the future, and then the comparisons of the prediction results obtained from the soil-water characteristic curve (SWCC) with field results are conducted, to validate the effect of GWT on water contents.

FIELD TESTING

The test section was selected at A11 expressway in Shanghai, which was built in 1996 and would be widen to accommodate the sharp increase in traffic volume. The test section has 16cm of asphalt concrete, 40cm of lime-flyash stabilized crushed stone base and 3m of silty clay embankment. The pavement was removed due to notable deterioration, so the soil drilling tests were carried out directly at the top of subgrade. The sample location layout is shown in Figure 1.

The GWT near the test site was monitored monthly over a period of one year. The seasonal variation of GWT was not significant and the water table was at a depth of approximately 0.5m, as illustrated in Figure 2.

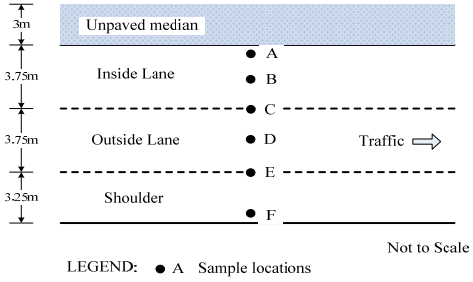

Fig.1. Sample location layout

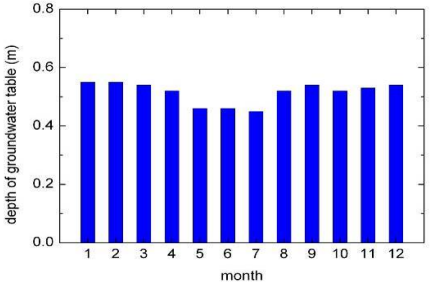

Fig.2. Fluctuation in GWT

The soil samples were transported to the laboratory at Tongji University for routine testing to determine grain-size distribution, liquid limit (LL), plastic limit (PL), specific gravity (G_S), OMC, maximum dry density (MDD), dry density (γ_d) and gravimetric water content (w). Table 1 presents a summary of the measured properties of soil samples. It is found that the dry density was very low and subgrade soils were insufficiently compacted, which may have resulted in the pavement damage of the test section.

Table 1. Summary of Soil Properties for Subgrade Soil

LL	PL	PI	G_S	γ_d (kN/m^3)	OMC (%)	MDD (kN/m^3)	Grain size distribution (%)		
							sand	silt	clay
31.1	19.2	11.9	2.71	15.04	16.1	18.10	2.0	82.9	15.1

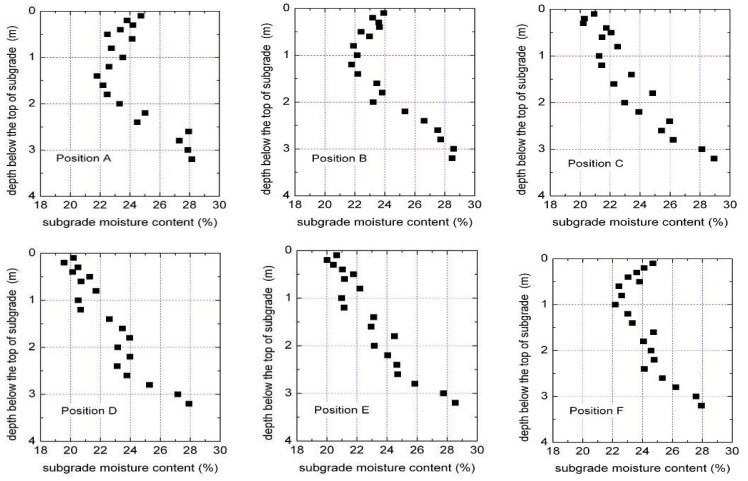

Fig.3. Subgrade moisture content variation with depth

In Figure 3 the measured gravimetric water contents (w) of subgrade soils at different sample locations are plotted versus depth below the top of subgrade. Vaswani (1975) noted that the higher the compaction and dry density of the subgrade soils were, the lower the moisture content would be. In the case of test section, due to the low degree of compaction, the values of water content were all relatively high ranging from 20% to 29% (1.04PL~1.51PL). It is also found that moisture contents beneath pavement, such as location C, D and E, increased with the decrease in depth to GWT, which indicated that groundwater was an influential factor controlling long-term moisture distribution in subgrade. On the contrary, the distribution characteristics were reverse within the depth of about 1m at location A, B and F, caused by infiltration through shoulder and unpaved median. It is worth mentioning that location B was beneath the center of inner lane, which suggested the efficacy of pavement drainage systems, especially the drainability of median facility, were not good to remove runoff completely and quickly. When the existing subgrades were dug, it was found that the aggregate drains were contaminated by the soils.

PREDICTED RESULTS

When dealing with unsaturated soils, the moisture content can be expressed in terms of soil suction. The suction, denoted h_s, was computed using the depth to GWT, specifically $y\gamma_w$, where y is the distance from the GWT to the point of interest, and γ_w is the unit weight of water (Perera, 2004). The relationship between soil suction and moisture content is depicted by the soil-water characteristic curve (SWCC). The SWCC function chosen to predict was the equation developed by Fredlund and Xing (1994):

$$\theta_w = \left[1 - \frac{\ln\left(1+\frac{h_s}{h_r}\right)}{\ln\left(1+\frac{10^6}{h_r}\right)}\right] \frac{\theta_s}{\left\{\ln\left[\exp(1)+\left(\frac{h_s}{a}\right)^b\right]\right\}^c} \tag{1}$$

Where θ_w is volumetric water content, θ_s is saturated volumetric water content and treated as a known determined by γ_d and G_s, a, b, c and h_r are soil parameters.

In this paper, the four parameters were calculated with test data from Ye (2005) as Figure 4 and presented in Table 2. The relationship between volumetric water content and gravimetric water content can be written as:

$$\theta_w = \frac{w\gamma_d}{\gamma_w} \tag{2}$$

Table 2. SWCC parameters for prediction

a (kPa)	b	c	h_r (kPa)
42.8839	0.72818	0.7421	370.09649

Figure 5 shows the plots of predicted versus measured gravimetric water content values for subgrade. It is shown that the predicted results are acceptable and can be used to depict the significant effect of GWT on EMC characteristic. The error may be

caused partially by uncertainty of calculated function parameters from test data, especially in the range of low suction (0~100kPa) where a few data were obtained, and the other reason may be the SWCC curve with these parameters could not account for the impact of compaction conditions in field.

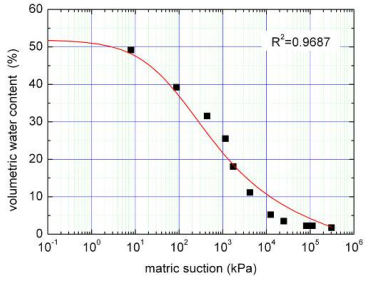

Fig.4. Soil-water characteristic curve for Shanghai silty clay

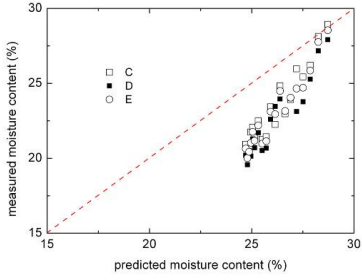

Fig.5. Predicted versus measured moisture content values

Perera (2004) stated that the error associated with the $y\gamma_w$ model is larger than TMI-P200 model and the TMI-P200/wPI model based on investigation of subgrade soils throughout the United States, but $y\gamma_w$ method is a good approximation to estimate the suction of the soil when the GWT is within three feet of the ground surface. In the case of Shanghai, the depth of GWT usually ranges from 0.5 to 1.5m, so it seem to be feasible to predict silty clay subgrade moisture content using $y\gamma_w$ model, where the GWT datum are easily available.

CONCLUSION AND DISCUSSION

Results from field investigation conducted in this study indicate that, the moisture contents of the whole test section were relatively high resulted from the low degree of compaction and high GWT, and further, the poor drainability increased the water accumulation near the pavement edge and unpaved median, even beneath the inner lane. The predicted results from $y\gamma_w$ model were shown to provide a satisfactory agreement with testing datum, it is suggested that the EMC of silty clay subgrade in Shanghai can be predicted from GWT. However, testing for SWCC should be conducted because the parameters presented in the paper could not consider the influence of compact effort in field, and more attention should be paid to the range of low suction.

ACKNOWLEDGEMENTS

The financial support of NSFC (50908176) and Program for Young Excellent Talents in Tongji University are gratefully acknowledged.

REFERENCES

Chu T. Y., Humphries K. W., Stewart R. L., et al. (1977). "Soil moisture as a factor in subgrade evaluation." *Transportation Engineering Journal*, ASCE, 103(1): 87-102.

Fredlund D. G. and Xing A. (1994). "Equations for the soil-water characteristic curve." *Can. Geotech. J.*, 31:521~532.

Han Y. P. (2005). "Resilient modulus estimation system." *Ph.D. Dissertation*, University of Missouri-Rolla.

Khoury, N. N., and Musharraf, M. Z. (2004). "Correlation among resilient modulus, moisture variation and soil suction for subgrade soils." *TRB 2004 Annual Meeting*, 2004.

Ling J. M., Wang W. and Wu H. B. (2002). "On residual deformation of saturated clay subgrade under vehicle load." *Journal of Tongji University*, 30(11):1315-1320. [in Chinese]

Perera Y. Y. and Zapata C. E. (2004). "Moisture equilibria beneath highway pavements." *83rd Annual Meeting of Transportation Research Board*, TRB.

Puppala A. J., Mohammad L. N. and Allen A. (1999). "Permanent deformation characterization of subgrade soils from RLT test." *Journal of Materials in Civil Engineering*, 11(4): 274-282.

Quintus H.V. and Killingsworth B. (1998). "Analyses relating to pavement material characterization and their effects on pavement performance." *Report No. FHWA-RD-97-085*, Federal Highway Administration.

Vaswani N. K. (1975). "Case studies of variations in subgrade moisture and temperature under road pavements in Virginia." *Highway Research Record No. 532*, Highway Research Board, Washington D .C., 30-42.

YE, W. M., Tang Y. Q. and Cui Y. J. (2005). "Measurement of soil suction in laboratory and soil-water characteristics of Shanghai soft soil." *Chinese Journal of Geotechnical Engineering*, 27(3):347-349. [in Chinese]

Zapata C. E. (1999). "Uncertainty in soil-water-characteristic curve and impacts on unsaturated shear strength predictions." *Ph.D. Dissertation*, Arizona State University.

Influence of lime on Alluvial Soil Strengthened with Pond Ash and Rice Husk Ash for Construction of Subgrade of Road

Tapash Kumar Roy

Sr.Lecturer, Department of Civil Engineering, Bengal Engineering & Science University,Shibpur, Howrah-711103, West Bengal. E Mail: tapash@civil.becs.ac.in, tapash122001@yahoo.com

ABSTRACT: Due to rapid development in the industrial sectors, huge quantities of waste materials are being produced as by-product and such wastes are to be located over dumping zones near the plants. These wastes not only need depositional land, but also create accumulation hazard and pollute environment around the plants. On the other hand procurement of conventional materials in huge quantity required for construction of subgrade of road is becoming very difficult in many locations due to various problems. So need has arisen for proper disposal of the waste materials. Utilizing these materials in the area of road construction after improving their characteristics suitably can provide useful solution of this problem. So keeping this in view, an experimental study was undertaken to explore the possibility of utilization of the alternative materials like pond ash, rice husk ash (RHA) by mixing with local alluvial soil by adding small percentage of lime for the construction of road subgrade as cost effective mix.

INTRODUCTION

The satisfactory performance of the pavement structure of road is essentially connected with the quality of subgrade materials, which may be found in-situ or that of filler materials for embankment required depending on the existing topography of the sites. However in many locations, the availability of conventional filling materials is in short supply or nonexistent due to various reasons like non-availability of adequate land to supply fill materials, land acquisition problems etc. Particularly in case of densely populated area, the procurement of such filler materials required for development of formation is becoming difficult and this problem becomes more severe due to increase in constructional activities in transportation sector in India like Pradhan Mantri Gram Sadak Yojona as well as National Highway Development Project are the prestigious projects undertaken by the Government of India. On the other hand, due to rapid economic growth and industrialization, a huge quantity of waste materials generated creates a tremendous threat to public health and ecology. With decreasing coal quality and increasing power generation, coal ash production is

projected to reach 90-100 million tons a year by the turn of the century. Only 2% of the ash produced is used for some gainful purposes; the rest is to be disposed as waste material (*www.worldbank.org*). So need has arisen for proper disposal of the wastes materials. Utilizing these materials in the area of road construction after improving their characteristics properly can provide useful solution of this problem. A large number of investigators are engaged in this field over last few decades. Bhasin et al. (1985) reported the improvement in the soaked CBR of soil on addition of rich husk ash and lime sludge and further extended their investigation on stabilization of black cotton soil by using RHA with or without lime. Ali et al. (2004) carried out an investigation on the influence of RHA and lime on Atterberg limits, strength, compaction, swell and consolidation properties of bentonite. An experimental study has been done for determining the stabilizing effect on clayey soil by using rice husk ash from rice mill and lime sludge from a paper factory (Chandra et al. 2005). By considering this objective, a research program has undertaken at the Transportation Laboratory of Bengal Engineering and Science University, Shibpur to examine the possible improvement in the engineering properties of the locally available alluvial soils by adding various proportion of pond ash and rice husk ash to evaluate the cost-effective mixing proportion. Further to study the effect of mixing lime over a small range of proportion to the soil using pond and rice husk ash in cost-effective proportion.

EXPERIMENTAL INVESTIGATIONS

Material Used

In these study four types of materials namely alluvial soil, pond ash, rice husk ash and lime have been used. The properties of materials are described below:

Soil: Soil used in this investigation is alluvial soil of blackish gray clayey silt, collected from the shallow depth of the nearby field in the campus of Bengal Engineering and Science University, Shibpur at Howrah. Evaluated properties for the same are shown in the following table1and based on liquid limit and plasticity index the soil may be classified as “MI”

Rice husk ash (RHA): Rice husk ash, a predominantly siliceous material is collected from local rice mill at Burdwan, a district of West Bengal. The physical properties of the said materials are reported in the following Table 1.

Pond ash: The pond ash is non-plastic materials and used in this investigation was collected from nearby Thermal Power Station at Kolaghat. The geotechnical properties of pond ash obtained in the laboratory tests are reported in the Table1.
The major constituents of pond ash are Silica (SiO_2), Alumina (Al_2O_3), Iron Oxide (Fe_2O_3), Calcium Oxide (CaO), Magnesium Oxide (MgO), Sulpher (SO_3). Loss on Ignition and Surface area (Sq.m/N) vary from 0.4-0.6% and 2300-5700 respectively (Rao, 1999). Ghosh and Subbarao (1998) had made detailed investigation on fly ash from Kolaghat Thermal Power Station (KTPS), West Bengal and shown the chemical

composition as 53.30% of SiO_2, 31.73% of Al_2O_3, 5.27% of Fe_2O_3, 1.40% of CaO, 0.10% of MgO, 5.50% of Loss of Ignition and others 2.70%.

Lime: Lime has been collected from the nearby market at Howrah, West Bengal and tested in the laboratory of the Department of Chemistry, Bengal Engineering and Science University, Shibpur. The constituents of lime by weight were 1.85% of SiO_2, 0.31% of Al_2O_3, 0.14% of Fe_2O_3, 55.48% of CaO, 0.10% of MgO, 0.15% of Na_2O, 0.43% of K_2O and 41.23% of LOI.

Table 1. Physical Properties of Soil, Pond ash and Rice husk ash used

Sl.No	Properties	Test values of Soil	Test values of Pond ash	Test values of RHA
1	Grain size Distribution by Sieve analysis & Hydrometer method (a) Sand size particles (b) Silt size particles (c) Clay size particles	 Nil 68% 32%	 31.25% 63.5% 5.25%	 72.0% 28.0% Nil
2	Atterberg's limit- (a) Liquid limit (b) Plastic limit (c) Plasticity Index	 47% 32% 15%	Non Plastic	Non Plastic
3	Light compaction- (a) MDD (b) OMC	 15.5 kN/m^3 23.00%	 11.4 kN/m^3 32.5%	 11.3 kN/m^3 28.0%
4	Specific gravity	2.63	2.25	2.06
5	(a) CBR Unsoaked at OMC (b) CBR Soaked	12.91% 4.90%	40.25% 5.26%	19.60% 14.70%

PROPORTIONS OF MATERIALS

For determining the quantitative information about the mixed soil, having 20% of rice husk ash and increasing percentages of pond ash as 20%, 40% and 60% were mixed with decreasing percentage of pure soil as 60%, 40% and 20% and indicated as series 1, 2 and 3. Further 0 to 3% of lime by weight of pure soil was added with the mixed soil as shown in the series 1, 2 and 3 for investigating their improvement in properties, if any. In total, 12 mixes were prepared having different proportions are used for the laboratory study and shown in Table 2. Now for determining the various characteristics of the soil mixed with pond ash, rice husk ash and lime, Standard Proctor compaction tests and CBR tests at optimum moisture condition both in unsoaked and soaked have been performed in the laboratory as per the standard procedure laid down in the relevant BIS codes.

Table 2. Mix Proportion of Soil, Pond ash, RHA and Lime by weight percentage

Series	Sl. No.	Mixed Soil			
		Soil (%)	Pond ash (%)	RHA (%)	Lime (%)
1	1	60	20	20	0
	2	60	20	20	1
	3	60	20	20	2
	4	60	20	20	3
2	1	40	40	20	0
	2	40	40	20	1
	3	40	40	20	2
	4	40	40	20	3
3	1	20	60	20	0
	2	20	60	20	1
	3	20	60	20	2
	4	20	60	20	3

EXPERIMENTAL RESULTS AND DISCUSSIONS

Compaction Characteristics

The effect of adding lime in varying percentage from 0% to 3%, on the maximum dry density (MDD) and optimum moisture content (OMC) of the soils mixed with pond ash and rice husk ash are plotted in Figs. 1 and 2 respectively.

From the Figs. 1 and 2, it is observed that addition of varying proportions of pond ash; rice husk ash and lime have considerable effect on the maximum dry density and optimum moisture content of the alluvial soil. Maximum dry density of tested soil is 15.6 kN/m^3 and this value of mixed soil decreases with the decreased proportion of soil but with the increased proportion of pond ash up to 60% and becomes 11.10 kN/m^3 due to deceased MDD of both pond ash and rice husk ash compared to the virgin soil. Further addition of lime in increasing amount from 1% to 3%, these values decrease gradually in all the cases of mixed soils in the series 1, 2 and 3 due to elimination of gaseous materials from the mixed soil at the time of chemical reactions.

The OMC of tested soil is 23.0%, but this value increases with the increased proportion of pond ash and the decreased proportion of soil without addition of any lime and these values become 29.15%, 31.25% and 29.99%, for series 1, 2 and 3 respectively. However with the addition of lime in increasing proportion from 1% to 3% with the series 1, 2 and 3, these values increase gradually due to demand of water for chemical reaction among soil, pond ash, rice husk ash and lime. These values for series-1 & 2 increase at slow rate and become 31.29%, 32.12%, 33.87% for series-1 and 33.17%, 33.26%, 34.35% for series-2 for addition of lime 1%, 2% and 3% respectively with both the series. However the same for series-3 increases at rapid rate compare to that of series-1 & 2 and become 32.12%, 34.34%, 36.08% for addition of lime 1%, 2% and 3% respectively

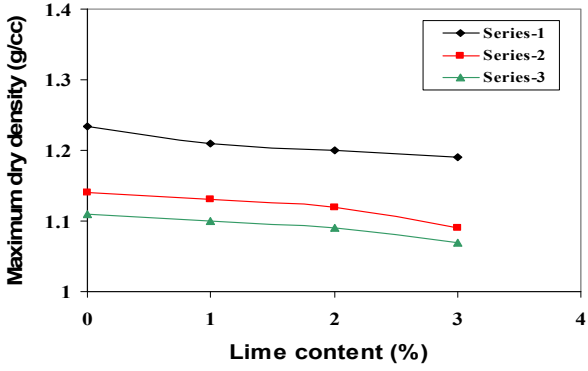

FIG. 1. Variation of MDD of Pond ash and Rice husk ash mixed alluvial soil with varying percentage of Lime

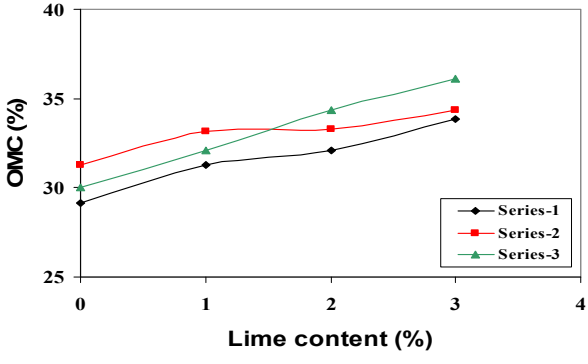

FIG. 2. Variation of OMC of Pond ash and Rice husk ash mixed alluvial soil with varying percentage of Lime

Strength Characteristics

The effect on CBR value of above cited mixed soil at OMC in soaked and unsoaked condition for addition of lime in varying percentage from 0% to 3% are evaluated and results are shown in the following Figure 3 and 4.

From the FIG. 3, it is obvious that California Bearing Ratio value of the tested soil in unsoaked condition is 12.91% and this value increases with the increasing percentage of pond ash and decreasing proportion of soil and becomes 16.17%, 19.19% and 18.17% for the ratio of soil, pond ash and rice husk ash as 60:20:20, 40:40:20 and 20:60:20 respectively without addition of any lime. However with addition of lime with the mixed soil in increasing ratios from 1% to 3%, this value increases gradually in all the series. But remarkable increment is observed in case of unsoaked CBR value

as 23.83% when lime is added by 3% with the series-2 of mixed soil, in where the proportion of RHA, pond ash and soil are remained as 40%, 40% and 20% respectively.

However from the FIG. 4, significant performance has been observed for soaked CBR value of the tested soil when mixed with pond ash, rice husk ash and lime. The soaked CBR of tested soil is 4.9% and with the increasing amount of pond ash and decreasing amount of soil these values increases to 10.12%, 12.52% and 8.36% for the ratio of soil, pond ash and rice husk ash as 60:20:20, 40:40:20 and 20:60:20 respectively without mixing of lime. Further when these mixed soil added with the increasing amount of lime from 1% to 3%, this value increases in all the cases. But significant observation is made when lime is added by 3% with the series-2 of mixed soil and this value becomes 17.46% for the proportion of RHA, pond ash and soil are remained as 40%, 40% and 20% respectively. This value is nearly four times the corresponding value of the virgin soil.

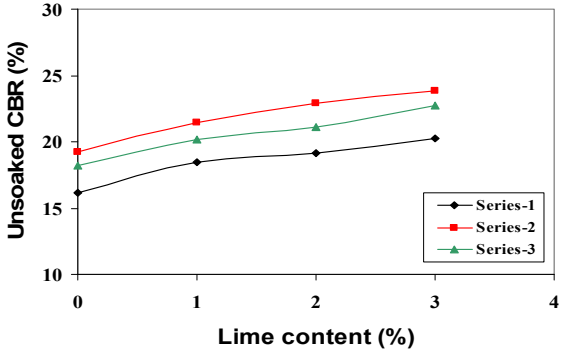

FIG. 3. Variation of CBR (unsoaked) of Pond ash and Rice husk ash mixed alluvial soil with varying percentage of Lime

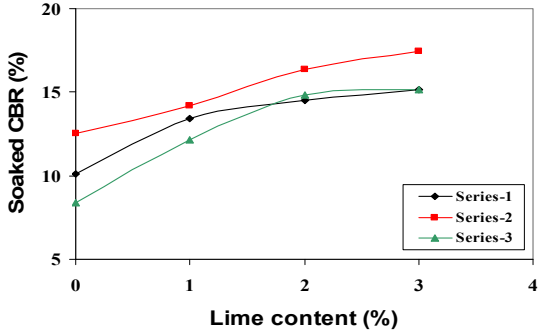

FIG. 4. Variation of CBR (soaked) of Pond ash and Rice husk ash mixed alluvial soil with varying percentage of Lime

CONCLUSION

From this experimental study, the following conclusions can be made:

1. Consumption of waste materials like pond ash and rice husk ash in bulk quantity in the construction of road project can be made with reducing the accumulation hazard and environmental pollution.
2. Addition of rice husk ash in increasing proportion with the alluvial soil decreases the maximum dry density of the mixed soil with or without mixing of lime due lower dry density of pond ash and rice husk ash. However the optimum moisture content of the mixed soil increases gradually with the increased percentage of pond ash, rice husk ash and lime due to higher demand of water of pond ash and rice hush ash for achieving maximum density compared to the virgin soil.
3. In strength characteristics, CBR value in soaked and unsoaked condition increases gradually for addition of increasing amount of pond ash and rice husk ash with alluvial soil. However addition of lime in increasing proportions with these mixed soils show the better increment in the CBR values both in the soaked and unsoaked conditions. Significant CBR value is observed for the local alluvial soil mixed with 40% pond ash, 20% rice husk ash and 3% lime, and the said value in unsoaked condition is nearly 2 times and in soaked condition is 4 times the corresponding value of the virgin soil. Such an increase seems due to greater pozzolanic action of pond ash and RHA with lime in presence of water.

REFERENCES

Ali, M.; and Sreenivasulu, V. (2004), "An Experimental Study on the Influence of Rice Husk Ash and Lime on Properties of Bentonite." *Proceedings of the Indian Geotechnical Conference,* Vol. I: 468-471.

Bhasin N.K, Goswami N.K., Oli P., Krishan N., Lal N.B. (1985) Utilization of waste material in construction of roads in rural areas." *Seminar on road and Road Transport in Rural area,CRRI, New Delhi* : 260-267.

Chandra, S., Kumar, S. and Anand, K. R., (2005) "Soil Stabilization with Rice Husk Ash and Lime Sludge." *Journal of Indian Highway, Indian Road Congress, (May)*: 87-98.

Ghosh, A., and Subbarao, C., (1998) "Hydraulic Conductivity and Leachate Characteristics of Stabilized Fly Ash." *Journal of Environmental Engineering, ASCE,* Vol.124, No.9, September: 812-820.

http://www.worldbank.org/html/dec/Publications/Abstracts97/03esd/esd22.html

IS 2720. Method of Test for Soil (Part ∇III) (1980) Laboratory Determination of Moisture Content & Dry Density.

IS 2720. Method of Test for Soil (Part XVI) Laboratory Determination of CBR.

Rao A.V.N., (1999). "Characteristics of Fly ash its applications – A brief review." *Proceedings`of the national seminar on Fly ash characterization and its Geotechnical applications, Fly ash Mission, TIFAC, Bangalore*: 1-8.

Sublayer Strength Evaluation with FWD in Semi-rigid Base Asphalt Pavement Rehabilitation Project

Lin CONG[1], Robert L Lytton[2], Zhaoxing XIE [1]

[1]Associate Professor, Key Laboratory of Road and Traffic Engineering of MOE, Tongji University, Shanghai, 201804, P.R. China, conglin@tongji.edu.cn
[2]Professor, Department of Civil Engineering, Texas A&M University, College Station, TX, 77843-3136, USA, r-lytton@civil.tamu.edu
[3]Engineer, Shanghai Municipal Planning Design and Research Institute, 609 Jianguoxi Road, Shanghai 200031, P.R. China, xzx9898@163.com

ABSTRACT: This paper used dynamic FEM model instead of continuum elastic layered system to simulate whole or broken semi-rigid base asphalt pavement response under FWD. Calculating results indicated that the sublayer strength can be evaluated by special FWD deflection basin parameter. Subgrade modulus (Esg) can be well evaluated by Curvature Index CI_7 and Shape Factor F_8 and the estimated results were not affected by pavement structure cracking condition. Whether Esg greater than 170MPa or not is defined as pavement subgrade failure criteria. Curvature Index CI_3 can use to indicate the semi-rigid base layer structural condition and its criteria is CI_3 value greater than 60um. This method have been applied and validated successfully in Jialiu Expressway rehabilitation project in Shanghai. It can more precisely distinguish weak sections for pavement rehabilitation design.

INTRODUCTION

After more than ten years continuing development, a large part of expressway pavements in China that mostly were semi-rigid base asphalt pavement type has stepped into rehabilitation phase. All the semi-rigid bases were made of lime and fly-ash stabilized aggregate or cement stabilized aggregate. These pavement structure rehabilitation projects require to divide the whole road into analysis sections by structural bearing capacity, service condition, etc, especially base layer structural condition and subgrade strength. One analysis section has one representative evaluation result used in design procedure. In China highway agencies used to using Benkelman Beam deflection data to analyze pavement strength and divide road section. But the B-B surface deflection reflects the full-depth pavement bearing capacity, but it can not show the base layer and subgrade condition, which impair designer making correct rehabilitation practice.

To date, Nondestructive testing (NDT) is widely recognized as an important tool for

pavement structural evaluation. Falling weight deflectometer (FWD) has gained acceptance as the most developed pavement structural testing device for its ability to apply heavy load and to simulate actual truck traffic wheel loading. Currently, a number of FWD backcalculation programs can estimate each layer modulus by modeling pavement as linear or nonlinear elastic system; these moduli are then used to compute the effective pavement structural capacity.

Actually, these semi-rigid base asphalt pavement in rehabilitation phase usually has been broken by cracking, interface sliding, so using continuum elastic layer system model to will cause unreasonable backcalculation moduli results. AASHTO(1993) suggests not to calculate existing pavement structural number (SN_{eff}) using inverse effective moduli of each layer in pavement rehabilitation evaluation. Uddin, Z. Pan found that broken or distressed pavement causes backcalculated moduli's difference, and developed new revised backcalculation software. Yusuf Mehta found that pavement structure condition such as layer broken, depth, and temperature variation effected deflection bowl shape more than the inverse moduli. Cong Lin demonstrated distressed and broken semi-rigid base pavement generates anomalistic deflection bowl under FWD load, which diminishes the usefulness of traditional backcalculation methods. Friedrich W.J. described a fast computer program (PROBE) that calculates important mechanistic response parameters and determines the quality of data and the degree of structural integrity of the pavement layers under whole or broken conditions. For this reason, the new approach should be adopted to interpret FWD data in order to evaluation the sublayer structure condition of semi-rigid base asphalt pavement.

OBJECTIVE

1. Build the dynamic hypothesis FEM model of whole and broken or cracked semi-rigid base asphalt pavement.
2. Using systematic statistic regression analysis, study the deflection bowl index to interpret the degree of structural integrity of the semi-rigid base layer and quality of soil subgrade strength and set up the base layer and subgrade strength failure criteria.
3. Apply and validate the new method through practical project.

WHOLE AND BROKEN PAVEMENT FEM MODEL

The FWD load is assumed as 0.7Mpa peak haversine impulse load in 30ms duration time and distributing over a circular contact pressure area 15cm in radius. According the field semi-rigid base asphalt pavement distressed condition survey, transverse cracking, longitudinal cracking and block cracking is the main distressed type. The pavement FEM models simulate the whole integrity structure and distress structures considering different cracking types, position, depth, extension and tensity.

In order to set up a reasonable deflection data ware, a series of semi-rigid base pavement structure combinations and materials properties is considered as Table 1. Assembling all above factors by random, 11808 pieces of pavement model were got finally. It took half a year to calculate all the FEM models to generate the deflection data ware.

Table.1 Parameters for Semi-Rigid Base Asphalt Pavement FEM Model

Parameter	AC layer	Base layer	Subbase layer	Subgrade
Thickness (cm)	9, 12, 15, 18, 21	20, 30, 40	15, 20, 30, 40	Infinity
Modulus（GPa）	1, 2, 4, 7, 11	1, 3, 6, 9, 20	0.4, 2, 4, 7, 13	0.035, 0.1, 0.2, 0.35
Density（kg/m^3）	2400	2200	2100	1800
Poisson's Ratio	0.30	0.25	0.25	0.30
Damping (%)	5	5	5	5

Five types of deflection bowl shape indexes were used to obtain the layer modulus and structure integrity condition through systematically statistic regression software SPSS, including: direct deflection; curvature Index; Shape Factor; Slope index; Area index.

SUB-GRADE SOIL MODULUS CALCULATION AND FAILURE CRITERIA

From the above extensively deflection systematically statistic analysis results, it was found that among all the five types deflection indexes, combination of Curvature Index CI_7 and Shape factor F_8 can uniquely determine the subgrade modulus, seeing Figure 1. Essentially, this statistic relationship was regressed from all the whole and broken semi-rigid base asphalt pavements, so it was also effective for the severely cracked and broken pavement evaluation in rehabilitation projects. The definition of CI_7 and F_8 is as follow:

$$CI_7 = d_7 - d_8 \tag{1}$$

$$F_8 = \frac{d_7 - d_9}{d_8} \tag{2}$$

Where: d_7、d_8、d_9 respectively are surface deflection of Number7, 8, 9 geophone of FWD, μm.

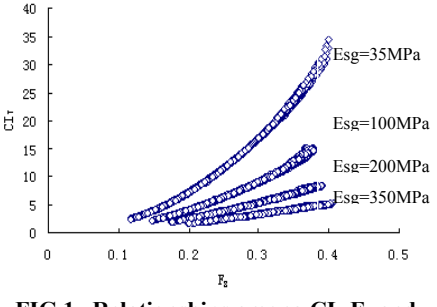

FIG.1. Relationships among CI_7,F_8,and subgrade modulus Esg

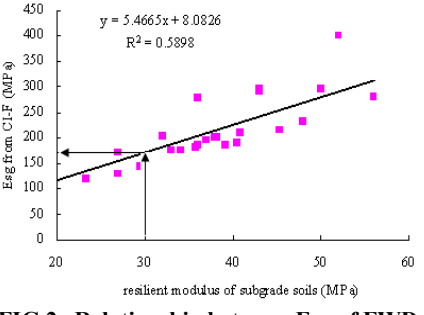

FIG.2. Relationship between Esg of FWD and static resilient modulus

In Huning Expressway rebuilding project and Jialiu Expressway rehabilitation project both in Shanghai, FWD deflection, Bearing Plate and Benkelman Beam deflection were well planned and measured on the whole and severely cracked pavement section. The

FWD was tested on the pavement surface, and at the same position the other tests were carried out on the subgrade surface right after the upper layer dismantled. By this way, for the same subgrade position dynamic modulus was calculated from FWD testing deflections using CI_7 and F_8 relationship; correspondingly, the static resilient modulus was calculated from the Bearing Plate and Benkelman Beam deflection testing data using standard method. The final calculation results were shown in FIG 2. the fine relationship between them demonstrates that the FWD sub-grade modulus calculation method is reasonable.

In asphalt pavement design specification of china, the static resilient modulus of subgrade soil is specified as no less than 30Mpa for high grade asphalt pavement. So according to the relationship between dynamic modulus back calculated Esg of FWD and static resilient modulus measured by bearing plate testing, Esg above the minimum limit 170MPa is defined as the expressway asphalt pavement's sub-grade failure criteria, shown as in Fig 2.

BASE LAYER BROKEN CONDITION DISCRIMINATION CRITERIA

Semi-rigid base layer contributes the large part bearing capacity of asphalt pavement, cracks and broken is its main deterioration types, so judging the base layer broken or not by NDT is the premise to determine whether to replace it in rehabilitation project. The above deflection data ware statistic regression shows that CI_3 is the most sensitive index to the base modulus and broken condition.

$$CI_3 = d_3 - d_4 \tag{3}$$

Where: d_3, d_4 are surface deflection of Number3, 4 geophone of FWD, respectively.

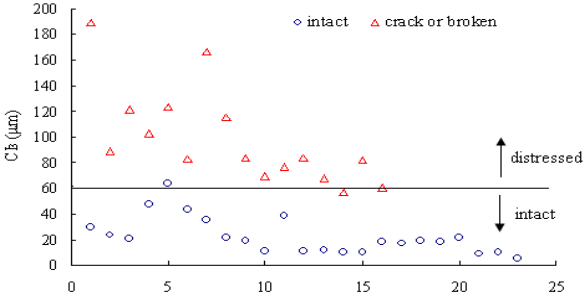

FIG.3. Intact and broken semi-rigid base layer comparison by CI_3 index.

This project chose a new expressway semi-rigid base asphalt pavement in Shanxi Province to test deflection basin by FWD, so its CI_3 results certainly reflected the whole intact base layer structure condition. Correspondingly, the same type pavement structure in Jialiu expressway rehabilitation project in Shanghai was tested by FWD. After surface deflection testing, surface asphalt layer was wiped out and semi-rigid base layer was well checked by experienced engineers by walk to find the cracked and distressed position in the semi-rigid base layer, these positions were screened on its

surface deflection. Totally, there were 23 effective testing points (listed on X-axis). By this way, it can get the relationship between CI_3 index and structural condition of the semi-rigid base layer. Both of the CI_3 index final result is shown in FIG 3.

Obviously, base layer in a distressed and broken condition, its CI_3 will increase over 60um, so this 60um CI_3 divining line is suggested to be the semi-rigid base layer broken condition discrimination criteria. Although there were 3 points not according with the law, this criterion can be accepted considering the complexity of field testing.

APPLICATION OF THE SUBLAYER STRENGTH EVALUATION METHOD

In May 2008, one 2 Km long road segment was tested by FWD in Jialiu Expressway to apply and verify the sublayer strength evaluation method to distinguish the failure or weak semi-rigid base asphalt pavement section. The deflections of nine geophones of total 35 points were drawn in Fig 4.

Using above relationship functions to calculate all of the subgrade soil dynamic modulus Esg and semi-rigid base layer CI_3, the results were shown in Fig 5 and Fig 6.

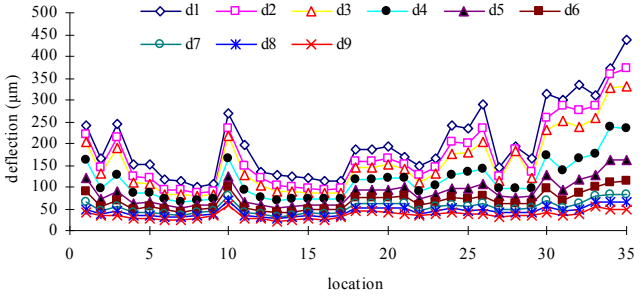

FIG.4. Intact and broken semi-rigid base layer condition comparison by CI_3 index

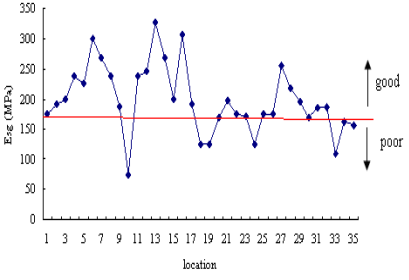

FIG.5. E_{sg} ranging in the tested segment

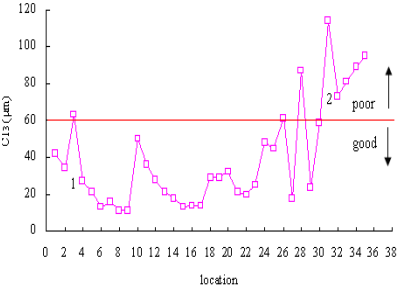

FIG.6. CI_3 index ranging in the tested segment

After milling out the surface asphalt layer, core the base layer at point 4 and 33, marking 1 and 2 in Fig6. The coring specimen showed that base layer at point 4 was

well and integrity, but the base was broken and loose at point 33 even not to get one integrity core. These was consistent with judgment result by CI_3 that base layer at point 33 was poor and broken. The Esg values from point 18 to point 35 in Fig 5 were almost below 170MPa, so the segment can be distinguished as poor subgrade section. In Fig 6, the base layer section from point 26 to point 35 was in broken condition. Finally in the rehabilitation practice, the section between points 24 to point 35 was designed to mill out asphalt layer and base layer, improve subgrade strength by mixing lime and compaction, and then rebuild the cement-treated base layer. This project got a satisfied appraise from all the attendant parts.

CONCLUSIONS

The investigations carried out have been particularly concerned with expressway rehabilitation project in Shanghai. This study has led to the following conclusions:

1. For the severely cracked and broken semi-rigid base asphalt pavement, it can not use FWD deflection bowl to estimate sublayer structural condition effectively for the rehabilitation project by backcalculation program based on the continuum elastic layer system.
2. Combination of Curvature Index CI_7 and Shape factor F_8 can uniquely determine the subgrade modulus even in the severely cracked and broken pavement condition. Whether Esg larger than 170MPa or not is defined as pavement subgrade failure criteria.
3. Curvature Index CI_3 can well indicate the semi-rigid base layer structural condition, the value 60um of CI_3 is suggested to be the semi-rigid base layer broken condition discrimination criteria.

Finally, due to space limitations, only the major parts are highlighted herein. The methods have been successfully applied in Jialiu Expressway rehabilitation project in Shanghai. Moreover further validation studies are ongoing in other practical projects.

REFERENCES

AASHTO. (1993). “AASHTO Guide For Design of Pavement Structures.” American Association of State Highway and Transportation Officials, Washington.

Cong Lin and Z.Y. Guo. (2006) “Analysis and Evaluation of Transverse-Cracked Semi-Rigid-Base Asphalt Pavements Using FWD Data.” *ASCE Geotechnical Special Publication*.

Friedrich W. Jung and Dieter F.E. Stolle. (1992). “Nondestructive testing with falling weight deflection on whole and broken asphalt concrete pavements*.” Transportation research record*, No.1377.

Lee, Y. (1997). “Condition Assessment of Flexible Pavements Using FWD Deflections.” Ph.D. thesis. North Carolina State University, Raleigh.

Uddin, W. and Pan, Z. (1997). “Finite Element Dynamic Analysis of Distress Asphalt Pavements.” *the 8th International Conference on Asphalt Pavements*, Washington.

Mehta, Y. and Roque, R. (2003). “Evaluation of FWD Data for Determination of Layer Moduli of Pavements.” *Journal of Materials in Civil Engineering*. Vol. 15, No. 1, January/February 2003, pp. 25-31.

Evaluation of Subgrade Modulus for Semi-Rigid Asphalt Pavement Using Deflection Basin Parameter

Zhaoxing Xie[1,2], Lin Cong[2], and Zhongyin Guo[3]

[1] Key Laboratory of Shanghai Road Engineering, Shanghai Municipal Planning Design and Research Institute, 609 Jianguoxi Road, Shanghai 200031, P.R. China;email::xzx9898@163.com

[2] Corresponding author. Key Laboratory of Road and Traffic Engineering of MOE,Tongji University, 4800 Caoan Road, Shanghai 201804,P.R. China; email: tjconglin@163.com

[3] Key Laboratory of Road and Traffic Engineering of MOE,Tongji University, 4800 Caoan Road, Shanghai 201804,P.R. China; email: zhongyin@tongji.edu.cn

ABSTRACT: The paper presents a method based on deflection basin parameters to evaluate the subgrade modulus. The paper develops 2-D and 3-D dynamic FEM to simulate semi-rigid asphalt pavement deflection basin response under FWD loading pulse. It is discovered that the relationship between Curvature Index CI_6 and Shape Factor F_6 may be used to determine the subgrade modulus. The moduli, thicknesses and cracked condition of upper layers have minimal effect on the relationship between CI_6 and F_6. Based on the calculation and analysis, the nomograph of subgrade modulus is presented.

INTRODUCTION

The Falling Weight Deflectometer (FWD) is an excellent device for evaluating the pavement structural. Most of the backcalculation programs which have been used to estimate moduli of pavement layers employ the static analysis as a forward model. Chang et al. (1992) concluded that static analysis-based programs often underestimate the subgrade modulus when deflections obtained from dynamic tests are used. Lee (1997) and Kim (2001) proposed the backcalculation procedures that incorporated the dynamic effect to assess the subgrade condition. However, the scope of their study is limited to full-depth asphalt pavement and aggregate base asphalt pavement. The semi-rigid base asphalt pavement (a pavement with semi- rigid material as base course and subbase course, such as cement-stabilized or lime fly-ash stabilized material) is one of major structural forms of asphalt pavement in China, and the performance and the state of stress of semi-rigid base asphalt pavement are quite different from full-depth asphalt pavement and aggregate base asphalt pavement. Thus, in the paper a backcalculation method to determine the subgrade modulus by deflection basin parameters is investigated for semi-rigid base asphalt pavement.

Pavement Model and Model Parameters

The 2-D FEM and 3-D FEM of semi-rigid base asphalt pavement are developed on the basis of ANSYS. The lengths of 2-D axi-symmetric FEM model are set to 8 m. The size of 3-D FEM model is 8m×8m×8 m. The nodal points at the bottom boundary are fixed whereas those on the vertical boundary are constrained from moving in the horizontal direction. The FEM mesh is designed finer at the loading area. At locations father from the load, the mesh becomes coarser to reduce the computation burden. For intact pavements when the load is away from the edges, a 2-D finite element model is proved to yield results suitable for the traffic loading analysis (Cho et al. 1996). However, transverse or longitudinal cracks can not be modeled using 2-D axi-symmetric finite elements since cracks do not occur in a circular shape (Lee 1997). Thus, in this paper the 2-D FEM model is employed for the intact pavements, and the 3-D FEM model is used to model pavement with transverse cracks.

Semi-Rigid base asphalt pavement is considered as a four-layered system with linear elastic material properties. It is known that soils are stress-state dependent materials. Because of the time limitations of the study, the stress-state dependent behavior will not be studied in the paper. The pavement layer properties are given in table 1. A half-sine load with 50KN peak load and duration of 0.03 s that simulates a typical FWD load is used for dynamic analysis. The deflection sensors are placed at distances of 0, 200, 300, 600, 900, 1200, 1500, 1800, and 2100 mm from the loading center. Because the use of transient data is too complicated, only peak deflections obtained from transient data are utilized in this study. The dynamic analysis shown that the effect of the stiff layer depth to the surface deflections vanishes when the depth of the stiff layer is greater than (or equal to) 6.0 m. Therefore, the 2-D and 3-D finite element model in this study could be considered semi-infinite when dynamic analysis is employed.

Table 1. Parameters for Semi-Rigid Base Asphalt Pavement

	AC layer	Base layer	Subbase layer	Subgrade
Modulus(MPa)	1000, 2000, 4000, 7000, 11000	1000, 3000, 6000, 9000, 20000	400, 2000, 4000, 7000, 13000	35, 100, 200, 350
Thickness (cm)	9, 12, 15, 18, 21	20, 30, 40	15, 20, 30, 40	Infinity
Density(kg/m^3)	2400	2200	2100	1800
Poisson's Ratio	0.30	0.25	0.25	0.30
Damping (%)	5	5	5	5

The single reflection crack is one of main distressed types for semi-rigid base asphalt pavement. Therefore, the single reflection crack is considered in this study and the computed deflections from cracked pavements will be compared against those of intact pavements to develop the subgrade strength evaluation method. Figure 1 presents the crack conditions in this study. The single reflection crack perforates both

base and AC layers and is placed between two sensors and at distances of 450, 750, 1050, and 1950 mm from the loading center, respectively. In this study the crack surfaces remain separate throughout the dynamic finite element analysis.

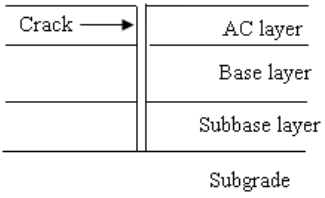

FIG. 1 Cracked condition considered in this study.

Curvature index and Shape Factor

The deflection basin parameters (DBPs) are good indicators of the pavement layer conditions. For example, the slope or deflection differences close to the load tend to reflect the strength of upper layers, while the outer deflections define the stiffness of the subgrade. All the DBPs investigated in this study are summarized in Table 2.

Table.2 Deflection Basin Parameters

Deflection Parameter	Formula
Curvature Indexes	$CI_1 = D_0 - D_{30}, CI_2 = D_{30} - D_{60}$ $CI_3 = D_{60} - D_{90}, CI_4 = D_{90} - D_{120}$ $CI_5 = D_{120} - D_{150}, CI_6 = D_{150} - D_{180}$
Shape Factors	$F_1 = \frac{D_0 - D_{60}}{D_{30}}, F_2 = \frac{D_{30} - D_{90}}{D_{60}}$ $F_3 = \frac{D_{60} - D_{120}}{D_{90}}, F_4 = \frac{D_{90} - D_{150}}{D_{120}}$ $F_5 = \frac{D_{120} - D_{180}}{D_{150}}, F_6 = \frac{D_{150} - D_{210}}{D_{180}}$
D_r Surface deflection, r Distance from the loading center (cm)	

Based on the synthetic database from dynamic FEM analysis, it is found that CI_6 and F_6 exhibits a better linear relationship in the log-log scale and the upper layers' moduli and thicknesses have no effect on the CI_6-F_6 relationship when subgrade modulus remains the same (Figure 2). Similar trends are discovered between other combinations of DBPs, such as CI_5 and F_5, CI_4 and F_4, CI_3 and F_3, as well as CI_2 and F_2 (Figure 2). It should be noted that when Curvature index is near the loading center, more variations are found in the CI-F relationship, which may be due to poor correlation between deflections close to the load and subgrade modulus. There is not a

linear relationship between CI_1 and F_1.

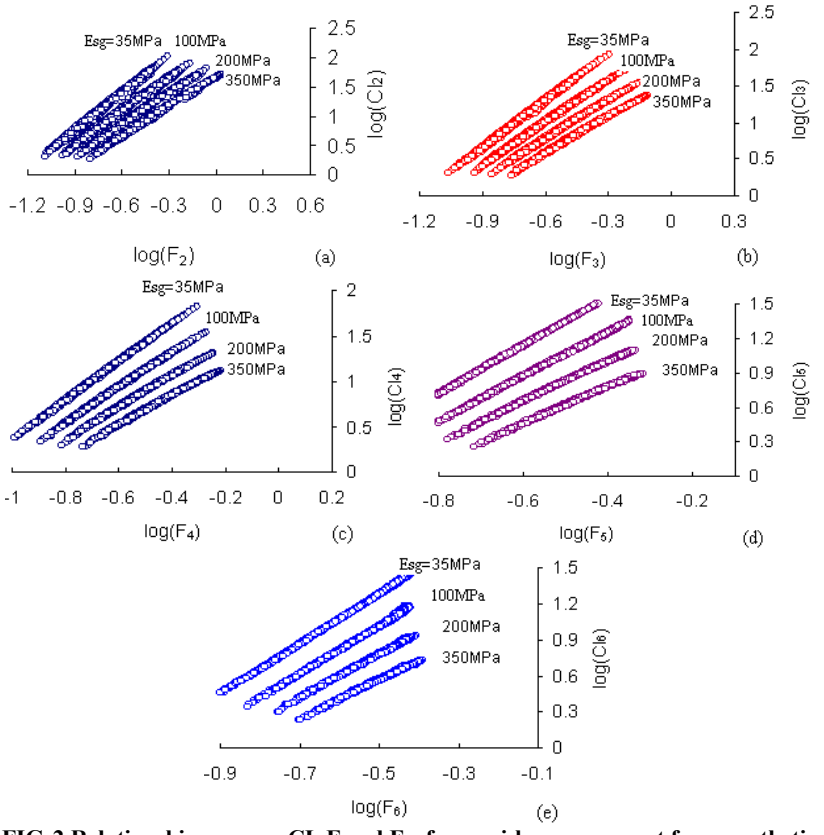

FIG. 2 Relationships among CI, F and E_{sg} for semi-base pavement from synthetic deflections

Effects of Cracked Conditions

FWD tests are often performed on cracked pavements. Therefore, the influence of the severe crack on the CI-F relationship is investigated. Figure 3 shows the effects of the single reflection crack on the CI-F relationship. In the figure, the symbol Crack-195, for example, refers to the single reflection crack at 195 cm from the loading center. It can be seen from Figure 3 that the effects of the single reflection crack on the CI-F relationships except for the CI_6-F_6 relationship are significant, when the reflection crack is placed close to the deflection sensors relating to Curvature index and Shape Factor. The effect of the single reflection crack on the CI_6-F_6 relationship is minimal, whether the single reflection crack is placed any distance from the loading

center. In Figure 3 (d), when the crack is farther away from the deflection sensors relating to CI_5 and F_5, the influence of the crack on the CI_5-F_5 relationship can be negligible.

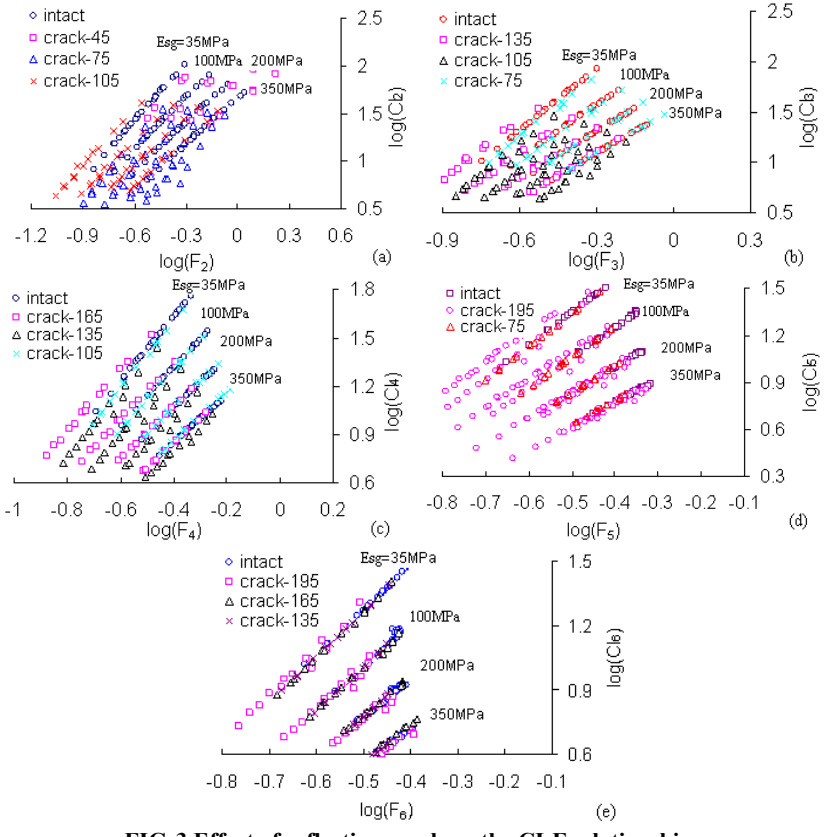

FIG. 3 Effect of reflection crack on the CI-F relationships

Nomograph of Subgrade Modulus

In summary, the combination of CI_6 and F_6 is the better indicator of the subgrade condition among the CI-F relationships. The CI_6-F_6 relationship may be expressed using the following equation.

$$\log(CI_6) = A * \log(F_6) + B \qquad (1)$$

Where, A and B are functions of E_{sg} and their values are presented in Table 3.

Table.3 Regression Constants for the CI_6-F_6 Relationship

E_{sg} (MPa)	A	B
70	2.0044	2.0987
125	1.8549	1.8423
175	1.7989	1.7165
225	1.7267	1.5942
275	1.6666	1.4907
350	1.5770	1.3525

A graphical method based Eq. 1 and Table 3 to predict E_{sg} is developed as shown in Figure 4. E_{sg} can be directly predicted by locating the point (CI_6, F_6) in Figure 4. It should be noted that this proposed method to determine Esg incorporates the dynamic effect.

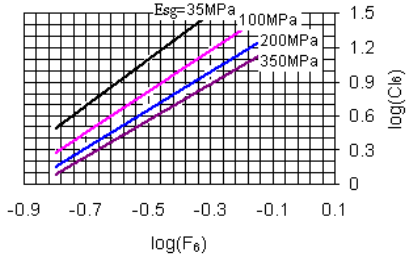

FIG. 4 Nomograph of subgrade modulus

CONCLUSIONS

The results presented in this paper have shown that the relationship between Curvature Index CI_6 and Shape Factor F_6 may be used to determine the subgrade modulus. The effect of the moduli, thicknesses and cracked condition of upper layers on the CI_6-F_6 relationship is minimal. The combination of CI_6 and F_6 is the better indicator of the subgrade condition among the CI-F relationships. This proposed method to determine E_{sg} incorporates the dynamic effect.

REFERENCES

Chang, D-W., Kang, Y. V., Roesset, J. M., Stokoe, K. H. II. (1992), "Effect of Depth to Bedrock on Deflection Basins Obtained with Dynaflect and Falling Weight Deflectometer Tests", *Transportation Research Record 1355*, TRB, National Research Council ,Washington, D.C., pp. 8-16.

Lee, Y-C. (1997). "Condition Assessment of Flexible Pavements Using FWD Deflections", Ph.D. thesis. North Carolina State University, Raleigh.

Kim, Y.R. (2001). "Assessing Pavement Layer Condition Using Deflection Data", NCHRP Project 10-48. North Carolina State University, Raleigh.

Cho,Y-h., B. F. McCullough and J. Weissmann. (1996). “Considerations on Finite-Element Method Application in Pavement Structural Analysis.” *Transportation Research Record 1539*, TRB, National Research Council, Washington, D.C., pp.96-101.

Comparison of FWD and Benkelman Beam in Evaluation of Pavement Structure Capacity

Liang Zhou[1], Qingfeng Wu[2], Jianming Ling[3]

[1]PhD Candidate, Key Laboratory of Road and Traffic Engineering of Ministry of Education, Tongji University, Shanghai P.R. China, 201804. Email: tinyzhou2014@sina.com
[2]Senior Engineer, Shanghai Highway Administration Department, Shanghai P.R. China, 200063. Email: wuqf5435@sina.com
[3]Professor, Key Laboratory of Road and Traffic Engineering of Ministry of Education, Tongji University, Shanghai P.R. China, 201804. Email: jmling01@yahoo.com.cn

ABSTRACT: This paper deals with the implementation and comparison of the falling weight deflectometer (FWD) and Benkelman Beam (BB) for pavement evaluation. Field measurements were made at an in-service pavement A30 in Shanghai, China. Based on the deflections measured by FWD and BB, the exact relation between the results of FWD and BB was established. The modulus of the subgrade was back-calculated with MODULUS, and the ratio of $E_{(sta)}$ and $M_{R(dyn)}$ was consistent with the suggestion of AASHTO 1993. Due to the fact that FWD test is very convenient and rapid, it indicates that FWD is an appropriate device for the pavement structural evaluation and the selection of optimal pavement rehabilitation strategy. It is believed that the dynamic modulus back-calculated from FWD test results can be used as a stiffness modulus for the subgrade of new pavement construction in China.

INTRODUCTION

With the increase of heavy traffic in China, highways become aged and the performances of roads become deteriorated. Different types of treatments, ranging from simple maintenance to complete reconstruction, are required to keep pavements safe and serviceable to the road users. Generally, laboratory and nondestructive testing (NDT) techniques are the main methods used to evaluate the structural integrity of pavements. Laboratory evaluation or existing pavements requires coring through pavement structure, which is expensive and time-consuming (EL-RAHIM 2001). Among NDT techniques, a widely used commercial NDT device is the falling weight deflectometer (FWD), which imparts an impulse load to the pavement. Complete deflection basins are used, with a procedure known as backcalculation, to estimate in situ elastic moduli for each pavement layer. The back-calculated results can be used to evaluate corrective measures such as overlays, rehabilitation or reconstruction (Chen et al. 2008).

Among the most widely used traditional methods for testing of pavement structural capacity are the plate loading (PLT) and Benkelman Beam (BB) tests. The two methods are widely used to establish the structural capacity of the pavement in situ. These tests are static and they are quite cumbersome to perform in situ. However, they are rather simple and easy to understand; therefore, they are quite widely used.

This paper focuses on comparing FWD and BB results of Section A30 in Shanghai, China.

TEST SECTION DESCRIPTION

The test section is the junction of in-service pavements located on A30 and A12 Highway in JiaDing District, Shanghai in China. The junction of A30 and A12 is a three-lane highway in each direction. The length of the junction is about 3.2 km. It is reported that there was an average of 5,000 vehicles per lane everyday in 2006. The percentage of trucks is approximately 42.7%.

The junction pavement was first constructed in 1998, and it was reconstructed for widening in 2004. The pavement structure comprised a total of three layers: 150mm asphalt surface, 450mm base/subbase, and subgrade. Due to heavy daily traffic in JiaDing District, the damages of the junction pavement were severe. Cracks first occurred in late 1999 and continued to occur during successive years. The pavement structure of the outside lane appears to be weaker than the inside lane, probably because it has carried roughly 90% of the regular traffic since 2000. There is also some subsidence at the junction, which lead to continual patching of the asphalt surface as a temporary remedy (Figure 1).

FIG. 1. Pavement condition on A30 test section

DATA COLLECTION

There have been several investigations reported using a falling weight deflectometer (FWD) to characterize the structural properties of pavements. Several researchers have used FWD to evaluate the structural performance or to determine material parameters (Zhou et al. 1997; Hossain et al. 1997; Pologruto, 2006).

Falling Weight Deflectometer

FWD test is performed by dropping a weight on the top of a circular plate with a

rubber-buffer system. The resulting load is a force impulse with duration of approximately 30 ms and the frequency distribution ranging from 0 to 50 Hz. The FWD load magnitude can vary from 30kN to 130kN by adjusting the drop height and/or drop weight. Several seismic sensors are mounted on FWD at some specified intervals along pavement surface. The sensors used in this study are in the center of the plate and at points located at 200, 300, 600, 900, 1200, 1500, 1800 and 2100mm, respectively, away from the center. The radius of the FWD loading plate is 150 mm, the FWD load in the study is 50 kN, and the pressure below the plate is assumed to be uniform (Xu, 2000). Figure 2 shows the typical deflection basin under the FWD setup (Mehta et al. 2003). The FWD test was repeated at each location followed by pavement coring for in-situ layer thickness of base and subbase, and the thicknesses served as inputs to backcalculate the layer moduli.

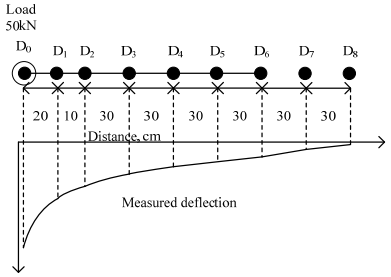

FIG. 2. Schematic of FWD loading configuration, deflection basin

The traditional backcalculation techniques use the deflection test conditions (i.e., load plate geometry, layer thickness) and estimated layer moduli to generate a theoretical deflection basin. The theoretical deflections are compared with the measured deflections and the error is minimized until the two basins show a good match. Subgrade elastic modulus $M_{R(dyn)}$ was backcalculated using the program MODULUS, developed at the Texas Transportation Institute. It uses a layered elastic computer program to generate a database of deflection basins for a range of layer moduli. A pattern search method and interpolation are employed to minimize the error between the measured and calculated deflection basins (EL-RAHIM 2001).

Benkelman Beam

According to the Specifications for Design of Highway Asphalt Pavement (JTG D50-2006) in China, the design deflection is the most important criterion to control the structural capacity of the asphalt concrete pavement. Therefore, the current deflection is an effective criterion to evaluate the remaining structural capacity of pavement. Highway Performance Assessment Standards (JTG H20-2007) provides an equation for determining the Pavement Structure Strength Index (PSSI). PSSI is a function of many data—Structure Strength Coefficient (SSI), design deflection of the pavement (l_d), testing deflection (l_0), and two model parameters which are readily

available from the statistical models. Deflection testing is done using the Benkelman Beam (BB) in China.

Field Test Methods of Subgrade and Pavement for Highway Engineering (JTJ 059-95) provide the following function (1) to determine the resilient modulus of the pavement.

$$E = \frac{2p\delta}{L}(1-\mu^2)\alpha \tag{1}$$

in which E=resilient modulus (MPa); p=average vertical load pressure (MPa); δ=radius of load (cm); L= deflection (0.01mm); μ=Poisson's ratio; α=coefficient of deflection. The process of BB was done according to the above specifications.

The equipments in the study were FWD and BB (Figure 3).

(a) (b)

FIG. 3. Devices used in structure capacity evaluation: (a)FWD and (b)BB

RESULTS AND DISCUSSION

Analysis of FWD and BB deflection data

Due to large amount of data available, the comparison is simply made in terms of test values in order to provide a gross evaluation. A correlation between BB and FWD deflection was thus achieved. The model was presented in the following form,

$$\text{FWD}=4.39\text{BB}-15.8 \tag{2}$$

The coefficient of determination, R^2, was 0.9578. It is observed that the results of FWD and BB are strongly correlated. The FWD users may use the correlation proposed above to transfer the measurements into BB to calculate PSSI. Taking also into account the fact that the test of FWD is much faster, simpler, and more accurate than BB, it is recommended to use FWD as a substitute to BB to evaluate the structural capacity. It is notable that the correlation above between FWD and BB is just for the junction of A30 and A12 in Shanghai, and the correlation for another section must be established with the field test data.

Analysis of FWD and BB modulus data

From the review of previous studies it becomes clear that there is a need, both from theoretical and practical viewpoint, to interpret FWD test results with a reliable and simple analysis technique. The BB results were analyzed to obtain the corresponding subgrade modulus defined as $E_{(sta)}$. Moreover, the dynamic subgrade modulus $M_{R(dyn)}$ was estimated from MODULUS using FWD test results. The mean value of the subgrade modulus for all tested points obtained by different methods of analysis is presented in Table1.

Table 1. Backcalculated Modulus of FWD and BB

Location	Result	Test No.			
		1	2	3	4
k167+360~ k167+390	$M_{R(dyn)}$/MPa	60.4	87.6	69.6	76.8
	$E_{(sta)}$/MPa	16.3	18.4	17.4	16.9
	$E_{(sta)}/M_{R(dyn)}$	0.27	0.21	0.25	0.22
k168+120~ k168+150	$M_{R(dyn)}$/MPa	68.5	112.6	57.0	79.6
	$E_{(sta)}$/MPa	17.8	21.4	11.4	18.3
	$E_{(sta)}/M_{R(dyn)}$	0.26	0.19	0.20	0.23
k168+690~ k168+720	$M_{R(dyn)}$/MPa	109.6	102.3	63.5	72.1
	$E_{(sta)}$/MPa	26.3	22.5	16.5	13.7
	$E_{(sta)}/M_{R(dyn)}$	0.24	0.22	0.26	0.19
k168+950~ k168+980	$M_{R(dyn)}$/MPa	61.2	57.7	64.4	76.5
	$E_{(sta)}$/MPa	15.3	12.7	11.6	17.6
	$E_{(sta)}/M_{R(dyn)}$	0.25	0.22	0.18	0.23

It is observed that the static analysis provides lower estimates compared to the corresponding back-calculated moduli of FWD. The ratios of $E_{(sta)}/M_{R(dyn)}$ are in the range of 0.18 to 0.27 with an average of 0.227. According to the aforementioned studies the dynamic modulus of the subgrade is higher than the static modulus obtained from traditional static analyses, such as the BB. This is consistent with the findings in AASHTO (1993) and other studies suggesting that dynamic testing provides a higher modulus compared to static, and the value of ratio varies from 0.2 to 0.33 (Ali et al. 1987; Von-Quintus et. al 1998).

Due to the fact that the FWD test is very convenient and rapid, it is accurate and inexpensive to evaluate the structure capacity. It is believed, also, that the dynamic modulus back-calculated from FWD test results can be used as a stiffness modulus for the subgrade of new pavement construction in China.

CONCLUSION

This study is an example of the evaluation of structural capacity with FWD, and the rehabilitation strategy was given based on the test results of FWD. It should be clarified that subgrade soil conditions are nonuniform, hence the modulus back-calculated is essentially an average value, and the rehabilitation strategy was

made on the basis of many factors. The main conclusions derived from the experimental evaluation presented herein are the following:

1. The exact relation between the results of falling weight deflectometer (FWD) and Benkelman Beam (BB) is established, and the coefficient of determination is very high. Therefore, it is recommended that the employment of FWD to substitute BB to evaluate the structural capacity.
2. It should be noted that the correlation between FWD and BB is merely for the junction of A30 and A12 in Shanghai, and the correlation for another sections must be established with the field test data.
3. The ratio of $E_{(sta)}$ and $M_{R(dyn)}$ ranges from 0.18 to 0.27, this finding is consistent with the findings in AASHTO (1993) and other studies suggesting from 0.2 to 0.33.
4. Due to the fact that the FWD test is very convenient and rapid, it is believed that the dynamic modulus back-calculated from FWD test can be used as a dynamic parameter for the subgrade of the structure capacity evaluation or new pavement constructions in China.

ACKNOWLDGEMENTS

This study was funded by a Foundation Grant of Shanghai Municipal Engineering Bureau (2008-1-4). The support is gratefully acknowledged. This research would not have been possible without QiuXin for his field support and insight in the data analysis. Grateful thanks are due to the workers for FWD data and BB data collection.

REFERENCE

Ali N.A., and Khosla N. P., "Determination of Layer Moduli Using a Falling Weight Deflectometer," *Transportation Research Record 1117*, TRB, National Research Council, Washington, DC., 1987, pp. 1-10.

ASHRAF M. ABD EL-RAHIM (2001). "In-situ tests for subgrade resilient modulus characterization" *The University of Mississippi*.

Bing Xu(2000). "Assessing pavement layer condition using FWD deflection data." *North Carolina State University*

Dar Hao Chen and Tom Scullion(2008). "Forensic Investigations of Roadway Pavement Failures". *Journal of Performance of Constructed Facilities*, Vol.22(1), 35-44.

Hossain, M., Habib, A., and LaTorella., T. M. (1997). "Structural layer coefficients of crumb rubber-modified asphalt concrete mixtures." *Transportation Research Record 1583*, Transportation Research Board, Washington, D.C., 62–70.

H. L. Von-Quintus, and B. M. Killingsworth, "Comparison of Laboratory and In situ Determined Elastic Layer Moduli," A Paper Presented at the 78th Annual Meeting of the Transportation Research Board, Washington, DC., January 1998.

Michael Pologruto(2006) "Study of In situ Pavement material properties determined from FWD testing " *Journal of Transportation Engineering*, Vol. 132(9),742-750.

Yusuf Mehta, A.M and Reynaldo Roque (2003), "Evaluation of FWD Data for Determination of Layer Moduli of Pavements." *Journal of Materials in Civil Engineering*, Vol. 15(1):25-31.

Zhou, H., Rada, G. R., and Elkins,G. E. (1997). "Investigation of backcalculated moduli using deflections obtained at various locations in a pavement structure." *Transportation Research Record 1570*, Transportation Research Board, Washington, D.C., 96–107.

Applications of Ground Penetrating Radar to Road Pavement: State of the Art and Novelties

Andrea Benedetto[1] and Maria Rosaria De Blasiis[2]

[1]Associate Professor, Dept. Sciences of Civil Engineering, University Roma Tre, via Vito Volterra, 60, 00146 Rome, Italy benedet@uniroma3.it
[2]Full Professor and Director, Inter Univerities Research Center on Road Safety (CRISS), University Roma Tre, via Vito Volterra, 60, 00146 Rome, Italy deblas@uniroma3.it

ABSTRACT: Ground Penetrating Radar (GPR) has been using in the pavement engineering since almost twenty years. The traditional and mostly diffused application is the evaluation of the thicknesses of pavement layers. Such a measure can be done at traffic velocity with no impact on safety and operability of the roads. The actual frontier is the evaluation of the thickness in the case of thin layers. More recently GPR has been used to evaluate the pavement conditions. In the paper we present the methods for the electronic detection of pavement singularities as for moisture and bulk densities evaluation. At this regards a novel approach in the frequency domain that has been recently developed and validated is presented in the paper.

INTRODUCTION

Non Destructive Technologies (NDTs) have been recently developed and applied to many sectors of engineering and environmental protection. NDTs are efficient, effective and reliable; moreover they are very significant if compared to traditional measurements and tests. Also in the field of pavement engineering NDTs are becoming always more diffused and utilized. In many cases they are assumed as a current standard for testing and monitoring. The importance of NDTs for pavement engineering is evident if we consider the actual poor conditions of roads pavements in many countries and the limited financial resources that governments plan to spend for maintenance. In this framework Ground Penetrating Radar has assumed a great relevance and it is used by many agencies for damage prevention, evaluation and monitoring so as for maintenance optimization (Smith and Scullion, 1993; Maser, 1996; Saarenketo and Scullion, 2000). More recently new principles for preventing damage that are based on safety aspects have been introduced in the pavement maintenance (Tighe and alii, 2000; Benedetto and Angiò, 2002). Under this perspective new objectives have been requested to monitoring technologies as: celerity of measurements, low cost, limited interference with traffic flow, safety of work-measurement zones, reliability and statistic significance of diagnosis, damage causes diagnostics. Referring to those

objectives, NDTs and GPR in particular are very effective tools. This paper presents a state of the art and an overview about the applications of GPR in the field of pavement engineering.

LAYERS THICKNESS EVALUATION

Principles and method

Standards for the application of radar in pavement engineering have been developing for few years (i.e. ASTMa, 1999; ASTMb, 1999). The principles of using GPR reflections to compute layer properties have been determined by Maser and Scullion (1991). By monitoring time delays between the peaks of the reflected signals, it is possible to evaluate layer thicknesses through the well known following equation:

$$h_1 = \frac{c \cdot \Delta t_1}{\sqrt{\varepsilon_a}} \tag{1}$$

Where, ε_a is the dielectric value of the asphalt surfacing layer, h_1 is the thickness of the top layer, c is the speed of radar wave in air; Δt_1 is the time delay between the peaks.

Resolution of the measurements

Radar resolution depends on the wave length of the signal. If f is the frequency [GHz] and v the propagation velocity [mm/ns] of the signal, the wave length λ is v/f [mm]. The propagation velocity depends on the dielectric characteristics of low-loss materials as it follows: $v = c/\varepsilon^{0.5}$ where ε is the dielectric permittivity and c the free space velocity of an electromagnetic wave ($3x10^8$ m/s). In dry asphalt ε is 2 to 4, in wet asphalt ε is 6 to 12 and v is 70 to 210 mm/ns. The theoretical resolutions of GPR are from about 90 mm, for a center frequency between 0.8 and 2.3 GHz, to 25 mm for f = 2.6 to 7.7 GHz.

The resolution of a GPR with two on-the-road antennas (600 and 1600 MHz) has been experimentally validated on a new pavement in real scale, in which 12 sections with different layers' thicknesses were developed (Benedetto and alii, 2006). In this work, according to other literature, the average velocity of the wave in the first and binder asphalt layers is 105.13 mm/ns using 600 MHz antenna, the standard deviation is 7.81 mm/ns; and v is 103.72 mm/ns using 1600 MHz antenna, with a standard deviation 12.51 mm/ns. The thickness of these two layers is about 110 mm. For 6 pavement sections the first layer is 40 mm and the second is 70 mm, for the other 6 the first layer is 60 mm and the second is 50 mm. The interface at 110 mm is unambiguously detected using both the antennas (error < 10%). The detection of the interfaces at 40 and 60 mm is affected by relevant uncertainty using the 1600 MHz antenna. In conclusion, the best configuration for GPR, according to penetration and resolution needs, is with two antennas (Scullion and alii, 1994; Benedetto and alii, 2003; Benedetto and alii, 2004): about 600 MHz, for base and sub-base, and 2 GHz, for thin layers (maximum 40 mm).

Reliability and thin layers evaluation

Two questions affect the evaluation of the thin layers: (1) the resolution of GPR, that has been yet shortly discussed and (2.1) the signal's analogical characteristics as (2.2)

the signal's processing procedures to reduce the noise from antenna's "end reflection" (main bang or ringing) that crucially biases the interface's peak from thin layers (Delbò and alii, 2000; Benedetto and alii, 2004). The problem of interference with the end reflection is not well known yet (Scullion and alii, 1994; Roberts, 2000). The end reflection has been studied as intrinsic effect of TX-RX systems. Here the problem of interference between this reflection and the first reflection from the surface asphalt thin layer is enlightened. In this case, the first reflection is convolved with the ringing of antenna. To avoid or reduce this interference two strategies are possible.

End reflection rises when antenna transmits the signal pulse and at the same time receives back the echo of the transmitted signal. If the transmitted pulse covers a time domain so long that the first reflection interferes with it, the signal processing is often unreliable. To solve the end reflection from the first reflection it is possible to reduce the duration of pulse increasing the frequency of signal. Of course the sampling period has to be strongly increased, but the resolution of Radar improves.

In general, Ground Penetrating Radar signal can be expressed as it follows:

$$Y(t) = y_1(t) \otimes y_2(t) = \int_{-\infty}^{\infty} [y_1(t) \cdot y_2(t-\tau)]\, d\tau \tag{2}$$

where $Y(t)$ is the received signal as the convolution between $y_1(t)$, the interface reflection, and $y_2(t\text{-}\tau)$, the end reflection, t is time and τ is the delay. Numerically it is:

$$\underline{A} = \underline{X} \cdot \underline{H} \tag{3}$$

Where, $\underline{A}$ is the matrix of received signals ($a_{i,j}$ is the amplitude at time $t=i$ and at the abscissa $s=j$) $\underline{X}$ is the signal reflected by the first interface that is convolved with $\underline{H}$ that is the end reflection. In many cases we must use the approach of the "pseudo-inverse" matrix ($\underline{H}^{1}_{pinv}$), of the same dimension of $\underline{H}$, so that:

$$\underline{H} \cdot \underline{H}^{-1}_{pinv} \cdot \underline{H} = \underline{H} \text{ and } \underline{H}^{-1}_{pinv} \cdot \underline{H} \cdot \underline{H}^{-1}_{pinv} = \underline{H}^{-1}_{pinv} \tag{4}$$

With the obvious consequence that $\underline{H} \cdot \underline{H}^{-1}_{pinv}$ and $\underline{H}^{-1}_{pinv} \cdot \underline{H}$ are Hermitian or self-adjoint. We remember that a matrix is Hermitian if $[\underline{AT}]^* = \underline{A}$ where * means complex conjugate and $\underline{T}$ means transposed matrix.

In conclusion we obtain a linear system in which each equation is represented by:

$$x_{i,j} = \sum_{k=1,n} a_{i,k} \cdot (h^{-1}_{pinv})_{k,j} \tag{5}$$

DEFECTS AND DAMAGES DIAGNOSIS IN PAVEMENT

Detection and classification

It is possible to identify three different categories of road damages that can be electrically distinguished by GPR (Benedetto and alii, 2004): point located singularity inside a homogeneous layer (i.e. void or water), long wave length singularity between

two different layers (i.e. depressions), and short wave length singularity between two different layers (i.e. pumping).

The road is scanned in a sequence of vertical radar reflections. The vertical sweep samples are regularly spaced. The proposed algorithm considers the generic time delay (τ_{ij}) of a radar signal, where (j) is the index of the longitudinal or transversal road scan sample and (i) is the index of the depth sample. The algorithm is based on a threshold analysis between the delay average ($<\tau_i>$), induced by a continuous interface of the layer (i), and the generic time delay (τ_{ij}). If the difference between these two delays is less than a minimum fixed threshold value (δ) the layer is a horizontal straight outline. On the other hand, if the above-mentioned difference is greater than the adopted threshold value, the analysis yields the presence of a singularity.

If e is the error induced by the singularity, the delay is recursively expressed as:

$$\tau_i^{(j)} = \tau_i^{(j-1)} + e \tag{6}$$

It is possible to compare this stochastic variable e with a second threshold. With reference to the above damage categories, it is:

$$\begin{aligned} \| e \| &> \lambda^* \quad \text{short wave length singularity} \\ \| e \| &< \lambda^* \quad \text{long wave length singularity} \end{aligned} \tag{7}$$

Where, λ^* is the second threshold value.

Structural damages

Structural damage in road pavements is frequently directly connected with the percentage of moisture in its deepest layers or in the sub-grade soils. Water infiltration and clayey soil pumping are the most important causes of the decrease of bearing capacity of the unbound layers (Al-Qadi et aii., 2004; Diefenderfer et alii, 2005). Measurement of soil water content is also important because as it increases, stiffness decreases, therefore the strains increase. A widely used method to measure soil water content, bulk electrical conductivity, and deformation of rock is based on Time Domain Reflectometry system (TDR). TDR inspection of wide roads is not generally efficient in terms of time and cost. On the contrary, GPR is suitable to the aim, in fact it is non destructive and quick also if used at a large scale. The relation between the dielectric constant of soils and their volumetric water content has been extensively studied in the past and various empirical relations have been proposed. Topp et alii (1980) suggested one among the more commonly used ones, which is supposed valid for any mineral soil material. A more theoretical approach to relate soil water content and permittivity is based on dielectric mixing models, which use the volume fractions and the dielectric permittivity of each soil's constituents to derive an approximate relationship (e.g. Saarenketo, 1998; Friedman, 1998; Hubbard and alii, 2002; Huisman et al., 2003; Serbin and Or, 2003; Benedetto, 2004). More recently the EMA (Effective Medium Approximation) model has been experimentally validated by Fiori et alii (2005). A new method based on signal processing in the frequency domain is mentioned in the following section (Benedetto and alii, 2009; Benedetto and Fattorini, 2009).

Measurements of moisture content in the time and frequency domain

Methods for measuring the moisture content under pavement have been investigated in the past (Saarenketo and alii, 1994; Grote and alii, 2005). The proposed method is based on Ground Penetrating Radar inspection and considers two-dimensional analysis of moisture distribution under pavement. The methodology, its accuracy and reliability has been experimentally tested (Benedetto and Pensa, 2006; Benedetto and Pensa, 2007). It is generally accepted that moisture content variation under pavement depends on the cycles of repeated loads increasing the pore water pressure. It is known that: structural damage of pavement is caused by water and plastic soil infiltration in sub-asphalt layers, it is not visible until the pavement cracks and consequently repair costs get high, groundwater and rain infiltration depend on the permeability of sub-asphalt layers, pavement permeability, initial (i.e. initial moisture, initial hydraulic permittivity) and boundary conditions (i.e. hydraulic permittivity of soils and pavement, drainage systems, rain intensity), infiltration can be studied according to the hydraulic laws. If we assume that: all the boundary and initial conditions are known and the spatial distribution of moisture under pavement is known at a specific time instant. Therefore: it is possible to invert the hydraulic laws of infiltration to extract the spatial distribution of the hydraulic permittivity from the moisture distribution. Finally knowing the hydraulic permittivity distribution in the unbound layer, it is possible to diagnose accurately if cohesive soil has penetrated the sub-asphalt layers. The analytical procedure is based on a Monte Carlo simulation cascade (Benedetto and Pensa, 2007). This method, developed in the time domain, is very effective but not very efficient, in fact a preventive calibration and an onerous computational phase is needed. Very recently a new approach, more efficient, has been developed in the frequency domain.

The GPR signals propagate in an unsaturated soil according to the theory of Rayleigh scattering (Benedetto and alii, 2009; Benedetto and Fattorini, 2009). In fact the "droplets" of water and the water adsorbed to the soil particles have dimensions much smaller rather than the wavelength of the EM waves. As the moisture content increases, the frequency spectrum shifts towards lower frequencies, according to Rayleigh scattering. These expectations are confirmed by the experiments. This phenomenon provides a way to measure the water content by using an FFT to find the shift of the peak of the frequency spectrum. A great advantage of this method is that no calibration is needed. This method has been tested also by the author in the field of pavement engineering (Benedetto and alii, 2009).

Principles for bulk density evaluation

Compaction of sub-grade and soils has the effect to reduce the voids in the composite material and, consequently, to increase the density. This reduction depends on two main facts: (1) the solid grains joint more closely, (2) some grains break and the little broken parts can fill some voids. It has been shown that the dielectric value increases when voids decreases. But the correlation is weak. Saarenketo and Scullion (2000) found an exponential regression curve $\varepsilon \propto \exp(-\theta)$ where θ is the voids content ($R^2=0.72$).

Analogously Benedetto and Benedetto (2002) found parabolic regression curves ($R^2=0.42 \div 0.87$). The reason of this weakness in the regression function is that the dielectric properties of compacted and loose material are not very different when it is

dry. In fact air dielectric permittivity (ε=1) and dry aggregate dielectric permittivity (about ε=2-6) are not very different.

ASPHALT MIX CHARACTERISTICS

GPR has been also used to evaluate asphalt mixes characteristics such as voids content and bitumen content (Aultman-Hall and alii, 2004). Liu and Guo (2002) have investigated firstly the correlations among the value of dielectric constant and the bitumen and voids content. A more comprehensive work has been presented by Benedetto and alii (2006) at the 11th International Conference on GPR. This is a real scale work where about hundred cores have been extracted after the GPR inspection. It has been found that the dielectric constant and voids content are inversely correlated with R^2 about 0.5. The GPR inspection has been carried out using two antennas at 600 and 1600 MHz. R^2 is greater (about 0.6) in the case of the 600 MHz antenna. In the experiment the propagation velocity of GPR signal increases about 5% as the voids content increases about 10%. Very poor correlations have been obtained in the case of dielectric constant value and bitumen content. Moreover the results are often contrasting. The reasons are probably the following two: during compaction (using the same energy) (1) voids are filled by bitumen and the dielectric constant increases because the dielectric constant of air is lower rather than the bitumen's one or (2) the bulk density of the material generally increases and the dielectric constant changes as the proportion of bitumen, air and aggregates changes. Consequently the bitumen content is very weakly correlated to the dielectric constant value and more in depth investigations are needed.

CONCLUSIONS

In conclusion GPR has been used for many applications in the field of pavement engineering. Layer thickness evaluation with GPR is actually a reliable and cost effective application. The case of evaluation of thin layers is not completely solved but good results and methods have been proposed basing on software and hardware improvements. The applications for pavement damage monitoring and diagnosis are very interesting. Especially the last novelties for moisture content evaluation under pavements have yet given significant and relevant results.

ACKNOWLEDGMENTS

The authors appreciate the support of the Ingegneria Dei Sistemi S.p.A. (IDS – Italy) providing the GPRs and thank Mr. Spartaco Cera for technical assistance.

REFERENCES

Al-Qadi I.L., Lahouar S., Loulizi A., Elseifi M.A., Wilkes J.A. (2004). "Effective approach to improve pavement drainage layers." *J. of Transp. Eng.*, 130(5), 658-664.

$ASTM_a$ American Society for Testing and materials (1999a). "Standard test method for determining thickness of bound pavement layers using short-pulse radar." Annual

Book of ASTM Standards, D 4748-98, 470-473.

ASTM$_b$ American Society for Testing and materials (1999b). "Standard test method for evaluating asphalt-covered concrete bridge decks using GPR." Annual Book of ASTM Standards, D 6087-97, 654-657.

Aultman-Hall L., Jackson E., Dougan C.E., Choi S.N. (2004). "Models relating pavement quality measures." *Transportation Research Record*, 1869, 119-125.

Benedetto A., Benedetto F. (2002). "GPR experimental evaluation of sub-grade soil characteristics for rehabilitation of roads." *Proc. IX Int. Conf. GPR* - Santa Barbara California USA.

Benedetto A., Angiò C. (2002). "Diagnosi del degrado delle pavimentazioni con Georadar e sicurezza stradale." *Proc. XII Convegno nazionale della SIIV*, Parma, Italy.

Benedetto A., Benedetto F., De Remigis E. (2004). "Problems and perspectives in evaluation with GPR of road pavement's thin layers." *Proc. VIII Int. Conf. on AATT* (ASCE) China.

Benedetto A., Angiò C., Manacorda G., Pinelli G., (2003). "GPR automatic inspection of road pavement layer thickness." *Proc. 3rd Int. Symp. on Rehab. Maint. Roads Mairepav*, Guimares, Portugal.

Benedetto A. (2004). "Theoretical approach to electromagnetic monitoring of road pavement." *Proc. 10th Int. Conf. GPR*, Delft, the Netherlands.

Benedetto A., Benedetto F., De Blasiis M.R., Giunta G. (2004). "Reliability of radar inspection for detection of pavement damages." *Int. J. of Road Material and Pavement Design*, Hermes Science, Vol.5 (1), 93-110.

Benedetto A., De Blasiis M.R., Crispino M., Pensa S. (2006). "Analysis of hot-mix asphalt properties: a full scale experiment", *11th Int. Conf. on GPR*, Columbus, USA.

Benedetto, A., Pensa S. (2006). "Diagnosis of pavement structural damages using GPR." *11th Int. Conf. GPR*, Columbus, USA.

Benedetto A., Pensa S. (2007). "Indirect diagnosis of pavement structural damages using surface GPR reflection techniques." *J. Appl. Geophysics*, Elsevier, 62: 107–123.

Benedetto A. Fattorini F. (2009). "GPR signal processing in frequency domain for efficient pavement damage prediction." *Proc. Mairepav*, Turin, Italy.

Benedetto A., D'Amico F., Fattorini F. (2009). "Measurement of moisture under road pavement: a new approach based on GPR signal processing in frequency domain." *Proc. Intern. Workshop Adv. GPR*, Granada, Spain.

Delbò, S., Gamba, P., Roccato D. (2000). "A Fuzzy Shell Clustering Approach to Recognize Hyperbolic Signatures in Subsurface Radar Images." *IEEE Transactions on geoscience and remote sensing*, 38(3), 1447-1451.

Diefenderfer, B., Galal K., Mokarem D. (2005). "Effect of Subsurface Drainage on the Structural Capacity of Flexible Pavement." VTRC05-R35; Pr. No. 66818, 29p.

Fiori A., Benedetto, A., M. Romanelli, (2005). "Application of the effective medium approximation for determining water contents through GPR in coarse-grained soil materials." *Geophysical Research Letters*, 32, L09404, doi:10.1029/2005GL022555.

Friedman S. P. (1998). "A saturation degree-dependent composite spheres model for describing the effective dielectric constant of unsaturated porous media." *Water*

Resour. Res., 34, 2949– 2961.
Grote K., Hubbard S., Harvey J., Rubin, Y. (2005). "Evaluation of infiltration in layered pavements using surface GPR reflection techniques." *J. Appl. Geoph.*, 57, 129–153.
Hubbard S., Grote K., Rubin Y. (2002). "Estimation of nearsubsurface water content using high frequency GPR ground wave." *Leading Edge of Exploration*, Society of Exploration Geophysics, vol. 21 (6). 552– 559.
Huisman J.A., Hubbard S.S., Redman J.D., Annan A.P. (2003). "Measuring soil water content with ground penetrating radar: A review." *Vadose Zone J.*, 2, 476– 491.
Liu L., Guo T. (2002). "Dielectric property of asphalt pavement specimens in dry, water-saturated and frozen conditions." *Proc. 9th Int. Conf. GPR, Santa Barbara*, USA.
Maser K.R. (1996). "Condition assessment of transportation infrastructure using ground-penetrating radar." *J. Infrastruct. Syst.*, 2 (2), 94– 101.
Maser K., Scullion T. (1991). "Automated detection of pavement layer thickness and subsurface moisture using Ground Penetrating Radar", *TRB paper.*
Roberts R. (2000). "Examination of the effect of antenna surface distance on the radiation of a GPR antenna." *Proc. 8th Intern. Conf. GPR*, Gold Coast Australia.
Saarenketo T. (1998). "Electrical properties of water in clay and silty soils." *J. Applied Geophysics*, 40, 73–88.
Saarenketo T., Scullion T. (2000). "Road evaluation with ground penetrating radar." *J. Appl. Geophys.*, 43, 119– 138.
Saarenketo T., Nikkinen T., Lotvonen S. (1994). "The use of ground penetrating radar for monitoring water movement in road structures." *Proc. 5th Intl. Conf. on GPR*, Kitchener, vol. 3 of 3, pp. 1181– 1192.
Scullion T., Lau C.L., Chen Y. (1994). "Pavement evaluations using ground penetrating radar in Texas." *Proc. 5th Intl. Conf. on GPR*, Kitchener, 1, 449– 463.
Serbin G., Or D. (2003). "Near-surface soil water content measurements using horn antenna radar: methodology and overview." *Vadose Zone J.*, 2, 500–510.
Smith S., Scullion T. (1993). "Development of ground-penetrating radar equipment for detecting pavement condition for preventive maintenance." Final Rep., Strategic Hwy. Res. Prog., Project H-104A, Nat. Res. Council, Washington, D.C.
Tighe S, Li N., Falls L.C., Haas R. (2000). "Incorporating road safety into pavement management." *Transportation Research Record*, 1699, 1-10.
Topp G.C., Davis J.L., Annan A.P. (1980). "Electromagnetic determination of soil water content: measurements in coaxial transmission lines." *Water Res.Res.*, 16(3), 574–582.

Research on detection to Moisture Content of Flexible Pavement by GPR

Chunlin Li [1], Linchang Miao, Ph.D. [2], and Jingchao Yue, Ph.D.[3]

[1]Ph.D. Student, Institute of Geotechnical Engineering, Southeast University, Nanjing, China, 210096; Lecturer, Department of Civil Engineering, Tongling University, China, 244000, lichunlin111@126.com
[2]Professor, Institute of Geotechnical Engineering, Southeast University, Nanjing, China, 210096, lc.miao@seu.edu.cn
[3]Professor, School of Environment and Water Conservancy, Zhengzhou University, Zhengzhou, china, 450002, yuejc@zzu.edu.cn

ABSTRACT: Moisture content is an important parameter due to its important influence on the serviceability of the pavement. Drainage is considered as one of most important factors in pavement projects. When water is trapped inside a flexible surface structure layer, it deteriorates surface layer and causes stripping, raveling and potholes in Hot Mixing Asphalt (HMA). Traditional methods to evaluate the pavement, for example, core-drilling can not meet the requirement to estimate the pavement moisture content effectively, because there are many disadvantages in this method such as low efficiency, bad representation, especially destruction to the pavement. Based on the above analysis, a new rapid, high efficient and nondestructive technology was proposed in this study. Ground Penetrating Radar (GPR) was developed recently, which is used widely for the pavement thickness detection. In this study, GPR was conducted to detect the moisture content of flexible surface, and the results demonstrate the effectiveness of the new kind.

INTRODUCTION

GPR is developed recently and is a nondestructive technology for the pavement thickness detection. GPR is based on radar principles and technology. A GPR system consists of transmitter, receiver, processor, and data display. GPR works at the surface of the pavement and transmits electromagnetic wave to the pavement layers, when the electromagnetic wave reaches the pavement layers, it will be reflected at the interface of two different kinds of medium. As we know, different medium has different dielectric properties. The reflected wave will be received by the receive antenna and transformed to digital signal. The data can be saved automatically to the computer of GPR, which can be utilized to determine the property, situation, location and moisture of medium. The last is the objective of this paper.

Highway embankment typically includes three layers: surface structure layer, base

layer and subgrade layer. The typical thickness of the surface structure layer has a range from 100 to 800mm. This layer is constructed by a dense graded HMA material. The thickness of the base course generally varies between 200 to 400mm. This is basically a crushed stone layer, which can either be untreated or stabilized by adding cement or asphalt into it. Subgrade layer is the surface of a roadbed upon which the pavement structure and shoulders are constructed. This subgrade supports all the layers mentioned above. When a location has good original soil, the subgrade can be simply treated using lime-soil layer; otherwise, ground improvement is needed.

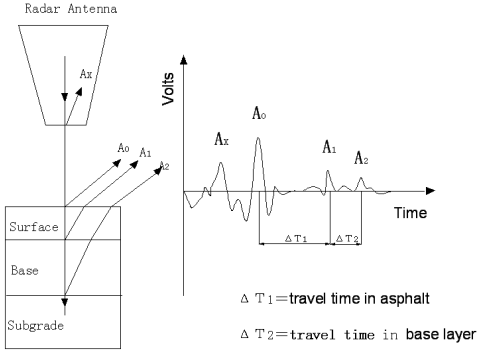

FIG. 1. GPR trace fundamentals

Figure1 shows an example trace from a two-layer pavement model (Dwayne Arthur Harris, 2006). There are four pulse waveforms in the example trace: Ax is amplitude of the waveform from radar wave reflected off the end of the antenna; A0 is amplitude of the waveform from the radar wave reflected off the pavement surface (surface echo); A1 is amplitude of the waveform from the radar wave reflected off the base of the asphalt layer (first interface return); and A2 is amplitude of the waveform from the radar wave reflected off the bottom of the base layer.A0,A1 and A2 can be used to estimate the dielectric values of a given material. For surface structure layer, the dielectric value of HMA can be calculated using Equation (1) (Brawijaya, 2005).

$$\sqrt{\varepsilon_{ac}} = \frac{1 + A_0 / A_m}{1 - A_0 / A_m} = \frac{A_m + A_0}{A_m - A_0} \tag{1}$$

where ac is dielectric constant of pavement surface asphalt mixture; Am is amplitude of the waveform reflected off metal plate.

THE PRINCIPLE OF GPR TO DETECT MOISTURE OF PAVEMENT

HMA is a mixture of aggregates, water, asphalt and air. Aggregates have a dielectric constant between 6 and 8, and asphalt has a dielectric constant between 2.4 and 3, and air has the dielectric constant of 1, while water has the dielectric constant of 81. Based on the studies on dielectric properties of HMA, the content of asphalt and mixed

manner have a weak influence on dielectric properties of HMA compared with moisture content of asphalt mixture (Huang , et.al., 2008).

The dielectric constant about HMA can be calculated by following equation：

$$\sqrt{\varepsilon_{ac}} = V_{air}\sqrt{\varepsilon_{ar}} + V_{as}\sqrt{\varepsilon_{as}} + V_r\sqrt{\varepsilon_r} + V_w\sqrt{\varepsilon_w} \tag{2}$$

Where Vair, Vas, Vr,Vw are the volume content percentage of air, asphalt, aggregates and water, respectively (Birchak, et.al., 1974). eair, eas, er,ew are the volume content percentage of air, asphalt, aggregates and water, respectively.

For a specific HMA, its dielectric constant is mainly a function of water content, because the dielectric constant of the water is much greater than that of the other components, that is, water content is the factor that most closely affects the dielectric constant of a HMA, so the humid HMA can be considered as combination of water and dry HMA. The Equation (2) can be simplified as the below equation:

$$\sqrt{\varepsilon_{ac}} = V_w\sqrt{\varepsilon_w} + V_{ac}\sqrt{\varepsilon'_{ac}} \tag{3}$$

After acquiring dielectric constant of HMA, the moisture of HMA can be calculate by formula as follows:

$$w = \frac{\sqrt{\varepsilon_{ac}} - \sqrt{\varepsilon'_{ac}}}{G(\sqrt{\varepsilon_w} - \sqrt{\varepsilon_{ac}})} = \frac{\sqrt{\varepsilon_{ac}} - \sqrt{\varepsilon'_{ac}}}{G(9 - \sqrt{\varepsilon_{ac}})} \tag{4}$$

where G is the density of dry Hot-Mix Asphalt，the value vary between 2.35 g/cm^3 and 2.37 g/cm^3; e'ac is the dielectric constant of dry HMA，which can be measured by Dielectric constant detector in laboratory using core-drilling and sampling method; eac is the dielectric constant of humid HMA, which can be calculated by waveforms.

As discussed above, the dielectric constant of asphalt mixture can be acquired from the radar wave amplitude reflected off the pavement surface. Subsequently, water content can be calculated based on the relationship between the humidity and the dielectric constant of asphalt mixture.

When Equation (4) is used, the following assumptions and approximations should be made:

(1) The density and dielectric properties of asphalt mixture are uniform along the highway, although some assumptions do not accord with the practice, the sections constructed at the same time, the differences is pretty small, which can be ignored;

(2) Pavement surface water content and internal water content are almost same, if not, the measured water content is the water content of pavement surface asphalt mixture; and

(3) Asphalt mixture is regarded as two-phase mixture consisting of water and non-continuous material approximately.

THE TEST RESULTS AND ANALYSIS

The purpose for this investigation is to determine the accuracy of the pavement surface water content with GPR and to establish the relationship between moisture and dielectric constant of asphalt mixture based on the real measured data in site.

GPR were conducted to investigate the moisture content of the highway from Anyang to Xinxiang in Henan province. Pulse radar equipment made in USA was employed in this investigation, which use Air-coupled antenna type 1.0GHZ. During data collection, the weather was good, and no rain was reported over at least the previous five days. Moving speed in collecting data varies from fifteen to twenty mile per hour.

It is important to discuss the relationship between Moisture contents and dielectric constants of HMA Firstly. Fifty sampling position were chosen and moisture contents of Hot-Mix Asphalt were measured by moisture-density nuclear gauge, which had been calibrated with core-drilling and sampling. Dielectric constant values of pavement surface asphalt mixture are calculated using Equation (1) in each sampling position.

Example: Figure 2 is a waveform of Anyang to Xinxiang Highway at the location of K599. Amplitude of the waveform reflected off metal plate (A_m) is 17.95V. Amplitude values reflected off pavement surface asphalt mixture (A_0) is 7.87V.

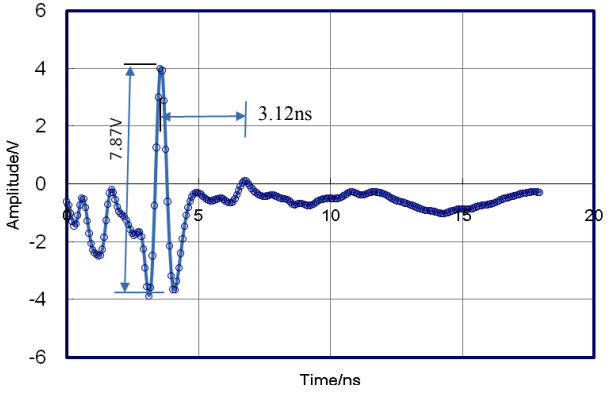

FIG. 2. The waveform of Anyang to Xinxiang Highway at the location of K599

Dielectric constants of Hot-Mix Asphalt in the sampling position can be obtained to rely on the amplitude of the reflected by below equation：

$$\sqrt{\varepsilon_{ac}} = \frac{A_0 + A_m}{A_0 + A_m} = \frac{17.95 + 7.87}{17.95 - 17.87} = 2.39 \tag{5}$$

The correlation about moisture contents and dielectric constants of HMA at different moisture content levels is presented in Figure 3.

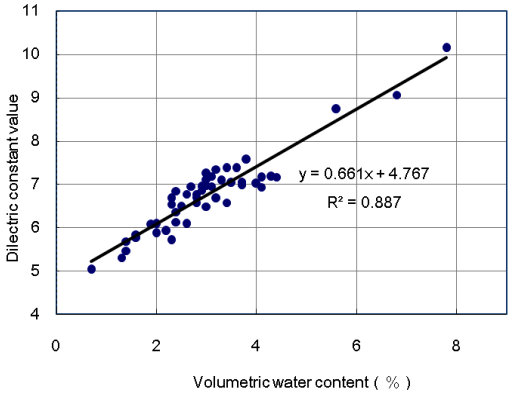

FIG. 3. The correlation of Moisture contents and dielectric constants of HMA

Figure 3 shows the relationship of moisture and dielectric constant of HMA. From this figure, it is apparent that this is approximately a linear correlation. Based on the dielectric constant, the moisture content of asphalt concrete pavement can be estimated roughly. Dielectric constant of asphalt concrete pavement surface generally varies in the range of 5 to 7.5. When dielectric constant is less than 5, it indicates that the void ratio of asphalt concrete pavement is pretty high. If dielectric constant of asphalt concrete surface is less than 4, it indicates basically that the asphalt desquamates from aggregate, so the strength of the pavement became insufficient and it is prone to extensive damage. If dielectric constant is greater than 7.5, it demonstrates excessive water exists in the surface structure layer and the efficacy of pavement drainage maybe be poor, which will affect the stability and service life of the project.

In order to study the accuracy to evaluate water content by reflected GPR signals, Equation (4) was used to evaluate the results tested using GPR. Subsequently, the results were compared with results which were measured with moisture-density nuclear gauge, then a statistical analysis was carried out to study the discrepancy of the two methods.

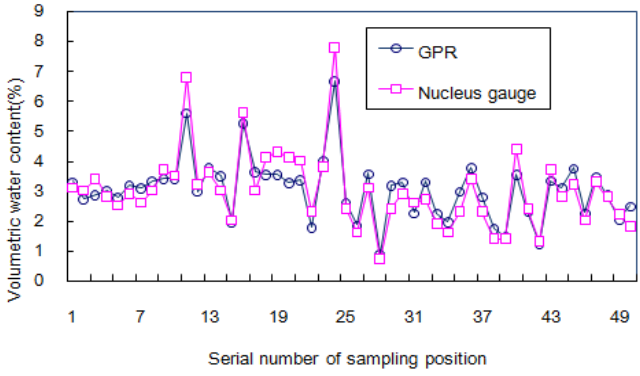

FIG .4. The comparison of GPR and moisture-density nuclear gauge in measuring moisture

Field data shows that GPR-based moisture is generally consistent with the results of moisture-density nuclear gauge. However, statistics shows that the maximum relative error is 37.7%, whilst an average relative error is 13.6%. One reason may be that the data measured by GPR is surface moisture content of asphalt mixture pavement, while the data measured with moisture-density nuclear gauge is internal average moisture content of asphalt mixture pavement. Although the accuracy of HMA moisture content measurement in field with GPR can not be assured due to the inhomogeneious and impurities of pavement, the proposed method is still amazing method to determine the water content of HMA efficiently and no-damage to the pavement.

CONCLUSIONS

This study shows that GPR signals can be used to estimate the asphalt concrete pavement surface moisture content. The moisture content can be obtained from waveform that is reflected from pavement surface, and GPR is a continuous, timely and nondestructive technology. . This technique is feasible and inexpensive. However, the accuracy of the tests still needs to be explored. Generally speaking, the detection about pavement moisture based on GPR needs refinements and improvements, and should be treated as an additional measurement to complement the existing techniques, rather than as a replacement of these techniques.

ACKNOWLEDGEMENT

This paper is a part of the project “Jiangsu Six Top Talent Project” which is supported by the Jiangsu Provincial Government. The authors wish to express their gratitude for the support given to this work.

REFERENCES

Dwayne Arthur Harris.(2006). "Pavement thickness evaluation using ground penetrating radar". PhD Thesis, *Purdue University*, West Lafayette, Indiana.

Brawijaya. (2005). "A new methodology to diagnose pavement subsurface condition using ground penetrating radar". PhD Thesis, *Rensselaer Polytechnic Institute*, Troy, New York.

Huang, X. C, Wang, Z. B, and Li, H. J (2008). "Application of pavement radar in asphalt pavement draining and Waterproofing".. *GuangDong gonglu JiaoTong*: 1-4.

J. R. Birchak, C. G. Gardner, J. E. Hipp. and J. M. Victor. (1974). "High dielectric contant microwave probes for sensing soil moisture". *Proc..IEEE*, 62: 93-98.

Improving Pavement Management System by Adding Pavement Preservation Component

DingXin Cheng[1], Sui Tan[2], R. Gary Hicks[3]

[1] Interim Director, California Pavement Preservation Center and California State University, Chico; dxcheng@csuchico.edu
[2] Program Manager of MTC pavement management program; stan@mtc.ca.gov
[3] Program Manager, California Pavement Preservation Center; rghicks@csuchico.edu

ABSTRACT: Pavement preservation can extend a pavement's effective service life, improve safety and pavement service condition, and is a cost-effective approach. There are many benefits of adding pavement preservation into pavement management system. Pavement management system (PMS) can identify pavement preservation needs and help program pavement preservation projects. Pavement preservation increases the effectiveness of pavement management system, which can allocate available funding more cost-effectively. Although integrating pavement preservation into pavement management system is not a new thing, 9 out of 41 state agencies still utilized "worst first" approaches in their project prioritization based on a survey results in 2008. It is a challenging task to add the pavement preservation component to a PMS. An example of integration of pavement preservation with pavement management system is provided. This paper also provides guidance on how to add the pavement preservation components to pavement management system using a stepwise method.

INTRODUCTION

With most of the United States roadway network are already constructed, the major activity has now shifted from new construction to maintaining and preserving existing roads. Ideally, we want to preserve our existing highway systems so that they are safer, smoother, and last longer. As a component of system preservation, pavement preservation is aimed at preserving the investment in our highway system, extending pavement life, and meeting our customers' needs. It is the timely application of carefully selected surface treatments to maintain or extend a pavement's effective service life. The potential benefits of a successful pavement preservation program can be numerous, including higher customer satisfaction, increased safety, cost savings/cost-effectiveness, improved pavement condition, improved strategies and techniques, and better informed decisions. A pavement preservation program should be a valuable tool included in an agency's pavement management system.

Adding pavement preservation components to PMS can benefit both PMS and pavement preservation program. Some early PMS consisted primarily of a database, a pavement condition index, and a ranking system to develop a prioritized list of projects following the traditional "worst first" approach. Pavement preservation is a proactive approach where pavement preservation treatments are applied at a right time and group together (Stroup-Gardiner and Shatnawi, 2009). A pavement management system can support systematic and effective pavement preservation treatment programming. On the other hand, a successful pavement preservation program can support a PMS by providing cost-effective funding allocation and optimized project programming.

Integrating pavement preservation into a pavement management system is not a new thing. Number of studies have described the theories and benefits of integrating pavement preservation (PP) into PMS (Hicks et. al, 2000; Smith, 2002; Zimmerman and Peshkin, 2003; Zimmerman and Peshkin, 2004). The United States Federal Highway Administration (FHWA) has also developed a training course to educate people on how to integrate PP with PMS (FHWA 2003). However, based on the survey results conducted on the U.S. State agencies, there were still 9 out of 41 surveyed State agencies utilizing "worst first" approach in their project prioritization (Saadatmand, 2008). Agencies should integrate preservation with their pavement management system as least at the network level.

It is a challenging task to add the pavement preservation component to a PMS. It requires the knowledge of pavement preservation treatments, asset management, system engineering, funding, and support from upper management. To assist agencies to successfully implement pavement preservation in their pavement management system, this paper provides guidance to support the successful implementation of this integration effort by a stepwise method. Due to technical challenge, long duration for development, and funding limitations, this paper recommends that an agency add pavement presentation components to its PMS stepwise, first at network level, then project level, and finally both levels with feedback loop.

PAVEMENT MANAGEMENT SYSTEMS SUPPORT PAVEMENT PRESERVATION EFFORTS

PMS can be used as a tool to effectively program preservation treatments for an agency. An effective PMS identifies good candidates for preventive maintenance since it has the roadway distress survey and maintenance history. Good candidates for preservation treatments generally are ones with a pavement condition index (PCI) of 55 or more. The PMS can also support to determine the optimum time for performing maintenance treatments. Reconstruction and maintenance costs rise as a pavement ages. However, if maintenance or rehabilitation is carried out too early, the life cycle costs are high. There is an optimum time at which maintenance should be performed to provide the maximum cost effectiveness (Hicks et al, 2000**,** MTAG, 2008). This is normally between 5 and 10 years depending on the treatment. If an agency's PMS does not include a pavement preservation component, the history of pavement preservation activities may not be traceable since maintenance crews do not always record preservation activities.

PAVEMENT PRESERVATION INCREASES EFFECTIVENESS OF PMS

A pavement preservation component within the PMS can help an agency allocate funding more cost effectively. It can support PMS to prioritize and select projects for right treatment.

Different pavement treatments can have very different treatment lives. Treatment lives are typically defined by the time the pavement condition index (PCI) drops to a level requiring more maintenance or a rehabilitation treatment. A higher PCI value means the road is providing good service. The pavement preservation approach (dashed line, FIG. 1) keeps good road in good condition has the best service to travelers. The rehabilitation strategy (thin line) has the intermediate serviceability while the reconstruction approach (thick line) has the poorest serviceability because it allows the pavement deteriorate until it needs to be replaced.

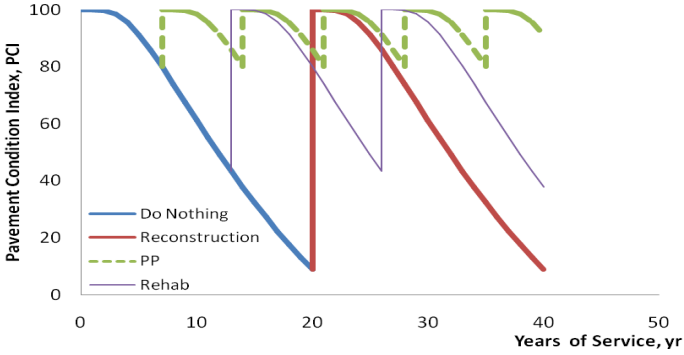

FIG. 1. Serviceability of Different Treatment Strategies

GUIDANCE ON ADDING PAVEMENT PRESERVATION COMPONENTS TO PMS

Adding a pavement preservation component to a PMS system can be a very demanding and challenging job. The following are a list of tasks an agency should undertake when integrating pavement preservation into PMS.

- Inventory, pavement condition survey, and information that supports pavement preservation activities.
- Identify pavement preservation techniques that reflect current state of practice and cost information.
- Develop family performance curves for grouped pavement preservation activities at the network level pavement management analysis.
- Develop performance curves for individual pavement preservation techniques so that project level pavement management analysis can be conducted.
- Create multiple year project assignment for each pavement management

section based on either critical PCI method (Shahin, 2005) or Dynamic Programming procedure (Feighan et al., 1989)
- Include remaining life analysis or life extension associated with the treatment.
- Integrate budget allocation and optimization to meet the objectives of backlog elimination, maintaining condition, or reaching a specific PCI.

Although there are numerous benefits of the integration, it usually requires significant initial funding and other resources such as data collection, computer programming, training, and operation cost. Therefore, it is very important to have good communication with upper management and obtain their support to integrate pavement preservation into the PMS. FIG. 2 shows a guideline flowchart for integrating PP into PMS. Based on the funding level and available resources, three different PP and PMS integration levels can be implemented. The network level integration requires the least effort, and integration at both network and project level requires the highest funding and most work. The integration of PP with PMS can be started from either a network (step 1) or project level (step 2) only. Eventually, a full integration at both network and project level with feedback loop (step 3) can be developed as shown in FIG. 2.

EXAMPLE OF INTEGRATING PAVEMENT PRESERVATION COMPONENTS WITH PMS

As an illustration, the PMS StreetSaver® program can be used to demonstrate the effectiveness of integrating pavement preservation into pavement management system. StreetSaver® is the popular PMS software developed by Metropolitan Transportation Commission (MTC) in the San Francisco Bay Area, California. StreetSaver® provides network-level analysis with some project-level components, supplemented with GIS mapping capability. It was developed in 1984 with a strong emphasis on preventive maintenance. The founding principle is *making good streets last longer so they cost less to maintain*.

Establishing Pavement Condition Categories

A five-category condition definition has been developed to provide realistic M&R treatment assignment. Condition Category I (CAT I) is preventive treatment; CAT II is light rehabilitation, predominantly non-load-related; CAT III is moderate rehabilitation, predominantly load-related; CAT IV is heavy rehabilitation; and CAT V is reconstruction. It is also required to set the PCI breakpoints. Since CATs I, II, and III are mainly pavement preservation treatments, different PCI breakpoints are used to trigger treatments in each condition category. When PCI is between 70 to 55, CAT II/III treatments will be applied; PCI between 90 to 70, CAT I. However, PCI from 100 to 90 will be ignored by the system because it is not cost effective to provide any maintenance.

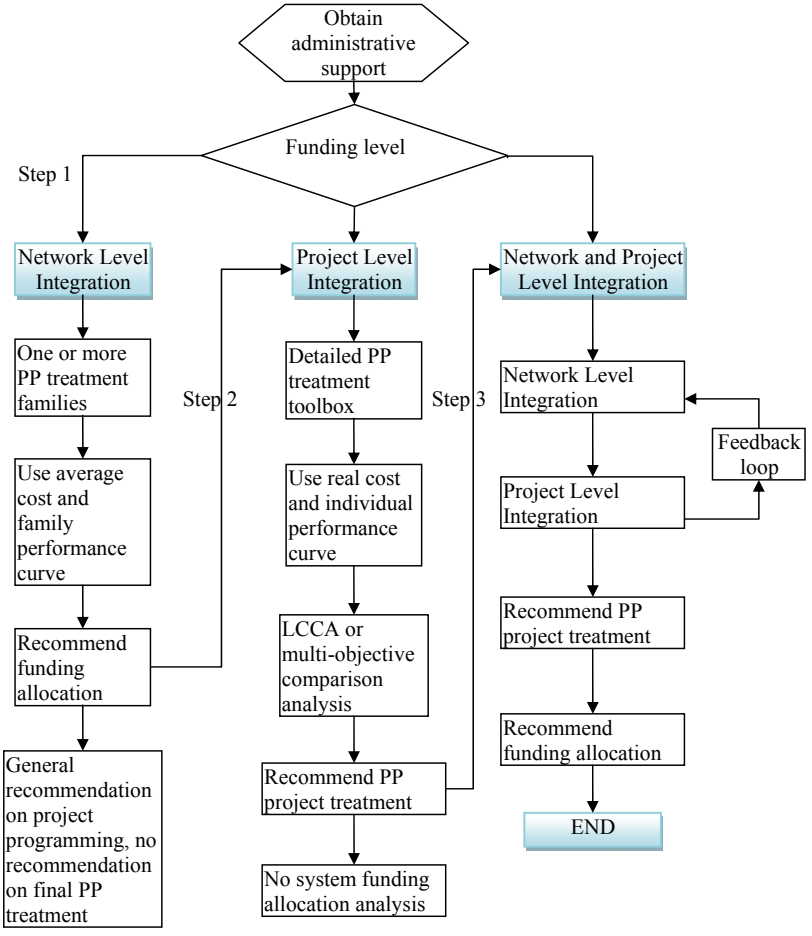

FIG. 2. Flowchart for developing different levels of integrating PP with PMS

Adding Pavement Preservation Treatment in StreetSaver®

StreetSaver® uses a decision tree to model the decision making process that agencies follow to select a maintenance or rehabilitation strategy. The decision tree contains "branches" for each functional classification, surface type, and condition category.

Jurisdictions can outline their M&R strategy, choosing a treatment for each branch. For example, a PP treatment strategy can be easily setup for a residential street with AC surface type. Under CAT I, crack seals will be applied at $1.00/LF at a 4-year interval between crack treatments, and slurry seal at $3.30/SY every eight years

between surface seals. After three surface seals, the pavement will receive a mill and thin overlay as a surface restoration. For CAT II, non-load related, a rubberized chip seal at $7.55/SY will be applied. If the condition is due to load related, then a thin AC overlay will be triggered.

Individual Performance Curve

Unlike other PMS that uses family performance curve for prediction, StreetSaver® maintains an individual performance curve for each street section. This unique curve, which incorporates local conditions such as climate, traffic, design, and workmanship, is used to predict future condition. For example, in FIG. 3, for the pavement management section Lurline Drive (000007-000003), the inspection results in 2002, 2004 and 2008 show that the pavement is performed better than its family curve (in red). The adjusted curve (in green), with a current real-time PCI of 74, is the performance curve of Lurline Drive.

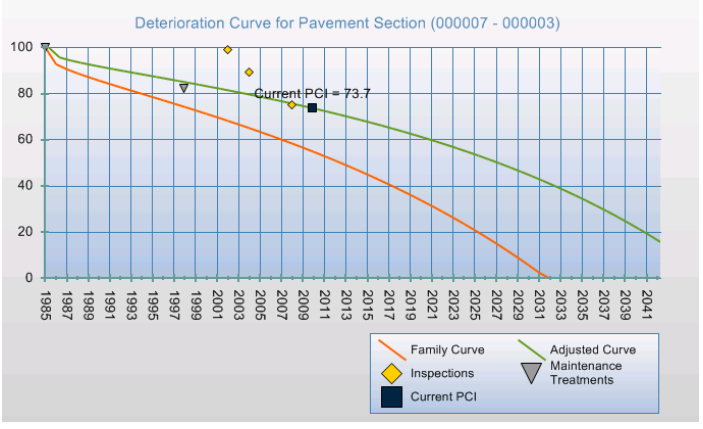

FIG. 3. Performance curve for a management section with PP strategies

The unit cost of pavement preservation is much less than that of rehabilitation or reconstruction. Based on national experiences, every dollar spent on pavement preservation, could potentially eliminate or delay 6 to 10 dollars on major rehabilitation or and more for reconstruction (FP2, 2001). By adopting effective preservation methods that proactively corrects minor road deficiencies early, the roadway lives can be extended at comparatively low cost. Running complex budget scenarios in StreetSaver® are beyond the scope of this paper. For simplicity, FIG. 4 illustrates the deferred maintenance and PCI over a 15-year period for three different alternatives, Do Nothing, Rehab and Reconstruction, and PP (PP+Rehab (30%PM)). The PP alternative shows the highest average network PCI, while rehabilitation and reconstruction alternative shows a lower average PCI than PP alternative. More importantly, the deferred maintenance for PP alternative is 50 percent lower than

rehabilitation and reconstruction alternative. With the same amount of the funding available, the pavement preservation approach can cover more roadways than rehabilitation or reconstruction does. The pavement preservation keeps the good roads in good condition. Therefore, the overall pavement conditions of the pavement preservation alternative are better than the "worst first" rehabilitation or reconstruction alternative.

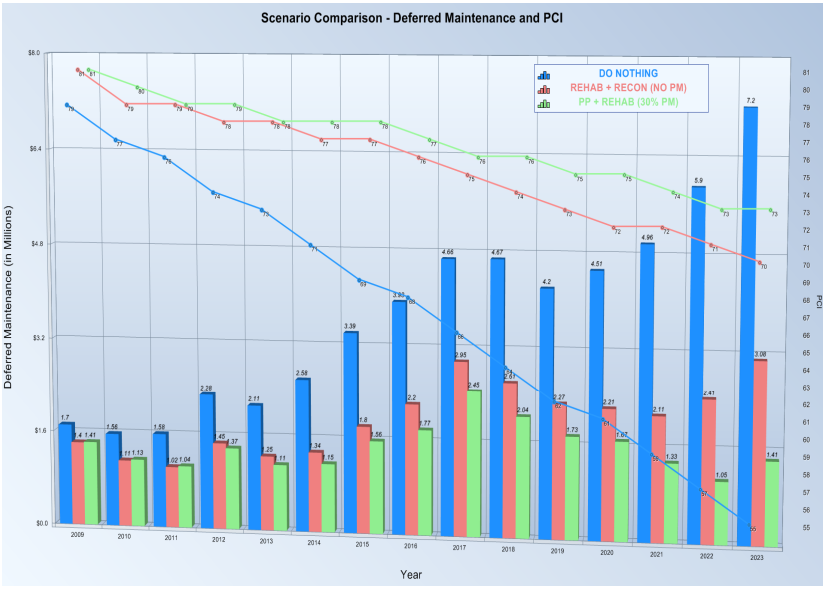

FIG. 4. Advantage of integrating PP with PMS (Graph from StreetSaver®)

CONCLUSIONS

Adding pavement preservation component to PMS has many advantages, especially when more pavements need to be preserved in good condition. Advantages include:

1. PMS can support programming of pavement preservation projects.
2. PMS with pavement preservation component can demonstrate the benefits of pavement preservation program. It can clearly show the advantages of having pavement preservation over "worst first" approach.
3. Pavement preservation programs make a PMS more effective by providing a component within the PCI range which is currently not used for treatment scheduling.
4. Adding pavement preservation component to PMS can be incrementally added to existing systems. Depending on funding and available resources, one can choose to integrate at either network level or project level at first step.
5. The integration of pavement preservation with PMS at both network level and

project level is the most complicated approach. However, it can provide the most benefits for both network and project level pavement management. The network level integration or project level integration can be later upgraded to full integration of PP with PMS with feedback loop.

REFERENCES

Caltrans (2008). "Maintenance Technical Advisory Guide." Second edition. California Department of Transportation, Sacramento, CA.

Feighan, K.J., Shahin, M.Y., Sinha, K.C., and White, T.D. (1989). "A Prioritization Scheme for the Micro PAVER Pavement Management System." *Transportation Research Record,* Transportation Research Board, Washington D.C., No 1215: 89-100.

FHWA (2003). "Pavement Preservation: Integrating Pavement Preservation Practices and Pavement Management." *FHWA-NHI-131104*, National Highway Institute, Publication No.: FHWA-NHI-04-050.

FHWA (2003). "Pavement Management System." Last revised in 2003, website address: http://www.fhwa.dot.gov/cadiv/techapps/pms.htm.

FP2, Foundation for Pavement Preservation. (2001) "Pavement Preventive Maintenance Guidelines - Strategies for initiating new or improving existing pavement preventive maintenance programs."

Hicks, R.G, Seeds, S.B. and Peshkin, D.G. (2000). "Selecting a Preventative Maintenance Treatment for Flexible Pavements", *FHWA Report*, FHWA-IF-00-027, 2000.

Robert M. Davies, R.M. and Sorenson J. (2000). "Pavement Preservation: Preserving Our Investment in Highways." *Public Roads,* Vol. 63 (4).

Saadatmand, N. (2008). "Pavement Management Applications in the U.S.A." *7th International Conference on Managing Pavement Assets*, Calgary, Canada.

Shahin, M.Y. (2005). "Pavement Management for Airports, Roads, and Parking Lots." Second edition, *Springer Science Business Media, Inc.*, New York, NY, U.S.A.

Smith, R.E. (2002). "Integrating Pavement Preservation into a Local Agency Pavement Management System." *Transportation Research Record*, National Research Council, Washington, D.C. , No. 1795: 27-32.

Smith, R.E. (2006). "Pavement Preservation and the MTC StreetSaver Pavement Management Program." *The 2006 StreetSaver user conference*, Newport Beach, CA.

Stroup-Gardiner, M., Shatnawi, S. (2009). "The Economics of Flexible Pavement Preservation." *Transportation Research Board*, *the 88th TRB Annual Meeting*, Washington, D.C.

Zimmerman, K.A. and Peshkin, D.G. (2003). "A Pavement Management Perspective on Integrating Preventive Maintenance into a Pavement Management System." *Transportation Research Record*, National Research Council, Washington, D.C. No. 1827: 3-9,

Zimmerman, K.A. and Peshkin, D.G. (2004). "Issues in Integrating Pavement Management and Preventive Maintenance." *Transportation Research Record*, National Research Council, Washington, D.C. No. 1889: 13-20.

Cost-Effectiveness Evaluation of Pavement Maintenance Treatments by OPTime

Qiao Dong[1] and Baoshan Huang[2]

[1]Graduate Research Assistant, University of Tennessee, 223 Perkins Hall, Knoxville, TN, 37996; qdong2@utk.edu
[2]Associate Professor, University of Tennessee, 223 Perkins Hall, Knoxville, TN, 37996; bhuang@utk.edu

ABSTRACT: The cost-effectiveness of different maintenance treatments including micro surfacing, HMA overlay and mill & fill were evaluated by using OPTime. The treatment effectiveness was calculated as the difference in computed areas associated with the post-treatment performance indicator curve and the do-nothing curve. It was found that mill & fill had the highest unit costs, followed by HMA overlay and micro surfacing. HMA overlay had the highest effectiveness, followed by mill & fill and micro surfacing. Micro surfacing was found to be the most cost-effective treatment due to its low cost.

INTRODUCTION

With more and more pavement maintenance projects applied, there is a need to evaluate the cost and effectiveness of various maintenance treatments from the perspectives of both cost and effectiveness (O'Brien 1989). Investigation indicates that more than 3000 pavement resurfacing maintenance projects were applied in Tennessee State from 1987 to 2008. With so many maintenance projects applied, evaluating the cost-effectiveness of different treatments is of great importance.

In order to evaluate the effectiveness of different treatment, appropriate measures of effectiveness need to be defined first. Several existing measures of effectiveness include the performance jump, the improved pavement performance, the expected treatment life, the expected extended treatment life, the area between the performance curve and the threshold (Labi 2006, 2003, Rajagopal 1990). NCHRP report 523 presented a cost-effectiveness analysis method for determining the optimal timing for the application of preventive maintenance treatments (Peshkin and Hoerner 2004). An Excel VBA designated OPTime software was presented in this report. As shown in Figure 1, the effectiveness (benefit) is defined as the difference in computed areas associated with the post-treatment performance curve and the do-nothing curve in the report. This method best reflects the effect of treatment since it not only involves both treatment service life and overall pavement condition, but also directly indicates how much the pavement performance is improved.

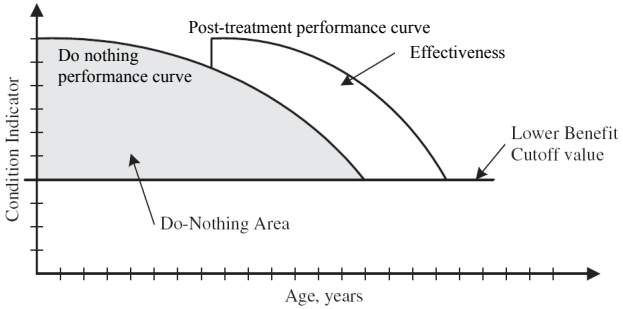

FIG. 1. Conceptual illustration of the effectiveness (D.G. Peshkin et al.)

OBJECTIVE

In this study, the methodology used in NCHRP 523 was investigated and a project case study was first conducted by using OPTime. Then, the cost-effectiveness of three pavement maintenance treatments were evaluated and compared by using OPTime.

ALGORITHM OF OPTIME

The OPTime software is a useful tool to determine the optimal application time of preventive maintenance based on the cost-effectiveness analysis of different maintenance scenarios. In OPTime, ***Benefit*** is defined as the quantitative influence on pavement performance as measured by one or more condition indicators. The optimal application of a preventive maintenance treatment occurs at the point at which the benefit per unit cost is greatest. The following are three important conceptions for the optimal timing analysis.

(1) Define Performance Indicators and Benefit Cutoff Values

The effect of a treatment on performance is determined by the changes in pavement performance indicators, such as International Roughness Index (IRI), or other measure of performance. As shown in Figure 1, Benefit cutoff values are defined as the y-axis boundary conditions for the performance curves that define the upper and lower limits for the benefit area calculations. Pavement failure trigger values are usually used as the benefit cutoff values.

(2) Determine Do-nothing and Post-treatment Performance Relationships

The benefit associated with the application of a maintenance treatment is based on the improvement in performance compared with that for the “do-nothing” alternative. The do-nothing relationship defines the pavement performance over time that would be expected if only no or minor routine maintenance was conducted. The post-treatment relationship defines the pavement performance over time that would be expected if a treatment is applied. The two relationships can be determined by investigating the historical pavement performance data from Pavement Management System (PMS).

(3) Identify Benefit of Treatments

As shown in Figure 1, for a specific condition indicator, the benefit is determined by the difference in computed areas associated with the post-treatment performance indicator curve and the do-nothing curve. When there are more than one performance indicator included in the analysis, benefit weighting factors are used to combine the individual benefit values associated with the different condition indicators together.

$$\text{Area}_{\text{Benefit(i)}} = \text{Area}_{\text{Post treatment(i)}} - \text{AREA}_{\text{Do nothing(i)}} \quad (1)$$

$$\%\text{Benefit}_i = (\text{Area}_{\text{Benefit(i)}})/(\text{Area}_{\text{Do nothing(i)}}) \quad (2)$$

PROJECT CASE STUDY

Project Summary

The micro surfacing treatment project applied at SR341 in Tennessee was investigated by using the OPTime. Micro surfacing is spreading a mixture of polymer modified asphalt emulsion, fine aggregate, mineral filler and water on an original pavement surface. The surface age, which is the time when the maintenance was applied, was 11 years. Three condition indicators: Roughness, rutting depth and PSI were selected. Benefit weighting factors for the three condition indicators were chosen as 20, 30 and 50, respectively. The average cost per mile was $42,173.

Do-nothing and Post-treatment Performance Curves

As shown in Figure 2, linear model was used to build the do-nothing and post-treatment performance curves. The pavement performance data of the adjacent road section, which had the same pavement structure, traffic and environmental condition, were used to build the do-nothing performance curves. The intercepts of the rutting depth linear model were set to be 0 while the intercepts of the IRI liner model were forced to be between 45in./mile to 60in./mile, since the IRI of newly constructed pavement are between 45~60 in./mile(Shafizadeh & Mannering 2003).

It is noted that the post-treatment performance relationship in Figure 2 only represented the pavement performance when the treatment was applied at the pavement age of 11 years. The post-treatment performance relationship would be different when the treatment was applied at different pavement service age. Thus, it is necessary to estimate the post-treatment performance relationships for different application time. As shown in Equation 3 and Figure 3, interpolation is utilized to estimate the slopes for the post-treatment performance model at different application time.

$$Slope_i = Slope_0 + \frac{(Slope_N - Slope_0)}{N} i \quad (3)$$

Where, $Slope_i$: slope of the performance model at pavement age of i years.

$Slope_0$: slope of the do-nothing performance model.

$Slope_N$: slope of the post-treatment performance model at age of N years.

i: Assumed treatment application time, year.

N: Actual treatment application time, year.

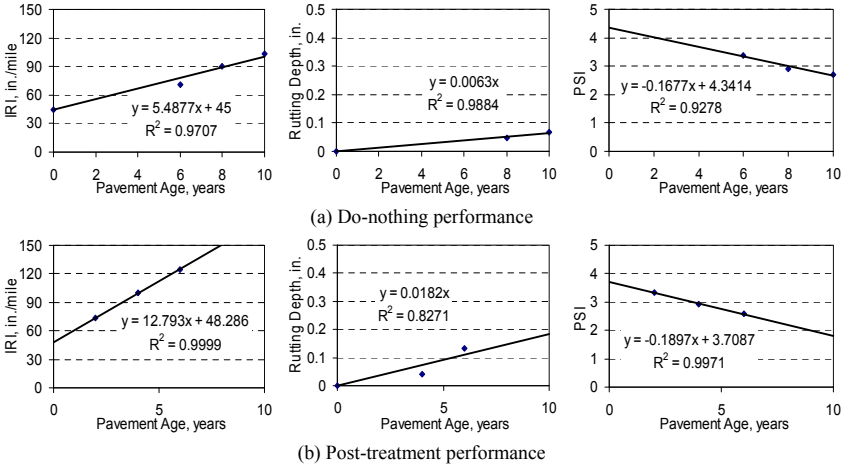

FIG. 2. Pavement performance relationships for project SR 341 (micro surfacing)

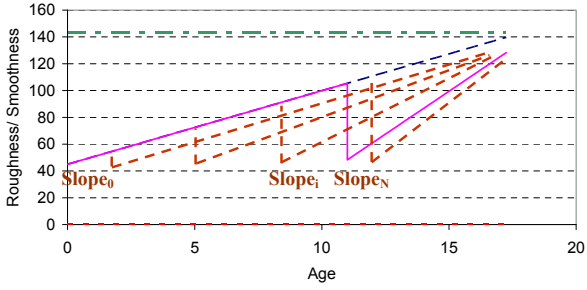

FIG. 3. Slopes of post-treatment performance curves at different application time

A value of 143 in./mile was chosen as the upper benefit cutoff value for roughness. According to the roughness do-nothing performance model, this value is predicted at an age of 17 years. 0.5 in. was chosen as the lower cutoff value for rutting depth and it was predicted at an age of 79 years. 2.5 was chosen as the lower cutoff value for PSI and it was predicted at an age of 11 years. Since the PSI value reached its lower cutoff value at 11 years, a maintenance scenario of applying micro surfacing at 3, 5, 7, 9 and 11 years was investigated. Slopes for the three investigated pavement performance indicators were estimated by equation 3. The intercepts of post-treatment performance curves were assumed to be the same at different application time.

Analysis Results Discussion

Table 1 presents the analysis result. It indicated that of the 5 investigated application

years; the optimal applicant year was 11 as indicated by the largest total benefit value (0.27) and the longest extension of life of 6.4 years. It can also be seen that negative benefit values occurred at early application age and the optimal application time was the year when PSI reached its lower thread. This is because the application of the treatment resulted in increased pavement deterioration rate as shown in Figure 2.

Table 1. Format and Layout of Tables in GSP Papers

Application Time (years)	Benefit	Expected Life (years)	Life Extension (years)
3	-0.16	10.0	-1.0
5	9.95E-03	11.8	0.8
7	0.14	13.7	2.7
9	0.23	15.5	4.5
11	**0.27**	**17.4**	**6.4**

TREATMENT COMPARISON

The cost-effectiveness (benefit/cost) of three maintenance treatment method: micro surfacing, HMA overlay and mill & fill were investigated by using OPTime. The benefits and benefit/cost ratios were calculated as an indicator of cost-effectiveness. The treatment application ages were the real application time of the maintenance treatment. Three typical projects with similar traffic level (<5000 AADT) were investigated for each maintenance treatment. Related project information and pavement performance data were collected and analyzed. Table 2 summarized the analysis results.

Table 2. Cost-effectiveness Comparison of Different Maintenance Treatment

Treatment	Cost ($/mile)	Benefit	Expected Life (years)	Life Extension (years)	Benefit/Cost ($\times 10^{-5}$)
Micro surfacing	32723	0.36	15	4.2	1.1
HMA overlay	72719	0.57	20	10.6	0.8
Mill & fill	175016	0.46	18	7.8	0.3

In order to compare the costs of different maintenance projects at different time, Asphalt Price Index, which is the historical asphalt price, were utilized to calculate the adjusted cost of asphalt materials. Besides, a discount rate of 4% percent was also used to calculate the current value of the costs. It can be seen from Table 2 that among the three investigated maintenance treatments, mill & fill has the highest cost, followed by HMA overlay and micro surfacing.

As indicated by the benefit, expected life and expected life extension, HMA overlay treatment has the highest benefit value, followed by mill & fill and micro surfacing. Similar conclusion could also be attained when life extension was used to evaluate the effectiveness. HMA overlay increases the pavement thickness and improves the pavement structure whereas mill & fill is usually applied on a relatively weak pavement structure and does not contribute to the pavement structure capacity. Thus, HMA overlay has higher effectiveness.

Micro surfacing had the highest cost-effectiveness (benefit/cost), followed by HMA overlay and mill & dill. Due to the low cost, micro surfacing was more cost-effective

than other two treatments. However, mill & fill and HMA overlay have the ability to overcome pavement distress and increase the pavement structure capacity. The two surface treatments can not simply replace the two new pavement layers when the pavement is in poor condition.

CONCLUSIONS

Based on the analysis above, several conclusions can be summarized as follows:

1. Practical optimal time can be calculated by using OPTime software and investigating the condition indicator performance relationships and is mainly determined by the do-nothing performance relationships.
2. Mill & fill had the highest costs, followed by HMA overlay and micro surfacing.
3. As indicated by the benefit value, expected life and expected life extension, HMA overlay had the highest effectiveness, followed by mill & fill and micro surfacing.
4. Due to the low cost, micro surfacing was the most cost-effective treatment, followed by HMA overlay and mill & fill. However, mill & fill has the ability to overcome severe pavement distress and HMA overlay can increase the structure capacity. Thus, micro surfacing maybe inapplicable in some situations.

ACKNOWLEDGMENTS

The authors appreciate the Tennessee Department of Transportation (TDOT) for their assistance on the project information and pavement performance data collection.

REFERENCES

L. G. O'Brien, "NCHRP Synthesis of Highway Practice 153: Evolution and Benefits of Preventive Maintenance Strategies". *Transportation Research Board*, National Research Council, 1989: 69.

S. Labi, S.H. Kong, G. Lamptey, and C. Nunoo, "Long-Term Benefits of Micro surfacing in Indiana-Methodology and Case Studies", *Transportation Research Board*, National Research Council, Washington, D.C., 2006.

S. Labi, and K.C. Sinha, (2003). "The Effectiveness of Maintenance and Its Impact on Capital Expenditures". *Technical Report FHWA/IN/JTRP-2002-27*, West Lafayette, Indiana.

A.S. Rajagopal and K.P. George, (1990). "Pavement Maintenance Effectiveness" *Transportation Research Record*, 1276: 62-68.

D.G. Peshkin, T.E. Hoerner, K.A. Zimmerman, (2004). "NCHRP Report 523: Optimal Timing of Pavement Preventive Maintenance Treatment Applications", *Transportation Research Board*.

K. Shafizadeh, and F. Mannering (2003). "Public Acceptability of Pavement Roughness on Urban Highways: An Empirical Analysis", *Transportation Research Record* 1860: 187 - 193.

Variable Slip Skid Resistance Testing for Road Safety Investigation and Pavement Management

Wei Liu[1] and Bryce Tinkler[2]

[1]Senior Engineer, Fugro Pavement Management Services Ltd, 31 Mckee Street, Te Rapa, Hamilton, New Zealand 3200; wei.liu@pmsnz.co.nz

[2]General Manager (NZ), Fugro Pavement Management Services Ltd, 31 Mckee Street, Te Rapa, Hamilton, New Zealand 3200; bryce.tinkler@pmsnz.co.nz

ABSTRACT: The relationship between surface friction and roadway safety has long been recognized by transportation agencies and concern with the number of accidents occurring in wet pavement conditions has grown. For this reason it is imperative for road safety and road asset management divisions to undertake pavement wet skid resistance survey on a routine and regular basis. Many kinds of equipment are available to measure skid resistance on road surface, such as side force tester, Lock Wheel Tester, Fix-Skip Tester and Variable Slip Tester. In this paper, Norsemeter ROAR MkII, a new kind of variable slip tester, is introduced. Norsemeter ROAR MkII can be operated on both fix slip mode and variable slip mode. It will be demonstrated in this paper that the testing results from Norsemeter ROAR MkII are useful for both road network condition monitoring and safety investigation of black spot area through stopping distance analysis and lose-of-controlled analysis. Therefore, it is believed that the application of Norsemeter ROAR MkII variable slip skid resistance testing can help various road controlling authorities to make better decision on road maintenance programs and road safety improvement programs.

INTRODUCTION

The World Health Organization (WHO) reports that motor vehicle crashes worldwide kill 1.2 million and injure 50 million people annually. The worldwide economic costs are estimated at $518 billion each year (WHO 2004). Motor vehicle crashes result from numerous contributing factors including driver's error, poor geometric alignment of the roadway, and a lack of sufficient friction at the tyre-pavement interface during wet weather. The relationship between surface friction and roadway safety has long been recognized by transportation agencies and concern with the number of accidents occurring in wet pavement conditions has grown. National Transportation Safety Board (NTSB) and Federal Highway Administration (FHWA) reports indicate that 13.5% of fatal crashes and 18.8% of all crashes occur

when pavements are wet (Dahir and Gramling 1990). For this reason it is imperative for public safety and pavement managers to undertake pavement wet skid resistance survey on a routine and regular basis.

Throughout the world there are numerous methods for measuring and reporting the skid resistance of a pavement, including locked wheel devices, sideway-force devices, fixed slip devices, and variable slip devices. Among these skid resistance testers, only variable slip devices can provide the full friction curve. After the whole friction curve is combined with the actual geometric attributes of the pavement, it is possible to then calculate the fundamental responses of a skidding vehicle i.e. the stopping distance and/or the loss of control speeds. In this paper, Norsemeter ROAR MkII, a new kind of variable slip tester, is introduced. Norsemeter ROAR MkII can be operated on both fix slip mode and variable slip mode. It will be demonstrated in this paper that the testing results from Norsemeter ROAR MkII are useful for both skid resistance survey in network level and safety investigation in project level.

NORSEMETER ROAR MKII SKID RESISTANCE MEASUREMENT SYSTEM

The Norsemeter ROAR MkII owned and operated by Fugro Pavement Management Services Ltd is pictured in Figure 1.

FIG. 1. Norsemeter ROAR MkII survey equipment

It uses a hydraulic braking system for both the measurement of the coefficient of friction and the application of braking forces to maintain or vary the slip ratio, which can operate in both fixed-slip and variable-slip modes. This equipment design to operate from a vehicle at normal traffic speeds (variable slip mode) or 50km/hr (fixed slip mode) and uses shaft encoder technology and optionally GPS equipment to record the location of measurements. The truck carries a water tank of approximately $8m^3$ capacity to allow the pavement to be sprayed prior to the passage of the standard friction tyre in large scale network survey. The ROAR uses a hydraulic braking system for both the measurement of the coefficient of friction and the application of braking forces to maintain or vary the slip ratio. In the fixed slip mode, the ROAR is

capable of providing skid resistance measurement like most of fixed slip testers and side force testers. In the variable slip mode, it measures the skid resistance of the road surface by computer controlled braking of the test wheel from free-rolling to fully-locked, while constantly monitoring the braking friction force that the road surface exerts against the test wheel. Figure 2 shows typical results obtained from the ROAR testing in variable slip mode for a full friction cycle along with that of the fitted Rado friction curve.

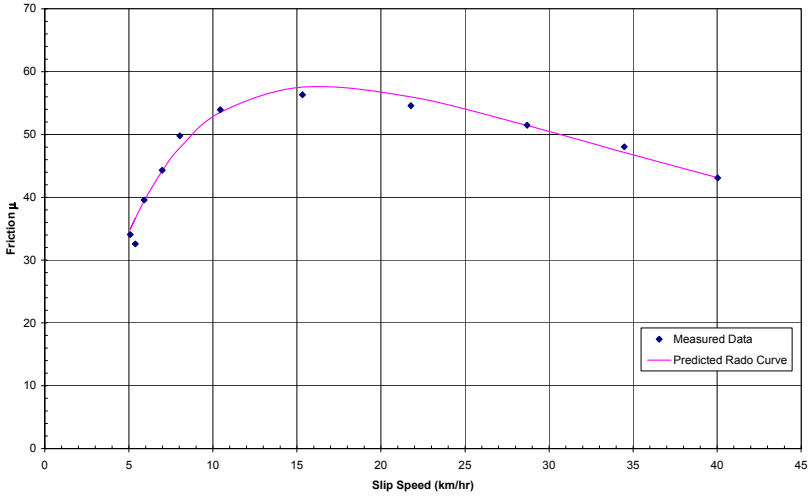

FIG. 2. Example of ROAR data in variable slip mode and the fitted Rado friction curve

By fitting the ROAR data into Rado friction curve, skid resistance parameters such as international friction index (IFI), Mupeak (the peak friction coefficient), and Vcrit (the critical slip speed) can be derived for each friction cycle. The IFI has two components F60 and Sp. F60 is the standardised friction measure (friction factor) at a 60 km/hr speed. Sp is the gradient of the friction versus slip speed relationship and is an indicator of the speed dependency of the recorded friction value.

STOPPING DISTANCE AND LOSS OF CONTROL ANALYSIS

Assuming that hysteresis energy loss is relatively small compared to the work done by friction, the stopping distance ds at small velocity interval dv is given by.

$$ds = \frac{v^2 - (v - dv)^2}{2gF_{60}e^{(\frac{60-v}{Sp})}} \quad (1)$$

From the equations of motion, the time interval *dt* is given by. (assuming constant friction across the small velocity *dv* interval)

$$dt = \frac{dv}{gF_{60}e^{\left(\frac{60-v}{sp}\right)}} \tag{2}$$

Since F60 and Sp are not constant, numerical integration needs to be applied for the two equations shown above to obtained the stopping distance and stopping time from speed v to 0.

Take a vehicle travelling around a bend of radius r with a cross fall of θdegrees the equations of static's for equilibrium give:

$$\cos(\theta)mg\mu - \cos(\theta)\frac{v^2}{r} + \sin(\theta)mg = 0 \tag{3}$$

Simplifying and solving for v gives

$$v = \sqrt{rg(\mu + \tan(\theta)} \quad \text{or} \quad v = \sqrt{rg(\mu + \%Crossfall)} \tag{4}$$

Considering the case of a loss of control accident, loss of control occurs when the In the above equation the value of $M\mu_{peek}$ can be substituted into the equation to obtain the maximum speed the curve of radius *r* can be negotiated at without a loss of control.

EXAMPLES AND DISCUSSIONS

Table 1 shows the skid resistance measurement results from Norsemeter ROAR MkII operated in variable slip mode for ten sections of roads.

Table 1. Skid Resistance Measurements of Test Sites

Section No	Start(m)	End(m)	Mu_{peak}		F60		Sp	
			Avg	Std	Avg	Std	Avg	Std
1	729	1166	0.72	0.11	0.38	0.07	67.68	29.72
2	1166	729	0.68	0.06	0.40	0.05	73.36	33.77
3	5763	6114	0.69	0.09	0.42	0.05	89.06	38.22
4	6114	5763	0.71	0.13	0.44	0.04	89.00	33.91
5	4215	4691	0.69	0.06	0.41	0.06	83.40	38.33
6	4691	4215	0.78	0.11	0.42	0.06	68.63	25.75
7	3334	3776	0.71	0.10	0.42	0.05	85.75	50.47
8	3776	3334	0.73	0.07	0.44	0.06	85.77	37.71
9	3955	4530	0.76	0.10	0.43	0.07	79.59	40.01
10	4530	3955	0.76	0.14	0.41	0.09	75.73	51.66

It can be seen from Table 1 that: the average Mu_{peak} value for these test sections is ranged from 0.68 to 0.76 and the standard deviation of Mu_{peak} value is ranged from 0.06 to 0.14; the average F60 value for these test sites is ranged from 0.38 to 0.44 and the standard deviation of F60 value is ranged from 0.04 to 0.09; the average Sp value for these test sites is ranged from 68 to 89 and the standard deviation of Sp value is ranged from 26 to 52.

Table 2 shows a summary of results for the loss of control and stopping distance analysis for the test sites listed in Table 1.

Table 2 Probabilities of Loss of Control and Failing to stop within 30m

Section No	Minimum Radius (m)	Crossfall (%)		Speed (kph)		Possibility of Loss of Control	Possibility of failingto stop within 30m
		Avg	Std	Avg	Std		
1	91	2.7	1.4	65	15	6.50%	5.56%
2	68	2.0	1.6	65	15	21.60%	6.16%
3	48	3.3	0.9	45	10	3.90%	12.05%
4	48	-9.5	1.0	45	10	13.60%	41.11%
5	104	-3.2	0.8	65	15	4.30%	13.48%
6	103	-1.8	1.4	65	15	2.70%	33.76%
7	84	-4.8	2.1	65	15	14.00%	24.58%
8	84	-4.8	2.1	65	15	11.40%	45.01%
9	37	10.5	2.7	65	15	58.50%	33.38%
10	37	7.8	0.9	65	15	58.00%	22.93%

It can be seen from the Table 2 that the results suggest that all sites having some probabilities of loss of control and some possibilities of failing to stop within 30m. The maximum possibility of loss of control occurs at Section No. 9 while the maximum possibility of failing to stop within 30m occurs at Section No. 8.

A closer inspection of the results of loss of control analysis shows that in most cases the standard distribution of the cross-fall was relatively high in comparison to the average value and it is quite possible that negative camber on curve was encountered, the result of which is an “effective” lowering of available friction on these curves. The implication of these results is that in all cases it would be better to treat these locations as being in need of minor safety improvements to improve pavement geometry rather than simply resurfacing the curve.

From the inspection of these sites identified as having a high potential for skidding accidents, it can be seen that potential skidding deficiencies can in no way be controlled by monitoring texture or friction alone, with skidding deficiencies being controlled by the combination of both.

The major implication of this finding is that if a skid resistance testing, inspection and solution regime is undertaken that is focused solely on surface friction, the results obtained could do little to lower the overall risk of skid resistance accidents occurring on the network and additionally geometric solutions need to be considered when assessing the potential for skidding type accidents.

CONCLUSIONS AND RECOMMENDATIONS

In this paper, Norsemeter ROAR MkII, a new kind of variable slip tester, is introduced. Norsemeter ROAR MkII can be operated on both fix slip mode and variable slip mode. This paper showed how the assessment of the skid resistance properties of a pavement is essentially an investigation into risk. The assessment process used in this paper was based on the recently developed Norsemeter ROAR MkII measurement, which was shown to account for both components of skid resistance and thus model the whole friction process. The paper also showed how the

use of one friction number can lead to greater overall risk to the road user; as the use of one friction number does not and can not model the whole friction process and thus can give meaningless results.

It is recommended that the following approach be undertaken for future skid resistance surveys, which in reality is a safety audit, combining skid resistance and pavement geometry:

1. A fixed slip survey is used to identify locations with potential skid resistance deficiencies. Each site with potential deficiencies then surveyed in variable slip test mode.
2. The current cross-fall, vertical and horizontal curvature is established from the high-speed laser profiler survey.
3. Accurate approach velocities are established from the traffic survey.
4. Loss of control and skidding probabilities established for each site and priorities established.

For each site identified as being deficient, an effective long-term solution should be established by improving the pavement geometry, surfacing or both.

REFERENCES

Dahir, S.H., and Gramling, W.L. (1990). "Wet-Pavement Safety Programs, NCHRP Synthesis of Highway Practice 158." Transportation Research Board, National Research Council, Washington, D.C.

Rado, Z. 1994. "Analysis of Texture Models." PTI Report No. 9510, Pennsylvania Transportation Institute, Penn State University, State College, Pennsylvania.

World Health Organization (2004). World Report on Road Traffic Injury Prevention.

The Application of Stepwise Regression in Analyzing Pavement Friction Data

Wenbing Song[1], P.E., Xin Chen[2], Ph.D., P.E. and Dan Sajedi[3]

[1]Office of Materials Technology, Maryland State Highway Administration, 7450 Traffic Dr., Hanover, MD 21076, U.S.A; wsong@sha.state.md.usa
[2]Office of Materials Technology, Maryland State Highway Administration, 7450 Traffic Dr., Hanover, MD 21076, U.S.A; xchen@sha.state.md.usa
[3]Office of Materials Technology, Maryland State Highway Administration, 7450 Traffic Dr., Hanover, MD 21076, U.S.A; dsajedi@sha.state.md.usa

ABSTRACT: The Maryland State Highway Administration (MDSHA) conducts periodical friction surveys on the pavement network to monitor its overall skid resistance condition. It was found from the survey data that pavement friction could be affected by numerous variables: rehabilitation activities, traffic patterns, traffic volumes, survey vehicle test speeds, weather-related factors, and etc. Those variables affect pavement friction condition simultaneously by different mechanisms and in different degrees. It is of importance to investigate the relative significance of those variables in affecting pavement friction so it can be used for friction data interpretation and engineering decision making. This paper applies a multivariate analysis on the friction data using stepwise regression. The stepwise regression provides a measure to assess the relative importance of those variables based on the order of their entry into the model. Cross-validation is then used to examine the effectiveness and generality of the developed model. The engineering implications of the developed model are discussed. The advantages and limitations of using stepwise regression and feasible alternatives for analysis are also discussed.

INTRODUCTION

Pavements friction is a very important factor for the highway safety as inadequate friction on pavement surface could increase the possibility of wet road accidents (FHWA, 1998; Kuttesch 2008). Pavement friction improvement programs have been applied to reduce wet road accidents in the United Sates and other counties (Lyon et al., 2008; Murad et al., 2008; Mayora et al., 2008).

To monitor pavement friction conditions, the Maryland State Highway Administration (MDSHA) annually collects friction data on its entire network using skid trailers (ASTM E-274 using ribbed tire (E501)). The friction number (FN) is measured at approximate three tenth mile intervals on the network. The FN is an indication of pavement friction conditions (the higher the FN, the better the friction

condition).

Previous studies revealed that pavement friction could be affected by a number of variables. The friction of the pavement surface generally deteriorates with the age of pavements in service. Rehabilitation activities can refurbish pavement surface and improve its friction. Particularly, some special treatments, such as the application of high polish value aggregates (HPVA) in hot mix asphalt (HMA) or the utilization of slurry seals on pavement surface, could improve friction notably - those practices had been commonly used in Maryland for friction improvement (Song et al., 2005). Meanwhile, researchers also found that the pavement friction could be affected by weather-related factors such as temperature and rainfall (Song et al., 2005; Anderson et al. 1986; Burchett et al. 1980; Hill et al. 1981). Also, test speed of survey vehicle could inversely affect measured friction measurements (Awoke et al, 2008; Henry 2000). In addition, real time pavement surface conditions such as the existence of small particles and/or spilled oil make friction measurements unpredictable.

The impacts from those variables coexist in the friction survey data. It is important to identify the relative significance of those influences as the knowledge gained can be used to interpret survey results, predict pavement friction performance and determine friction improvement alternatives

For this purpose, this paper conducts a multivariate analysis of friction data using stepwise regression, which models dependent variable in a parsimonious manner by including in the model only explanatory variables that make significant contributions in explaining dependent variables. Stepwise regression also provides a mechanism to assess the relative importance of explanatory variables based on the order of entry of those variables into the model. To analyze the effectiveness of the model, cross-validation is implemented - the full data set is randomly divided into a training sample and a validation sample, accounting for 70% and 30% of the full data set respectively (Afifi et al., 2004; UTexas, 2009). The validation sample is used to examine the model developed by the training sample.

This paper also summarizes the engineering implications and discusses the advantages and limitations of using stepwise regression and then provides feasible alternatives for multivariate analysis.

DATA SET

The MDSHA pavement network covers 10270 directional miles, where Hot Mix Asphalt (HMA) surfaced pavements, flexible or composite pavements, account for 98% of the network. Friction survey is annually conducted on approximately 97% of the network. This paper uses 4 years' survey data, total 161,000 samples, from HMA surfaced pavements. The FN values range from 20 to 70 with a mean of 47 (outliers have been excluded).

Vehicle tires continuously polish pavement surface and therefore pavement friction deteriorates with accumulated traffic volumes, which are calculated by the logarithm of accumulated traffic (Equation 1) since the application of new overlays:

$$Accumulated \quad Traffic = Log(AADT_{per\_lane} * Age_{pavement} * 365 days) \tag{1}$$

Where AADT is the annual average daily traffic, and age is the years between when pavements were overlaid and when they were surveyed.

In addition to the traffic volumes, traffic patterns in urban or rural roads were different (Song et al., 2005): vehicles on urban roads are more frequently accelerated and decelerated due to traffic lights, stop signs or traffic jams, while on rural roads vehicles speeds are relatively consistent. As a result, pavement surface is polished faster on urban roads than on rural roads. Rural roads and urban roads account for approximately 70% and 30% of the MDSHA pavement network respectively.

In general, a new overlay provides a refurbished pavement surface and therefore would improve pavement friction. Particularly, two types of treatments are believed to improve pavement friction notably (Song et al., 2005): One is to use high polish value aggregates (HPVA) in HMA. Polish value of aggregates reflects how aggregates could resist repeating polishing by vehicle tires: The higher the polish value, the greater and the more lasting the friction of aggregates.

The other is slurry seal that provides a thin surface treatment with mixtures composed of crushed aggregates, asphalt emulsion and fillers. Slurry seal is commonly used as a preventive or corrective maintenance activity and most suitable for low speed roads. It was found that slurry seal effectively improved pavement friction (Song et al., 2005).

In the data set under investigation, approximately 12% samples are HPVA HMA and 2% are slurry seal.

This paper uses seasonal variation of weather conditions in terms of monthly accumulated rainfall and monthly average air temperature recorded at the Baltimore Washington International (BWI) airport station to represent the weather conditions.

In general, there is an inverse relationship between test speed and friction values. Specifically, the friction number could be related to test speed by the following Equation (Hall et al., 2006):

$$FN(60) = FN(s) * e^{(\frac{S-60}{S_p})} \tag{2}$$

Where, $FN(60)$ is the adjusted FN at a test speed S to a test speed of 60 km/hr. S is the speed and $FN(S)$ is the FN at a test speed S. S_p is the international friction index (IFI) speed number determined by the macro-texture of pavement surfaces.

In this paper, a majority of test speed samples were centered around 39~41 mph. Depending on the speed limit of roads under survey, test speeds also cluster around 25, 30 and 35 mph. This paper uses test speeds ranging from 20 ~50 mph in analysis.

IMPLEMENTATION AND RESULTS

Stepwise regression is used to develop a predictive model for friction as a function of explanatory variables described above. To validate the effectiveness of the model, the full data set is randomly split into a 70% training samples and a 30% validation samples, and the training samples are used to develop the model and the validation samples are used to examine the model developed by the validation samples. Statistic Analysis System (SAS) is used to implement the stepwise regression, and the 0.15 significant level is pre-set for explanatory variables to be selected into the model and remain in the

model.

Applying the model developed by the training data set on the validation dataset, we obtained a R^2 of 0.268. Comparing to the R^2 of training data set (0.269), the difference is trivial, which validates the generality of the model. The stepwise regression model indicates that:

- Traffic is the most important factor in predicting pavement friction. Pavement surface would be polished faster by urban traffic than by rural traffic, causing urban pavements have lower FNs than rural pavements, by 5.3 units on average; In addition, pavement friction decreases with the traffic volume at a rate of 1.9 units per logarithm of accumulated traffic.
- Rehabilitation activities, next to traffic, play a second important role. Particularly, slurry seals and using high polish value aggregates improve pavement FNs by 7 and 1.7 units on average respectively.
- With statistic significance less than traffic and rehabilitation activities, weather related variables, temperature and rainfall, also contribute to the fluctuation of friction data measurements. FNs tend to decrease with higher temperature and increase with more rainfall. This information helps explain the fluctuation of friction data collected in different seasons or years.
- Testing speed inversely affects friction, but its statistic significance is the weakest comparing to other variables under investigation, for the given range (20 mph ~ 50 mph).

DISCUSSION AND CONCLUSIONS

This paper uses the stepwise regression to investigate the relationship between pavement friction and explanatory variables including traffic volumes, traffic patterns, rehabilitation activities, weather conditions and test speeds. The stepwise regression has numerous advantages:

1. It examines all the explanatory variables that may help explain dependent variables. It is of great help when multiple variables might be involved and one does not have a conclusive proof.
2. It includes in the model only explanatory variables that exhibit significant influences so that one can focus on those significant factors.
3. It provides a mechanism to access the relative importance of explanatory variables based on their order of entry into the model or the partial R-square they contribute. Understanding the relative importance of explanatory variables help engineers interpret the variation in the friction data, and take effective measures to improve pavements friction.

However, to apply the stepwise regression in data analysis, one would pay attention to the following issues that might undermine its effectiveness or provide misleading information.

1. The effectiveness of stepwise regression could be affected by the “co-linearity” problem, which arises when two or more explanatory variables are highly correlated with each other. As a result, stepwise regression may not produce the best model if there are redundant explanatory variables.
2. Stepwise regressions do not always select the best set of explanatory variables

because the selection of next variable depends on the previously selected variables in the model, and the final set of variables may not always be the best.

3. Stepwise regressions inflate the risk of capturing chance features of the data. Therefore the models could be specific to the data set and may not be able to replicate in future.

To alleviate above concerns, some researchers suggested an all-possible-subset method - applying stepwise regression on all possible subsets of explanatory variables and using the model providing the best predictive results. This approach involves examining models on $2^k - 1$ combinations of explanatory variables.

In addition, all types of regressions pre-define a relationship (linear, in most circumstances) between a dependent variable and explanatory variables, which may limit the chances to find the most representative relationships. In this case, other multivariate analysis techniques such as neural network, Bayesian network and so on would be more appropriate.

ACKNOWLEDGMENTS AND DISCLAIMER

The authors appreciate the supports from management team, designers, and field technicians at the Office of Materials Technology, Maryland State Highway Administration. The contents of this paper reflect the views of the authors and do not necessarily reflect the official views of policies of the Maryland State Highway Administration. This paper does not constitute a standard, specification, or regulation.

REFERENCES

Lyon, C. and Persaud, B. (2008). "Safety Effects of a Targeted Skid Resistance Improvement Program." *TRB Annual Meeting 87th*, Washington, D.C. CD-ROM.

Murad, M. M. and Abaza, K. A. (2008). "Pavement Friction in a Program Aimed at Reducing Wet-Weather Traffic Accidents as the Network Level." *TRB Annual Meeting 87th*, Washington, D.C. CD-ROM.

Mayora, J. M. P. and Pina, R. J. (2008). "Effects of Pavement Friction Improvements on Crash Rates on Spanish Two-Lane Rural Roads." *TRB Annual Meeting 87th*, Washington, D.C. CD-ROM.

Song, W., Chen, X., Smith, T. and Hedfi, A. (2005). "Investigation of Hot Mix Asphalt Surfaced Pavements Skid Resistance in Maryland State Highway Network System." *TRB 84th Annual Meeting*, Washington, D.C. CD-ROM.

Anderson, D. A., Meyer, W. E., and Rosenberger, J. L. (1986). "Development of procedures for correcting skid-resistance measurements to a standard end-of-season value." *Transportation Research Record 1084*, TRB, National Research Council, Washington, D.C :40-48.

Burchett, J. L., and Rizenbergs, R. L. (1980) "Seasonal Variations in the skid Resistance of pavements in Kentucky." *Transportation Research Record 788*, TRB, National Research Council, Washington, D.C: 6-17.

Hill, B. J., and Henry, J. J. (1985). "Short-term, weather-related skid resistance variations." *Transportation Research Record 836*, TRB, National Research Council, Washington, D.C: 76-86.

Awoke G. S. and Goulias, D. (2008). "Review of Maryland Pavement Friction Survey and The Impact of Variable Test Speed on Friction Values." *TRB Annual Meeting 87th*, Washington, D.C. CD-ROM.

Henry J. J. (2000). "Evaluation of Pavement Friction Characteristics". *NCHRP Synthesis 291*. Transportation Research Board, Washington, D. C.:

Afifi, A., Clark, V.A., May, S. (2004). "Computer-Aided Multivariable Analysis, Fourth edition." Chapman & Hall/CRC, Boca Raton/London/ New York/ Washington, D.C.: 174-180.

Hall, J.W., Titus-Glover, L., Smith, K.L., etc. (2006). "Guide for Pavement Friction - Final Guide". *NCHRP Project (1-43)*. Washington D.C.: 17-17.

Long-Term Field Monitoring of Moisture Variations under Asphalt Pavement with Different Drainable Base Materials

Madhar Taamneh [1] and Robert Y. Liang [2]

[1] Ph.D, Dept. of Civil Engineering, Tafila Technical University, Tafila 66110, Jordan. Email: mmtaamneh@yahoo.com
[2]Professor, Dept. of Civil Engineering, The University of Akron, Akron, OH 44325-3905, (corresponding author). Email: rliang@uakron.edu

ABSTRACT: This paper presents long-term (six-year in duration) field monitoring results of moisture in six completely rehabilitated highway pavement sections on Interstate I-90 in Ashtabula county, Ohio. There were a total of six monitoring sections for six different drainable base materials used in construction. The Time Domain Reflectometery (TDR) was used to measure moisture contents in different pavement layers and cohesive subgrade soils (up to 1.829 m below the pavement surface). Statistical analysis was performed to exam the time history of moisture variations at different pavement layers as well as seasonal variations of moisture profile with depth. The comparative effectiveness of six different drainable base materials in alleviating excess moisture in the pavement system was also evaluated based on statistical analysis of moisture data.

INTRODUCTION

The sustained long period of free water existing within a pavement structure is undesirable because it can not only adversely affect the load carrying capacity of the pavement but also cause premature pavement failures. The current trend to remove the water from different layers of a pavement system is to use a subsurface drainage system. This is accomplished by different approaches, such as using open graded drainable base, asphalt or cement stabilized bases, edge drains, and geosynthetics.

There have been some recent field monitoring research undertaken by several researchers, including Sargand (2002), Heydinger (2003), Wolfe and Butalia (2004), Figueroa (2004) and Thang et al. (2008). Generally, subgrade moisture content beneath the pavement was found to oscillate from season to season, with maximum values occurred in summer season and minimum values occurred in winter season. In some instances, the subgrade moisture content was found to approach the full saturation level. The effect of precipitation on measured or observed soil moisture content is not well defined. While some studies have suggested that precipitation has a considerable influence on subgrade moisture content (Figueroa 2004, Thang et al.

2008), others could not establish a firm relationship (Sargand 2002, Diefenderfer 2002, Heydinger 2003,). In the above mentioned research, however, none of them was dedicated to specifically comparing the effectiveness of various types of drainable base materials on the moisture regime in the pavement layers, including base, subbase, and subgrade. The main purpose of this paper is to evaluate the effectiveness of various types of drainable base courses by analysis the filed monitored moisture data over a long term service life of pavement sections built with different drainable base materials.

PROJECT DESCRIPTION

For the purpose of evaluating effectiveness of different drainable base materials in flexible pavement, a section of totally re-built I-90 in the Ashtabula County, Ohio, was selected for extensive instrumentation and monitoring of moisture regimes under six different drainable base materials. The length of pavement with each type of drainable base material is 152.4 m long. The subsurface drainage system included two perforated underdrain pipes The shallow underdrain was a 10 cm diameter pipe within the shoulder edge, which was used primarily to drain the water in the base course and subbase course. The underdrain pipe was a 15.24 cm diameter perforated pipe placed underneath the outer edge of highway lane for draining water infiltrated to that depth. The 10.16 cm diameter underdrain pipes were wrapped with fabric cover to prevent potential clogging due to migration of fine materials.

BASE MATERIALS

Five different drainable base materials and one controlled base material (ODOT 304) in the Ohio Department of Transportation Materials Specifications were built in six monitoring pavement sections (each section was 500 ft long). The designation of the base materials are as follows: unbound base materials include ODOT 304, ODOT 307-IA, ODOT 307-NJ, and ODOT 307-CE, and bound base materials include ODOT 306 (cement treated base) and ODOT 308 (asphalt treated base). The thickness of base layer in all pavement sections was 4 inches except for ODOT 307-CE where 6 inches was used. The cement treated base (ODOT 306) was made by mixing AASHTO #57 stones with cement at 250 lb per cubic yard and a water cement ratio (w/c) of 0.36. The asphalt treated base (ODOT 308) was made by mixing AASHTO #57 stone with 1.5 to 3.5 percent by weight of PG 64-22 asphalt binder. The average measured moisture content was 5.7% and 4.8% for the ODOT 304 base and ODOT 307 series, respectively. The average dry density was 134 lb/ft3 and 126 lb/ft3 for ODOT 304 and ODOT 307 series, respectively.

FIELD INSTRUMENTATIONS

In this study, TDR probes manufactured by Campbell Scientific Inc. were used to measure the variations in pavement moisture contents. A total of 20 TDR probes and 18 TDR probes are used in unbounded and bounded base material sections, respectively. For each monitored section, two complete duplicate sets of sensors were

installed: one beneath the centerline of the driving lane and the other one beneath the centerline of the passing lane. The CR10X data loggers were used to monitor and store the data at each test section. A 12 volt DC power was used to provide power source to each data logger. The depth and spacing of each TDR sensor are depicted in Fig. 1 for pavement sections with both bound and unbound base courses.

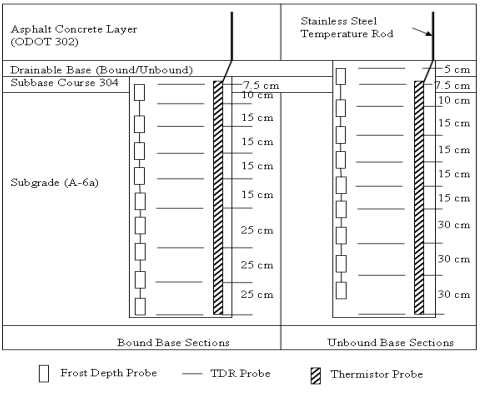

FIG. 1. Typical instrumentation profiles.

MOISTURE VARIATION WITH TIME

Gravimetric moisture from the instrumented pavement sections was recorded every 8 hours. Due to space limitations, only moisture variation near the top of subgrade layer is presented in this paper. The average daily gravimetric moisture contents (calculated as the average of the three 8-hours readings for the day) at the top of the subgrade layer on driving lanes are plotted with date in Fig. 2. The gravimetric water content calculated to be corresponding with 100 percent degree of saturation for each layer is also presented inside the box in the figure.

The degree of variation of moisture at the subgrade layer near the subbase was seen to be the least in the pavement sections built with bound drainable base, thus confirming a superior performance of bound drainable base in preventing moisture migration into the top elevation of the subgrade soils. Almost all the measured gravimetric moisture content was at the level less than the estimated gravimetric moisture content corresponding to 100 percent degree of saturation, with the exception at the pavement section built with ODOT 304 as base layer (i.e., no drainable base material was used). This observation leads to a suspicion that due to less than satisfactory hydraulic conductivity, ODOT 304 may not be effectively draining the infiltrated water in a timely manner.

After spring 2007, sharp jumps in the measured gravimetric moisture contents can be noticed at both pavement sections built with ODOT 304 and ODOT 307-IA drainable base materials. At ODOT 304 section, jumps occurred at driving lane at subgrade layers, whereas at ODOT 307-IA section, jumps occurred at both driving and

passing lane at the top elevation of the subgrade layer. It is worthy of mentioning that, up to now, all pavement sections are free of surface cracks.

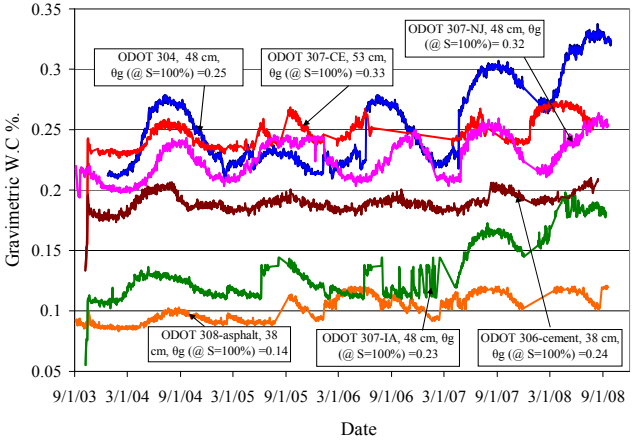

FIG. 2. Average daily water content measurements in top subgrade layer (top 30 cm of subgrade layer).

MOISTURE VARIATION WITH DEPTH

The average of six years moisture content profiles with depth at four seasons are presented in Fig. 3 for cement treated pavement sections. It is apparent from this figure that the gravimetric moisture content in the late spring and early summer seasons are greater than those in the late fall and early winter seasons. The subgrade at shallow depth (top 30.48 cm of subgrade layer) exhibits higher gravimetric moisture content variations compared with base and subbase layers. Moisture content variations at the bottom of the subgrade (177.8 to 223.5 cm from the pavement surface) were much lower than those near the subgrade surface. This implies that moisture content near the subgrade surface is affected by surface water. No clear correlation between the moisture regimes under the pavement system and the type of the base materials could be observed in this study.

STATISTICAL ANALYSIS OF MOISTURE DATA

Using the data from the entire monitoring period (from October 2003 to September 2008), the COV is calculated as the ratio of the standard deviation to the mean and presented in Tables 1. In general, large variation of the computed COV was observed in the base and subbase materials, whereas relatively small variation was observed at the top 30.48 cm of the subgrade layer. The smallest COV was actually observed at the bottom of the subgrade (i.e., 182.9 cm from the pavement surface). If using COV values at the shallow depth of the subgrade layer as a criterion of judging the

effectiveness of drainable base in preventing moisture migration into subgrade, then the ranking from best to worst of the six base materials can be as follows: ODOT 306-cement treated base, ODOT 308-asphalt treated base, ODOT 307-CE, ODOT 307-NJ, ODOT 307-IA, and finally ODOT 304.

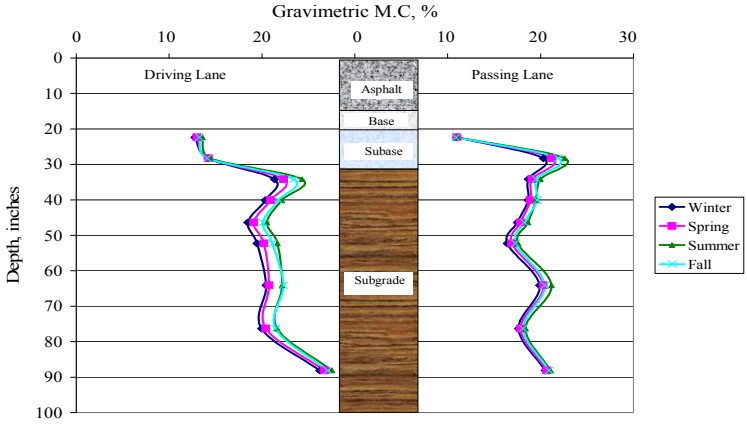

FIG. 3. Average 6 year water content measurements versus depth for ODOT 306-cement treated.

In this section, more analysis of the moisture regime in the soils is presented, including the average degree of saturation and the percent of time when the moisture content is greater than or equal to the moisture content at full saturation. The average degree of saturation is calculated according to the following equation:

$$\text{Average degree of saturation } \% = \left(\frac{\theta_{g_{avg}} - \theta_{g@S=100\%}}{\theta_{g@S=100\%}} \right) \times 100\% \qquad (1)$$

Where: $\theta_{g@S=100\%}$ = estimated gravimetric water content at full saturation, $\theta_{g_{avg}}$ = average gravimetric water content over 6 years of monitoring. The percent of time when the measured water content is greater than or equal to the water content at full saturation is calculated according to the following equation:

$$\text{Percent of Time when } (\theta_g \geq \theta_{g@S=100\%}) = \left(\frac{N_{\theta_g \geq \theta_{g@S=100\%}}}{N_T} \right) \times 100\% \qquad (2)$$

where: $N_{\theta_g \geq \theta_{g@S=100\%}}$ = number of measurement points during the duration of the six year monitoring period when the measured water content is greater than or equal to

the water content at full saturation, N_T = total number of measurement points for TDR sensors during the entire monitoring period.

Table 1. Statistical Moisture Content Data

Pavement Layer	Pavement Section	COV	$\Theta_{g@S=100\%}$	Saturation, %	Time percent of fully saturation
Base Course	ODOT 304	11.9	0.21	56.2	0.00
	ODOT 307-NJ	14.3	0.18	66.1	0.00
	ODOT 307-IA	5.8	0.22	39.1	0.00
	ODOT 307-CE	11.4	0.17	46.5	0.00
Subbase Course	ODOT 304	17.8	0.18	67.4	0.06
	ODOT 307-NJ	15.9	0.22	61.0	0.00
	ODOT 307-IA	10.3	0.18	50.1	0.00
	ODOT 307-CE	12.0	0.15	46.6	0.00
	Asphalt	6.7	0.23	66.8	0.00
	Cement	8.7	0.21	62.6	0.00
Subgrade Top layer	ODOT 304	13.5	0.23	110.7	63.40
	ODOT 307-NJ	7.5	0.30	75.7	0.00
	ODOT 307-IA	8.4	0.16	82.3	0.00
	ODOT 307-CE	7.3	0.33	75.2	0.00
	Asphalt	6.9	0.15	68.0	0.00
	Cement	6.3	0.29	65.2	0.00
Subgrade Bottom layer	ODOT 304	3.6	0.28	87.3	0.00
	ODOT 307-NJ	6.5	0.34	68.4	0.00
	ODOT 307-IA	5.3	0.28	73.2	0.00
	ODOT 307-CE	2.9	0.32	67.3	0.00
	Asphalt	4.3	0.22	83.0	0.00
	Cement	3.9	0.30	88.6	0.00

The calculated average degree of saturation and the time percent of full saturation are shown in Table 1. According to the results shown in Table 1, none of the drainable base materials showed the measured water content exceeding the estimated water content at full saturation. This observation also holds true for subbase layers and subgrade bottom layers. The exception to the above observation was noticed at the top elevation of the subgrade layer underneath the ODOT 304 pavement section. In fact, the percent of saturation time for this section for this elevation was found to be 64 percent. A lesser severe percent of time (i.e., about 5 to 10 percent) when top elevation of subgrade was in full saturation can be observed in the pavement sections built with ODOT 307-NJ and ODOT 307-IA. Both cement treated and asphalt treated permeable base materials showed the lowest degree of saturation in the subgrade soils when compared to other pavement sections built with other types of drainable base materials.

CONCLUSION

In this paper, field measured moisture data for the regime underneath asphalt concrete layers of the flexible pavement sections built with different drainable base materials were analyzed to investigate the effect of drainable base material types on the subsurface moisture regimes. Pavement sections built with cement treated and asphalt treated permeable base materials showed the lowest variation in the gravimetric moisture contents, especially at the top of the subgrade layer. Furthermore, using COV values at the top elevation of the subgrade soils as an evaluation index, the effectiveness of different drainable base materials to drain the infiltrated water can be ranked from the best to worst as follows: ODOT 306-cement treated base, ODOT 308-asphalt treated base, ODOT 307-CE, ODOT 307-NJ, ODOT 307-IA, and finally ODOT 304. It seems that it is prudent to avoid using ODOT 304 and ODOT 307-IA as drainable base materials for poor performance in preventing moisture from migrating toward cohesive subgrade soils.

Contrary to other field monitoring programs cited in the literature, there was no evidence of full saturation in base and subbase materials for the entire monitoring period. In some cases, particularly in ODOT 304 pavement section, subgrade soils at the top elevation of the subgrade layer experienced full saturation for 64 percent of the monitoring duration. Underneath passing lanes, subgrade layers at both ODOT 307-NJ and ODOT 307-IA sections experienced full saturation for about 5 and 10 percent of the monitoring duration. Both cement treated and asphalt treated permeable base materials showed the lowest degree of saturation among other base materials.

REFERENCES

Diefenderfer, B.K. (2002) “Moisture Content Determination and Temperature Profile Modeling of Flexible Pavement Structures.” Ph.D Dissertation, Virginia Polytechnic Institute and State University.

Figueroa, J.L. (2004) “Long Term Monitoring of Seasonal and Weather Stations and Analysis of Data from SHRP Pavements.” Final Report for Project ODOT 8880, Ohio Department of Transportation, Report No. FHWA/OH-2004/004.

Heydinger, A. (2003). “Monitoring Seasonal Instrumentation and Modeling Climatic Effects on Pavements at the Ohio/SHRP Test Road.” Report No. FHWA/OH-2003/018, U.S. Department of Transportation.

Sargand, S. (2002). “Continued Monitoring of Pavement in Ohio.” Sate Job Number 14652(0), Report No. FHWA/OH-2002/035, University of Ohio.

Thang, H.P., Matthew, C., David, J.W., Chuck, J., Vern, S., and Radhey, S. (2008). “Case study of seasonal Variation in the Subgrade and Subbase Layers of Highway US 20.” Report No. CTRE Project 04-172, IHRN Project TR-516, Iowa State University.

Wolfe, W. E., and Butalia, T. S., (2004). “Continued monitoring of SHRP pavement instrumentation including soil suction and relationship with resilient modulus.” Sate Job Number 14691(0), Report No. FHWA/OH-2004/007. University of Ohio.

Method of Design for Improving the Drainage Layer of Asphalt Pavement

Hancheng Dan[1], Liang Li[2], Hui Yao[3], Lianheng Zhao[4] and Xiaoli Yang[5]

[1]Ph.D. candidate, School of Civil engineering and Architecture, Central South University, Changsha 410075, Hunan, P.R.China, danhancheng@163.com
[2]Professor, School of Civil engineering and Architecture, Central South University, Changsha 410075, Hunan, P.R.China, liliang_csu@126.com
[3]Ph.D. candidate, School of Civil engineering and Architecture, Central South University, Changsha 410075, Hunan, P.R.China, jianxin_yaohui@163.com
[4]Ph.D. candidate, School of Civil engineering and Architecture, Central South University, Changsha 410075, Hunan, P.R.China, zlh8076@163.com
[5]Professor, School of Civil engineering and Architecture, Central South University, Changsha 410075, Hunan, P.R.China, yxnc@yahoo.cn

ABSTRACT: A method for improving the design of drainage layer in pavement was presented. Based on the percolation theory, the mathematical physics model for calculating the water exchanges were established, involving drainage layer with a constant cross-width thickness and drainage layer with a varying cross-width thickness. Then, the analytical solutions of flux distribution in drainage layer with a constant cross-width thickness and drainage layer with a varying cross-width thickness were obtained to verify the improvement of discharge capacity of proposed drainage layer. Then, the models were calculated and analyzed. The analysis results showed that the drainage layer with a varying cross-width thickness can improve the water drainage capacity well. Additionally, through the parameter analysis, it demonstrated that the parameters of n and H' play a significant role in improving the discharge capacity of drainage layer.

INTRODUCTION

Water can infiltrate into the pavement structure by various means, which can cause and accelerate the pavement damage. Inner drainage system in pavement can drain the accumulated water promptly, and it is useful to promote the service performance and greatly prolong service life thereby acquiring considerable economic benefit. The comparison analysis and observation results have shown that the service life of pavement which is set the drainage layer or permeable base can be improved up to approximately 30% in concrete pavement and 50% in asphalt pavement respectively than that of pavement with no drainage layer (MATHIS, 1989). In order to drain surface infiltration water effectively, the common experience drainage design is that the discharge capacity of drainage facilities should be greater than the water quantity

infiltrating the pavement structure, and the discharge capacity of drainage facilities downstream should be greater than that of upstream(JTJ018297, 1998), i.e. the kinds of drainage facilities must have enough discharge capacity in order to drain the free water in the pavement away. The cross section of drainage layer in general road is rectangular shape i.e. the drainage layer with a constant cross-width thickness (See Fig.1). In this case, this design consideration can meet the demand of drainage at the transverse direction of pavement. Nevertheless, at the superelevation road section or the sections that transverse slope is large; the transverse hydraulic gradient is also large which give rise to accelerate the velocity of the free water in the drainage layer and also lead to the non-uniform infiltration of water. Therefore, on the condition of long duration and large density of rainfall, the water ponding will occur at the pavement edge. Moreover, at the superelevation transition, the drainage path originates near the highway crown at a location upslope from the zero cross slope station. Because of the negative cross slope, the drainage path is initially directed towards the outer travel lane edge. However, the cross slope superelevation results in the drainage path turning inward to the inside pavement edge of the roadway curvature(Jeong, 2008). Therefore, the water path is longer than the general road section. Further, at the superelevation transition, the water-collecting wells to drainage the excessive water on the pavement surface are set at the side close to the median, but on the another side away from the median is not set the water-collecting wells but curb instead i.e. concentrated drainage. Thus, on the condition of long rainfall duration and larger rainfall density, the pavement edge is ponding and the water is easier to infiltrate into the pavement structure. The literature by AL-Qadi (Al-Qadi, Lahouar, Louizi, Elseifi and Wilkes, 2004) presented a method to improve the drainage layer from the perspective of pavement materials rather than the design method. To conclude, the author figures that the drainage layer with a varying cross-width thickness (See Fig.2) should be taken into account and tried at the superelevation transition or the special road sections need to improve the discharge capacity of drainage layer in the highway.

In this paper, a study of water drainage in the drainage layer with a varying cross-width thickness and one design method are presented on the basis of the percolation theory in order to support the feasibility of application.

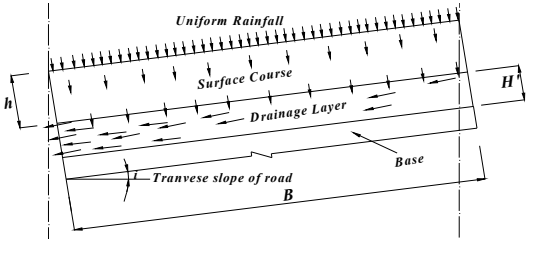

FIG.1. Schematic diagram of the drainage layer

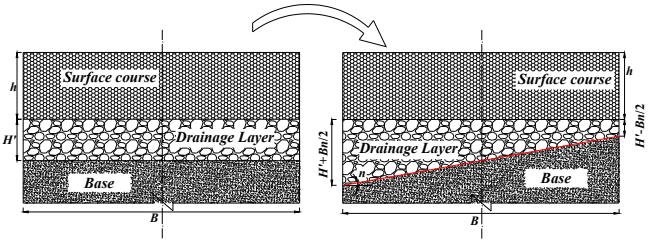

FIG.2. Design of improved drainage layer

ESTABLISHMENT AND SOLUTION OF DRAINAGE LAYER WITH A CONSTANT CROSS-WIDTH THICKNESS MODEL

Provided that the surface course is permeable with certain permeability coefficient and the rainfall infiltrates the surface course uniformly. In order to establish the calculation model for modeling the water seepage in drainage layer, the assumptions can be given as bellow:

(a). Ignore the transverse water seepage in surface course;
(b). Regard pavement base as the non-drainage layer;
(c). Generate water seepage only between the surface course and drainage layer;
(d). Neglecting the velocity head at the end section of drainage layer.

Based on these assumptions above, the model can be illustrated as FIG.3.

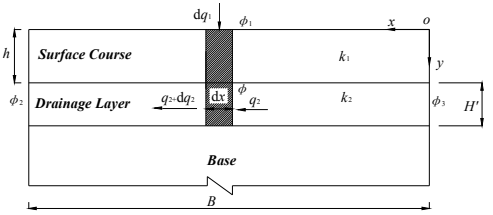

FIG.3. Drainage layer with a constant cross-width thickness model

It can be seen from FIG.3 that *dx* is the differential section in which the water infiltrates the drainage layer via surface course (largely via the cracks for instance). And the water head loss is ϕ_1- ϕ if the top water head is ϕ_1 and the down water head is ϕ. Define the thickness of surface course is *h*, thus, the hydraulic gradient is $J = \frac{\varphi_1 - \varphi}{h}$. In addition, dq_1 is seepage flux through *dx*. k_1 is the permeability coefficient of surface course, *B* is the width of pavement, J_0 is the resultant gradient of pavement which equals to $J_0 = \sqrt{i_h^2 + i_z^2}$, where the i_z and i_h are longitudinal and transverse slopes of road respectively.

According to the *Darcy Law*, the flux in surface course can be given

by $dq_1 = k_1 \frac{\varphi_1 - \varphi}{h} dx$, and the seepage flux in drainage layer through *dx* of surface course can be expressed as $q_2 = k_2 H' \frac{d(\varphi_3 - \varphi)}{dx}$. Therefore, the increment of seepage flux in drainage layer is $dq_2 = k_2 H' \frac{d^2(\varphi_1 - \varphi)}{dx^2} dx$

With the continuity of seepage flow, the flux in drainage layer through *dx* of surface course should be equal to the increment of seepage flux in drainage layer. Thus, we can obtain the differential equation which is expressed as

$$\frac{d^2(\varphi_1 - \varphi)}{dx^2} = \frac{k_1}{k_2 hH'}(\varphi_1 - \varphi) \tag{1}$$

In summary, the equation (1) is the seepage balance differential equation which illustrates the water exchange between the surface course and drainage layer of equal thickness.

The equation (1) can be solved whose solution is given by

$$\varphi_1 - \varphi = C_1 e^{(\alpha x)} + C_2 e^{-(\alpha x)} \tag{2}$$

where, $\alpha = \sqrt{\frac{k_1}{k_2 hH'}}$, the fluxes of surface course and drainage layer at *x* can be expressed as bellow respectively

$$\begin{cases} q_1 = \frac{k_1}{\alpha h}\left[C_1 e^{(\alpha x)} - C_2 e^{-(\alpha x)}\right] \\ q_2 = k_2 H' \alpha \left[C_1 e^{(\alpha x)} - C_2 e^{-(\alpha x)}\right] \end{cases} \tag{3}$$

where C_1 and C_2 are integral constants.

Provided that the boundary conditions are $q_2|_{x=0} = 0$， $\varphi_1 - \varphi|_{x=B} = \Delta\varphi_B$

We can obtain the constant coefficients and the equations as bellow

$$q_1 = \frac{k_1}{\alpha h} \frac{\Delta\varphi_B}{e^{(\alpha B)} + e^{-(\alpha B)}}\left[e^{(\alpha x)} - e^{-(\alpha x)}\right] \tag{4}$$

$$q_2 = k_2 H' \alpha \frac{\Delta\varphi_B}{e^{(\alpha B)} + e^{-(\alpha B)}}\left[e^{(\alpha x)} - e^{-(\alpha x)}\right] \tag{5}$$

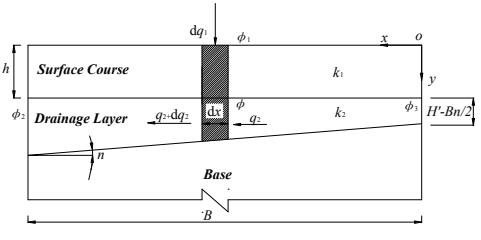

FIG.4. Drainage layer with a varying cross-width thickness model

ESTABLISHMENT AND SOLUTION OF DRAINAGE LAYER WITH A VARYING CROSS-WIDTH THICKNESS MODEL

Based on the assumptions of the model as equal thickness, the unequal thickness model can be established accordingly (see FIG.4).

In FIG.4, *n* is the slope of drainage layer, *dx* is differential calculation section. In the model of unequal thickness, the flux in drainage layer through *dx* of surface course should be equal to the increment of seepage flux in drainage layer. Thus, we can obtain the differential equation expressed as equation (6).

$$(H+nx)\frac{d^2(\varphi_1-\varphi)}{dx^2}+n\frac{d(\varphi_1-\varphi)}{dx}+\frac{k_1}{hk_2}(\varphi_1-\varphi)=0 \tag{6}$$

where $H=H'-Bn/2$.

Defined β with $\beta=\frac{k_1}{hk_2n}$, the equation (6) can be transformed into

$$\left(\frac{H}{n}+x\right)^2\frac{d^2(\varphi_1-\varphi)}{dx^2}+\left(\frac{H}{n}+x\right)\frac{d(\varphi_1-\varphi)}{dx}+\beta\left(\frac{H}{n}+x\right)(\varphi_1-\varphi)=0 \tag{7}$$

In summary, the equation (7) is the seepage balance differential equation which illustrates the water exchange between the surface course and the drainage layer of unequal thickness.

Though the equation can be solved by means of quadrature of power series, it is convenient to transform the functions into the form of *Bessel Function*.

And the general solution of equation (7) is

$$\varphi_1-\varphi=C_1I_0\left(2\sqrt{\beta(x+H/n)}\right)+C_2K_0\left(2\sqrt{\beta(x+H/n)}\right) \tag{8}$$

Given the boundary conditions as below

$$\left.\begin{aligned}\varphi_1-\varphi\big|_{x=B}&=\Delta\varphi_B\\ Q_2\big|_{x=0}&=0\end{aligned}\right\} \tag{9}$$

We have

$$\begin{cases}Q_1=\dfrac{k_1}{2\beta h}Z\left[C_1I_1(Z)+C_2K_1(Z)\right]\\ Q_2=k_2(H+xn)\dfrac{2\beta}{Z}\left[C_1I_1(Z)+C_2K_1(Z)\right]\end{cases} \tag{10}$$

where

$$\left.\begin{aligned}C_1&=\frac{-\Delta\varphi_BK_1(Z_0)}{I_1(Z_0)K_0(Z_B)-I_0(Z_B)K_1(Z_0)}\\ C_2&=\frac{\Delta\varphi_BI_1(Z_0)}{I_1(Z_0)K_0(Z_B)-I_0(Z_B)K_1(Z_0)}\\ Z&=2\sqrt{\beta(x+H/n)}\end{aligned}\right\} \tag{11}$$

COMPARISON ANALYSIS OF MODEL

Based on the assumption (d), we have

$$q_2=k_2H'a(h+BJ_0)\frac{\sinh(ax)}{\cosh(aB)} \tag{12}$$

$$Q_2=\frac{2\beta k_2[h+B(J_0+n)]}{Z}\left[H'+\frac{(2x-B)n}{2}\right]\frac{K_1(Z)I_1(Z_0)-I_1(Z)K_1(Z_0)}{I_1(Z_0)K_0(Z_B)-I_0(Z_B)K_1(Z_0)} \tag{13}$$

We can obtain the flux ratio at $x=B$ under the condition with same areas of drainage

layers in order to compare the efficiency of drainage layers with different thickness.

$$\left.\frac{Q_2}{q_2}\right|_{x=B} = \frac{(2H'+Bn)\cdot\beta}{H'\alpha\tanh(\alpha\cdot B)\cdot Z_B}\frac{h+B(J_0+n)}{h+BJ_0}\frac{I_1(Z_0)K_1(Z_B)-I_1(Z_B)K_1(Z_0)}{I_1(Z_0)K_0(Z_B)-I_0(Z_B)K_1(Z_0)} \tag{14}$$

where

$$\left.\begin{aligned} Z_0 &= 2\sqrt{\frac{k_1}{hk_2n^2}\left(H'-\frac{Bn}{2}\right)} \\ Z_0 &= 2\sqrt{\frac{k_1}{hk_2n^2}\left(H'+\frac{Bn}{2}\right)} \end{aligned}\right\} \tag{15}$$

In this paper, the permeability coefficient of surface course (k_1) and drainage layer (k_2) were 0.01cm/s and 1.0 cm/s respectively. Moreover, other corresponding parameters were listed in the Table 1, and the parameter analyses were shown in FIG.5 and FIG.6.

Table 1. Calculation Parameters for the Analysis of Flow in Drainage Layer

Parameters	k_1 (cm/s)	k_2 (cm/s)	h (cm)	H' (cm)	J_0	B (m)
Value	10^{-2}~10^{-6}	0.135~2.4	9~15	8~15	0.02	10
References	(Maupin, 2000, Dan,et.al, 2009)	(Lv, et.al, 2003; Sasaki,et.al, 2006)	(Bi, et.al, 2001)	(Bi, et.al 2001)	(JI, 2005)	(JI, 2005)

In Fig.5, when x the transverse direction along the pavement is between 0m and 10m, the flux of q_2 and Q_2 both increase nonlinearly. Moreover, the difference between the q_2 and Q_2 is relatively obvious which can be illustrated by the flux ratio of Q_2/q_2 from the Fig.5. The flux ratio Q_2/q_2 approximately reaches the peak which is up to 1.58 at x=6m and then fall down to about 1.5. In other words, the percent of improvement of discharge capacity is about 50%.

FIG.6 shows that the value of n play an important role in improving the drainage capacity of drainage layer and the Q_2/q_2 at x=B increases from 1.00 to 1.9 at H'=8cm, while from1.00 to 2.4 at H'=16cm. Furthermore, it is significant that the thinner the thickness of drainage layer is; the more effective improvement of drainage is.

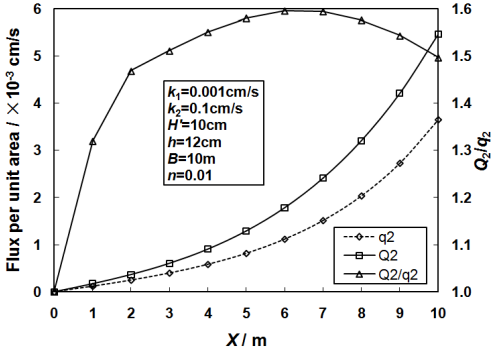

FIG.5. Flux distribution and comparison profiles along transverse direction

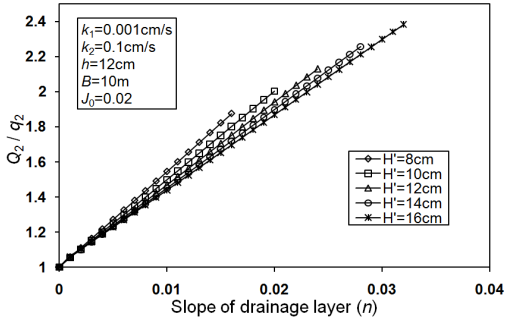

FIG.6. Effect of *n* and *H'* on the flux ratio

CONCLUSIONS

On the basis of the percolation theory, the mathematical physics model for illustrating the water seepage in surface course and drainage layer, involving drainage layer with a constant cross-width thickness and drainage layer with a varying cross-width thickness, were established. By solving the model using the *Bessel Function* solution, the analytic solutions of flux distribution in drainage layer with a constant cross-width thickness and drainage layer with a varying cross-width thickness were obtained to describe the difference between these two kinds of drainage layers and to verify the improvement of discharge capacity of proposed drainage layer.

With the calculated comparison, the drainage layer model with a varying cross-width thickness presented in this paper made a better improvement of discharge capacity than that of drainage layer with a constant cross-width thickness. The parameters analysis indicated that the parameters of *n* and *H'* play a significant role in improving the discharge capacity of drainage layer.

ACKNOWLEDGEMENT

Financial support for the work reported here was provided through a project (No.2007-29) supported by Hunan Communications Department and another project (No.2009ybfz05) supported by Central South University. Moreover, the authors owe a debt of gratitude to Miss Zhang Ting for her generous help on checking English spellings and grammar.

REFERENCES

Al-Qadi, I. L., Lahouar, S., Louizi, A., Elseifi, M. A., and Wilkes, J. A. (2004). "Effective approach to improve pavement drainage layers." *Journal of Transportation Engineering-Asce*, 130(5), 658-664.

Bi, Y. X., Yao, Z. K., Guo, Y. B., and Jiang, A. F. (2001). "Structure analysis of semi-rigid asphalt pavement with asphalt treated permeable base." *China Journal of*

Highway and Transport, 14(3), 17-20.
Dan, H. C., Li, L., He, Y. C., Zhao, L. H., and Wang, F. (2009). "Study on Permeability Test of Asphalt Pavement." *Journal of Highway and Transportation Research and Development*, 26(08), 16-21.
Jeong, J. (2008). "A Hydrodynamic Diffusion Wave Model for Stormwater Runoff on Highway Surface at Superelevation Transitions." Dissertation PHD, The University of Texas at Austin, Austin.
Ji, Q. K. (2005). "Design of road infiltration based on infiltration coefficient of pavement." *Chinese Journal of Geotechnical Engineering*, 27(9), 1045-1049.
JTJ018297. (1998). "Specifications of drainage design for Highways." People's Communications Press, Beijing.
Lv, W. J., Wu, S. S., and Dai, J. L. (2003). "Permeability coefficient test of permeable base materials." *Journal of Xi'an Highway University*, 29(02), 22-24.
Mathis, D. M. (1989). "Permeable Base Design and Construction." *Proc., 4th International Conference on Concrete Pavement Design and Rehabilitation*, Purdue University, 663-670.
Maupin, G. W., and Jr. (2000). "Investigation of Test Methods, Pavements, and Laboratory Design Related to Asphalt Permeability." Virginia Transportation Research Council, Charlottesville, VTRC 00-R24.
Sasaki, I., Moriyoshi, A., and Hachiya, Y. (2006). "Water/gas permeability of bituminous mixtures and involvement in blistering phenomenon." *J. Jpn. Petrol. Inst.*, 49(2), 57-64.

Determination of Subgrade Resilient Modulus for Existing Pavement Based on Moisture Condition Coupled with Stress

Jianming Ling[1], Xin Qiu[2], Jie Yuan[3]

[1]Professor, Key Laboratory of Road and Traffic Engineering of Ministry of Education, Tongji University, Shanghai P.R. China, 201804. Email: jmling01@yahoo.com.cn
[2]PhD, Key Laboratory of Road and Traffic Engineering of Ministry of Education, Tongji University, Shanghai P.R.China,201804. Email: tonyxinqiu@163.com
[3]Associate professor, Key Laboratory of Road and Traffic Engineering of Ministry of Education, Tongji University, Shanghai P.R. China, 201804. Email: yuanjie@tongji.edu.cn

ABSTRACT: Subgrade resilient modulus (E_R) is a crucial parameter for pavement design and evaluation with a mechanistic-empirical method. To existing pavement overlaying and reconstruction, E_R is difficult to determine because it is a function of both water content and stress level. In this paper, a 3-stage method to determine E_R considering moisture condition coupled with stress is presented. Firstly, the equilibrium moisture of every sublayer of an existing subgrade was predicted by soil water characteristic curve and validated by in-situ water content tests. Secondly, a constitutive model of resilient modulus (M_R) was established for the subgrade soil on the basis of triaxial repeated loading tests. Its parameters related to water content were regressed as well. Finally, according to the equivalent principle of deflection at the top of pavement structure, a prediction function of subgrade E_R was proposed based on moisture-stress coupling condition and KENLAYER pavement analysis program. Its validity was verified by Falling Weight Deflectometer (FWD) tests. The presented 3-stage method has successfully been applied to predict E_R of the existing subgrade in widening engineering of Shanghai A11 Expressway.

INTRODUCTION

According to a lot of case investigation, some pavement diseases, such as cracking and permanent deformation, are attributed to inadequacy of subgrade resilient modulus E_R (Ling, 2006). As a result, the determination of E_R has been a key point for pavement design and evaluation with a mechanistic-empirical method. For a new pavement design, triaxial repeated loading tests in laboratory (AASHTO, 1992) could be used to characterize subgrade soil and calculate its resilient modulus M_R. For the existing pavement structures, some field tests, such as loading plate test, deflection measurement and dynamic cone penetration test, are frequently adopted to evaluate the subgrade structure and acquire its E_R. However, in consideration of field condition and

time-consuming, there is a great need for a simpler yet reliable method. To an existing subgrade structure, its E_R depends mainly on two outer factors: equilibrium moisture state and stress level (Li, 1994). In the past, some experiential regression function were used in terms of physical parameters of subgrade soils to predict E_R of the existing subgrade (Powell, 1984 and Carmichael, 1986), but stress condition as an important factor was often ignored.

In this paper, an attempt was made to present an efficient function to predict E_R considering the effect of moisture condition coupled with stress. FWD test was also conducted to verify the validity of the E_R prediction function.

EQUILIBRIUM MOISTURE OF SUBGRADE

Prediction Method and Model Coefficients

In general, subgrade soil is unsaturated, its equilibrium moisture can be expressed in terms of soil suction. The suction, denoted h_s, could be computed by the depth to ground water table (GWT), specifically $h\gamma_w$. Where h is the height of any interest point in subgrade to the GWT, and γ_w is the unit weight of water (Perera, 2004). The relationship between soil suction and water content is depicted by soil water characteristic curve (SWCC). The chosen SWCC model in this paper is the equation developed by Fredlund and Xing (Fredlund and Xing, 1994), shown as Equation 1.

$$\theta_w = \left[1 - \frac{\ln\left(1+\frac{h_s}{h_r}\right)}{\ln\left(1+\frac{10^6}{h_r}\right)}\right] \frac{\theta_s}{\left\{\ln\left[\exp(1)+\left(\frac{h_s}{a}\right)^b\right]\right\}^c} \tag{1}$$

Where, θ_w is volumetric water content, θ_s is saturated volumetric water content, a, b, c and h_r are model coefficients.

For the purpose of analysis and application, a testing section was selected on A11 Expressway in Shanghai. Some related physical parameters of the drilled subgrade soil were tested in laboratory. Its plastic index (PI) and percent passing No.200 (P_{200}) are 11.9 and 0.98 respectively. Then the parameter wPI (= $P_{200}\times PI$) is equal to 11.66. According to equations proposed by Zapata (1999), the coefficients of Equation 1 were calculated and shown in Table1.

Table 1. Calculated coefficients for the chosen SWCC model

a	b	c	h_r (kPa)
11.47	1.71	0.52	372.78

Verification of Predicted Results

The GWT of A11 Expressway was monitored monthly over a period of one year and

its average depth from ground was approximately 0.5m. Using $h\gamma_w$ model and Fredlund and Xing SWCC, gravimetric water contents at different depths in subgrade were predicted as shown in Fig.1. In-situ test of equilibrium moisture of subgrade was performed by drilled soil samples, which were retrieved from 0.3 m intervals reaching a depth of 2.7m. The comparison of the prediction results with In-situ test results is illustrated in Fig.2. It is shown that the predicted results are acceptable.

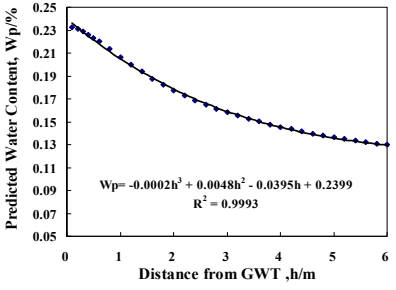

FIG.1. Predicted water content

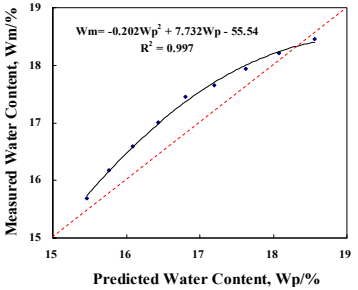

FIG.2. Predicted vs. measured water content

M_R MODEL OF SUBGRADE SOIL

M_R Tests

Table 2. M_R Test Results of The Subgrade Soil

Load Number	Stress Level/kPa		M_R/MPa at Different Water Contents(%)					
	σ_d	σ_c	8.6	10.2	12.5	14.1	16.3	18.6
1	30	60	129.13	111.17	92.08	79.53	61.61	28.98
2	30	45	116.56	99.29	82.32	68.46	56.19	25.27
3	30	30	108.10	91.75	71.57	59.67	47.83	21.51
4	30	15	100.99	70.71	62.51	43.77	38.09	18.46
5	55	60	107.53	81.00	71.97	58.73	48.63	25.93
6	55	45	92.10	74.27	63.11	52.75	44.38	23.27
7	55	30	86.48	66.87	53.54	47.86	38.99	20.17
8	55	15	74.61	57.63	47.19	38.73	31.56	15.20
9	75	60	88.57	81.18	60.66	50.13	40.20	20.07
10	75	45	81.28	69.89	55.28	47.76	38.28	18.65
11	75	30	76.20	62.74	46.59	44.14	33.70	14.76
12	75	15	64.62	53.40	40.66	36.45	25.50	9.97

It has been customary to use M_R to represent the elastic performance of subgrade materials defined as the repeatedly applied wheel load stress divided by the recoverable strain(Seed,1962). To the subgrade soil of A11 Expressway, M_R tests, in accordance

with AASHTO TP46 protocol (1992), were conducted by employing repeated triaxial equipment of USA Sensotec-SA-Series at Tongji University. A total of 18 cylinder samples (Φ38mm×80mm) were prepared and were divided into 6 kinds of subsets with different water contents. Deformation of each sample was monitored using two Linear Variable Differential Transformers (LVDTs) mounted outside of a testing chamber. The last five loading cycles of a 100-cycle sequence yielded average M_R value. The detailed M_R test results are listed in Table2.

M_R Model Correlated to Stress and Moisture Condition

It has been reported that M_R of fine-grained subgrade soils typically decreases at increasing stress levels. The bilinear model (Thompson and Elliott, 1985) was commonly used for fine-grained subgrade soils expressed by the resilient modulus-deviator stress relationship given in Equation 2.

$$\begin{aligned} M_R &= k_1 + k_3(k_2 - \sigma_d) \qquad k_2 \geq \sigma_d \\ M_R &= k_1 - k_4(\sigma_d - k_2) \qquad k_2 < \sigma_d \end{aligned} \quad (k_1>0,\ k_2>0,\ k_3>0,\ k_4>0) \tag{2}$$

Where, σ_d is deviator stress, k_1,k_2,k_3 and k_4 are parameters.

Since the effects of k_2, k_3 and k_4 are not obvious at different moisture conditions, the constant values are chosen as 42.75,1110 and 178 respectively according to the test results. The nonlinear regression option was employed to determine the relationship between k_1 and water content, and the regression equation is shown as following.

$$k_1 = e^{(5.458 - 0.0658\ w)} \quad (R^2=0.98) \tag{3}$$

Where, k_1 is a model parameter, w is the water content of sub-grade

Verification of M_R Model

The predicted moduli are plotted against the measured ones as illustrated in Fig.3. A good relation between predicted and measured M_R of the soil is shown in the figure.

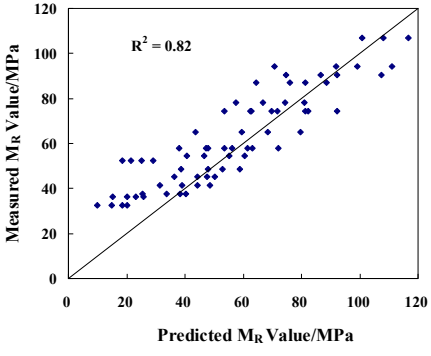

FIG.3. Predicted vs. measured M_R value

EQUIVALENT RESILIENT MODULUS OF SUB-GRADE E_R

Calculation Scheme and Assumptions

Based on the models of equilibrium moisture and resilient modulus of subgrade soils as mentioned above, the equivalent resilient modulus of subgrade, E_R, could be determined according to the calculation scheme shown in Fig.4.

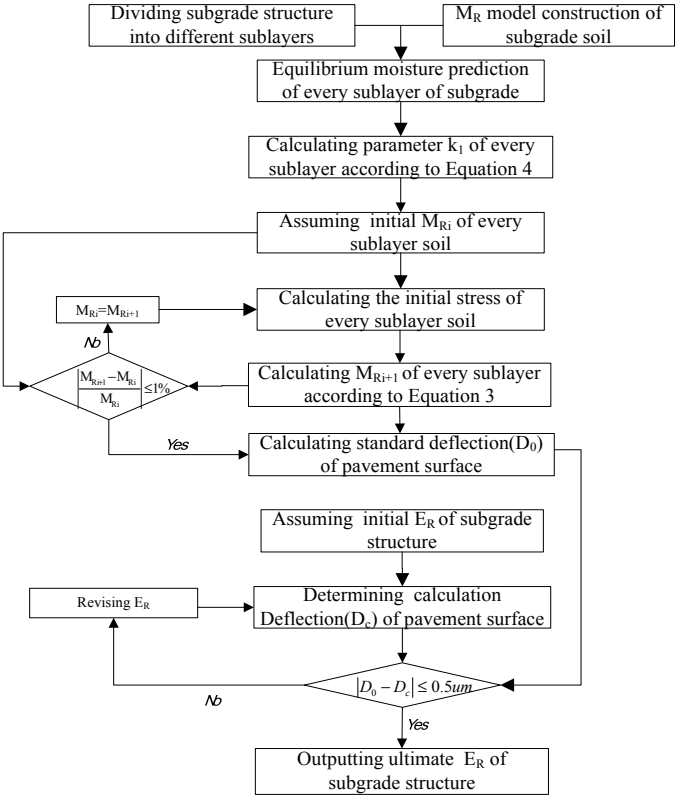

FIG.4. Calculation scheme of subgrade E_R

The KENLAYER finite element model was used for solving pavement surface deflections and other critical pavement stresses and strains under applied wheel loading. In addition, the following basic assumptions were considered.

1. Self-weights of subgrade and pavement are considered and there is initial stress and not initial strain in the subgrade structure.
2. The imposed vehicle load on the pavement structure is assumed to be circular and

uniform with 0.7MPa of pressure stress and 30cm in diameter.

3. Deviator stress (σ_d) is calculated by Equation 4.

$$\sigma_d = \sigma_1 - \frac{\sigma_2 + \sigma_3}{2} + \gamma \cdot z \cdot (1 - K_0) \tag{4}$$

Where, σ_1, σ_2 and σ_3 are the three direction principal stress in subgrade structure; γ is the soil unit weight density; z is the depth of calculation point from subgrade surface; K_0 is the coefficient of earth pressure at rest condition.

Prediction Function of E_R

A typical asphalt pavement with cement treated base (CTB) in China was modeled as a multi-layered system. The geometrical and material parameters of the analyzed pavements are given in Table 3.

Table 3. Geometrical and Material Parameters of Pavements

Material Type	Layer Thickness/cm	Layer Modulus/MPa	Poisson Ratio
Asphalt concrete(AC)	16~24	2000~6000	0.35
Cement Treated Soils(BC)	38~46	4000~12000	0.25
Subgrade (SG)	—	E_R	0.4

According to the scheme as mentioned above, different pavements were analyzed by KENLAYER program and their subgrade resilient moduli E_R were respectively calculated based on the equivalent principle of deflection at the top of pavement structure. Using the calculated E_R database, a correlation function between E_R and other selected variables was found, and it is defined as follows:

$$Ln(E_R) = -0.441Ln(E_{AC}) + 0.177Ln(E_{BC}) - 0.162Ln(h_{AC}) + 0.863Ln(h_{BC}) + 3.96 \quad (R^2=0.79) \tag{5}$$

Where, E_R is the equivalent resilient modulus of subgrade, E_{ac} and E_{bc} are the elastic modulus of asphalt concrete course and CTB course, h_{ac} and h_{bc} are the layer thickness of asphalt concrete course and CTB course, respectively.

Appraisal of E_R Prediction Function

The field FWD data from A11 Expressway in Shanghai were used to backcalculate the equivalent E_R of the existing subgrade, which were plotted against the predicted values from Equation 5, as presented in Fig.5. A good agreement between backcalculated and predicted results shows the applicability of the E_R prediction function.

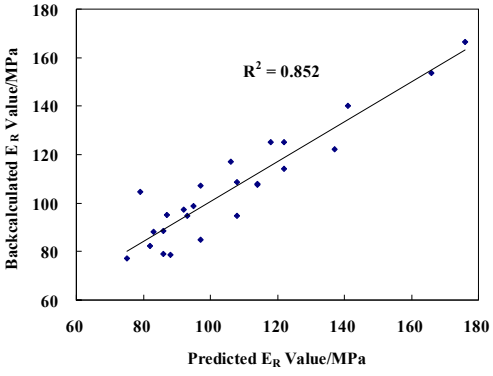

FIG.5. Backcalculated vs. rredicted E_R of subgrade

CONCLUSIONS

An effective method to determine subgrade resilient modulus for existing pavement is proposed by considering moisture condition coupled with stress level. The detailed conclusions are drawn as follows:

1. The equilibrium moisture condition of the existing subgrade of A11 Expressway in Shanghai could be predicted by $h\gamma_w$ model and Fredlund and Xing SWCC based on basic physical parameters tests of subgrade soils.
2. A bilinear model of resilient modulus of the existing subgrade soil, was discussed by correlating modulus values with stress and moisture condition. The predictability of the model was verified.
3. An effective calculation scheme to determine the equivalent resilient modulus of subgrade was presented and a prediction function was established. And FWD tests were conducted to verify the validity of the prediction function as well.

ACKNOWLEDGMENTS

The authors appreciate the support of the Scientific and Technical Committee of Shanghai, China.

REFERENCES

Ling, J.M., Guo, R.H. and Yuan, J. (2006). "A method to monitor and evaluate seasonal variation in resilient modulus of pavement subgrade." *Geotechnical Special Publication*, ASCE, 154: 150-156.

AASHTO (1992). Standard Method of Test for Resilient Modulus of Unbound Granular Base/Subbase Materials and Subgrade Soil-SHRP Protocol P46, AASHTO Designation: T294-92, Washington, D.C..

Li, D., and Selig, E.T. (1994). "Resilient Modulus for fine-grained subgrade Soils." *Journal of Geotechnical Engineering*, Vol. 120 (6): 939-957.

Powell, W.D., Potter, J.F., Mayhew, H.C., and Nunn, M.E. (1984). "The Structural Design of Bituminous Roads." *TRRL Report* LR 1132: 62.

Carmichael, R.F. III and Stuart, E. (1986). "Predicting Resilient Modulus: A Study to Determine the Mechanical Properties of Subgrade Soils." *Transportation Research Record: Journal of the Transportation Research Board*, 1043: 145~148.

Perera, Y. Y. and Zapata, C. E. (2004). "Moisture equilibria beneath highway pavements." *83rd Annual Meeting of Transportation Research Board*, TRB.

Fredlund, D.G. and Xing, A. (1994). "Equations for the soil-water characteristic curve." *Can. Geotech. J.*, Vol. 31: 521~532.

Zapata, C.E., Houston, W. N., Houston, S. L. and Walsh, K. D. (2000). "Soil-Water Characteristic Curve Variability." *Proceedings of Sessions of Geo-Denver 2000: Advance in Unsaturated Geotechnics*: 84~124.

Seed, H.B., Chan, C.K. and Lee C.E. (1962). "Resilience Characteristics of Subgrade Soils and Their Relations to Fatigue Failures in Asphalt Pavements." *Proceedings International Conference on Structural Design of Asphalt Pavement*, University of Michigan: 611~636.

Thompson, M.R. and Elliott, R.P. (1985). "ILLI-PAVE Based Response Algorithms for Design of Conventional Flexible Pavements." *Transportation Research Record* No. 1043: 50-57.

Performance of Pavements with Blast Furnace Base Courses

L.J.M. Houben[1], S.Akbarnejad[2], and A.A.A. Molenaar[3]

[1]Associate professor of Delft University of Technology, Delft, the Netherlands:l.j.m.houben@tudelft.nl
[2]Ph.D researcher of Delft University of Technology, Delft, the Netherlands: s.akbarnejad@tudelft.nl
[3]Professor of Delft University of Technology, Delft, the Netherlands: a.a.a.molenaar@tudelft.nl

ABSTRACT: In the Netherlands Blast Furnace Slags (BFS) are used as a self-cementing road base material on a wide scale for many decades. An example is the motorway A32 which was built in the years 1986-1988. Some 10 years after construction the first transversal heaves occurred at the asphalt pavement surface. Since then the number of heaves has considerably increased and the heaves kept on growing in height. Finally the pavement was fully reconstructed in 2008 and 2009.
In 2007 an extensive research was initiated into the performance of the BFS base material on the motorway A32. This research included:

1. Inventory of the number, length and height of the transversal heaves at the pavement surface.
2. Falling Weight Deflection measurements at some heaves, but also in between some heaves, from which the modulus value of the BFS road base was backcalculated. The modulus values show an extreme variation.
3. Materials research on bound BFS base material obtained by taking cores. The modulus of elasticity, compressive strength, tensile strength and coefficient of linear thermal expansion has been investigated.
4. Development of a mechanical model which describes the birth and growth of the heaves. The model enables to quantify the effects of the magnitude of the mechanical properties of the BFS road base and the season of construction of the base on the development of the pattern of transversal heaves.
5. Chemical and mineralogical analyses of the BFS road base material. This research is intended to indicate possible deleterious reactions and their effects on the long-term performance of BFS.

INTRODUCTION

In the Netherlands, BFS is used as a self-cementing road base material on a wide scale for many decades. An example is a 9.3 km long stretch of the motorway A32. Around 10 years after construction the first transversal heaves occurred at the pavement surface. Such heaves not only have a negative effect on the driving comfort and the traffic noise but also may affect traffic safety. It seems that the heaves at the

pavement surface are caused by slow but long lasting chemical processes in the BFS road base which cause an increase of the volume of the base.

In 2007 an extensive research was initiated to investigate the performance of the BFS as a road base material. First, the results of ARAN (Automated Road ANalyser) and FWD (Falling Weight Deflection) measurements, carried out on the A32 will be presented. In this way the patterns of the heaves, i.e. the height, the length of the heaves and their spacing, and the modulus of elasticity of the pavement layers have been determined.

Then the results of the laboratory research on the bound BFS base material obtained through coring on the A32 are presented. The stiffness and strength properties have been measured on the field aged base material.

After that a very brief description is given of the mechanical model that was developed to enable the calculation of the birth and growth of the transversal heaves. It became clear that the BFS performance may vary considerably many years after construction due to chemical processes rather than by thermal effects.

Then attention is paid to the long-term physical and mechanical performance of BFS which is investigated by means of chemical-mineralogical techniques to study potential degradative processes. This part of the study, allows a systematic exploration of the combined interactions of both developmental and potential degradative chemical processes on the long-term performance of the BFS to be made. This step is designed to provide fundamental information for further analysis of these materials.

Finally, the last chapter gives the conclusions and recommendations of the research into the performance of BFS road bases application.

FIELD MEASUREMENTS ON MOTORWAY A32

ARAN measurements were performed in 2007 on both traffic lanes of both A32 carriageways and it appeared from the analysis of the ARAN measurement that the average distance between the heaves varied per road section between 5 m and 100 m. The height of the heaves varied from 3 mm to 27 mm, while the length of the heaves usually is 1 m to 6 m. Previous ARAN measurements revealed that the growth rate (increase of the height) of the heaves is on average about 1 mm per year.

Based on the analysis of the ARAN measurements results, 2 road sections were selected for FWD measurements using a standard 50 kN load. From the measured FWD deflection curves the dynamic modulus of elasticity of the BFS base has been backcalculated. The dynamic modulus of elasticity of the BFS base near the centre of the transversal heaves was dramatically low, namely 30 MPa to 50 MPa. In some other locations the modulus of elasticity amounted 100 MPa to 300 MPa, while on the remaining locations the modulus of elasticity had a value between 500 MPa and 4200 MPa. The conclusion from the analysis of the FWD measurements is that, 20 years after construction, at all transverse heaves the asphalt pavement structure of the A32 had a low bearing capacity, mainly due to the (very) low modulus of the crushed BFS road base.

From the measured longitual unevenness the IRI (International Roughness Index) has been calculated. In this study the IRI records for the A32 were determined for different years and over an average length of 10 and 100 meter. Accordingly the

probability of exceeding the maximum allowable IRI value of 3.5 and 5.1 was studied based on the normal distribution of the IRI values.

MATERIALS RESEARCH

The materials investigation was done on the BFS road base material, obtained through 29 cores taken from the A32. One core was taken in the centre of 5 selected heaves and 2 cores were taken at either side of each heave, at a distance of maximum 1.8 m. Furthermore, 4 cores were taken halfway between the heaves.

The following results were obtained:

Dry density: the dry density was on average 2029 kg/m^3.

Coefficient of thermal expansion: was measured on 4 specimens and varies from 6.8.10^{-6}/°C to 8.8.10^{-6}/°C, with an average value of 8.10^{-6}/°C (Figure 1).

Dynamic modulus of elasticity: varied very strongly, from 800 MPa to 12500 MPa (6 specimens). The modulus appeared to be independent on the loading frequency.

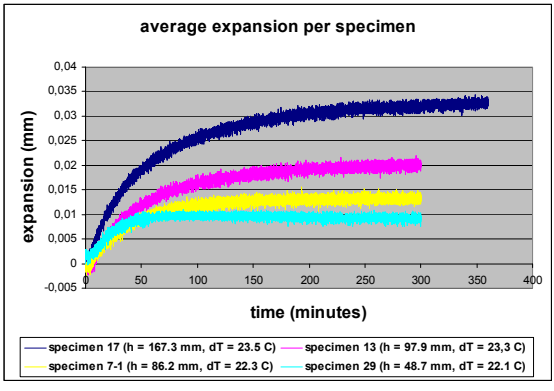

FIG. 1. Average expansion of the specimens as a function of time; at start of every test: temperature of specimen is 5°C.

Indirect tensile strength: measured in a force controlled test (speed of loading 0.2 kN/s), varied from 0.4 MPa to 0.7 MPa, with an average value of 0.52 MPa. The specimens exhibited brittle failure behaviour.

Compressive strength: measured in a force controlled test (loading rate 2 kN/s), varied from 2.0 MPa to 3.8 MPa, with an average value of 2.7 MPa. Also under compression the specimens exhibited brittle failure behaviour.

MECHANICAL MODEL FOR BIRTH AND GROWTH OF TRANSVERSAL HEAVES

Introduction

A mechanical model has been developed which enables the analysis of the birth and the growth of transversal heaves in (asphalt) pavements with a hydraulic BFS base. In this model it is assumed that the binding of the hydraulic BFS leads to, in the longitudinal direction of the road obstructed, expansion resulting in increasing compressive stresses in the road base. The binding of the slags also leads to (relatively small) temperature effects. On the other hand, the binding of the slags also results in an increasing compressive strength of the road base.

Transversal heaves occur when the compressive stress exceeds the compressive strength, present at that moment. Because of the heaves a certain amount of stress relaxation occurs in the still bound material in between the crushed zones. The long-lasting chemical process of the still bound base however proceeds and at a certain moment new transversal heaves occur in between the existing heaves. In case of the A32, this mechanism repeated itself a number of times and it became the reason for the recent complete reconstruction.

Time-Dependent Behaviour of Blast Furnace Slags Road Base

The model to describe the time dependent mechanical behaviour of BFS was selected in accordance to Eurocode 2 (2005). The mechanical model was calibrated on the basis of materials research and in situ ARAN measurements on the A32. The development of the influential mechanical properties is graphically shown in the figures 2 and 3.

Figure 2-left shows the development of the total deformation, in the case that the road base is constructed at May 1 at a temperature of 15°C. When the road base is constructed at February 1 (temperature of the base 5°C), August 1 (25°C) or November 1 (15°C) the cyclic thermal strain is somewhat different.

Figure 2-right shows the development of the modulus of elasticity.

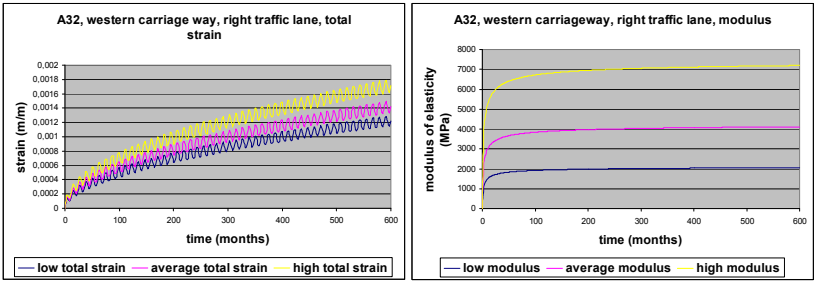

FIG. 2. Development of the total (obstructed) strain (in case of construction at May 1) and the modulus of elasticity of the bound BFS road base of A32.

Figure 3 shows the development of the compressive strength (as well as the tensile strength, but this is not a relevant factor in the mechanical model).

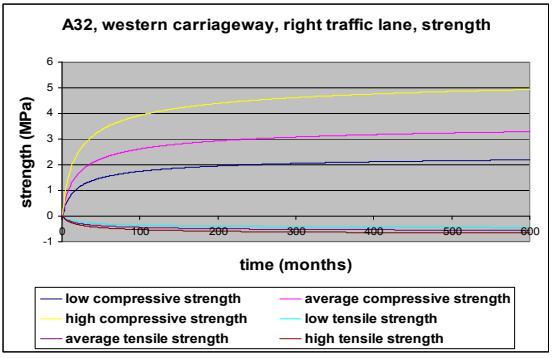

FIG. 3. Development of the compressive strength and the tensile strength of the bound BFS road base of A32.

Calculation Results from Mechanical Model

Calculations with the mechanical model have been done, for a period of 50 years (600 months), for 12 combinations of mechanical properties of the BFS road base (low, average, high) and time of construction (February 1, May 1, August 1, November 1, when the temperature during construction is minimum, average, maximum and average, respectively).

As an example, figure 4 gives an overview of the times of birth of the subsequent series of transversal heaves and the spacing between adjacent heaves if the pavement is constructed at May 1 and if the BFS base has low, average and high mechanical properties respectively.

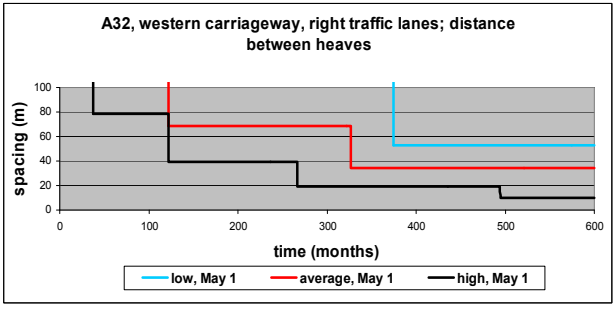

FIG. 4. Example of calculated times of birth of subsequent series of transversal heaves and the spacing between adjacent heaves.

The time of birth of the first series of transverse heaves is also visible in figure 5 that shows primarily the growth of these heaves. In the case of average and high

mechanical properties of the BFS road base, after this first series of transversal heaves there grow other series of heaves which can be deducted from figure 4.

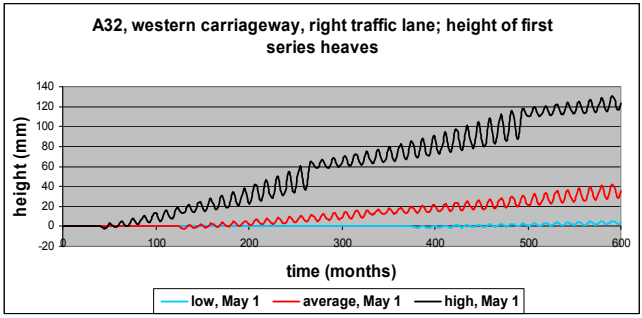

FIG. 5. Example of the calculated (growth of the) height of the first series of transversal heaves.

The combination of average mechanical properties of the bound BFS road best and construction of the base at May 1 agrees best with the pattern of vertical heaves as observed on the A32. This is logical as the mechanical model was calibrated for this combination.

The practical consequence is that, in order to limit the birth and growth of transversal heaves, the blast furnace slags road base material should be lightly hydraulic and preferably constructed in the summer period.

CHEMICAL AND MINERALOGICAL ANALYSES

Introduction

In the previous section a phenomenological model has been described which allows to estimate the number and severity of the heaves. This model however doesn't provide information about the main reason that these heaves occur. Therefore it was decided to study the chemical-mineralogical composition and also to examine the interrelation between the physical and mechanical behaviour, as it relates to potential degradative mechanisms. The experimental study includes the fresh (unhydrated) BFS and also field aged aggregates.

Experimental Procedure

As mentioned above, both unhydrated material (obtained from a Dutch producer) and field aged materials from the A32 were investigated. Both types of aggregates were examined through XRD techniques and XRF spectrometry to establish the chemical as well as mineralogical composition. The XRD analysis was performed using a Siemens D5005 diffractometer, with incident beam monochromator and position sensitive detector, allowing determination of the mineralogical phases within

the constituents. Diffraction patterns were recorded in the angular range 5-70 °2θ, with 5 s/step. For the XRD analysis a search/match procedure was used to identify the crystalline phases in the diffraction patterns. It employs the database to compare the sample diffraction patterns with patterns of pure phases.

Subsequently major elements (Si, Ti, A1, Fe, Mn, Mg, Ca, Na and K in % by mass) were determined by the XRF on pressed powder using a Philips PW2400 Rh 60kV spectrometer.

Results and Discussion

It was tried to identify important mineral phases including Ettringite ($Ca_6Al_2(SO_4)_3(OH)_{12}$-$26H_2O$), Quartz ($SiO_2$), Akermanite ($Ca_2MgSi_2O_7$) and Calcite ($CaCO_3$). In addition, an estimate of the elemental and the oxide content was made.

The XRF analysis of the aggregates shows that the major elements Al, Si and Ca were almost equal in concentration in the field aged material and fresh samples (Table 1). Additionally there are indications that the BFS was suspected for some degradative reactions due to relatively high concentrations of some chemical elements such as MgO and SO_3.

In addition XRD was performed on the hydrated BFS road base material and its results identified the existence of some hydration products such as Ettringite and Calcium Silicate Hydrate. The existence of unhydrated phases in some samples from undeformed locations on the A32 can be corresponded to a different hydration rate.

Similarities and differences in the mineral phases present in the fresh and field aged BFS were noted. Quartz, Aluminium oxide (Al_2O_3), Mg and Fe oxide were identified in all samples. Calcium Silicate Hydrate and Ettringite were only detected at aged materials. Ettringite was expected to occur in the aged samples (Taylor, 1992). In order to decrease uncertainties further investigation is however required on the concentration of the mineral phases.

In this preliminary chemical - mineralogical study unexpected mineral phases were not detected in the available fresh BFS but there is some doubt about their long term performance and accordingly their application for road base construction needs further investigations.

Table 1. XRF chemical composition of the main constituents of BFS.

Constituent of the fresh BFS	% by mass
Na_2O	1.06
MgO	4.02
Al_2O_3	6.63
SiO_2	16.18
CaO	46.98
SO_3	7.80
TiO_2	1.26
MnO	2.62
Fe_2O_3	11.00
K_2O	0.51
P_2O_5	0.2

Constituent of the field aged BFS	% by mass
Na_2O	0.23
MgO	4.33
Al_2O_3	7.57
SiO_2	17.01
CaO	47.95
SO_3	5.51
TiO_2	1.26
MnO	2.28
Fe_2O_3	18.31
K_2O	0.51

CONCLUSIONS AND RECOMMENDATIONS

From the extensive research on the 20 years old hydraulic and fresh BFS material, the following conclusions are drawn:

1. The hydraulic BFS has transformed into a bound material, with accompanied chemical expansion and thermal effects.
2. Compressive stresses develop in the bound BFS (due to obstructed expansion) that at a certain moment exceed the compressive strength, resulting in crushed zones and the birth of heaves.
3. With progress of time an increasing number of heaves keeps on growing in height. The pattern of heaves (i.e. height, length and spacing between the heaves) on the A32 has been investigated.
4. A mechanical model has been developed which describes the birth and growth of subsequent series of heaves. The long-lasting chemical process and consequent expansion appears to be dominant over the thermal effects.
5. The model clearly demonstrates that with increasing mechanical properties of the hydraulic BFS the transversal heave problem is getting worse. The higher the mechanical properties the more heaves occur.
6. A compromise should be sought between desired high modulus of elasticity and a low risk for the occurrence of crushing and the subsequent grow of transversal heaves.
7. The cause of the internal chemical deterioration of BFS road base is being under investigation. Recent chemical – mineralogical investigations show the presence of chemically suspected phases which can provoke a series of chemical reactions leading to expansion.

ACKNOWLEDGEMENTS

The authors thank the Dutch Ministry of Traffic, Public Works and Water Management for their cooperation in providing data and all its assistance in material collection.

REFERENCES

Eurocode 2: Design and calculation of concrete structures – Part 1-1: General rules and rules for buildings (in Dutch)

Taylor, H.F.W. (1992). “Cement Chemistry”, *Academic Press*, Boston, USA: 277-290.

Subgrade Stress Measurements under Heavy Aircraft Gear Loading at FAA National Airport Pavement Test Facility

Navneet Garg, M. ASCE, Frank Pecht, and Qingge Jia

Federal Aviation Administration William J. Hughes Technical Center, Airport Technology R&D Branch, NJ, U.S.A. Navneet.Garg@faa.gov, Frank.Pecht@faa.gov, Qingge.Jia@faa.gov

ABSTRACT: The National Airport Pavement Test Facility (NAPTF) is a fully enclosed instrumented test track 274.3 m (900 ft) long by 18.3 m (60 ft) wide. In construction cycle three (CC3), four new flexible pavement test items (LFC1 through LFC4) were constructed. The pavement structures were of conventional construction with 127-mm (5-in) asphalt surface, 203-mm (8-in) crushed stone base, varying subbase thickness, and a silty clay subgrade of 3 to 4 CBR. The test items were named LFC1 (thinnest subbase) through LFC4 (thickest subbase). Traffic tests were performed with 6-wheel loading in one wheel track and 4-wheel loading in the other wheel track. Rut depth and profile measurements were made on the asphalt surface during traffic testing. A fixed wander pattern was applied to the traffic during the tests. The wander pattern consisted of 66 repetitions, 33 traveling east and 33 traveling west. Sensors were embedded into the pavement layers to measure the pavement response to applied loads and included asphalt strain gages (ASG), multiple depth deflectometers (MDD), and soil pressure cells (PC). Subgrade pressure cells (2 inches, Kulite) were placed only in test item LFC4 and were placed 10 cm (4 inches) and 43 cm (17 inches) below the subgrade surface. This paper summarizes the subgrade vertical stress measurements under 6-wheel and 4-wheel landing gears at 245 kN (55,000 lb) and 289 kN (65,000 lb) wheel loads at different wander positions. There was no evidence of structural failure in LFC4 at the end of traffic testing.

INTRODUCTION

Failure in pavements is not a phenomenon of chance, but a phenomenon that has a definite mechanical cause. When the pavement is incapable of performing the task it was designed for, it has failed. Failure could be structural (deep structure rutting, alligator cracking, longitudinal or transverse cracks in slabs, etc.) or functional (surface rutting, roughness, loss of skid resistance, etc.). In mechanistic-empirical design procedures, pavement responses such as stresses and strains are related to pavement life through the use of transfer functions. For flexible pavements, the tensile strain at the bottom of asphalt concrete layer is related to the fatigue life of the pavement. Reduced

strain corresponds to increased fatigue life. Subgrade compressive strain is used to consider pavement surface rutting. The failure models used in the Federal Aviation Administration (FAA) pavement thickness design procedures (AC 150/5320-6E) are developed based on full-scale test results. Generally, the pavement test sections in full-scale tests are instrumented to measure critical pavement responses. Pavement instrumentation data helps in a better understanding of pavement system responses and can also be used for the validation/calibration of analytical response prediction models. Full-scale tests for airport pavements have used embedded instrumentation since 1948 (Porter, 1948). Most of the subsequent full-scale tests performed by U.S. Army Corps of Engineers have used embedded instrumentation to measure pavement responses. Currently, pavement instrumentation is extensively used in full-scale testing at the FAA National Airport Pavement Test Facility (NAPTF). This paper presents the subgrade vertical stress measurements under 6- and 4-wheel landing gears at 245 kN (55,000 lb) and 289 kN (65,000 lb) wheel loads at different wander positions during Construction Cycle 3 (CC3).

NATIONAL AIRPORT PAVEMENT TEST FACILITY

The FAA NAPTF is located at the FAA William J. Hughes Technical Center, Atlantic City International Airport, New Jersey. The primary objective of the tests is to generate full-scale pavement performance and response data for development and verification of airport pavement design criteria. It is a joint venture between the FAA and the Boeing Company, which became operational on April 12, 1999. The test facility consists of a 274.3-m (900-ft) long by 18.3-m (60-ft) wide test pavement area, embedded pavement instrumentation and a dynamic data acquisition system, environmental instrumentation and a static data acquisition system, and a test vehicle for loading the test pavement with up to 12 aircraft tires at wheel loads of up to 334 kN (75,000 lb). Figure 1 shows the NAPTF and the test vehicle.

FIG. 1. National airport pavement test facility

The target lives of the CC3 test items varied from 200 to 36,000 passes of dual tandem

(2D) landing gear configuration with a wheel load of 245 kN (55,000 lb). All four test items were constructed on a low-strength subgrade (CBR≈4) and were labeled LFC1, LFC2, LFC3, and LFC4. A MH-CH soil classification material known as County Sand and Stone Clay (CS&SC) was used for the low-strength subgrade. The thicknesses of FAA specification P-401 plant mix bituminous surface and FAA specification P-209 crushed aggregate base course (for all four test items) were 127 mm (5 in) and 203 mm (8 in), respectively. The thickness of FAA specification P-154 subbase course varied from 406 mm (16 in) for LFC1 to 1092 mm (43 in) for LFC4. Pavement cross sections are shown in Figure 2.

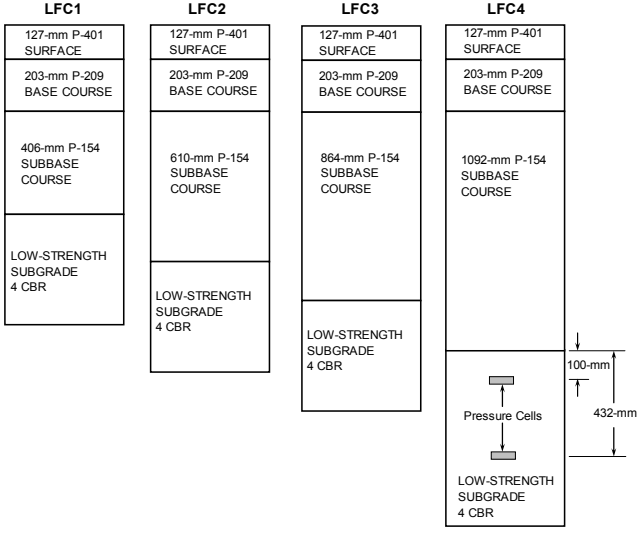

FIG. 2. Test pavement cross sections

PAVEMENT INSTRUMENTATION AND TRAFFIC TESTING

Pavement instrumentation in CC3 consisted of multiple-depth deflectometers (MDD), asphalt strain gages (ASG), subgrade pressure cells (PC), compression gages, and temperature gages. A fixed wander pattern (Hayhoe, 2006) was applied to the traffic during the tests. The wander pattern consisted of 66 repetitions, 33 traveling east and 33 traveling west. The transverse position of the gears was changed only at the start of the eastward repetitions. The north lane was trafficked by a 6-wheel (3D) configuration at 1372-mm (54-in) dual spacing and 1449-mm (57-in) tandem spacing. The south lane was trafficked by a 4-wheel (2D) configuration at 1372-mm (54-in) dual spacing and 1449-mm (57-in) tandem spacing. Wheel loads were set at 245 kN (55,000 lb) each.

The failure criterion was the presence of at least 25.4 mm (1 inch) of surface upheaval adjacent to the traffic lane, which is indicative of shear failure in the subgrade. This is

the same criterion used by the U.S. Army Corps of Engineers in previous full-scale tests of flexible airport pavements for the multiple wheel heavy gear load (MWHGL) test series run by the U.S. Army Corps of Engineers Waterways Experiment Station.

LFC1 north (6-wheel) and LFC1 south (4-wheel) failed in 90 and 132 passes, respectively. For test item LFC2, the north and south sides failed in 1,584 and 2,970 passes, respectively. Subgrade failure was observed (surface upheaval adjacent to the traffic lane). Since LFC3 and LFC4 showed little distress at 4,000 passes, the wheel loads were increased to 289 kN (65,000 lb) for the remainder of the tests. Test item LFC3 showed signs of subgrade failure. Test item LFC4 did not show any signs of structural (subgrade) failure at the completion of 20,000 passes.

SUBGRADE STRESS MEASUREMENTS IN CC3

Subgrade PCs were installed only in test item LFC4 at a 102-mm (4-inch) and 432-mm (17-inch) depth below the subgrade surface in different orientations to measure the complete stress field (Figure 2). PCs were Kulite Model 0234 Soil Pressure Cells. They are small diameter soil pressure cells consisting of a liquid-filled hollow steel cell 51 mm (2 inches) in diameter and 13 mm (0.5 inch) thick, with an electrical pressure transducer housed within the cell. The transducer responds to changes in pressure applied to the surface of the sensor by the material in which the sensor is embedded. Four PCs were installed to measure vertical stress in the subgrade. P2-1D and P2-3D were installed (in the 6-wheel traffic lane) at a 432-mm (17-inch) and 100-mm (4-inch) depth below the subgrade surface, respectively. P2-2D and P2-4D were installed (in the 4-wheel traffic lane) at a 432-mm (17-inch) and 100-mm (4-inch) depth below the subgrade surface, respectively. The P2-3D failed and did not work.

Before the start of traffic tests, the pavements were conditioned with one complete wander pattern (66 passes) at 89 kN (20,000-lb) wheel load with 6-wheel landing gear configuration on the north lane and 4-wheel landing gear configuration on the south lane. Figure 3 shows the maximum vertical subgrade stress measured at a 432-mm (17-inch) depth below the subgrade surface under 6-wheel and 4-wheel landing gear configurations at wheel loads of 89 kN (20,000 lb), 245 kN (55,000 lb) and 289 kN (65,000 lb).

The best fit curve through the data points was an exponential curve signifying some degree of nonlinearity in subgrade stresses with increase in load. Figure 4 shows the variation in subgrade stress as a function of gear or strut load (number of wheels on the gear times the wheel load) and the relationship shows nonlinearity.

A fixed wander pattern (66 passes in one wander pattern) was applied to the traffic during the tests, which resulted in different gear positions from the location of PC in the transverse direction. Figure 5 shows the vertical subgrade stress measurements at different wander positions during the first 66 passes. The results show fairly high degree of repeatability (except for few exceptions) in the measurements. Higher variability was observed when the gear was away from the PCs.

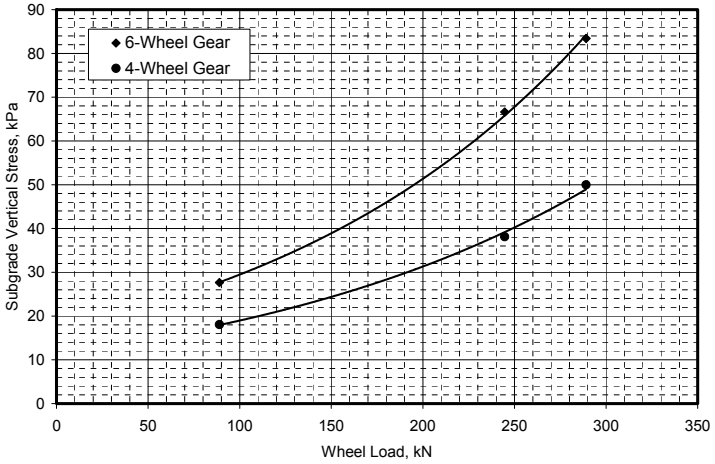

FIG. 3. Vertical stress at a 432-mm depth below subgrade surface

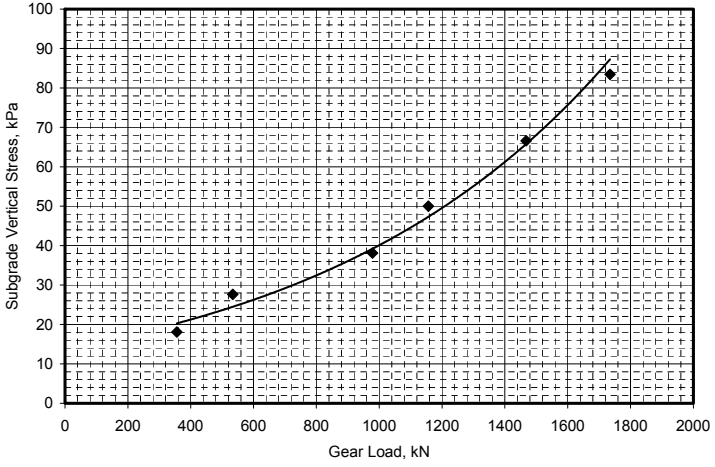

FIG. 4. Vertical stress at a 432-mm depth below subgrade surface

Maximum vertical subgrade stress occurred when the center of landing gear was on top of the gage. Maximum vertical subgrade stress at a 432-mm (17-inch) depth below the subgrade surface from traffic tests is summarized in Figures 6 and 7.

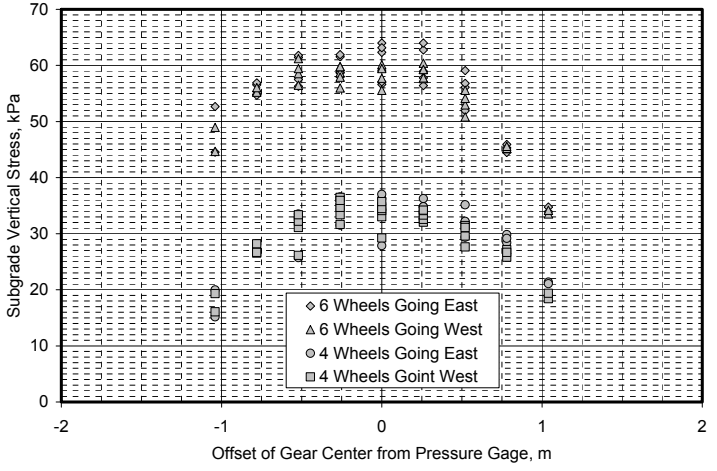

FIG. 5. Vertical subgrade stress at different wander positions (Wheel Load – 245 kN)

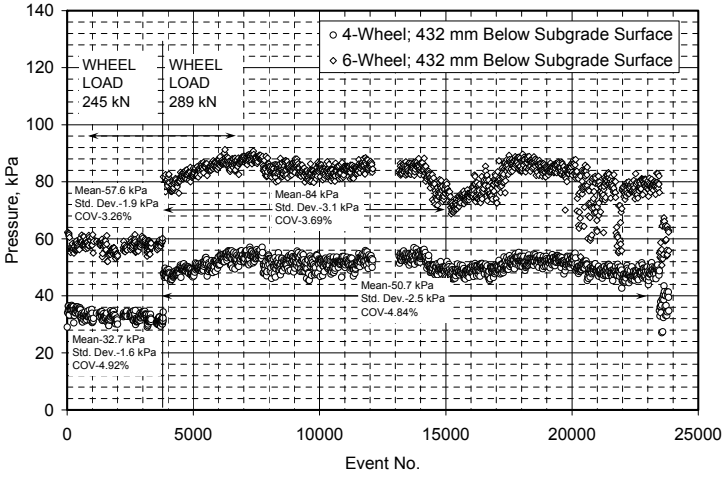

FIG. 6. Vertical subgrade stress during traffic tests

Variation in stresses after 15,000 passes (event no.) is related to fluctuations in pavement temperatures during the early fall season (month of October). Variations in stresses are more significant under 6-wheel landing gear. The 6-wheel gear load is 1.5 times the 4-wheel gear load; however, the vertical subgrade stresses are about 1.7 times higher under 6-wheel gear. Figure 7 shows vertical subgrade stresses at two different depths under 4-wheel landing gear. At 245 kN (55,000-lb) wheel load, the stresses at a

100-mm (4-inch) depth below subgrade surface are about 2.1 times higher than the stresses at a 432-mm (17-inch) depth below subgrade surface and at 289 kN (65,000-lb) wheel load they are about 1.8 times higher. Detailed information about pavement performance and posttraffic testing can be found in (Hayhoe, 2006). Figure 8 shows the pavement layer thickness after the completion of traffic tests. No clear signs of surface upheaval outside the traffic path were observed. Most of the rutting was contributed by the P-154 subbase layer. Rutting in the subgrade material was minimal.

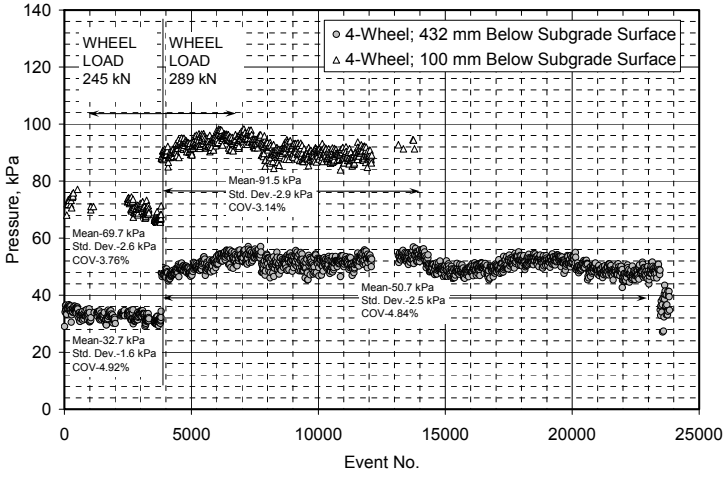

FIG. 7. Vertical subgrade stress during traffic tests (under 4-wheel gear)

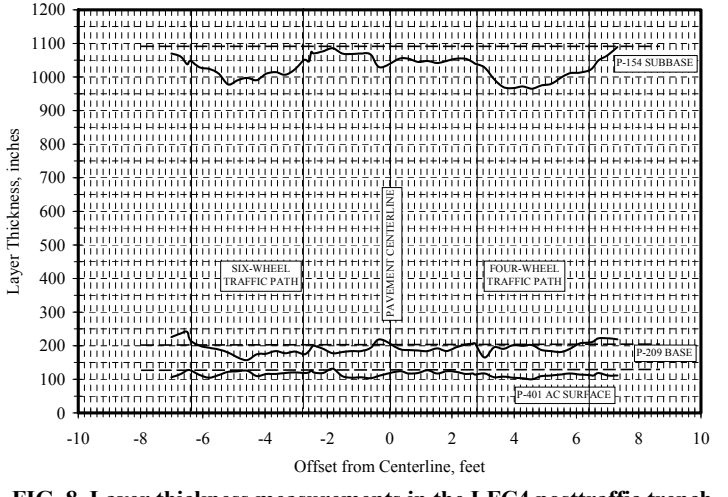

FIG. 8. Layer thickness measurements in the LFC4 posttraffic trench

CONCLUSIONS

Vertical subgrade stress measurements under heavy aircraft gear loads are presented. The results show that subgrade stress measurements can be made with a very high degree of repeatability and reliability. The standard deviations ranged from 0.23 to 0.45 psi and coefficient of variation ranged from 3.26 to 4.92 percent. Nonlinear behavior (stress-softening) of subgrade was observed. The pavement surface rutting at the end of trafficking was about 7.6 cm (3 inches). Posttraffic tests showed no signs of shear failure or rutting in the subgrade. Most of the rutting was contributed by the subbase layer. The thicker subbase in test item LFC4 helped in protecting the subgrade reducing the vertical stress compared to test items LFC1 and LFC2.

ACKNOWLEDGMENTS

The work described in this paper was supported by the FAA Airport Technology Research and Development Branch, AJP-6310, USA, Dr. Satish K. Agrawal, Manager. The contents of the paper reflect the views of the authors, who are responsible for the facts and accuracy of the data presented within. The contents do not necessarily reflect the official views and policies of the FAA, USA. The paper does not constitute a standard, specification, or regulation.

REFERENCES

Porter, O. J. (1948). "Accelerated Traffic Test at Stockton Airfield, Stockton, California." Report, Department of the Army Corps of Engineers, Sacramento District.

Hayhoe, G. F. and Garg, N. (2006). " Traffic Testing Results from CC3 Flexible Pavements at the FAA'S NAPTF." *Conf.Proc., ISAP-2006,* Quebec City, Canada.

PREDICTING RUTTING OF UNBOUND AGGREGATE LAYERS USING TOTAL VOID CALCULATION UNDER FULL-SCALE TESTING AT THE FAA NATIONAL AIRPORT PAVEMENT TEST FACILITY

Jeffrey Gagnon[1], P.E., M. ASCE and Navneet Garg[1], Ph.D., M. ASCE

[1] FEDERAL AVIATION ADMINISTRATION, Airport Technology R&D Branch, William J. Hughes Technical Center, Atlantic City International Airport, NJ 08405, United States

ABSTRACT: The Federal Aviation Administration (FAA) National Airport Pavement Test Facility (NAPTF) is located at the William J. Hughes Technical Center, Atlantic City International Airport, New Jersey. The primary objective of the tests performed at the NAPTF is to generate full-scale pavement performance and response data for development and verification of airport pavement design criteria. Four construction cycles (CC1, CC2-OL, CC3, CC5-TS) for testing flexible pavements under heavy aircraft loading have been completed and the fifth one is under way. In both CC1 and CC3, deformation of the aggregate base and aggregate subbase due to densification was noted and contributed to the rutting of the asphalt pavement test sections. This paper will discuss if the Total Void (TV) calculation based upon historic data of CC1 and CC3 can be used to predict the total deformation of the aggregate base and subbase layers in flexible pavements, as well as, to investigate whether the FAA gradation specifications for subbase and base courses are susceptible to deformation based upon the total void calculation.

INTRODUCTION

Poor performances of unbound granular layers contribute to the poor performance of both flexible and rigid pavements, leading to reduced life and costly maintenance. In flexible pavements, the poor performance results in rutting, fatigue cracking, longitudinal cracking, depressions and frost heaving (Saeed, et al. 2001). Rutting is a progressive accumulation of plastic strain in each layer of the flexible pavement that occurs under repeated loading. Rutting can be the result of both densification and permanent shear deformation (Saeed, et al. 2001). At the Federal Aviation Administration (FAA) National Airport Pavement Test Facility (NAPTF), the primary objective of the tests performed was to generate full-scale pavement performance and response data for development and verification of airport pavement design criteria. The primary objective of full scale flexible pavement tests was to generate shear failure in the subgrade as evidenced by subgrade flow and upheaval outside the traffic

path. More detailed information about failure criterion can be found in (Hayhoe, et al. 2003 and Hayhoe and Garg, 2003).

AGGREGATE MATERIAL SPECIFICATIONS

The materials used for all construction cycles at NAPTF follow the FAA Advisory Circular 150/5370-10D, "Standards for Specifying Construction of Airports." For unbound aggregate subbases, the specification followed is P-154, "Subbase Course" and for unbound bases P-209, "Crushed Aggregate Base Course," is followed. Tables 1 and 2 summarize the specified gradation requirements for P-154 and P-209 and the gradation used at NAPTF. For both P-154 and P-209, the material passing the No. 40 sieve must have a liquid limit not more than 25 and plasticity index of not more then 6 for P-154 and 4 for P-209 materials.

The same P-154 materials were recycled and reused for each of the construction cycles, and therefore, the gradations for CC1, CC2, and CC5 are the same.

The compaction acceptance criteria for both P-154 and P-209 in the field shall be at least 100 percent of the maximum dry density of laboratory specimens (tested in accordance with ASTM D 1557, Modified Proctor).

TABLE 1. P-154 Gradation Requirements

Sieve Size	Percentage by Weight Passing Sieves	
	Specification	NAPTF CC1, CC2 & CC5
3 inch (75.0 mm)	100	100
No. 10 (2.0 mm)	20-100	44.2
No. 40 (0.450 mm)	5-60	11.7
No. 200 (0.075 mm)	0-8	5.6

TABLE 2. P-209 Gradation Requirements

Sieve Size	Design Range Percentage by Weight	Job Mix Tolerances Percent	Percentage by Weight Passing Sieves		
			CC1	CC3	CC5
2 in (50.0 mm)	100	0	100	100	100
1-1/2 (37.0 mm)	95-100	+/- 5	95.9	100	100
1 in (25.0 mm)	70-95	+/- 8	86.2	90.0	94.5
3/4 in (19.0 mm)	55-85	+/- 8	79.5	73.2	83.2
No. 4 (4.75 mm)	30-60	+/- 8	46.5	49.8	34.7
No. 30 (0.60 mm)	12-30	+/- 5	17.7	15.0	13.1
No. 200 (0.075 mm)	0-8	+/- 3	6.7	3.8	4.3

OPTIMUM AGGREGATE GRADATION

In general, specifications target a dense grading for aggregate base and subbase materials due to their strength and stability from interlocking particles and fewer voids. Having fewer voids means less densification can occur. Rounded stones do not interlock and will quickly deform under loading. The particle size distribution is expressed by Talbot's grading curve represented by the value of the exponent *n* in the equation below (Arnold, et al. 2007)

$$\rho = 100(\frac{d}{D})^n \quad (1)$$

where $\rho =$ percent passing sieve size *d, D* = maximum particle size.

In most specifications, *n* is found to be between 0.3 (fine grading) and 0.5 (coarse grading) with values of 0.45 to 0.5 indicating better compactibility (Arnold, et al. 2007). However, a New Zealand Report (Bartley 2007) noted better compactibility is achieved with *n*-value of 0.35, as the fine-graded materials can pack down more readily to form a dense grading. A grading with *n* = 0.5 is historically known as Fuller's maximum density curve, although the actual maximum density may occur at *n*-values less than 0.5 for some aggregates (Arnold, et al. 2007). Table 3 summarizes the average values of *n* for the materials used at NAPTF.

Table 3. N-Value for P-154 and P-209

Materials	Specification Range		Cycle	Average *n-value*
	Lower Limits (coarse side)	Upper Limits (fine side)		
P-154 Subbase	0.51	0.23	CC1	0.35
			CC3	0.35
			CC5	0.35
P-209 Base	0.46	0.22	CC1	0.29
			CC2	0.34
			CC5	0.33

TOTAL VOIDS

An alternate specification that can be used as a replacement for percent compaction is the calculation of Total Voids (TV) in the compacted base and subbase layers. Voids are the spaces between individual particles of rock that make up the layer. Total voids are the sum of these spaces and are defined below (Bartley 2007):

$$TV = \left(1 - \frac{\gamma_d}{\gamma_s}\right)100 \quad (2)$$

where γ_d = dry density in lb/ft^3 and γ_s = Apparent Specific Gravity in lb/ft^3.

The Apparent Specific Gravity is used because it provides the most appropriate measure of the overall dry mass of rock in the system. It should be noted that the value for a rock type from a particular area is constant and will only vary depending on the amount of weathering that has occurred in the rock (Bartley 2007). The risk of rutting in aggregate layers can be minimized by compacting the layers to a low level of TV prior to new layers being placed on top. From the Land Transport New Zealand research, densification was likely to occur when the total voids content was greater than 15%. The optimum grading for maximum dry density was found to lie between *n* = 0.33 and 0.39 (Bartley 2007).

Table 4 below summarizes the French Design Manual for Pavement Structures specifications for total voids at the modified optimum of the proctor scale (PMO):

Table 4. French Void Content

Type of untreated granular material	Void Content at PMO (%)
Category "A"*	20
Category "B":B1	17
Category "B":B2	18
* D equals 31.5 mm maximum	

Category "A" gradations is obtained in a single fraction without addition of water but the evenness of the grain size distribution. Category "B" aggregates are obtained by combining several separate granular fractions, in defined portions and are mixed at a mixing plant (LCPC 1997).

FLEXIBLE PAVEMENT TESTING

In both CC1 and CC3, the 5-inch asphalt surface course showed no signs of densification. P-154 subbase showed signs of densification. The question arose as to whether the specifications for aggregate base, P-209, and aggregate subbase, P-154, were comprehensive enough to withstand densification under aircraft loading or if there is a need to either improve the specifications or investigate additional requirements such as total voids in the aggregate base and subbase layer.

Construction Cycle 1

CC1 consisted of six flexible test items (two each on low-, medium-, and high-strength subgrades). The target material strength was a California Bearing Ratio (CBR) of 4 for low-strength subgrade, 8 for medium-strength subgrade, and 20 for the high-strength subgrade. The pavement test item cross sections for the flexible pavements (measured thickness) are shown in Table 5.

Table 5. CC1 Pavement As-Built Cross-Sectional Details

Item ID	Surface Layer		Base Layer		Subbase Layer		Subgrade		
	Type	Thickness inch	Type	Thickness inch	Type	Thickness inch	Soil Type	CBR	Strength
LFS	P-401	5.0	P-401	4.88	P-209	29.63	MH-CH	4	Low
LFC	P-401	5.13	P-209	7.75	P-154	36.38	MH-CH	4	Low
MFC	P-401	5.13	P-209	7.88	P-154	12.13	CL-CH	8	Medium
MFS	P-401	5.0	P-401	4.88	P-209	8.5	CL-CH	8	Medium
HFS	P-401	5.13	P-401	4.5	-	-	SW-SM	20	High
HFC	P-401	5.25	P-209	7.88	-	-	SW-SM	20	High

P-401 Surface: asphalt concrete surface; P-401 Base: asphalt stabilized base; P-306: econocrete base; P-209: crushed stone base; P-154: subbase

The north wheel track was loaded with a 3D (six-wheel triple-dual-tandem) gear configuration. The south wheel track was loaded with a 2D (four-wheel dual-tandem) gear configuration. On test items MFC and MFS, the wheel loads were set at 45,000 lb (20.4 tonnes) each throughout the tests. Traffic speeds were 5 mph (8 km/h) initially and 2.5 mph (4 km/h) during the tests. The traffic tests on test items LFC and LFS began with a 45,000-pound (20.4 tonnes) wheel load, but after approximately 20,000

load cycles the pavements on the low-strength subgrade showed few signs of subgrade distress, so final loading was set at 65,000 pounds (29.47 tonnes). A fixed wander pattern was applied to the traffic during the tests. The wander pattern consisted of 66 repetitions, 33 traveling east and 33 traveling west. Posttraffic tests showed significant rutting in the P-154 subbase.

Test item MFC was declared failed after 12,000 passes and exhibited ruts of 4 to 6 inches (100 to150 mm) deep with upheaval outside the traffic lane and asphalt surface cracking inside the traffic lane. Subgrade intrusion into subbase was observed. Density measurements in P-154 were made using a 6-inch sand cone apparatus (ASTM D 1556-90). Table 6 summarizes the density and total void results for LFC and MFC. The apparent specific gravity of P-154 subbase is 2.74.

Table 6. Summary of Results for CC1 Test Items - LFC and MFC

Test Item	Location	Offset, feet	Dry Density, pcf	Total Voids, %
LFC	Pretraffic	-	133.60	21.86
	ONWT	-23.00	146.52	14.31
	NWT	-13.42	150.52	11.96
	CL	0.00	145.24	15.05
	SWT	12.33	150.84	11.78
	OSWT	23.00	145.97	14.62
MFC	Pretraffic	-	131.10	23.32
	ONWT	-25.33	135.00	21.04
	NWT	-12.75	118.70	30.58
	CL	0.00	117.70	31.16
	SWT	11.50	122.60	28.29
	OSWT	26.25	121.10	29.17

ONWT – Outside North Wheel Track (no traffic); NWT – North Wheel Track; OSWT – Outside South Wheel Track (no traffic); SWT – South Wheel Track; CL – Centerline (no traffic)

In test item LFC, rutting was primarily contributed by the P-401 asphalt concrete layer and subbase (Figure 1) and the reduction in total voids was observed (Table 6). In test item MFC, slight rutting was observed in the P-209 base (Figure 2), and shear failure was observed in the P-154 subbase. Subgrade intrusion into the subbase and loss of density (increase in TV) in the wheel tracks was observed.

Construction Cycle 3 (CC3)

Construction Cycle 3 (CC3) consisted of four flexible test items on low-strength subgrade. The test items were labeled LFC1, LFC2, LFC3, and LFC4. The thicknesses of P-401 plant mix bituminous surface and P-209 crushed aggregate base course were 5-inches and 8-inches for all four test items. The thickness of P-154 subbase course varied from 16-inches for LFC1 to 43-inches for LFC4.

The north lane was trafficked by a 3D configuration. The south lane was trafficked by a 2D configuration. Wheel loads were set at 55,000 lb each and the traffic speed was 2.5 mph. The wander pattern was similar to one used in CC1.

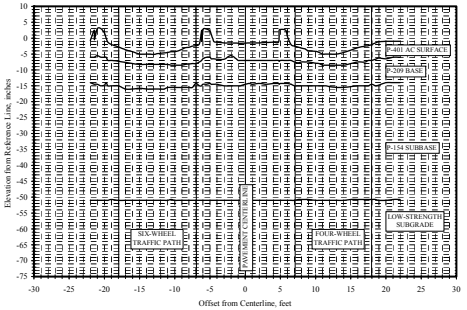

FIG. 1. Layer profiles from test item LFC trench

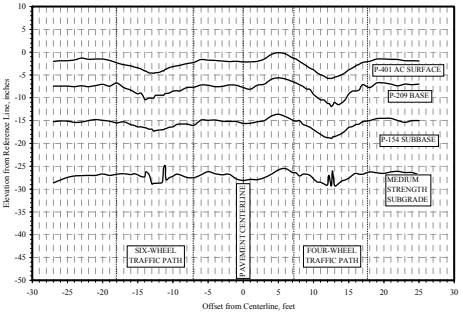

FIG. 2. Layer profiles from test item MFC trench

LFC1 north (3D) and LFC1 south (2D) failed in 90 and 132 passes, respectively. For test item LFC2, the north and south sides failed in 1,584 and 2,970 passes, respectively. Since little distress was observed at 4,000 passes in LFC3 and LFC4, the wheel loads were increased to 65,000 lb. The north side of LFC3 failed at 20,000 passes. The number of passes to failure for LFC3 south side (2D) was estimated to be approximately 40,000 passes by extrapolation of the rut depth curve. Test item LFC4 did not show any signs of structural failure.

Posttraffic testing showed significant rutting in the P-154 subbase. Density measurements were made using a 6-inch sand cone apparatus (ASTM D 1556-90). Table 7 summarizes the density and total void results. The apparent specific gravity of P-154 subbase was 2.74.

The deformations within the LFC1 pavement structure were so large throughout the trafficking period that significant consolidation did not occur and the shape of the surface rut tended to be flat or W-shaped in the center of the wheel track (Hayhoe and Garg 2006). The results in Table 7 show a significant increase in density in the wheel tracks for test item LFC2. Significant portions of the rutting in the P-154 layer are due to consolidation (or change in density) and not shear failure in the material (Garg and Hayhoe 2007). Compaction of the P-154 subbase layer also resulted in higher CBRs inside the wheel tracks. In test item LFC3, density increased in the wheel track but

reduced outside the wheel track. The effect was most pronounced in the north (3D) wheel track since the north wheel track failed completely, while the south wheel track did not, when trafficking was stopped. An increase in subbase thickness outside the wheel track and decrease in thickness inside the wheel track was observed. This indicates the rutting in the subbase was caused by a combination of shear flow and consolidation. In test item LFC4, contrary to expectations, no significant degree of consolidation occurred in the P-154. The total air voids pretraffic and posttraffic were similar.

Table 7. Summary of Results for CC3 Test Items

Test Item	Location	Offset, feet	Dry Density, pcf	Total Voids, %
LFC1	Pretraffic	-	126.00	26.31
	ONWT	-26.00	135.98	20.47
	NWT	-16.50	134.59	21.28
	CL	-1.00	129.57	24.22
	SWT	16.00	137.24	19.73
	OSWT	26.00	130.19	23.85
LFC2	Pretraffic	-	126.00	26.31
	ONWT	-26.00	132.97	22.23
	NWT	-16.50	148.20	13.32
	CL	-1.00	134.46	21.36
	SWT	16.00	147.62	13.66
	OSWT	26.00	127.44	25.46
LFC3	Pretraffic	-	126.00	26.31
	ONWT	-26.00	108.84	36.34
	NWT	-16.50	130.95	23.41
	CL	-1.00	111.81	34.60
	SWT	16.00	127.37	25.50
	OSWT	26.00	117.28	31.41
LFC4	Pretraffic	-	126.00	26.31
	ONWT	-26.00	106.17	37.90
	NWT	-16.50	124.39	27.25
	CL	-1.00	115.61	32.38
	SWT	16.00	124.33	27.28
	OSWT	26.00	109.27	36.09

ONWT – Outside North Wheel Track (no traffic); NWT – North Wheel Track; OSWT – Outside South Wheel Track (no traffic); SWT – South Wheel Track; CL – Centerline (no traffic)

CONCLUSIONS

Based upon the *n*-value of the specified gradations for P-209 and P-154, both P-209 and P-154 have a lower limit (coarse side) of 0.46 and 0.51, respectively, which should provide adequate resistance to rutting if adequately compacted. The upper limit of these materials is 0.22 and 0.23, which may be easier to handle and compact but may be susceptible to additional densification and thus, lead to rutting. The NAPTF P-209 and P-154 with *n*-values from 0.34 to 0.29 and 0.35 are very close to their maximum compactability and should provide adequate rutting resistance as long as maximum densities are achieved.

In CC1 test item LFC1, the TV after construction was 21.86% and posttraffic was between 11.78% and 15.05% and exhibited rutting. This supports the requirements in

the French design manual and recommendations from New Zealand. The P-154 material TV at placement was too high at 21.86% and was bound to become compacted (densification) by trafficking. Conversely in CC1 MFC, TV actually increased counter to densification since shear failure occurred in the subbase layer. In CC3 the pretraffic TV was 26.31% and in three of the four test items, densification occurred in the trafficked areas but not to the expected range of 15% to 20%. In LFC4, the TV actually increased from 26.3% to a high of 27.28%. More analysis of the existing data and the data to be collected during Construction Cycle 5 is recommended to see if there is a correlation between the TV amount and densification of the unbound aggregate layers and if TV should be an added requirement to the FAA construction specifications.

ACKNOWLEDGEMENTS

The work described in this paper was supported by the FAA Airport Technology Research and Development Branch, AJP-6310, United States of America, Dr. Satish K. Agrawal, Manager. The contents of the paper reflect the views of the authors, who are responsible for the facts and accuracy of the data presented within. The contents do not necessarily reflect the official views and policies of the FAA, USA. The paper does not constitute a standard, specification, or regulation.

REFERENCES

Arnold, G., Werkmeister, S., and Alabaster, D. (2007) "The Effects of Grading on the Performance of Basecourse Aggregate." Land Transport New Zealand Research Report 325.

Bartley, F.(2007) "Total Voids in Unbound Granular Pavements." Land Transport New Zealand Research Report 332.

French Design Manual for Pavement Structures. (1997) Laboratoire Central des Ponts et Chaussées (LCPC), pp. 105.

Garg, N., and Hayhoe, G. F. (2007) "Consolidation of aggregate base and subbase layers under heavy aircraft loading at the National Airport Pavement Test Facility." Proceedings, Advanced Characterisation of Pavement and Soil Engineering Materials.

Hayhoe, G. F., and Garg, N.(2003) "Posttraffic Testing On Medium-Strength Subgrade Flexible Pavements at the NAPTF." Proceedings, 2003 Airfield Pavement Specialty Conference, Airfield Pavements – Challenges & New Technology.

Hayhoe, G. F., and Garg, N. (2006) "Traffic Testing Results from CC3 Flexible Pavements at the FAA's NAPTF." Proceedings, 10th International Conference on Asphalt Pavements, International Society for Asphalt Pavements.

Hayhoe, G. F., Garg, N., and Dong, M. (2003) "Permanent Deformations During Traffic Tests on Flexible Pavements at the NAPTF." Proceedings, 2003 Airfield Pavement Specialty Conference Airfield Pavements – Challenges & New Technology.

Saeed, A., Hall, J., and Barker, W. (2001) "Performance-Related Tests of Aggregates for Use in Unbound Pavement Layers." NCHRP Report 453.

The Performance and Economic Benefits of Thick Granular Base for Flexible Pavement Design in Frost Susceptible Regions

Randy Beck[1], Bill Yu[2*], and Roger Green[3]

[1]Department of Civil Engineering, Case Western Reserve University, randall.f.beck@gmail.com
[2*]Department of Civil Engineering, Case Western Reserve University, xxy21@case.edu, 216-368-6247, corresponding author
[3]Office of Pavement Engineering, Ohio Department of Transportation, roger.green@dot.state.oh.us, 649-995-5993

ABSTRACT: This paper describes the economic analyses of using thick granular base design in cold regions. The use of thick granular bases is believed to lead to higher and uniform structural support. For regions in freeze-thaw zones, the use of thick granular base helps to move the weaker and frost susceptible subgrade material further down in the pavement structure where stress, strain, and frost penetration are lower. To implement such design in cold regions, the performance benefits must overcome the initial high investment and results in longer term economic benefits. This paper discusses results of analyses on the design, economic and performance of pavements of different granular base thickness. The effects of local environmental conditions such as freeze-thaw are assessed. Recommendations are provided on the use of thick granular base for flexible pavement design in cold regions.

ENGINEERING CONSIDERATIONS OF APPLYING THICK GRANULAR BASES FOR FLEXIBLE PAVEMENT

The asphalt pavement in states such as Ohio is typically constructed on a 4" or 6" dense graded aggregate base (DGAB). Pavement constructed with a thick granular base (>=12") is common practice for many countries (i.e. South Africa, New Zealand, Australia, etc.). An important function of granular base for pavement in cold regions is to reduce the effects of frost actions. Frost actions in pavement include 1) frost heaving resulting mainly from the accumulation of moisture (ice lenses) in the frost susceptible soil during the freezing period; and 2) the weakening of soil when thawing temperature occurs. Both factors affect pavement structure and its service. As a consequent of frost actions, spring road closure or controls are routinely implemented in many state routes for pavement protection, which causes inconveniences for private and commercial traffic.

To alleviate the effects of frost action, a few US states, including Washington State Department of Transportation (WSDOT), traditionally use non-frost susceptible

material constructed equal to half of the design depth of frost penetration. The State of Idaho adopted the use of "rock cap" for frost protection. Experience in Idaho indicated the use of rock cap is a technical and economic feasible approach, which in many route eliminated the requirements of road closure. The rock cap material is an open graded aggregate with 100 percent passing the 75mm (3 in.) sieve and 0 to 15 percent passing the 12.5mm (1/2 in.) sieve. The free draining material placed immediately on top of embankment or existing pavement intercepts the flow of water before entering the newly constructed upper pavement layers from lower water sources. The same capillary break also provide open drainage blanket to reduce the amount of thawing moisture (Uhlmeyer et al. 2003). Similar practice of using free draining gravel and sand layer under pavement is adopted in European Countries, Canada, South Africa and Austria. The following Table 1 summarizes the practice in a few countries and U.S. states.

Table 1. Type and Thickness of Permeable Base Layer of Freeze-thaw Mitigation

Country	**Type**	**Thickness**
Sweden	Sand layers	8 in. (200mm) (Rengmark et al. 1963)
Finland	Sand (or gravel) layer	6 in to 8 in. (150 to 200mm) (Taivainen 1963)
Estonia	Free draining sand or capillary break	12 in. (300mm) (Uhlmeyer et al. 2003)
Austria	Granular	At least 8 in. (200 mm)
Australia	Granular	Typically at least 8 in. (200mm)
Canada	Thick layer of clean sand	12 in. (300 mm) (Armstrong and Csathy 1963)
US States	Type	Thickness
Maryland	Granular cap	12 in. (305mm)
Idaho	Rock cap	7.2 in to 31 in.
Washington State	Rock cap (Open Graded Dense Aggregate)	18 in.

The type of base layer design and its construction quality poss important impact on pavement service conditions. It is estimated 30% to 40% of rutting in flexible pavement originates from permanent deformation of aggregate base layer (NCHRP 453). About 50% of rutting originate from permanent deformation of subgrade (Sargand et al. 2006). Experiment data shows the use of thick granular base brings about a stronger base layer and more uniform base deformation. This reduces the amount of rutting and structural failure in pavement. Pavement constructed with thicker granular base (DGAB of more than 8 in. (200mm)) has significantly reduced deflection and variations as indicated by the FWD 1st sensor deflection magnitude and variation. The thicker the granular base layer, the smaller the absolute deflection in pavement, i.e., the higher the stiffness.

To prompt the use of thick granular base in cold regions, the performance benefits of thick granular base must overcome the initial high investment and results in life cycle economic benefits. In this paper, the pavement performance is predicted using the new Mechanistic-Empirical Pavement Design Guide (MEPDG) (Ohio DOT 2009).

The performance prediction is combined with life cycle analyses to determine the benefits of using thick granular base for flexible pavement in cold regions.

EFFECTS OF GRANULAR BASE ON PAVEMENT PERFORMANCE USING MECHANISTIC-EMPIRICAL PAVEMENT DESIGN GUIDE (MEPDG)

Design input for MEPDG software

Figure 1 shows the assumed pavement structure in MEPDG analyses. In this analysis, the pavement is assumed to consist of four major layers, i.e., the AC layer, granular base layer, compacted subgrade and natural soil (Fig. 1).

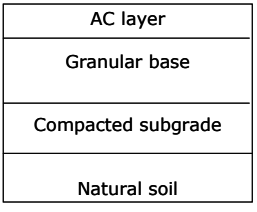

FIG. 1 Pavement structure in MEPDG analyses

MEPDG software requires the input of traffic, climate data, structural design and materials.

Design Traffic: The design traffic is obtained by referring to the traffic count record in LTTP database in typical sections in Ohio (version 17.0). Considering the observed trends in AADTT from LTTP data, the following input parameters were assumed for MEPDG traffic input.

1) Design AADTT 8000
2) Linear growth with 3%
3) Two lane traffic with 50% split
4) 90% on design lane
5) Operation at 60 mph
6) Default adjustment factors

Default adjustment factors for traffic spectra are used since it is very hard to sort out data in LTTP and fit into MEPDG Format. Besides, there are significant yearly variations in traffic spectra.

Materials Input: The materials input include those for Asphalt Concrete (AC), granular base materials, compacted subgrade and natural subgrade.

Asphalt Concrete

By referring to reports and published literature, the following properties were assumed for AC, as is show in Table 2.

Table 2. Input Parameters for Asphalt Concrete

General properties	Reference temperature (°F): 70
	Poisson's ratio 0.35
	Volumetric effective binder content (%) 9
	Air voids (%) 6.2
	Total unit weight (pcf) 148
Gradation	Cumulative % Retained 3/4 inch sieve 23
	Cumulative % Retained 3/8 inch sieve 46
	Cumulative % Retained #4 sieve 60
	% Passing #200 sieve 2.9
Thermal properties	Thermal conductivity asphalt (BTU/hr-ft-F°) 0.67
	Heat capacity asphalt (BTU/lb-F°) 0.23
Binder grade PG 64-22	

Granular Base

One of the major input parameters for granular base materials are the resilient modulus. A literature survey was conducted to determine a representative value for the resilient modulus of the granular base. Example results are summarized in Table 3. The resilient moduli were typically obtained from backcalculation of FWD data or from CBR data together with correlations between CBR values and resilient modulus. From these previous data, a value of 40 ksi is selected as representative for the resilient modulus of granular base materials.

Table 3 Examples of Resilient Modulus for Granular Base Materials

State	Modulus	Thickness	
Idaho DOT	170-415MPa (23,000-60,000 psi) backcalculation	0.60-2.67ft	Uhlmeye et al. 2003
Maryland DOT	8,800 psi (using CBR=7)	12 in	
Ohio SHRP Testing Road FWD backcalculation	Ranges between 250-300MPa 36,000 psi-43,000psi	6-12 inch	

Compacted Subgrade

The resilient moduli of compacted subgrade on Ohio SHRP Testing Section has been extensively studied in the past (ORITE report 1996). The resilient moduli over each testing section has been documented. An average resilient modulus for Ohio. SHRP Testing Sections is of 15.18 ksi or (104.6 MPa) (ORITE 1996). In addition, the following assumptions are made in the analyses

1) Resilient modulus of 104.7 MPa or 15,180 psi
2) Extend 1 ft

Natural Subgrade

To account for the effects of natural soils, a layer of less compacted subgrade or natural soil is assumed to underlain the compacted subgrade. This material is assumed to

1) Extends to infinite
2) Resilient moduli is assumed to range between 7,5000 to 10,000 psi

Local Calibrations for MEPDG Software

Preliminary calibrations of MEPDG distress models in Ohio are used to replace the default calibration parameters used in the national wide calibration. These models are summarized in the following:

Alligator crack model

$$\beta_{fs} = 1.47655 - 0.03562 * V_a + 0.0302 * V_{be} - 0.01858 * H_{ac} + 0.010864 * PATBHTHK - 0.22169 E_{ac} \quad (1)$$

where V_a is the percentage of air void

V_{be} is the volume percentage of binder content

H_{ac} is the thickness of AC layer in inch

PATHBHTHK is the thickness of permeable asphalt layer, =0 if no permeable asphalt layer is used.

E_{ac} dynamic modulus of bottom HMA sublayer, millions of psi

Rutting Model

The rutting model for AC, Base and Subgrade are as follows

AC layer:

$$\beta_{1r} = 5.137 * H_{HMA}^{-0.4762} \quad (2)$$

Base Layer

$$\beta_{B1} = 1 \quad (3)$$

Subgrade

$$\beta_{s1} = \frac{1.6177}{H_{HMA}} \quad (4)$$

Results of Sensitivity Study using Ohio Calibrations as Representative of Those in Cold Regions

Figure 2 plots the variations of predicted IRI with the thickness of granular base layer for 7 inch asphalt pavement. As the thickness of granular base layer increases, the IRI numbers decreases. The trend of decreases, however, is at a decreasing rate. A turning point lies somewhere between granular base layer of 10 to 15 inch thick.

Figure 2(b) plots the variations of predicted surface cracking with the thickness of granular base layer for 7 inch AC asphalt pavement. As the thickness of granular base layer increases, the predicted surface cracking decreases and then increases. A minimal value lies somewhere between granular base layer of 12 to 15 inch thick

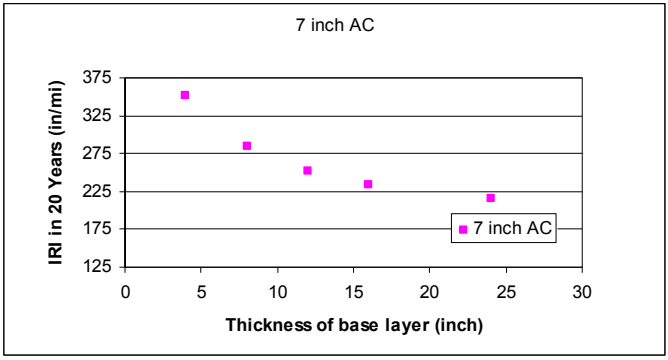

(a)

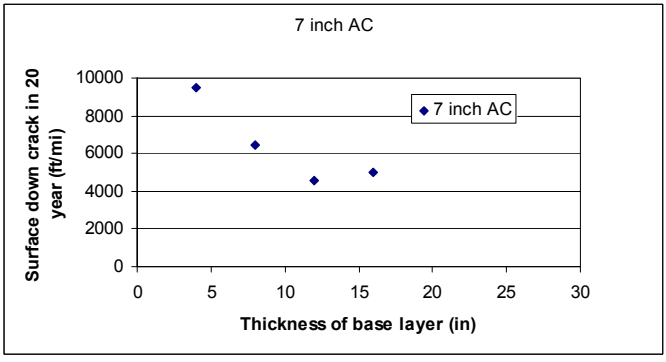

(b)

FIG. 2 a) Sensitivity of IRI to the thickness of base layer using Ohio calibrations, b) Sensitivity of surface cracking to the thickness of base layer using Ohio calibrations

.

Table 4 summarizes the results of sensitivity analyses on the effects of base layer thickness on the performance of 7 inch AC pavement. The table presents the service life (in months) based on the criteria for each type of distresses. Four major types of distresses are included for the comparison. The table indicates, for 7 inch AC pavement design, as the thickness of base layer increases, the service life based on IRI number and bottom crack all increases. The service life based on rutting decreases. For surface crack criterion, the service life first increases and then decrease. The controlling criteria are the bottom crack.

Table 4 Summary of the Effects of Base Layer Thickness on the Service Life of 7 inch AC Pavement Using Different Distresses Criteria (unit in months)

Base thickness (in.)	IRI	Rutting	Bottom crack	Surface crack
4	95	155	22	23
8	123	131	32	81
12	142	118	36	120
16	155	106	46	109
24	172	94	57	56

The percentage of service life change (increase) due to per unit increase in base layer thickness is derived from Table 4 and shown in Table 5. This table indicates that the increases of base layer thickness typically results in increases in the service life. The benefits, however, gradually decrease at the thickness of base layer continues to increase. The thickness of base layer where the maximum benefits can be obtained is around 12 inch. After that, continue increasing the thickness of base layer does not result in appreciable about return (in terms of further increase in the service life).

The controlling distress is the bottom crack. Between thickness of 8 inch to 12 inch, increases in every inch of granular base result in 5% increase in the service life (the total 4 inch brings 20%) increase in service life. Similarly, between thickness of 4 inch to 8 inch, increases in every inch of granular base result in 11% increase in the service life (the total 4 inch brings 44%) increase in service life.

Table 5 Percentage of service life change per unit increase in the base layer thickness for 7 inch AC pavement (unit in months)

Thickness (in.)	Incremental	Benefits			
4	4	IRI	Rutting	Bottom crack	Surface crack
8		0.07	-0.04	0.11	0.63
12	**4**	**0.05**	**-0.02**	**0.05**	**0.42**
16	4	0.03	-0.02	0.11	-0.12
24	8	0.02	-0.01	0.06	-0.29

Economic Aspects of Thick Granular Base Design for Flexible Pavement

Simplified Life Cycle Economic Analyses Model

The life cycle construction cost is estimated based on the assumption of the following economic terms:

x_1: inflation rate of construction cost

x: inflation rate

m: reconstruction cycle (assuming decided by pavement selection)

n: number of reconstruction cycle

The equivalent monetary value at the first year for a period of n*m years is:

$$Cost = C_1 + C_1\frac{(1+x_1)^m}{(1+x)^m} + C_1\frac{(1+x_1)^{2m}}{(1+x)^{2m}} + ... + C_1\frac{(1+x_1)^{nm}}{(1+x)^{nm}}$$
$$= C_1\left(1 + q^m + q^{2m} + ... + q^{nm}\right) = C_1\left(\frac{1-q^{(n+1)m}}{1-q^m}\right) \quad (5)$$

where C_1 is the pavement construction cost at year 1, $q = \frac{1+x_1}{1+x}$

Assume there are two alternative design that result in reconstruction cycle of m and n years respectively. The ratio of equivalent current cost for the life cycle of these two designs is:

$$\frac{Cost_1}{Cost_2} = \frac{C_1\left(\frac{1-q^{(m+1)n}}{1-q^n}\right)}{C_2\left(\frac{1-q^{(n+1)m}}{1-q^m}\right)} = \frac{C_1\left(1-q^{(m+1)n}\right)\left(1-q^m\right)}{C_2\left(1-q^{(n+1)m}\right)\left(1-q^n\right)} \quad (6)$$

The ratio should be 1 for the life cycle construction cost to break even.
Assuming pavement design resulted in reconstruction period of 20 and 15 years respectively, the initial construction cost are c_2 and c_1 respectively (c_2>c_1), to break even the life-cycle construction cost. The ratio of construction cost in 60 years should be:

$$\frac{Cost_1}{Cost_2} = \frac{\left(1+q^{15}+q^{30}+q^{45}+q^{60}\right)C_1}{\left(1+q^{20}+q^{40}+q^{60}\right)C_2} = 1 \quad (7)$$

At the break even point, there is

$$\frac{C_2}{C_1} = \frac{\left(1+q^{15}+q^{30}+q^{45}+q^{60}\right)}{\left(1+q^{20}+q^{40}+q^{60}\right)} \quad (8)$$

A plot between *q* and the ratio of initial construction cost at the break even points is shown in the following Figure 3. As long as the ratio of initial construction cost for alternative design is controlled below this curve, the performance benefits (in terms of service life extension) would offset the higher initial construction cost. For example, for the *q* value of 1 (inflation and inflation of construction cost equal), as long as the increase in the initial construction is below 25%, the higher initial construction cost will be offset by the life cycle performance extension from 15 years to 20 years (an 33% increase in service life). This simplified model does not explicitly account for cost associated with rehabilitation, traffic delay, safety, etc.

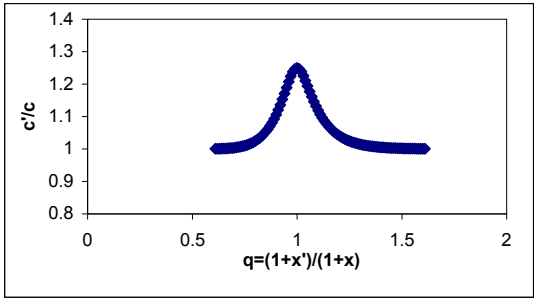

FIG. 3 Plot of q ($q = \frac{1+x_1}{1+x}$) and the ratio of initial construction cost (C_2/C_1)

The previous analyses show that as long as C_2/C_1 lies below the line specified, the life cycle cost for a better base design should be lower despite of higher initial cost.

Economic Comparison Based On ODOT Material and Construction Cost

The average material cost for each materials were obtained from Ohio DOT construction materials database. With these information, the average cost of pavement base to the total construction cost of pavement is determined. It was found that on average, the base layer accounts for around 1/3 of total pavement cost.

For pavement design that extended the reconstruction time from 15 years to 20 years. Assuming 1) an interest rate of 5.25% and 2) inflation rate of construction cost of 7%, 3) the cost of base layer is 30% of the total cost for base layer and pavement layer. The life cycle cost analyses indicated that doubling the thickness of base layer will still save the life-cycle cost. Based on the performance prediction using MEPDG, the 33% increase in the service life is achievable by using thicker granular base design. This means increasing the currently used 6 inch granular base to 12 inch will still bring down the life cycle construction cost.

CONCLUSIONS

This paper used MEPDG and simplified life cycle economic model to study the use of thick granular base in cold regions. Ohio is used as representative of cold regions. The results indicate that the use of thick granular base, while requires higher initial construction cost, will reduce life cycle cost by increasing the pavement service life. An optimal thickness of granular base appears to be around 12 inch for Ohio climate conditions. The use of thick granular base will make it more sustainable for flexible pavement in cold regions.

REFERENCES

Uhlmeyer, J.S., Piece, L. M., Lovejoy, J.S., Gribner, M.R., Mahoney, J.P. and Olson, G.D. (2003). “Design and Construction of Rock Cap Roadways: Case Study in Northeast Washington Stat.” TRR 1821

Rengmark, F. (1963). “Highway Pavement Design in Frost Areas in Sweden.” Highway Research Record No. 33, Highway Research Board, Washington D.C., pp. 137-149.

Taivainen, O.A. (1963). “Preventive Measures to Reduce Frost Action on Highways in Finland.” Highway Research Record No. 33, Highway Research Board, Washington, D.C., pp. 202-210.

Armstrong, M.D., and Csathy, T.I. (1963). “Frost Design Practices in Canada.” Highway Research Record No. 33, Highway Research Board, Washington D.C., pp. 170-196.

NCHRP Report 453: “Performance-Related Tests of Aggregates for Use in Unbound Pavement Layers”

Washington State DOT, “Use of Rock Cap Material as a Capillary Break”, Washington State DOT Tech Note,
http://www.wsdot.wa.gov/biz/mats/pavement/technotes/rockcaptechnote.pdf.

Sargand S.M, Wu, S. and Figueroa,J. (2006). Rational Approach for Base Type Selection, Journal of Transportation Engineering, Vol. 132, No. 10, October 2006, pp. 753-762.

Guidelines for Implementing NCHRP I-37A M-E Design Procedures in Ohio, SJN 134300, draft final report

Numerical Analysis and Geo-mechanism Study on the Subgrade Cracking Process Based on RFPA

Xiao-jing Li[1,2], Guo-ren Lu[2],Wei-min Yang[2], Shu-cai Li[2]

[1]Shandong Jianzhu University, School of Civil Engineering, Jinan 250101, China; li8021@163.com
[2]Geotechnical and Structural Engineering Research Center of Shandong University, Jinan 250061, China

ABSTRACT: Based on the typical highways widening approaches used in the process of expressway extension in China, the differential settlement and cracking mechanism in the pavement while widening unilaterally and bilaterally were studied using the FEM software RFPA. The results showed that the cracks initially appeared from the toe of side slope of the new foundation. As time went on, the settlement increased and cracks arised from the toe of side slope of the old foundation. Then these cracks propagated gradually and eventually formed a clear sliding surface, leading to glides along the interfaces between the old and new foundations. The interfaces were apt to be the potential gliding planes. If the embankment was higher, the global stability would be worse and the differential settlement would be larger. While the differential settlement and glide increased, the generated additional flexural-tensile stress and shear stress also increased progressively. The consequences were that the longitudinal cracks would appear in the foundation and further brought about the cracking of the asphalt pavement.

INTRODUCTION

The typical widening methods were simulated in this paper adopting RFPA software (Sha 2001). A numerical analysis model was established to analyze the differential settlement in the expressway extension project. Furthermore, the generation and propagation mechanism of longitudinal cracks in the roadbed and surface layer was studied.

THE NUMERICAL ANALYSIS PRINCIPLE AND IMPLEMENTATION OF THE ROADBED CRACKING PROCESS

The basic principle of RFPA centrifuge was the principle of the geo-technical centrifuge model tests, which studied the geotechnical engineering problems by increasing the magnitude of body force, which was responding to the prototype. Adopting RFPA, the unit weight of the model was gradually superimposed by a certain coefficient. The relative weak elements would damage while the stress was beyond their

capacity. With the number of the damage elements increasing, they coalesced and formed a macroscopic rupture surface finally(Chen 2006; Su and Xu 2000; Tang and Zhu 2002; Tang et al. 2007; Yu and Tang 2007; Zhang and Tang 2006; Zhu and Tang 2003).

CALCULATION MODEL

The background of numerical simulation was Wei'ru expressway in China.

Model simplification and assumption

Based on the widening methods of typical expressway project constructed in China, several simplified models were constructed which were model 1 for unilateral widening and heightening; model 2 for unilateral widening; model 3 for bilateral widening and heightening; model 4 for the bilateral widening and an increase of 0.54m cement stabilized macadam acting as basement, 0.18m asphalt concrete layer.

Model calculation parameters

The detailed parameters of Model 1 ~ 3 were listed in Table 1 and the order of the assignment values in the table was: the old embankment, the new embankment, the old roadbed, the new roadbed. The order of strength was that the new embankment> the old embankment> the old roadbed> the new roadbed. The parameters of Model 3 were in Table 2. The width and filling height of the old roadbed were 18m and 3m. The roadbed was widened by three methods and slope was 1:1.5.

Table 1. List of the Parameter in Model 1~3

Category	Modulus MPa	Poisson's Ratio μ	Friction Angle φ	Cohesion c（kPa）
New Embankment	50	0.35	20°	25
Old Embankment	40	0.35	20°	25
Old roadbed	4	0.35	20°	25
New roadbed	3	0.35	15°	25

PS: Unit Density is 18 kN/m^3

Table 2. List of the Basement Parameter in Model 3

Category	Modulus MPa	Poisson's Ratio μ	Friction Angle φ	Cohesion c（kPa）
Cement Stabilized Macadam	1500	0.25		
Asphalt Concrete	1200	0.25		

SIMULATION AND ANALYSIS OF THE MODEL FAILURE ROCESSES

The failure process of Model 1 and the analysis of the failure process

The establishment and the failure process of Model 1

In Model 1, the old embankment was 18m width and 3m height. The new roadbed was widened unilaterally, which was 28m width and 6m height. The slope of both the new roadbed and the old roadbed was 1:1.5, as shown in Figure 1:

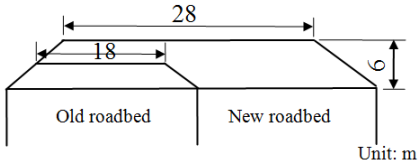

FIG. 1. Schematic diagram of Model 1

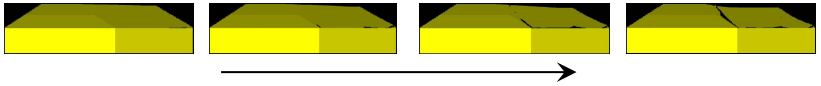

FIG. 2. Simulation of the failure process of Model 1

Movement vector and the road surface settlement of Model 1

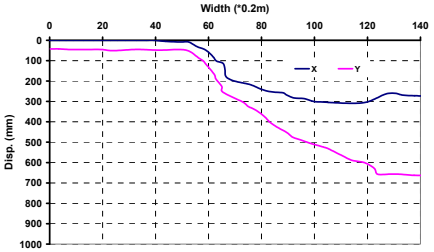

FIG. 3. Displacement vector and the settlement of the embankment surface in Model 1

Analysis of calculation results of Model 1

From Fig. 2 and Fig. 3, it could be seen that the settlement firstly appeared at the edge of the shoulder of the new roadbed. Small cracks emerged at the foot of the slope on the outside of the new roadbed after unilateral roadbed widening. With the time going on after the construction, the settlement gradually approached the inside of road. There was also a bottom-up crack, which aggregated at the bottom of the new roadbed and gradually produce slippage at the junction between the new roadbed and the old roadbed. Therefore, it produced a longitudinal crack on embankment surface along the interface between the old roadbed and the new roadbed.

The failure process and analysis of Model 2

The establishment and destruction process of Model 2

In Model 2, the old embankment was 18m width and 3m height. The new roadbed was widened unilaterally, which was 28m width and 3m height. Both the slope of new roadbed and that of old roadbed were 1:1.5, as shown in Fig. 4.

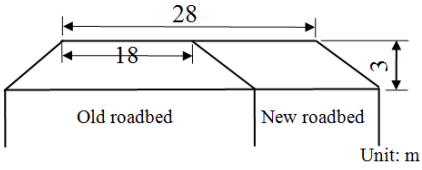

FIG. 4. Schematic diagram of Model 2

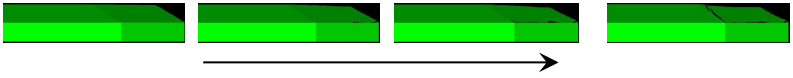

FIG. 5. Simulation of the failure process of Model 2

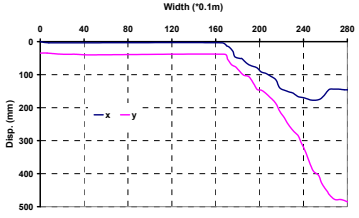

FIG. 6. Displacement vector and the settlement of the embankment surface in Model 2

Analysis of the calculation results of Model 2

Model 2 was actually a special case of model 1. Since this kind of widening mode was more widely used contrasting to that of model 1, it was studied individually. Comparing Model 2 (the embankment height of 3m) to Model 1 (the embankment height of 6m), it could be seen that both the settlement trends and the shape of the settlement curve were similar, as well as cracking mode in the roadbed. The maximum settlement was less than 0.50m at the edge of new roadbed shoulder (as shown in Fig. 6), while that of Model 1 was 0.75m. The area of old roadbed which was affected by the settlement of new roadbed was very small. There was nearly no further extension to the inside of the road and the affected area of cracking and the slippage was much smaller than that of Model 1.

The failure process and analysis of Model 3

The establishment and destruction process of Model 3

The new roadbed which was widened bilaterally was 28m width and 6m height. The slopes of new roadbed and old roadbed were both 1:1.5. Based on Model 1, 0.54m cement stabilized macadam for basement layer and 0.18m asphalt concrete layer were adopted in Model 3. Compared to macadam, the foundation and roadbed could be considered as relatively homogeneous medium. Macadam and asphalt concrete layer were considered as non-homogeneous material, whose homogeneity coefficients were assumed 10 and 15 respectively. The compressive strength parameters were 3.37 and 3.98 MPa.

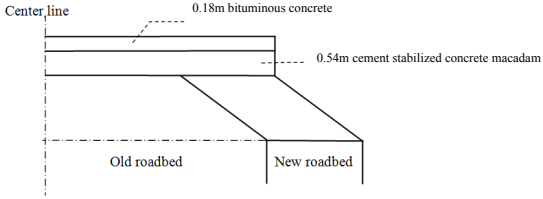

FIG. 7. Schematic diagram of Model 4

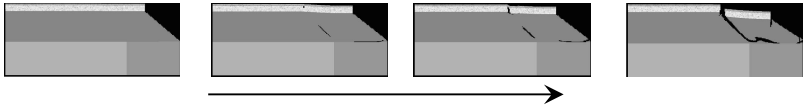

FIG. 8. Simulation of the failure process of Model 4

Movement vector and the road surface settlement figure of Model 1

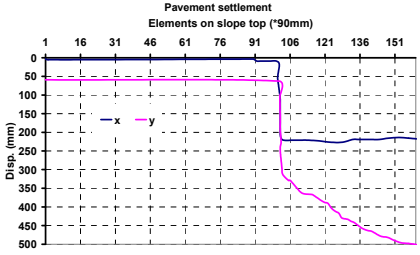

FIG. 9. Displacement vector and the settlement of the embankment surface in Model 4

Analysis of the calculation results of Model 3

The cracking generated in the roadbed extended to the pavement for Model 3 and biased to the roadbed centerline, as shown in Fig. 8. The additional shear stress generated in the road surface, the basement and the base course since the differential

settlement. The shear capacity of the surface layer and the base material was much bigger than that of the roadbed soil, so shear failure firstly occurred in the roadbed. Then the stress concentrated in the basement layer and surface layer where failure happened. Therefore, the basement layer also failed and longitudinal crack in the layers led to the failure of surface layer, whose flexural-tensile strength was relatively bigger. Eventually, the longitudinal crack of the overall road structure happened.

From the settlement curves, it could be seen that the maximum settlement of the edge of the road shoulder reduced and its value was about 0.45m compared to the 0.50m settlement in situation of the unilateral widening (as shown in Fig. 9). The settlement in the central line of the road was almost zero and the settlement of the entire old roadbed was stable. It indicated that the settlement was larger due to the effect of eccentricity.

ENGINEERING PRACTICE

According to the principles laid down by "roadbed Design standard" of the Ministry of Communication of China, when the value of the transverse slope of the road camber in the widening roadbed was more than 0.5%, cracking occurred on the road surface. Checking according to the formula proposed by Wang Xuan-cang and Chen Xing-guang, all the increment of the transverse slope of the road camber in the above model were more than 0.5%. The crack situation of the basement layer and the road surface after the road widening construction were shown in Fig. 10 and Fig. 11.

FIG. 10. Crack in the base layer and surface layer in-situ

FIG. 11. Longitudinal crack of the surface layer in-situ

SUMMARY

According to the widening mothods in the typical projects of expressway constructed in China, three simplified models were established. Utilizing RFPA, the cracking process of longitudinal cracks in the road reconstruction was simulated and analyzed, in addition, the cause of the longitudinal cracks was explored. It came to the conclusions as follows:

1. The maximum settlement of the widened roadbed generally occurred near the edge of the shoulder in the new roadbed, while the settlement in the old roadbed centerline was small.
2. The longitudinal cracks firstly occurred at the foot of the slope in the new roadbed. As the time elapse, the settlement gradually increased. Then, the crack occurred at the foot of the old roadbed and propagated and produced slippage finally.
3. The mechanics impact of the differential settlement on the roadbed surface was mainly embodied in the additional stress, which led to the longitudinal cracks of the road surface. The location of the longitudinal cracks was in the interface between the old roadbed and the new roadbed and biased to the central position of the old road.
4. The authenticity for the longitudinal cracks phenomenon by RFPA indicated that RFPA was an effective tool to study the mechanism and regularity of the longitudinal cracks in the road reconstruction.

ACKNOWLEDGMENTS

This research is supported by the Key Project for Science and Technology Research of Ministry of Education (Grant No. 108158).

REFERENCES

Chen, X.G.(2006). "Different settlement control technique research of expressway expansion project." *Master thesis*.

Sha, Q.L. (2001). "Asphalt pavement failure and prevention of expressway." *Beijing :People Traffic Press*.

Su, C. and Xu, Z.Z.(2000). "Back analysis method of foundation parameters for connection section of highways and its application." *Journal of Hohai University,* Vol.28(6):38-42

Tang, C.A., Tang, L.X. and Li, L.C.(2007). "Centrifugal loading method of RFPA for the failure process analysis of rock and soil structure." *Chinese Journal of Geotechnical Engineering*, Vol.29(1):71-76.

Tang, C.A. and Zhu, W.C. (2002). "Numerical photo elastic fringe of stress distribution during failure process of material." *Mechanics and Engineering*, Vol.24(5):47-50

Yu, Q.L. and Tang, C.A.(2007). "Digital image based characterization method of rock's heterogeneity and its primary application." *Chinese Journal of Rock Mechanics And Engineering*, Vol.26(3):551-559

Zhang, Y.B. and Tang, C.A.(2006). "Stress parallel computing in rock failure process analysis system." *Chinese Journal of Rock Mechanics And Engineering,* Vol.25(3):479-483

Zhu, W.C., Tang, C.A. (2003) "Constitutive relationship of mesoscopic elements used in rfpa and its validations. " *Chinese Journal of Rock Mechanics And Engineering*, Vol.22(3):24-29

The Analysis and Recommended Solutions for Rural Roads in China

Xiaoping Lin[1], Runhua Guo[2], and Jianming Ling[3]

[1]China Academy of Transportation Sciences, Beijing 100029, China; xplin2005@yahoo.com.cn
[2]Tsinghua University, Beijing 100084, China; guorh@tsinghua.edu.cn
[3]Tongji University, Shanghai 200092, China; jmling01@yahoo.com.cn

ABSTRACT: China has developed her expressway system after 10 years' intensive construction with most of its expressway systems concentrated in the coastal areas. In the central and western parts a majority of the highway system is comprised of rural roads with low volume traffic. The objective of this article is to display the current rural roads situation in China, the existing problems in the rural road system, and some of the main factors impacting rural road infrastructures, and dedicate the rural road development strategies to preserve China's extensive rural road system. This paper also focuses on the main problems and the development objectives of rural roads in different areas of China. Base on the study, the solutions to typical rural roads of each area are organized and strategies for rural roads are also recommended.

INTRODUCTION

As one of the fastest growing country among the world, China developed her expressway system after 10 years' intensive construction started 2005. By 2015, the highway system in China will be strategically in the same scale as that in U.S. with most of its expressway systems concentrated in the coastal areas due to the well developed economy in those areas.

China is in many aspects a rural country with 58.07 percent of its total population living in rural areas (CAST, 2001), especially in the central and western parts of China, where a majority of the highway system is comprised of rural roads. By the end of 2008, the total length of China's rural highways has reached 3.21 million kilometers (2 million miles), through which 99 percent of the township administrative centers and 93 percent villages are connected (MOT, 2009).

In China, The current situation of limited budgets, limited technique supports, increasing truck numbers and axle loads on rural pavements, special subgrade or base condition, sustainable development requirement and the identified rural pavement maintenance needs obviously suggest that the rural road network will find it increasingly challenging to develop extensive rural road system in the future if these

trends maintain. China should develop its own strategies to deal with all these challenges. This paper will focus on the main problems and the development objectives of rural road in different areas of China. Base on the study, the solutions to typical rural roads of each area are enumerated and strategies for rural roads are also recommended.

The objective of this article is to display the current rural roads situation in China, discuss the existing problems in the rural road system, highlight some of the main factors that impact rural road infrastructures, and dedicate the rural road development strategies to preserve China's extensive rural road system.

RURAL ROAD NETWORK IN CHINA

The hierarchical rural road network in China consists of three main parts: roads connecting county seats, towns and villages. By the end of 2001, the length of rural roads reached 1.28 million km (795,525 miles). Especially in 2008, 391,000 km of rural roads were built or rebuilt (Figure 1), with 263,000 km (119,329 miles) blacktop and cement roads paved. 99 percent of the township administrative centers and 93 percent villages are connected through this rural network (XNA, 2009).

FIG. 1. Typical rebuilt rural road in China

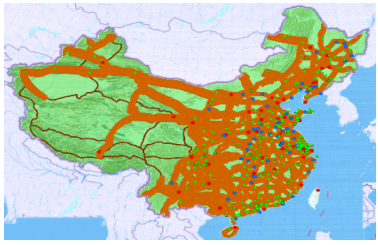

FIG. 2. National highway network

The Chinese government has invested huge funds to build rural roads. During the country's tenth Five-Year Plan (2001~2005), China had invested 417.8 billion yuan (US$ 51 billion) in rural road construction, three times that in the previous five years. Local transportation departments have been urged to put more effort and investment in rural roads. By the end of 2010, 1.2 million km (745,805 miles) of rural roads will be built or rebuilt, a quarter of which will be brand new roads. 95 percent of towns and 80 percent of villages in the country will be covered by this building and rebuilding program. China will have 1.8 million km (1.1 million miles) of rural roads and all administrative villages in China will be connected by highways. The new roads will be mainly built in old revolutionary bases, border areas, poor areas and major grain producing areas.

DEVELOPMENT OBIECTIVE OF RURAL ROADS IN CHINA

The overall objective of the development of rural roads in China is to achieve a rural road network extended in all directions. As shown in figure 2, the time length

should be less than half hour for any vehicle to reach the highway system through the rural road network in the eastern part of China; this criterion is 1 hour and 2 hours for middle part and western part respectively.

In the first twenty years of the 21st century, the rural road network is required to be very well developed. In other words, a very well extended network will connect all counties, towns, and villages with higher service level.

During the period of 2011~2020, 1.05 million km (652,279 miles) rural roads will be built or rebuilt, more than half of them will be newly built. 98 percent of the township administrative centers and 90 percent villages will be blacktop and cement roads paved. The overall length of rural road will reach a number of 2.5 million km (1.55 million miles).

According to the strategy of the Ministry of Transport, China planed to have its rural road conditions and traffic service greatly improved by the year 2005, with roads reaching 99.8 percent of towns and 96 percent of villages.

Along with a national highway network, the Ministry plans to build a bus network in rural areas so that farmers can easily go outside their hometowns (XNA, 2005).

By the end of 2010, China will have all its towns and villages connected to roads and more than 95 percent of those village roads will be available to public traffic. By the end of 2020, all village roads will be built into high-standard roads and all will be available to public traffic (XNA, 2006).

MAIN CHALLENGES OF RURAL ROADS DEVELOPMENT

At present, roads in many rural areas are not in good condition. Owing to funds shortage, technology support limitation and anfractuous local environment, it is difficult to build highways for all China's villages. Except for all this huge progress, there are still 167 towns and 49,339 administrative villages currently not linked with highways (XNA, 2009). More than 300,000 villages have not been linked by blacktop or cement roads, and about 40,000 villages even do not have paved roads (XNA, 2005).

Unlike major intercity roads, government policy generally could not direct resources to the improvement of rural roads, which will lead the rural roads into a situation of short of system support (XNA, 2003). Road construction is also facing the shortage of funds. The positive fiscal policy will “fade out" stage by stage and the investment from budget will be reduced from the tax system, also the sustainable development strategies require to be more stringent on environment and land resources, which increase the difficulty in financing rural projects.

The continual increasing in output, specialization, and mobility in countryside put tremendous pressure on the rural road system (Figure 3) (People’s web, 2005). The continuing reliance on the traditional Road Maintenance Tax as the major source of fiscal support for road construction and maintenance were seriously limited, which restrained the needs for a higher level of funding.

FIG. 3. Over-weighted trucks

FIG. 4. Bad traffic conditions in rural area

The problems can be summarized as bad traffic condition (Figure 4), low technique level (Figure 5), and short of funds, self development capacity and support (Figure 6).

FIG. 5. Low technique levels in rural area

FIG. 6. Short of support sections

Moreover, China is a country with various kinds of physiognomies. This makes the rural road network construction more difficult (Figure 7). Sometimes many rural roads will have to be built on poor or special property subgrade or base, which will finally present very bad traffic condition. This special subgrade conditions include saline soils, desert (Figure 8), frozen area (Figure 9), loessial area (Figure 10) and wetlands area (Figure 11).

FIG.7. Execrable construction environments

FIG. 8. Rural roads in desert area

In the following 15 years, most of the existing rural road network will be updated, rebuilt or reorganized. How to achieve the goal efficiently and economically is a key problem faced by engineers and planners.

As a responsible nation on the earth, China's sustainable development strategy requires that any built or rebuilt rural road project should harmonize with its environment, which will increase the cost potentially or in short term and sometimes

hold back the development of rural road network for the limitations in funds or environment.

FIG. 9. Rural roads in frozen area

FIG. 10. Rural roads in loessial area

STRATEGY ANALYSIS OF RURAL ROADS DEVELOPMENT

Lack of finance, limited technique supports, heavy traffic and axle loads on rural pavements, unsatisfactory subgrade etc., all these factors make us realize that the rural road network needs to be constructed extensively despite difficulties. To solve the urgent issue, some feasible measures are suggested as follows.

Low cost road construction technology

It is necessary to develop low cost road construction technology in rural area, especial in western low volume traffic area. To face the shortage of funds, engineers should employ any possible technologies to decrease the cost of road construction such as inventing new construction materials, new equipments,

Private-Public Partnership

When the nation-financed rural roads are locally used or locals are not the predominant users of the road, the construction and maintenance of rural roads will be serious problems. Therefore, Private-Public Partnership will be an effective and reasonable solution to this problem.

Toll roads

Usually increasing numbers of heavier trucks will result in faster pavement structural capacity deteriorating and shorter pavement life. Tolling on over-weighted trucks will efficiently solve the problem.

Rural road network rebuilding technology

Except the newly built roads, almost all the existing rural roads need to be rebuilt to have its rural road conditions and traffic service greatly improved. Rural road network rebuilding technology will systematically optimize available resources and provide the best service.

Special area road construction technology

Since many rural roads are built on poor or special property subgrade or base, it is necessary to develop special area road construction technology to meet the local environment conditions. These technologies should focus on saline soils, desert, frozen area, loessial area and wetlands area. Also, geological defect investigation and treatment technologies should also be developed.

CONCLUSIONS AND RECOMMENDATIONS

China will have all its towns and villages connected to highway system and more than 95 percent of those village roads will be available to public traffic during the Eleventh Five-Year Plan (2001~2010). At the end of 2020, all village roads will be built into high-standard roads and all will be available to public traffic. The overall length of rural road will reach a number of 2.5 million km (1.55 million miles)

Challenges such as budgets shortage, technique supports deficiency, poor subgrade or base condition, sustainable development requirement and the identified rural pavement maintenance needs indicate the necessity of speeding up the rural road system construction. Though these problems will exist for a long time, the national infrastructure construction will be carried out step by step to benefit rural areas.

To achieve the goal of high level rural road network, recommended strategies include low cost road construction technology, Private-Public Partnership, toll roads, rural road network rebuilding technology, and special area road construction technology. The overall objective of the development of rural roads in China is to achieve a road network extended in all directions rural.

REFERENCES

A Survey of Scientific Accomplishment on Chinese People (2001). Chinese Association of Science and Technology (CAST).

Minister of Transportation (MOT), Summary lecture on transportation. Jan. 16, 2009 http://www.mot.gov.cn/zhuzhan/buzhangwangye/lishenglin/zhongyaojianghua/200901/t20090116_552042.html. Accessed Dec 26, 2009.

Xinhua News Agency (XNA): China's Rural Road Length Reaches 2.9 Million Km: China Development Gateway, October 24, 2005. http://www.chinagate.com.cn/english/45146.htm. Accessed March 30, 2006.

Xinhua News Agency (XNA): China to build 1.2 million km rural roads in five years: People's Daily Online, February 08, 2006. http://english.people.com.cn/200602/08/eng20060208_240928.html. Accessed March 30, 2008.

Xinhua News Agency (XNA): Rural Road Construction Speeded Up: China Development Gateway, May 16, 2003. http://www.chinagate.com.cn/english/3903.htm. Accessed March 30, 2006.

http://www.people.com.cn: What's going on in China about treating over-weighted trucks: October 24, 2005. http://finance.people.com.cn/GB/8215/35535/. Accessed March 30, 2008.

Bitumen Quality, Pavement LCCA and Contractor's Expectations

Filippo G. Praticò[1], Domenico Tramontana[2], Antonio Casciano[3]

[1, 2, 3]Mediterranea University at Reggio Calabria –Via Graziella – Feo di Vito – 89100 Reggio Calabria – Italy - [1]filippo.pratico@unirc.it; [2] ratio85@libero.it; [3] casciano.antonio@libero.it.

ABSTRACT: QC/QA (Quality Control/ Quality Assurance) tests on asphalt binder may assess that the as-constructed pavement has characteristics different from the ones set out in the contract for the as-designed pavement due to the insufficient quality of the bitumen. Therefore, a Pay Adjustment (PA) is needed.

In the light of the above facts, the objective of this paper was the assessment of a quantitative relationship between asphalt binder quality and the consequent Pay Adjustment, for a given class of boundary conditions.

Once the problem was modelled, experiments and simulations were carried out through the use of M-E PDG (Mechanistic-Empirical Pavement Design Guide, 2007).

Consequences in terms of pavement life cycle cost analysis (LCCA) and contractor's expectations were derived. Results demonstrated how bitumen quality and cost influence Pay Adjustment and contractor's strategy.

PROBLEM STATEMENT

Pavement expected life depends on many material and construction factors. In general, asphalt cement can be modified to achieve several classes of improvements.

The main reasons for using polymer modified bitumens rely in the fact that pavements constructed by using binders are usually more resistant to fatigue, thermal cracking, rutting, stripping, and temperature susceptibility than neat binders (Yildirim, 2007). The choice of a bitumen of given penetration grade (European system) or performance grade (U.S. system) depends on material, traffic, and environmental factors. As a matter of fact, in practice, even if an adequate choice was carried out, the real asphalt binder can be unsatisfactory.

Indeed, unfortunately many classes of issues and variables are involved in pavement construction: contractor's strategy, timetable and scheduling drawbacks (which can affect the number of tests), defects due to transportation and/or storage.

As a consequence, QC/QA (Quality Control/ Quality Assurance) tests on asphalt binder can assess that the as-constructed pavement (and, in particular, bitumen) has characteristics different from the ones set out in the contract for the as-designed

pavement. Therefore, pavement life cycle cost (see figure 1) and Pay Adjustment (PA) need to be evaluated.

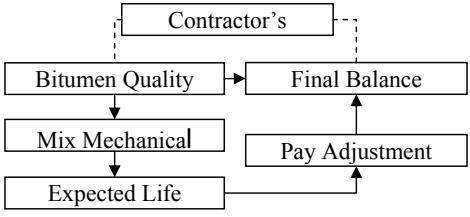

FIG. 1. Conceptual framework.

In the light of the above-mentioned issues, the objective of this paper was the assessment of a quantitative relationship between asphalt binder quality and the consequent Pay Adjustment, for a given class of boundary conditions. This section deals with the problem modelling, while the experiments and simulations carried out are described in the next section.

In order to try to model the dependence of pavement life cycle cost on asphalt binder quality two problems were addressed. The first is the relationship between the expected life of the pavement and bitumen quality (equations 1 to 4). The second issue is the derivation of the corresponding Pay Adjustment (PA, equation 5). PA and (bitumen) cost are intended to be the key-factors which affect contractor's strategy.

It is well known that the penetration of the bitumen affects the viscosity-temperature relationship according to the following algorithm:

$$\log\log\eta = A + VTS\log T_R \tag{1}$$

where:

A = regression intercept of viscosity-temperature susceptibility;
VTS = regression slope of viscosity-temperature susceptibility;
η = viscosity, in cP (mPa·s);
T_R = reference temperature, in Rankine

where A and VTS depend on the class of penetration (M-E PDG, 2007).

The Modulus – frequency relationship can be given by the following formula (M-E PDG, 2007):

$$\log(E^*) = \delta + \frac{\alpha}{1 + e^{\wedge}\left[\beta + \gamma(\log t_r)\right]} \tag{2}$$

where:

E^* = dynamic modulus, in psi;
δ = limiting minimum value of E*;
$\delta+\alpha$ = limiting maximum value of E*;
β, γ = parameters describing the shape of the sigmoidal function;
t_r = time of loading at the reference temperature, in sec., depending also on bitumen class.

Also fatigue, rutting and thermal cracking can be affected by the changes in composition or moduli.

As for fatigue, a general mathematical form of the relationship between the number N_f of load repetitions and the modulus (E_S) is shown in equation below (M-E PDG, 2007):

$$N_f = C' k_1 \left(\frac{1}{\varepsilon_t}\right)^{k_2} \left(\frac{1}{E_S}\right)^{k_3} \tag{3}$$

where: N_f = number of repetitions to fatigue cracking;
ε_t = tensile strain at the critical location;
E_S = stiffness of the material;
k_1, k_2, k_3 = laboratory regression coefficients;
C' = laboratory to field adjustment factor.

As for the Rutting prediction model, it is usually expressed in terms of the vertical compressive strain (ε_V) at the top of the sub-grade layer (WSDOT Pavement Guide, 1998):

$$N_r = 1.077 \cdot 10^{18} \left(\frac{10^{-6}}{\varepsilon_V}\right)^{4.4843} \tag{4}$$

where: N_f = number of cycles to failure;
ε_V = vertical compressive strain at the top of the sub-grade layer, (function of all the moduli of the multilayered pavement).

Finally, the amount (C_f) of transverse cracking expected in the pavement system (thermal cracking) can be predicted by relating the crack depth (C_D) to an amount of cracking (crack frequency) for example through the expression after (Loh and Olek, 1999).

For a given traffic and climate, as far as only the bearing properties are considered, the above-specified factors are the structural elements needed to determine the expected life of the as-designed pavement (D) and the expected life of the as-constructed pavement (E). E depends mainly on three classes of failure mechanisms: fatigue cracking (equation 3 illustrates a typical fatigue law), thermal cracking and plastic deformation (e.g. equation 4). Elaborations are quite complex and a software routine is usually needed.

Pay Adjustment will depend on the relationship between D and E. Therefore an algorithm able to take into account for the expected lives, following the methodology of the LCCA (Life Cycle Cost Analysis), is needed (Weed, 2001; Praticò, 2007):

$$PA = C\left[\frac{R^D - R^E}{1 - R^O}\right] \tag{5}$$

where C is the cost, D is the design life of the as-designed pavement, E is the expected life of the as-constructed pavement, R is the ratio (1 + INF) / (1 + INT) where INF and INT are the inflation and interest rates, O is the expected life of successive resurfacing/reconstruction.

Due to the fact that bitumen quality affects the abovementioned expected life (equations 1 to 4), the equation (5) provides a quantitative relationship between pavement life cycle costs and bitumen quality.

EXPERIMENTS AND RESULTS

Experiments and simulations were carried out based on the synergetic application of the (M-E PDG, 2007) and equation 5.

Input data related to:

1) layer 1 (asphalt concrete)
   - layer thickness (5 in≅13cm);
   - aggregate gradation;
   - general properties (reference temperature: 70°F = 21°C, effective bitumen volume content: 10.5%, air voids content: 8%);
2) layer 2 (granular base)
   - layer thickness (13 in≅33cm);
   - strength properties (Poisson's ratio: 0.35, coefficient of lateral pressure: 0.5, modulus: 28000 psi; 1psi=6.9kPa);
3) layer 3 (sub-grade)
   - layer thickness (infinite);
   - strength properties (Poisson's ratio: 0.35, coefficient of lateral pressure: 0.5, modulus: 11000 psi);
4) Traffic conditions (AADTT: 1550, number of lanes in design direction: 2, percent of trucks in design direction: 50%, percent of trucks in design lane: 90% operational speed: 95 km/h);
5) Annual climate statistics (mean annual air temperature: 17°C, mean annual rainfall: 350 mm, etc.);
6) Performance criteria and limits (e.g. asphalt concrete surface down cracking with limit of 370 m/km);
7) Characteristics of bitumens. The bitumen quality ranged from A_b (pen=4.5 mm, class 40-50, A=10.5254, VTS=-3.5047, see eq.1, Performance Grade PG 70-16, average viscosity=3287230 Pa*s) up to E_b (pen=21.5 mm, class 200-300, A=11.8107, VTS=-4.0068, Performance Grade PG 52-28, average viscosity=74386 Pa*s) as in (M-E PDG, 2007). Note that the abovementioned discretization of bitumen quality is a key work hypothesis.

Given the above-mentioned design of experiments (control factors: 1~6; variable: 7), from the four classes of inputs (Structure, Climate, Traffic, Performance Criteria), through the algorithm of the M-E PDG, the corresponding plots were obtained, each one related to a failure criterium. From the expected lives related to each of the above-mentioned diagrams, a minimum expected life was derived.

Under the above-mentioned hypotheses, results demonstrated that (see figures 2 to 4):

a) longitudinal cracking (m/km), alligator cracking (%), hot mix asphalt, HMA, rutting (cm), unbound layer rutting (cm), total rutting (cm) and IRI, international roughness index, depend on time (months);
b) longitudinal cracking and rutting were the main failure causes;
c) for a type A_b bitumen the expected life was 254 months (higher than the design life D, failure for longitudinal cracking), for type B_b (which was assumed to be the as-designed bitumen) was 244 (design life D, failure for longitudinal

cracking), for type C_b was 237 (lower than D, failure for longitudinal cracking), for type D_b was 211 (lower than D, failure due to rutting of the HMA), for type E_b was 94 months (lower than D, failure for rutting of the first layer).

From equation 5 the following values of PA/C (%) were derived (see figure 3):

- bitumen A_b PA/C=5;
- bitumen B_b PA/C=0;
- bitumen C_b PA/C=-5;
- bitumen D_b PA/C=-18;
- bitumen E_b PA/C=-93.

It is important to point out that for the asphalt binder type B_b (as-designed bitumen) the Pay Adjustment is zero, while for A_b (high viscosity) there will be a bonus (PA > 0) and for C_b, D_b and E_b (low viscosity) a penalty (PA < 0).

Note that the higher the viscosity (Pa·s), from E_b to A_b, the higher is the PA/C ratio (%).

In order to better examine the results it seems relevant to focus on the following key-factors, for a given length of road and for a given contractor's strategy:

- the Pay Adjustment, PA (which is positive for A_b or negative for C_b);
- the cost of the as-designed bitumen (B_b), C_1;
- the cost of the as-constructed bitumen, C_2 (higher than C_1 for A_b, lower than C_1 for A_c);
- their difference $D_C = C_1 - C_2$ (negative for A_b, positive for C_b), i.e. the eventual, immediate and temporary gain for the contractor;
- the sum of the above-mentioned D_C and the Pay Adjustment, which represents the final balance between immediate gain (D_C) and posticipate losses (PA);
- the economical reinforcement, R_E, for choocing the type-A_b bitumen instead of the type-C_b bitumen, that is to say $[D_C+PA]_A-[D_C+PA]_C$.

Under the above-mentioned hypotheses, it is possible to derive that, if the contractor's choice is A_b:

- if all the bitumens (from A_b to E_b) have the same cost, the immediate gain D_C for the contractor is null and the economical reinforcement R_E for doing such a choice is high (9%, see figure 4, left bar);
- if there is a very high cost difference among the different types of bitumen (for example 0.36 €/kg to make an upgrade from E_b to A_b, see x-axis in figure 4), then the immediate gain D_C is negative (about -11%) and in this case the economical reinforcement R_E will be strongly negative (-16%, see figure 4, bar on the right). Therefore, in this case both immediate and overall consequences for choosing A_b will be negative and a poor class bitumen will be probably selected (C_b to E_b);
- for a given economic scenario there will be a particular cost difference (in our hypothesis 0.09 €/kg, see x-axis in figure 4) in which the overall balance R_E will be close to zero and the choice of A_b or C_b basically will not affect contractor's budget.

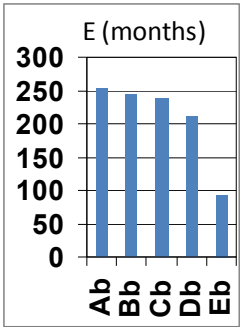

FIG. 2. Ex. life of different bitumens.

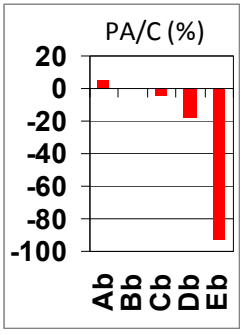

FIG. 3. PA/C for different bitumens.

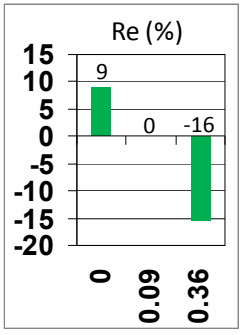

FIG. 4. Reinforcement for different Dc values.

MAIN FINDINGS

In the light of the above results, under the given hypotheses, the following main findings can be drawn:

- the higher the quality of the asphalt binder (among the selected work hypotheses) the higher is the expected life of the as-constructed flexible pavement and the more probable is a failure *per* longitudinal cracking;
- the lower the quality of the asphalt binder the more probable a failure due to Rutting;
- from a contractor's perspective, the critical factor relies in the comparison between immediate and sure gains *vs.* future and possible gains of the same order of magnitude. The cost for bitumen modification seems to play a crucial role in this process of check and balance;
- it is noteworthy to point out that the pay adjustment can play an important role in terms of "tuning" of contractor's *vs.* agency strategy.

Future research will aim to extend the simulations and studies in order to obtain a wider spectrum of responses.

REFERENCES

AASHTO TP 62-03 (2005). "Standard Method of Test for Determining Dynamic Modulus of Hot-Mix Asphalt Concrete Mixtures." American Association of State Highway and Transportation Officials, Washington, D.C.

AA.VV. (2007). "Guide for Mechanistic-Empirical Design of New and Rehabilitated Pavement Structures." Retrieved May 2008 from www.trb.org/mepdg, National Cooperative Highway Research Program, Transportation Research Board, Washington, D.C.

AA.VV (1998). "WSDOT Pavement Guide: Flexible - Mechanistic-Empirical Method." Retrieved May 2008 from http://training.ce.washington.edu/WSDOT. Washington Department of Transportation.

American Society for Testing and Materials (1998). "ASTM D2493 Viscosity-Temperature Chart for Asphalt." *Annual Book of ASTM Standards*.

Bonaquist, R. and Christensen, D.W. (2005). "A Practical Procedure for Developing Dynamic Modulus Master Curves for Pavement Structural Design." *84th Annual Meeting of the Transportation Research Board*, Paper No. 05-0389, Washington D.C.

Clyne, T. R. et alia (2004). "Determination of HMA Modulus values for use in Mechanistic-Empirical Pavement Design." University of Minnesota, Department of Civil Engineering. Office of Materials and Road Research.

Garcia, G. and Thompson, M. (2007). "HMA Dynamic Modulus Predictive Models (A Review)." Illinois Center for Transportation - Department of Civil and Enviromental Engineer.

Loh, S. and Olek, J. (1999). "Contributions of PG Graded Asphalt to low Temperature Cracking Resistance of Pavement." Joint Transportation Research Program. Purdue University - Department of Civil Engineering.

Praticò, F.G. (2007) "Quality and timeliness in highway construction contracts" a new acceptance model based on both mechanical and surface performance of flexible pavements." *International Journal of Construction Management and Economics*, Volume 25, Issue 3, pages 305-313, Routledge – Taylor and Francis.

Yildirim, Y. (2007). "Polymer modified asphalt binders." *Construction and Building Materials*, Volume 21, Issue 1.

Weed, R.M. (2001). "Derivation of equation for cost of premature pavement failure." *Paper presented at the 80th TRB Annual Meeting*, Washington, DC.

Predicted Pavement Life-Cycle Costing of Surface Maintenance Treatments

Dr Tim Martin[1]

[1]Chief Scientist, Sustainable Infrastructure Management, ARRB Group Ltd (formerly Australian Road Research Board), Vermont South, Victoria, 3133, Australia; tim.martin@arrb.com.au

ABSTRACT: Some 85% of Australia's sealed road network is comprised of unbound granular pavements with a wearing surface treatment of stone aggregate embedded in a thin bituminous binder seal. Experimental pavement deterioration data gathered by means of accelerated load testing (ALT) on various forms of binder seal and stone aggregate over separate test pavements was used to estimate relative performance factors for cumulative rutting and roughness deterioration under these surface treatments. The ALT experiments were under controlled environmental conditions that were either continuously wet or continuously dry to allow modification of these relative performance factors for other environmental conditions. These relative performance factors have been applied to the observed deterioration of given surface treatments to develop road network deterioration (RD) models that allow prediction of the influence of various surface treatments on pavement deterioration. This paper demonstrates that when the relative performance factors are applied to the observed pavement deterioration under a given surface treatment to predict pavement deterioration under other forms of surface treatment, selection of a surface treatment option with the lowest pavement life-cycle cost is possible for a given traffic load and environmental condition.

INTRODUCTION

Australia's sealed road network is comprised of around 85% of sprayed unbound granular pavements (Oliver 1999). Figure 1 details the three main types of sprayed seal which are designated as follows: (i) single seal; (ii) double seal; and, (iii) geotextile seal. Provided these seals are kept from surface cracking, the unbound granular pavements can withstand heavy traffic loads if they are well constructed, designed and maintained.

Experimental work using accelerated load testing (ALT) was untaken to quantify the influence of the above surface maintenance treatments on pavement deterioration (Martin et al. 2000, Martin et al. 2001). This experimental work covered 12 separate

test pavements with different surface treatments and testing conditions. A total of 46 data points were collected. This quantification was in the form of a relative performance factor for maintenance effects, rpf_m, which was based on the deterioration of a sprayed seal relative to that of a single seal under ALT conditions.

Separate ALT experiments were also undertaken for increases in axle load to quantify the increases in distress on sealed unbound granular pavements (Yeo and Koh 2003). Again this quantification was in the form of a relative performance factor for load effects, rpf_l.

This paper will compare, on a pavement life-cycle costing basis of road agency costs, and select the lowest life-cycle cost surface treatment from the three main types of sprayed seal under the following three maintenance scenarios all under constant environmental conditions:

1. a seal choice immediately post pavement construction or rehabilitation (zero pavement age) a under constant traffic load
2. a reseal choice after 10 years over an existing single seal to a 10 year old pavement under constant traffic load to a pavement that is 10 years old
3. a reseal choice after 10 years to an existing single seal to a 10 year old pavement under traffic load increase of 25%.

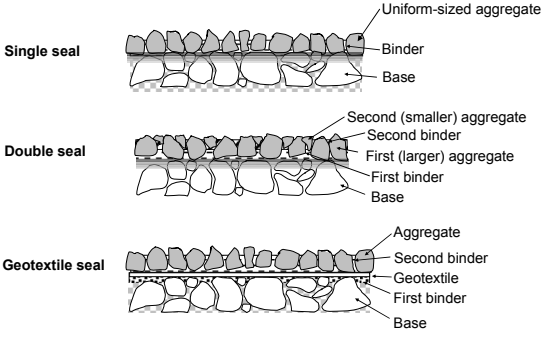

FIG. 1. Three types of sprayed seal

EXPERIMENTAL EVIDENCE FOR MAINTENANCE TREATMENT PERFORMANCE

A relative performance factor for maintenance effects, rpf_m, was defined as follows:

$$\text{relative performance factor } (rpf_m) = \frac{\Delta d_i \text{ (treatment } 'i')}{\Delta d_j \text{ (treatment } 'j')} \quad (1)$$

where;

Δd_i = cumulative distress (rutting and roughness) due to treatment *'i'* measured from the initial densification phase

Δd_j = cumulative distress (rutting and roughness) due to treatment *'j'* measured from the initial densification phase.

Separate relative performance factors were developed both for rutting, rpf_{mrut}, and roughness, rpf_{miri}, using equation (1) by substituting the deterioration relationships developed under the ALT experiments for each surface maintenance treatment. The resulting relative performance factors, rpf_{mrut} and rpf_{miri} are summarised in Table 1 (Martin 2008). For all these treatments in Table 1, the reference treatment '*j*' was an uncracked single seal (unckdss).

The relative performance factor, rpf_m, for treatment '*i*' relative to treatment '*j*' was applied to observed cumulative rutting and roughness deterioration, Δd_j, for the treatment '*j*' to predict the cumulative deterioration, Δd_i, of treatment '*i*' by re-expressing equation (1) as follows:

$$\Delta d_i = rpf_m \times \Delta d_j \quad (2)$$

Table 1. Summary of Estimated Relative Performance Factors for Maintenance Treatments

Treatment ratio	rpf_{mrut}	rpf_{miri}
unckdds[3](d)/unckdss (d)[1]	0.76	0.56
unckdds (w)/unckdss (w)[2]	0.76	0.56
unckdgeo[4](w)/unckdss (w)	0.47	0.48
unckdgeo (d)/unckdss (d)	0.47	0.48

Note:
1. d = dry test condition
2. w = wet test condition
3. unckdds = uncracked double seal
4. unckdgeo = uncracked geotextile seal.

Table 1 indicates that the deterioration of uncracked double seals and geotextile seals relative to uncracked single seals was not influenced by the testing conditions being either wet or dry.

EXPERIMENTAL EVIDENCE FOR INCREASED TRAFFIC LOADING PERFORMANCE

Relative performance factors, defined in a similar way as equation (1) for maintenance effects, were developed both for rutting, rpf_{lrut}, and roughness, rpf_{liri}, under increased wheel loading using deterioration relationships developed from the ALT experimental data. This experimental work covered 10 separate test pavements under varying loading conditions. A total of 64 data points were collected. The relative performance factor for roughness, rpf_{liri}, was found to be as follows (Martin 2008):

$$rpf_{liri} = (LR)^{3.536} \quad (3)$$

where;

LR = load ratio = actual wheel load / reference wheel load.

Where the observed roughness rate is Δd_{iri} under a load ratio of LR and the load ratio is increased, designated as LR^l, the predicted roughness rate, Δd^l_{iri} is given by (Martin 2008) for relatively small increases in wheel load:

$$\Delta d^l_{iri} = \frac{\Delta d_{iri} \times (LR^l)^{3.536}}{(LR)^{3.536}} \quad (4)$$

ANALYSIS OF MAINTENANCE TREATMENT OPTIONS

A pavement life-cycle costing analysis of the three scenarios was conducted using a real discount rate of 5% over two different analysis periods: 20 years and 50 years based on roughness deterioration. Using a typical observed roughness deterioration rate of 0.08 International Roughness Index units (IRI, m/km) per year for an unbound granular pavement with a single seal, the deterioration rate was reduced by 0.56 if a double seal was chosen and 0.48 if a geotextile seal was chosen (see Table 1) under all three scenarios. The typical cost of a single seal in Australian dollars (AUD) was 12,250/lane-km (year 2000), while the cost of a double seal was 1.75 times the cost of a single seal and the cost of a geotextile seal was 2.0 times the cost of a single seal (Holtrop 2000).

Using the observed roughness deterioration rate of 0.08 IRI per year, the predicted increased roughness deterioration was estimated to be 0.176 IRI per year based on equation (4) when the existing load ratio, LR, of 1.132 was increased 25% to 1.415, this being a 25% increase in traffic load under scenario (3).

Over the life-cycle analysis period the pavement roughness was limited to a maximum acceptable value of 4.2 IRI and reduced by rehabilitation to reduce the roughness to a lower value. The following relationship based on road agency before and after roughness measurements of sealed unbound granular sealed overlays was used (Austroads 2007):

$$IRI_a = 1.46 + 0.119 \times IRI_b \quad (5)$$

where;

IRI_a = roughness (IRI) after the sealed unbound granular overlay
IRI_b = roughness (IRI) before the sealed unbound granular overlay.

The notional cost of this rehabilitation was AUD 175,000/lane-km (year 2000). Resealing of the unbound granular pavement was assumed to occur every 10 years as this is a typical life of a seal (Oliver 1999). The road agency costs over the analysis periods of 20 years and 50 years were reduced to a present value (PV) and equivalent uniform annual cost (EUAV) (Haas et al. 1994). Figures 2(a), 2(b) and 2(c) show the predicted pavement performance for the three maintenance scenarios.

Figure 2(a) for scenario (1) shows that rehabilitation was needed for a pavement with a single seal choice to maintain the roughness below the acceptable value of 4.2 IRI. However, a pavement with either the double seal or the geotextile seal, due to lower rates of deterioration, was not rehabilitated during the analysis period.

Figure 2(b) for scenario (2) shows that during the analysis period, rehabilitation was eventually needed for a pavement sealed with any of the three seal options, although the geotextile seal deferred rehabilitation the longest.

Figure 2(c) for scenario (3) under increased traffic load with increased roughness deterioration shows that a higher number of rehabilitations occur on a pavement with a single seal relative to the other seal choices.

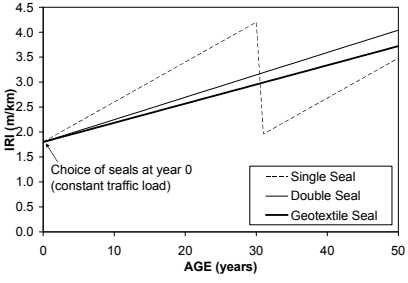

FIG. 2(a). Choice of seal at year 0 (constant traffic)

FIG. 2(b). Choice of reseal at year 10 (constant traffic)

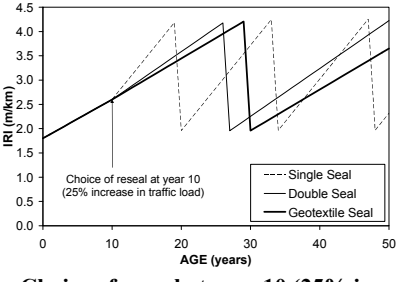

FIG. 2(c). Choice of reseal at year 10 (25% increase in traffic)

RESULTS OF ANALYSIS

Table 2 summarises the pavement life-cycle cost analysis outcomes for the three maintenance scenarios.

Table 2 shows, under the maintenance scenario (1) of constant traffic, that the double seal had the lowest PV and EUAC over the 50 year analysis period. However, when the analysis period was reduced to 20 years, the single seal was found to have the lowest PV and EUAC. This was because the 20 year analysis did not include the rehabilitation required for the single seal in year 30.

Table 2 shows, under the maintenance scenario (2) of constant traffic with a reseal option at year 10, that the geotextile seal had the lowest PV and EUAC over the 50 year analysis period. However, when the analysis period was reduced to 20 years, again the single seal was found to have the lowest PV and EUAC. Again this was

because the 20 year analysis did not include the rehabilitation required for the single and double seals in years 30 and 46, respectively.

Table 2 shows, under the maintenance scenario (3) of increased traffic with a reseal option at year 10, that the geotextile seal had the lowest PV and EUAC over the 50 year analysis period. However, this time when the analysis period was reduced to 20 years, the double seal was found to have the lowest PV and EUAC. The double seal had the lowest PV and EUAC over the 20 year analysis because the single seal required rehabilitation in year 20 with the increased traffic load. The impact of increased deterioration with the increased traffic load influenced the choice of a more costly reseal that had reduced deterioration compared to that of a single seal. This reseal selection did not consider the potential loss of surface stone under increased traffic load which would make the selection of a more costly reseal more compelling.

Table 2. Summary of Life-Cycle Costs of Surface Maintenance Treatments

Maintenance Scenario	PV ($)		EUAC ($)	
	50 yr.	**20 yr.**	**50 yr.**	**20 yr.**
1. Reseal Choice at Year 0 (constant traffic)				
- single seal (ss)	67,687	**24,387**	3,708	**1,957**
- double seal (ds)	**52,554**	42,679	**2,879**	3,425
- geotextile seal (geo)	60,060	48,775	3,290	3,914
2. Reseal Choice at Year 10 (constant traffic)				
- single seal (ss)	67,687	**24,387**	3,708	**1,957**
- double seal (ds)	60,046	33,491	3,289	2,687
- geotextile seal (geo)	**47,810**	36,525	**2,619**	2,931
3. Reseal Choice at Year 10 (25% traffic increase)				
- single seal (ss)	146,147	89,024	8,006	7,143
- double seal (ds)	104,241	**33,490**	5,710	**2,687**
- geotextile seal (geo)	**84,938**	36,524	**4,653**	2,931

CONCLUSIONS

Experimental evidence has quantified that more costly surface maintenance treatments on sealed unbound granular pavements can reduce the expected deterioration of these pavements. In practice under increased traffic load it is highly likely that the lowest life-cycle cost of existing pavements will occur when the more costly surface maintenance treatments are used.

The pavement life-cycle costing analysis period can have a significant bearing upon the surface maintenance treatment option selected. This is particularly the case when highly costly rehabilitation works are not included in the analysis period as these works can have a significant impact of the resulting PV and EUAC, particularly when the real discount rate is relatively low, which is appropriate for road infrastructure.

ACKNOWLEDGEMENTS

The author acknowledges the support received from Prof. William Young of Monash University, Dr John McLean, independent consultant, and Mr Thorolf Thoresen of the ARRB Group.

REFERENCES

Austroads. (2007). "Interim Works Effects Models." prepared by T. Martin, AP-R 300/07, Austroads, Sydney, Australia.

Haas, R., Hudson, W.R. and Zaniewski, J. (1994). "Modern Pavement Management." Krieger Publishing Co., Malabar, Florida, USA.

Holtrop, W. (2000). Personal communication, Australian Asphalt Pavement Association (AAPA), Kew, Victoria, Australia.

Martin, T.C. (2008). "Predicting sealed granular pavement deterioration at a road network level." PhD Thesis, Civil Engineering Department, Monash University, Clayton, Victoria, Australia.

Martin, T., Gleeson, B., Johnson-Clarke, J., Tredrea, P. and Fossey, D. (2000). "The effect of maintenance on pavement performance: the accelerated load testing in 1999/2000." ARRB TR Contract Report, RC90264, ARRB TR, Vermont South, Victoria, Australia.

Martin, T., Gleeson, B., Johnson-Clarke, J., Tredrea, P., Luke, R. and Fossey, D. (2001). "The effect of maintenance on pavement performance: accelerated load testing in 2000/2001." ARRB TR Contract Report RC1739, ARRB TR, Vermont South, Victoria, Australia.

Oliver, J. (1999). "The performance of sprayed seals, ARRB TR Report." ARR 326, ARRB TR, Vermont South, Victoria, Australia.

Yeo, R. and Koh, S.L. (2003). "Impact of new heavy vehicles on pavements and surfacings – report on load equivalence using ALF." ARRB TR Contract Report for Austroads Project T+E.P.N.504, Vermont South, Victoria, Australia.

Effect of Traffic Data Coverage on the M-E PDG Traffic Characterization

Joel T. Brown[1], Syed Waqar Haider[2], Ph.D., P.E. Neeraj Buch[3], Ph.D. and Karim Chatti[4], Ph.D.

[1] Graduate Research Assistant, Department of Civil and Environmental Engineering, Michigan State University, 3546 Engineering Building, East Lansing, MI-48824, e-mail: brown121@msu.edu
[2] Assistant Professor, Department of Civil and Environmental Engineering, Michigan State University, 3546 Engineering Building, East Lansing, MI-48824; Tel: (517) 432-7798; Fax: (517) 432-1827, e-mail: syedwaqa@egr.msu.edu
[3] Professor, Department of Civil and Environmental Engineering, Michigan State University, e-mail: baladi@egr.msu.edu
[4] Professor, Department of Civil and Environmental Engineering, Michigan State University, e-mail: chatti@egr.msu.edu

ABSTRACT: The Mechanistic-Empirical Pavement Design Guide (M-E PDG) requires detailed traffic data to characterize the axle loads and their repetitions, and subsequently predict pavement performance. For level 1, the M-E PDG requires, at 95% confidence level, 84 days of coverage for traffic data i.e., one week per month (OWPM). The data coverage can produce 1 to 2% errors in axle load and truck traffic distributions, as well as 5 to 10% error in AADTT values. In preliminary analyses of five WIM sites in Michigan, it was found that OWPM data produced significant variation in monthly distribution factors and AADTT, especially for sites with AADTT less than 1000 vehicles. Subsequent M-E PDG analyses using OWPM versus continuous traffic data yielded significant variation in predicted pavement performance. Therefore, the objective of this paper is to investigate whether using OWPM WIM data is equivalent to continuous WIM data when determining traffic characteristics—truck traffic classification (TTC), axle load distribution, monthly distribution factors (MDFs), hourly distribution factors (HDFs), axle groups per vehicle (AGPV) and AADTT. To accomplish the study objective, traffic characterizations from one week and continuous data coverage from 34 WIM sites in Michigan were obtained and compared in order to provide confidence intervals in terms of traffic characterization and pavement performance differences between OWPM and continuous data.

INTRODUCTION

An investigation was initiated to establish if using one week of data coverage for each month out of the year (OWPM) is reliable enough for use in the ME-PDG as compared to using continuous data for the entire year. This satellite investigation is part of a larger project with the Michigan Department of Transportation (MDOT) that involves the

determination of baseline traffic characteristics in the state of Michigan for the M-E PDG. The six traffic characteristics included in the investigation are: average annual daily truck traffic, (AADTT), axle groups per vehicle (AGPV), monthly distribution factors, (MDFs), hourly distribution factors (HDFs), truck traffic classification (TTC), and axle load spectra (ALS).

The TrafLoad software (NCHRP Project 1-39 2005), which was used in the conversion of the raw WIM data to actual traffic characterizations suggested that OWPM data is acceptable for level 1 site specific data (highest available for a given site). The traffic data was extracted from the first week of each month from November 2005 to October 2007. Further investigation of five selected sites comparing continuous data (all available days) and OWPM data suggested that use of continuous data may be warranted. Subsequent provision of continuous data coverage for 2 years for all sites by the MDOT has allowed for a more extensive examination into the differences between OWPM and continuous data.

The differences between OWPM and continuous data coverage were assessed in two ways; (a) first, the comparison was made between the numerical differences in the traffic input values yielded by OWPM and continuous data, (b) second, the differences between one-week and continuous data inputs was assessed through an evaluation of predicted performance life of rigid pavements in the M-E PDG (NCHRP 1-37A 2004). There were several traffic characteristics that yielded a distribution of values rather than a single variable—ALS, MDFs and HDFs. It was desirable to ascertain a single value that would capture the difference in the distributions and provide a practical and relatable quantity to draw conclusions. This method was preferred over performing statistical analysis for comparing different distributions through tests like the Kolmogorov-Smirnov (K-S). The use of a single value allows for easy application of statistics on the difference between OWPM and continuous data. For the latter case, a base design was used and PCC slab thicknesses were determined through AASHTO design methods and ESAL calculations. The M-E PDG runs were executed for continuous and OWPM data from each site. The predicted performance life based on the limiting distress, percent slabs cracked, was recorded for both OWPM and continuous data. It should be noted that all other inputs (e.g., layer thicknesses, materials, and environmental variables) were held constant so as to attribute any difference in performance life solely to the differences in inputted traffic parameters based on the data coverage.

The following sections outline the procedures for assessing the difference between OWPM and continuous data both from a traffic characterization and the M-E PDG predicted pavement performance standpoints.

BACKGROUND AND LITERATURE REVIEW

A literature review was performed in order to provide more insight into the reliability of traffic data based on the coverage. A study with the objective of characterizing truck traffic in California concluded that WIM stations showed little differences between

weeks in the same month (Lu and Harvey 2006). The TrafLoad program accepts as a minimum OWPM of data for all 12 months in order for a site specific inputs at Level 1A (NCHRP Project 1-39 2005). The same study revealed that utilizing continuous 7-day data produced mean absolute percent errors of 10.1% and 9.9% for factored and un-factored ESAL counts, respectively, when compared to "annual" (8 months of continuous data) estimates. Chapter 4 of the M-E PDG manual specifies confidence intervals and associated error in prediction of axle load distribution, truck traffic distribution and AADTT for a given amount of traffic collection days based on LTPP data. Utilizing 12 weeks at 7 days per week yields a total of 84 collection days for a given year. The manual states that at a 95% confidence level, 84 days of collection will produce a 1-2% error in axle load distribution, 1-2% error in truck traffic distribution, and a 5-10% error in AADTT (NCHRP 1-37A 2004).

A related FHWA study assessed the actual variability in pavement life prediction due to different traffic data coverage (FHWA 2006; Papagiannakis et al. 2006). The study involved analyzing WIM stations, automatic vehicle classification (AVC) and automatic traffic recorder (ATR). Results that are most similar to the one week per 12 months WIM station collection scheme included regional data from AVCs over 1 month per 4 seasons and 1 week per 4 seasons. For the given pavements considered, at a 95% confidence level, the overall range in error from variation in traffic data prediction and difference in flexible performance prediction from continuous data is approximately 38% and 50%, respectively. It should be noted that continuous site specific WIM data was regarded as the "true" measure of truck traffic and performance prediction (FHWA 2006; Papagiannakis et al. 2006). Little research on the influence the traffic data collection coverage on rigid pavement performance was found. The Traffic Monitoring Guide (FHWA 2001) recommends that for any truck weight road group (TWRG) formed, at least one continuous WIM station should be incorporated to provide the most accurate truck traffic factors. Most analyses on the subject of evaluating the effect of traffic sampling recognizes continuous site specific WIM data as the actual truck traffic pattern of the site and should be used whenever possible.

METHODOLOGY

Continuous weight and classification data from thirty four WIM stations were extracted from the MDOT database for the period of November 2005 to October 2007. Data from the first week of each month was taken as a subset of the continuous data to serve as the OWPM data. It was assumed that a small difference exists between weeks within a month. The TrafLoad software was then used to process the raw weight and classification data from the WIM stations into the traffic characterizations needed as inputs in the M-E PDG. Upon processing, the numerical differences between the two data sets, in terms of traffic characterizations and predicted pavement performance, could be established.

Traffic Characterization Comparison

As previously mentioned, it was highly desirable to create a single value which

captured the difference between the two data sets (week vs. continuous) for statistical analyses of the data. Due to the nature of the traffic characterizations varying from a single unit value (AADTT) to a full distribution such as axle load spectra, the creation of a single unit value(s) was different for each traffic characterization. As a result, it is necessary to review the process for creation of a single value for each traffic characteristic. To avoid repetition, the variables used in the equations to follow are summarized below:

d = difference value
c = continuous data
w = OWPM data
i = VC or VC grouping
j = Month/hour/axle Type
k = Axle load category

Average Annual Daily Truck Traffic (AADTT)

As AADTT is a single variable itself, the difference in AADTT was measured as the difference between continuous AADTT and OWPM AADTT. It should be noted that these AADTT values are for a single design lane direction and not two-way totals. For statistical purposes, it is necessary to normalize these "raw" AADTT value differences into percentages as the physical magnitude of the difference for a given site would misconstrue the data. Equation 1 shows the relative difference in AADTT:

$$AADTT\%_d = \frac{AADTT_c - AADTT_w}{AADTT_c} \times 100 \quad (1)$$

Truck Traffic Classification (TTC)

In preliminary analyses of the data, it was found that the traffic stream was largely dominated by Vehicle Class (VC) 5 and VC9 and, to a lesser extent by VC13 trucks. Rather than comparing all 10 vehicle classes, it was decided to compare the distribution between single unit trailers (VC 4-7), tractor trailer combinations (VC8-10) and multi trailer combinations (VC11-13). Grouping in this way allowed more dominant truck classes to be separated, and minimized the differences that would be seen in VC that are rarely present in the traffic stream. The creation of the single value for TTC for each grouping was done by summing the vehicle class percentages from each category and subtracting one week from continuous values as shown in Equation 2. Unlike AADTT, it was not necessary to calculate a relative percentage difference, as TTC percentages were already normalized values.

$$TTC_{di} = \sum TTC_{ci} - \sum TTC_{wi} \quad (2)$$

Monthly Distribution factor (MDF)

The default MDFs created by TrafLoad were separated into the same groupings as mentioned in the case of TTC. For each truck grouping of single unit trailers (VC 4-7), tractor trailer combinations (VC8-10) and multi trailer combinations (VC11-13), there were 12 factors corresponding to each month of the year. As an alternative, rather than having 36 values for each site, an average difference in MDFs between one week and continuous data across the 12 months was taken for each truck grouping as

demonstrated by Equation 3. It is important to note that the absolute value of the difference had to be taken since the MDFs must always sum to 12, and thus it follows that the average difference (or sum of differences) will always be zero. The result of this computation yields a single average positive difference for each truck grouping. Since MDFs are normalized values, there was again no need to establish a percentage difference.

$$MDF_{di} = \frac{\sum_{j=1}^{12} \left| MDF_{cij} - MDF_{wij} \right|}{12} \tag{3}$$

Hourly Distribution Factor (HDF)

The difference in HDF values was assessed in a similar manner to that of MDFs. Since the HDF must add to 100%, differences found between OWPM and continuous data for each hour of the day would sum to zero. As such, the absolute value of the difference was taken for each hour and averaged to create a single positive value for each site. The calculation can be seen in Equation 4.

$$HDF_{d} = \frac{\sum_{j=0}^{23} \left| HDF_{cj} - HDF_{wj} \right|}{24} \tag{4}$$

Axle Group per Vehicle (AGPV)

The axle group per vehicle is the average number of axle type (e.g., single, tandem etc) per vehicle class. The single value for AGPVs was created through a straight difference between continuous and OWPM data for each axle type and vehicle class. The calculation is shown in Equation 5.

$$AGPV_{dij} = AGPV_{cij} - AGPV_{wij} \tag{5}$$

Axle Load Distributions

Single and tandem axles were chosen to be compared as they are the most prevalent axle types in all vehicle classes (Haider and Harichandran 2007; Lu and Harvey 2006). The VC5, VC9 and VC13 were analyzed only as they were shown to be the most prevalent in the traffic stream in Michigan. To determine the variation in axle load spectra, a single average axle load value for OWPM and continuous data was created by multiplying the proportion in each axle load category (ALP_{kij}) by the loading value of that category (ALV_{kij}) as shown in Equation 6. These individual products were summed to determine the weighted average for both OWPM and continuous axle load spectra. Since TrafLoad produces monthly axle load spectra for each axle, a total of 24 values were available for comparison for each VC. As it has been stated in the literature (Haider and Harichandran 2007), little month to month variation exists in axle load spectra, annual axle load spectra values were utilized by averaging monthly spectra. The numerical difference between OWPM and continuous data was calculated by subtracting the OWPM average axle load value from the continuous average axle load value for each site, as shown in Equation 7. These values were then normalized by calculating percentage difference for the same reasoning as AADTT.

$$AL_{ij} = \sum_{k=1}^{39} ALV_{kij} \times ALP_{kij} \quad (6)$$

$$AL\%_{dij} = \frac{AL_{ijc} - AL_{ijw}}{AL_{ijc}} \times 100 \quad (7)$$

M-E PDG Rigid Performance Comparison

A base design was created for a typical rigid pavement to establish differences in pavement performance between OWPM and continuous data inputs. The base design parameters are presented in Table 1. It should be noted that all other input variables were held constant (i.e., the M-E PDG default) for all the runs performed in this analysis.

Table 1. M-E PDG Rigid Base Design for Traffic Comparison

Layer/Detail	Elastic Modulus (psi)	Thickness (in)
JPCP	550 (MOR) 4.2M (EM)	Variable
Crushed Gravel	25000	6
Sand Subbase-A3	15000	13
Clay Roadbed-A6	10000	Semi-Infinite
Joint Spacing	15 ft	
Dowel Bar Diameter	1.25 in (<10in) 1.5in (=>10in)	
Climate	Lansing, MI	

The pavement thickness for each site was established by calculating ESALs for a 20 year design period (using continuous data) and applying AASHTO 1993 design using 95% reliability.

The M-E PDG predicted pavement surface roughness in terms of international roughness index (IRI), percent slabs cracked and faulting. A FHWA study specifies maximum design thresholds for the rigid pavement performance predictors for various design lives (Khazanovich et al. 1998). In a preliminary analysis, 20 year performance predictors proved to be too stringent using 95% reliability in the M-E PDG; failure was occurring in half the design life. As a result, a combination of the M-E PDG default and FHWA (Khazanovich et al. 1998) 30 year thresholds were used as failure criteria. The following thresholds were adopted:

- IRI-173 in/mi (the M-E PDG default)
- Faulting- 0.236 in (FHWA 30 years)
- Percent Slabs Cracked- 15% (FHWA 30 years/M-E PDG default)

The limiting distress in the M-E PDG for the sites analyzed was percent slabs cracked. The software was first run using the AASHTO pavement design thicknesses

and the design life at which the percent slabs cracked reached 15% was recorded. It was desirable to obtain a 20 years design life to represent a practical pavement performance. Consequently, the pavement thicknesses were adjusted in the M-E PDG (if needed) to ensure that the percent slabs cracked threshold was close to 20 years for achieving consistency of performance across designs. The program was then re-run using all OWPM traffic characterizations again and revised pavement design lives were determined for all sites.

RESULTS AND DISCUSSIONS

Statistical Significance of Traffic Characterization Differences

Once numerical differences were calculated and normalized for all inputs, statistical analysis was conducted to summarize data and draw conclusions. The mean, standard deviation, and 95% confidence intervals (CIs) for the normalized differences from each traffic input were calculated. It was assumed that the WIM stations were independent sites and the traffic characterizations created were random independent samples from a normal population. One sample *t*-test and paired *t*-tests for the differences between continuous and OWPM data were performed to determine if the difference was significantly different than zero (*p*-value less than 0.05 for 95% two-tailed test). The *t*-test could not be performed for the MDF and HDF values as the differences were all positive values. The results of the statistical analyses are presented in Table 2.

Table 2. Statistical Analysis Results for Difference in Traffic Characterizations Using OWPM and Continuous Data

	Mean difference	Std. Dev.	Std. Error	CI Min	CI Max	*t*-value	df	Sig. 2 Tailed
AADTT	3.22%	2.46%	0.42%	2.36%	4.08%	7.63	33	0.000
TTC VC4-7	-0.30%	1.21%	0.21%	-0.73%	0.12%	-1.46	33	0.153*
TTC VC8-10	0.36%	1.11%	0.19%	-0.03%	0.75%	1.88	33	0.068*
TTC VC11-13	-0.06%	0.62%	0.11%	-0.27%	0.16%	-0.52	33	0.606*
MDF VC 4-7	0.12	0.07	0.01	0.09	0.15	N/A	N/A	N/A
MDF VC8-10	0.08	0.02	0.00	0.07	0.08	N/A	N/A	N/A
MDF VC11-13	0.16	0.12	0.02	0.11	0.20	N/A	N/A	N/A
HDF	0.07%	0.04%	0.01%	0.05%	0.08%	N/A	N/A	N/A
Single AGPV	0.0112	0.2733	0.0148	-0.0180	0.0404	0.76	339	0.450*
Tandem AGPV	-0.0001	0.0237	0.0013	-0.0033	0.0018	-0.57	339	0.567*
Tridem AGPV	-0.0019	0.0265	0.0026	-0.0070	0.0032	-0.74	104	0.464*
Quad AGPV	0.0047	0.0296	0.0029	-0.0011	0.0104	1.62	104	0.109*
SA VC5	-0.21%	1.82%	0.31%	-0.84%	0.43%	-0.67	33	0.510
TA VC5	0.03%	1.43%	0.25%	-0.47%	0.53%	0.12	33	0.905
SA VC9	-0.07%	0.41%	0.07%	-0.21%	0.07%	-1.02	33	0.314
TA VC9	-0.26%	0.62%	0.11%	-0.48%	-0.05%	-2.50	33	0.018
SA VC13	-0.13%	1.74%	0.30%	-0.74%	0.47%	-0.45	33	0.656
TA VC13	0.44%	1.32%	0.23%	-0.02%	0.90%	1.95	33	0.059

* Indicates Paired t-test

The results in Table 2 show that with the exception of AADTT and tandem axle average load for VC9, the differences between OWPM and continuous traffic

characterizations were not statistically significant. Actual differences in AGPV approached zero. Confidence intervals at 95% for the difference in average axle load values and TTC percentages for all assessed values fell within 1 % of zero. Both traffic characterization differences were within the 1-2% difference specified by the M-E PDG manual. The average AADTT difference is about 3.2% with a CI roughly between 2.3% and 4.1%. The AADTT average difference seems to be lower than the M-E PDG research findings of 5-10%. Besides AADTT, the MDFs seemingly experienced the most variation. Knowing that the default value for MDFs is 1 in the M-E PDG, average magnitude differences between 0.08 (VC 8-10) up to 0.16 (VC 11-13) suggesting possible differences in values of 10% to 20%.

Statistical Significance of M-E PDG Output

The comparison between OWPM and continuous data was established by subtracting OWPM performance life from continuous performance life (in years). This resulted in 34 values for comparison. The mean, standard deviation, and 95% confidence intervals (CIs) for the difference in performance life were calculated and are shown in Table 3. A paired *t*-test was utilized to establish if the difference varied significantly from zero.

Table 3. Statistical Summary of Difference in the M-E PDG Rigid Pavement Performance Life (in yrs) when Using OWPM vs. Continuous Data

	Mean	Std. dev.	Std. error	CI min	CI max	*t*-value	df	Sig.
Performance life	-1.25	1.42	0.24	-1.74	-0.75	-5.11	33	.000

Table 3 reveals that using OWPM data over continuous data produces a significant difference in pavement performance from a statistical perspective. From a practical standpoint, using OWPM data, with 95% confidence level, results in an overprediction of pavement performance ranging from 9 months to 21 months (0.75 to 1.75 years) with a mean value of 15 months (1.25 years). It should be noted that this mean life difference of 15 months represents the difference in performance life between OWPM and continuous data for a given slab thickness based on a threshold of 15% slabs cracked. This also means that the analysis presented in the paper is based on evaluating the difference in performance lives as opposed to difference in pavement thicknesses due to data coverage.

CONCLUSIONS

This paper presents a comparison between usages of OWPM and continuous traffic data as part of a MDOT project investigating traffic characterizations found in the state of Michigan. The analyses compared differences between the actual traffic characterizations produced between the two data sets from 34 WIM stations in the state of Michigan. A difference in the M-E PDG rigid pavement performance was also assessed by using different data coverage scenarios. The following conclusion can be made based on the result of analyses:

1. Paired *t*-tests revealed that with the exception of AADTT and VC9 tandem axle load

differences in traffic characterization values based on OWPM versus continuous, were not statistically different from zero.
2. The 95% confidence interval for TTC and average axle load differences were within 1% of zero, which was comparable to the M-E PDG manual's findings.
3. AADTT percentage difference between the two data sets had a 95% CI of 2.36% to 4.08% which was less than the 5-10% specified in the M-E PDG manual.
4. OWPM and continuous data AGPV and HDF differences are negligible.
5. MDFs showed some variability, having average difference magnitudes of 0.07 to 0.20 across various VC groupings, which translates to possible differences of 10-20%.
6. Use of OWPM instead of continuous data in the M-E PDG rigid pavement analysis led to over prediction of the performance life with a 95% confidence interval between 0.75 to 1.75 years.

While the findings reflect that OWPM data could be used in place of continuous data, it is recommended that continuous data be used whenever available.

REFERENCES

FHWA. (2001). "Traffic Monitoring Guide." FHWA-PL-01-021, <http://www.fhwa.dot.gov/ohim/tmguide/index.htm>.

FHWA. (2006). "LTPP Data Analysis: Optimization of Traffic Data Collection for Specific Pavement Design Applications." TechBrief FHWA-HRT-06-111.

Haider, S. W., and Harichandran, R. S. (2007). "Characterizing Axle Load Spectra by Using Gross Vehicle Weights and Truck Traffic Volumes." *CD ROM, 86th Annual Meeting of Transportation Research Record*.

Khazanovich, L., Darter., M., Bartlett, R., and McPeak., T. (1998). "Common Characteristics of Good and Poorly Performing PCC Pavements." FHWA-RD-97-131, Federal Highway Administration,.

Lu, Q., and Harvey, J. T. (2006). "Characterization of Truck Traffic in California for Mechanistic Empirical Design." *CD ROM 85th Annual Meeting Transportation Research Record*.

NCHRP 1-37A. (2004). "Guide for Mechanistic-Empirical Design of New and Rehabilitated Pavement Structures." *NCHRP Project 1-37A, National Cooperative Highway Research Program*, National Research Council, Washington, D.C.

NCHRP Project 1-39. (2005). "Traffic Data Collection, Analysis, and Forecasting for Mechanistic Pavement Design." *Report 538, National Cooperative Highway Research Program, National Research Council*, Transportation Research Board, Washington, D.C.

Papagiannakis, A., Bracher, M., Li, J., and Jackson, N. (2006). "Sensitivity of NCHRP 1-37A Pavement Design to Traffic Input." *Transportation Research Record: Journal of the Transportation Research Board*, 1945(-1), 49-55.

Study on Pavement Superposition Effects under Multiple Aircraft Tires

Hongduo Zhao[1], Jianming Ling[2] and Zukang Yao[3]

[1]Associate Professor, Key Laboratory of Road and Traffic Engineering of Ministry of Education, Tongji University, Shanghai 200092 China; hdzhao@tongji.edu.cn
[2]Professor, Key Laboratory of Road and Traffic Engineering of Ministry of Education, Tongji University, Shanghai 200092 China; jmling01@yahoo.com.cn
[3]Professor, Key Laboratory of Road and Traffic Engineering of Ministry of Education, Tongji University, Shanghai 200092 China; zkyao@yahoo.cn

ABSTRACT: Superposition effects of runway asphalt pavement under multiple aircraft tires load are discussed in this paper. 30×20×10 m (Full Size Model), 15×20×10 m (1/2 Model) and 15×15×10m (1/4 Model) size models are established on ABAQUS 3D numerical analysis platform. Using those models, asphalt pavement responses under single tire, double tires, single tandem, dual tandem, dual triple, and compound landing gear are studied. Results show that multiple superposition effects are apparent. The pavement surface deflection under full landing gear is larger than any other tire groups; the maximum vertical strain on the top of the sub-grade and the horizontal stress at the bottom of the base appear in 6 tires group for A 380 and rear 8 tires group for B-777; the largest strain or stress can reach 1.15 times of the full landing gear's value. Based on the pavement responses under multiple tires load, the fatigue life of pavement is analyzed. Functions developed by LEDFAA, APSDSR and UC Berkeley are used in the fatigue analysis. The results of flexible and semi-rigid pavements show that the allowed load repetitions of runway asphalt pavement under full landing gear are 20~30% higher than 6 or 4 tires group. Therefore, the full landing gear is recommended to be used in asphalt pavement structure design.

INTRODUCTION

Complex landing gear, such as 2 dual triple configuration of B-777, 2 dual tandem and 2 dual triple configuration of A380, exists popular in New Large Aircraft (NLA). Because of the heavy loads, high tire pressure and close tire distance, the responses of runway asphalt pavement is a combination of all landing gear tires. However, only up to 4 tires can be considered in the traditional airport pavement design method, which is called design aircraft method. For example, if B-747 is selected as the design aircraft, only one dual tandem group can be used in the analysis, and the superposition effects among tire groups are neglected. Furthermore, a new pavement design method should be developed to support the dual triple configuration in B-777 and A380 landing gear.

In order to enhance the accurate of pavement structure design, superposition effects under multiple aircraft tires are studied through ABAQUS 3D numerical analysis.

3D NUMERICAL ANALYSIS MODELS

The width of runway subject to NLA can reach 60 m. The span of NLA landing gear is about 10m. If full size pavement is taken into account in the ABAQUS model, it is a time-consuming work to run the analysis on current PC. In order to satisfy various landing gear configurations, 30×20×10 m (Full Size Model), 15×20×10 m (1/2 Model) and 15×15×10 m (1/4 Model) size model are established on ABAQUS. The C3D8R finite element is selected as the basic element of those models. The size of single element is controlled less than 200 mm at critical positions, such as the elements under the tire. The pavement responses under B-777 obtained from various size 3D models and BISAR elastic layer system are compared. The results show that those 3D models are accurate enough for pavement engineering.

ANALYSIS PARAMETERS

Several civil aircrafts with various landing gear configurations are considered in this paper. Major parameters used in analysis are listed in Table 1. The footprint of a single tire is assumed as a rectangular, and its length width ratio equal 1.452. The contact stress is assumed uniform and as large as the tire inflation pressure.

Table 1. Parameters of Aircraft Main Landing Gear

No.	Aircraft Group	Single Tire Load (kN)	Tire Pressure (MPa)	Landing Gear Configuration	Total Tires	Size of Single Tire (mm)	
						Width	Length
1	A320-200	175.63	1.441	Double tires	4	290	421
2	A330-300	272.58	1.448	Dual tandem	8	360	523
3	B-777-300ER	265.27	1.524	Dual triple	12	346	503
4	B-747-400ER	236.64	1.586	Compound	16	321	465
5	A380-800	260.95	1.500	Compound	20	346	503

Four types of runway asphalt pavement are considered in the analysis, such as flexible conventional (FC), flexible stabilized (FS), full depth (FD), and semi rigid (SR) structure. Parameters of pavement structures and materials are listed in Table 2**.**

Table 2. Parameters of Pavement Structures and Materials

Layer	Layer Thickness (mm)/ Modulus of Resilience (MPa)			
	FC	FS	FD	SR
AC Surface	150/1800	50/1800	5/1800	160/1800
Base	400/400	400/800	600/800	200/2000
Subbase	400/300	300/300	--	300/1500
Bedding Course	--	--	--	200/200

GEAR GROUPS

In order to explore the superposition effects of pavement responses under multiple aircraft tires, compound landing gear is divided into different tire groups. The responses of asphalt pavement under each tire group are studied. The tire groups of B-747 and A380 are shown in FIG. 1 and FIG. 2.

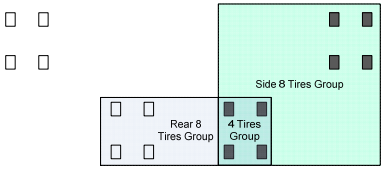

FIG. 1. Tire groups of B-747

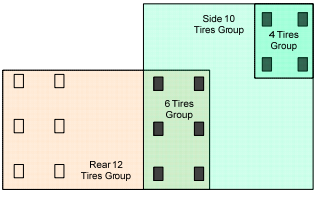

FIG. 2. Tire groups of A380

SUPERPOSITION EFFECTS

Superposition Effects of Pavement Responses

Using the 3D numerical models, runway asphalt pavement responses under single tire, various tire groups and full landing gear are explored. The ratios of maximum responses under full landing gear divided by maximum responses under single tire are listed in Table 3. It can be concluded that the pavement responses difference between full landing gear and single tire are significant. The level of the superposition effects are increased with the pavement stiffness. The superposition effects of surface deflection and vertical strain on the top of the sub-grade are greater than the stress and strain at the bottom of the pavement layers.

Table 3. Ratios of Maximum Responses under Full Gears and Single Tire

Pavement Structure		FS			SR		
Aircraft		A320	A330	B-777	A320	A330	B-777
Surface Deflection		1.637	2.134	3.040	1.800	2.615	3.696
Horizontal Strain at Layer Bottom	Transversal	0.912	1.209	1.209	1.041	1.702	1.702
	Longitudinal	1.295	0.970	0.970	1.573	1.306	1.306
Horizontal Stress at Layer Bottom	Transversal	0.980	1.158	1.158	1.120	1.636	1.636
	Longitudinal	1.243	0.990	0.990	1.481	1.361	1.361
Vertical Strain on Top of Sub-grade		1.444	1.401	1.845	1.600	1.720	2.413

Note: For FS, layer bottom is the bottom of base; for SR , layer bottom is the bottom of subbase

The superposition effects become more complex with compound landing gear. Pavement responses under different tire groups of A380 and B-747 are listed in Table 4 and Table 5. As the results, the superposition effects are obvious. The surface deflection under full landing gear is larger than any other tire groups. The maximum vertical strain on the top of the sub-grade and the horizontal stress at the bottom of the base appears in

6 tires group for A 380 and rear 8 tires group for B-777. The largest strain or stress can reach 1.15 times of the value of full landing gear. Those superposition effects will affect the results of pavement structure design.

Table 4. Maximum Responses under Tire Groups of A380 (FS)

Tire Group	Surface Deflection (0.01mm)	Vertical Strain on Top of Sub-grade (με)	Horizontal Strain at the Bottom of Base (με)		Horizontal Stress at the Bottom of Base (MPa)	
			X*	Y	X	Y
Single	279.81	1196.51	373.1	342.9	0.331	0.313
4 Tires	600.24	1787.29	392.4	392.6	0.345	0.327
6 Tires	762.41	1966.95	427.5	321.9	0.359	0.293
Side 10 Tires	863.38	1947.56	419.4	370.8	0.349	0.321
Rear 12 Tires	884.5	1927.88	409.1	330.5	0.344	0.292
Full 20 Tires	933.32	1902.75	399.1	371.3	0.331	0.32

*Note: X is the direction of Transversal; Y is the direction of Longitudinal

Table 5. Maximum Responses under Tire Groups of B-747 (SR)

Tire Group	Surface Deflection (0.01mm)	Vertical Strain on Top of Sub-grade(με)	Horizontal Stress at the Bottom of Subbase (MPa)	
			Transversal	Transversal
Single	171.2	635.31	0.383	0.374
4 Tires	460.08	1380.35	0.559	0.541
Rear 8 Tires	616.01	1442.61	0.473	0.595
Side 8 Tires	577.92	1393.85	0.538	0.539
Full 16 Tires	703.96	1433.77	0.516	0.592

Superposition Effects of Load Repetitions

In pavement design, airport engineer pays more attention to allowed load repetitions (fatigue life) of pavement than pavement responses themselves. The allowed load repetitions of pavement are various, when they are calculated based on different failure mode. Typical pavement performance functions are used in this paper (see Table 6), which are developed by different institutes and used widely in pavement engineering.

Table 6. Performance Function used in Load Repetitions Analysis

Failure mode	Performance Function	Developed by
Failure of base (Crack)	$\log N_f = 16.086 - 3.29 \times \log \varepsilon_t - 0.854 \times \log S_{mix}$	Berkeley
	$\log N_f = 2.68 - 5 \times \log \varepsilon_H - 2.665 \times \log E_A$	LEDFAA
	$\frac{\sigma_t}{f_r} = 0.972 - 0.0825 \log N_f$	Demnsey
Failure of sub-grade (Rut)	$\varepsilon_z = 0.004276 N_f^{-0.1507}$	APSDS
	$N_f = 10,000 \times \left(\frac{0.000247 + 0.000245 \times \log E_{SG}}{\varepsilon_V} \right)^{0.0658 \times E_{SG}^{0.559}}$	LEDFAA

Using the performance functions listed in Table 6 and corresponding pavement

responses, allowed load repetitions of asphalt pavement under different gear groups are analyzed. Results of A380 are listed in Table 7; results of B-747 are listed in Table 8. The maximum pavement responses are produced by 6 tires group for A380, so the allowed load repetitions is minimal. For A380, when the failure mode is the crack, the allowed load repetitions under full landing gear are about 20~30% more than under 6 tires group; when the failure mode is the rut, the allowed load repetitions under full landing gear are about 20% more than under 6 tires group. For B-747, the maximum pavement responses are produced by full landing gear (16 tires). In the FS pavement, the allowed load repetitions under full landing gear are about 5~10% less than 4 tires group. However, in the SR pavement, the allowed load repetitions under full landing gear are about 40% less than 4 tires group.

Table 7. Allowed Load Repetitions under Different Gear Groups of A380

Pavement Structure	**FS**				**SR**
Failure Mode	Failure of base (Crack)		Failure of sub-grade (Rut)		Fatigue of base
Function	Berkeley	LEDFAA	APSDS	LEDFAA	Demnsey
Single	722739	2107653	4677	7020	6135907
4 Tires	611179	1633706	326	404	172331
6 Tires	461794	1067198	173	204	23101
Side 10 Tires	491800	1174311	185	219	40370
Rear 12 Tires	533738	1329775	197	236	162975
Full 20 Tires	579027	1504932	215	259	215443

Table 8. Allowed Load Repetitions under Different Gear Groups of B-747

Pavement Structure	**FS**				**SR**
Failure Mode	Failure of base (Crack)		Failure of sub-grade (Rut)		Failure of base
Function	Berkeley	LEDFAA	APSDS	LEDFAA	Demnsey
Single	855208	2721725	7983	12455	13784593
4 Tires	614263	1646247	205	245	101405
6 Tires	611179	1633706	198	236	37128
Rear 8 Tires	642407	1762198	221	266	177209
Side 8 Tires	610667	1631627	227	273	40370
Full 16 Tires	855208	2721725	7983	12455	13784593

According to the results of superposition effects obtained from above analysis, the full landing gear of aircraft is recommended to be used in asphalt pavement structure design.

CONCLUSIONS

In this paper, superposition effects of New Large Aircrafts, such as B-747, B-777 and A380 are studied using ABAQUS. The results can be concluded as follows:

1. 30×20×10 m, 15×20×10 m and 15×15×10m size models are established on ABAQUS, which are accurate enough for pavement engineering application.
2. Using 3D models, asphalt pavement responses under single tire, double tires, single tandem, dual tandem, dual triple and compound landing gear are studied. The results

show that multiple superposition effects are apparent. The pavement surface deflection under full landing gear is larger than any other tire groups; the maximum vertical strain on the top of the sub-grade and the horizontal stress at the bottom of the base appear in 6 tires group for A 380 and rear 8 tires group for B-777; the largest strain or stress can reach 1.15 times of the full landing gear's value.

3. Based on the responses under various tire groups and typical performance functions, which are developed by LEDFAA, APSDSR and UC Berkeley, the allowed load repetitions of pavement are analyzed. For A380, the allowed load repetitions of runway asphalt pavement under full landing gear are 20~30% higher than 6 or 4 tires group. However for B-747, the full landing gear produces the minimum allowed load repetitions.
4. The full landing gear is recommended in runway asphalt pavement design.

ACKNOWLEDGEMENT

This paper is supported by the Chinese National Natural Science Foundation project: Research on Airport Asphalt Pavement Design Theory and Indexes based on Spatial Response Analysis (No. 60776818).

REFERENCES

Zhao, H. (2006). "New generation large aircraft oriented load analysis method and parameters for asphalt pavement design." *A dissertation submitted to Tongji University in conformity with the requirements for the degree of Doctor of Philosophy.*

Yao, Z. (2003). "Asphalt pavement design index system." *Research report of Tongji University*.

Monismith, C.L., Finn, F.N., Ahlborn, G. and Markevich, N. (1987). "A general analytically based approach to the design of asphalt concrete pavements." *Proceedings, 6th International Conference on the Structural Design of Asphalt Pavements,* University of Michigan and Delft University: 345-365.

Gopalakrishnan, K. and Thompson, M. R (2006). "Assessing Damage to Airport Pavement Structure due to Complex Gear Loads". *Journal of Transportation Engineering, ASCE, Vol. 132(11)*: 888-897.

Wardle, L., Rodway, B. and Rickards, I. (2001). "Calibration of advanced flexible aircraft pavement design method to S77-1 method. " *Advancing Airfield Pavements, American Society of Civil Engineers*, 2001 Airfield Pavement Specialty Conference, Chicago, Illinois : 192-201.

U.S. Department of Transportation, Federal Aviation Administration (1995). "Airport Pavement Design for the Boeing 777 Airplane, AC No: 150/5320-16." *U.S. Department of Transportation,* Federal Aviation Administration.

Analysis of Loading Stresses in Asphalt Overlay on Existing Concrete Pavements Based upon a Simplified Three-dimensional Model

Yumin Zhou[1], Zhiming Tan[2]

[1]Key Laboratory of Road and Traffic Engineering at Tongji University, Ministry of Education, Shanghai, 201804, PRC. [1] Lecturer, Ph.D, pavement engineering, E-mail: zhouym69@163.com. [2] Professor, Ph.D, pavement engineering, E-mail: tanjk@online.sh.cn.

ABSTRACT: A simplified three-dimensional model is established to analyze the responses in asphalt overlay (AC) paved on existing concrete pavements (PCC) slabs under vehicle loads, by using the finite element method, through some examples, the convergence of loading stresses in AC nearby the joint of PCC slabs and interface forces are discussed, the expressions of the nominal maximum tensile stress σ_{1max} in AC are then formulated, and the influences of load position x, structural parameters (E_1, h_1, h_2, k_0, δ), interlayer stiffness and void underneath PCC slabs on the stresses σ_{1max}, τ_{1max} in AC and the internal forces q_{2max}, τ_{2max} are analyzed, in the end, the damage modes of AC on PCC structure are issued based on the strength theory. The study indicated that the sectional internal forces (axial force N and moment M) can be taken as convergence criteria to reasonably determine the model meshing density. The stress σ_{1max} can be calculated upon corresponding sectional internal forces N, M and a stress concentration factor ξ_p; the stresses σ_{1max}, τ_{1max} may reach peak values when the load position x not exceeding ±0.2m; the influences of structural parameters E_1, h_1 on the stresses σ_{1max}, τ_{1max} and the interface forces q_{2max}, τ_{2max} are much significant; eliminating the void underneath PCC slabs will have a disadvantageous effect on the stress σ_{1max} but an active effect on the interface forces q_{2max}, τ_{2max}; a higher joint spring stiffness C_w will considerably reduce the stresses σ_{1max}, τ_{1max} and the interface forces q_{2max}, τ_{2max}; the placing width of soft interlayer over the joint should be 0.3~0.4m; the soft interlayer with higher stiffness will reduce the stress σ_{1max}, but raise the interface force q_{2max}, therefore increase the risk of interface damage.

INTRODUCTION

A commonly adopted rehabilitation measure to existing concrete pavements (PCC) is to pave an asphalt overlay (AC) on it, but the problem is how to prevent so-called reflective crack from appearing on AC nearby the joints of PCC slabs (AASHTO, 2004, China Communication Press, 2002). Study showed that the vehicle load is one of the primary causes of reflective crack in AC. In fact, when a vehicle load just acting on a joint of PCC slabs, a bending stress occurs in AC nearby the joint, whereas moving off

the joint a distance, a higher tensile stress and shearing stress produce, therefore, if the stresses created exceeding the material strength a crack initiates on AC nearby the joint, under repeated vehicle loads the cracks initiated will develop upward through the AC thickness. The history of research on reflective crack caused by vehicle loads is more than 30 years. In 1977, Austin Research Engineers issued a two-dimensional stress (strain) method for analysis of reflective crack based on a static equilibrium approach. By using a finite element program ANSR-I, N. F. Coetzee and C. L. Monismith (1980) obtained the distribution of stresses in AC nearby the joint of PCC slabs with or without a SAMI interlayer, and discussed the influences of some parameters on the stresses (C. L. Monismith and N. F. Coetzee, 1980), Rashid (1982) firstly advocated to use the crack band theory to analyze the problem of reflective crack on AC, and pointed out that the element size should not be less than the summation of several grain diameters (Rashid, 1982). Majidzadeh et al (1985) discussed the methods to eliminate the reflective crack (K.Majidzadeh, et al., 1985). A.A.A. Molenaar et al (1986) analyzed the effects of stress absorbing membrane interlayers in preventing reflective crack (A.A.A. Molenaar, J.C.P. Heerbens, et al., 1986). P. W. Jayawickrama and R. L. Lytton (1987) put forward a set of overlay design equations based on Paris law (P.W. Jayawickrama and R.L. Lytton, 1987). R. L. Lytton (1989) established an overlay design method based on the fracture mechanics theory, and issued a group of calculating formulas of stress intensity factors for I and II types of cracks upon a model of beam on elastic foundation (R. L. Lytton., 1989). By applying 2D and 3D models, Deyun Zhou (1990), Baoming Yu (1991) studied the influences of structural parameters on the stresses in AC (Deyun Zhou, Zukang Yao, 1990; Baoming Yu, 1991). L. Francken and A. Vanelstraete (1992), P. Blankenship et al (2003) discussed the modeling and experimental testing methods of interface systems (L. Francken and A. Vanelstraete, 1992, P. Blankenship, N. Iker and J. Drbohlav, 2003). J. M. Rigo et al (1993) studied the crack propagation in an overlay subjected to vehicle and thermal effects upon a 2D model by using SAPL15 program (J.M. Rigo, et al., 1993). A. H. De Bondt et al (1997), J. B. Sousa et al (2005), Yumin Zhou (2007) issued a mechanistic-empirical based overlay design method for preventing reflective crack (A. H. De Bondt and A. Searpas , 1997; J. B. Sousa, J. C. Pais and G. B. Way, 2005; Yumin Zhou, 2007). Up to date, there still existed some problems on analysis of loading stresses in AC on PCC structure including: (1) selection of convergence criterion and determination of proper meshing density; (2) treatment of arbitrary contact conditions in interface; (3) consideration of local void underneath PCC slabs and joint load transfer capacity etc. In fact, because of the discontinuity of PCC slabs, the application of soft interlayer and the local contact conditions between AC and PCC slabs, the stresses (strains) in AC nearby the joints vary remarkably and sometimes exhibit singularity, however, it is necessary to establish a model of AC on PCC structure and reasonably analyze the influences of all aspects mentioned.

METHODOLOGY

A simplified 3D model of AC on PCC structure

Normally a typical AC on PCC structure consists of many layers, subsequently AC, interlayer (if any), PCC slabs, base, sub-base and sub-grade etc, for simplicity, a three-dimensional model of two-layered structure including AC and PCC slabs is

established, and the following assumptions are employed:

1. Materials for AC and PCC slabs are homogenous and linear elastic;
2. Interface between AC and PCC slabs can be regarded as a special thin interlayer, and simulated using a set of dual linear springs with stiffness in normal and tangential directions;
3. A Winkler foundation can be used to reflect the function of structural layers below PCC slabs;
4. The joint load transfer capacity can be simulated by using a joint shearing spring with stiffness C_w;
5. Void underneath PCC slabs is permitted in the model.

A three-dimensional model of AC on PCC structure is shown in FIG.1, L and B are the length and width of PCC slab respectively, δ is the width of joint.

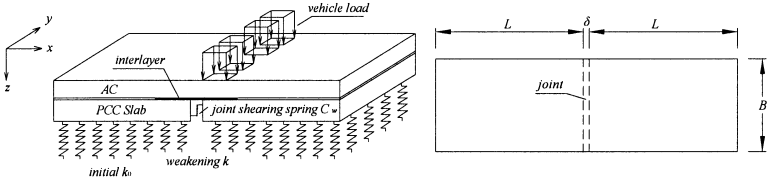

(a) perspective view (b) plane view

FIG.1. 3D model of AC on PCC structure

To reflect the contact conditions of interface between AC and PCC slabs, the interface forces q_2 and τ_2 shall satisfy the following equations (Zienkiewicz O. C., Taylor R. L., 2009):

$$q_2 = \begin{cases} k_{n0}^c \cdot \Delta v & q_2 < 0 \\ k_{n0}^l \cdot \Delta v & q_2 \geq 0 \end{cases}$$
$$\tau_2 = \begin{cases} k_{t0} \cdot \Delta u + c & \Delta u < \Delta u_0 \\ k_{t0} \cdot \Delta u_0 + c & \Delta u \geq \Delta u_0 \end{cases} \quad (1)$$

Where: q_2 is the normal pressure in interface; τ_2 denotes the shearing stress in interface; $k_{n0}{}^c$ is the normal spring stiffness in interface under compression state; $k_{n0}{}^l$ is the normal spring stiffness in interface in tension state; k_{t0} is the tangential spring stiffness in interface; c is the cohesive force in interface; Δv expresses the relative displacement of AC to PCC slabs in normal direction in interface; Δu is the relative displacement of AC to PCC slabs in tangential direction in interface; Δu_0 is the critical relative displacement in tangential direction in interface when sliding occurs.

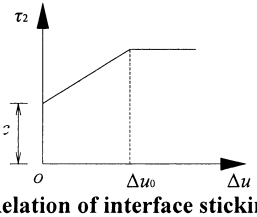

FIG.2. Relation of interface sticking-sliding

The interface sticking-sliding relation is illustrated in FIG.2. In fact, the spring stiffness in interface is not only related to interlayer itself, but also closely in conjunction with the material properties of AC and PCC slab, therefore, taking into account the shear and compression deformation effects of AC and PCC slab, the normal and tangential spring stiffness in interface is then referred to as generalized stiffness k_t and k_n, they are written as:

$$k_{\mathrm{t}}^{-1} = k_{\mathrm{t0}}^{-1} + C_{\mathrm{t}} \sum_{i=1}^{2} 2(1+\mu_i) \frac{h_i}{E_i} \quad , \quad k_{\mathrm{n}}^{-1} = k_{\mathrm{n0}}^{-1} + C_{\mathrm{n}} \sum_{i=1}^{2} \frac{(1+\mu_i)(1-2\mu_i)}{1-\mu_i} \frac{h_i}{E_i} \tag{2}$$

Where: C_{t}, C_{n} stand for the tangential shear effect coefficient and normal compression effect coefficient of AC and PCC slab respectively, C_{t}=1/4, C_{n}=2; μ_{i} is the Poisson's ratio of i layer, i=1 for AC, and 2 for PCC slab.

When the bending and shear deformation effects of interlayer itself are neglected, the tangential and normal spring stiffness k_{t0}, k_{n0} for interlayer can be computed as:

$$k_{\mathrm{t0}} = \frac{1}{2(1+\mu_3)} \frac{E_3}{h_3} \quad , \quad k_{\mathrm{n0}} = \frac{(1-\mu_3)}{(1+\mu_3)(1-2\mu_3)} \frac{E_3}{h_3} \tag{3}$$

Where: h_3 is the thickness of interlayer itself; E_3, μ_3 are the elastic modulus and Poisson's ratio of interlayer respectively.

When the interface between AC and PCC slabs is in fully bonded, the generalized stiffness k_{n} and k_{t} take the maximum values, that is, the spring stiffness k_{t0}, k_{n0} for interlayer itself tends to be infinite, however, the contact conditions of interface may also be represented by relative stiffness factors λ_{t} and λ_{n}:

$$\lambda_{\mathrm{t}} = k_{\mathrm{t}} / k_{\mathrm{tmax}} \quad , \quad \lambda_{\mathrm{n}} = k_{\mathrm{n}} / k_{\mathrm{nmax}} \tag{4}$$

Three typical contact conditions of interface are given below:

λ_{t} =1, $\lambda_{\mathrm{n}}{}^{c}$=1 and $\lambda_{\mathrm{n}}{}^{l}$=1 represents fully bonded contact condition;

λ_{t} =0, λ_{n}=1 and $\lambda_{\mathrm{n}}{}^{l}$=0 is for unbonded contact condition;

0<λ_{t} <1, λ_{n}=0.1~1 and 0<$\lambda_{\mathrm{n}}{}^{l}$<1 is on behalf of semi-bonded contact condition.

When considering the effect of interlayer, only the spring stiffness k_{t0}, $k_{\mathrm{n0}}{}^{\mathrm{c}}$ and $k_{\mathrm{n0}}{}^{l}$ need to be input.

Extensive field investigations showed that the void underneath PCC slabs existed objectively in highways in some areas; the schematic of void underneath PCC slabs is shown in FIG.3 (Yumin Zhou, 2007).

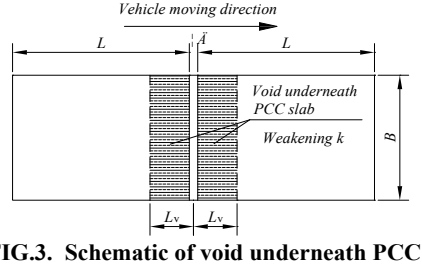

FIG.3. Schematic of void underneath PCC

However, two parameters such as void length L_v and sub-grade weakening index λ_k can be used to reflect the extent of void underneath PCC slabs, the void length L_v is about 0.4~0.8m, and the sub-grade weakening index λ_k is directly defined as:

$$\lambda_k = k / k_0 \tag{5}$$

Where: k_0 is the initial reaction modulus of sub-grade; k represents the reaction modulus of sub-grade while weakening (Yumin Zhou, 2007).

Numerical solution

The general finite element software ANSYS is selected to do the stress analysis of AC on PCC structure due to its powerful functions (ANSYS Inc., 2005).

Element type

As per AC and PCC slabs, the solid45 element is used, for sub-grade the surface154 element is applied to simulate a Winkler foundation support, for interface between AC and PCC slabs, the contact pairs targe170 and conta173 are used to simulate an arbitrary contact condition.

Structural parameters

Taking a typical AC on PCC structure, L=5.0m, B=3.75m, δ=0.01m, assuming the cohesive force c=0, the joint shearing spring stiffness C_w=0, the structural parameters are listed in Tab.1, and the interlayer spring stiffness k_{t0}, k_{n0}^{c}, k_{n0}^{l} are given in Tab.2.

Table 1. Material Properties for Typical AC on PCC Structure

Structure layer	Modulus /MPa	Poisson's Ratio	Thickness /m
AC	1200	0.35	0.10
PCC	30000	0.15	0.22
soft interlayer	20	0.45	0.003
Sub-grade	50 MN/m^3		

Table 2. Interface Parameters

case	Interlayer width	stiffness /(MN/m^3)	segment1	segment2
1	W_1=5m,W_2=0	k_{t0}	6.61e+07	-
		k_{n0}^{c}	8.77e+06	-
		k_{n0}^{l}	8.77e+06	-
2	W_1=4.6m,W_2=0.4m	k_{t0}	6.61e+07	2.30e+09
		k_{n0}^{c}	8.77e+06	2.53e+10
		k_{n0}^{l}	8.77e+06	2.53e+10
3	W_1=4.6m,W_2=0.4m	k_{t0}	6.61e+07	2.30e+09
		k_{n0}^{c}	8.77e+06	2.53e+10
		k_{n0}^{l}	8.77e+06	0

In Tab.2, case1 corresponds to a fully bonded contact condition in interface, case2 matches to a bonded contact condition by placing a soft interlayer over the joint of PCC slabs with a side width W_2=0.4m, and case3 is same as case2 except for the interface force q_2=0 when tension occurring.

A dual-wheel single axle load is applied on the AC on PCC structure, P =100kN, tire-print area A=0.189m×0.189m, and tire-pavement contact pressure p=0.700MPa, the configuration of dual-wheel single axle load is shown in FIG.4, the load position is just on the side of joint (x=(0.189+δ)/2 , see FIG.1).

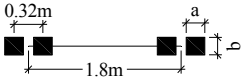

FIG.4. Configuration of a dual-wheel single axle load

Model Meshing

The model meshing of AC on PCC structure is shown in FIG.5. In thickness direction, the AC and PCC slabs are uniformly meshed with n layers and 4 layers respectively; in transverse and longitudinal directions, the model is meshed in a biased manner from 0.025m to 0.4m, nearby the joint of PCC slabs the element size is 0.025m, see FIG.5.

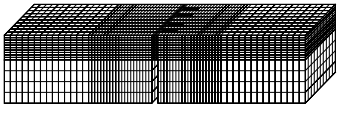

FIG.5. Model meshing of AC on PCC structure

Stress, sectional internal forces and interface forces

At location of the maximum stress σ_{1xmax}, the distribution of σ_{1x} through AC thickness is shown in FIG.6. We can see a remarkable stress concentration in AC.

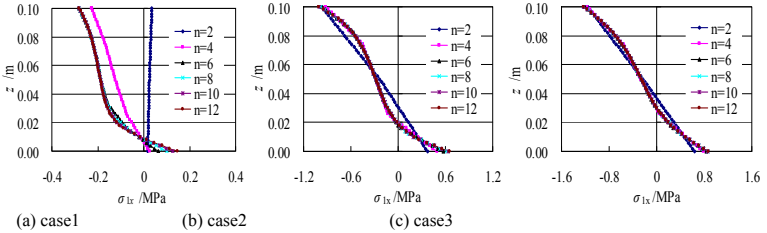

FIG.6. Diagrams of stress σ_{1x} ~ z curves

The sectional internal forces N and M can be calculated as:

$$N_x = \int_0^{h_1} \sigma_{1x}(z)dz, \quad N_y = \int_0^{h_1} \sigma_{1y}(z)dz$$
$$M_y = \int_0^{h_1} \sigma_{1x}(z)(z-0.5h_1)dz, \quad M_x = \int_0^{h_1} \sigma_{1y}(z)(z-0.5h_1)dz \tag{6}$$

The diagrams of ratio α (σ_{1x}, σ_{1y}, σ_{1z}, τ_{1max}, N_x, M_y, q_{2max}, τ_{2max} related to n=2, 4, 6, 8, 10, 12 against that of n=12) vary with n are shown in FIG.7~FIG.9.

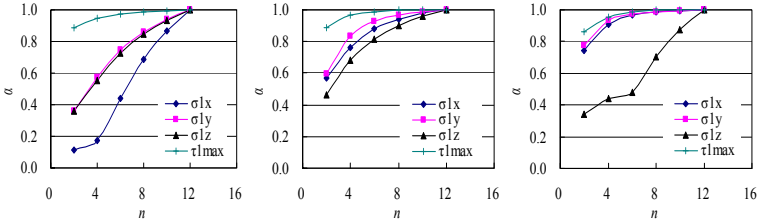

FIG.7. Diagrams of stresses ratio α ~ *n* curves

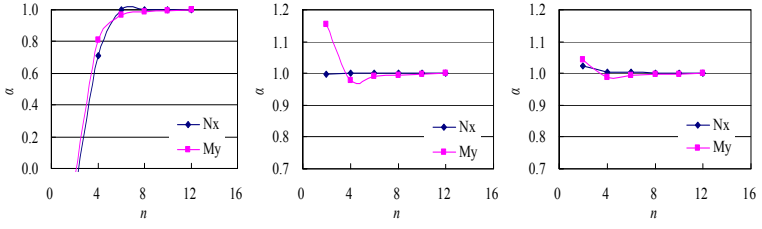

FIG.8. Diagrams of sectional internal forces ratio α ~ *n* curves

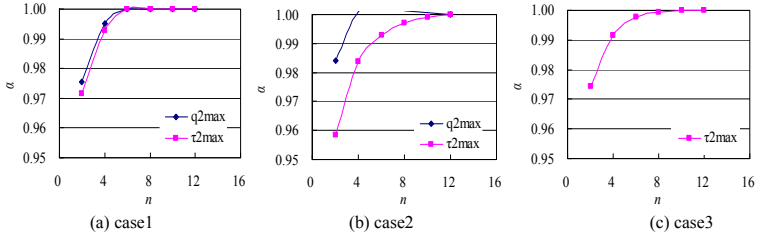

FIG.9. Diagrams of interface forces ratio α ~ *n* curves

From FIG.7 it is seen that most of the stress components in AC near the joint of PCC slabs are difficult to converge when the interface between AC and PCC slabs is fully bonded, if a soft interlayer is placed over the joint, the convergence of stresses in

AC may considerably improve, but some stress components are still not converged, however, it is not appropriate to use a stress index to judge the reasonability of model meshing. From FIG.8 it can be found that the sectional internal forces N_x and M_y are much easy to converge, for all 3 cases, when n=8, the sectional internal forces N_x and M_y are almost identical to that of n=12, therefore, the sectional internal forces N and M may be taken as convergence criteria for the finite element solution. From FIG.9 we can see that with increase of n the interface forces q_{2max}, τ_{2max} also exhibit a well-converged characteristics.

Since maximum shearing stress τ_{1max} in AC and maximum interface forces q_{2max}, τ_{2max} have no convergence problem, we can get more precise results as long as the model meshing is fine enough; regarding the maximum tensile stress σ_{1max} in AC nearby the joint of PCC slabs, due to the convergence problem, our concern is how to get a reasonable value of it upon the finite element results.

EXPRESSION OF LOADING STRESSES IN AC

As discussed above, the loading stresses on the bottom surface of AC nearby the joint of PCC slabs are growing up with increase of the model meshing density, that is to say, the loading stresses in AC nearby the joint are somewhat singularity, and therefore are out of reality. However, a scheme is proposed to deal with the "growing" loading stresses in AC.

In terms of the size of aggregates in AC (1~2cm), we may adopt an averaged method to get the nominal maximum tensile stress σ_{1max} (see FIG.10), as:

$$\sigma_{1\max} = \frac{M_{y(x)} - \int_{h_e}^{h_1} \sigma_{1x(y)}(z)(z - 0.5h_1)dz}{0.5(h_e - h_1)h_e} \tag{7}$$

Where: h_e is the effective size of aggregate in AC for stress averaging.

The schematic of the nominal maximum tensile stress σ_{1max} on the bottom surface of AC nearby the joint of PCC slabs is illustrated in FIG.10.

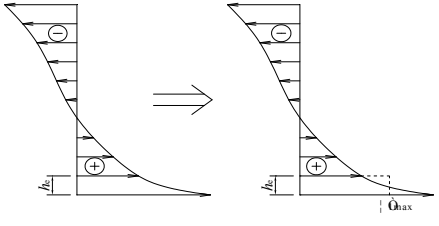

FIG.10. Schematic of the nominal maximum tensile stress σ_{1max}

By using the sectional internal forces N, M, the nominal maximum tensile stress σ_{1max} may also be approximated as:

$$\sigma_{1\max} = \xi_p \left(\frac{N}{h_1} \pm \frac{6M}{h_1^2} \right) \tag{8}$$

Where: ξ_p represents the stress concentration factor of σ_{1max}.

The stress concentration factor ξ_p varies sharply with contact conditions between AC and PCC slabs, for given cases in Tab.2, supposing h_e=1cm, corresponding to case1, ξ_p is not available, case2, ξ_p =1.34, case3, ξ_p =1.09.

SENSITIVITY ANALYSIS

The factors of influencing the stresses σ_{1max}, τ_{1max} in AC and the interface forces q_{2max}, τ_{2max} include the load position x, AC modulus E_1, AC thickness h_1, PCC slab thickness h_2, sub-grade reaction modulus k_0, width of joint δ, void length L_v and sub-grade weakening index λ_k, and the interlayer width W_2, stiffness k_{t0}, k_{n0} etc., in general, the stresses σ_{1max}, τ_{1max} and the interface forces q_{2max}, τ_{2max} are a function of all factors listed above. Supposing the elastic modulus E_2=30000MPa, v_2=0.15, and a group of typical AC on PCC structures are given in Tab.3 for the following analysis.

Table 3. Typical AC on PCC structures

case	x	E_1	v_1	h_1	h_2	k_0	δ	W_2	L_v	λ_k	C_w	k_{t0}	k_{n0}
1	-	1200	0.35	0.10	0.22	50	0.01	0.6	0	1	0	-	-
2	0.1	-	0.35	0.10	0.22	50	0.01	0.4	0	1	0	2.30e9	2.53e10
3	0.1	1200	0.35	-	0.22	50	0.01	0.4	0	1	0	2.30e9	2.53e10
4	0.1	1200	0.35	0.10	-	50	0.01	0.4	0	1	0	2.30e9	2.53e10
5	0.1	1200	0.35	0.10	0.22	-	0.01	0.4	0	1	0	2.30e9	2.53e10
6	0.1	1200	0.35	0.10	0.22	50	-	0.4	0	1	0	2.30e9	2.53e10
7	0.1	1200	0.35	0.10	0.22	50	0.01	0.4	0.8	-	0	2.30e9	2.53e10
8	0.1	1200	0.35	0.10	0.22	50	0.01	0.4	0.8	-	-	2.30e9	2.53e10
9	0.1	1200	0.35	0.10	0.22	50	0.01	-	0	1	0	2.30e9	2.53e10
10	0.1	1200	0.35	0.10	0.22	50	0.01	0.4	0	1	0	-	-

Effect of moving vehicle Load

Assuming that a dual-wheel single axle load P=100kN moving on AC along the longitudinal edge of PCC slabs (see FIG.11). Because the locations of σ_{1max}, τ_{1max}, q_{2max}, τ_{2max} are at a narrow zone nearby the joint and hardly change with the load position x, however, we will mainly discuss their magnitudes varying with x.

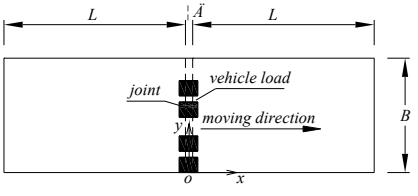

FIG.11. Schematic of vehicle load moving on AC

The parameters are as listed in Tab.3 case1, the diagrams of ratios λ (σ_{1max}, τ_{1max}, q_{2max}, τ_{2max} related to load position x against its relevant peak value) changing with the load position x are shown in FIG.12.

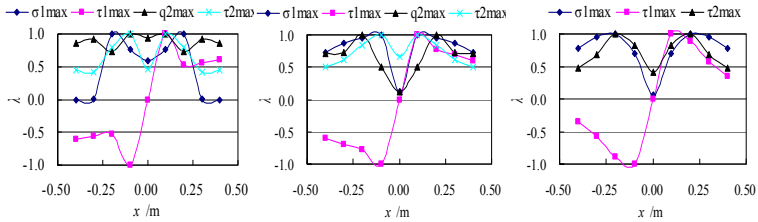

(a) k_{t0}=6.61e13,k_{n0}=8.77e12 (b) k_{t0}=2.30e9,k_{n0}=2.53e10 (c) k_{t0}=2.30e9,k_{n0}=2.53e10_open

FIG.12. Diagrams of ratio λ of σ_{1max}, τ_{1max}, q_{2max}, τ_{2max} ~ x curves

It can be found from FIG.12 that the ratios λ almost reach peak values when the load position is at x=±0.2m or at x=±0.1m, however, it is only necessary to discuss the loading stresses in AC and the interface forces where the vehicle load just acting on x=±0.1m or x=±0.2m.

Elastic modulus E_1

The elastic modulus E_1 for AC is not a constant but a function of environmental temperature, normally it drops while environmental temperature rising, vice versa.

Supposing that the elastic modulus E_1 varies from 400~12000MPa, the other parameters are given in Tab.3 case2, the diagrams of the stress σ_{1max}, τ_{1max}, the sectional internal forces N_x, M_y and the interface forces q_{2max}, τ_{2max} changing with E_1 are shown in FIG.13. It can be found that with increase of the elastic modulus E_1 the stresses σ_{1max}, τ_{1max} rise up, the interface forces q_{2max}, τ_{2max} drop down, whereas the sectional internal force N_x decreases and M_y grows up, obviously under vehicle loads it is disadvantageous for an AC on PCC structure in cold season. With increase of the elastic modulus E_1, the factor ξ_p drops from 1.75 to 1.

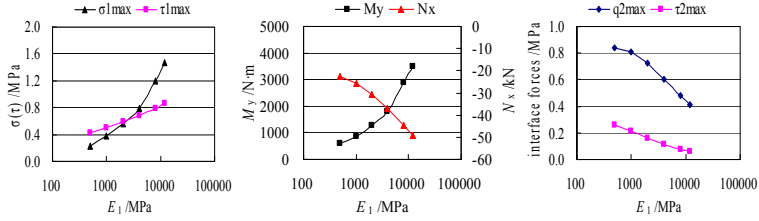

(a) σ_{1max}, τ_{1max} (b) N_x, M_y (c) q_{2max}, τ_{2max},

FIG.13. Diagrams of σ_{1max}, τ_{1max}, N_x, M_y, q_{2max}, τ_{2max} ~ E_1 curves

AC thickness h_1

Practically the AC thickness h_1 may vary from 0.05m to 0.25m, the other parameters are provided in Tab.3 case3, the diagrams of the stress σ_{1max}, τ_{1max}, the sectional internal forces N_x, M_y and the interface forces q_{2max}, τ_{2max} changing with h_1 are shown in FIG.14.

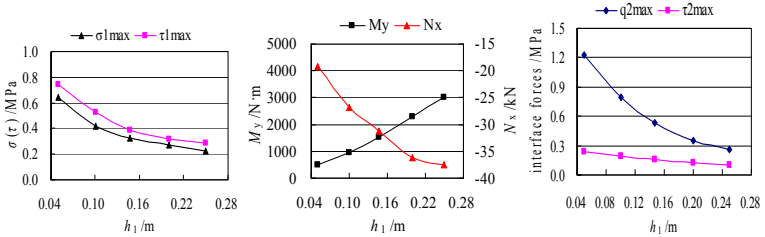

(a) σ_{1max}, τ_{1max} (b) N_x, M_y (c) q_{2max}, τ_{2max},

FIG.14. Diagrams of σ_{1max}, τ_{1max}, N_x, M_y, q_{2max}, τ_{2max} ~ h_1 curves

We can see from FIG.14 that with increase of the AC thickness h_1 the stresses σ_{1max}, τ_{1max} and the interface forces q_{2max}, τ_{2max} all drop down, among which the interface force τ_{2max} drop slightly, the stresses σ_{1max}, τ_{1max} and the interface force q_{2max} fall relatively quick, whereas the sectional internal force N_x decreases and M_y grows up, however, a fairly thicker AC is effective to enhance its performance of tension and shearing resistance. The factor ξ_p takes 1.34 when h_1=0.05, 0.10cm, then falls from 1.67 to 1.60.

PCC slab thickness h_2

Provided that the PCC slab thickness h_2 changing from 0.18m to 0.34m, the other parameters are presented in Tab.3 case4, the diagrams of the stress σ_{1max}, τ_{1max}, the sectional internal forces N_x, M_y and the interface forces q_{2max}, τ_{2max} varying with h_2 are presented in FIG.15.

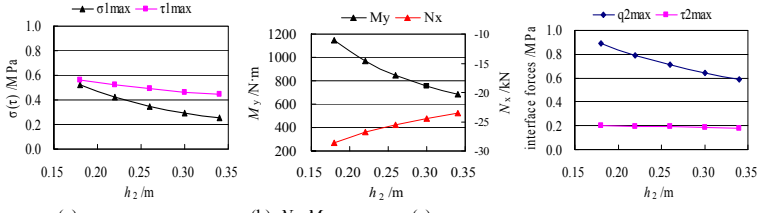

(a) σ_{1max}, τ_{1max} (b) N_x, M_y (c) q_{2max}, τ_{2max},

FIG.15. Diagrams of σ_{1max}, τ_{1max}, N_x, M_y, q_{2max}, τ_{2max} ~ h_2 curves

It can be seen from FIG.15 that with increase of the PCC slab thickness h_2 the stresses σ_{1max}, τ_{1max} and the interface forces q_{2max}, τ_{2max} all drop down, among which the interface force τ_{2max} remains nearly unchanged, whereas the sectional internal force N_x decreases and M_y grows up, basically, it is quite limited to reduce the stresses σ_{1max}, τ_{1max}, the sectional internal forces N_x, M_y and the interface forces q_{2max}, τ_{2max} by a thicker PCC slab. With increase of the PCC slab thickness h_2, the factor ξ_p rises from 1.31 to 1.41.

Initial reaction modulus k_0

Assuming that k_0 varies from 50 to 400 MN/m^3 and without void underneath PCC slabs, the other parameters see Tab.3 case5, the diagrams of the stresses σ_{1max}, τ_{1max}, the sectional internal forces N_x, M_y and the interface forces q_{2max}, τ_{2max} changing with k_0 are shown in FIG.16.

It is found from FIG.16 that with increase of the initial reaction modulus k_0 the stresses σ_{1max}, τ_{1max} and the interface forces q_{2max}, τ_{2max} drop down, among which the stresses σ_{1max}, τ_{1max} and the interface force τ_{2max} fall slightly, whereas the sectional internal force N_x decreases and M_y grows up, obviously it is not significant to reduce the stresses σ_{1max}, τ_{1max}, the sectional internal forces N_x, M_y and the interface forces q_{2max}, τ_{2max} with a higher initial reaction modulus k_0.

With increase of the initial reaction modulus k_0, the factor ξ_p comes down gradually from 1.34 to 1.25.

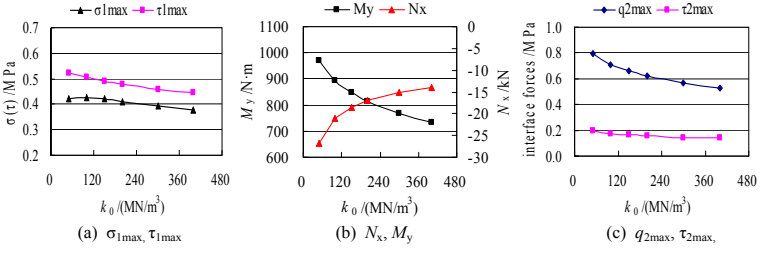

FIG.16. Diagrams of σ_{1max}, τ_{1max}, N_x, M_y, q_{2max}, τ_{2max} ~ k_0 curves

Width of PCC joint δ

Normally the width of joint δ changes from 4mm to 20mm, the other parameters refer to Tab.3 case6, the diagrams of the stresses σ_{1max}, τ_{1max}, the sectional internal forces N_x, M_y and the interface forces q_{2max}, τ_{2max} changing with δ are shown in FIG.17. We can see that the stresses σ_{1max}, τ_{1max} grow up when the width of joint δ changing from 4mm to 10mm, then tend to be stable, so do the sectional internal force N_x and M_y, the interface force q_{2max} fluctuates with δ, and τ_{2max} remains nearly unchanged. When δ>10mm, the influence of δ on the stresses σ_{1max}, τ_{1max}, the sectional internal forces N_x, M_y can be neglected, whereas $\delta \leq 10$mm, the influence of δ shall be considered. When δ<6mm, the factor ξ_p stands at 1.30, otherwise ξ_p takes 1.34.

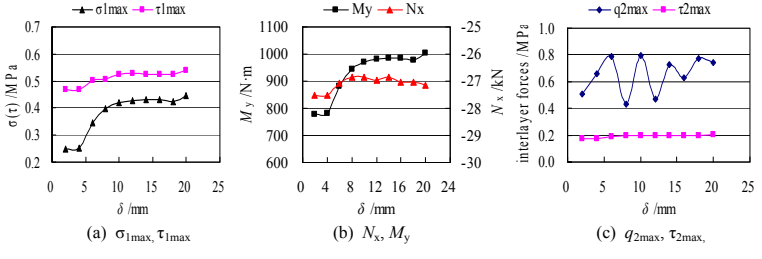

FIG.17. Diagrams of σ_{1max}, τ_{1max}, N_x, M_y, q_{2max}, τ_{2max} ~ δ curves

EFFECTS OF VOID AND JOINT LOAD TRANSFER CAPACITY

Void underneath PCC slabs

The void underneath PCC slabs can be described by using two parameters L_v and λ_k defined previously, herewith taking L_v=0.8m, C_w=0, λ_k changing from 0 to 1, the other parameters are listed in Tab.3 case7, the diagrams of ratios α (σ_{1max}, τ_{1max}, N_x, M_y, q_{2max}, τ_{2max} related to an arbitrary λ_k against that of λ_k=1) changing with λ_k are drawn in FIG.18. We can see that with increase of λ_k the stress σ_{1max} rises up, the shearing stress τ_{1max} keeps nearly unchanged, whereas the sectional internal forces N_x, M_y and interface forces q_{2max}, τ_{2max} come down, it seems that eliminating the void underneath PCC slabs will lead to a disadvantageous effect on the stress σ_{1max}, but an active effect on the interface forces q_{2max}, τ_{2max}, thus reduce the risk of interface damage. While the sub-grade weakening index λ_k varies from 0 to 1, the factor ξ_p decreases from 1.43 to 1.34.

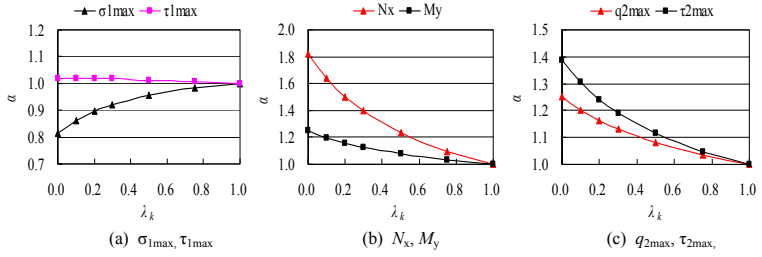

FIG.18. Diagrams of ratios of σ_{1max}, τ_{1max}, N_x, M_y, q_{2max}, τ_{2max} ~ λ_k curves

Joint load transfer capacity

Assuming that the joint shearing spring stiffness C_w changes from 1 to 10000 MPa/m, the other parameters are given in Tab.1 case8, the diagrams of ratios α (σ_{1max}, τ_{1max}, N_x, M_y, q_{2max}, τ_{2max} related to arbitrary C_w against that of C_w=1 MPa/m) changing with C_w are shown in FIG.19 and FIG.20.

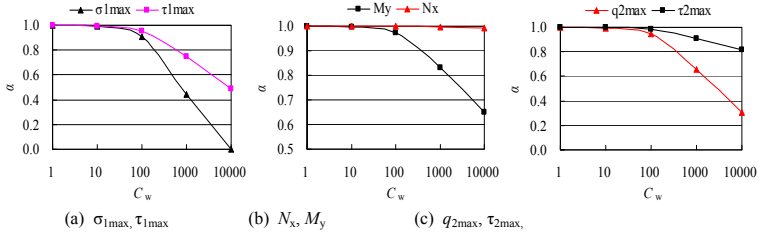

FIG.19. Diagrams of ratios of σ_{1max}, τ_{1max}, N_x, M_y, q_{2max}, τ_{2max} ~ C_w curves (λ_k=0)

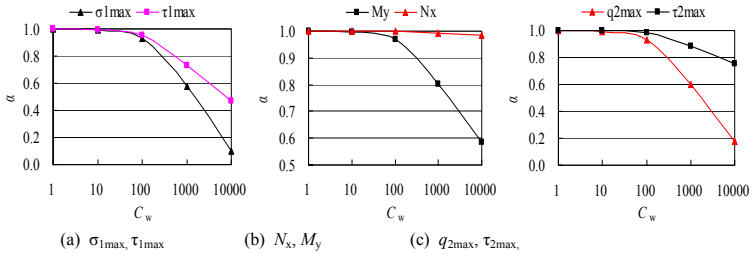

FIG.20. Diagrams of ratios of σ_{1max}, τ_{1max}, N_x, M_y, q_{2max}, τ_{2max} ~ C_w curves (λ_k=1)

It can be found from FIG.19 and FIG.20 that with increase of the joint shearing spring stiffness C_w the stresses σ_{1max}, τ_{1max}, the sectional internal N_x, M_y and the interface forces q_{2max}, τ_{2max} all drop down, among which the axial force N_x drop slightly, when C_w>100 MPa/m, the variation of σ_{1max}, τ_{1max}, M_y, q_{2max}, τ_{2max} rise up rapidly, that means a relative higher joint shearing spring stiffness C_w will be effective to reduce the stresses σ_{1max}, τ_{1max} and the interface forces q_{2max}, τ_{2max}. Compared the results of λ_k=0 with that of λ_k=1, the trends of ratios α changing with C_w are almost the same, and the differences are not significant, however, it is important to improve the joint shearing spring stiffness C_w rather than the sub-grade weakening index λ_k before paving AC on PCC slabs to reduce the loading stresses in AC and the interface forces.

With increase of the joint shearing spring stiffness C_w, the factor ξ_p falls from 1.43 to 1.26 at λ_k =0, and 1.34 to 1.20 at λ_k =1.

INTERLAYER EFFECTS

Width of interlayer

In order to retard the reflective crack caused by the thermal stresses, a soft interlayer with finite width is often placed over the joint of PCC slabs before paving AC, this measure is proven to be most effective to reduce the thermal stresses but disadvantageous to lower the loading stresses in AC, nevertheless, it is necessary to determine a proper width of soft interlayer to balance the thermal stresses and the loading stresses in AC.

For case9 in Tab.3, the stresses σ_{1max}, τ_{1max}, the sectional internal N_x, M_y and the interface forces q_{2max}, τ_{2max} changing with soft interlayer width W_2 are shown in FIG.21. It can be seen clearly that with increase of the soft interlayer width W_2 the stresses σ_{1max}, τ_{1max} keep nearly unchanged, the interface forces q_{2max} firstly grows up when W_2 changing from 0.3m to 0.5m, then comes down at 0.6m，following stands at a stable level, the interface forces τ_{2max} remains unchanged. Therefore, a 0.3~0.4m soft interlayer width shall be enough.

With increase of the soft interlayer width W_2, the factor ξ_p changes from 3.05 to 2.99.

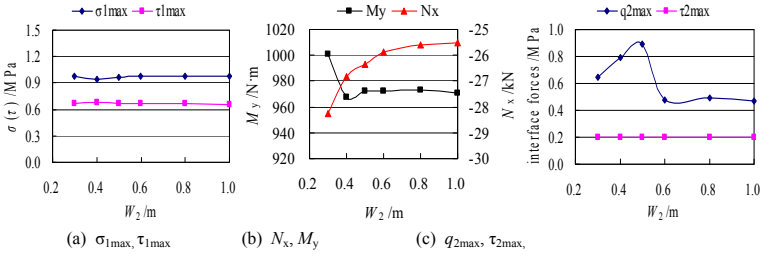

(a) σ_{1max}, τ_{1max} (b) N_x, M_y (c) q_{2max}, τ_{2max},

FIG.21. Effects of soft interlayer width W_2

Stiffness of interlayer

The stiffness of interlayer will vary with its elastic modulus E_3 and thickness h_3, for commonly used interlayer materials, the material properties along with its stiffness are listed in Tab.4 (Yumin Zhou, 2007).

Assuming the soft interlayer width W_2=0.4m, the other parameters are presented in Tab.3 case 10, the lowest and highest stiffness of each type of interlayer given in Tab.4 are used to compute the stresses σ_{1max}, τ_{1max} in AC, the sectional internal forces N_x, M_y and the interface forces q_{2max}, τ_{2max}, the results are listed in Tab.5. It can be found that with increase of the interlayer stiffness the stress σ_{1max} may be close to zero, or even becomes negative, the shearing stress τ_{1max} decreases and its variation is less than 24.1%, and the interface forces q_{2max}, τ_{2max} increase considerably. As per the factor ξ_p, with increase of the interlayer stiffness, the stress σ_{1max} shifts from tension to compression state, thus it is not necessary to discuss.

Table 4. Material Properties and Corresponding Stiffness of Interlayer (Yumin Zhou, 2007)

Type	E_3 /MPa	h_3 /mm	μ_3	k_{t0} /MPa	k_{n0} /MPa
A-stress absorption	10~100	1~5	0.45	690~35000	7500~380000
B-unwoven geotextile	10~160	0.4~4	0.35	900~150000	4000~650000
C-geotextile	400~1500	0.4~0.7	0.35	210000~1400000	910000~6100000

Table 5. Loading Stresses in AC and Interface Forces

Type	σ_{1max}	τ_{1max}	q_{2max}	τ_{2max}	N_x	M_y
A1	0.6918	0.584	0.379	0.000	-14649	-1319
A2	0.0560	0.521	1.470	0.738	-29355	-328
B1	0.7033	0.610	0.191	0.113	-21068	-1703
B2	0.0413	0.606	1.480	1.010	-28769	-278
C1	0.0353	0.603	1.480	1.040	-28203	-264
C2	0.0000	0.492	2.070	2.850	-25054	-136

DAMAGE MODES

Under vehicle loads, the damage of AC on PCC structure takes two basic modes, one is the AC damage arising from much higher tensile or shearing stress in AC nearby the joint of PCC slabs, the other is related to the interface damage nearby the joint, such as interface between AC and PCC slabs sliding or open, the damage controlling equations of AC on PCC structure are given by:

$$\begin{aligned} \sigma_{1\max} \le [\sigma_1], \quad \tau_{1\max} \le [\tau_1] \\ q_{2\max} \le [q_2], \quad \tau_{2\max} \le [\tau_2] \end{aligned} \tag{9}$$

Where: (σ_1) is the allowable tensile stress of AC material; (τ_1) represents the allowable shearing stress of AC material; (q_2) stands for the allowable tensile stress in interface; (τ_2) is on behalf of the allowable shearing stress in interface.

As per the strength of interlayer materials, (q_2) normally varies from 0.5MPa to 1.0MPa; and (τ_2) is not less than 0.3MPa (Fujie Zhou, 1998; Shuming Li, 2002), based on the analysis made above, however, the damage process of AC on PCC structure is quite complicated, the damage may occur first in AC nearby the PCC joint, or the damage may initiate in the interface between AC and PCC slabs, most probably the damage in the AC and the interface occur simultaneously or alternatively. The schematic of damage in AC on PCC structure is illustrated in FIG.22.

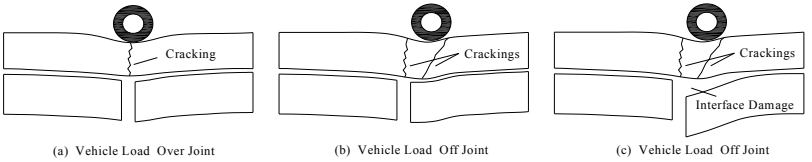

FIG.22. Schematic of damage in AC on PCC structure

CONCLUSIONS

Based upon a simplified three-dimensional model of AC on PCC structure, established by using the finite element method, through examples, the stresses $\sigma_{1\max}$, $\tau_{1\max}$ in AC, the sectional internal forces N, M and the interface forces q_2, τ_2 caused by vehicle load are studied, and the conclusions are drawn as follows:

1. The finite element results indicated that the loading stresses in AC nearby the joint of PCC slabs are sometimes quite difficult to converge, but corresponding sectional internal forces N, M are well-converged, therefore, the sectional internal forces can be taken as convergence criteria to judge the reasonability of model meshing.
2. By adopting an averaged method, the nominal maximum tensile stress $\sigma_{1\max}$ on the bottom surface of AC near the joint of PCC slabs can be calculated upon the corresponding sectional internal forces N, M and a stress concentration factor ξ_p.
3. When the load position x not exceeding ±0.2m, the stresses $\sigma_{1\max}$, $\tau_{1\max}$ reach relevant peak values, the influences of structural parameters E_1, h_1 on the stresses

σ_{1max}, τ_{1max} and the interface forces q_{2max}, τ_{2max} are much significant.

4. Eliminating the void underneath PCC slabs will have a disadvantageous effect on the stress σ_{1max} but an active effect on the interface forces q_{2max}, τ_{2max}. A higher joint spring stiffness C_w would considerably reduce the stresses σ_{1max}, τ_{1max} in AC and the interface forces q_{2max}, τ_{2max}.
5. A 0.3~0.4m placing width of soft interlayer is enough. The higher the stiffness k_{t0}, k_{n0} of interlayer, the lower the stress σ_{1max}, but the interface force q_{2max} will rise up, therefore increase the risk of interface damage.
6. The damage of AC on PCC structure takes 2 basic modes: direct reflective crack in AC or interface damage then reflective crack in AC.

REFERENCES

AASHTO, 2004. AASHTO Guide for Mechanistic-Empirical Design of New and Rehabilitated Pavement Structures. Washington, D. C.

P. R. China. Ministry of Communications, (2002) Specification of Cement Concrete Pavement Design for Highway(S). Beijing: China Communication Press, 2002 (in Chinese).

Monismith, C.L. and Coetzee, N. F. (1980) "Reflective Cracking: Analyses, Experimental Laboratory Studies, and Design Considerations," *Proceedings of AAPT*, Vol.49, 1980, pp268~311.

Rashid, (1982)"ASCE State-of-the-art Report on Finite Element Analysis of Reinforced Concrete," Prepared by a Task Committee Chaired by A. Nilson, American Society of Civil Engineers, New York.

Majidzadeh, K. et al., (1985)"Improved Methods to Eliminate Reflection Cracking," *FHWA/RD-86/075*, Federal Highway Administration, Washington, D.C.

Molenaar, A.A.A.. Heerbens, J.C.P. et al., "Effects of Stress Absorbing Membrance Interlayers," *Proceedings of AAPT*, Vol.55, 1986, pp206~219.

Jayawickrama, P.W. and Lytton, R.L. (1987)"Methodology for Predicting Asphalt Concrete Overlay Life against Reflection Cracking," *Proceedings of 6th International Conference Structural Design of Asphalt Pavements*, Vol.1, pp912~924.

Lytton, R.L. (1989). Use of Geotextiles for Reinforcement and Strain Relief in Asphalt Concrete. Geotextiles and Geomembranes, *Special Issue on Geotextiles and Geogrids in Pavements*, Vol.8(3), pp217-237.

Zhou, D. andYao, Z. (1990)"Three dimensional finite element analysis of asphalt overlay on concrete pavements", *China Journal of Highway and Transport*, Vol.3(3), 1990, pp18~26 (in Chinese).

Yu, B. (1991)"Study on reflective cracking and design for asphalt overlay on concrete pavements", Shanghai: Department of Road and Traffic Engineering, Tongji University, 1991 (in Chinese).

Francken, L. and Vanelstraete, A. (1992) "Interface Systems to Prevent Reflective Cracking: modeling and experimental testing methods," *Proc. of 7th International Conference on Asphalt Pavements*, Vol.1, pp45~60.

Blankenship, P., Iker, N. and Drbohlav, J.(2003) "Interlayer and design considerations to retard reflective cracking," *Paper submitted to 2003 Annual Meeting of TRB*.

Rigo, J.M. et al. (1993) "Evaluation of Crack Propagation in an Overlay Subjected to

Vehicle and Thermal Effects", *Reflective Cracking in Pavements*, Published by E& FN Spon, 1993, pp146~158.

De Bondt, A. H. and Searpas, A.(1997) Design of (Reinforced) Asphaltic Overlays. *8th International Conference on Asphalt Pavement Structural Design*. August 10-14, 1997. Seattle, Washington, pp1161~1180.

Sousa, J. B., Pais, J. C. and Way, G. B. (2005) "A Mechanistic-Empirical Based Overlay Design Method for Reflective Cracking," Road Materials and Pavement Design. Vol.6-No.3/2005, pp339-363.

Zhou, Y. (2007) "A Study on Mechanism of Reflective Cracking and Design Method of Asphalt Overlay Paved on Cement Concrete Pavements", Shanghai: School of Transportation Engineering, Tongji University,(in Chinese).

Zienkiewicz, O.C., Taylor, R.L. (2009) "The Finite Element Method for Solid and Structural Mechanics (M)", sixth edition, Elsevier (Singapore) Pte Ltd., 2009.

ANSYS Inc. (2005), *ANSYS Contact Technology Guide 10.0(R)*,

Zhou, F., "Prevention Measures and Analysis of Reflective Cracking"，Shanghai: Department of Road and Traffic Engineering, Tongji University, 1998 (in Chinese).

Li, S. (2002) "Study on Design Method of Asphalt Overlay on Existing Concrete Pavements", Shanghai: School of Transportation Engineering, Tongji University, (in Chinese).

Visco-elastoplastic response of flexible pavement under traffic loads

Chen Yekai[1], Wang Jinchang[2]

[1] School of Civil Engineering and Transportation, South China University of Technology, Guangzhou, China, 510640; chenyekai@163.com
[2]Architecture engineering institute, Zhejiang University, Hangzhou,China,310027; wjc501@126.com

ABSTRACT: In this paper, liner Drucker-Prager creep model was used to simulate the visco-elastoplastic response of flexible pavement under traffic loads. The effect of asphalt layer thickness, asphalt stiffness, interactive properties between the asphalt and base layers, base and sub-grade modulus, and the traffic loads level were considered in parametric study.

INTRODUCTION

Rutting develops with an increasing number of load applications. Rutting is caused by a combination of densification and shear-related deformation and may occur in any layer of a pavement structure (Witczak et al. 1997; Simpson 1999). For years, researchers and practitioners alike in the pavements and materials industry have been performing forensic investigations to determine the origin of asphalt pavement permanent deformation failures (Brown E. R., & S. A. Cross. 1992; Odermatt et al. 1999; Wang et al. 2009). Usually, the investigations involve traffic control, coring, excavation, and significant materials testing. These investigations are costly and can be very inconvenient for road users.

In this study, nonlinear visco-plastic FEA were performed using the general-purpose finite element (FE) program ABAQUS. In order to understand the developing mechanism and influence factors of rutting for in-service flexible pavements. parametric study was carefully conducted considering the effect of asphalt layer thickness, asphalt stiffness, base and sub-grade modulus, the traffic loads level, and the interactive properties between asphalt and base layers was studied in detail.

MATERIAL PROPERTIES

Asphalt layer

Flexible pavement permanent deformation, which occurs as a result of repeated loading, depends on the total cumulative traffic loading time. In order to simulate flexible pavement permanent deformation, a creep model is used to characterize layer

materials. Permanent deformation of pavement asphalt and unbound aggregate and foundation materials is a time- and stress-dependent response. In the case of asphalt layers, there is also temperature dependence. The finite element software ABAQUS was used for analysis of rutting. Stress and time dependency is accounted for using a creep rate model from the ABAQUS material model library. In equation form, the creep rate is represented as (Hibbit, K. & Sorenson. 2008):

$$\dot{\varepsilon} = \mathrm{A}\sigma^{n} t^{m} \tag{1}$$

Where: $\dot{\varepsilon}$ =creep strain rate

σ =uniaxial equivalent deviatoric stress

t = total loading time, and

A, m, n, parameters related to material properties

Aggregate base and sub-grade

One of the most typical structures in flexible pavements is unbound granular base pavement, which is composed of asphalt surface layer, aggregate base course, and compacted sub-grade on top of the natural ground. The deformation response of the aggregate base and sub-grade materials is modeled in this study using a stress state dependent yield plastic model from the ABAQUS material model library, which is the linear extended Drucker-Prager model.

The linear model is written in terms of all three stress invariants. It provides for a possibly noncircular yield surface in the deviatoric plane to match different yield values in triaxial tension and compression, associated inelastic flow in the deviatoric plane, and separate dilation and friction angles.

The linear Drucker-Prager criterion (see Fig.1) is written as:

$$F = t - p\tan\beta - d = 0 \tag{2}$$

Where: $t = \frac{1}{2}\left[1 + \frac{1}{K} - \left(1 - \frac{1}{K}\right)\left(\frac{r}{q}\right)^{3}\right]$

β = the slope of the linear yield surface in the p–t stress plane and is commonly referred to as the friction angle of the material;

d = the cohesion of the material

K = the ratio of the yield stress in triaxial tension to the yield stress in triaxial compression and, thus, controls the dependence of the yield surface on the value of the intermediate principal stress (see Fig.2, Hibbit 2008).

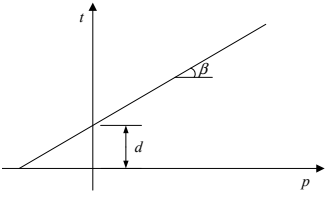

FIG. 1. Yield surfaces in the meridional plane

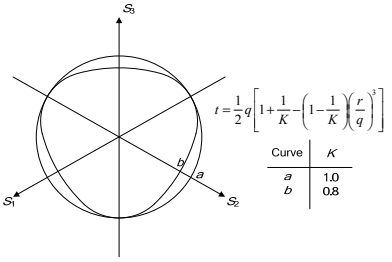

FIG.2. Typical yield/flow surfaces of the linear model in the deviatoric plane

In this study, flexible pavements comprised of asphalt layer, aggregate base, and sub-grade are selected for the investigation. The model parameters of each layer in pavement system are shown in table 1 and table 2. The material properties of asphalt concrete were obtained by uniaxial compression creep test (Zhang, 2009). AC I is referred as unmodified asphalt mixture and AC II is modified asphalt mixture. The creep properties of the asphalt mixture were tested up to 3600s of loading time at temperature 25^0C. Both stiff and weak modulus were considered in the base and sub-grade layers, as listed in table 2.

Table 1. Material Properties of Asphalt Layer Used in Analyses (Zhang, 2009)

AC Type	E(MPa)	v	$\beta(^0)$	σ_0(MPa)	A	n	m
AC I	1000	0.3	38.3	0.66	1.65e-06	0.943	-0.890
AC II	1500	0.3	50.19	0.78	3.86e-06	0.726	-0.885

Table 2. Material Properties of Base and Subbase Layer Used in Analyses

Pavement layer	Type	E(MPa)	v	$\beta(^0)$	σ_0(kPa)
Base	Stiff	1500	0.25	43.2	728.2
	Weak	500	0.3	33.6	365.7
Subbase	Stiff	50	0.3	30.8	46.2
	weak	25	0.35	20.6	30.2

LOADING SYSTEM

A moving load was represented by the haversine load with a peak magnitude of 100 kN to simulate a single and dual tire loads respectively, as followed (Huang, 1993, see Fig.3):

$$q(t) = q_{\max} \sin^2\left(\frac{\pi t}{T}\right) \tag{3}$$

where, $q_{\max}$ = contact pressure; T is the duration of the load, written as (Huang, 1993):

$$T = \frac{12a}{v} \tag{4}$$

where, a = the radius of load contact area; v is the vehicle speed.

In this study, a loading duration of 0.081 second (v=80km/h) and a rest period of 0.919 second were selected. For a tire-pavement contact pressure distribution on pavement surface, Although recent studies[10] have revealed that the contact pressure is non-uniform and the effect of the non-uniform distribution of the contact pressure is important in accurate pavement response computation. The uniform contact pressure distribution was studied in this paper.

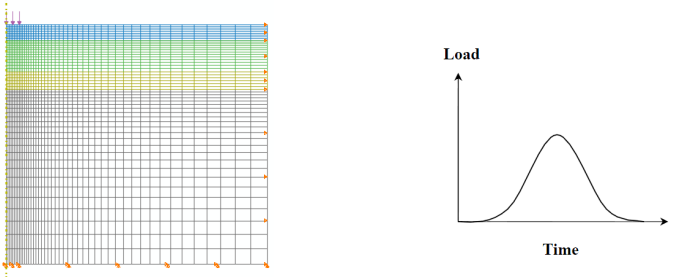

FIG.3. Axisymmetric pavement structure modeling subject to cyclic loadings

RESULTS AND DISCUSSIONS

Fig.4 shows radial stress-strain curves under the uniform contact pressure in cyclic mode. The hysteresis loops shifted to the right side demonstrating the accumulation of radial strains in tension. Fig.5 presents the equivalent creep strain contours at different number of cycles. It is noted that the intensity of creep increases as the number of cycles increases. Another observation to be made in this figure is that the pattern of creep contour (i.e., shape and relative intensities of creep at different locations) remains relatively the same at different cycles. This observation is important in this study because of the computing time required in simulating long-term creep behavior.

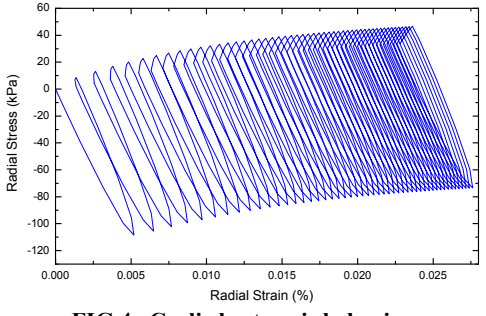

FIG.4. Cyclic hysteresis behavior

Simulation of the cyclic behavior of asphalt pavements using the ABAQUS takes between 10 and 15 seconds per cycle on a 3.00 GHz Intel Core™2 Due computer with 4.00 GB memory, and the simulation of 500 cycles takes about 1.4 to 2.1 hours. Based on this rate, one million cycles will take about 2,800 to 4,200 hours. In this study, the stress and equivalent creep strain contours at the peak load of the 10th cycle are used in

the evaluation of the creep initiation mechanisms. Comparison of the contours at the 500th cycle yields pretty much the same conclusions as those made from longer cycles.

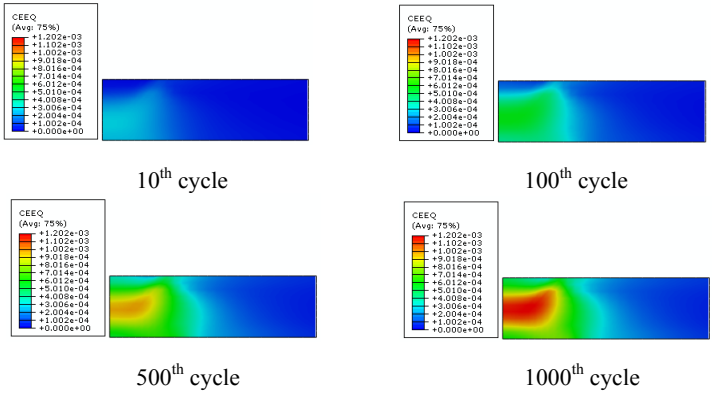

FIG.5. Equivalent creep stain(CEEQ) contours at different cycles

Various pavement structures with changing layer thicknesses, layer stiffness, contact pressure distributions, and load levels were modeled using the ABAQUS program. Combinations of these variables are selected such that effects of individual variables on stress and creep states can be evaluated effectively. Values selected for each variable are summarized below:

1. AC layer thickness: 12, 18, 24, and 30 cm, referred as thin, medium, and thick respectively;
2. AC stiffness: AC I for softer asphalt mix and AC II for stiffer asphalt mix;
3. Base and sub-grade stiffnesses: full factorial combinations of stiff and weak base and stiff and weak sub-grade, i.e., stiff base and stiff sub-grade (referred as SS), stiff base and weak sub-grade (SW), weak base and stiff sub-grade (WS), and weak base and weak sub-grade (WW);
4. Friction coefficients between AC and Base layers: 0.0, 0.5, 1.0, 5.0, referred as frictionless, poor, medium, and rough respectively;
5. Load levels of 100 and 200 kN.

Effect of AC Thicknesses

An important observation is that the level of creep is greatly affected by the asphalt layer thickness. In Fig.6, the equivalent creep strain decreases significantly as the asphalt layer thickness increases. Another observation is the asphalt thickness influences the location of the maximum creep in the asphalt layer. As shown in Fig.6, when the thinnest layer is modeled, the severe creep is found at the bottom of the layer. As the asphalt layer becomes thicker, the location of the creep moves up to the layer's center.

Fig.7 presents the cumulative creep strain in the asphalt layer as the traffic loads increase, the creep strain is represented by equivalent creep strain, which defined as

$\int_0^t \dot{\bar{\varepsilon}}^{cr} dt$. It also can be concluded that the thin asphalt thickness will lead to more cumulative creep strain. And as the creep strain occur in the asphalt layer, unrecoverable deformation may be accumulated in the pavement system, which means the pavement rutting. Fig.8 shows the permanent deformation results of different asphalt thickness, although the creep strain is the largest in the thin asphalt layer, the rutting is the least, and the thick (30 cm) asphalt layer has the largest rutting.

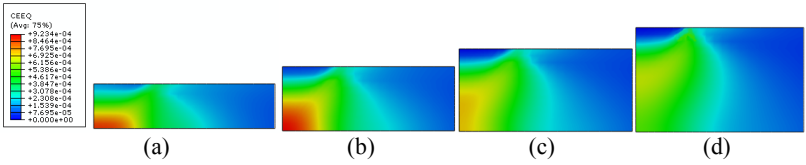

FIG.6. Equivalent creep strain contours in asphalt layer with different thickness (a) 12 cm, (b) 18 cm, (c) 24 cm, (d) 30 cm

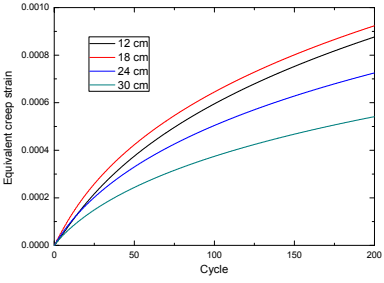

FIG.7. Cumulative creep strain with loads cycle

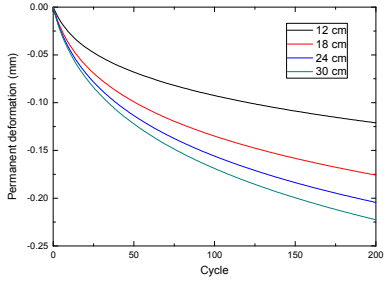

FIG.8. Cumulative rutting with loads cycle

Effect of AC Stiffnesses

Fig.9 presents the creep contours calculated using two asphalt stiffness (AC I and AC II in table 1). It can be concluded from this figure that the creep strain decreases as the asphalt layer becomes stiffer, and the creep distribution in the asphalt layer is almost the same if the layer thickness and the contact condition between the AC and base is the same.

The creep strain in the asphalt layer accumulate as the traffic loading cycle increase, as shown in Fig.10, and less creep occurs in the stiffer asphalt layer (AC II). As creep strain arises in the asphalt layer, unrecoverable deformation may develop in the pavement system, which means the pavement rutting. Fig.11 shows the permanent deformation results of this two asphalt type, rutting becomes deeper as the traffic loading cycle increase, and the stiffer asphalt will lead to less rutting in the pavement system. This means that the modified asphalt (AC II) has more rutting resistance than the unmodified asphalt does.

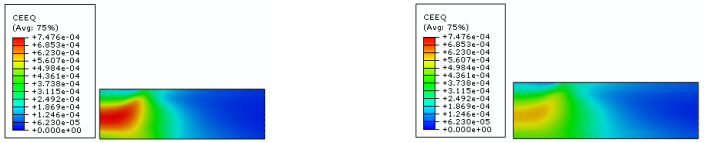

(a) AC I, (b) AC II

FIG.9. Equivalent creep strain contours with different AC stiffnesses

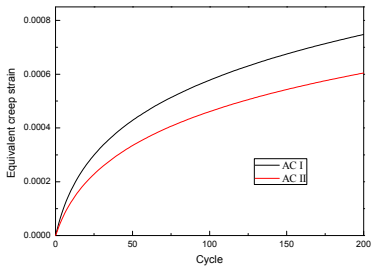

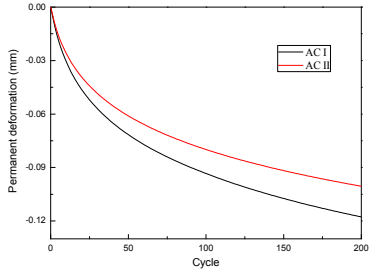

FIG.10. Cumulative creep strain with loads cycle **FIG.11. Cumulative rutting with loads cycle**

Effect of Base and Sub-grade Modulus

The effect of base and sub-grade modulus can be evaluated by comparing four subfigures under each response parameter in each figure (table 2), the effect of sub-grade modulus on pavement creep is much less than the effect of the base modulus, as shown in Fig.12, the difference of the creep strain between SS (Fig.12a) and SW (Fig.12b) is quite small. In this condition, the stiffness of base layer is same. The similar result can be concluded between WS and WW base and sub-grade modulus.

Fig.13 is the creep strain cumulative curve in the asphalt layer, and Fig.14 is the pavement rutting cumulative curve with traffic loading cycle. It can be seen that the results of creep and rutting under SS and SW, WS and WW are almost the same. In this condition, the stiffness of the base layer is the same, whether the sub-grade moduli are stiff or weak. However, changing the base stiffness will lead to significantly different creep strain in the asphalt layer and rutting in the pavement system, and this difference will become lager as the traffic loading cycle increase.

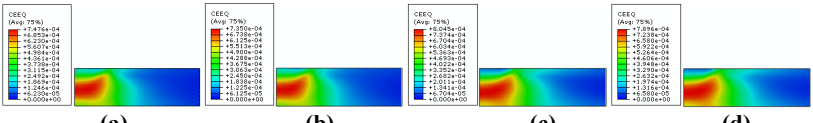

(a) (b) (c) (d)

FIG.12. Equivalent creep strain contours in asphalt layer under different base and sub-grade modulus: (a) SS, (b) SW, (c) WS, (d) WW

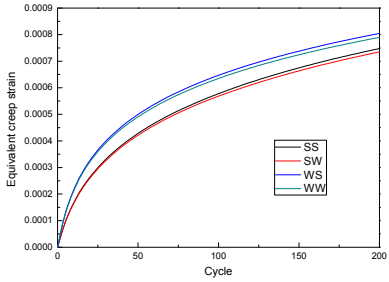

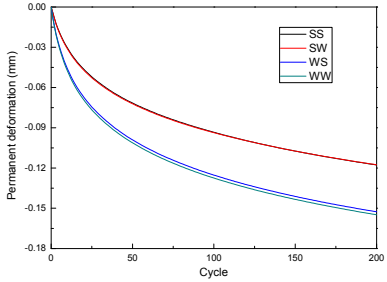

FIG.13. Cumulative creep strain with loads cycle FIG.14 Cumulative rutting with loads cycle

Effect of interactive properties between AC and Base layers

Fig.15 presents the equivalent creep contours in asphalt layer under different friction coefficients between AC and base layer. This figures show that frictionless condition between AC and base layer results in a greater amount of creep in all cases (see Fig.15a), and the creep strain in the asphalt layer decreases as the friction coefficient increases, and the least amount of creep occurs under the rough condition (see Fig.15d). Another observation is that the location of the largest creep strain in the asphalt layer is greatly affected by the interactive conditions between AC and layers. When the contact condition is frictionless, the location of the largest creep is closer to the bottom of AC layer, and as the friction coefficients increases, the location of the maximum creep strain moves up to the center of asphalt layer.

Fig.16 presents the creep strain cumulative curve in the asphalt layer, and Fig.17 is the pavement rutting cumulative curve with traffic loading cycle. It can be seen that the frictionless contact condition lead to more cumulative creep strain and pavement rutting, and less creep strain and rutting developed in the rough contact condition.

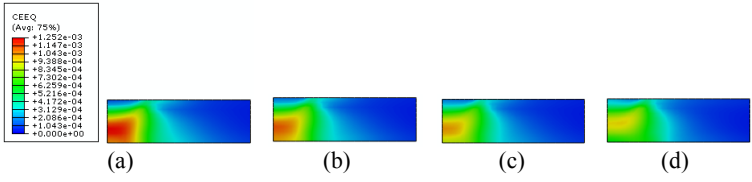

FIG.15. Equivalent creep strain contours in asphalt layer under (a) f=0, (b) f=0.5, (c) f=1.0, (d) f=5.0

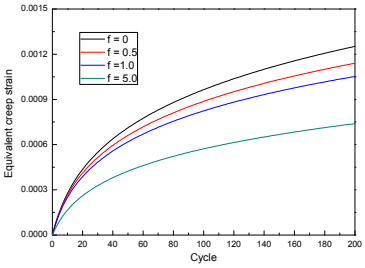

FIG.16. Cumulative creep strain with loads cycle

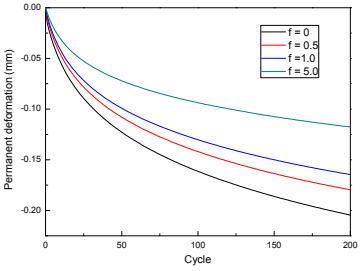

FIG.17. Cumulative rutting with loads cycle

Effect of Load Levels

Fig.18 presents the creep contours calculated under different traffic loading level (100 kN and 200 kN). It can be concluded from this figure that more creep strain occur in the asphalt layer under heavier traffic loading (200 kN), and considerable plastic strain arises near the bottom of the asphalt layer also in this load condition, as shown in Fig.19. This means that viscous plastic property of the asphalt material must be considered when the traffic loading is relatively heavier.

(a) (b)

FIG.18. Equivalent creep strain contours in asphalt layer under different traffic loading level: (a) 100 kN, (b) 200 kN

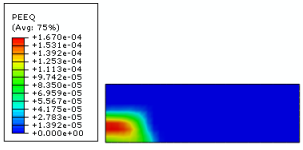

FIG.19. Equivalent plastic strain contours in asphalt layer under

CONCLUSIONS

The visco-elastoplastic behavior of asphalt pavement was simulated using FEA. The main conclusion from this parametric study can be summarized as follows:

1. The asphalt layer thickness has a significant effect on the magnitude and location of creep strain in the asphalt, while the asphalt layer stiffness mainly affects the magnitude of the creep strain.

2. The creep is more affected by the base stiffness than by the sub-grade stiffness.
3. The frictionless contact condition between the asphalt and base layers lead to more creep strain than rough contact condition does.
4. The viscoplastic of asphalt layer becomes more important as the traffic load level increase.

REFERENCES

Brown, E. R. and Cross, S. A. (1992). "A National Study of Rutting in Hot Mix Asphalt (HMA) Pavements." *NCAT Report 92-5*, National Center for Asphalt Technology, Auburn, Alabama.

Hibbit, K. and Sorenson. (2008). ABAQUS Theory and Users Manual Version 6.8. Pawttucket, Inc., Rhode Island.

Hua, J. (2000). "Finite element modeling and analysis of accelerated pavement testing devices and rutting phenomenon." Purdue University.

Huang, Y. H. (1993). Pavement analysis and design, Prentice–Hall, Englewood Cliffs, N.J.

Huhtala, M., Philajamaki, J., and Pienimaki, M. (1989). "Effects of tires and tire pressures on road pavements." *Transportation Research Record*, 1227, Transportation Research Board, Washington, D.C., 107-114.

Odermatt, N. Janoo, V. and Magnusson, R. (1999). "Analysis of Permanent Deformation in Sub-grade Material Using a Heavy Vehicle Simulator." *Preprint of Proceedings of the International Conference on Accelerated Pavement Testing*, Reno, Nevada.

Sebaaly, P.E. and Tabatabaee, N. (1993). "Influence of Vehicle Speed on Dynamic Loads and Pavement Response." *Transportation Research Board 1410*, TRB, National Research Council, Washington D.C., 107-114.

Simpson, A. (1999). "Characterization of Transverse Profile." Transportation Research Record 1655, *Transportation Research Board*, National Research Council, Washington, D.C., 185-191.

Uzan, J. (1999a). ''Granular material characterization for mechanistic pavement design.'' J. Transp. Eng., 125(2), 108-113.

Uzan, J. (1999b). ''Permanent deformation of a granular base material.'' Transportation Research Record No. 1673, *Transportation Research Board*, Washington, D.C., 89-94.

Wang, H., Zhang, Q.S., and Tan, J.Q. (2009). "Investigation of Layer Contributions to Asphalt Pavement Rutting." *Journal of Materials in Civil Engineering*, ASCE, 21(4),181-185.

Witczak, M. W., Von Quintas, H., and Schwartz, C. W. (1997). "Super-Pave support and performance models management: Evaluation of the SHRP performance models system." *Proc., 8th Int. Conf. on Asphalt Pavements*, Vol. III, ISAP, Seattle, Wash., 175–195.

Zhang, L. (2009). "Research on constitutive relations for asphalt mixtures and method of rutting prediction based on creep test." South China University of Technology.

Zhang, W. (2001). "Finite element simulation of rutting on superpave pavements." Kansas State University.

The Rutting Resistant Surface Course Combination for Continuous Uphill Section of Expressway

Yang Xu[1,2]， Hongxing Guan[3],Qisen Zhang[4], Libo Zhou[5]

[1]Ph.D.candiate, college of Architecture Engineering, Central South University, Changsha 410075; xyhnjt@163.com

[2] Manager, Hunan Province Transportation Planning Survey and Design Institute, Changsha 410008; xyhnjt@163.com

[3] Associate professor, School of Traffic and Transportation Engineering, Changsha University of science and technology; guanhxin@sina.com

[4] Professor, College of Architecture Engineering, Changsha University of science and technology;zhangqisen@163.com

[5] Associate professor, School of Traffic and Transportation Engineering, Changsha University of science and technology;zgoulibo@163.com

ABSTRACT: Rut is always serious when asphalt pavements sustain heavy loading and slow moving vehicles. This indicates that traditional asphalt pavements structural combination design methods can not offer sufficient rutting resistance performance for the special section. In this study, full-thickness rutting tests under heavy load and slow speed were developed for many surface course combinations. The contribution rate of each surface layers to the whole surface course's rutting resistance performance was studied. Test results show that the rutting resistance performance of top surface layer, middle surface layer and bottom surface layer should be improved simultaneously to prevent rut in the continuous uphill expressway; the use of modified bituminous or anti-rut agents is an effective way to improve the rutting resistance performance of asphalt mixture. Finally, a suitable asphalt surface course was recommended for a 13km continuous uphill asphalt pavement maintenance project.

INTRODUCTION

Rut is a main disease type of asphalt pavements. Many scholars have studied on it for many years. One of the main solution ways is to use rutting resistant materials. From GTM test and APA test, Huang, et al (2009) noted that aggregate play a important role on rutting resistance performance; Sirin et al (2008) reported that modified bituminous can improve the rutting resistance performance of asphalt mixture. Wu et al (2008) studied the factors influencing rutting resistance performance with full-thickness Loaded Wheel Tester; Yang et al (2007) analyzed the contribution rate of top surface layers and middle surface layer to their combination's rutting resistance performance.

These conclusions can be used to guide asphalt pavement structure design and material design for normal highways. However, for steep and long uphill highway, the pavement rutting resistance design has to take account of the influence of heavy loading trucks moving slowly. The research about this is rare. Paulo, et al (1998) verified the influence of trucks moving slowly on asphalt mixture with field rut data and laboratory rutting test data, which testing method was Repetitive Simple Shear Test at Constant Height.

Currently, Loaded Wheel Testers(LWT for short) is used popularly to analyze the rutting resistance performance of asphalt mixtures in China. LWT is designed to simulate vehicle wheels moving on asphalt pavements. The testing condition of LWT is unified by STANDARD TEST METHODS OF BITUMINOUS AND BITUMINOUS MIXTURES FOR HIGHWAY ENGINEERING（JTJ 052-2000）in China. LWT's testing wheel diameter is 200 mm and testing wheel width is 50 mm. LWT's specimen dimension is 300mm×300mm×50mm. Under standard testing condition, the testing wheel pressure on asphalt mixture specimen is 0.7Mpa, the testing wheel moves back and forth at speed 42 times/minute at 60℃.

In this study, LWT will be improved to perform full-thickness, heavy load and slow speed rutting tests, which is named as Improved LWT(ILWT for short); Then the rutting resistance performance of different asphalt surface course combination will be compared. Based on this, a suitable asphalt surface course combination will be recommended for a 13 km continuous uphill expressway.

RUTTING TESTS FOR SERVING UPHILL EXPRESSWAY

This study's object is a 13 km continuous uphill section in Beijing-ZhuHai expressway, which initial asphalt surface course is SMA-16 + AC-20 + AC-25. The top surface layer is basalt modified asphalt mixture, the middle surface layer and bottom surface layer are limestone asphalt mixtures. Only one year after opening traffic, serious rut disease appeared in the uphill section pavement. Then the surface course FAC-13 + FAC-20 + FAC-25 was introduced to replace the old damaged surface course. The three layers are all basalt modified asphalt mixture. Rut investigation results in this section show that rutting resistance performance of the latter course is better than that of the former course. Even so, ruts still appear in the latter course.

In this study, rutting resistance performance of the two surface courses mentioned above is compared with LWT and ILWT respectively. In china, the LWT standard testing methods is only appropriate for a single layer asphalt mixture. ILWT can work under heavy load and low speed, which photo is shown in Fig.1; Its specimen thickness can achieve 200mm; Its testing wheel pressure is adjustable from 0.7Mpa to 1.4Mpa; Its testing wheel moving speed is adjustable from 10 to 56 times/minute.

Firstly, rutting tests for the six kinds of asphalt mixture used in the two surface course mentioned above were performed with LWT. The testing wheel moving speed and testing temperature were set at 42 times/minute and 60℃. The specimens were shaped with rut shaping instrument. The test results are shown in Fig.2.

FIG.1. ILWT photo

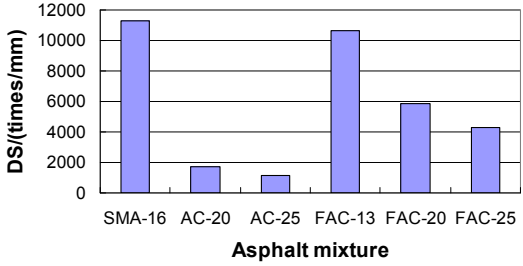

FIG.2. The dynamic stability(DS for short) of asphalt mixture (under condition of 0.7Mpa, 42times/min, 60℃)

In Fig.2, the symbol "DS" is the index used in China to reflect rut deformation developing speed of asphalt mixture; DS is defined as $(d_2-d_1)/(t_2-t_1)$, where t_1 and t_2 is the 45th minute and the 60th minute respectively, d_1 and d_2 is the rut deformation at t_1 and t_2 respectively.

According to the DS controlling criteria regulated in Chinese Specifications, the DS value listed in Table 1 are all more than the criteria. Based on this, the surface course SMA16+AC20+AC25 and FAC13+FAC20+FAC25 should all be able to resist rut disease. But the rut investigation results in the uphill section don't support it. That is to say the DS controlling criteria regulated in Chinese Specifications for normal highway are not appropriate for the long and steep uphill highway such as the 13 km continuous uphill section in Beijing-Zhuhai expressway. Because heavy loading and slow moving trucks account for a large proportion in the uphill section, the LWT testing methods can not simulate its actual traffic situation. In other words, rutting test results obtained under

LWT standard testing conditions can not reflect the rut characteristics in the 13 km continuous uphill expressway.

Secondly, ILWT was used to test the whole surface course's rutting resistance performance. Its testing wheel pressure and testing wheel moving speed was changed to 1.1Mpa and 14 times/minute respectively. Its testing specimen was the full-thickness surface course. The full-thickness surface course specimens were shaped successively from bottom layer to top layer with rut shaping instrument. The test results are shown in Table 1.

The data in Table 1 show clearly that FAC-13 + FAC-20 + FAC-25 surface structure has better rutting resistance performance than SMA-16 + AC-20 + AC-25. The rut investigation results also verify this conclusion. However, the two surface course structures still fail to resist rutting when they sustain heavy loading and slow moving trucks. These indicate that the whole surface course's rutting resistance performance of the section still needs to be improved.

Table 1. The DS Results Of Asphalt Surface Structures (under condition of 1.1Mpa, 14times/min,60℃)

Surface structure	DS(times/mm)
SMA-16+AC-20+AC-25	1338
FAC-13+FAC-20+ FAC-25	2657

SURFACE COURSE COMBINATION ANALYSIS

To evaluate the rutting resistance performance of different surface course combination, many other surface course combinations was designed. The mixtures used in these surface course combinations are listed in Table 2. The LWT test results of these asphalt mixtures are shown in Fig.3. The ILWT test results of different surface course combination are shown in Fig.4.

Table 2. Asphalt Mixtures Used in Different Surface Course Combination

No.	Row A (top surface layer)	Row B (middle surface layer)	Row C (bottom surface layer)
Line 1	AC-13	AC-20	AC-20(limestone)
Line 2	FAC-13	modified bituminous AC-20	modified bituminous AC-20(limestone)
Line 3	SMA-13	AC-20 +0.3% anti-rut agent	modified bituminous AC-20(basalt)

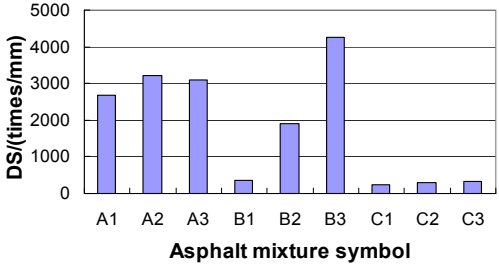

FIG.3. DS results of single layer asphalt mixture (under condition of 1.1Mpa, 14times/min,60℃)

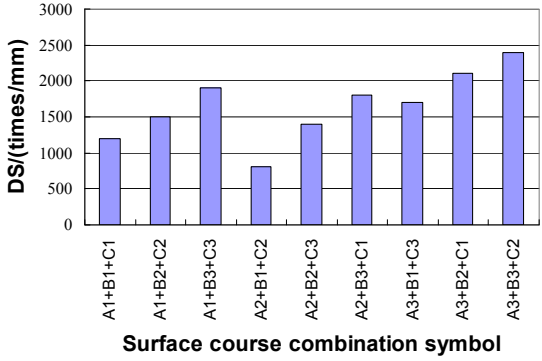

FIG.4. DS results of different surface course combination (under condition of 1.1Mpa,14times/min,60℃)

The symbol "A1" in Fig.3 represents the mixture listed in Row A and Line 1 in Table 2, that is AC-13; The other symbols in Fig.3 have the similar meanings.

The data in Fig.3 indicate that modified bituminous and anti-rutting agent can significantly improve the rutting resistance performance of asphalt mixtures, the rutting resistant effect of adding anti-rutting agent is better than that of using modified bituminous. Comparing with other factors, aggregate size and aggregate type has little influence on rutting resistance performance of asphalt mixtures. The data in Fig.4 indicate that the surface course of A3+B3+C2, that is SMA-13 + modified bituminous AC-20 (0.3% of anti-rutting agent) + modified bituminous AC-20 (limestone), has the best rutting resistance performance. Comparing the surface course A3+B3+C2 with SMA-16 + AC-20 + AC-25 in Tab.2, we find that their top surface layer mixtures have almost the same rutting resistance performance, the former's middle surface layer mixture has better rutting resistance performance than the latter's, the whole surface

course's rutting resistance performance of the former improves about 60 percents than that of the latter. These indicate that improving the middle surface layer mixture's rutting resistance performance has significant effect for the whole surface course's rutting resistance performance. Comparing the surface course A3+B3+C2 with FAC-13 + FAC-20 + FAC-25 in Tab.2, we find that their top surface layer mixtures have almost the same rutting resistance performance, the former's middle surface layer mixture rutting resistance performance is about twice as large as the latter's, the former's bottom surface layer mixture rutting resistance performance is about one quarter of the latter's, but the whole surface course's rutting resistance performance of the latter is better than that of the former. These indicate that the influence of bottom surface layer on the whole surface course's rutting resistance performance can not be ignored.

THE RECOMMENDED SURFACE STRUCTURE

The above analysis results indicate that it does not obtain sufficient whole surface course's rutting resistance performance to only improve the top surface layer's rutting resistance performance. We also need to focus on improving the rutting resistance performance of the bottom surface layer. In this study a new asphalt surface course was proposed and tested. The new surface course is modified bituminous SMA-13 + modified bituminous AC-20 (0.3% of anti-rutting agent) + modified bituminous FAC-20. The full -thickness rut tests were performed for the new surface course with ILWT. Its testing load and testing wheel moving speed is 1.1Mpa and 14 times/min respectively at 60℃. Test results show that the whole surface course's DS is 3200 times/mm. If the rut disease is acceptable when the whole surface structure's DS value is greater than 3000 times/mm that is the criterion regulated in Chinese Specifications for SMA mixture. According to this criterion, we can explain why serious rut disease appear in the surface course of SMA-16 + AC-20 + AC-25 and FAC-13 + FAC-20 + FAC-25 of the 13km continuous uphill section in Beijing-Zhuhai expressway. Also according to this criterion, we suggest the surface course of modified bituminous SMA-13 + modified bituminous AC-20 (0.3% of anti-rutting agent) + modified bituminous FAC-20 as the second maintenance solution for the 13km continuous uphill section in Beijing-Zhuhai expressway.

CONCLUSIONS

(1)The standard LWT test conditions can not reflect the characteristics of heavy loading trucks moving slowly on long and steep uphill pavements. It is difficult to judge whether rut will appear or not with LWT test results.

(2)To evaluate the rutting resistance performance of long and steep uphill pavements, it is necessary to perform the full-thickness rutting test under heavy load and slow speed condition.

(3)Using modified bituminous and adding anti-rutting agents can effectively improve rutting resistance performance of asphalt mixtures. To meet the requirement of rutting resistance performance for heavy loading and slow moving traffic, it is best to use modified bituminous in all the three surface layers.

Because the full-thickness rutting test data is few, especially the relationship study between laboratory full-thickness rut and the actual pavement structure rut is rare, the

rutting resistance criteria for full-thickness rutting test can not be recommended in this study. For various reasons, it need a long time to verify whether the recommended surface course in this study is able or not able to resist rut.

ACKNOWLEDGEMENTS

This study was supported by Western Transportation Construction Science and Technology Project of China(No.200731800003 and No.2009318000070) and Educational Commission of Hunan Province of China(No.06C109).

REFERENCES

Huang, B. and Shu, X. (2008) "Effects of coarse aggregate angularity and asphalt binder on laboratory - measured permanent deformation properties of HMA." *International Journal of Pavement Engineering,* Vol. 10 (1): 19-28.

Sirin Okan Kim and Hong-Joong (2008). "Comparison of rutting resistance of unmodified and SBS-modified Superpave mixtures by accelerated pavement testing." *Construction and Building Materials*, Vol. 22(3): 286-294.

Wu, R. and Shi, L.(2008). "Total thickness rutting research on key influencing factors of asphalt pavement." J*ournal of Wuhan University of Technology,* Vol. 30(1): 58-61.

Yang, J, Cui, J, Wan, J and Shi X(2007). "Strategy of improving rutting resistance based on contribution rate of different layers." *Journal of Southeast University (Natural Science Edition)*, Vol. 37(2):350-354.

Korkila-Tanttu. and Lenna(2007). "Speed and reloading effects on pavement rutting." *Proceedings of the Institution of Civil Engineers: Geotechnical Engineering,* Vol. 160(3): 123-127.

Paulo A, Pereira, Pais Jorge and Sousa Jorge. "Validation of SHRP A-698 Permanent Deformation Concepts for Different Truck Speeds." *Fifth International Conference on Bearing Capacity of Roads and Airfields, Trondheim, Norway,*1998.

Wang, H. and Li X. (2009) . " Rutting in asphalt pavement under heavy load and high temperature." *China Civil Engineering Journal*, Vol. 42(5): 139-144.

Author Index

Page number refers to the first page of paper

This page intentionally left blank

Subject Index

Page number refers to the first page of paper